Metal-uronide interactions and their relevance to the thermolysis of kelp

A thesis submitted for the Degree of Doctor of Philosophy

by

J. S. Rowbotham

M.Sci (Cantab)

University of Durham

Department of Chemistry

December 2016

Statement of copyright

This thesis is based on work conducted by the author, in the Department of Chemistry at Durham University, during the period October 2011 to December 2015.

All work described in this thesis is original, unless otherwise acknowledged in the text or in the references. None of this work has been submitted for another degree in this or any other University.

Signed: J. Rowbotham Date: 22/12/16

Jack S. Rowbotham

Cover art kindly provided by Natalie Patel

Thesis Abstract

This thesis describes investigations into the coordination- and thermo-chemistry of metal-uronide complexes (namely alginates). The work probes the importance of such metal-saccharide interactions in the thermolysis of kelp, with a view to deriving valuable fuels and chemicals from this aquatic bioresource. In this regard, **Chapter 1** justifies the model-compound approach adopted in this thesis, and outlines the wider context in which the work is set.

Chapter 2 describes the isolation of the composite monosaccharides of alginate (D-mannuronate and L-guluronate) and their characterisation by NMR spectroscopy. A combination of 1- and 2-D ^{1}H and ^{13}C experiments were utilised to provide the most comprehensive assignments of algal mono-uronates to-date. Subsequently, the well-defined mono-uronate spectra were used to probe the conditions that favour hydrothermal uronolactone formation.

Chapter 3 probed the response of the algal mono-saccharides (prepared and characterised in Chapter 2) to a range of metal ions (Na^{+}, K^{+}, Mg^{2+}, Ca^{2+}, Sr^{2+}, Ba^{2+}, Zn^{2+}, and Cu^{2+}) to explore the validity of the well-known "Egg-box model" of metal ion/alginate coordination. By observing changes to anomeric equilibria, *α*-L-gulopyranuronate was found to coordinate (*via* an axial-equatorial-axial arrangement of hydroxyl groups) to large, divalent cations, in a manner consistent with "Egg-box binding". In contrast, in the presence of Na^{+}, Mg^{2+}, Zn^{2+}, and, Cu^{2+} *α*-L-gulopyranuronate interacted *via* its carboxylate moiety (and possibly ring oxygen), demonstrating the unsuitability of these ions for Egg-box binding.

Chapter 4 describes the impact of the metal ions discussed in Chapter 3 on the subsequent pyrolysis behaviour of alginates (and related mono- and poly-uronides). Thermogravimetric analysis (TGA), pyrolysis-gas chromatography mass spectrometry (Py-GCMS), and solid-state studies of the post-thermolysis chars were all conducted. The uronides were generally found to demonstrate unfavourable thermal behaviour (high yields of char, CO_2, and H_2O, and low yields of condensable hydrocarbons). Complexation of Cu^{2+}, however, had a beneficial impact on subsequent thermolysis, by increasing the low-temperature, selective formation of 2-furfural. The presence of Cu^{0} in the alginate char is indicative of Cu(II)-mediated alginate decomposition occurring via a *Hofer-Moest* type decarboxylation.

Chapter 5 tested the validity of the model compound approach by enriching samples of kelp with either Cu^{2+} or Ca^{2+} ions and studying the thermal degradation of the resulting materials by TGA and Py-GCMS. The thermochemical outcomes for the whole biomass mirrored those found for the model compounds studied in Chapter 4.

Finally, in **Chapter 6**, the results of Chapter 2 – 5 are analysed synoptically, and the success of the model compound approach is appraised. Ultimately, it is concluded that the ability of a metal ion to inhibit or promote thermal decarboxylation of a uronide (in isolation or within kelp) is more important in dictating pyrolysis behaviour than any differences in coordination to various hydroxyl groups around the saccharide ring. The results could find application in the development of a phytoremediative kelp-based thermal biorefinery.

Acknowledgments

First and foremost, I would like to thank my supervisors, Dr. Phil Dyer and Prof. Chris Greenwell, for supporting me through this work, and for granting me the academic freedom to chase golden eggs and wild geese (in roughly equal measure). They have both been incredibly generous in terms of time and resources, and, importantly, have taught me an awful lot about chemistry. Naturally, all three of us are grateful to those bodies who have financially facilitated our work (The Engineering and Physical Sciences Research Council, The Centre for Process Innovation, and The Durham Energy Institute).

Durham has been an excellent doctoral home these last few years, and I have found the Department of Chemistry a friendly and exciting place to work. As such, the long list of people who I would like to thank cannot be produced in full here. Instead, I express my general thanks to all those at Durham who have been willing to lend me a few milligrams of reagent, or a few minutes of their time whilst I have worked here. For those colleagues who made experimental contributions to the project, their efforts are recognised in individual chapter acknowledgements throughout the thesis.

Of course, working in the lab would not be half as fun without my fellow group members. So, barmy as they all are, I would like to thank Antonis, Luke, Michael(s), Anna, Jas, Stephen, Josie, Emma-Kate, Rikan, and James (the Tweedledum to my Tweedledee) for making my time here so special. I will miss them all very much. In addition, I am grateful to the three brilliant postdocs who I have been lucky enough to work with: Drs. Li Li, Benjamin Smith, and Hilary Redden, all of whom helped me immensely.

I would also like to briefly acknowledge the support of my new supervisors (at the University of Oxford), Prof. Kylie Vincent and Dr. Holly Reeve, for their patience and generosity whilst I finished writing up this thesis.

Naturally, I could not have achieved any of the work presented here without the love and support of my parents, to whom I am eternally grateful. Likewise, my brothers (Simon and Harry) and aunts (Denise and Glynis) have all played a part in keeping my spirits up (and my stomach full) through my time at Durham. Finally, I reserve a special thanks for Natalie, for patiently forgiving the many late nights and “lab weekends”, and for being there when they were over.

The work in this thesis
is dedicated to

Henry Rowbotham

on the occasion of his 90th birthday

Contents

Chapter 1

An introduction to the thermochemistry of kelp, and the relevance of metal-alginate interactions

Chapter 2

Preparation, characterisation, and solution-state behaviour of algal mono-uronic acids

Chapter 3

Opening the Egg-Box: exploring metal-uronide interactions by solution state NMR spectroscopy

Chapter 4

The metal-mediated thermolysis of alginates and related uronides

Chapter 5

The metal-mediated thermolysis of alginate-rich kelp biomass

Chapter 6

Summary, appraisal, and outlook

Appendices

- **<u>Appendices A-O:</u> Additional results and methodology**
- **<u>Appendices P-Q:</u> Additional literature reviews**
- **<u>Appendices R-T:</u> Papers published during the preparation of this thesis**

List of abbreviations

Alg	Alginate
Gul	L-guluronate
Man	D-mannuronate
Gal	D-galacturonate
Glc	D-glucuronate
Pec	Pectinate
MAlg, MPec…	A metal salt of the above uronates
HAlg, HPec…	The acidic form of the above uronates
M	D-mannuronate unit within alginate polymer
G	L-guluronate unit within alginate polymer
GlcLac	Glucuronic acid lactone
ax-eq-ax	Axial-equatorial-axial arrangement of hydroxyl oxygens
2-FF	2-furaldehyde, 2-furfural
LG/LGO	Levoglucosan/Levoglucosenone
NMR	Nuclear Magnetic Resonance
SSNMR	Solid State Nuclear Magnetic Resonance
COSY	Correlation Spectroscopy
NOSEY	Nuclear Overhauser Effect Spectroscopy
HMQC	Heteronuclear Multiple Bond Correlation Spectroscopy
HSQC	Heteronuclear Single Quantum Coherence Spectroscopy
J	Scalar coupling constant
d	doublet
dd	doublet of doublets
*p*t	*pseudo*-triplet
m	multiplet
ppm	Parts per million
δ	Chemical Shift
$\Delta\delta$	Change in chemical shift
T	Temperature
λ	Wavelength
TGA	Thermogravimetric Analysis
TGA–MS	Thermogravimetric Analysis−Mass Spectrometry

TGA−FTIR	Thermogravimetric Analysis−Fourier Transform Infra−Red spectra
DTG	Differential Thermogravimetric Analysis
DSC	Differential Scanning Calorimetry
PXRD	X−ray powder diffraction
CHN	Carbon Hydrogen Nitrogen analysis
XPS	X−ray photoelectron spectroscopy
GC–MS	Gas Chromatography Mass Spectrometry
Py–GCMS	Pyrolysis Gas Chromatography Mass Spectrometry
FGA	Fixed gas analyser
ESI–MS	Electrospray Ionization Mass Spectrometry
ICP	Inductively Coupled Plasma
ICP–MS	Inductively Coupled Plasma Mass Spectrometry
ICP-OES	Inductively coupled plasma optical emission spectrometry
wt.%	Percent by Weight
vol.%	Percent by Volume
mol.%C	Percent by molar carbon content in the sample
FTIR	Fourier Transform Infra−Red Spectroscopy
ATR	Attenuated Total Reflectance
UV−VIS	Ultra Violet−Visible Spectroscopy
DFT	Density Functional Theory
HPLC	High Performance Liquid Chromatography
E_a	Energy of activation
A	Pre−exponential factor
a, b, c	unit cell dimensions
α, β, γ	unit cell angles
V	unit cell volume
μ	linear absorption coefficient
Z	number of formula units per cell
ρ_{calcd}	calculated density
e	electron
R	R–factor (unweighted)
$\omega R2$	R–factor (weighted)
S	goodness of fit
ϑ	angle of data collection

More specialised abbreviations (especially those pertaining to specific measurements of chemical shift, or definitions of characteristic thermochemical temperatures), are defined in the text where required.

Chapter 1

Chapter 1

An introduction to the thermochemistry of kelp, and the relevance of metal-alginate interactions

1.1 Chapter overview

This chapter provides an introduction and justification for the experimental work contained in the later chapters of the thesis. The use of biomass and, specifically, the carbohydrates within biomass, to produce fuels and chemicals sustainably is briefly discussed, followed by a summary of the thermochemical methods that may be used to achieve such conversions. The mediating role of intrinsic metal ions within the pyrolysis of biomass is highlighted as being a relatively unexplored, but important, phenomenon. The notion of using kelp as a chemicals' feedstock *via* pyrolysis is subsequently introduced, highlighting the substantial difference in its carbohydrate profile compared to conventional terrestrial (lignocellulosic) sources of biomass. In this regard, alginate, an anionic polysaccharide abundant in brown seaweeds, is discussed, including its potential use as a model compound with which to probe the pyrolysis of kelp more generally. Ultimately, the discussions lead to the posing of three key questions for research:

1) **How do different metal ions coordinate to alginates of varying compositions?**
2) **What is the impact of metal-alginate coordination on subsequent pyrolysis behaviour?**
3) **Can the pyrolysis of kelps be more easily understood and, subsequently, optimised through a knowledge of the metal-mediated degradation of its composite alginate?**

The strategy adopted in attempting to answer these questions is then explained, and a summary of the thesis structure is provided.

1.2 Routes to fuels and chemicals from carbohydrate-rich biomass: cellulose and beyond

As rapid technological development dominated the 20th century, our civilisation has become ever dependent on fossil-derived hydrocarbon fuels and chemicals. The rapid depletion of reserves of such compounds is not only unsustainable in terms of maintaining a consistent supply, but is also causing a dangerous (and unprecedented) perturbation of the global carbon cycle, manifested as anthropogenic climate change. Hence, a key challenge for chemists is to minimise the rate at which such crude oil reserves are extracted, by providing substitutes containing carbon already available in the biosphere. In this regard, biomass-derived carbohydrates represent a promising opportunity with, for example, over one trillion tons of cellulose (Figure 1.1), the most abundant organic compound on Earth, being produced annually by terrestrial plants.[1] A plethora of methodologies has now been developed to transform carbohydrate-rich biomass into the desired hydrocarbons, of which thermochemical upgrading (see Section 1.3) represents just one.

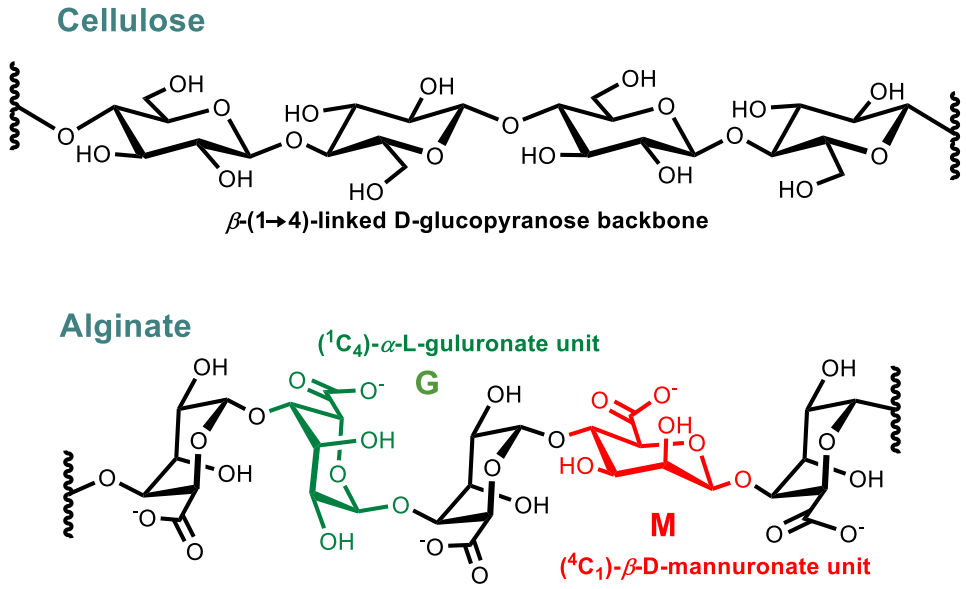

Figure 1.1 Cellulose (a principal constituent of terrestrial biomass), and alginate (a principal constituent of aquatic biomass).

Of course, utilisation of such carbohydrates (either in an isolated state, or within the parent biomass) requires for additional considerations beyond developing the necessary conversion processes. Cultivation of plants for fuels and chemicals demands land and fresh water that would usually be devoted to food production. In a world where access to such resources is also becoming increasingly scarce, recent attentions have focussed on the utilisation of unconventional sources of feedstock carbohydrates, including waste products and non-terrestrial biomass.[2] Here kelp represents an interesting example as a source of fast-growing, carbohydrate-rich biomass, capable of thriving in waste and saline waters.[3–5] However, the contrasting physiological requirements of kelp compared to terrestrial biomass gives rise to a whole new assortment of available carbohydrates, low in cellulose

and high in alginate (see Figure 1.1).[6] Alginate is a linear polyuronide comprised of (1→4)-linked *α*-L-guluronate and *β*-D-mannuronate, which as anionic saccharides, possess metal binding abilities not observed for neutral carbohydrates.[7] This thesis will seek to understand and exploit such metal-binding properties in promoting favourable effects in the thermochemistry of alginate-rich kelps for the sustainable production of chemicals.

1.3 Thermochemical upgrading of carbohydrate-rich biomass

There are many biological and chemical methodologies that have been developed to convert carbohydrates (and carbohydrate-rich biomass) into valuable fuels and chemicals. A full review of such methods here is not required (though Appendix S and references therein can be consulted for further information). Instead, this thesis highlights thermochemical methodologies as a possible route to carbohydrate conversion, whereby the action of heat is utilised to depolymerise and deoxygenate the saccharides to the desired platform chemicals. Of course, there is opportunity to vary the processing parameters to optimise the formation of various products, giving rise to the techniques of pyrolysis, gasification, hydrothermal liquefaction (HTL), and combustion (see Figure 1.2). Each of these technologies shows varying potential for the conversion of kelp into fuels, chemicals, or heat, and a full review is provided in Appendix S. In this thesis, however, pyrolysis is discussed as the principal mode of kelp conversion, owing to the requirements of heat and pressure being lowest for this technology.

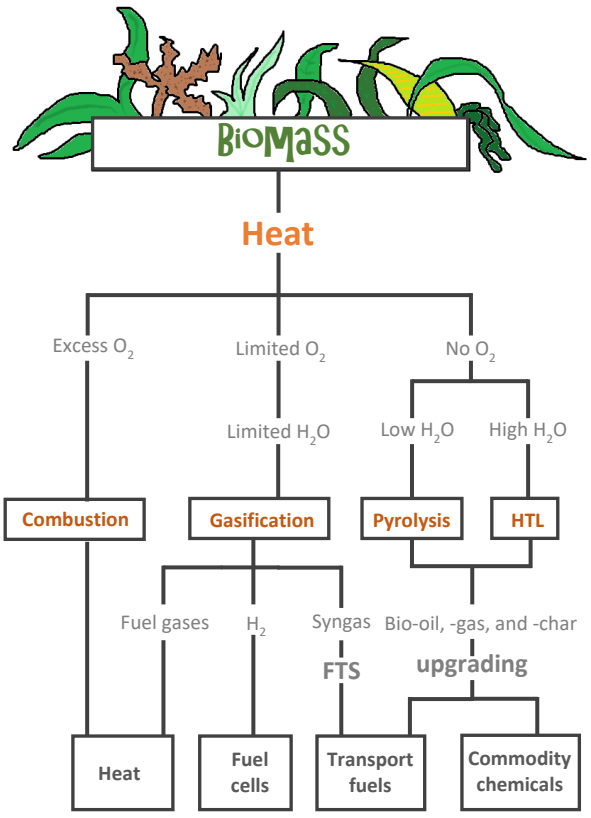

Figure 1.2 Routes to the thermochemical upgrading of biomass. Redrawn and modified with permission from Balat *et al.*[8] (© Elsevier 2009)

Pyrolysis is simply the degradation of a compound through the action of heat, typically under inert atmospheres (to minimise oxidative processes such as combustion). Its use for the upgrading of biomass has been reviewed extensively,[8–13] with a wide variety of different feedstocks having been investigated.[14] For carbohydrate-rich biomass, three phases of product can be expected to arise from pyrolysis, each with different applications (see Figure 1.3):[8–13]

- **Bio-oil:** the condensable organic species arising from pyrolysis may be collected as a dark, viscous, liquid, typically composed of organic- and aqueous-soluble fractions. The organic-phase of the bio-oil is often cited as being the most valuable commodity to arise from pyrolysis, as it contains molecules that could be used as liquid fuels or as platform chemicals (though varying degrees of additional processing would be required).[10,13] The diversity of compounds found in the pyrolysis of carbohydrates can be extremely extensive, and improving selectivity in this regard is a fundamental priority to facilitating commercialisation.[15]

- **Bio-gas:** non-condensable gases such as CO_2, CO, C_1-C_4 hydrocarbons, and H_2 (in decreasing order of abundance) are often liberated from pyrolysed biomass. The raw bio-gas is of low energy density in itself, and requires further upgrading (either by purification or, for example by Fischer-Tropsch processing) to be of significant value.[10,13]

- **Bio-char:** the solid material remaining following pyrolysis. The char forms from both biomass that has failed to volatilise, and also the secondary reaction and polymerisation of liberated reactive organic compounds. Often enriched in carbon, pyrolytic bio-char has been cited as a candidate for soil remediation.[16,17] However, the char also contains inorganic material, which is residual from the parent biomass, which should be borne in mind when potential applications are considered.[10,13]

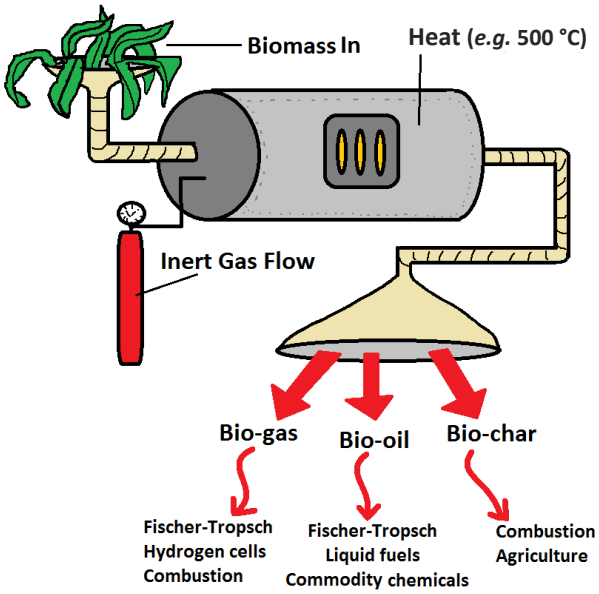

Figure 1.3 A summary of the products from the pyrolysis of carbohydrate-rich biomass

Naturally, the relative distribution of the bio-oil, -gas, and -char phases heavily depend on conditions under which the pyrolysis is performed. Here, the heating rate is known to be particularly influential, and is used to classify the pyrolysis process as being either *slow*, *intermediate*, *fast*, or *flash* (see Table 1.1 for full definitions), with the latter giving rise to maximal yields of bio-oil.[10]

Whilst the heating rate is, to some degree limited by the available apparatus, the thermochemical behaviour of a particular feedstock may also be altered in a more straightforward fashion by inclusion of an additive during the pyrolysis process itself. In many cases, the additive is usually an inorganic material with catalytic properties, such as a zeolite or a metal oxide, giving rise to so-called "catalytic pyrolysis".[18–21] Co-feeding catalyst material with the biomass in pyrolysis (primary catalysis) is now a widely-accepted strategy for improving yields and selectivities towards desired compounds. Similarly, passing the escaping vapours over a catalyst *ex situ* (secondary catalysis) has also been recognised as a route to improving selectivity towards valuable compounds.[22] However, some authors have questioned the degree to which metal ions already bound within the biomass matrix might also play a modifying role (see Figure 1.4).[23] These so-called "intrinsic" metal ions have been claimed to act as "*natural catalysts*", though the true nature of their effects has been relatively unexplored.[23] Some authors have argued that doping-in metal ions with more advantageous properties, compared with those found naturally, may be a route to improving the commercial viability of the thermochemical processing of lignocellulosic biomass (see mini-review in Appendix P).[24] In the latter half of this chapter, however, the role of intrinsic metal ions in the pyrolysis of kelp biomass is considered.

Table 1.1 Different classes of pyrolysis and the typical resultant product distribution. Adapted with permission from Bridgewater[9] (© Society of Chemical Industry 2009).

Pyrolysis Class	Heating Rate (°C min^{-1})	Temperature (°C)	Residence Time	Approx. Product Distributions (wt.%)		
				Oil	Char	Gas
Flash	1000-10000	900-1300	< 0.5 s	75 (25 % H_2O)	12	13
Fast	100-1000	500 – 900	< 2 s	60 (30 % H_2O)	20	20
Intermediate	50-100	400-500	10-20 s	50 (50 % H_2O)	25	25
Slow	10	400	Mins - Hours	30 (70 % H_2O)	35	35

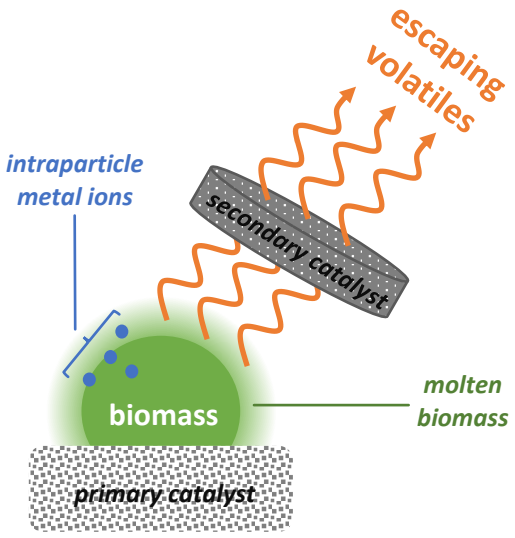

Figure 1.4 Types of catalyst that can be included in the pyrolysis of biomass, including metal ions bound intrinsically within particles of biomass.[23]

1.4 The metal-mediated pyrolysis of alginate-rich kelp

As stated in Section 1.2, being comprised of up to 40 wt.% of alginate,[25] kelp is chemically distinct from more conventional (lignocellulosic) biomass, which has been the subject of significant focus in the pyrolysis arena. Furthermore, the anionic nature of the polyuronide, coupled with the saline environment in which kelp grows, means that up to 15 wt.% of the seaweed feedstock may comprise metallic cations.[25] The exact profile of these metal ions in the kelp is determined by a combination of the concentration of the cations in the surrounding water, and the affinity of the alginate for the metal in question.[26] Over the years, an empirical series for the affinity of divalent metal ions to alginate-rich kelps has been established, with the metals showing a preference to bind in place of naturally-occurring Na^+ in the following order:[27,28*]

$$\mathbf{Pb^{2+} > Cu^{2+} > Cd^{2+} > Ba^{2+} > Sr^{2+} > Ca^{2+} > Co^{2+} > Ni^{2+} > Mn^{2+} > Mg^{2+}}$$

Whilst the origins of the affinity series have never fully been established (see Chapter 3), a hypothesis was proposed in 1973 by Grant and co-workers to explain the data,[29] formulating what is now widely recognised as *the Egg-Box model*. The Egg-Box model posits that a suitable cation will coordinate to an arrangement of hydroxyl groups, ring oxygens, and carboxylate moieties provided by chains of parallel *α*-L-guluronate dimers (see Figure 1.5), binding the strands firmly together. Meanwhile, cations which do no "fit" within the Egg-Box cavities, or in situations where no such sites exist (such as in poly-D-mannuronate chains), coordination of the metal is simply achieved through the carboxylate moiety.[7]

*From a technological point of view, the preference of alginate-rich kelps to bind to environmentally toxic metals (Pb^{2+}, Cu^{2+}, and Cd^{2+}) is particularly noteworthy for the application of seaweed biomass as a potential bioremediation agent.[26]

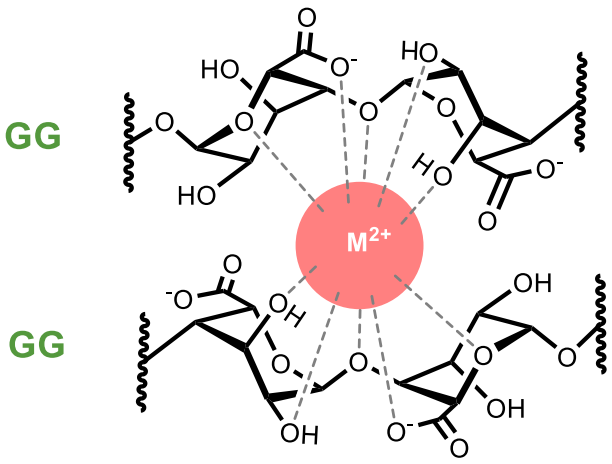

Figure 1.5 A divalent metal ion bound to alginate according to the Egg-Box model[29]

Differences in binding at the molecular level can result in drastic differences to the macro-scale physical properties of the alginate.[30,31] For example, varying the alginate structure (particularly the ratio of mannuronate:guluronate, **M**:**G**) can influence the gelation behaviour of the sample.[23] From the point of view of pyrolysis, where the interactions of metal ions with different hydroxyl groups on a saccharide are known to influence subsequent degradation,[32,33] two questions can be asked of alginate-rich kelp:

1) What is the impact of the coordinated cation on the pyrolysis of alginate within seaweed biomass?
2) In different kelp samples (containing alginates with varying **M**:**G** ratio), does the metal ion have differing effects?

The answer to these questions may have important implications for the pyrolysis of kelp biomass, though they are not easily addressed. As such, in Section 1.5, a strategy for investigating the pyrolysis of alginate-rich kelp is proposed, based on a model-compound approach. Ultimately, work contained in this thesis could be applied towards the development of a phytoremediative kelp-based thermal biorefinery. Here, samples of alginate-rich kelp would be employed to soak-up toxic metals in polluted water-streams, prior to being pyrolysed to derive valuable products (see Figure 1.6).[34,35]

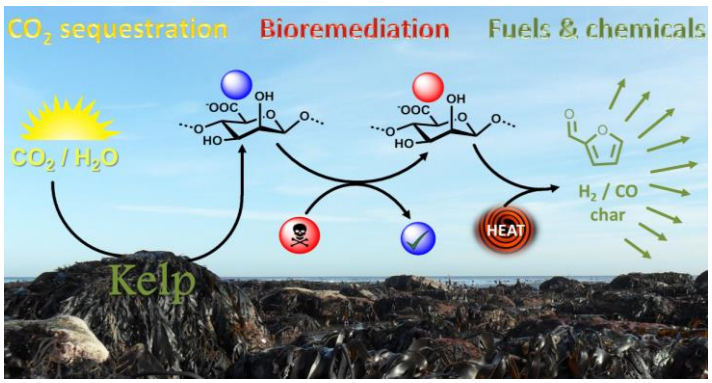

Figure 1.6 A scheme for the utilisation of alginate-rich kelp *via* combined phytoremediation and thermochemical upgrading.

1.5 A model compound approach to the pyrolysis of kelp

The pyrolysis of carbohydrates is a highly complex field, with even simple sugars giving rise to many hundreds of products. Similarly, from a chemists' perspective, biomass is a difficult starting material to work with, especially macroalgae, which varies in composition depending on species, season, geographical location, and the local growth environment.[25,36–38] Researchers must take care therefore, to avoid presenting results with little general applicability, specific only to the particular batch of biomass that was tested. To combat the problems of sample variability, and to simplify the subsequent analysis, a model compound approach can be adopted. Here, a simple starting material (D-glucose or guaiacol, for example) is selected to represent a more complex biomass constituent (cellulose or lignin), which in turn is used to derive information about the parent biomass.[39–42] Given the success of the strategy in the research of the pyrolysis of lignocellulosic biomass, it is proposed here that alginate would make a suitable model compound for exploring the pyrolysis of kelp. However, given the variability in structure and, hence, metal-binding behaviour of alginates described above, the composite monosaccharides of alginate (mono-L-guluronate and -D-mannuronate) are also worthy of exploration (see Figure 1.7). Unfortunately, unlike D-glucose and guaiacol, the algal mono-uronates are not currently commercially available, nor have they been well-characterised in previous works in the literature, and so their isolation will be a major challenge in this thesis. With access to these simple chemical building blocks, it is hoped that the complicated fields of kelp coordination- and thermochemistry may be significantly simplified.

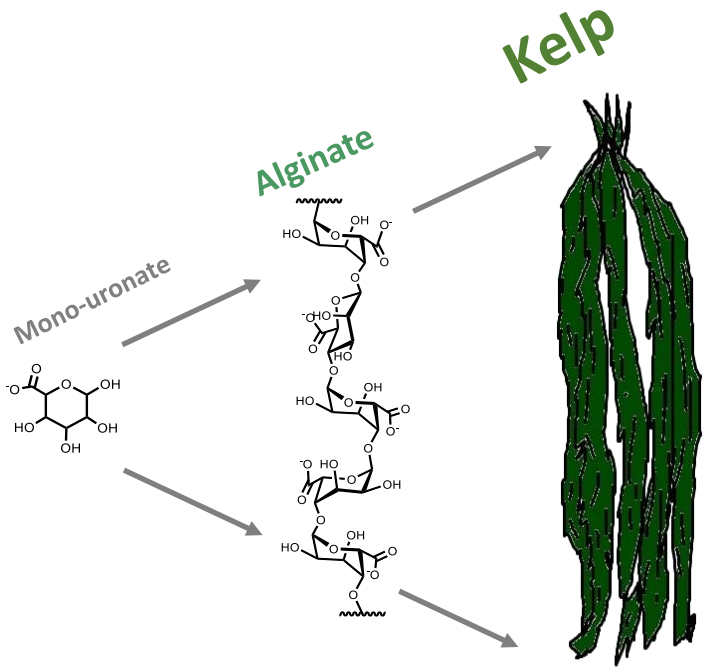

Figure 1.7 Proposed model compounds for research into the metal-binding and pyrolysis behaviour of kelp.

1.6 Thesis aims and structure

Following the discussions in Section 1.2-1.5, this thesis aims to answer three key questions:

1) **How do different metal ions coordinate to alginates of varying compositions?**
2) **What is the impact of metal-alginate coordination on subsequent pyrolysis behaviour?**
3) **Can the pyrolysis of kelps be more easily understood and, subsequently, optimised through a knowledge of the metal-mediated degradation of its composite alginate?**

In attempting to answer these questions, the thesis adopts the following structure:

- **Chapter 2 details the synthesis and characterisation of algal mono-uronates.**
  The algal mono-uronates were successfully isolated, but only in the solution state. Their properties were studied under aqueous conditions (such as their response to heat and pH changes) to inform later discussions on uronide pyrolysis behaviour**.**

- **Chapter 3 probes the ligand behaviour of algal mono-uronates.**
  The algal mono-uronate samples from Chapter 2 were investigated for their response to various s- and d-block metal ions. Evidence is sought for signs of "Egg-Box" coordination, and metal ions are classified according to whether they conform to the model or not.

- **Chapter 4 explores the metal-mediated pyrolysis of uronides**
  Screens a number of metal ions to assess their impact on the pyrolysis of alginates (and related uronides). Many aspects of pyrolysis behaviour are studied, including kinetics, product formation, and char structure.

- **Chapter 5 investigates the metal-mediated pyrolysis of kelps**
  The insight gained from the work in Chapter 4 is utilised in order to attempt to optimise the thermolysis of alginate-rich kelp. The collection of a number of kelps also facilitated an assessment of the degree to which varying alginate structure affects pyrolysis.

As each of these research challenges demanded for very different techniques to be employed, each chapter is designed to be stand-alone so that the relevant method development can be explained in detail. Furthermore, the subject matter of this thesis is both complex and somewhat unconventional. The study of metal-saccharide interactions is not commonly encountered, and is rarely discussed in tandem with carbohydrate thermochemistry. As such, reviewing and appraising the literature on these two topics is also a major aim of this thesis, and each chapter contains an extensive background section (which can be skipped if the reader is already familiar with the topic).

Finally, **Chapter 6** provides a synoptic appraisal of the arguments in each chapter, from which a single, unified set of conclusions are provided to address the key questions quoted above.

1.7 Chapter References

1 D. Klemm, B. Heublein, H.-P. Fink and A. Bohn, *Angew. Chemie Int. Ed.*, 2005, **44**, 3358–3393.

2 A. Singh, P. S. Nigam and J. D. Murphy, *Bioresour. Technol.*, 2011, **102**, 10–16.

3 K. Gao and K. R. McKinley, *J. Appl. Phycol.*, 1994, **6**, 45–60.

4 M. Song, H. Duc Pham, J. Seon and H. Chul Woo, *Renew. Sustain. Energy Rev.*, 2015, **50**, 782–792.

5 A. Ross, J. Jones, M. Kubacki and T. Bridgeman, *Bioresour. Technol.*, 2008, **99**, 6494–6504.

6 D. Manns, a L. Deutschle, B. Saake and S. Meyer, *RSC Adv.*, 2014, **4**, 25736–25746.

7 P. Gacesa, *Carbohydr. Polym.*, 1988, **8**, 161–182.

8 M. Balat, M. Balat, E. Kırtay and H. Balat, *Energy Convers. Manag.*, 2009, **50**, 3147–3157.

9 A. V. Bridgwater, *J. Sci. Food Agric.*, 2006, **86**, 1755–1768.

10 A. V. Bridgwater, *Biomass and Bioenergy*, 2012, **38**, 68–94.

11 H. B. Goyal, D. Seal and R. C. Saxena, *Renew. Sustain. Energy Rev.*, 2008, **12**, 504–517.

12 E. Butler, G. Devlin, D. Meier and K. McDonnell, *Renew. Sust. Energ. Rev.*, 2011, **15**, 4171–4186.

13 A. Demirbas, *Energy Convers. Manag.*, 2009, **50**, 2782–2801.

14 M. Verma, S. Godbout, S. K. Brar, O. Solomatnikova, S. P. Lemay and J. P. Larouche, *Int. J. Chem. Eng.*, 2012, **2012**, 1–18.

15 M. J. Antal, in *Advances in Solar Energy*, Springer New York, Boston, MA, 1983, pp. 61–111.

16 M. I. Bird, C. M. Wurster, P. H. de Paula Silva, A. M. Bass and R. de Nys, *Bioresour. Technol.*, 2011, **102**, 1886–1891.

17 M. I. Bird, C. M. Wurster, P. H. De Paula Silva, N. A. Paul and R. De Nys, *GCB Bioenergy*, 2012, **4**, 61–69.

18 C. Hu, Y. Yang, J. Luo, P. Pan, D. Tong and G. Li, *Front. Chem. Sci. Eng.*, 2010, **5**, 188–193.

19 A. Aho, N. Kumar, K. Eränen, T. Salmi, M. Hupa and D. Y. Murzin, *Fuel*, 2008, **87**, 2493–2501.

20 K. Shi, S. Shao, Q. Huang, X. Liang, L. Jiang and Y. Li, in *2011 International Conference on Materials for Renewable Energy & Environment*, IEEE, 2011, vol. 1, pp. 317–321.

21 R. French and S. Czernik, *Fuel Process. Technol.*, 2010, **91**, 25–32.

22 K. Wang, P. a. Johnston and R. C. Brown, *Bioresour. Technol.*, 2014, **173**, 124–131.

23 M. S. Mettler, D. G. Vlachos and P. J. Dauenhauer, *Energy Environ. Sci.*, 2012, **5**, 7797–7809.

24 G. N. Richards and G. Zheng, *J. Anal. Appl. Pyrolysis*, 1991, **21**, 133–146.

25 P. Schiener, K. D. Black, M. S. Stanley and D. H. Green, *J. Appl. Phycol.*, 2015, **27**, 363–373.

26 T. A. Davis, B. Volesky and A. Mucci, *Water Res.*, 2003, **37**, 4311–4330.

27 A. Haug, J. Bjerrum, O. Buchardt, G. E. Olsen, C. Pedersen and J. Toft, *Acta Chem. Scand.*, 1961, **15**, 1794–1795.

28 R. Kohn, *Pure Appl. Chem.*, 1975, **42**, 371–397.

29 G. T. Grant, E. R. Morris, D. A. Rees, P. J. C. Smith and D. Thom, *FEBS Lett.*, 1973, **32**, 195–198.

30 O. Smidsrød and A. Haug, *Acta Chem. Scand.*, 1965, **19**, 329–340.

31 A. Haug, S. Myklestad, B. Larsen, O. Smidsrød, G. Eriksson, R. Blinc, S. Paušak, L. Ehrenberg and J. Dumanović, *Acta Chem. Scand.*, 1967, **21**, 768–778.

32 H. B. Mayes, M. W. Nolte, G. T. Beckham, B. H. Shanks and L. J. Broadbelt, *ACS Catal.*, 2015, **5**, 192–202.

33 A. Saddawi, J. Jones and A. Williams, *Fuel Process. Technol.*, 2012, **104**, 189–197.

34 G. W. Roberts, M.-O. P. Fortier, B. S. M. Sturm and S. M. Stagg-Williams, *Energy & Fuels*, 2013, **27**, 857–867.

35 A. Cole, Y. Dinburg, B. S. Haynes, Y. He, M. Herskowitz, C. Jazrawi, M. Landau, X. Liang, M. Magnusson, T. Maschmeyer, A. F. Masters, N. Meiri, N. Neveux, R. de Nys, N. Paul, M. Rabaev, R. Vidruk-Nehemya and A. K. L. Yuen, *Energy Environ. Sci.*, 2016, **9**, 1828–1840.

36 E. Marinho-Soriano, P. C. Fonseca, M. A. A. Carneiro and W. S. C. Moreira, *Bioresour. Technol.*, 2006, **97**, 2402–2406.

37 W. A. P. Black, *J. Mar. Biol. Assoc. United Kingdom*, 1950, **29**, 45–72.

38 J. M. M. Adams, A. Ross, K. Anastasakis, E. M. Hodgson, J. A. Gallagher, J. Jones and I. S. Donnison, *Bioresour. Technol.*, 2011, **102**, 226–234.

39 M. S. Mettler, A. D. Paulsen, D. G. Vlachos and P. J. Dauenhauer, *Green Chem.*, 2012, **14**, 1284–1288.

40 M. Asmadi, H. Kawamoto and S. Saka, *J. Anal. Appl. Pyrolysis*, 2011, **92**, 88–98.

41 R. Vinu and L. J. Broadbelt, *Energy Environ. Sci.*, 2012, **5**, 9808–9826.

42 A. Khelfa, A. Bensakhria and J. V. Weber, *J. Anal. Appl. Pyrolysis*, 2013, **101**, 111–121.

Chapter 2

Chapter 2

Preparation, characterisation, and solution-state behaviour of algal mono-uronic acids

2.1 Chapter abstract

This chapter concerns the isolation of the sodium salts of the algal uronic-acids, D-mannuronic (**HMan**) and L-guluronic acids (**HGul**), and their characterisation by nuclear magnetic resonance (NMR) spectroscopy. A combination of one- and two-dimensional ^{1}H and ^{13}C NMR experiments (including pure shift techniques) was utilised in order to provide confident assignments of the pyranose forms of the two uronic acids at various pH values (from 7.0 – 1.0) with previous inconsistencies in the literature being addressed. The changes in chemical shift observed upon titrating NMR solutions of the uronates were subsequently used to establish logarithmic values of the acid dissociation constants of the various anomers of algal pyranuronic acids: $pK_a(^{1}C_4$-α-L-gulopyranuronic acid) = 3.45 ± 0.03, $pK_a(^{1}C_4$-β-L-gulopyranuronic acid) = 3.44 ± 0.03, $pK_a(^{4}C_1$-α-D-mannopyranuronic acid) = 3.33 ± 0.03, $pK_a(^{4}C_1$-β-D-mannopyranuronic acid) = 3.21 ± 0.03. The configurational equilibria ([pyranose]/[furanose] and pyranose [α]/[β] ratios) of **HMan** and **HGul** are reported and the dominance of the $^{1}C_4$-β-L-gulopyranuronic and $^{4}C_1$-α-D-mannopyranuronic acid configurations is demonstrated at all of the pH values studied. The lactonisation behaviour of **HMan** and **HGul** was also investigated with the compounds being found to form furanurono-6,3-lactones readily at pH 1.0 in an analogous manner to D-glucuronic acid (**HGlc**). Whilst **HMan** formed lactones to a roughly similar degree to **HGlc**, **HGul** was found to be much harder to convert, and **HGal** did not undergo lactonisation at all. None of the uronic acids were found to lactonise at pH 7.0, leading to the conclusion that the carboxylate moiety must be protonated in order for lactonisation to occur.

2.2 Background

2.2.1 Uronic acids in biomass

2.2.1.1 An introduction to the uronic acids relevant to biomass and macroalgae

The uronic acids (specifically aldouronic acids)* are a family of sugar acids derived from aldoses through oxidation of the terminal carbon (C6 in the case of the aldohexuronic acids considered in this thesis) to yield a carboxylate moiety. The relationship of such uronic acids to the parent aldose and similarly related sugar acids (aldaric and aldonic acids) is depicted in Figure 2.1.[1] Of the 16 possible isomeric hexuronic acids,[2] four are found both naturally and abundantly in biomass: D-glucuronic (**HGlc**), D-galacturonic (**HGal**), D-mannuronic (**HMan**), and L-guluronic (**HGul**) acids, the occurrence of each of these acids is described in detail below.[3] Whilst the chemistry of **HGlc** and **HGal** has been studied extensively, the latter pair (**HMan** and **HGul** - referred to here as the *algal uronic acids* owing to their role as the constituent co-monomers of alginic acid) have been comparatively unexplored. The discrepancies in the degree to which the various uronic acids have been investigated appears to have arisen largely due to historical reasons (the order of their discoveries, the growth of the pectin industry etc.) rather than the existence of any particularly lucrative properties from one set over another. Hence, whilst **HGlc** and **HGal** are readily and cheaply available (on the order of £10/g), **HMan** and **HGul** can only be purchased from speciality companies for prohibitively expensive prices (on the order of £2000/g and £10,000/g, respectively). Consequently, as chemists have sought to develop novel catalysts and processing options for the conversion of biomass-derived monosaccharides,[4] including mono-uronic acids, algal acids are currently typically overlooked in such trials (see references for recent examples).[5–8]

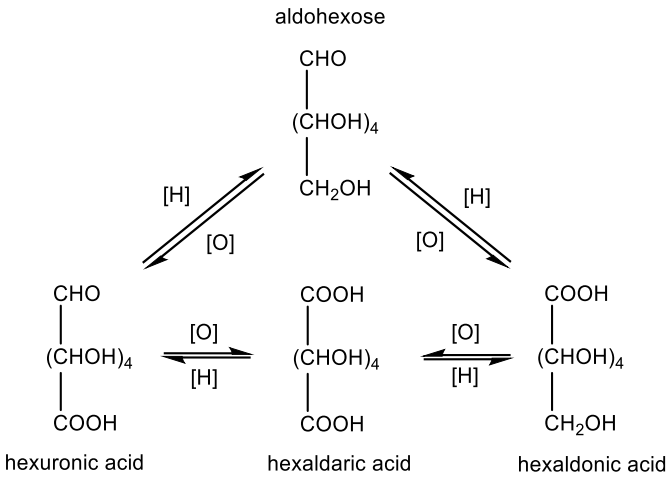

Figure 2.1 The relation between six-membered sugar acids and a parent aldose

* Also referred to as *alduronic* and *glycuronic acids* in some texts

The role, in part, of this chapter is to subject the algal uronic acids to some of the same scrutiny as has been afforded to their molecular cousins and, in doing so, to provide fundamental information to underpin the investigations in the remainder of the thesis. The particular motivation in this case is ultimately to shed light on the thermal behaviour of algal biomass. Hence, as glucose is used to explore the thermochemistry of cellulose,[9] and cellulose accordingly offers insight into the thermochemistry of complex cellulosic biomass,[10] it is hoped that the study of algal mono-uronic acids will be able to help to better explain and exploit the thermochemistry of polyuronides and uronide-rich kelp. Of course, one of the key differences between the aldoses and aldouronic acids is the ability of the latter to form ionic complexes with metal ions, a facet that has a number of implications both in regards to their thermochemistry (explored in Chapters 4 and 5) and in the utilisation of uronides (or their uronate salts) in broader medical and technological applications (explored in Chapter 3).[11,12] Again, knowledge of the chemical behaviour of the individual mono-uronic acids will ultimately be required to fully understand the complexities of uronate-metal binding behaviour. As such, the investigations conducted within this chapter into the solution-state behaviour of **HMan** and **HGul** will likely have implications to work conducted beyond the bounds of this thesis and hopefully go some way to promoting their routine study alongside the more familiar **HGal** and **HGlc**.

2.2.1.2 Stereochemical definitions and representations of uronic acids

As stated above, the aldouronic acids can be considered as the oxidised derivatives of a parent aldose and accordingly the stereochemistry of D-glucuronic, D-galacturonic, D-mannuronic, and L-guluronic acids stem from D-glucose, D-galactose, D-mannose and L-gulose, respectively (see Figure 2.2). It is of interest to note that guluronic acid is the only L-isomer of the four uronic acids considered (L-aldoses are generally much less common in nature than D-aldoses),[13] which is a consequence of it being formed from the C5 epimerisation of D-mannuronic acid in the biosynthesis of alginic acid.[14,15]

The mono-uronic acids shown in Figure 2.2 are depicted in a number of projections. In this thesis, the projections are used interchangeably to suit the particular circumstance in question. Thus, perspective (or 3D) projections are particularly convenient for describing the orientation of, for example, saccharide-metal binding (see Chapter 3), whilst pyrolysis mechanisms are usually most straightforwardly expressed in either Haworth of Fischer projections (see Chapter 4).

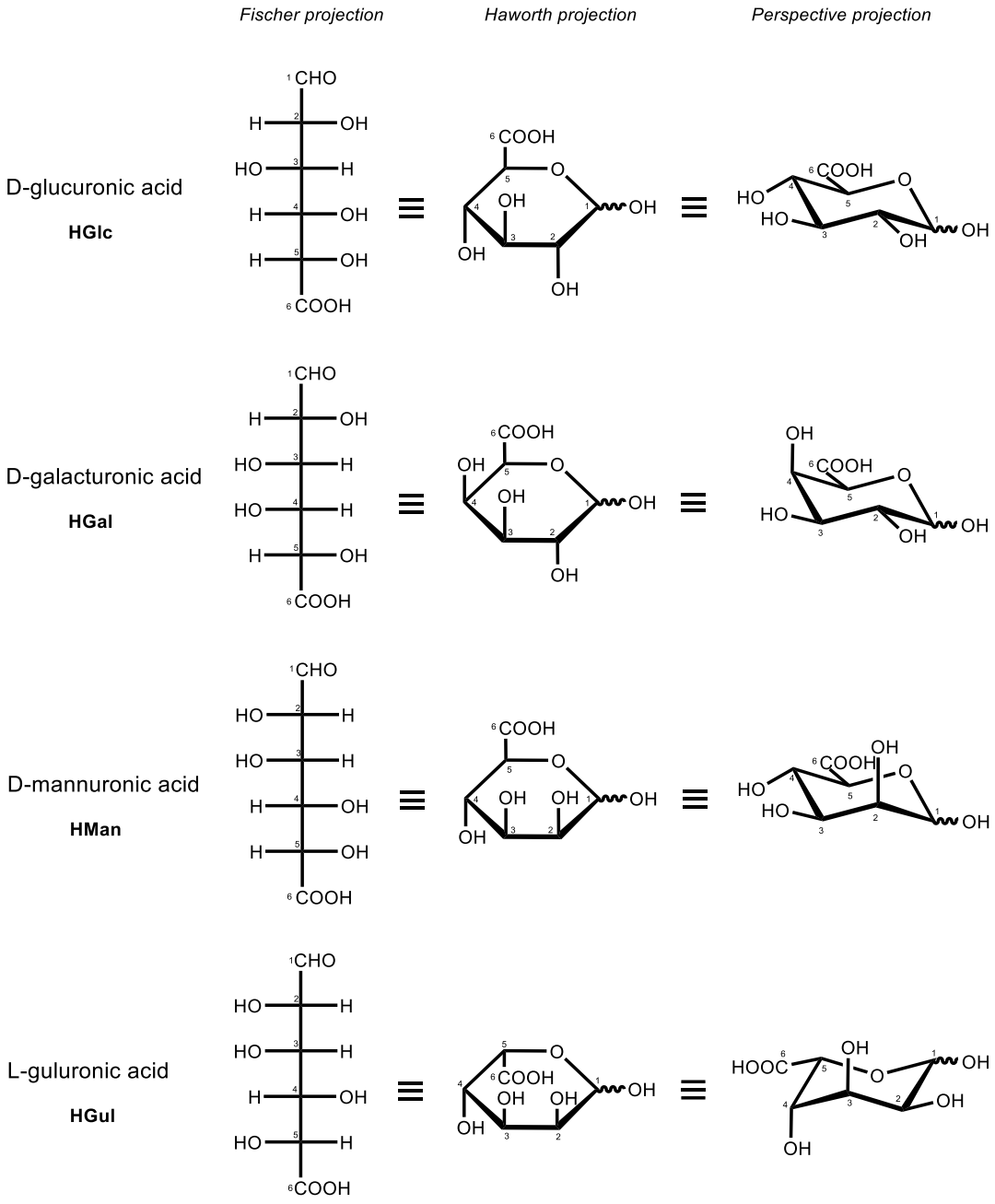

Figure 2.2 Stereochemical definitions of hexuronic acids

2.2.1.3 D-Glucuronic acid (HGlc)

D-Glucuronic acid was the first of the aldohexuronic acids to be discovered (being prepared as a lactone by Schmiedeberg and Meyer in 1879) and attracted considerable attention over the first part of the twentieth century.[1] Indeed, it is from **HGlc** that the term "uronic acid" originates, as the compound was first detected as a common constituent of mammalian urine. It has since been established that enzymatic glycosylation with a D-glucuronic acid moiety is an important route to the solubilisation and subsequent excretion of toxic substances from the body.[16] Hence, the appearance of **HGlc** in biomass is of little surprise as it provides a readily accessible detoxifying agent to herbivorous animals.*[,17] For the purposes of this thesis, **HGlc** is of interest as a principle constituent of hemicellulose, with 4-O-methyl-D-glucuronide forming the branched units of the *β*-D-xylan backbone (see Figure 2.3).[3] However, it is worth mentioning that **HGlc** can also occur in substantial degrees in many other biomass-derived polysaccharides such as gum arabic (acacia gum)[18] and U-fucoidan derived from brown algae.[19]

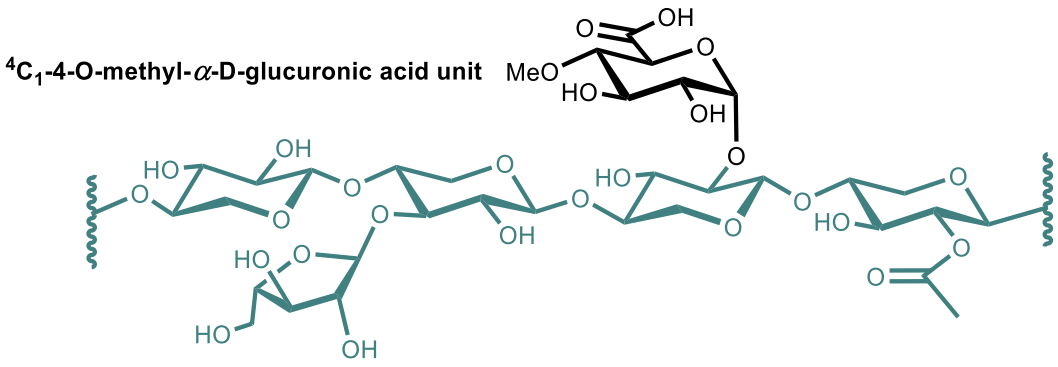

Figure 2.3 D-Glucuronic acid as it is found in the *β*-D-xylan fraction of hemicellulose

2.2.1.4 D-Galacturonic acid (HGal)

First isolated independently in 1917 by Saurez and Ehrlich, galacturonic acid is best known as being the principle monomeric unit of pectins (see Figure 2.4).[20] Pectins may be found in the cell walls of many terrestrial plants and to a very high degree in citrus fruits where they provide structure to the peel.[3] Depending on the origin, pectins can have varying degrees of methyl esterification of the carboxylic acid moiety, up to 80 % for apple pectin for example.[21] Occasional substitution of the hydroxyl groups with acetyl groups, or neutral sugars, and interruption of the chain with rhamnose units are all also common deviations from the poly-D-galacturonic acid backbone.[3,21] The ability of pectin to gel means that it has found utilisation in a range of areas, particularly as a thickening agent in the production of jams and marmalades.[21,22]

* A eucalyptus leaf-eating koala bear typically excretes 2-3 grams of D-glucuronic acid per day![17]

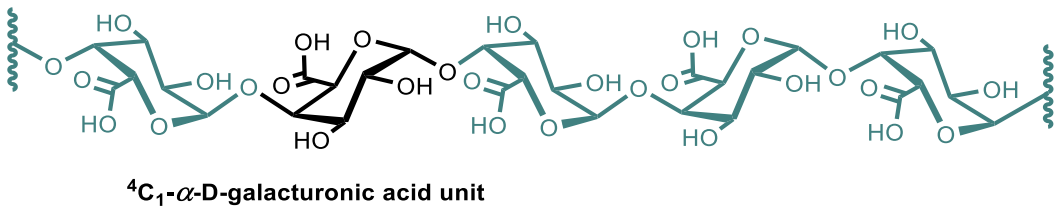

Figure 2.4 D-galacturonic acid as it is found in pectin

2.2.1.5 D-Mannuronic acid (HMan)

In 1928 Nelson and Cretcher isolated a previously unidentified uronic acid (initially as a lactone) as a hydrolysis product of alginic acid.[23] The authors went on to characterise the unknown saccharide and identify the D-mannose stereochemistry, confirming its identity as D-mannuronic acid.[24–26] Whilst crystalline samples of both the α- and β- pyranose forms of the acids have been prepared by Schoeffel and Link, these authors noted the low yields and difficulties associated with the crystallisations, which has contributed to there being very limited information regarding the solid state properties of **HMan**.[27] Along with L-guluronic acid (see Section 2.2.1.6), **HMan** is a constituent co-monomer of alginic acid where it is found unsubstituted and in a 1,4-linked $^4C_1$-β-D-configuration (see Figure 2.5).[28]

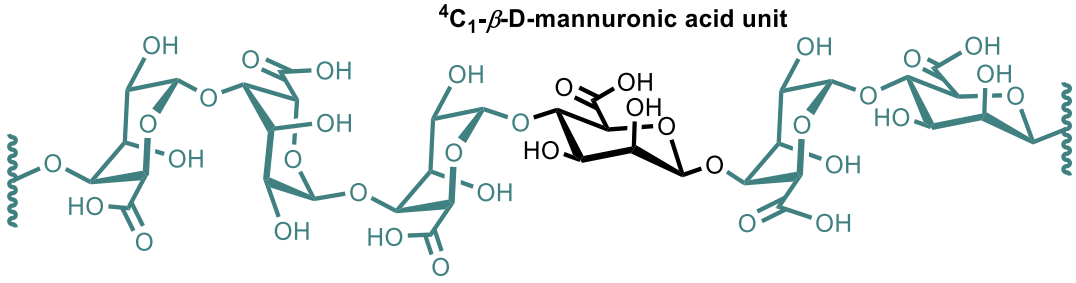

Figure 2.5 D-Mannuronic acid as it is found in alginic acid

2.2.1.6 L-Guluronic acid (HGul)

In their discovery of D-mannuronic acid from the hydrolysate of brown algae (See Section 2.2.1.5), Nelson and Cretcher left open the possibility of other, undiscovered uronide units existing within the alginic acid structure. This turned out to be an astute allowance as, in 1955, Fischer and Dörfel provided the first positive characterisation of L-guluronic acid as a hydrolysis product of alginate.[29] Upon confirmation that the **HGul** had not arisen as a result of C5-epimisation of hydrolysed mannuronide, guluronic acid was confirmed as the secondary co-monomer of alginic acid.[30] Subsequent X-ray diffraction and polarised infrared studies confirmed that **HGul** exists in a 1,4-linked $^1C_4$-α-L-pyranose configuration when bound in the polymer (see Figure 2.6).[31] The crystallisation of **HGul** in either the free

acid form or as a lactone has been found to be extremely elusive,[32] and similarly little work has been reported on the crystallisation of guluronate salts.[33–36]

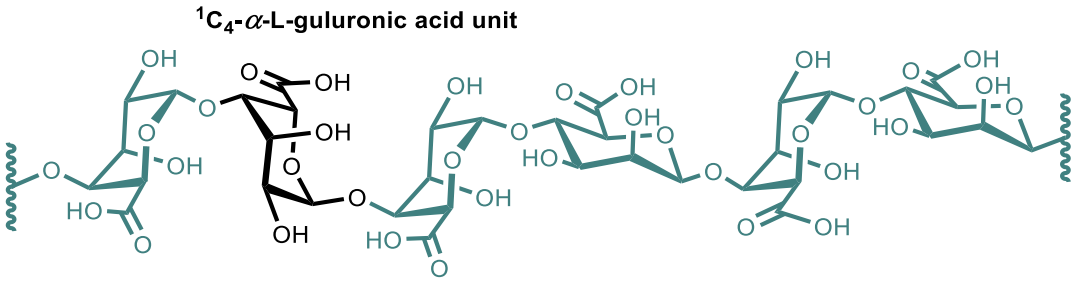

Figure 2.6 L-Guluronic acid as it is found in alginic acid

2.2.2 Solution state equilibria of aldohexosaccharides

Whilst frequently depicted as single structures, the uronic acids are known to exist in dynamic equilibria between a number of constitutional, configurational and conformational isomers when dissolved in aqueous solution.[37] Whilst such equilibria are generic to all aldo-sugars, they are qualitatively summarised in the exemplar case of D-glucuronic acid in Figure 2.7.

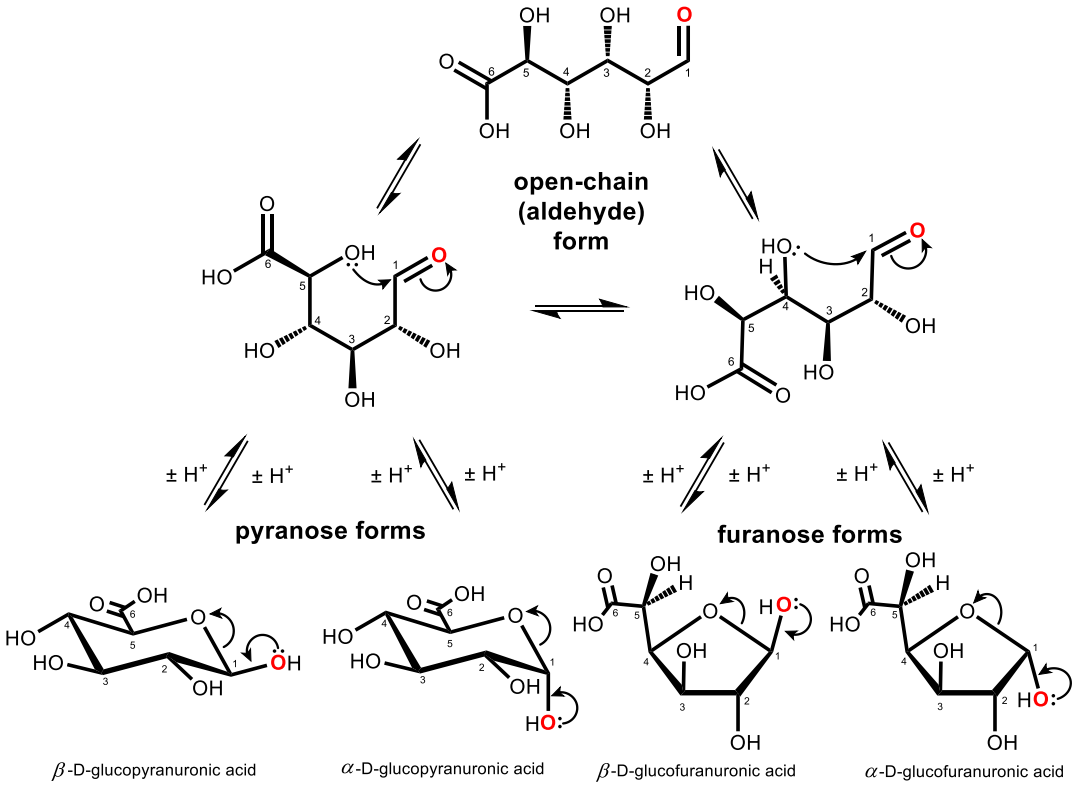

Figure 2.7 Isomeric equilibria exhibited by D-glucuronic acid in aqueous solutions

In fact, there has been very little work to probe these various equilibria in the cases of uronic acids, but the following section will draw insights from the aldohexoses (which have been studied in much greater depth) in order to inform the later discussions in this chapter.[37–41] Hence the following equilibria should be considered when discussing aqueous aldose (and aldouronic acid) chemistry:

- **Cyclic and acyclic constitutional isomerism:** The cyclic form of an aldose (also known as the hemiacetal or lactol form) is in equilibrium with an acyclic isomer (also known as the open-chain or aldehyde form).[*] The open chain is relatively high in energy and exists in sufficiently low abundance to make detection difficult (for example, in aqueous conditions less than 0.01 mol.% of glucose molecules exist in the acyclic form at 25 °C).[42] Hence, the majority of aldose monosaccharides in solution exist in the cyclic form.

- **Pyranose and furanose constitutional isomerism:** An aldose sugar may re-cyclise as either a six-membered ring (with the C6 carboxylate carbon exocyclic) known as the *pyranose* form, or as a five-membered ring (with both C6 and C5 exocyclic) in the *furanose* form. When the stereochemical arrangements of substituents are ignored, a saturated six-membered ring is known to be lower in energy than a saturated five-membered ring, and hence the pyranose form typically dominates in aqueous solutions of aldohexoses.[41]

- **Anomeric configurational isomerism:** A further isomeric equilibrium exhibited by pyranose and furanose forms of aldose sugars arises as a consequence of differing relative stereochemistry of the hydroxyl group on C1 (the anomeric carbon) following cyclisation. Two configurations (anomers) of cyclic aldoses are formed as a result, and are termed "*α*" and "*β*". In the four pyranose forms of **HGlc**, **HGal**, **HMan**, and **HGul**, the *α*-configuration is defined as having an axial arrangement of the hydroxyl group on C1, and the *β*-configuration is defined as having an equatorial arrangement of the hydroxyl group on C1. Anomeric equilibria are established much less rapidly than pyranose and furanose equilibria leading to the phenomenon of "complex mutarotation"[†] whereby an isomerically pure crystalline sugar may be dissolved in solution and traverse through several values of specific rotation before finally settling.[38] The steric and electronic factors that dictate the position of anomeric equilibria are explored in more detail later in this section.

[*]The aldehyde form can also be partially hydrated to yield a second acyclic compound bearing a *gem*-diol on C1 and known as the *aldehydrol* form, though this is not depicted in Figure 2.7.[37]

[†]Mutarotation is the change in the rotation of polarised light through a solution of saccharide following the perturbation of an optically active equilibrium. The term is commonly used to refer to the observable manifestation of an anomeric tautomerisation.[38]

- **Conformational isomerism:** Aside from the constitutional and configurational equilibria listed above, pyranose rings can also adopt a number of different conformations, namely the *chair*, *boat*, and *skew* forms (familiar from cyclohexane chemistry).[38] Of these, the boat form is the lowest in energy and has been studied in some detail for all of the aldohexoses.[37,41] Two forms of the boat are possible, the so-called $^{4}C_{1}$ and $^{1}C_{4}$ structures (as depicted in the exemplar case of *β*-D-glucuronic acid in Figure 2.8). From theoretical calculations, it has been shown that the $^{4}C_{1}$ conformer is far lower in energy for both *α*- and *β*-pyranose configurations of D-glucose, D-mannose, D-galactose, and the $^{1}C_{4}$ conformer is far lower in energy in the case of the *α*- and *β*-pyranose configuration of L-gulose.*[37,43–45] In the case of the four uronic acids considered in this thesis, the preferred conformations discerned for the parent aldoses are presumably even more favoured as they all locate the bulky carboxylate moiety in the sterically favoured equatorial position. Whilst furanose configurations can also exist in different conformations (namely the *envelope* and *twist* forms), the arguments to determine which is the lower in energy are much more subtle, and not considered in depth here.[41]

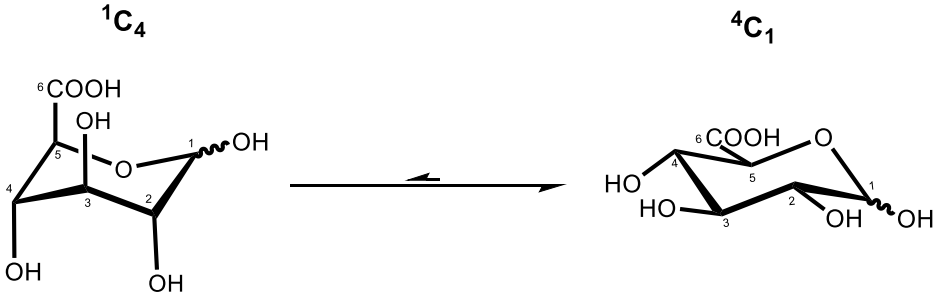

Figure 2.8 Interconversion of chair conformations ($^{1}C_{4}$ and $^{4}C_{1}$) of D-glucuronic acid

- **Additional equilibria:** Some aldohexoses are capable of reversibly forming anhydrosugars in acidic solution.[38] Such equilibria are particularly relevant in the case of aldohexuronic acids, which are capable of intramolecular esterification to form lactones (see discussions in Section 2.2.3).

Whilst optical rotation has previously been the routine method of choice for investigating these various equilibria,[37] nuclear magnetic resonance (NMR) spectroscopy has emerged as a much more versatile tool.[39,40] Through NMR spectroscopic studies, the composition of aqueous solutions of D-glucose, D-galactose, D-mannose and L-gulose have all been investigated and reveal that, overwhelmingly, the cyclic, pyranoid, $^{4}C_{1}$ (or $^{1}C_{4}$ in the case of L-gulose) forms dominate.[37] The anomeric equilibrium between *α*- and *β*-pyranose forms in all cases is, however, much more finely balanced and worthy of more in-depth discussion.

*In fact the calculations were carried out using the $^{4}C_{1}$ form of D-gulose, but as the $^{1}C_{4}$ form of L-gulose is enantiomeric with this compound and hence energetically equivalent under aqueous or gas phase conditions, the results may be considered to be transferable.[41]

Stoddart provided an excellent account of the factors governing the stability of one pyranose anomer over another, and they may be summarised in terms of electronic and steric factors:[41]

- **Electronic factors**: The electronic influences governing the *α*/*β*-pyranose epimeric equilibrium are dominated by the *anomeric effect*,[38] which is manifested as an energetic preference for axial over equatorial substituents (hydroxyl groups in the cases discussed here) at the anomeric carbon (C1). The origin of the effect has been ascribed to a combination of the reduction in dipole-dipole repulsion between the lone pair on the anomeric oxygen and the hydroxyl oxygen (the electrostatic influence – see Figure 2.9), and the lowering of the energy of the anomeric oxygen lone electron pair through donation into the C-O σ* of the C1-hydroxyl bond (the hyperconjugation influence - see Figure 2.10).[46]

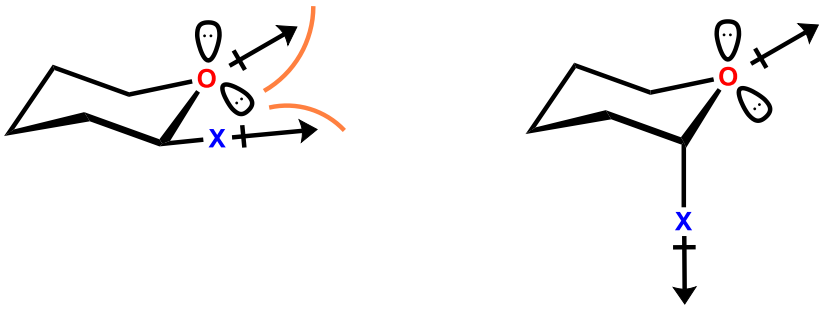

Figure 2.9 Dipole-dipole interactions in equatorially and axially substituted pyranoses

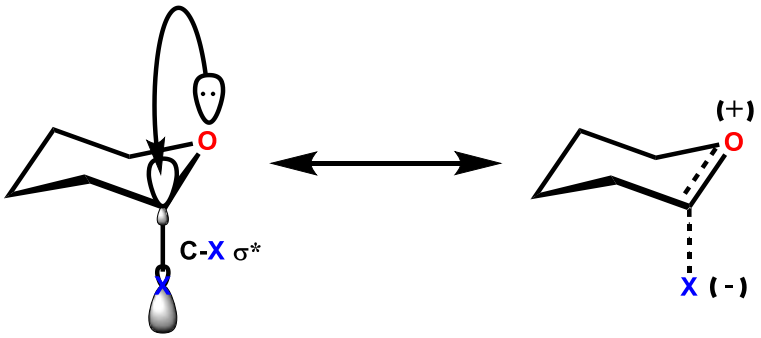

Figure 2.10 Stabilisation of an axially-substituted pyranose by hyperconjugation

- **Steric factors**: The steric factors governing anomeric stability arise from the varying repulsive influences of the axial and equatorial substituents around the pyranose ring. At a low, but surprisingly insightful, level of theory the order of stability for different combinations of axial and equatorial hydroxyl groups can be predicted (see Figure 2.11).[37] This analysis indicates that the 1,3-diaxial arrangement of hydroxyl groups is particularly destabilising.[38]

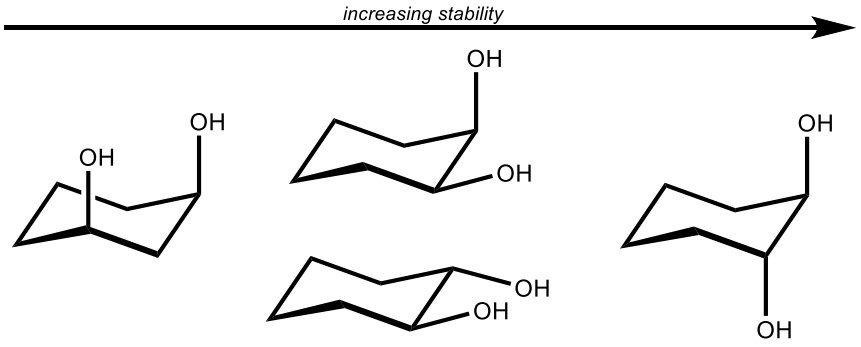

Figure 2.11 Stability of various arrangements of axial and equatorial substituents on a six-membered ring in an idealised chair conformation under aqueous conditions.[38,41]

When both steric and electronic influences are considered for the aldohexoses, it is possible to predict the equilibrium constitution between the two pyranose anomers based on their calculated free energy difference (ΔG) in aqueous conditions (see Table 2.1).[37] The correlation between theoretically derived and experimentally observed values prove to be quite satisfactory, confirming the role particularly of the steric factors of dictating the relative stabilities of the monosaccharides. Whilst additional discussions on this topic are made in Chapter 3, it is worthy to note especially that the *α*-L-gulose stereochemistry is one of the highest in energy of all of those calculated.

Table 2.1 The difference in free energy between anomers of different aldopyranoses under aqueous conditions at 25 °C. The data is taken from Angyal and quoted relative to an imaginary aldopyranose molecule possessing no interactions between its substituents.[37]

Aldopyranose	Free energy (kJ mol^{-1})		Calculated
	α	*β*	[*α*]/[*β*]
Allose	16.1	12.3	0.22
Altrose	14.0	14.0	1.00
Galactose	11.9	10.5	0.56
Glucose	10.0	8.6	0.56
Gulose	16.1	12.8	0.27
Idose	15.3	16.7	1.78
Mannose	10.5	12.3	2.13
Talose	14.8	16.7	2.13

Of course, whilst carbohydrate chemists are frequently most interested in which conformations and configurations predominate in neutral aqueous conditions at room temperature, knowledge of the higher energy states is also valuable as the ambient equilibria may be considerably perturbed when parameters are changed (including the pH, temperature, presence of metal ions, *etc.*) particularly in the case of the uronic acids. The effect of such perturbations will be considered extensively in this chapter and others.

2.2.3 Lactonisation of aldohexuronic acids

2.2.3.1 General comments on the lactonisation of aldohexuronic acid

The presence of carboxylic acid moieties in uronic acids within close proximity to hydroxyl groups means that such species can readily undergo reversible internal cyclising esterification (*lactonisation*). Hence, an additional equilibrium must be considered in the case of aldohexuronic acids compared to their aldohexose counterparts: one between the free acid and the corresponding lactone. Whilst a number of combinations of pyranurono- and furanurono-, *γ*- and *δ*- lactones can be imagined, the discussion here will focus on the furanurono-6,3-lactone (furanurono-*γ*-lactone). Though pyranurono-6,1-lactones have been prepared synthetically in the case of **HGlc**, **HMan**, and **HGal**, they require specialised strategies to facilitate the necessary inversion of conformation from stable $^4C_1$ to high-energy $^1C_4$ (see Figure 2.12).[47–49] The furanurono-6,3-lactones on the other hand form much more readily for all but D-galacturonic acid.[20] Indeed, the propensity of such urono-6,3-lactones to form under acidic conditions mean that **HGlc**, **HGul**, and **HMan** were all first isolated in their internally esterified form.[1,24,29]

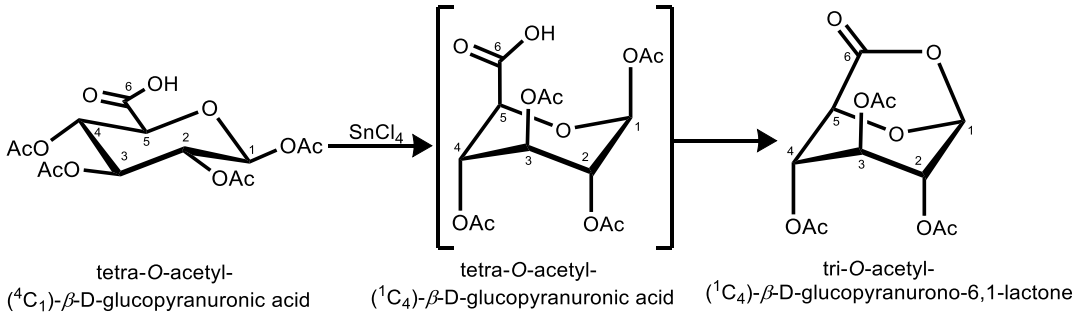

Figure 2.12 Formation of a pyranurono-6,1-lactone *via* conformation inversion[47,48]

2.2.3.2 D-Glucofuranurono-6,3-lactone

As in the case of the free aldohexuronic acids discussed in Section 2.2.1, the lactone of D-glucuronic acid (D-glucofuranurono-6,3-lactone or *glucurone*) was discovered far before those of the other uronic acids, and consequently, has benefited from much more extensive study.[1,50,51] Of particular relevance to the discussion here, the instability of the lactone at higher pH values has been noted,[1] as has the preferential formation of the lactone from the uronic acid at elevated temperatures (see Figure 2.13).[52] The energy of activation for conversion of D-glucopyranuronic acid to D-glucofuranurono-6,3-lactone (in subcritical water at pH 2-3) has been calculated as 88.5 kjmol^{-1} with an associated enthalpy change of +25.4 kjmol^{-1}, confirming the entropic driving force behind the change.[6] Whilst Stoddart ascribed the favourable entropic factor in lactone formation to the flexibility of the *cis*-fused five-membered ring of the furanurono-6,3-lactone,[52] the elimination of water from the molecule also presumably plays a significant role (see Figure 2.13).

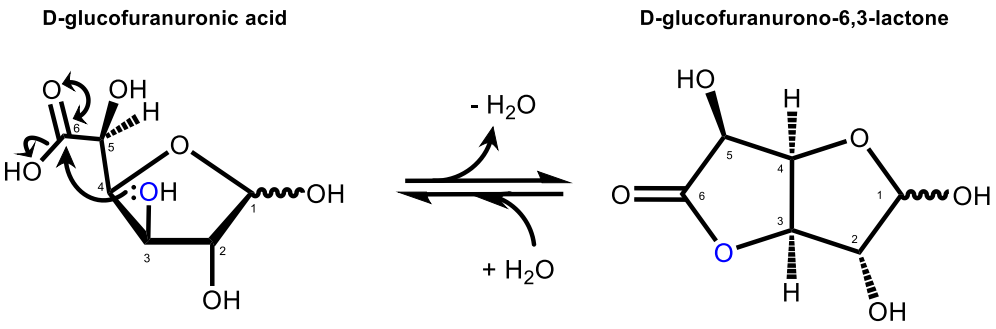

Figure 2.13 Reversible formation of D-glucofuranurono-6,3-lactone

2.2.3.3 D-Mannofuranurono-6,3-lactone

Crystalline D-mannuronic acid lactone (D-mannofuranurono-6,3-lactone or *mannurone*) readily forms from concentrated aqueous solutions of **HMan**[20,24,29,53,54] and was first characterised in 1946 by celebrated carbohydrate chemist Horace Isbell and his assistant Harriet Frush.[2] Here, Isbell and Frush were able to demonstrate by chemical means that the structure most likely consisted of a 6,3-*γ*-lactone fused to 1,4-furanose ring (see Figure 2.14). However, subsequent infra-red spectroscopy data from Fisher and Dörfel supported the hypothesis of a 6,3-*γ*-lactone and $^4C_1$-1,5-pyranose ring structure.[1,29] It was not until almost 50 years later that Shalaby *et al.* used a crystal directly from Prof. Isbell's collection of rare sugars to confirm by X-ray diffraction the originally proposed bicyclic furanose structure.[55] Indeed, Isbell and Frush's early work also demonstrated the anomerisation of the furanose ring of the lactone,[2] which again was observed later by ^{1}H NMR experiments in both D_2O and DMSO.[55] Whilst it has been recognised that the mannuronic lactone can be completely cleaved by neutralisation to yield the free uronate salt,[27] the equilibrium between the two forms has not been probed to the same extent as in the case of D-glucuronolactone (see Section 2.2.3.2).[2,26] Apart from a few studies into the glycosylation of D-mannuronolactone,[56,57] literature on the reactivity of the compound is relatively scarce.[51]

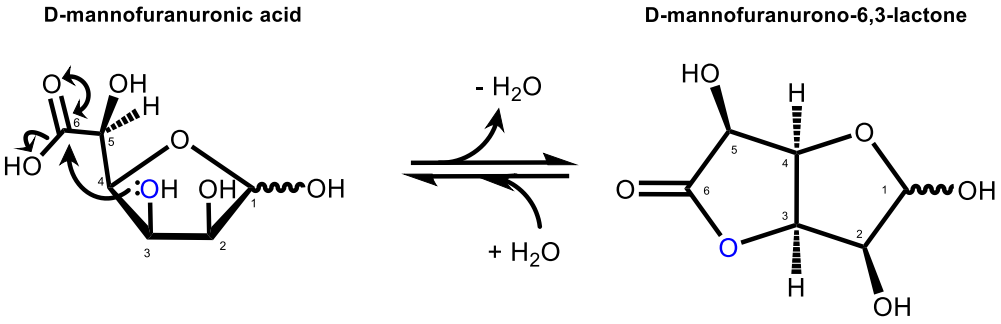

Figure 2.14 Reversible formation of D-mannofuranurono-6,3-lactone

2.2.3.4 L-Gulofuranurono-6,3-lactone

The structure and reactions of L-guluronic acid lactone (L-gulofuranurono-6,3-lactone or *gulurone*) are even less well studied than its mannuronic counterpart. The difficulty of preparing L-guluronic lactone has been noted,[58] and there are correspondingly very few literature precedents for isolating crystalline material.[29] Hence, structural characterisation of gulurone has relied on indirect evidence from the methyl glycoside derivatives, which again display a bicyclic structure with a 6,3-*γ*-lactone fused to the 1,4-furanose ring (see Figure 2.15).[58] Otherwise, the conditions that favour the formation of L-gulofuranurono-6,3-lactone are assumed to be similar to those of glucurone and mannurone.[1]

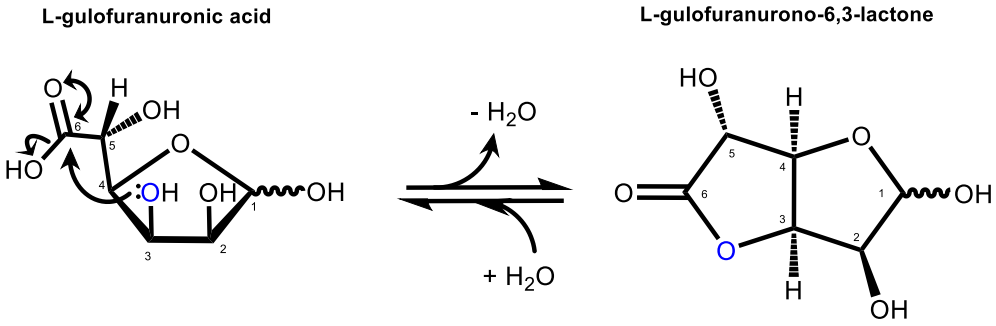

Figure 2.15 Reversible formation of L-gulofuranurono-6,3-lactone

2.2.3.5 D-Galactofuranurono-6,3-lactone

Some authors have referred to the formation of a galacturonic acid lactone under treatment with heat and acid, but they provide no analytical evidence to support this phenomenon.[5,59] Several textbooks also make reference to the formation of D-galactopyranurono-6,3-lactone (based on the analogous formation of 6,3-anhydrogalactose from galactopyranose),[13,60] however, the conditions necessary to induce galacturonic acid to undergo such a reaction were not described. Whilst galactopyranuron-6,1-lactone motifs can be formed from specialist, multistep reaction conditions (required to overcome the energetic hurdle of inverting the conformation from $^4C_1$ to $^1C_4$), such transformations cannot occur spotaneously in aqeous solution.[48,49] It is clear, however, that it is impossible for D-galactofuranurono-6,3-lactone to form in an analogous manner to those from **HGlc**, **HMan**, and **HGul** as, when **HGal** adopts a furanose configuration, the *trans* relationship between O3 and the exocyclic C5-C6 chain prevents intramolecular esterification (see Figure 2.16).[3]

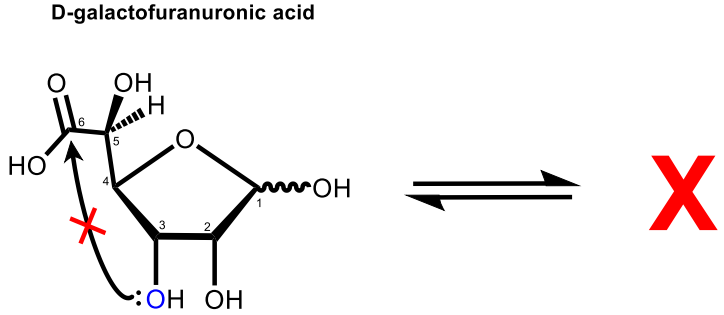

Figure 2.16 The formation of D-galactofuranurono-6,3-lactone from the corresponding uronic acid is stereochemically impossible

2.2.3.6 The relevance of aldohexuronic acid lactone formation to pyrolysis

The lactonisation displayed by uronic acids is pertinent to the discussion of uronide pyrolysis chemistry as there are clear similarities between the formation of 1,6-anhydroglucose (levoglucosan) in the pyrolysis of glucose and glucan-based polymers (see Figure 2.17.[61] Hence, whilst levoglucosan is known to be the most prominent product in the thermal degradation of glucans,[62] so to might it be anticipated that some form of lactone may dominate the thermochemistry of uronides (see Figure 2.18). As parallels between carbohydrate hydrothermolysis and anhydrous pyrolysis behaviours have been noted,[61,63] studying the response of mono-uronic acids to heat under aqueous conditions (including their lactonisation) could help to inform the discussion into their thermal degradation mechanisms (see Chapter 4).[5,6,64,65]

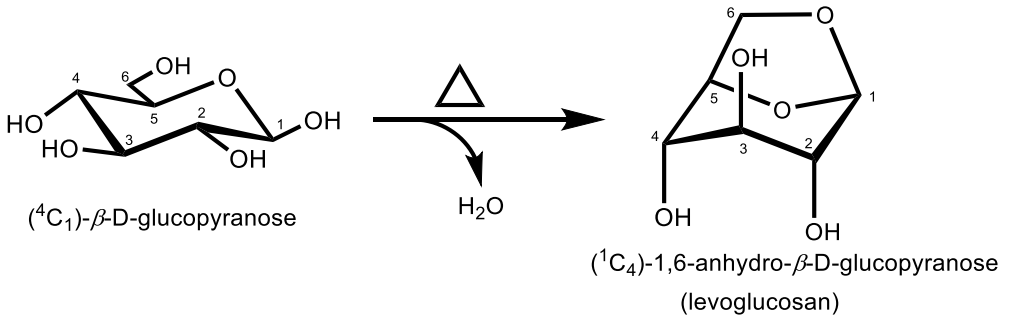

Figure 2.17 Thermal dehydration and rearrangement of glucose to yield levoglucosan

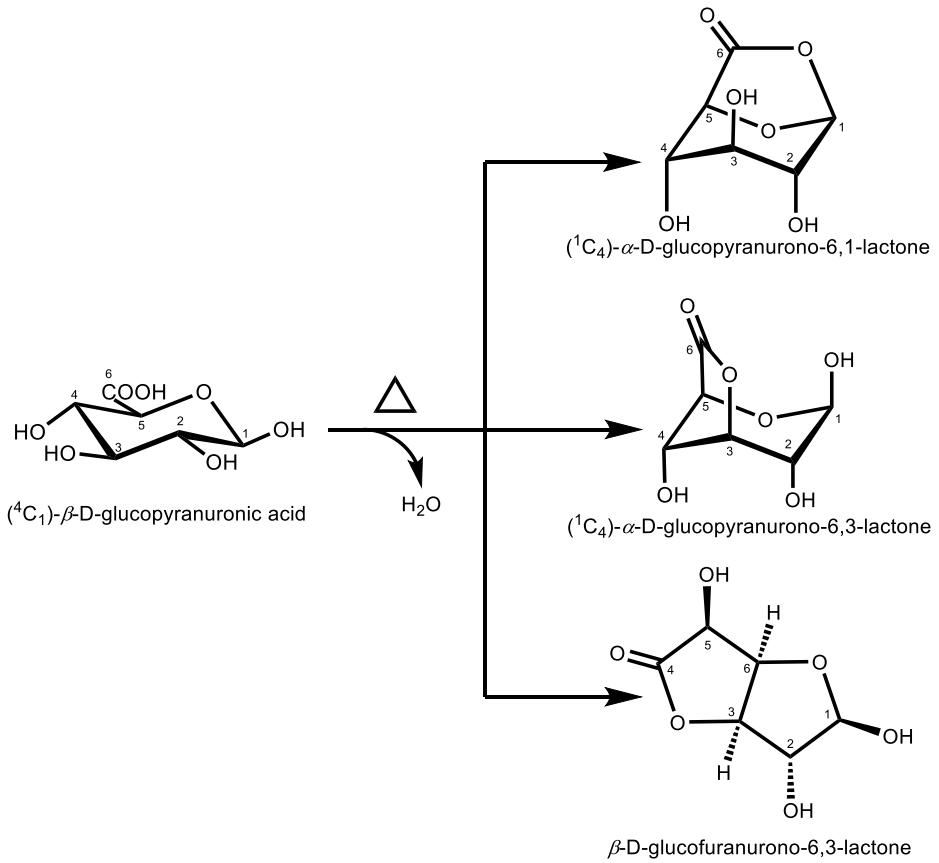

Figure 2.18 Anhydrosugars that may form in the thermal conversion of a uronic acid

2.2.4 Previous studies of monomeric algal aldohexuronic acids in aqueous solution

The solution state chemistry of alginic acid and alginates including their metal binding properties (see discussions in Chapter 3),[66–68] hydrothermolysis[64,69–73] (see discussions in Appendix C), and responses to changes in pH,[74–76] have all been extensively studied for a variety of reasons,[77,78] generally with a view to exploiting the technological potential of seaweeds.[11,12,67,79–81] Despite such high levels of interest, the corresponding properties of the monomeric units of alginic acid, namely **HMan** and **HGul**, have received very little attention. This is in contrast to the mono-uronic acids **HGal** and **HGlc**, for which many solution-based studies have been carried out in order to probe the response of the acids to the presence of metal ions (see extensive discussions in Chapter 3), changes in temperature (see discussions in Appendix C),[5,6,82,83] and changes in pH (amongst many others).[84–8787]

In previous investigations of the solution state chemistry of poly-, oligo- and mono-uronic acids, ^{1}H and ^{13}C NMR spectroscopy has proved to be an insightful tool.[14,66,78,87–91] In this regard however, the investigation of the algal mono-uronic acids by NMR spectroscopy has been extremely limited, with the reported data either being incomplete, poorly resolved, or inconsistent.[14,36,92–95] Whilst the few existing literature studies of **HMan** and **HGul** have been sufficient to demonstrate that, under neutral conditions and ambient temperatures, the algal mono-uronates appear to speciate in a similar manner to their parent aldohexoses (D-mannose and L-gulose), few other conclusions have been drawn.[37,40] However, changes in the pH of solutions of the algal uronic acids may be particularly impactful owing to changes in the level of dissociation of the carboxylate moiety, an effect that has not been well studied.[84,85,87] Indeed, whilst numerous measurements of the pK_a for **HGlc** ($pK_a \approx 3.20$) and **HGal** ($pK_a \approx 3.42$) have been made, only one value exists both for **HMan** ($pK_a \approx 3.38$) and for **HGul** ($pK_a \approx 3.65$).[75,84,86] Significantly, the single pK_a values established for **HMan** and **HGul** were both determined from a weighted average of the various pK_a values of all of the species in solution for each system, and hence the dissociation behaviour of *β*-D-mannopyranuronic acid, and *α*-L-gulopyranuronic acid (the forms of the saccharides as they are found in alginic acid) has not been determined.[75]

With this in mind, there is a clear need to obtain more complete NMR spectroscopic data for the algal-uronic acids, as this will facilitate a better understanding of their reactivity in aqueous solutions. Ultimately, it is hoped that, with more complete characterisation of the algal mono-uronic acids derived from the most up-to-date NMR spectroscopic methodologies, their chemistry may be explored more routinely alongside that of **HGal** and **HGlc** in the development of new techniques to utilise uronide-rich biomass. Indeed, the extensive insights available from NMR spectroscopic analysis of reaction solutions means that the technique could find future utility in the monitoring of aqueous phase processing of either alginates,[72,73,97,98] or whole kelp biomass[97,98] (see Appendix C for additional discussions in this regard).

2.2.5 Strategies towards the isolation of algal mono-uronic acids

In order to probe the aqueous phase behaviour of algal mono-uronic acids there are a number of strategies available for the isolation of suitable solutions of **HGul** and **HMan**. Such preparations are typically either purely synthetic in nature, or they proceed through a controlled hydrolysis of a parent polyuronide. Synthetic strategies involve either selective oxidation of a suitable aldose or reduction of the corresponding aldaric acid.[1,29,51,58,99] Such synthetic routes to **HMan** and **HGul** are not trivial and suffer from low yields, the need for multi-step protection procedures, complex separations, ill-defined crystallisations, and the requirement for costly starting materials.[1,58] In contrast, preparation of **HGul** and **HMan** from controlled hydrolyses of alginic acid, whilst being somewhat chemically inelegant, holds a number of advantages over the established synthetic routes.[100] Primarily, the reagents for hydrolysis (usually alginic acid) tend to be extremely low cost, facilitating scale-up of the procedure to compensate for the low product yields. Additionally, hydrolysis methodologies typically yield both of the target uronic acids simultaneously, reducing the requirement for duplicated preparations. For these reasons, only the hydrolysis methodologies are considered in detail here.

A survey of the literature concerning the hydrolytic isolation of algal mono-uronic acids (or mono-uronate salts) reveals that the process is typically achieved in three stages:

I. **Hydrolysis of alginic acid:** The glycosidic links of the polymer chain are cleaved by thermal treatment with formic acid,[101,102] methanolic HCl,[103] sulphuric acid,[32,33,54,94] trifluoroacetic acid,[93] or enzymatically[104,105] to yield a crude hydrolysate rich in mono-uronic acids.

II. **Separation of HMan and HGul:** Algal mono-uronic acids can be separated by electrophoresis,[106] complexation with a chiral resolving agent (such as brucine[33,34] or cinchonine[36]), by anion exchange chromatography,[94,107,108] or by high performance liquid chromatography (HPLC).[93]

III. **Isolation of uronic acid or uronate salt:** Solutions of the algal mono-uronic acids must first be neutralised to reverse any lactonisation that may have occurred,[59] with the opportunity for subsequent crystallisation of the resultant uronate salt being possible at this stage if required.[27,33–36,54,92] Alternatively, the uronate can be returned to an acidic state by exchange of the counter cation on a resin,[75] though crystallisation of the resulting parent acid is much more difficult from this point.[27]

Elements from each of these methodologies established from the literature could subsequently be combined to inform the approach utilised later in this chapter, with the final route adopting those elements that were found to be both successful and convenient. Finally, it should be realised that, throughout all of the steps, precautions must be taken to remove unwanted hydrolysis products (including lactones, oligo-uronides, and degradation products of the type discussed in Appendix C) and to avoid epimerisations of the uronic acids (which occur with ease at elevated pH values).[59,82,109]

2.3 Chapter aims

The arguments expounded in the previous sections highlight a lack of fundamental knowledge about algal mono-uronic acids, which is concerning as such understanding could help greatly in the development of technologies to exploit algal biomass. In order to address this situation, the following sections will explore the basic solution state behaviour of algal mono-uronic acids and explore properties such as their lactonisation under hydrothermal conditions (which could inform later discussions on the pyrolysis behaviour of the compounds). Isolation and characterisation of the uronates will also provide material with which to probe the coordination of metal ions, with a view to understanding cation binding within alginates (see Chapter 3). Accordingly, the principal aims of this chapter are:

I. **^{1}H and ^{13}C NMR spectroscopic assignments:** by preparing solutions of algal mono-uronate salts in D_2O, high field one- and two-dimensional NMR spectroscopic techniques (that were largely unavailable at the time of previous studies) will be used to provide confident assignments for the α- and β-pyranose anomers of those saccharides. Such assignments will facilitate a quantitative study of the position of the various configurational equilibria outlined in Section 2.2.2 in the cases of both Na-D-mannuronate and Na-L-guluronate.

II. **Determining response to changes in pH:** titration experiments follow by ^{1}H and ^{13}C NMR spectroscopy will be conducted to observe changes in the solution-phase structure and composition of **NaMan** and **NaGul** upon lowering the pH of the solution. The changes in chemical shift will be used to calculate pK_a values for the different pyranose configurations in the solutions.

III. **Exploring lactonisation behaviour:** by heating solutions of the algal uronic acids under different conditions and analysing them by ^{1}H NMR spectroscopy, a comparison of their lactonisation behaviour will be possible.

IV. **Comparisons of HGul and HMan with HGlc and HGal:** where relevant, comparisons will be made between the solution state behaviour of algal mono-uronic acids and other uronic acids (namely **HGlc** and **HGal**) studied under similar conditions.

Ultimately, the isolation of anomerically pure crystals of algal mono-uronic acids and their salts would be greatly beneficial to carrying out further investigations into their properties and reactivity (especially their pyrolysis chemistry). Whilst such crystallisations are beyond the scope of this chapter, it is hoped that the work conducted here may better enable future researchers to achieve the aim of obtaining well-defined solid samples of **HMan** and **HGul** (as are currently readily available for **HGal** and **HGlc**).

2.4 Results and discussion

2.4.1 Characterisation of algal mono-uronates in solution by multinuclear NMR spectroscopy

2.4.1.1 General comments on the analysis of algal mono-uronates by NMR spectroscopy

As was outlined in Section 2.2, part of the aim of this chapter was to obtain clear, unambiguous ^{1}H and ^{13}C NMR spectroscopic assignments of solutions of L-guluronic and D-mannuronic acids. As the systems in question are sensitive to the sample conditions (including the bound countercation, temperature, uronate concentration, and pD)[40,84,85] as well as the spectrometer employed, the following discussions all refer to spectra acquired at 600 MHz with solutions of 0.26 ± 0.02 M Na-uronate salt at 295 ± 2 K (unless stated otherwise), with the pD (or, rather, pH*)[*] being varied systematically and indicated as required. In some cases, as is demonstrated below, adjusting the pH* proved to be a useful tool for assigning particularly convoluted regions of the ^{1}H or ^{13}C spectra, as the shifts induced by the addition of D_3O^+ sometimes yielded better separated peaks.

The ^{1}H and ^{13}C assignments of both the pyranose forms of both algal mono-uronates are reported in Table 2.2 and Table 2.3. The ^{1}H NMR spectra at various pH* values are depicted in Figure 2.20 for Na-L-gulopyranuronate, and Figure 2.21 for Na-D-mannopyranuronate. Additional figures, including the ^{1}H-^{1}H COSY and ^{13}C NMR spectra are provided throughout the discussions in Sections 2.4.1.2 - 2.4.1.5.

In each ^{1}H NMR spectrum, the arguments of Angyal and others[37–39,42,110–112] were employed to make the assignments of carbohydrates (locating anomeric peaks, discerning pyranose signals from furanose signals etc.). Here, the relationships discerned by Karplus between the magnitude of vicinal ^{1}H-^{1}H coupling constants and the size of the dihedral angle, and subsequent modifications to the original equations were particularly useful.[110,113,114] In addition, 2D NMR spectra (namely ^{1}H-^{1}H COSY and ^{1}H-^{13}C HSQC)[†] provided further evidence to support assignments, as well as "pure shift" techniques to improve resolution.[‡,115] Once assignments had been made, the relative positions of the peaks were mostly in good agreement with those reported by previous authors (though absolute peak positions were influenced by the choice of reference), and the few discrepancies will be highlighted and analysed in the following discussions.[14,36,92–95]

---

[*]It should be noted that, as the pH-electrode used here was not calibrated in deuterated solutions, the term pD may only be used following a correction of about 0.4 units.[120] Alternatively, the term pH* can be used to refer to the uncorrected reading of a $[H_3O^+]$-calibrated electrode in solutions of varying $[D_3O^+]$.[120] For consistency, and to simplify calculations of acid dissociation constants later in this chapter, the term pH* is adopted in preference to pD from this point forward.

[†]Whilst additional experiments (including TOXY, HMBC and ROESY) were also acquired, they were not used to inform the discussions provided here and hence the results are not included.

[‡]Pure shift NMR spectroscopy involves broadband homodecoupling in the acquisition of a proton spectrum to remove the effects of spin-spin coupling and render all ^{1}H NMR peaks as singlets, dramatically reducing the signal density in busy regions.[115]

Once acquired, the ^{1}H NMR spectra for Na-D-mannuronate (at pH* 7.01) contained groups of signals with intensities in the ratio 100:50:6:4. From the discussions in Section 2.2.2, it was clear that the two larger sets of signals corresponded to two $^{1}C_{4}$-pyranose anomers and the smaller sets to two furanose species.* Similarly, for Na-L-guluronate under the same conditions, a spectrum was acquired with peaks of intensity ratio 100:22:6:3, with the larger sets being assigned to the two $^{4}C_{1}$-pyranose anomers and, again, the sets with lower intensity being attributed to the furanose species.* Hence, the pyranose configurations dominate for both Na-L-guluronate and Na-D-mannuronate under the conditions stated (see Figure 2.19). Accordingly, the following analysis is heavily centred around six-membered ring pyranoid structures, rather than the five-membered furanoid arrangement.† Whilst some reference is made to the signals arising from furanuronates where necessary, NMR experiments with longer acquisition times or more concentrated solutions would be required to make full assignments. Furthermore, no peaks could be identified in spectra of either uronate that corresponded to either of the open-chain forms, indicating their presence was especially low in solution.[38] However, whilst the furanose and open-chain configurations of the monosaccharides are given only secondary consideration in this thesis, they should be borne in mind when considering possible degradation pathways of uronates – especially *via* lactone formation (see Section 2.2.3.6).

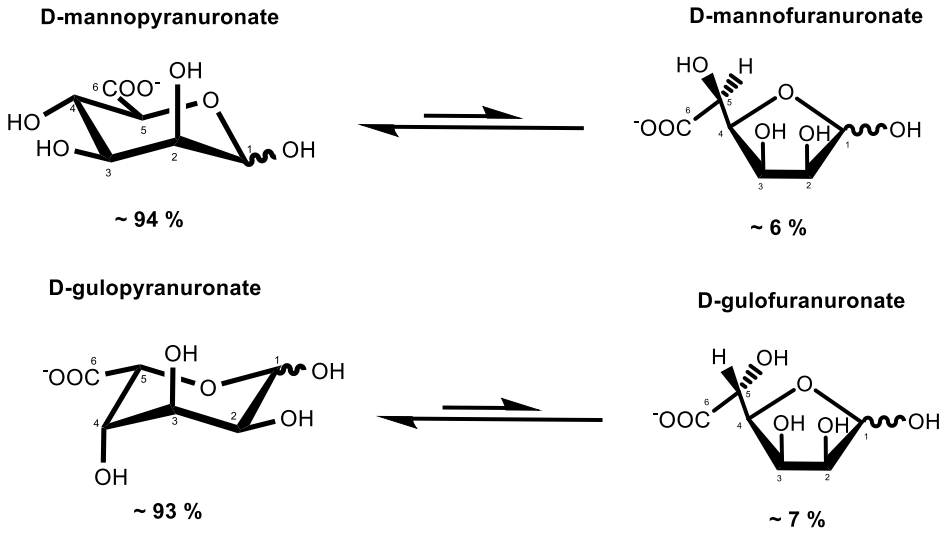

Figure 2.19 The position of the equilibrium between the pyranose- and furanose-forms of NaMan and NaGul determined from the intensities of signals in the ^{1}H NMR spectra in D_2O (pH* 7.01, 0.26 ± 0.02 M, 295 ± 2 K).

*The conformation of a pyranose anomer can be discerned through Karplus-type arguments, where the $^{1}C_{4}$ form would give a radically different coupling pattern than the $^{4}C_{1}$ form.[38] In the cases reported here, the uronates were found to be entirely in the conformations predicted by the discussions outlined in Section 2.2.2.

†Especially given that the uronates exist in a pyranoid arrangement in the alginate polymer chain

Table 2.2 ^{1}H NMR spectroscopic assignments of sodium mono-uronate salts in D_2O (0.26 ± 0.02 M) at 600 MHz, pH* 7.0 – 7.2, 295 ± 2 K (relative to $C_6\underline{H}_6$ in C_6D_6, δ = 7.15 ppm). Scalar coupling constants (J) quoted to a precision of ± 0.1 Hz.

δ (ppm) J (Hz)[a]	Na-D-mannopyranuronate		Na-L-gulopyranuronate	
	α	β	α	β
δH1	**5.17, d**	**4.87, s**	**5.17, d**	**4.84, d**
$J_{1,2}$	1.7	n.d.[b]	3.7	8.4
δH2	**3.86, *pt***	**3.89, d**	**3.91, *pt***	**3.61, dd**[c]
$J_{1,2}$	2.0	n.d.[b]	3.7	n.d.
$J_{2,3}$	3.3	3.2	4.0	n.d.
δH3	**3.83, dd**	**3.63, dd**	**3.99, *pt***	**4.05, m**
$J_{2,3}$	3.3	3.2	3.8	n.d.
$J_{3,4}$	9.2	8.9	4.3	n.d.[d]
δH4	**3.78, *pt***	**3.67, *pt***	**4.15, dd**	**4.05, m**
$J_{3,4}$	9.2	9.4	4.3	n.d.[d]
$J_{4,5}$	9.4	9.6	1.8	n.d.
δH5	**4.03, d**	**3.61, d**	**4.55, d**	**4.31, d**
$J_{4,5}$	9.3	9.6	1.8	0.8

Key: d = doublet, dd = doublet of doublets, *pt* = *pseudo*-triplet, m = multiplet, n.d. = not determined

[a] Scalar coupling constants (J) quoted to a precision of ± 0.1 Hz.

[b] Whilst $J_{1,2}$ is not resolved for β-**NaMan** at 600 MHz, at 400 MHz a value of $J_{1,2}$ = 1.1 Hz was measured.

[c] Additional splitting due to virtual coupling is also visible. At pH* 1.0, βH3 and βH4 are sufficiently separated to remove the effects of virtual coupling to βH2 to give a well resolved dd with $J_{1,2}$ = 8.4 Hz and $J_{2,3}$ = 3.3 Hz

[d] A value for $J_{3,4}$ could not be measured for **NaGul** at pH* 7.2 as βH3 and βH4 are superimposed. However, at pH* 1.0 the two signals are sufficiently separated to measure their mutual coupling as $J_{3,4}$ = 3.7 Hz.

Table 2.3 ^{13}C NMR spectroscopic assignments of sodium mono-uronate salts in D_2O (0.26 ± 0.02 M) at 600 MHz, pH* 7.0 – 7.2, 295 ± 2 K (relative to $C_6\underline{H}_6$ in C_6D_6, δ = 7.15 ppm).

δ (ppm)	Na-D-mannopyranuronate		Na-L-gulopyranuronate	
	α	β	α	β
δC1	94.29	93.99	93.26	93.89
δC2	70.81	71.49	64.82	69.14
δC3	70.49	73.26	71.46	71.64
δC4	69.39	68.97	71.32	71.46
δC5	73.33	76.73	67.75	74.77
δC6	177.41	176.67	176.98	176.29

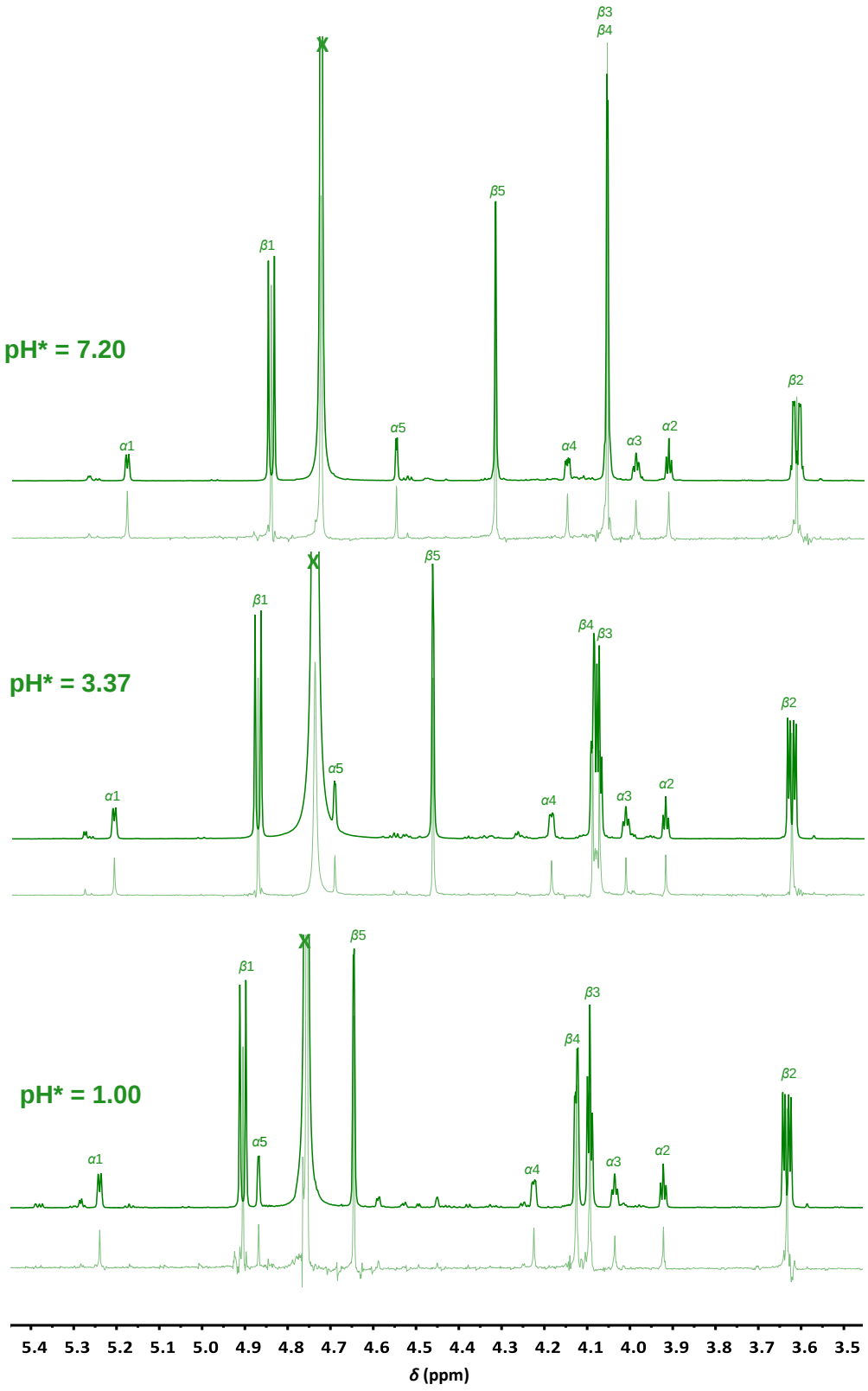

Figure 2.20 ^{1}H NMR spectroscopic assignments of sodium-L-gulopyranuronate in D_2O (0.26 ± 0.02 M) at 600 MHz, and 295 ± 2 K upon addition of DCl (relative to $C_6\underline{H}_6$ in C_6D_6, δ = 7.15 ppm). Dark green traces represent the fully coupled spectra and light green lower traces show the equivalent pure shift experiments.

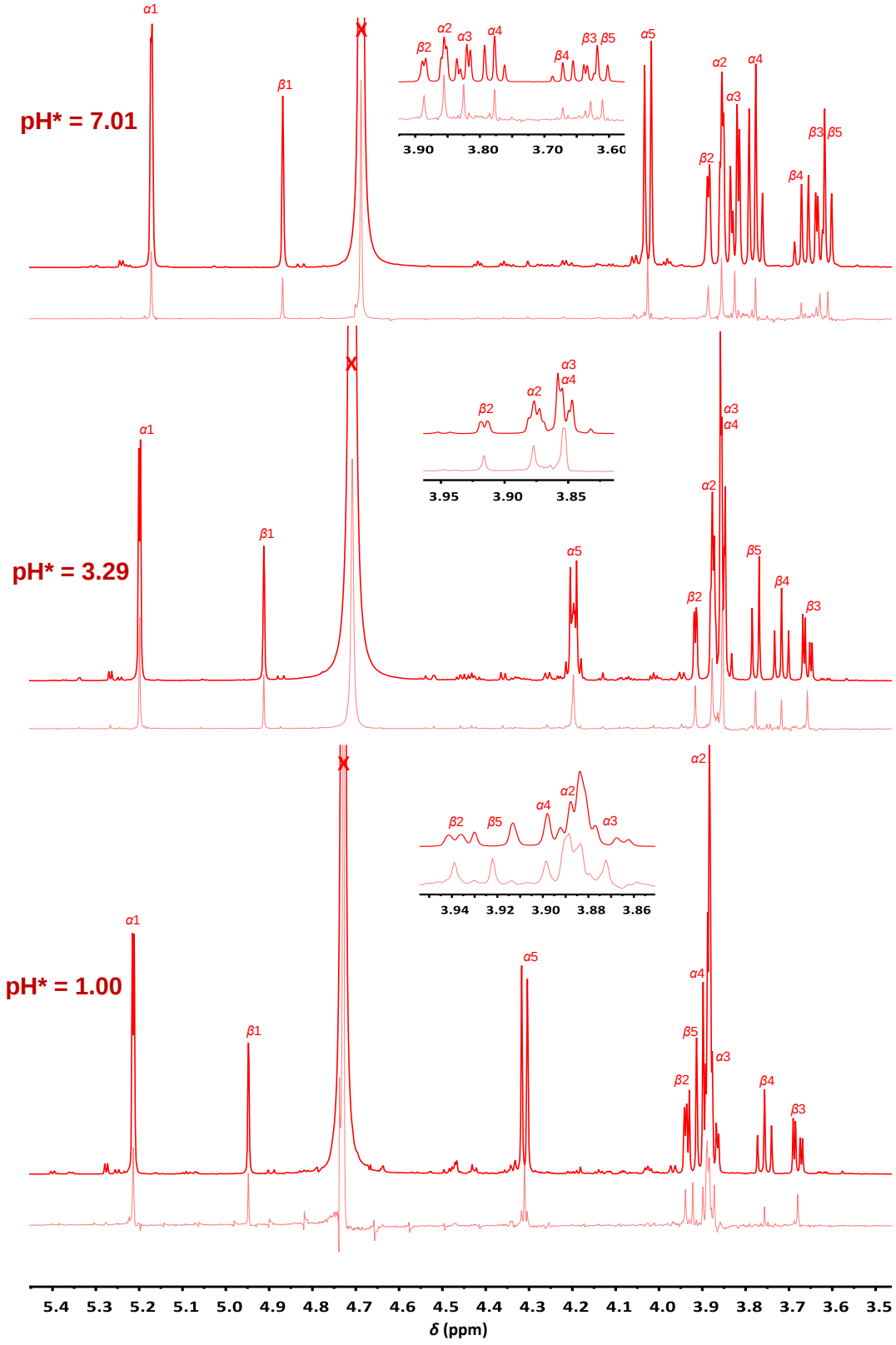

Figure 2.21 ^{1}H NMR spectroscopic assignments of sodium-D-mannopyranuronate in D_2O (0.26 ± 0.02 M) at 600 MHz, and 295 ± 2 K upon addition of DCl (relative to $C_6\underline{H}_6$ in C_6D_6, δ = 7.15 ppm). Dark red traces represent the fully coupled spectra and light red lower traces show the equivalent pure shift experiments.

2.4.1.2 Characterisation of sodium-L-gulopyranuronate by ^{1}H NMR spectroscopy

The NMR spectroscopic signals arising from the pyranoid anomeric protons, αH1 and βH1, can be readily identified (they possess the highest frequency chemical shift of all the protons in their respective ring systems) and then assigned to either the α- or β-anomer according to the arguments that $\delta(\alpha H1) > \delta(\beta H1)$ and $J_{\alpha H1\text{-}\alpha H2} < J_{\beta H1\text{-}\beta H2}$ (based on a Karplus relationship).[38] Hence αH1 (δ = 5.17 ppm, $J_{1,2}$ = 3.7 Hz) and βH1 (δ = 4.84 ppm, $J_{1,2}$ = 8.4 Hz) are assigned and can be used to show that the set of signals with the greater intensity arise from the β-anomer, with [α]:[β] = 0.22 ± 0.01.* Once the two sets of **NaGul** signals have been separated according to their respective intensities, ^{1}H-^{1}H COSY can be utilised to sequentially assign α and β -H2, -H3, -H4, and -H5 (See Figure 2.22).

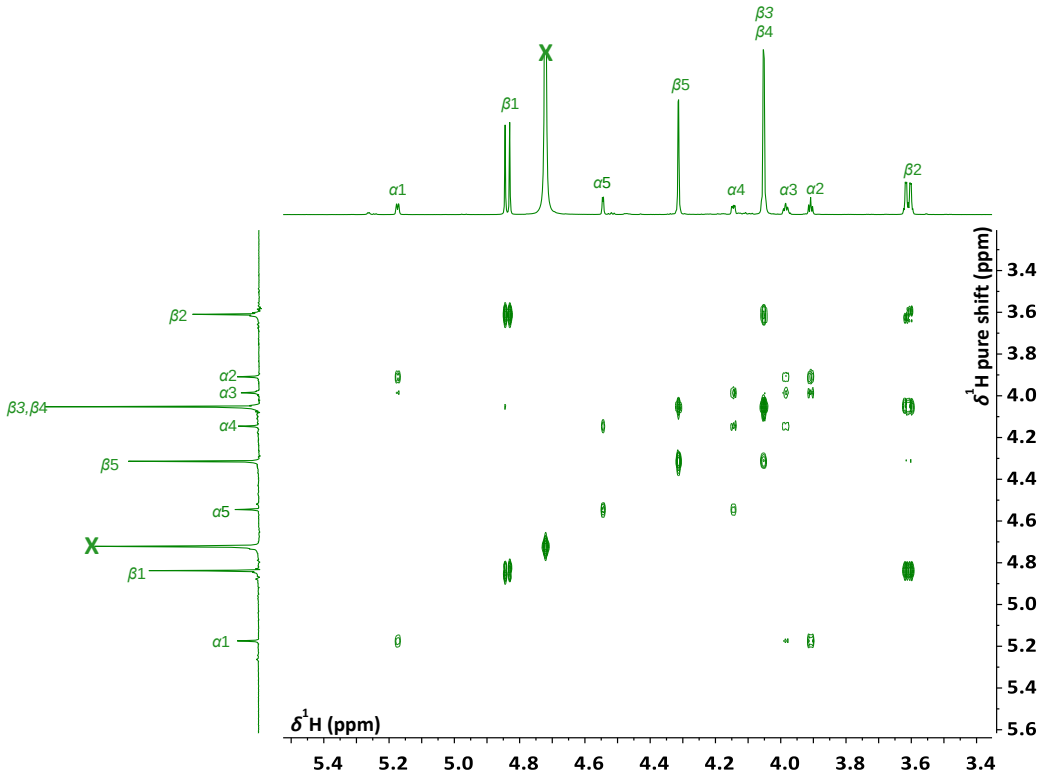

Figure 2.22 ^{1}H-^{1}H COSY spectrum of sodium-L-gulopyranuronate in D_2O (0.26 ± 0.02 M) at 600 MHz, pH* 7.20, 295 ± 2 K (relative to $C_6\underline{H}_6$ in C_6D_6, δ = 7.15 ppm). The horizontal trace is the fully coupled ^{1}H NMR spectrum and vertical trace is the ^{1}H pure shift NMR spectrum.

The full ^{1}H NMR spectral assignments for both anomers of L-gulopyranuronate are given in Table 2.2. The coupling constants recorded at 600 MHz are mostly consistent with those calculated by modified Karplus arguments (see Figure 2.23),[113] though a few cases are worthy of further discussion. The vicinal coupling between H4 and H5 (measured as 0.8 Hz and 1.8 Hz at 600 MHz for the α- and β-pyranose anomers respectively) seem to be lower

*It is worth noting that there are strong similarities between the proton NMR spectra of Na-L-gulopyranuronate and L-gulopyranose both in terms of the chemical shifts, relative intensities, and coupling constants of the signals arising from the anomeric protons, as might be expected.[40,111]

than might be expected (3 - 4 Hz) from their dihedral angle alone. This reduced coupling is, however, a known consequence of the H4 and H5 atoms occupying anti-periplanar relationships to electronegative oxygen atoms.[110,113] In addition, some second order effects are also visible in the guluronate spectrum at pH* 7.20, including i) the virtual coupling of *β*H2 with *β*H3 and *β*H4 to yield a complex multiplet, and ii) when the spectrum was recorded at 400 MHz, a long-range coupling between *α*H1 and *α*H3 of $J \approx 1$ Hz owing to a "W-type" interaction.[39,110] Finally, whilst the resonances for *α*H2, *α*H3, and (at low pH*) *β*H3 are expected to appear as doublets of doublets, they in fact appear as *pseudo*-triplets because in each case they possess two coupling constants that have very similar magnitudes.

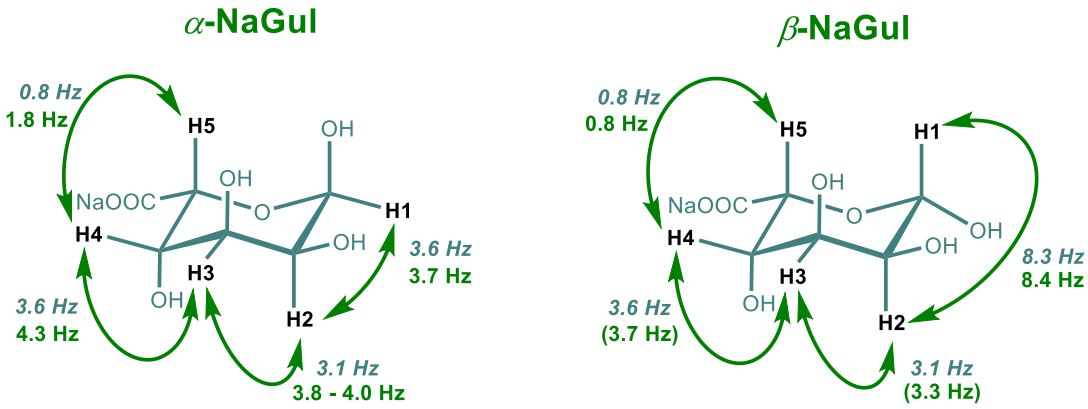

Figure 2.23 Theoretical[113] (grey) and observed (green) coupling constants of sodium-L-gulopyranuronate anomers in D_2O (0.26 ± 0.02 M) measured at 600 MHz, pH* 7.20, and 295 ± 2 K. Values in parentheses were measured at pH* 1.0.

Whilst the assignments provided above for the two gulopyranuronate anomers are in good agreement with the majority of the published data,[14,36,92–94] there have been two sources of confusion in studies by previous authors. The first arises from the fact that *β*H3 and *β*H4 have identical chemical shifts at pH* 7.20 (δ = 4.06 ppm), leading Matsumoto *et al.* to assign this signal to having arisen from a single proton: *β*H3. The discrepancy in the case of Matsumoto and co-workers has most likely arisen as a consequence of the authors' incomplete HDO suppression, which yielded an additional signal of similar intensity to the *β*-protons that was then mistakenly attributed to *β*H5. Following this error, the subsequent assignments of Matsumoto *et al.* are incommensurate with the 2D data recorded for during thesis and provided in Figure 2.22.

A second ambiguity has arisen in attempts to assign the NMR spectroscopic response to *α*H5 of L-gulopyranuronate. Whilst some authors could not observe or did not report a signal from *α*H5,[92–94] Steginsky *et al.*[14] concluded that it was "buried in the 3.91 – 4.15 ppm envelope" (referring to the region of the spectrum encompassing *α*H2, *α*H3, and *α*H4 and a broad peak brought about by the superimposition of signals from *β*H3 and *β*H4). However, in the work presented in this thesis, *α*H5 appears as a well resolved doublet at

pH* 7.20 with δ = 4.55 ppm and $J_{4,5}$ = 1.8 Hz. The discrepancies between this and previous studies can be attributed to differences in the experimental conditions, namely the temperature at which the spectra were acquired. Indeed, by recording the spectrum of Na-L-guluronate at both 25 °C and 45 °C (at 500 MHz and pH* 7.20) the difference is quite marked (see Figure 2.24). At the lower temperature the αH5 signal is clearly visible (as mentioned above), however, at 20 °C higher (the temperature used in the studies of previous authors)[14,94] the same signal coincides with the peak arising from HDO (with the position of the hidden αH5 signal being confirmed in the latter case by reference to the αH4-αH5 cross peak in a simultaneously acquired ^{1}H-^{1}H COSY spectra). Whilst such arguments may appear to be merely semantic, in fact an accurate determination of the position of the αH5 signal is of critical importance in pH sensitive experiments (see Section 2.4.1.6) and metal-ion binding studies (see Chapter 3).

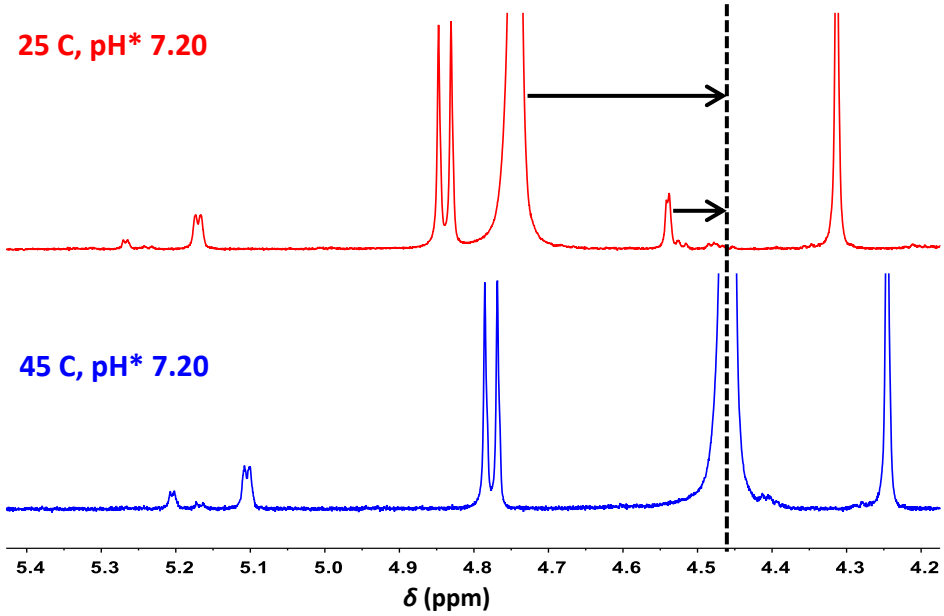

Figure 2.24 ^{1}H NMR spectrum of sodium-L-gulopyranuronate in D_2O (0.05 ± 0.01 M) at 500 MHz, pH* 7.20, and differing temperatures (relative to $C\underline{H}Cl_3$ in $CDCl_3$, δ = 7.26 ppm). The small αH5 signal can be "lost" under the HDO peak at elevated temperatures.

Upon gradual titration of the guluronate solution with DCl from pH* 7.20 to 1.00, there are a number of observable changes (explored in detail in Section 2.4.1.6). As anticipated, the H5 signals undergo the most drastic change, moving to higher frequencies by approximately 0.3 ppm in both cases (with the αH5 signal again coinciding with the HDO peak at pH* ≈ 3.0). The signals for βH3 and βH4 are also found to separate (leaving βH3 at δ = 4.09 ppm and βH4 at δ = 4.13 ppm at pH* 1.00) with the effects of the virtual coupling to βH2 correspondingly disappearing to yield a well-resolved doublet of doublets. Whilst all of the signals move to higher frequencies to different degrees by pH* 1.00 (see Section 2.4.1.6), the relative peak order does not change beyond those stated (see Figure 2.20).

2.4.1.3 Characterisation of sodium-L-gulopyranuronate by ^{13}C NMR spectroscopy

Once an unambiguous set of proton assignments for the anomers of Na-L-gulopyranuronate has been established by ^{1}H NMR spectroscopy, they can be used in the interpretation of the corresponding ^{13}C NMR spectrum *via* ^{1}H-^{13}C HSQC experiments, which for both *α*-**NaGul** and *β*-**NaGul** is a relatively trouble-free exercise (see assignments in Table 2.3 and Figure 2.25). A small complication arises due to the fact that *β*H3 and *β*H4 occur at the same chemical shift at pH* 7.20, and hence the HSQC experiment cannot be used to distinguish which carbon signal is associated to each proton. However, by gradually lowering of the solution's pH* to separate the two superimposed proton signals (see discussion in Section 2.4.1.6) the peaks at δ = 71.46 ppm and δ = 71.32 ppm in the original pH* = 7.20 spectrum can be assigned to *β*C3 and *β*C4 respectively (whilst previous authors left them unassigned).[36] Similarly, *α*C3 and *β*C4 exhibit only a very small difference in chemical shift (< 0.08 ppm), which appears to be susceptible to small changes in starting conditions (pH, concentration, temperature, *etc.*) such that the two peaks are not always well resolved. Again however, gradually lowering the pH* of the solution induces sufficient separation to resolve the peaks and confirm their original position (see Figure 2.25). Lowering the pH* further beyond this point causes the *β*C4 to move to a lower frequency chemical shift than *α*C4, which is in fact the only exchange of relative peak orderings to occur in the ^{13}C NMR spectrum of L-gulopyranuronate upon changing from neutral to acidic conditions.

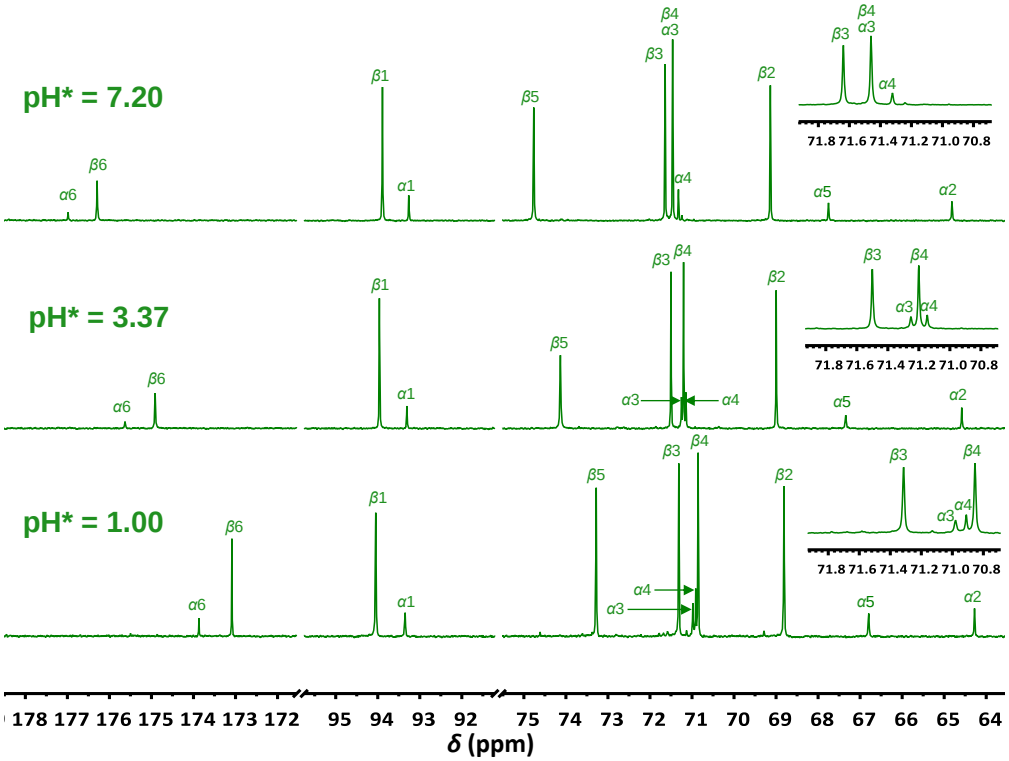

Figure 2.25 ^{13}C NMR spectral assignments of sodium-L-gulopyranuronate in D_2O (0.26 ± 0.02 M) at 600 MHz, and 295 ± 2 K upon addition of DCl (relative to $\underline{C}_6D_6$, δ = 128.06 ppm)

2.4.1.4 Characterisation of sodium-D-mannopyranuronate by ^{1}H NMR spectroscopy

A similar process to that described in Section 2.4.1.2 has been applied in the assignment of the proton NMR spectra of *α*- and *β*-Na-D-mannopyranuronate (see Table 2.2, Figure 2.21, and Figure 2.26). Again, when the anomeric protons have been assigned, two sets of signals corresponding to a [*α*]:[*β*] ratio of 2.02 ± 0.05.* can clearly be identified. At pH* 7.01, whilst *α*H2, *α*H3, *α*H4 and *β*H2 all produce signals very close to each other (in the region 3.74 to 3.95 ppm), at 600 MHz they are all well resolved and do not overlap, allowing ready assignment. However, when the spectrum is acquired at 400 MHz, the same region becomes excessively convoluted, rendering assignment much more difficult. This is the most likely source of the discrepancies between the assignments of the *α*-anomer in the work of Steginsky *et al.*[14] (who performed experiments on lower field instruments) and the work presented here at 600 MHz. *β*H3, *β*H4, and *β*H5 overlap considerably at pH* 7.01 in both the 400 and 600 MHz spectra, though the pure shift experiment assists considerably in locating the centre of the peaks (see Figure 2.21). It is interesting to note that of all of the H5 signals for all of the *α*- and *β*-pyranose anomers of **NaGlc**, **NaGal**, **NaGul** and **NaMan**, the **NaMan**-*β*H5 proton is the most shielded by some margin, with a chemical shift of 3.61 ppm compared to a mean value of 4.08 ppm. This shielding is conceivably an indication of the degree to which the lone electron pair of the anomeric oxygen is available to delocalise into the C5-H5 σ* orbital of the *β*-**NaMan** anomer, something that is relevant to the discussions on the metal binding properties of uronates contained in Chapter 3.

As with L-gulopyranuronate, the observed coupling constants for D-mannopyranuronate are largely in agreement with those predicted from modifications of the Karplus equation (see Figure 2.27).[113] Again, an exception to the expected *J*-values can be found in the case of the vicinal coupling between **NaMan**-*β*H1 and -*β*H2, which should be in the region of 3-4 Hz from geometrical arguments alone but are, in-fact, not observable at 600 MHz (though a value of 1.1 Hz can be measured at 400 MHz). As with $J_{4,5}$ in L-gulopyranuronate, the smaller than expected coupling between H1 and H2 of *β*-D-mannopyranuronate is a product of the anti-periplanar relationship of those two protons with electronegative oxygen atoms around the ring.[110] Finally, whilst *α*H2, *α*H4, and *β*H4 are expected to form doublets of doublets, they in fact appear as *pseudo*-triplets because in each case they possess two coupling constants that have very similar magnitudes.

* It is worth noting that there are strong similarities between the proton NMR spectra of Na-D-mannopyranuronate and D-mannopyranose both in terms of the chemical shift, relative intensities, and coupling constants of the signals arising from the anomeric protons, as might be expected.[40,111]

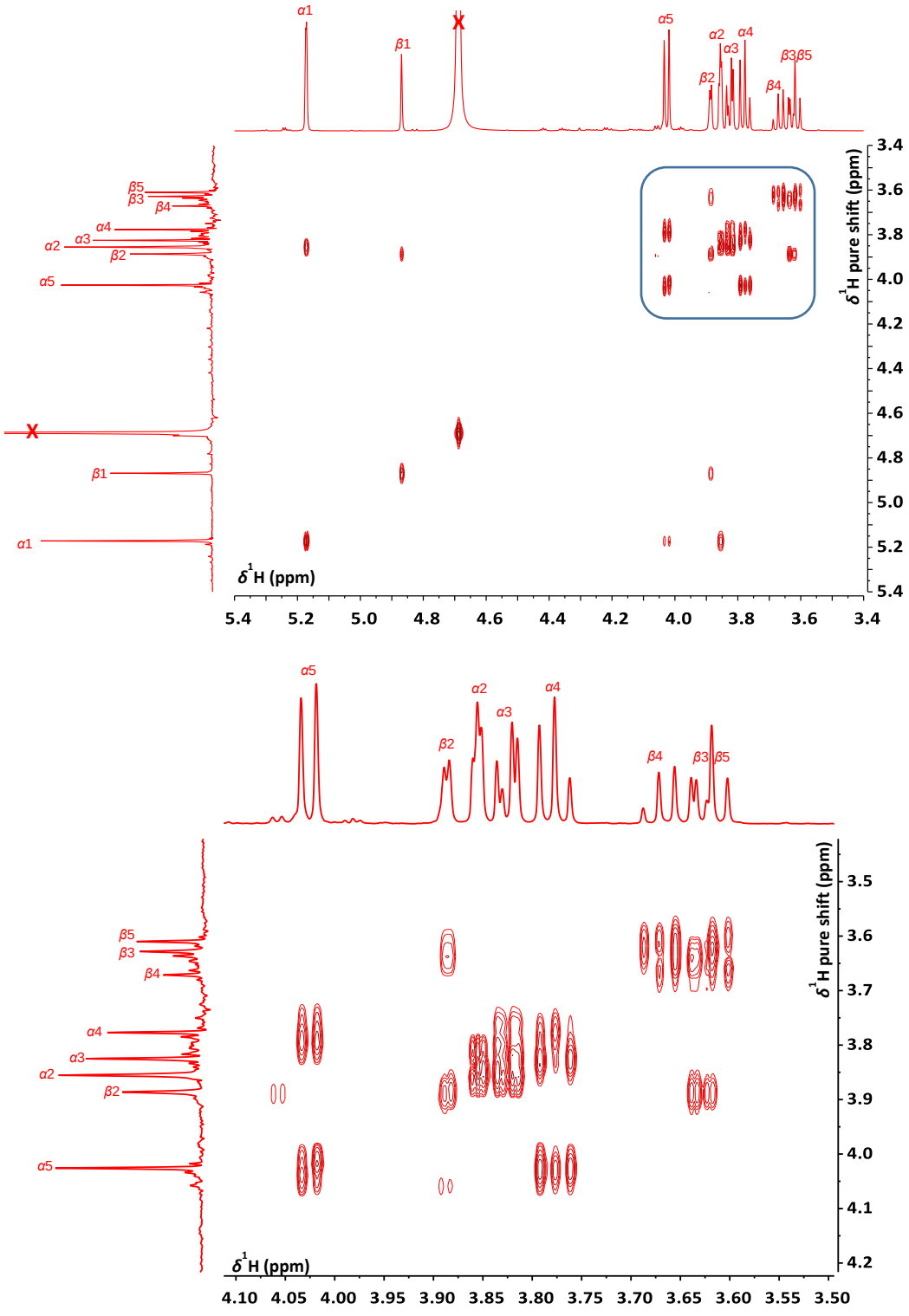

Figure 2.26 ^{1}H-^{1}H COSY NMR spectra (upper) and expansion (lower) of sodium D-mannopyranuronate in D_2O (0.26 ± 0.02 M) at 600 MHz, pH* 7.01, 295 ± 2 K (relative to $C_6\underline{H}_6$ in C_6D_6, δ = 7.15 ppm). The horizontal trace is the fully coupled ^{1}H NMR spectrum and vertical trace is the ^{1}H pure shift NMR spectrum in both cases.

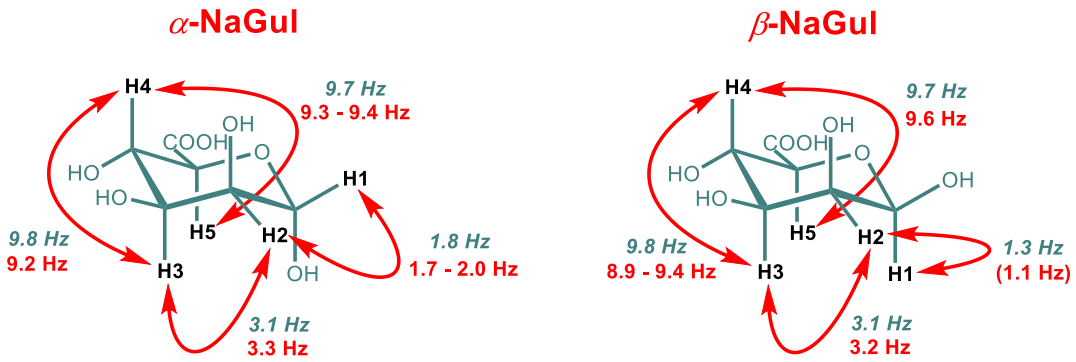

Figure 2.27 Theoretical[113] (grey) and observed (green) coupling constants of sodium-D-mannopyranuronate anomers in D_2O (0.26 ± 0.02 M) measured at 600 MHz, pH* 7.01, and 295 ± 2 K. Values in parentheses were measured at 400 MHz.

Whilst the full effects of lowering the pH* on the acquired Na-D-mannopyranuronate proton NMR spectrum are considered elsewhere (see Section 2.4.1.6), it is useful to note that the *β*H5 peak shifts to higher frequency, leaving the *β*H3 and *β*H4 signals to become clearly resolved (see Figure 2.21). However, below pH* 2.0 the *β*H5 signal moves into the region of *β*H2, *α*H2, *α*H3, and *α*H4, with the effect of making the resulting spectrum much harder to deconvolute. The peak corresponding to *α*H4 also gradually shifts to a slightly higher frequency than that of *α*H3 on moving from pH* 7.01 to pH* 1.00, and the NMR spectrum at pH* 3.4 represents the point at which the peaks possess the same chemical shift, giving rise to the appearance of virtual coupling effects in *α*H5 (see Figure 2.21).

2.4.1.5 Characterisation of sodium-D-mannopyranuronate by ^{13}C NMR spectroscopy

In a similar approach to that adopted for Na-L-guluronate in Section 2.4.1.3, the ^{13}C NMR spectrum of Na-D-mannuronate can be assigned by reference to ^{1}H-^{13}C HSQC spectrum once the corresponding proton NMR spectrum has been fully resolved. As with **NaGul**, the task of assignment can be simplified by the gradual addition of DCl to separate out signals and confirm the assignments of the spectra obtained at pH* 7.01 (particularly in the case of *β*H3/*β*H4 and *β*C3/*β*C4). The full effects of lowering the pH* of the solution in which the spectrum is acquired from 7.01 to 1.00 are considered in Section 2.4.1.6, but it is worth noting that there are few changes in the relative peak ordering, with the *α*C4 signal shifting to a lower frequency than that of *β*C3, and the *α*C2 and *α*C3 signals becoming significantly overlapped. The ^{13}C NMR spectra of **NaMan** obtained at different pH* values are shown in Figure 2.28 and the assignments at pH* 7.01 are fully listed in Table 2.3.

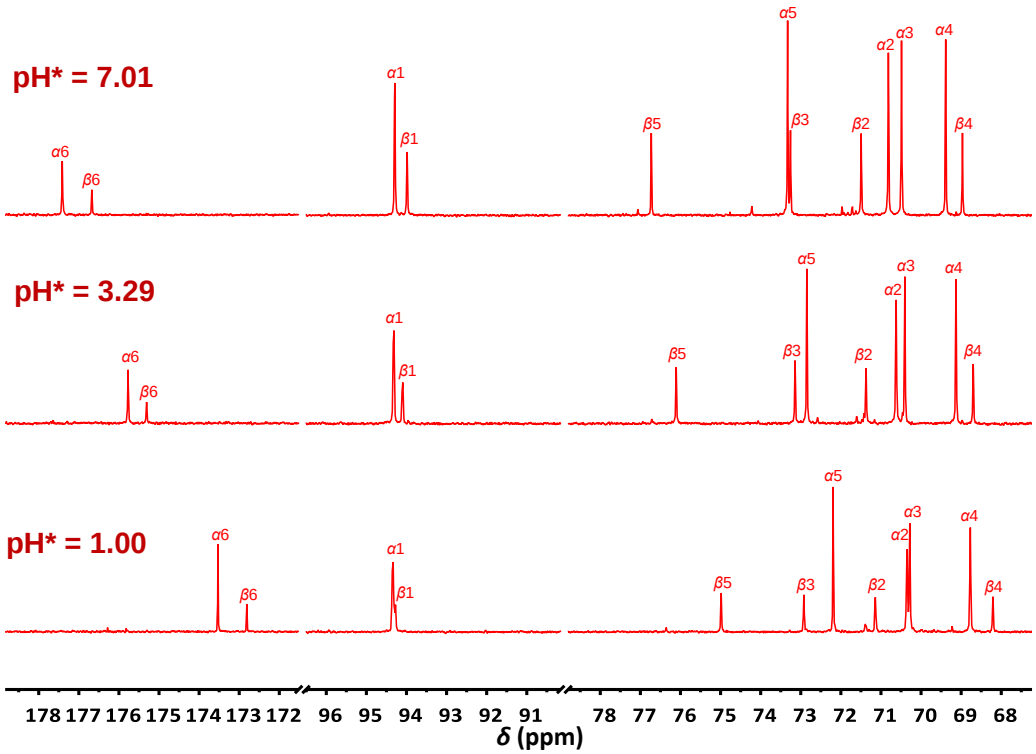

Figure 2.28 ^{13}C NMR spectra assignments of sodium D-mannopyranuronate in D_2O (0.26 ± 0.02 M) at 600 MHz, and 295 ± 2 K upon addition of DCl (relative to $\underline{C}_6D_6$, δ = 128.06 ppm).

*2.4.1.6 Changes to the ^1H and ^{13}C NMR spectroscopic chemical shifts of algal mono-uronates with decreasing pH**

The ^1H and ^{13}C NMR chemical shifts (δ) from analysis of Na-D-mannuronate and Na-L-guluronate (D_2O, 0.26 ± 0.02 M, 295 K) were recorded in the presence of increasing concentrations of DCl (from pH* 7.00-7.20 to pH* 1.00). The changes in δ ($\Delta\delta$) with decreasing pH* for both anomers of the pyranoid forms of the two uronates are shown in Figure 2.29 - Figure 2.32, in an analogous manner to those determined for Na-D-galacotpyranuronate and Na-D-glucopyranuronate by Jaques *et al*.[85] The data presented in Figure 2.29 and Figure 2.31 show that in the case of the ^{13}C NMR spectrum of **NaMan** and **NaGul**, C6 (the carboxylate carbon) experiences the greatest $\Delta\delta$ upon protonation of the uronate (for all of the observed anomers). The result is somewhat unsurprising and the $\Delta\delta$ values of -3 to -4 ppm are in line with those determined for **NaGal** and **NaGlc**.[85] What is surprising, however, is that the C6 signals move to lower chemical shift values with decreasing pH*, corresponding to shielding influences on the nuclei in question, when it might be assumed that the binding of H^+ would have a deshielding effect. The reasons for the size and direction of $\Delta\delta$ are complex and not fully understood.[87,116,117] Previous analyses have invoked linear electric field shift (LEFS) theory to help explain the observed trends in δ upon protonation of various functional groups, but such an advanced analysis is not required here.[118] It is sufficient to note that the shifting of C6 in all cases corresponds to the degree of protonation of the uronates and, hence, can be used to derive a value for the logarithmic acid dissociation constant (pK_a) (see Section 2.4.2.1).

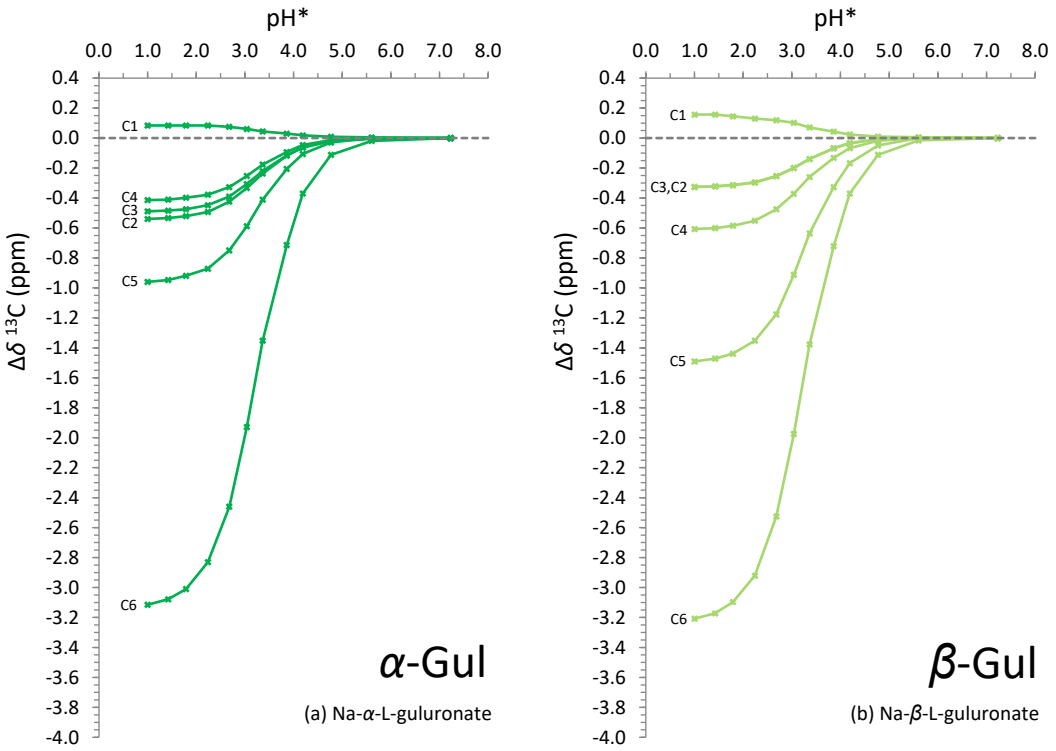

Figure 2.29 Plots of Δδ in the ^{13}C NMR spectra *versus* pH* for the sodium salt of (a) α- and (b) β-L gulopyranuronate in D_2O (0.26 ± 0.02 M) at 600 MHz, and 295 ± 2 K. The starting pH* is 7.20, which is lowered by addition of small volumes of DCl. Horizontal error bars of ± 0.03 pH units omitted for clarity.

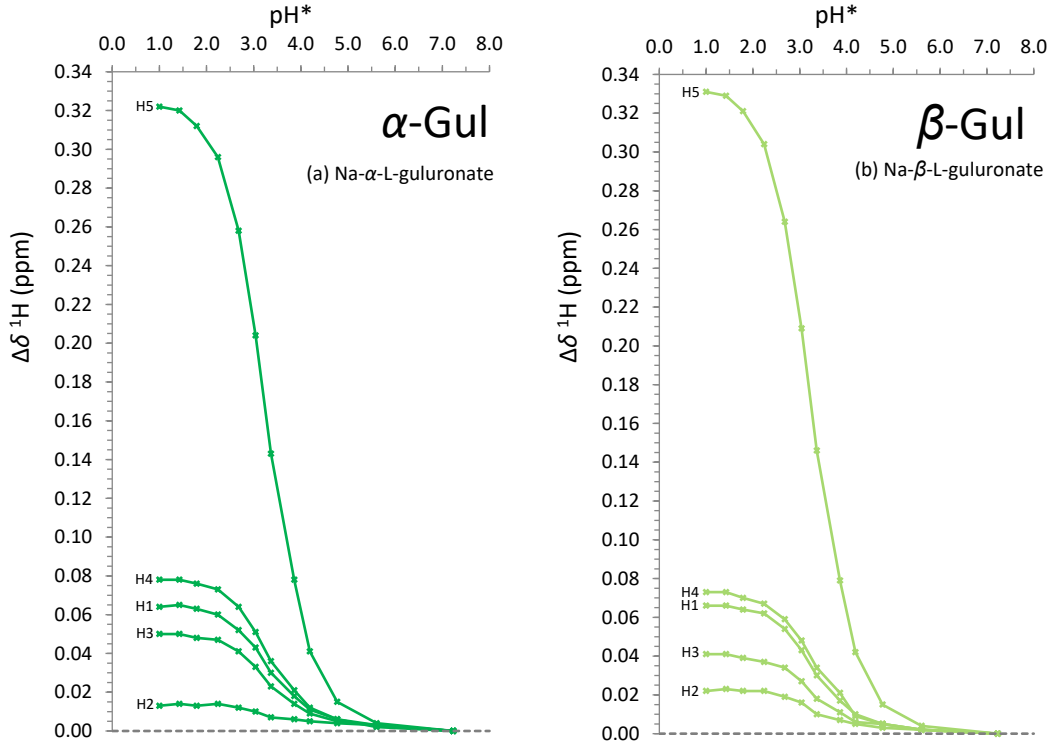

Figure 2.30 Plots of Δδ in the ^{1}H NMR spectra *versus* pH* for the sodium salt of (a) α- and (b) β-L-gulopyranuronate in D_2O (0.26 ± 0.02 M) at 600 MHz, and 295 ± 2 K. The starting pH* is 7.20, which is lowered by addition of small volumes of DCl. Horizontal error bars of ± 0.03 pH units omitted for clarity.

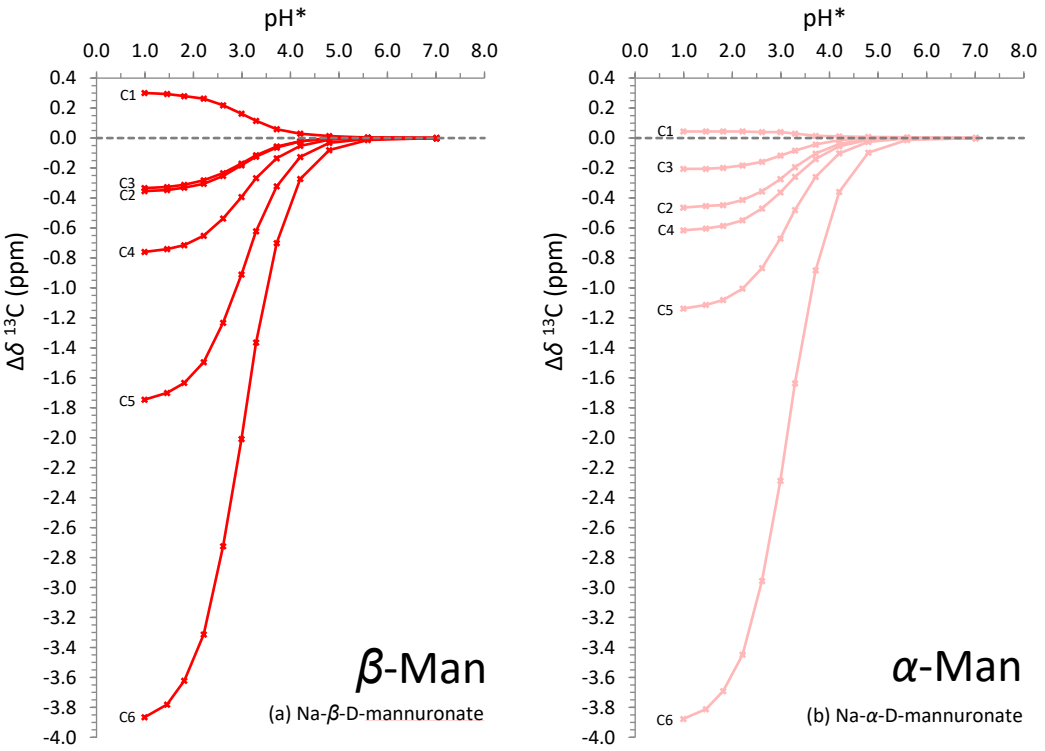

Figure 2.31 Plots of Δδ in the ^{13}C NMR spectra *versus* pH* for the sodium salt of (a) β- and (b) α-D-mannopyranuronate in D_2O (0.26 ± 0.02 M) at 600 MHz, and 295 ± 2 K. The starting pH* is 7.01, which is lowered by addition of small volumes of DCl. Horizontal error bars of ± 0.03 pH units omitted for clarity.

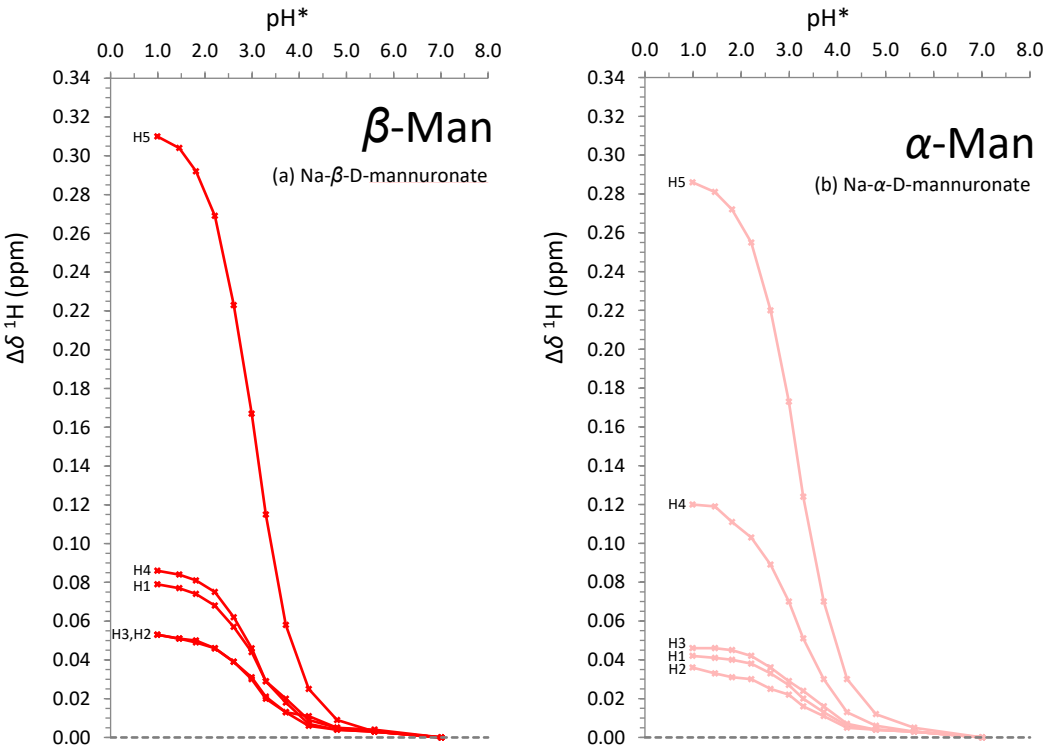

Figure 2.32 Plots of Δδ in the ^{1}H NMR spectra *versus* pH* for the sodium salt of (a) β- and (b) α-D-mannopyranuronate in D_2O (0.26 ± 0.02 M) at 600 MHz, and 295 ± 2 K. The starting pH* is 7.01, which is lowered by addition of small volumes of DCl. Horizontal error bars of ± 0.03 pH units omitted for clarity.

The Δδ values determined for the ring-carbon nuclei of **HGul** and **HMan** upon changing pH* found roughly to decrease with increasing through-bond distance from the carboxylate, such that Δδ C5 > C4 > C3 ≈ C2 > C1, mirroring the trend observed for **NaGal** and **NaGlc**.[85] Interestingly, both the results presented here and those of Jaques *et al.*, indicate that C1 is the only carbon nucleus to be deshielded upon lowering the pH. This deshielding of C1 is presumably a consequence of increased electron withdrawal and/or decreased electron donation by the anomeric oxygen neighbouring the carbon.

For the analogous analysis of Δδ in the ^{1}H NMR spectra of **NaGul** and **NaMan** on lowering the pH*, pure shift experiments were found to be particularly helpful, as they facilitated rapid measurement of the centre of a particular peak without the need to deconvolute splitting patterns. Figure 2.30 and Figure 2.32 show that, unlike the ^{13}C NMR experiments, the ^{1}H Δδ values from all protons in both pyranose anomers of **NaMan** and **NaGul** are positive in all cases with increasing [D_3O^+], corresponding to a deshielding of these nuclei. The magnitudes of the Δδ values again correspond roughly to the distance of the proton from the acidic group, such that Δδ H5 > H4 > H1> H3 > H2, in further agreement with the work of Jaques *et al.* for the **NaGlc** and **NaGal** systems.[85] It is interesting to note the trends in ^{1}H NMR spectroscopic Δδ values observed for increasing concentrations of deuterium chloride are in contrast with those determined for the addition of metal chlorides, with the latter effect being heavily dependent on the particular cation and uronate anomer under investigation (see Chapter 3). Finally, whilst a systematic study was not conducted, no obvious changes in the ^{1}H-^{1}H scalar coupling values (*J*) were observed in the ^{1}H NMR spectra on traversing the pH* scale, aside from those noted in Sections 2.4.1.1 and 2.4.1.4 arising from varying second order effects as the relative positions of the signals change.

2.4.2 Behaviour of uronic acids in neutral and acidic solution

2.4.2.1 Determination of pK_a of algal uronic acids

As was discussed in Section 2.4.1.6, the Δδ values determined by ^{13}C NMR spectroscopy for C6 (the carboxylate carbon) of a particular uronate can be plotted against pH* to determine the logarithmic acid dissociation constant (pK_a) of that species (with full details of the calculation being provided in Section 2.7.2.2).[119] This NMR titration-based methodology is able to resolve individual pK_a values for each of the anomers studied, in contrast to conventional potentiometric methods that essentially give a "weighted average" of all species in solution possessing dissociation constants within a similar range.[84] Of course, the disadvantage of NMR-based methods in this regard, is that the activity of a functional group in D_2O may differ substantially from that in H_2O.[119] However, Krężel and Bal have derived semi-empirical methods to convert a measured pK_a(H*) (the pK_a of a compound as measured in D_2O with an electrode calibrated in H_2O) into an equivalent pK_a(H) (the pK_a of a compound in H_2O).[120] The results of the measurements of pK_a(H*), pK_a(H), and pK_a(soln) (the pK_a obtained by calculating an average of the individual pK_a values of all species in solution weighted by their relative concentration) are reported in Table 2.4 for both anomers of the pyranose forms of **HMan** and **HGul**.

Table 2.4 pK_a values for individual anomers of algal mono-pyranuronic acids and the weighted average pK_a of their resulting solutions.

Uronic acid	Relative concentration[a]	pK_a (H*)	pK_a (H)[b]	pK_a (soln)[c]	pK_a (soln)-lit[75]
$^1C_4$-α-L-gulopyranuronic acid	18 %	3.26	3.45	3.44	3.65
$^1C_4$-β-L-gulopyranuronic acid	82 %	3.25	3.44		
$^4C_1$-α-D-mannopyranuronic acid	70 %	3.13	3.33	3.29	3.38
$^4C_1$-β-D-mannopyranuronic acid	30 %	3.00	3.21		

[a]Determined at a point close to the pK_a
[b]Calculated from the Krężel and Bal[120] equation: $pK_a(H) = 0.929pK_a(H^*) + 0.42$. Standard error ± 0.03
[c]Omitting small contributions from furanuronic acids. Standard error ± 0.03.

The results presented in Table 2.4 indicate that, whilst the two anomers of L-gulopyranuronic acid have virtually the same $pK_a(H)$ (approximately 3.25), the β-anomer of D-mannopyranuronic is a slightly stronger acid than its α-counterpart by between 0.7 to 0.19 pK_a units. From the calculated $pK_a(H)$ values, the corresponding $pK_a(soln)$ values for **HGul** and **HMan** were found to be 3.44 ± 0.03 and 3.29 ± 0.03, respectively, slightly lower than those derived by potentiometric titration by Haug (3.65 for **HGul** and 3.38 for **HMan**).[75] Interestingly, Wang *et al.*, who performed a similar NMR-based titration on α- and β-glucopyranuronic acids, also reported slightly lower values than those that they had determined by potentiometric means under similar conditions.[84] Regardless of the absolute values, the relative order of the acidities of **HGul** and **HMan** is preserved with a difference in $pK_a(soln)$ of 0.15 ± 0.06 units. It is worthy of note that the two constituent monomers of alginic acid (α-**HGul** and β-**HMan**) have a $pK_a(H)$ difference of between 0.24 ± 0.06, which is large enough to substantially influence the properties of kelps possessing alginates of differing mannuronate:guluronate ratios (**M**:**G**).[67,75,76,121–123] Whilst an exact explanation of the varying acidities of uronic acids has eluded explanation, Kohn and Kovác noted that a *trans*-relationship between mutually equatorial carboxylate and C4 hydroxyl groups favours lower pK_a values, whilst a *cis*-relationship with an axial C4 hydroxyl yields weaker acids.[86] However, the same authors also noted the possibility that intermolecular hydrogen bonding may play an equally important role in determining the pK_a of a uronic acid in addition to any intramolecular stereochemical influences.

2.4.2.2 Configurational equilibria of algal uronic acids in neutral and acidic solutions

At pH* 7.01, the ^{1}H NMR spectrum of D-mannuronic acid contains signals in the ratio 100:50:6:4 that correspond to a [pyranose]/[furanose] value of 15.0 ± 1.0 and, of the pyranose configurations, a [α]/[β] value of 2.00 ± 0.07. Interestingly, literature values for the equilibria of D-mannose measured under similar conditions show a significantly different [pyranose]/[furanose] value (111.1), but a very similar ratio for the [α]/[β] ratio of the pyranose anomers (1.90).[37] Hence, whilst the difference in energy between pyranose and furanose configurations is much larger in the case of D-mannose compared to Na-D-mannuronate, the relative stability of the pyranose anomers with respect to each other is very similar for both compounds. Upon lowering the pH* from 7.0 to 1.0 with DCl, the peak intensities of Na-D-mannuronate change to 100:42:8:6, yielding a [pyranose]/[furanose] value of 10.1 ± 0.09 and, for the pyranose configurations, a [α]/[β] value of 2.38 ± 0.05, with the changes mostly occurring at values close to the measured pK_a (see Section 2.4.2.1). This very slight relative stabilisation of the α-pyranose anomer with respect to the β-anomer of **HMan** is also found to occur for **HGal** and **HGlc** when the pH is lowered in a similar fashion (see experimental results in Chapter 3). Whilst such changes are small, the changes for **HGul** are found to be even smaller. **HGul** gives rise to signals in the ratio 100:22:6:3 at pH* 7.2, and 100:23:5:4 at pH* 1.0 corresponding to [pyranose]/[furanose] values of 13.6 ± 0.9 and 13.7 ± 0.9, respectively and, for the pyranose configurations, [α]/[β] values of 0.22 ± 0.01 and 0.23 ± 0.01, respectively. Such values are also fairly close to those measured by Angyal for L-gulose at pH 7.0 ([pyranose]/[furanose] = 32.3, [α]/[β] = 0.20),[37] which further demonstrates the extreme instability of the α-pyranose configuration of the gulose stereochemistry regardless of pH.

The results presented in this section therefore demonstrate relatively modest changes to the configurational equilibria of uronic acids with upon variation of the pH of the solution. The findings are worthy of note when considering the effects of metal-ion coordination to the same uronates, which, as is shown in Chapter 3, can cause much larger perturbations to the relative energies of the various configurations.

2.4.2.3 Lactonisation of algal uronic acids

Whilst lactones of algal uronic acids (**HMan** and **HGul**) are known to exist (see discussion in Section 2.2.3), their formation under thermal and hydrothermal conditions has never been studied systematically. In order to compare the lactonisation behaviour of **HMan** and **HGul** (and **HGal** and **HGlc** also), 0.05 M solutions of their respective sodium salts were subjected to various heating regimes. The solutions were then analysed by ^{1}H NMR spectroscopy where, in some cases, two new sets of peaks could be discerned in addition to those arising from the α- and β-pyranose and furanose signals (see Figure 2.33), corresponding to the formation of α- and β-furanurno-6,3-lactones (see Figure 2.34). Whilst overlapping in the NMR spectra prevented a full analysis of the newly formed lactone signals, tentative assignments of the peaks are provided in Section 2.7.3, which facilitated an approximate %acid:%lactone ratio to be calculated by integration. Additional evidence for lactonisation in the uronate/uronic acid solutions was provided by electrospray ionisation mass spectrometry (ESI-MS), in which a signal of *m/z* 199.0 (corresponding to $[C_6H_8O_6 + Na]^+$) was prominent only for samples displaying peaks corresponding to lactones in their ^{1}H NMR spectrum.

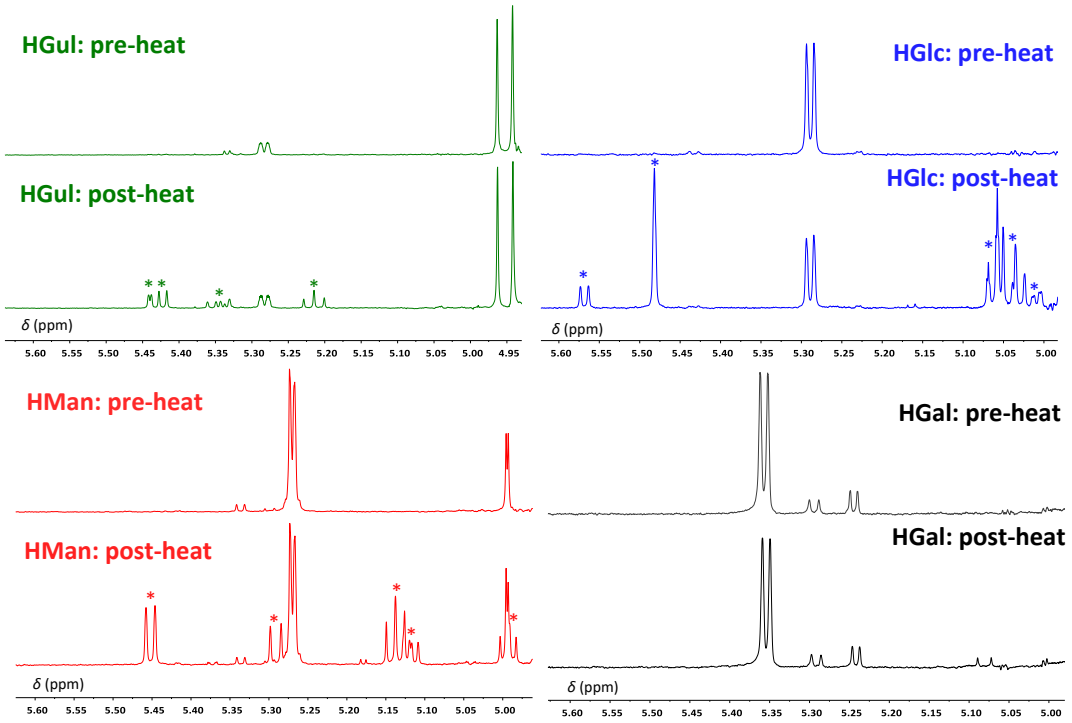

Figure 2.33 Anomeric region of the ^{1}H NMR spectra (400 MHz) of various mono-uronic acids in D_2O (0.05 M) at pH* 1.0 before and after heating for 12 hours at 60 °C. Starred peaks correspond to furanurono-6,3-lactones.

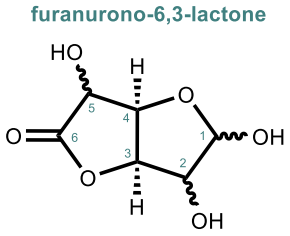

Figure 2.34 The generic structure of a bicyclic furanurono-6,3-lactone

The results from the lactonisation experiments are summarised in Table 2.5. Here it was found that no lactones form in the uronate solutions at pH* 7.0 (Experiment **A**), even upon heating for 12 hours at 60 °C (Experiment **B**). Upon lowering the pH* to 1.0 and allowing the samples to stand for 12 hours at room temperature (after which point the pyranose-furanose and associated anomeric equilibria had settled), no lactones were detected in any sample (Experiment **C**). However, after 24 hours at room temperature and pH* 1.0 small peaks appeared in the spectra of **HGlc**, **HMan**, and **HGul**, which, upon standing for five weeks (Experiment **D**), gave equilibrium %acid:%lactone ratios of 83:17, 80:20, and 96:4, respectively. For **HGlc**, a literature value of 80:20 derived from polarimetry data under similar conditions to Experiment **D** is in good agreement with the figure reported here.[1] Further heating of the solutions under experimental conditions **E** and **F** pushed the equilibrium increasingly towards lactone formation in all but solutions of **HGal**, which

displayed no new saccharide peaks (see Figure 2.33). The results of Experiments **E** and **F** are also in good agreement with previous polarimetry studies, which determined a %acid:%lactone value of 60:40 for a sample of **HMan** heated at 80 °C for 19.5 hours (but unreported pH),[26] and a ratio of 40:60 for a sample of **HGlc** heated at 100 °C for 2 hours at pH 2.5 – 3.5.[1]

It is interesting to note that, under the conditions of Experiment **F**, the uronic acid solutions were found to yellow, with the precipitation of brown humin substances and the evolution of a furfural-like odour being indicative of the irreversible degradation of the samples (discussed further in Appendix C). The hydrothermolysis of the uronic acids observed here demonstrates that such a process need not necessarily proceed *via* initial lactone formation,[5,6] as **HGal** clearly undergoes degradation but, for the reasons outlined in Section 2.2.3.5 and evidenced by the results in Table 2.5, clearly does not undergo lactonisation. Following Experiment **F**, the samples were left to stand at room temperature, and eventually returned to the same equilibrium positions as was found following Experiment **C**. Neutralisation of the solutions after this final stage induced complete hydrolysis of any lactones present and returned the uronates to their initial state found following Experiment **A**.

Table 2.5 Lactonisation of mono-uronic acids under various conditions

	Experiment conditions	**A**	**B**	**C**	**D**	**E**	**F**
	Duration (hours)	Eq[a]	12	12	Eq[a]	12	60
	Temperature (°C)	RT[b]	60	RT[b]	RT[b]	60	90
	*pH**	7.0	7.0	1.0	1.0	1.0	1.0
Approximate constitution of solution (% acid : % lactone)	**HGlc**	100:0	100:0	100:0	83:17	64:36	48:52[c]
	HMan	100:0	100:0	100:0	80:20	68:32	48:52[c]
	HGul	100:0	100:0	100:0	96:4	83:17	71:29[c]
	HGal	100:0	100:0	100:0	100:0	100:0	100:0[c]

[a] The constitution of the solutions at equilibrium at room temperature were determined by allowing the samples to stand for at least 5 weeks
[b] RT = room temperature
[c] Yellowing of the solution was observed along with the formation of solid humins

Through Experiments **A**-**F** it is possible to demonstrate the similarities in the lactonisation behaviour of **HGlc** and **HMan** as, under all of the conditions investigated, both compounds retain a similar %acid:%lactone ratio. In contrast, **HGul** does not appear to be as readily

susceptible to lactonisation, and **HGal** is completely resistant to the reaction. With the exception of **HGal**, which has been discussed in Section 2.2.3.5, it is not immediately clear as to what stereochemical arrangements particularly stabilise or destabilise the lactone structures, and a more detailed theoretical interpretation would most likely need to incorporate the interactions of locally coordinated water molecules.[124,125] Finally, these results demonstrate the necessity for the uronic acid to be protonated in order for lactonisation to occur as all of the lactones were hydrolysed when solutions were returned to pH* 7.0.

2.5 Chapter summary and conclusions

The algal mono-uronic acids (L-guluronic and D-mannuronic acids) were successfully isolated as their sodium salts in solutions of D_2O. Subsequent analysis using a host of NMR experiments (including 2D and pure shift methods) facilitated full assignments of the ^{1}H and ^{13}C NMR signals arising from $^{1}C_4$-*α*- and $^{1}C_4$-*β*-L-gulopyranuronate, and $^{4}C_1$-*α*- and $^{4}C_1$-*β*-mannopyranuronate. Whilst the pH of the solution was found to have profound effects on the chemical shifts of signals in both the ^{13}C and ^{1}H NMR spectra of both **HGul** and **HMan**, the aldose-type equilibria were not significantly altered in going from pH* 7.0 to pH 1.0. In this regard, $^{1}C_4$-*β*-L-gulopyranuronic acid and $^{4}C_1$-*α*-mannopyranuronic acid were found to be the most stable configurations in their respective solutions under all of the conditions tested, (just as has been demonstrated elsewhere for their parent aldoses).[37]

However, in contrast to aldose chemistry, both **HMan** and **HGul** exhibited considerable lactonisation at pH values below their pK_a. In the case of **HMan**, the equilibrium [acid]:[lactone] ratio was around 80:20 at pH* 1.0 (very similar to **HGlc** under the same conditions), whilst the equivalent value for **HGul** was 96:4. In all three cases, heating the solutions at low pH values increased the concentration of lactones, whilst returning the samples to pH* 7.0 hydrolysed the cyclic ester to yield the free acid form (see Figure 2.35). It is expected that similar lactonisation behaviour may occur in the anhydrous pyrolysis of uronides described later in this thesis. In contrast to all of the other uronic acids, **HGal** did not undergo lactonisation under any of the conditions tested, as it is stereochemically prevented from doing so.

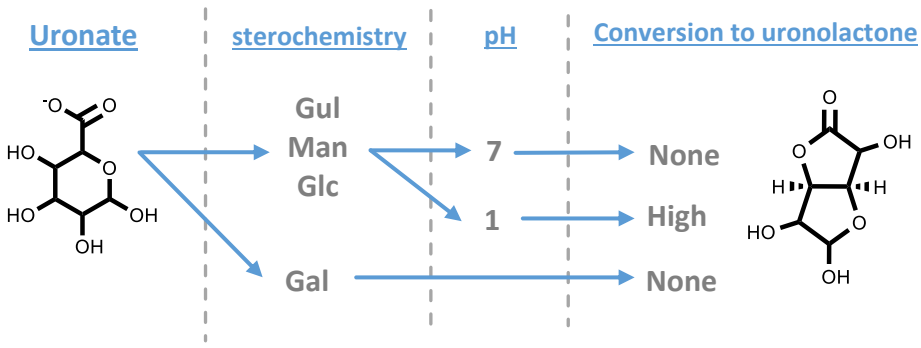

Figure 2.35 Summary of the hydrothermal lactonisation of various mono-uronates

Finally, titrations of **NaGul** and **NaMan** (as followed by NMR spectroscopy) enabled calculations for the pKa values of the individual anomers of L-gulo- and D-mannopyranuronic acids. Here it was found that, whilst *α*- and *β*-**HGul** possess virtually the same pK_a (≈ 3.45 and 3.44 respectively), *β*-**HMan** (pK_a ≈ 3.21) is more acidic than the *α*-**HMan** (pK_a ≈ 3.33). Whilst the reasons behind the variations in pK_a of the various configuration are unclear, the large difference between *α*-**HGul** and *β*-**HMan** has implications for the observed acid dissociation behaviour of alginates and alginate-rich kelps.

Ultimately, the work in this chapter has not yielded the solid-state samples of **HMan** and **HGul** (or their salts) that would be required to conduct the types of micropyrolysis experiments described in Chapter 4 of this thesis. However, preparing the algal mono-uronates in the solution-state, and characterising them by NMR spectroscopy, will facilitate a study of their aqueous behaviour, which, as Chapter 3 demonstrates, can also provide valuable insight into metal-binding by alginates (and hence, kelp). It is also hoped that the solution-state characterisation data provided here will also allow for more involved studies of uronide hydrothermolysis in the future.

2.6 Further work

2.6.1 Crystallisation of algal mono-uronic acids and their salts

Crystallisation of a saccharide facilitates study of the molecular structure by X-ray diffraction analysis (amongst other methods). Whilst such an approach has been used to great effect in the analysis of **HGlc** and **HGal** (and their salts),[126–132] only one structure has been reported in the case of the algal mono-uronic acids.[35] Whilst some authors have reported conditions for the crystallisation of various forms of the free acid and salt forms of **HGul** and **HMan**,[20,27,33,34,54] attempts to replicate their work in the preparation of this thesis were unsuccessful. Hence, it is recommended that further effort be dedicated to obtaining and characterising such algal uronate crystals, and additional discussions are provided in Appendix C to this end. Anomerically pure crystalline samples of algal mono-uronic acids would be particularly useful as they offer the potential to follow the kinetics of equilibrium formation by, for example, NMR spectroscopy.[92] Single crystalline material would also serve as a well-defined starting materials for the thermal analysis of mono-uronic acids or uronate salts (see Chapter 4).

2.6.2 Further characterisation of furanose and acyclic forms of algal mono-uronic acids by NMR spectroscopy

Furanose and acyclic forms of uronic acids are likely intermediates in uronolactone formation (see Figure 2.36), and hence assignment of their NMR spectra could prove to be insightful. Whilst signals clearly corresponding to the furanoid configurations of **HGul** and **HMan** were identified in the ^{1}H NMR spectra of the algal mono-uronic acids, such peaks were of a very low intensity compared to those arising from the pyranoid forms. The high signal density of the spectra coupled with the generally increased complexity for assigning furanose anomers[40] makes full assignment of the proton and carbon signals of algal furanuronic acids a difficult task. Increased acquisition times and the use of more highly

concentrated uronate solutions may better increase the chances of providing a successful set of assignments for the furanose configurations, as well as potentially revealing signals corresponding to the high energy acyclic forms of the uronic acids. Ultimately, however, the task of fully assigning the NMR spectra of algal mono-furanuronic acids will best be achieved by preparing anomerically pure crystals of the compounds (see Section 2.6.1) and acquiring data immediately after their dissolution (and hence before substantive speciation has occurred).[37]

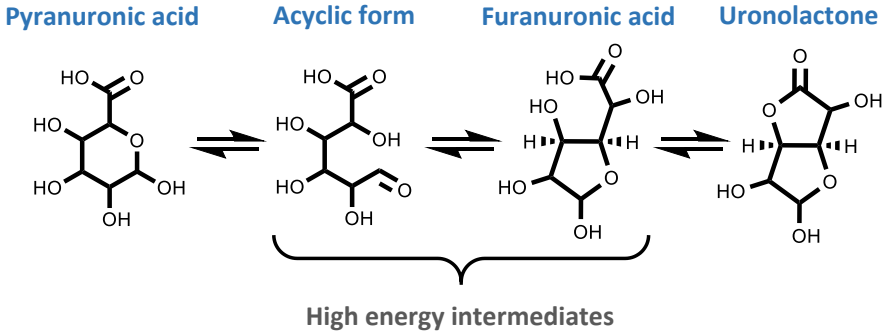

Figure 2.36 Likely intermediates in the solution-state hydrothermal conversion of uronolactones from pyranuronic acids

2.6.3 Computational analysis of algal mono-uronic acids

Whilst computational investigation have been carried out elsewhere to model the solution state properties of uronides (particularly with respect to their metal binding properties),[87,133–137] the anomeric equilibria described in this chapter have not been studied. Preliminary experiments utilising density functional theory (DFT) were attempted in order to replicate the results determined for the **HMan** and **HGul** *α*/*β*-pyranose interconversion, however it soon became apparent that the assembly of locally bound water molecules was not trivial and that a far more in-depth theoretical treatment would be required in order to fully account for the energy differences between the various configurations.[124,125] Further computational investigations may also be of use in attempting to define the electronic and steric traits that favour (and disfavour) lactone formation from the parent uronic acid.

2.6.4 Utilising aqueous algal mono-uronic acids in model compound studies on the hydrothermal conversion of alginates and kelps

Part of the motivation for isolating solutions of algal mono-uronic acids was their utilisation as model compounds for the hydrothermal conversion of kelps and alginates to platform chemicals.[71–73,96–98] Whilst an extensive hydrothermolysis study was not carried out in the preparation of this thesis, Appendix C describes the preliminary steps taken in order to facilitate such investigations in the future (including a literature review, testing of analytical procedures, and the isolation of reductic acid – a key intermediate in uronide degradation chemistry). The work in Appendix C, clearly indicates that the NMR spectroscopic data described in this chapter will be invaluable in the optimisation of the hydrothermolysis of alginate-rich kelps.

2.7 Materials and methods

2.7.1 Isolation of solutions of algal mono-uronic acids

2.7.1.1 Hydrolysis of alginic acid to yield mono-uronic acids

A method based on that of Isbell and Frush[54] was used to hydrolyse alginic acid (purchased from Sigma Aldrich with a reported **M**:**G** ratio of 1.6). Alginic acid (8.0 g, 46 mmol equivalents of mono-uronic acids) was added to ice cold H_2SO_4 (10.0 mL, 18.0 M) and stirred, giving rise to a thick brown paste. The paste was left at 5 °C for 18 hours. Ice cold deionised H_2O (800 mL) was added slowly to the paste with stirring, before the solution was heated at reflux at 100 °C for 16 hours. The resulting slurry was cooled to room temperature for 1 hour, before $Ba(OH)_2$ was added to attain a pH of 2.35 - 2.40. The resulting $BaSO_4$ precipitate was removed *via* filtration and the retentate washed with distilled water (2 × 100 mL). The solution and washings were combined and filtered through activated carbon (approximately 5.0 g) giving rise to a colour change from amber to pale yellow. The yellow solution was further neutralised to pH 7.5 – 8.0 by the addition of 2.0 M NaOH, giving rise to a brown coloured solution. Upon standing for 24 hours and re-adjusting the pH to 7.0, the solution was filtered and concentrated *in vacuo* (40 °C, 40 mbar) to approximately 10 mL to afford a cloudy syrup that was clarified by filtration through a 0.45 μm nylon syringe filter. AcOH (40 mL, 17.4 M) was added to the syrup to precipitate a dull grey solid that was recovered by centrifugation (3000 rpm, 15 min). The solid was washed with acetone (3 × 40 mL) with recovery each time by means of centrifugation (3000 rpm, 15 min). The off-white powder was dried *in vacuo* (40 °C, 40 mbar) to afford approximately 1.4 – 1.6 g of crude hydrolysate, which was stored at 5 °C until use.

2.7.1.2 Separation of mono-uronic acids by anion exchange-chromatography

A scaled-up method based on the chromatographic procedures of Haug and Larsen[107] and Larsen *et al.*[94] was developed to separate the uronic acids obtained through the hydrolysis of alginic acid in Section 2.7.1.1 based on their differing pK_a values.

An anion exchange column was prepared as follows: Approximately 400g of Dowex® 1X8 anion exchange resin (Cl^- form, 200 – 400 mesh) was washed sequentially with deionised H_2O (2 × 500 mL), NaOH (2.0 M, 3 × 600 mL), deionised H_2O (3 × 600 mL), AcOH (2.0 M, 3 × 600 mL), and deionised H_2O (3 × 600 mL). The resin was then transferred to an empty Thomson 650 mL SingleStep® plastic column and washed with AcOH (1.0 M, 2000 mL) pumped at 7.0 mL/min through Viton tubing (ID 1/8”, OD 3/16”, Wall 1/32”) *via* a LKB-BROMMA 2120 Varioperpex® II peristaltic pump. A layer of Dowex was sandwiched between two frits at the top of the column to act as a guard and to provide a level surface onto which the column could be loaded, giving a resin bed of length 190 mm and radius 32 mm.

In a typical separation experiment, crude hydrolysate powder (800 mg), as isolated in Section 2.7.1.1, was dissolved in deionised H_2O (5.0 mL) and filtered through a 0.45 μm nylon syringe filter. The brown solution was loaded on to the frit at the top of the column and AcOH (1.0 M) was added dropwise for 10 minutes whilst the uronic acids absorbed

onto the resin. An isocratic flow of AcOH (1.0 M) of 7.0 mL/min was maintained over the course of the run, with the eluent being monitored by means of a qualitative phenol-H_2SO_4 assay.[138] Under these conditions, L-guluronic acid was found to elute between 500 – 700 minutes and D-mannuronic acid between 770 – 1000 minutes, with the column running for a total of 20 hours. Approximately 200 mg (1.0 mmol) of each uronic acid in 1.5 L of AcOH (1.0 M) was collected in each run. The AcOH was removed by repeated co-evaporation of the solutions *in vacuo* (40 °C, 40 mbar) with de-ionised H_2O (10 × 500 mL), followed by reduction to approximately 100 mL. Following filtration through a 0.22 μm nylon syringe into a Duran® bottle (previously sterilised by heating at 110 °C) the solutions of uronic acid (with an approximate concentration of 10 mM) were stored at 5 °C until required.

2.7.1.3 Preparation of solutions of algal mono-uronates for NMR spectroscopy

The solutions of D-mannuronic and L-guluronic acid prepared by the procedure described in Section 2.7.1.2 were further processed to facilitate various NMR experiments (see Section 2.4 and Chapter 3). The uronic acids were first neutralised to pH 7.0 by careful addition of NaOH (0.2 M) and NaOH (0.01M) to yield solutions of Na-D-mannuronate and Na-L-guluronate. The pH at this stage was found to drift downwards as lactones in the solutions were hydrolysed to liberate free uronic acids, consequently, small additions of NaOH (0.01 M) were periodically made until the pH remained stable at 7.0 for a period of 48 hours.[59] Solutions were then filtered once again through a 0.22 μm nylon syringe filter prior to reduction *in vacuo* (40 °C, 40 mbar) to near dryness. At this stage, the viscous syrup was repeatedly re-dissolved and re-evaporated *in vacuo* (40 °C, 40 mbar) with D_2O (4 × 2.0 mL) before finally being dissolved in D_2O (2.0 mL) to yield solutions of approximately 100 mg uronate / mL D_2O. These stock solutions were stored at 5 °C until required, with small amounts of precipitate forming over this time being removed by micro-centrifugation in an IKA® mini-G centrifuge (6000 rpm, 5 mins).

Solutions of Na-D-glucuronate and Na-D-galacturonate were prepared in an identical manner to those of Na-D-mannuronate and Na-L-guluronate by dissolving commercial (Sigma Aldrich) D-glucuronic acid (200 mg, 1.0 mmol) and D-galacturonic acid monohydrate (220 mg, 1.0 mmol) in deionised H_2O (100 mL) and proceeding to neutralise, concentrate, and exchange with D_2O as described above.

D_2O solutions of uronate of the correct concentration for NMR spectroscopic analysis were subsequently made up by appropriate dilution of the stock solutions (typically 0.26 ± 0.02 M). The concentration was established by two methods (the details of which are elaborated in Appendix A). In the first instance, a standard phenol-H_2SO_4 assay (see Section 2.7.2.4) was employed to derive the concentration of the stock solution. Following dilution, fine-tuning of the concentration was achieved by comparison of the integrals of selected peaks in the ^1H NMR spectrum of the solution (measured against a $CHCl_3$ internal standard) with a calibration line derived from standard solutions of 0.0 - 50.0 mg Na-D-glucuronate /mL D_2O.

2.7.2 Analytical methods for studying solutions of algal mono-uronic acids

2.7.2.1 ^{1}H and ^{13}C NMR spectroscopy: general parameters

All deuterated reagents for NMR experiments were obtained from Apollo Scientific and clean Norell® XR-55-7 NMR tubes (5.0 mm) were used throughout. Sodium salts of the appropriate uronate in D_2O (0.26 ± 0.02 M) were used in all cases, unless stated otherwise. ^{1}H and ^{13}C one- and two-dimensional NMR spectroscopic experiments were variously conducted on Varian VNMRS-600 MHz, Varian Inova-500 MHz, and Bruker Avance-400 MHz spectrometers, according to the experimental requirements and equipment availability. The parameters pertaining to specific experiments are listed in full in Appendix D, including details of the pure shift and comprehensive sensing HSQC experiments.[139,140] All spectra for direct comparison were conducted under identical conditions, with a flame-sealed glass capillary (1.0 mm OD) containing either $CHCl_3$ in $CDCl_3$ (5:95 vol.%) or C_6H_6 in C_6D_6 (30:70 vol.%) inserted co-axially into each 5.0 mm NMR tube to act as a reference.[141,142] Data processing were carried out in MestReNova 10.0.2-15465.

2.7.2.2 NMR Titration and pK_a calculation

In order to determine the effect of reducing the pH of the solution on the ^{1}H and ^{13}C NMR spectrum of the uronates isolated in Section 2.7.1, a series of titration experiments were conducted. A preliminary experiment was first employed to determine the approximate volumes and concentrations of DCl to be added to obtain data at pH* values close to the pK_a. Thus, the minimal possible volume of DCl (typically around 3 μL, dispensed with an Eppendorf® Research® variable volume pipette) of varying concentrations (5.0 M – 0.5 mM) was added each time such that any effect arising from the changing uronate concentration was sufficiently small as to be undetectable. Furthermore, the pH was only changed in a downward direction (7 to 1) without the addition of NaOD to ensure that the $[Na^+]$:[uronate$^-$] ratio remained constant throughout. The pH* of the solution was determined by means of a Sigma-Aldrich® micro pH combination electrode (glass body, 183 mm L, 3.5 mm OD) connected to an Orion Star™ A111 pH-meter, and was measured once after adding the DCl and again following the NMR experiment to give a repeat reading from which an average could be derived. The solutions were shaken and allowed to equilibrate for 60 minutes prior to the NMR spectral acquisition. It should be noted that the reported value for $-\log[D_3O]^+$ cannot correctly be called the pD, as the electrode was calibrated in non-deuterated solutions. Hence, the term pH* is used to refer to the actual reading obtained, with no additional correction applied.[120]

A combination of one- and two-dimensional ^{1}H and ^{13}C NMR spectroscopic experiments were employed to follow the changes in the uronate signals at varying values of pH*, including: ^{1}H-^{1}H COSY, ^{1}H-^{13}C HSQC, and pure shift techniques. Chemical shift (δ) values were measured relative to signals from a reference solution of C_6H_6/C_6D_6 30:70 vol.% ($\delta^{1}H(C_6\underline{H}_6)$ = 7.15 ppm, and $\delta^{13}C(\underline{C}_6D_6)$ = 128.06 ppm) contained in a separate capillary.[141,142] The change in the chemical shift of the nuclei in question ($\Delta\delta$, ppm) at different values of

pH* was then calculated according to Equation 2.1, where δ(pH* X) is the chemical shift at a particular value (X) of pH*, and δ(pH* 7) is the chemical shift at pH* = 7.

$$\Delta\delta = \delta(\text{pH* X}) - \delta(\text{pH* 7}) \qquad \text{[Eq.2.1]}$$

Plotting $\Delta\delta$ *versus* pH* for C6 (the carboxylate carbon) of each compound yields a plot to which a sigmoidal curve could be fitted *via* a non-linear least-squares regression analysis in SciDavis 1.D009 with an R^2 value of ≥ 0.9998. The inflexion point of the curve was determined to derive a value for pK_a(H*), which could be converted to pK_a(H) by the method of Krężel and Bal.[120] As the error in $\Delta\delta$ is very small, the main source of uncertainty in the reported value of the pK_a arises from the measurement of pH*, for which duplicate readings typically did not vary by more than 0.05 units. Hence, pK_a(H) and pK_a(H*) values are reported with a standard error of ± 0.03.

2.7.2.3 ESI-MS and LC-ESI-MS analysis of solutions of uronic acids

The Na-uronate solutions prepared in Section 2.7.1 were analysed by liquid chromatography-electrospray ionisation mass spectrometry (LC-ESI-MS). Samples of 1.0 mg/mL in distilled water were transferred to a TQD mass spectrometer equipped with an Acquity Ultra Performance Liquid Chromatography (UPLC) unit (Waters Ltd. UK). The UPLC was conducted with a mobile phase of water/methanol, spiked with formic acid (0.1 vol.%) at flow rate of 0.6 mL min^{-1} through an Acquity UPLC BEH C18 column (1.7μm x 2.1mm x 50mm). The mass spectrometry electrospray ionisation source operated at 70 eV, and a mass range of 100 – 2000 amu was scanned. An Acquity photodiode array detector provided absorbance data from 210 nm to 400 nm. Under these conditions, all uronate salts (both those prepared from alginic acid and the commercial samples) gave a single peak in the negative ion chromatogram at 0.28 minutes, consisting largely of *m/z* = 193.1 (corresponding to $[\text{uronic acid} - H^+]^-$) and, to a lesser extent, *m/z* = 387.2 (corresponding to $[2(\text{uronic acid}) - H^+]^-$) and *m/z* = 409.0 (corresponding to $[2(\text{uronic acid}) - 2H^+ + Na^+]^-$) (see exemplar LC-MS trace in Figure 2.37).

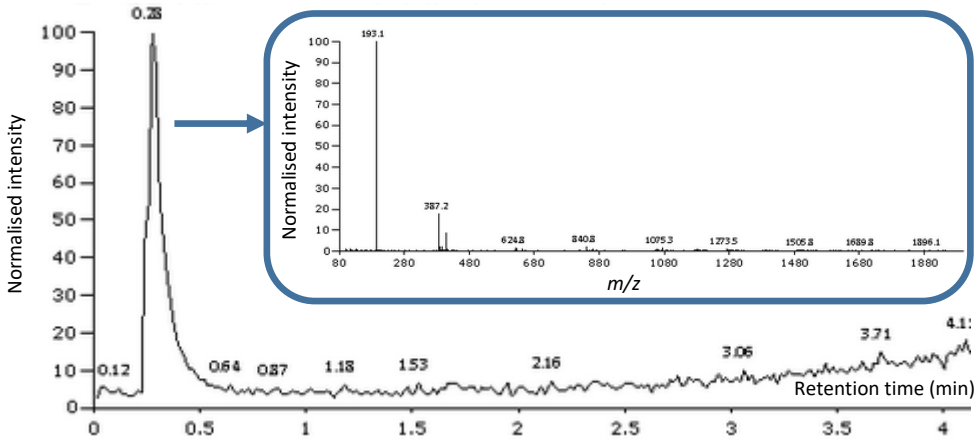

Figure 2.37 LC chromatogram and expanded negative ion ESI-MS spectrum at 0.28 minutes of a uronic acid in H_2O (1.0 mg/mL)

Some solutions (including those from the lactonisation experiments reported into Section 2.7.3) were analysed in an identical manner by ESI-MS, but without the initial liquid chromatography. For these latter samples, the signal in the positive ion chromatogram at m/z = 199.0 was assigned to $[\text{lactone} + Na^+]^+$.

2.7.2.4 Standard phenol-H_2SO_4 assay for determining uronic acid concentrations in solution

Standard phenol-H_2SO_4 assays were used both quantitatively and qualitatively to ascertain the concentration of uronic acid or uronate salts in aqueous solutions at various stages of their preparations.[138] In general, aqueous phenol (0.5 mL, 0.3 M) was added to 2.0 mL of the solution to be studied (or some dilution made up to 2.0 mL by deionised H_2O) in a glass test tube. H_2SO_4 (5.0 mL, 18.4 M) was added quickly by the action of an Eppendorf® Variable Volume pipette (500 – 5000 μL), causing instantaneous boiling of the solution. The formation of a brown colour was indicative of the presence of aldohexuronic acids, which could be further quantified by UV-VIS spectrophotometry as follows: Upon standing the sample in ice for exactly 60 minutes, the absorbance at 485 nm of 200 μL of the solution was measured by a 96-well Thermo Scientific Multiskan™ GO Microplate Spectrophotometer. Quantification was achieved by comparison with a calibration line derived from standard solutions of 0 – 200 μg D-glucuronic / mL deionised H_2O and 0 – 200 μg D-galacturonic acid / mL deionised H_2O, with the varying sensitivities of different uronic acids being accounted for according to the work of Haug and Larsen (see Appendix A).[32]

2.7.3 Hydrothermal lactonisation of uronic acids

Solutions of uronic acids in D_2O (0.05 M, 1.0 mL) were carefully heated in sealed NMR tubes (fitted with a J. Young's valve) at either pH* 7.0 or pH* 1.0 according to the conditions defined in Table 2.5. Following the heating regime, the solution was cooled to room temperature before immediately acquiring the ^{1}H NMR spectrum at 400 MHz. Peaks arising from the lactones were immediately recognisable as their furanoid anomeric protons are known to give signals at higher frequencies than the pyranose configurations.[37,38] The assignments for the detected lactones are reported in Table 2.6 and are based on the structures defined in Figure 2.38. For D-mannofuranurono-6,3-lactone, assignments were made based on those previously determined from crystalline material.[55] For the **HGlc**- and **HGul**-lactones, tentative assignments were made from the initial assumption that, when H1 and H2 are *trans* to each other (corresponding to the α-anomers in both of these cases) $J_{1,2}$ is expected to be very small (0-2 Hz), whilst for a *cis* arrangement (corresponding to the β-anomers) $J_{1,2}$ should be larger (3-5 Hz).[40] Hence, from integration of the appropriate peaks, α/β ratios of 1.28, 0.58, and 0.26 were calculated for α/β-L-gulo-, α/β-D-manno-, and α/β-D-glucofuranurono-6,3-lactones respectively. No evidence was found for the lactone open chain configurations being present in significant proportions in any of the solutions.[2,38] The ^{13}C NMR spectra were not acquired for the lactonisation experiments as the solutions were too dilute. The large initial sample size (1.0 mL) facilitated the periodic removal of aliquots from the NMR solution to study by electrospray ionisation mass spectrometry (ESI-MS) (see Section 2.7.2.3).

Table 2.6 Tentative ^{1}H NMR (400 MHz, 295 K) assignments of furanurono-6,3-lactones formed in solutions of uronic acids in D_2O (0.05 M) at pH* 1.0 (acidified with DCl) after heating for 12 hours at 60 °C (relative to C<u>H</u>Cl_3 in $CDCl_3$, δ = 7.26 ppm)

Lactone		Chemical shift assignments (δ, ppm)					Coupling constants (J, Hz)[a]			
		H1	H2	H3	H4	H5	$J_{1,2}$	$J_{2,3}$	$J_{3,4}$	$J_{4,5}$
Gul	***α***	5.42 d	4.29 dd	5.22 *p*t	n.d.[b]	4.50 d	4.1	5.4	5.7	1.2
Gul	***β***	5.44 d	4.30 dd	5.35 dd	n.d.[b]	4.58 d	1.5	4.7	7.0	3.9
Man	***α***	5.29 d	4.30 dd	5.12 dd	4.99 dd	4.78 d	5.5	4.3	3.3	5.1
Man	***β***	5.45 d	4.37 *p*t	5.14 *p*t	4.87 dd	4.74 d	4.5	4.8	4.7	6.5
Glc	***α***	5.57 d	4.40 d	5.01 dd	4.97 dd	4.76 d	3.9	0.8	3.5	5.1
Glc	***β***	5.48 s	4.37 s	5.06 d	5.04 dd	4.75 d	n.d.[c]	n.d.[c]	4.6	6.2

Key: s = singlet, d = doublet, dd = doublet of doublets, *p*t = pseudo-triplet, n.d. = not determined

[a] Scalar coupling constants (J) quoted to a precision of ± 0.1 Hz.

[b] Obscured by the HDO peak at 295 K (4.8 – 4.9 ppm). Varying the temperature revealed αH4 is a dd and βH4 a d.

[c] Too small to be measured at 400 MHz

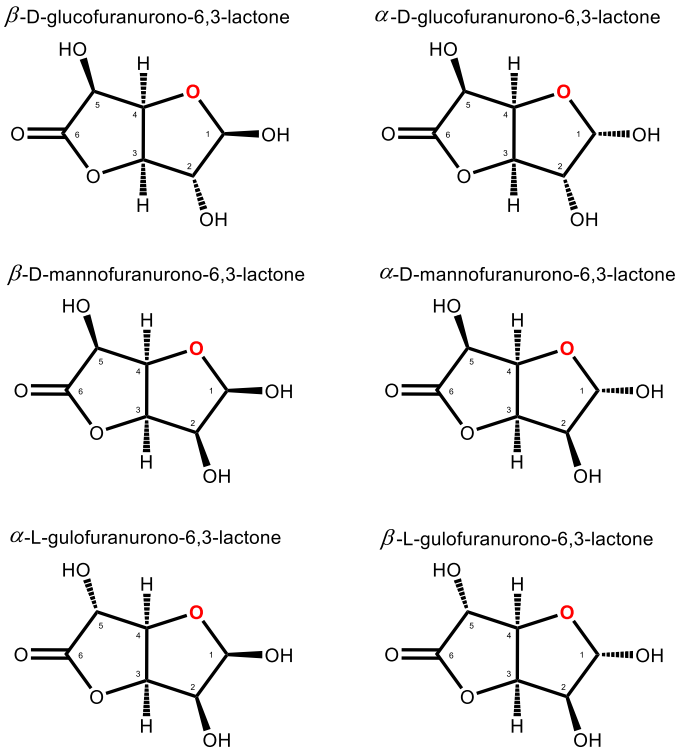

Figure 2.38 Stereochemical definitions of furanurono-6,3-lactones.

2.8 Chapter acknowledgments

Particular thanks are owed to Dr. Juan A Aguilar Malavia and other staff of the Durham university NMR service. Juan designed and conducted the advanced NMR methodologies employed in this Chapter (see Appendix D for details), and the work presented here owes much to his endeavours. The Durham University Mass Spectrometry service are also thanked for their assistance.

2.9 Chapter references

1 C. A. Marsh, in *Glucuronic Acid Free and Combined*, Elsevier, New York 1966, pp. 3–136.

2 H. S. Isbell and H. L. Frush, *J. Res. Natl. Bur. Stand.*, 1946, **37**, 43-49.

3 R. M. De Lederkremer and C. Marino, *Adv. Carbohydr. Chem. Biochem.*, 2003, **58**, 199-306.

4 C. Chatterjee, F. Pong and A. Sen, *Green Chem.*, 2015, **17**, 40–71.

5 R. Wang, T. Kobayashi and S. Adachi, *J. Appl. Glycosci.*, 2009, **56**, 181–184.

6 R. Wang, T. L. Neoh, T. Kobayashi, Y. Miyake, A. Hosoda, H. Taniguchi and S. Adachi, *Biosci. Biotechnol. Biochem.*, 2010, **74**, 601–605.

7 F. van der Klis, A. E. Frissen, J. van Haveren and D. S. van Es, *ChemSusChem*, 2013, **6**, 1640–1645.

8 S. Rautiainen, P. Lehtinen, J. Chen, M. Vehkamäki, K. Niemelä, M. Leskelä and T. Repo, *RSC Adv.*, 2015, **5**, 19502–19507.

9 M. S. Mettler, A. D. Paulsen, D. G. Vlachos and P. J. Dauenhauer, *Green Chem.*, 2012, **14**, 1284-1288.

10 M. S. Mettler, D. G. Vlachos and P. J. Dauenhauer, *Energy Environ. Sci.*, 2012, **5**, 7797-7809.

11 K. I. D. Skja, in *Renewable Resources for Functional Polymers and Biomaterials : Polysaccharides, Proteins and Polyesters*, RSC, Cambridge, 2011, pp. 186–209.

12 P. Gacesa, *Carbohydr. Polym.*, 1988, **8**, 161–182.

13 C. Peter and R. Ferrier, *Monosaccharides: Their Chemistry and Their Roles in Natural Products*, Wiley, New York, 1995.

14 C. A. Steginsky, J. M. Beale, H. G. Floss and R. M. Mayer, *Carbohydr. Res.*, 1992, **225**, 11–26.

15 A. Haug and B. Larsen, *Biochim. Biophys. Acta - Gen. Subj.*, 1969, **192**, 557–559.

16 K. Bachmann, in *Pharmacology: Principles and Practice*, Academic Press, Elsevier, Burlington, 2009, pp. 131-173

17 S. McLean, S. Brandon, N. W. Davies, R. Boyle, W. J. Foley, B. Moore and G. J. Pass, *J. Chem. Ecol.*, 2003, **29**, 1465–1477.

18 D. M. W. Anderson, M. C. L. Gill, A. M. Jeffrey and F. J. McDougall, *Phytochemistry*, 1985, **24**, 71–75.

19 B. Larsen, A. Haug and T. J. Painter, *Acta Chem. Scand.*, 1966, **20**, 219–230.

20 R. L. Whistler and M. L. Wolfrom, *Volume 2. Reactions of carbohydrates*, Academic Press, New York, 1963.

21 C. D. May, *Carbohydr. Polym.*, 1990, **12**, 79–99.

22 P. Sriamornsak, *Silpakorn Univ. Int. J.*, 2003, **3**, 206–228.

23 L. H. Cretcher and W. L. Nelson, *Science*, 1928, **67**, 537–538.

24 W. L. Nelson and L. H. Cretcher, *J. Am. Chem. Soc.*, 1930, **52**, 2130–2132.

25 W. L. Nelson and L. H. Cretcher, *J. Am. Chem. Soc.*, 1929, **51**, 1914–1922.

26 W. L. Nelson and L. H. Cretcher, *J. Am. Chem. Soc.*, 1932, **54**, 3409–3412.

27 E. Schoeffel and K. P. Link, *J. Biol. Chem.*, 1933, **100**, 397–405.

28 E. D. T. Atkins, I. A. Nieduszynski, W. Mackie, K. D. Parker and E. E. Smolko, *Biopolymers*, 1973, **12**, 1865–1878.

29 F. G. Fischer and H. Dörfel, *Hoppe-Seyler´s Zeitschrift für Physiol. Chemie*, 1955, **302**, 186–203.

30 D. W. Drummond, E. L. Hirst and E. Percival, *J. Chem. Soc.*, 1962,**1**, 1208-1216.

31 E. D. T. Atkins, I. A. Nieduszynski, W. Mackie, K. D. Parker and E. E. Smolko, *Biopolymers*, 1973, **12**, 1879–1887.

32 A. Haug, B. Larsen, O. Fykse, A. Block-Bolten, J. M. Toguri and H. Flood, *Acta Chem. Scand.*, 1962, **16**, 1908–1918.

33 I. R. Siddiqui, *Carbohydr. Res.*, 1980, **80**, 343–345.

34 I. R. Siddiqui, *Carbohydr. Res.*, 1978, **63**, 312–314.

35 F. Mo, T. J. Brobak and I. R. Siddiqui, *Carbohydr. Res.*, 1985, **145**, 13–24.

36 Japan Patent Office, JP4897310 (B2), 2007, 1–11.

37 S. J. Angyal, *Adv. Carbohydr. Chem. Biochem.,* 1984, **42**, 15–68.

38 S. J. Angyal, *Angew. Chemie Int. Ed. English*, 1969, **8**, 157–166.

39 S. J. Angyal and V. A. Pickles, *Carbohydr. Res.*, 1967, **4**, 269–270.

40 S. J. Angyal and V. Pickles, *Aust. J. Chem.*, 1972, **25**, 1695.

41 J. Stoddart, in *Stereochemistry of Carbohydrates*, John Wiley & Sons Inc, London, 1971, pp. 47–122.

42 W. A. Bubb, *Concepts Magn. Reson. Part A Bridg. Educ. Res.*, 2003, **19**, 1–19.

43 M. Appell, J. L. Willett and F. A. Momany, *Carbohydr. Res.*, 2005, **340**, 459–468.

44 U. Schnupf, J. L. Willett, W. B. Bosma and F. A. Momany, *Carbohydr. Res.*, 2007, **342**, 196–216.

45 M. Appell, G. Strati, J. L. Willett and F. A. Momany, *Carbohydr. Res.*, 2004, **339**, 537–551.

46 C. M. Filloux, *Angew. Chemie Int. Ed.*, 2015, **54**, 8880–8894.

47 E. M. Fry, *J. Am. Chem. Soc.*, 1955, **77**, 3915–3916.

48 C. Vogel, B. Liebelt, W. Steffan and H. Kristen, *J. Carbohydr. Chem.*, 1992, **11**, 287–303.

49 A. E. Christina, L. J. van den Bos, H. S. Overkleeft, G. A. van der Marel and J. D. C. Codée, *J. Org. Chem.*, 2011, **76**, 1692–1706.

50 A. Rauter, *Rev. Port. Quim.*, 1989, **31**, 1–16.

51 V. A. Timoshchuk, *Russ. Chem. Rev.*, 1995, **64**, 675–703.

52 J. Stoddart, in *Stereochemistry of Carbohydrates*, John Wiley & Sons Inc, London, 1971, pp. 185–186.

53 E. Schoeffel and K. Link, *J. Biol. Chem.*, 1932, **95**, 213–218.

54 H. L. Frush and H. S. Isbell, *J. Res. Natl. Bur. Stand.*, 1946, **37**, 321–324.

55 M. Shalaby, F. R. Fronczek, D. Vargas and E. S. Younathan, *Carbohydr. Res.*, 1994, **265**, 197–206.

56 M. Roussel, S. Moutard, B. Perly, M. Lefeuvre, T. Benvegnu and D. Plusquellec, *Carbohydr. Res.*, 2003, **338**, 375–378.

57 H. W. H. Schmidt, *Tetrahedron Lett.*, 1967, **8**, 235–240.

58 I. Macher, K. Dax, H. Inselsbacher and H. Weidmann, *Carbohydr. Res.*, 1979, **77**, 225–230.

59 J. D. Blake and G. N. Richards, *Carbohydr. Res.*, 1968, **8**, 275–281.

60 R. D. Guthrie, *Introduction to carbohydrate chemistry*, Clarendon Press, Oxford, 1974.

61 S. C. Moldoveanu, in *Techniques and Instrumentation in Analytical Chemistry*, Elsevier, Amsterdam, 2010, **28**, pp. 471–526.

62 H. B. Mayes and L. J. Broadbelt, *J. Phys. Chem. A*, 2012, **116**, 7098–7106.

63 O. Theander and D. A. Nelson, *Adv. Carbohydr. Chem. Biochem.,* 1988, **46**, 273–326.

64 K. Matsushima, H. Minoshima, H. Kawanami, Y. Ikushima, M. Nishizawa, A. Kawamukai and K. Hara, *Ind. Eng. Chem. Res.*, 2005, **44**, 9626–9630.

65 S. Daneshvar, F. Salak, T. Ishii and K. Otsuka, *Ind. Eng. Chem. Res.*, 2012, **51**, 77–84.

66 T. A. Davis, F. Llanes, B. Volesky and A. Mucci, *Environ. Sci. Technol.*, 2003, **37**, 261–267.

67 E. Fourest and B. Volesky, *Appl. Biochem. Biotechnol.*, 1997, **67**, 215–226.

68 T. A. Davis, M. Ramirez, A. Mucci and B. Larsen, *J. Appl. Phycol.*, 2004, **16**, 275–284.

69 C. G. Oates and D. a. Ledward, *Food Hydrocoll.*, 1990, **4**, 215–220.

70 A. Haug, B. Larsen, O. Smidsrød and J. Munch-Petersen, *Acta Chem. Scand.*, 1963, **17**, 1466–1468.

71 T. M. Aida, T. Yamagata, C. Abe, H. Kawanami, M. Watanabe and R. L. Smith, *J. Supercrit. Fluids*, 2012, **65**, 39–44.

72 T. M. Aida, T. Yamagata, M. Watanabe and R. L. Smith, *Carbohydr. Polym.*, 2010, **80**, 296–302.

73 W. Jeon, C. Ban, G. Park, H. C. Woo and D. H. Kim, *Catal. Sci. Technol.*, 2016, **6**, 1146–1156.

74 H. Andriamanantoanina and M. Rinaudo, *Polym. Int.*, 2010, **59**, 1531–1541.

75 A. Haug, *Acta Chem. Scand.*, 1961, **15**, 950–952.

76 A. Haug, B. Larsen, B. Samuelsson, J. Sjövall and J. Munch-Petersen, *Acta Chem. Scand.*, 1963, **17**, 1653–1662.

77 O. Smidsrød, D.Sc. thesis, University of Trondheim, Trondheim: NTNF's Institutt for Marin Biokjemi, 1973.

78 A. I. Usov, *Russ. Chem. Rev.*, 1999, **68**, 957–966.

79 T. A. Davis, B. Volesky and A. Mucci, *Water Res.*, 2003, **37**, 4311–30.

80 F. M. Kerton, Y. Liu, K. W. Omari and K. Hawboldt, *Green Chem.*, 2013, **15**, 860-871.

81 Q. Yu, J. T. Matheickal, P. Yin and P. Kaewsarn, *Water Res.*, 1999, **33**, 1534–1537.

82 B. Carlsson and O. Samuelson, *Carbohydr. Res.*, 1969, **11**, 347–354.

83 J. N. BeMiller and G. V. Kumari, *Carbohydr. Res.*, 1972, **25**, 419–428.

84 H. M. Wang, D. Loganathan and R. J. Linhardt, *Biochem. J.*, 1991, **278**, 689–695.

85 L. W. Jaques, J. B. Macaskill and W. Weltner, *J. Phys. Chem.*, 1979, **83**, 1412–1421.

86 R. Kohn and P. Kovác, *Chem. Zvesti*, 1978, **32**, 478–485.

87 P. Selvarengan, J. D. Kubicki, J.-P. Guégan and X. Châtellier, *Chem. Geol.*, 2010, **273**, 55–75.

88 H. Grasdalen, B. Larsen and O. Smidsrød, *Carbohydr. Res.*, 1979, **68**, 23–31.

89 C. DeRamos, A. Irwin, J. Nauss and B. Stout, *Inorganica Chim. Acta*, 1997, **256**, 69–75.

90 D. Ramos, PhD thesis, University of Cincinnati, 1995.

91 W. Mackie, R. Rizzo, F. Taravel and M. Vignon, *Int. J. Biol. Macromol.*, 1983, **5**, 329–341.

92 H. Grasdalen, F. Mo, J. Olav Bjørgum and I. R. Siddiqui, *Carbohydr. Res.*, 1990, **203**, 281–286.

93 A. Matsumoto, S. Hosoyama, K. Higashi and T. Toida, *Carbohydr. Res.*, 2012, **358**, 82–88.

94 B. Larsen, D. M. S. A. Salem, M. A. E. Sallam, M. M. Mishrikey and A. I. Beltagy, *Carbohydr. Res.*, 2003, **338**, 2325–2336.

95 A. Penman and G. R. Sanderson, *Carbohydr. Res.*, 1972, **25**, 273–282.

96 K. Niemelä and E. Sjöström, *Carbohydr. Res.*, 1985, **144**, 241–249.

97 R. Matsumoto, T. Aki, Y. Okamura, T. Tajima, Y. Nakashimada and Y. Matsumura, *J. Japan Inst. Energy*, 2014, **93**, 531–535.

98 A. Meillisa, H.-C. Woo and B.-S. Chun, *Food Chem.*, 2015, **171**, 70–77.

99 M. Stacey and P. I. Wilson, *J. Chem. Soc.*, 1944, **4**, 587–588.

100 S. N. Pawar and K. J. Edgar, *Biomaterials*, 2012, **33**, 3279–3305.

101 N. Chandía, *Carbohydr. Polym.*, 2001, **46**, 81–87.

102 H. Spoehr, *Arch. Biochem.*, 1947, **14**, 153–155.

103 E. L. Hirst, J. K. N. Jones and W. O. Jones, *J. Chem. Soc.*, 1939, **1**, 1880-1885.

104 L. Li, X. Jiang, H. Guan and P. Wang, *Carbohydr. Res.*, 2011, **346**, 794–800.

105 Y. Liu, X. L. Jiang, H. Cui and H. S. Guan, *J. Chromatogr. A*, 2000, **884**, 105–11.

106 A. Haug, B. Larsen, R. Nilsson, G. E. Olsen, C. Pedersen and J. Toft, *Acta Chem. Scand.*, 1961, **15**, 1395–1396.

107 B. Larsen, A. Haug, R. Nilsson, G. E. Olsen, C. Pedersen and J. Toft, *Acta Chem. Scand.*, 1961, **15**, 1397–1398.

108 Chinese Patent Office, CN 103755750 A, 2014.

109 K. Larsson and O. Samuelson, *Carbohydr. Res.*, 1973, **31**, 81–86.

110 J. Stoddart, in *Stereochemistry of Carbohydrates*, John Wiley & Sons Inc, London, 1971, pp. 129–146.

111 K. Bock and H. Thøgersen, *Annu. Reports NMR Spectrosc.*, 1982, **13**, 1–57.

112 R. U. Lemieux and J. D. Stevens, *Can. J. Chem.*, 1965, **43**, 2059–2070.

113 C. Altona and C. A. G. Haasnoot, *Org. Magn. Reson.*, 1980, **13**, 417–429.

114 M. J. Minch, *Concepts Magn. Reson.*, 1994, **6**, 41–56.

115 J. A. Aguilar, S. Faulkner, M. Nilsson and G. A. Morris, *Angew. Chemie Int. Ed.*, 2010, **49**, 3901–3903.

116 R. Hagen and J. D. Roberts, *J. Am. Chem. Soc.*, 1969, **91**, 4504–4506.

117 J. Batchelor, J. Feeney and G. C. Roberts, *J. Magn. Reson.*, 1975, **20**, 19–38.

118 J. Batchelor, *J. Am. Chem. Soc.*, 1975, **97**, 3410–3415.

119 J. Bezençon, M. B. Wittwer, B. Cutting, M. Smieško, B. Wagner, M. Kansy and B. Ernst, *J. Pharm. Biomed. Anal.*, 2014, **93**, 147–155.

120 A. Krężel and W. Bal, *J. Inorg. Biochem.*, 2004, **98**, 161–166.

121 F. Delben, À. Cesaro, S. Paoletti and V. Crescenzi, *Carbohydr. Res.*, 1982, **100**, C46–C50.

122 C. Rey-Castro, P. Lodeiro, R. Herrero and M. E. Sastre de Vicente, *Environ. Sci. Technol.*, 2003, **37**, 5159–5167.

123 A. Haug, S. Myklestad, B. Larsen, O. Smidsrød, G. Eriksson, R. Blinc, S. Paušak, L. Ehrenberg and J. Dumanović, *Acta Chem. Scand.*, 1967, **21**, 768–778.

124 J. L. Dashnau, K. A. Sharp and J. M. Vanderkooi, *J. Phys. Chem. B*, 2005, **109**, 24152–24159.

125 J. P. Simons, B. G. Davis, E. J. Cocinero, D. P. Gamblin and E. C. Stanca-Kaposta, *Tetrahedron: Asymmetry*, 2009, **20**, 718–722.

126 J. Hjortås, B. Larsen, S. Thanomkul, I. Szabo-Lin, C. Guthenberg and B. Mannervik, *Acta Chem. Scand.*, 1974, **28b**, 689–689.

127 H.-R. Tang, P. S. Belton, S. C. Davies and D. L. Hughes, *Carbohydr. Res.*, 2001, **330**, 391–399.

128 H. A. Tajmir-Riahi, *J. Inorg. Biochem.*, 1985, **24**, 127–136.

129 H. A. Tajmir-Riahi, *J. Inorg. Biochem.*, 1986, **26**, 23–33.

130 L. DeLucas, C. E. Bugg, A. Terzis and R. Rivest, *Carbohydr. Res.*, 1975, **41**, 19–29.

131 H. A. Tajmir-Riahi, *Carbohydr. Res.*, 1984, **125**, 13–20.

132 S. E. B. Gould, R. O. Gould, D. A. Rees and W. E. Scott, *J. Chem. Soc. Perkin Trans. 2*, 1975, **3**, 237-242.

133 W. Plazinski and M. Drach, *J. Phys. Chem. B*, 2013, **117**, 12105–12112.

134 W. Plazinski and M. Drach, *New J. Chem.*, 2015, **39**, 3987–3994.

135 P. Agulhon, V. Markova, M. Robitzer, F. Quignard and T. Mineva, *Biomacromolecules*, 2012, **13**, 1899–1907.

136 U. T. D. Huynh, A. Lerbret, F. Neiers, O. Chambin and A. Assifaoui, *J. Phys. Chem. B*, 2016, **120**, 1021–1032.

137 C. Menakbi, F. Quignard and T. Mineva, *J. Phys. Chem. B*, 2016, **120**, 3615–3623.

138 M. DuBois, K. A. Gilles, J. K. Hamilton, P. A. Rebers and F. Smith, *Anal. Chem.*, 1956, **28**, 350–356.

139 M. Foroozandeh, R. W. Adams, N. J. Meharry, D. Jeannerat, M. Nilsson and G. A. Morris, *Angew. Chemie Int. Ed.*, 2014, **53**, 6990–6992.

140 J. A. Aguilar, R. Belda, A. Botana and A. M. Kenwright, *RSC Adv.*, 2016, **6**, 83380–83385.

141 H. E. Gottlieb, V. Kotlyar and A. Nudelman, *J. Org. Chem.*, 1997, **62**, 7512–7515.

142 G. R. Fulmer, A. J. M. Miller, N. H. Sherden, H. E. Gottlieb, A. Nudelman, B. M. Stoltz, J. E. Bercaw and K. I. Goldberg, *Organometallics*, 2010, **29**, 2176–2179.

Chapter 3

Chapter 3

Opening the Egg-Box: exploring metal-uronide interactions by solution state NMR spectroscopy

3.1 Chapter abstract

This chapter concerns the metal ion coordination behaviour of algal mono-uronates (and related compounds), specifically with a view to gaining fundamental insight into the so-called "Egg-Box" model of alginate-cation binding. To this end, the well-defined NMR spectroscopic characterisation of sodium mono-L-gulopyranuronate and -D-mannopyranuronate demonstrated in Chapter 2 are exploited in order to study the effect of various s- and d-block metal ions on those compounds. Here it is found that the α/β ratio of pyranose anomeric equilibria of L-guluronate is grossly perturbed from its starting value (α/β = 0.21) upon the inclusion of 1.0 M Ca^{2+}, Sr^{2+}, and Ba^{2+} (α/β = 1.50, 1.20, and 0.58, respectively), but not in the presence of Na^{+}, K^{+}, or Mg^{2+} (α/β = 0.24, 0.19, and 0.26, respectively). Such changes are unparalleled in the spectra of D-mannuronate, D-glucuronate and D-galacturonate under the same conditions. An analysis of changes to the ^{1}H and ^{13}C NMR chemical shifts of α-L-gulopyranuronate reveals that the affinity of the molecule for larger divalent cations is a consequence of the axial-equatorial-axial (*ax-eq-ax*) arrangement of hydroxyl groups found uniquely on that uronate anomer. The *ax-eq-ax* arrangement participates in metal-ion coordination even in the presence of a secondary binding mode involving the carboxylate and ring oxygens of the uronate unit, and so the effect of varying the pH of the solution on metal complexation is also explored. This study represents the most comprehensive analysis of mono-uronate metal-ion coordination behaviour to-date and presents conclusions that are contrary to recent theoretical assessments. Ultimately, it is suggested that variations of the Egg-Box model that exclude interactions by hydroxyl ions of the guluronate moieties may not be correct.

3.2 Chapter introduction and context

This chapter contains experiments that aim to probe the fundamental metal-binding behaviour of alginates, particularly evidence for so-called "Egg-Box" coordination (see Figure 3.1). Whilst there are many reasons why a better understanding of such chemistry is useful,* the particular focus in this thesis is to attempt to rationalise the impact of different metal ions on the thermochemical behaviour of alginates (see Chapter 4) and alginate-rich kelps (see Chapter 5). In these latter chapters, a stark difference in the effect of Cu^{2+} and Ca^{2+} on the pyrolysis of alginates is noted, and so information on the coordination of these two ions is of particular value to the thesis as a whole. In order to garner fundamental insight into the manner in which Cu^{2+} and Ca^{2+} (alongside other metal ions) interact with alginates, this Chapter utilises the algal mono-uronates (**Gul** and **Man**, as prepared and characterised in Chapter 2) as model compounds. The binding of mono-uronates is readily investigated by NMR spectroscopy, and can give detailed insight into the oxygen atoms around the saccharide ring that are involved in metal binding, information that is not easily obtainable in polymeric samples. In particular, evidence is sought for coordination of metal ions to uronate oxygen atoms other than those of the carboxylate (such as the hydroxyl groups and ring oxygens that contribute to binding in the Egg-Box model). Prior to these investigations, however, Section 3.3 provides an extensive literature review of topics necessary to support the following experimental discussions:

- **Metal-saccharide coordination chemistry**
- **The classical Egg-Box model and subsequent revisions**
- **Mono-uronate coordination chemistry**
- **Probing metal-saccharide coordination by NMR spectroscopy**

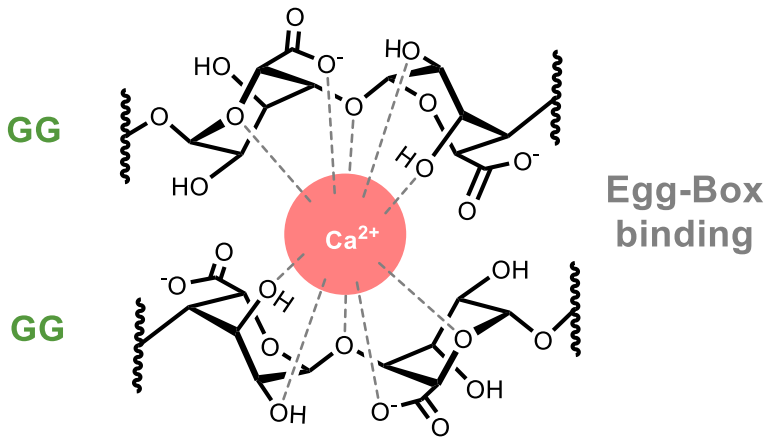

Figure 3.1 Ca^{2+} coordinated within an Egg-Box site created by two alginate chains

Ultimately, this chapter aims to build on the successful preparation and characterisation of algal-mono-uronates from Chapter 2, to derive fundamental insight into their metal binding behaviour to inform the discussions of metal-uronide thermochemistry in Chapters 4 and 5.

* With metal-bound alginates finding utility in areas as diverse as the manufacture of glacé cherries to drug delivery systems

3.3 Background

3.3.1 The coordination of metal ions to neutral and anionic carbohydrates

3.3.1.1 An introduction to metal-carbohydrate coordination chemistry

In the presence of a suitable cation, the electron-rich oxygen centres of carbohydrates can act as ligands. Whilst the study of such metal-saccharide chemistry can be dated back as far as 1825 with the isolation by Calloud of an adduct between NaCl and D-glucose, historically the low stability constants of such complexes (typically less than 0.1 M^{-1} for neutral monosaccharides) made their detection extremely difficult.[1] Indeed, in 1871, following a spate of unsuccessful experiments into the binding between sucrose and NaCl, Charles Haughton Gill presented a paper to The Chemical Society of London in which he stated:[2]

"Having obtained some positive results, I beg to lay them before the Society, for though of little interest in themselves, their publication may prevent the necessity of some other worker wasting so much time on an ungrateful subject"

Whilst some authors denied the possibility of complex formation between metals and neutral carbohydrates,[2] tantalising empirical evidence (such as the ability of sucrose to prevent the precipitation of $CaCO_3$ from limewater bubbled with CO_2) helped to maintain interest in the field.[3] With the advent of more sensitive analytical techniques such as electrophoresis and nuclear magnetic resonance (NMR) spectroscopy, the ability to detect and study metal-carbohydrate complexes became much more widespread, and the field grew considerably. In recent years, the term "metalloglycomics" has been coined to refer to the study of such metal-carbohydrate coordination,[4] and a number of reviews by Rendellmen,[3,5,6] Angyal,[1,7] and others[8–10] detail the rich chemical knowledge that has developed in this area.

The following sections include summarised discussions of the factors that favour metal-carbohydrate binding and the methods available to discern such information. Particularly, the case of metal binding to algal mono- and poly-uronic acids (including the renowned "Egg-Box" model, see Section 3.3.1.4) will be given special attention and, whilst knowledge in this area has applications in a wide realm of sectors, the relevance to uronide pyrolysis chemistry will be highlighted for the sake of advancing discussions in Chapters 4 and 5.

3.3.1.2 The role of stereochemistry and cation nature in metal-carbohydrate coordination

Negating any covalency that may be present in the binding of d-block elements, the coordination of a carbohydrate hydroxyl group to a metal ion may simply be considered to arise from the attraction between the dipolar charge of the oxygen atom with the positive nuclear charge of the cation (See Figure 3.2). In aqueous solutions however, the coordination of a cation by surrounding water molecules is far stronger than the attractive

forces arising from a single carbohydrate hydroxyl group, which is why the metal complexes of many neutral saccharides possess such low stability constants.[1]

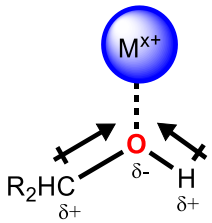

Figure 3.2 The coordination of a cation to a neutral carbohydrate through the attraction towards the dipolar charge of a hydroxyl moiety.

Whilst the binding of a single saccharide hydroxyl group may be of little practical significance, Angyal discerned that in the correct combination, certain arrangements of hydroxyl groups could bind strongly to a cation with observable effects on, for example, the electrophoretic mobility of the carbohydrate in question.[7] Indeed, the field of metal-sugar chemistry owes a great deal to the work of Stephen Angyal,[11] who devoted much of his career to elucidating the stereochemical requirements for the favourable binding of polyols and saccharides to metal ions.[1,7,12–16] A summary of Angyal's stereochemical rules for metal-binding ability in the cases of cyclohexane- and cyclopentane-based polyols (and, by analogy, pyranose and furanose rings) is depicted in Figure 3.3. Whilst a discussion of each example is not required here, it is pertinent to highlight the case of the axial-equatorial-axial (*ax-eq-ax*) arrangement of hydroxyl groups on a cyclohexane/pyranose ring, which has a particular affinity for divalent cations owing to the nature of the binding mode portrayed in the exemplar case of *epi*-inositol in Figure 3.4.[7]

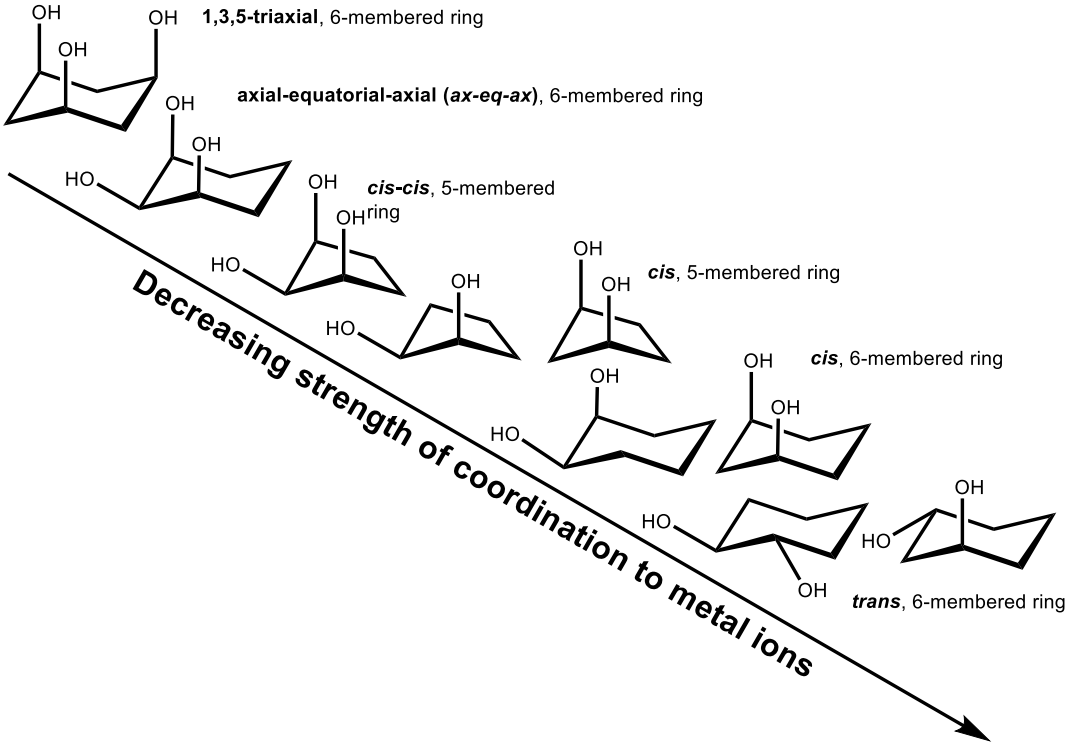

Figure 3.3 The abilities of combinations of hydroxyl groups to coordinate cations on five- and six-membered rings[1]

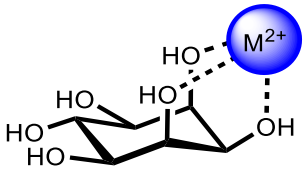

Figure 3.4 The axial-equatorial-axial (*ax-eq-ax*) metal-coordination mode determined for *epi*-inositol[7]

In studying Figure 3.3, it is interesting to note that the arrangements of hydroxyl groups that offer the strongest metal-binding on a pyranoid ring (namely 1,3,5 triaxial and *ax-eq-ax* configurations) are also the most sterically destabilising (see discussions in Section 2.2.2 of Chapter 2). This inherent energetic conflict in the synthesis of pyranose molecules with hydroxyl groups in suitable metal-binding formation means that, in fact, such arrangements are rarely found to occur naturally – with α-L-guluronic acid therefore providing an exceptional example.[1]

As one might expect, in order for strong complexation to occur, the stereospecific binding environment manifested in some polyols must also be matched by appropriate requirements of the coordinating cation.[*] In this regard, di- and tri-valent cations with ionic radii in the range of 100 – 110 pm (including Ca^{2+}, Cd^{2+}, and Eu^{3+}) possess an ideal size and charge density to coordinate to the *ax-eq-ax* arrangement of hydroxyl groups.[1] It is unclear as to whether the lack of complexation between smaller (≤ 80 pm) cations (such as Mg^{2+} and Zn^{2+})[3] and the *ax-eq-ax* binding mode is a consequence of the prohibitively low ionic radius of the metal, or the presence of a strongly coordinated solvation sphere precluding interaction.[3,7]

3.3.1.3 The strength of metal-binding by anionic mono-saccharides

Within the field of metalloglycomics, uronic acids are an interesting class of compound as they possess four potentially ligating functional groups: hydroxyl, carboxylate, ring oxygen, and aldehyde. However, whilst the metal-binding behaviour of other multifunctional monosaccharides has received much attention,[4,8,17–19] the equivalent properties of uronic acids have been studied much less intensively – especially the commercially unavailable algal mono-uronic acids (prepared in Chapter 2). Such a deficit is unfortunate, as the binding properties of the anionic mono-uronates[†] are likely to be very strong compared to

[*] Of course, in reality many other factors must be considered when promoting the formation of metal-saccharide complexes, including the ionic strength of the solution, the solvent, the temperature, the metal:ligand ratio, the role of counter anions and cations, and the presence of competing species. However, as such considerations are generic to all metal-ligand coordination chemistry, they are not discussed in detail here.

[†] The term "anionic" is used here only to refer to those saccharides that possess readily ionised functional groups. Whilst all carbohydrates may be considered to be anionic to some degree following deprotonation of their hydroxyl groups, the high pH values required to induce such behaviour is unlikely to arise naturally.

both their neutral counterparts and to simple carboxylate ligands,* a claim supported by comparison of suitable stability constants. Angyal defined values for strong, weak, and negligible carbohydrate-metal complexation as having stability constants of ≥ 5.0, ≈ 3.0, and ≤ 0.1 M^{-1}, respectively, which (especially under the low ionic strengths encountered in physiological conditions) are sufficiently small to be of little biological relevance.[7] However, calcium-uronate complexes have been reported with stability constants of greater than 100 M^{-1} [20] (though consensus values for galacturonate- and glucuronate-calcium complexes are in the lower range of 10 – 40 M^{-1});[8,9,21,22] a dramatic increase in coordination strength compared to their neutral equivalents. The extent to which the vast increase in stability constant in calcium-uronate complexes is simply a consequence of straight-forward binding between the metal and the carboxylate moiety has been questioned.[1] The exact coordination environment of metal ion bound to a mono-uronate, and the significance (if any) of the stereochemical arrangement of hydroxyl groups will be a key area of investigation in this chapter.

3.3.1.4 An introduction to alginates and the classical Egg-Box model

Alginic acid is found (as an alginate salt) inside and between the cell walls of kelps, where it acts as a principal structural polysaccharide to confer flexibility to the alga (which typically live in a turbulent coastal marine environments).[23] The polymer was first discovered by Scottish chemist ECC Stanford in the 1880s and, whilst unaware of its composition, Stanford was impressed by this "unique substance of remarkable properties"; naming it *algin*.[24†] Following more than a century of research, Stanford's original enthusiasm was well founded, with the metal-binding abilities of alginic acid (and corresponding alginate salts) finding widespread use in many diverse areas (discussed briefly below).[25,26] Alginic acid is now known to be a linear copolymer of di-equatorially (1→4) linked ($^4C_1$)-*β*-D-mannopyranuronic and di-axially (1→4) linked ($^1C_4$)-*α*-L-gulopyranuronic acids (see Figure 3.5), sometimes referred to as **M** and **G** units, respectively.[27,28] The polymer, which is typically found to have M_w values in the region of 10^5 g mol^{-1} when freshly extracted from the kelp,[29] contains both homo-polymeric (**MM** and **GG**) and hetero-polymeric (**MG**) blocks (see Appendix J for further discussion on this topic). Through X-ray fibre diffraction experiments, polymannuronic acid blocks have been found to possesses a flat, ribbon-like structure with a repeat unit (along the fibre axis) of 10.4 Å, whilst polyguluronic forms a buckled chain with a slightly smaller repeat unit of 8.7 Å.[27,28] Intramolecular H-bonding between oxygen atoms and the hydroxyl protons has been identified as being important for maintaining the secondary structures (highlighted in Figure 3.5). These X-ray fibre

* For example, alpha-hydroxy acids are known to have metal-binding stability constants around a factor of three times higher than the unfunctionalised parent acid.[1,5]

†The inconsistent situation in which the term *algin* has been superseded by *alginic acid*, but *pectin* has remained in universal usage (instead of the analogous *pectic acid*), is simply a matter of historic convention. In either case, the terms *alginate* and *pectinate* are used to distinctly identify the salts of these polyuronic acids, respectively.

diffraction experiments also revealed the electron-rich cavities that exist in the buckled polyguluronic acid arrangement.[27] Although occupied by water molecules, these cavities offer a clearly favourable cation binding site.[30]

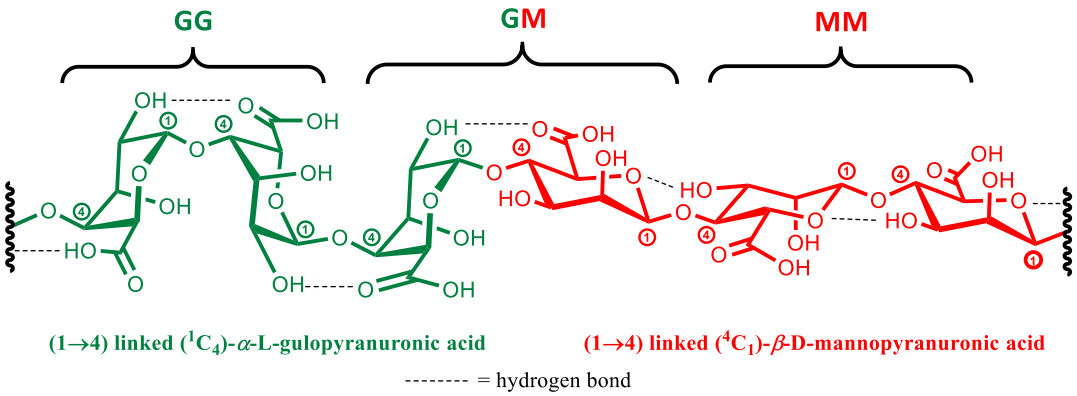

Figure 3.5 The structure of alginic acid

The importance of the *ax-eq-ax* arrangement of hydroxyl groups in metal-saccharide complexation (as recognised by Angyal, see Section 3.3.1.2), and the appearance of the same motif in the α-L-gulopyranuronic units of alginate lead to the development of the so-called "Egg-Box" model of divalent cation binding. Independently proposed by Angyal[15] and Smidsrød *et al.*,[31] the Egg-Box Model was formalised by Grant and co-workers in 1973,[32] in a paper that has since been cited almost 2000 times to-date. In the classical formulation of the model, the five available oxygen atoms from two guluronic units arranged in the buckled formation described above, chelate to a divalent cation in a pentadentate arrangement (see Figure 3.6).

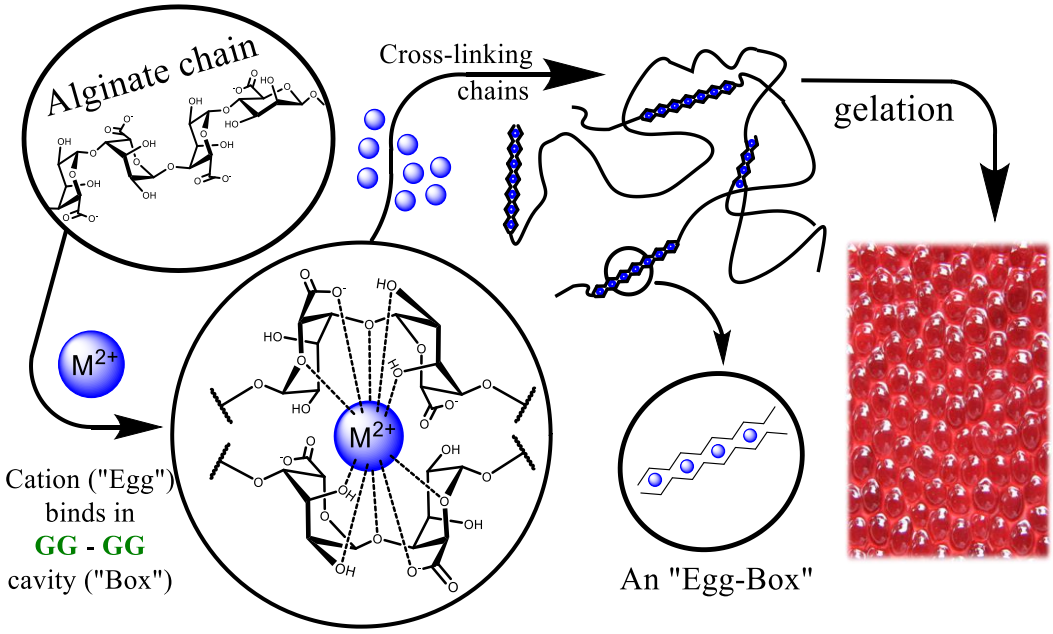

Figure 3.6 Alginate gelation through the classical "Egg-Box" model of cation binding. Each GG dimer provides a pentadentate coordination of the metal ion.[32]

Following the initial Ca^{2+} coordination in the first **GG** site, a second guluronate chain then chelates the cation in a similar manner. Whilst the coordination of a single cation between two chains is too weak to hold the polymers chains together permanently, a cooperative effect occurs[33–36] whereby local alignment of the chains around the metal ion facilitates the next cation to bind in the next uronate pocket, which is repeated until a critical number of about 20 sequentially bound units is achieved (see Figure 3.6).[34,37] The arrangement of cations bound in aligned guluronate cavities is reminiscent of eggs placed in an Egg-Box, from which the model derives its name.

The Egg-Box model was born out of a large amount of interest into the gelation behaviour of alginates in the presence of divalent metal ions, which was investigated extensively by a team lead by Arne Haug in Trondheim, Norway, throughout the 1960s and 70s.[31,32,38–44] In this regard, the Egg-Box model successfully explains many of the observed alginate gelation phenomena such as the ready formation of gels with Ca^{2+} (which sits comfortably in the Egg-Box sites) in contrast to Mg^{2+} (too small for Egg-Box sites),[45] or the strong gels formed by **GG**-rich alginates (with many Egg-Box sites) compared to **MM** or **MG** chains (lacking Egg-Box sites).[32,34,37,46] Since this early research, alginate have found use in a range of applications, from culinary uses,[47] to cosmetics, [48] and multifarous biomedical applications (drug delivery systems, cell encapsulation, wound dressings, gastro-oesophageal linings, treating cystic fibrosis *etc.*).[25,36,49–51] Perhaps most interesting property of alginates, from the point of view of biomass-utilisation, is the highly selective nature of metal-binding, following a generalised affinity series:[37,38]

$$\mathbf{Pb^{2+} > Cu^{2+} > Cd^{2+} > Ba^{2+} > Sr^{2+} > Ca^{2+} > Co^{2+} > Ni^{2+} > Mn^{2+} > Mg^{2+}}$$

Whilst the trend can, in-part, be rationalised by the relative hydration enthalpies of the metal species[52] and by reference to the *Irving-Williams Series*,[53] a satisfactory explanation for the exact ordering has yet to be proposed. However, despite such theoretical shortcomings, the potential for technological exploitation of the series has been widely recognised.[23] Particularly, the high affinity of alginate for toxic metals (Pb^{2+}, Cu^{2+}, and Cd^{2+}) gives rise to the possibility of the utilisation of kelp as a bioremediation agent (an idea explored extensively in Chapter 5).[54–56]

Given the far reaching applications of metal-bound alginates, verification of the Egg-Box model has been the subject of a great deal of experimental investigations in the solution-, gel-, and solid-states by a diversity of techniques, including circular dichroism,[32,57–60] NMR spectroscopy,[36,58,61–65] X-ray fibre diffraction,[30] small-angle X-ray scattering (SAXS),[66] and Fourier transform infra-red spectroscopy (FTIR).[67–69] However, the advent of computational methods has led to a number of (in some cases drastic) revisions to the classical model, casting significant doubts on the existence of Egg-Box type binding as it was originally proposed. A brief summary of the most significant challenges to the classical Egg-Box model is provided in the following section.

3.3.1.5 Alternative interpretations of the Egg-Box model

Initial doubts of the classical Egg-Box model (as is defined in Section 3.3.1.4) were first raised by Angyal, who queried the plausibility of a deca-coordinated calcium ion.[1] Indeed, a systematic review of calcium-saccharide complexes demonstrated that a di-pentadentate chelation of Ca^{2+} has no precedent.[70] As a consequence, researchers began to probe the

local coordination environment of a cation bound within an Egg-Box site by computational means. Three successive revisions of the Egg-Box model have all returned differing results. De-Ramos *et al.* proposed a model where only 6 oxygen atoms (of the 10 available from two **GG** units) were bound to Ca^{2+},[62] and Braccini and Pérez provided evidence to suggest that only 4 would bind.[71] However, the most radical divergence from the classical Egg-Box model came in a recent study by Plazinski and Drach, who investigated the coordination of a Ca^{2+} ion to a **GG** dimer through a hybrid density functional theory-molecular dynamics (DFT-MD) approach.[72,73] Here the authors reported that, rather than the Ca^{2+} ion remaining in the cavity of a **GG** dimer, the system was around 90 KJ mol^{-1} more stable with the cation outside of the central site, bound simply (in a bidentate arrangement)[43] to a single carboxylate group (see Figure 3.7) – over 3.2 Å away from any other the other oxygen atoms of the saccharide![70*] The authors concluded that coordinated water molecules in the hydration sphere of the Ca^{2+} showed a greater affinity for the metal ion than the hydroxyl and ring oxygens of the individual guluronate units. .

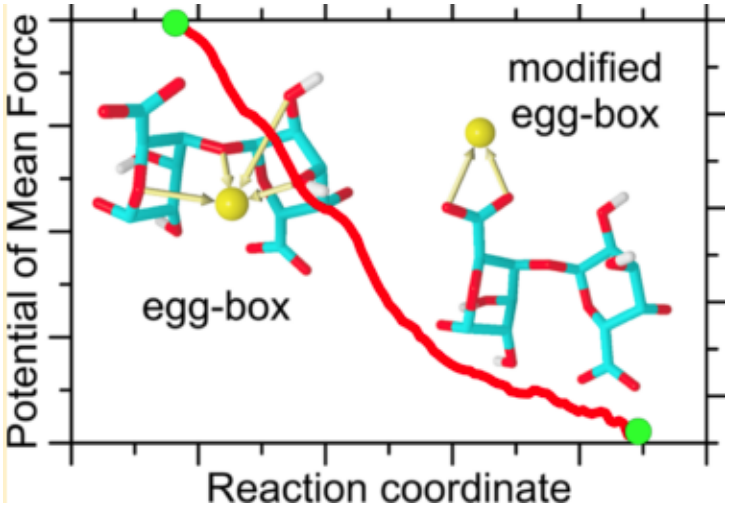

Figure 3.7 Energy minimisation of a **GG** dimer bound to Ca^{2+} in an Egg-Box arrangement (water molecules not shown). Reprinted with permission from by Plazinski and Drach.[42] © 2013 American Chemical Society.

Hence, whilst the classical Egg-Box model is an elegant representation of the interactions of metal ions with alginate, there is a growing degree of scepticism surrounding its accuracy. It is notable, however, that challengers to the model have not yet reached a consensus as to a suitable alternative, possibly owing to the complex demands of probing and modelling such complicated polymers. As such, the following section aims to simplify the task of investigating alginate-cation binding by considering the coordination behaviour of its constituent monosaccharides: L-guluronate and D-mannuronate.

3.3.2 Monopyranuronate-metal coordination

3.3.2.1 Monopyranuronate-metal coordination: general comments

With such uncertainty surrounding the binding of polyuronides to metal ions, an analysis of the properties of the composite monomeric units of such oligo- and poly-saccharides could provide a sensible starting point to test underlying assumptions. Unfortunately,

* As a point of reference, the average Ca-O distance in metal-saccharide binding is 2.48 Å.[70]

however, such appraisals are distinctly lacking – especially in the case of algal mono-uronates. The following sections will survey the limited available information with a view to designing experiments that can explore and explain differences between various mono-uronates and, potentially, their polymeric forms. Studies in the literature that seek to simultaneously compare all four significant mono-uronates (L-guluronate (**Gul**), D-mannuronate (**Man**), D-glucuronate (**Glc**), and D-galacturonate (**Gal**)) are extremely rare,[74,75] making comparisons between them difficult to draw. It is hoped that this chapter will remedy the situation to some extent by instigating tandem experiments on all four uronates such that their metal-binding behaviour may be compared directly.

3.3.2.2 Algal monopyranuronate-metal coordination: L-guluronate

Despite the importance of mono-*α*-L-gulopyranuronate to the understanding of the alginate-metal coordination, the compound has received very little attention in its own right. In the 1930s Isbell observed changes in the mutarotation behaviour of solutions of D-gulose (a neutral counterpart to L-guluronate, see Figure 3.8)* upon the addition of $CaCl_2$, corresponding to a shift of the pyranose anomeric equilibrium towards the formation of the sterically unstable (see discussions in Chapter 2) *α*-anomer.[76–78] Following crystallisation of a *α*-D-gulopyranose.$CaCl_2$.H_2O adduct,[76] the aqueous Ca^{2+}-gulose complex was found to have a stability constant of 3.7 M^{-1} (over 30 times larger than that of other neutral sugars with Ca^{2+}).[1] Lanthanide-induced changes to the ^1H NMR spectra of the methyl glycoside of *α*-D-gulose later indicated that the *ax-eq-ax* arrangement of oxygens described in Section 3.3.1.2 was responsible for the metal-binding properties displayed by the saccharide.[79]

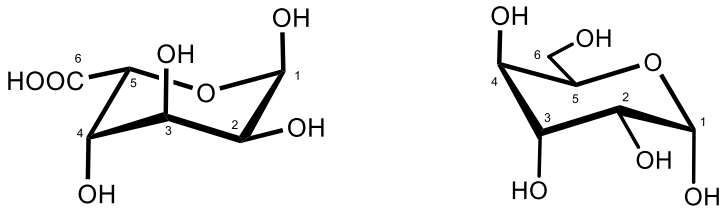

Figure 3.8 *α*-D-gulopyranose is a useful neutral comparator for the behaviour of mono-*α*-L-gulopyranuronic acid

Whilst *ax-eq-ax*-type binding may be important for cation chelation in the neutral *α*-gulopyranose monosaccharide, the same is not necessarily true for the guluronate counterpart. A hybrid DFT-MD computational investigation by Plazinski and Drach indicated that the interaction between Ca^{2+} and monogulopyranuronate is essentially one between the cation and a carboxylate group (see Figure 3.9).[72,80] Whilst this computational model suggested that mono- or bi-dentate coordination of the oxygen were very close in energy (separated only by a small energetic barrier associated with the re-arrangement of water molecules) any involvement from the hydroxyl oxygens or ring oxygen in binding was energetically unfavourable.

* As explained in Chapter 2, the $^4C_1$ stereochemical arrangement of D-gulose is enantiomeric with the $^1C_4$ form of L-gulose. As the two molecules are energetically equivalent, they may be considered to be synonymous for our purposes.

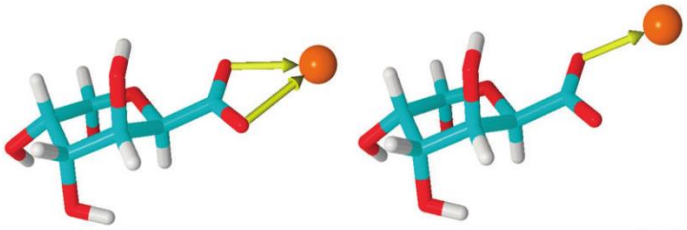

Figure 3.9 Energy minimisation by Plazinski and Drach of a monogulopyranuronate molecule in the presence of Ca^{2+} (water molecules omitted from diagram).[80] Reproduced with permission from both the Centre National de la Recherche Scientifique (CNRS) and The Royal Society of Chemistry (RSC) 2015.

The computational results of Plazinski and Drach are somewhat at odds with the crystal structure of sodium mono-*α*-L-gulopyranuronate (the only known mono-guluronate structure determined to-date).[81] Here, the Na^+ ion appears to rest in the *ax-eq-ax* site, but the distances from O1, O2, and O3 (2.375, 2.849, and 2.344 Å, respectively) do not suggest that all three hydroxyl groups contribute equally to the binding. The second binding site in the crystal structure places the Na^+ cation equidistant from O4 and O6 (a carboxylate oxygen). Hence, this tantalising molecular structure comes no closer to resolving the question of whether the *ax-eq-ax* site would actively bind metal ions in solutions of mono-guluronate, or whether the cation simply adopts such a position in the solid state for purposes of crystal packing.

Some authors have questioned the degree to which the stereochemical arrangement of mono-L-guluronate is anticipated to lead to observable differences in its metal-binding abilities compared to **Man**, **Gal**, and **Glc**. For instance, Kohn *et al.* demonstrated that Ca^{2+} ions show a nearly identical decrease in potentiometric activity* in the presence of **Gul** as in solutions of **Man**, **Glc**, **Gal** and, surprisingly, Cl^-.[74] Furthermore, Triffit also observed that mono-guluronate demonstrated no selectivity in the binding of Ca^{2+} and Sr^{2+}, despite the polymeric form of the molecule being able to discriminate between such cations.[82] Whilst these two studies did not consider the different anomeric forms of L-guluronate separately, the authors were led to the conclusion that the stereochemistry of **Gul** is relatively unimportant for governing the metal-binding properties of alginic acid, with the secondary structure of the polymer playing a much more significant role.

Given the uncertainties surrounding the metal-binding behaviour of mono-gulopyranuronate, it is perhaps surprising that more solution-state work has not been carried out to gain a better understanding. Indeed, only a single NMR spectroscopic investigation has been conducted in which the effect of a metal ion (Eu^{3+}) on **Gul** has been studied, and, whilst significant changes to the ^1H NMR spectrum of guluronate were noted, little could be interpreted from the results.[75] A key aim of this chapter will be to build on this early data in order to shed light on the nature of metal-mono-guluronate interactions in solution.

* Potentiometric measurements can be used to quantify the activity of a species in solution. Hence, upon coordination to a ligand, the observed potentiometric activity of a metal should decrease.

3.3.2.3 Algal monopyranuronate-metal coordination: D-mannuronate

Whilst studies into the metal binding properties of mono-D-mannuronate are, as with mono-L-guluronate, somewhat limited, all indications to-date are that **Man** behaves in a similar manner to its C2 epimer, D-glucuronate. Indeed, both **Glc** and **Man** show similar stability constants in complexes with Ca^{2+} and Cu^{2+},[21] and both compounds show similar responses to the addition of Eu^{3+} in their ^{1}H NMR spectra.[75,83] Hence, it might be assumed that the metal-binding modes available to **Man** are similar to those of **Glc** (described fully in Section 3.3.2.4), essentially utilising just the carboxylate oxygen or carboxylate and ring oxygens (see Figure 3.10). The predominance of the carboxylate binding is evidenced somewhat by the > 100-fold reduction in Ca^{2+} stability constant upon exchanging D-mannuronate for D-mannose (see Figure 3.11).[21] Indeed, whilst computational studies have suggested that a number of neutral coordination modes might be available for divalent metal ions in D-mannopyranose,[84] the stability of such complexation has been discounted elsewhere in the literature.[1,85] It is worth noting however that, whilst the mannopyranose stereochemistry does not appear to facilitate strong, selective binding to divalent cations, the *β*-furanose configuration is able to bind Ca^{2+} through the *cis-cis* arrangement of hydroxyl oxygens O1, O2, and O3 (see Figure 3.12).[86]

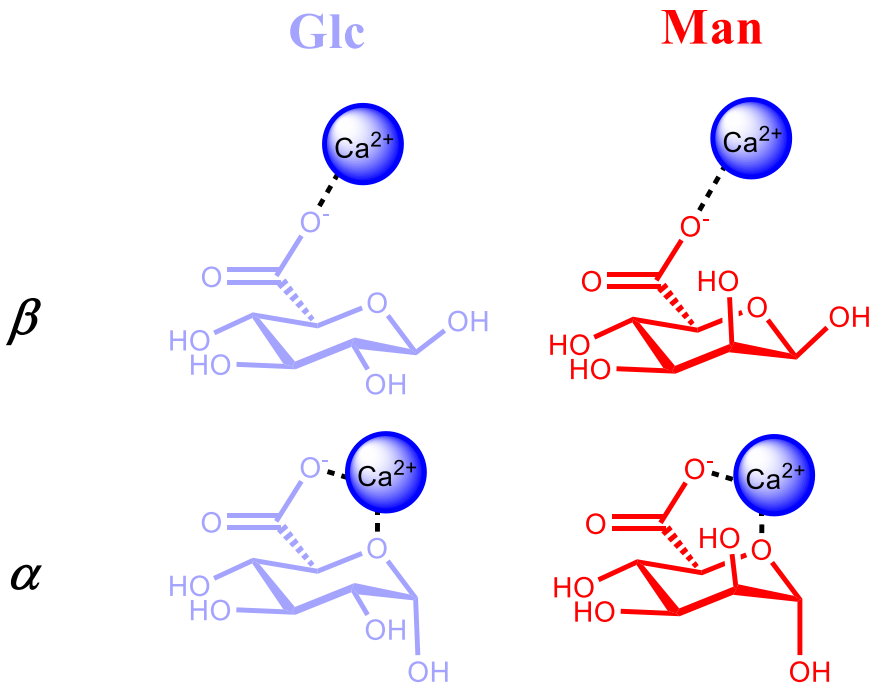

Figure 3.10 Possible parallels between the cation binding modes of D-glucopyranuronate (left) and D-mannopyranuronate (right)

β-D-mannopyranuronic acid

β-D-mannopyranose

Figure 3.11 *β*-D-mannopyranose is a useful neutral comparator for the behaviour of mono-*β*-D-mannopyranuronic acid

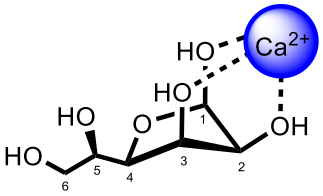

Figure 3.12 Observed Ca^{2+} binding to *β*-D-mannofuranose through the *cis-cis* arrangement of hydroxyl oxygens O1, O2, and O3[86]

3.3.2.4 Non-algal monopyranuronate-metal coordination: D-glucuronate and D-galacturonate

As was explained in Chapter 2, a historical imbalance exists in the degree to which the properties of **Gal** and **Glc** have been studied in comparison to the algal mono-uronic acids, **Gul** and **Man**. As such, the metal-binding behaviour of the former pair of saccharides has been investigated quite extensively compared to the algal-uronates discussed in Sections 3.3.2.2 and 3.3.2.3. Though the absolute values of stability constants of complexes between divalent metal ions and **Gal**/**Glc** in aqueous solutions vary quite widely,[8,20–22] their relative sizes consistently show that **Gal** can bind, for example, Ca^{2+} about two to three times more strongly than **Glc**. Detailed work by Jaques *et al.*[22] indicated that the *α*-anomer in both **Gal** and **Glc** will bind to Ca^{2+}-like cations more strongly than the respective *β*-counterparts (see values in Figure 3.13). The high affinity of mono-*α*-**Gal** for divalent cations has been invoked as an explanation into the gelling behaviour of pectins (polygalacturonates) (see references for examples).[1,71,87]

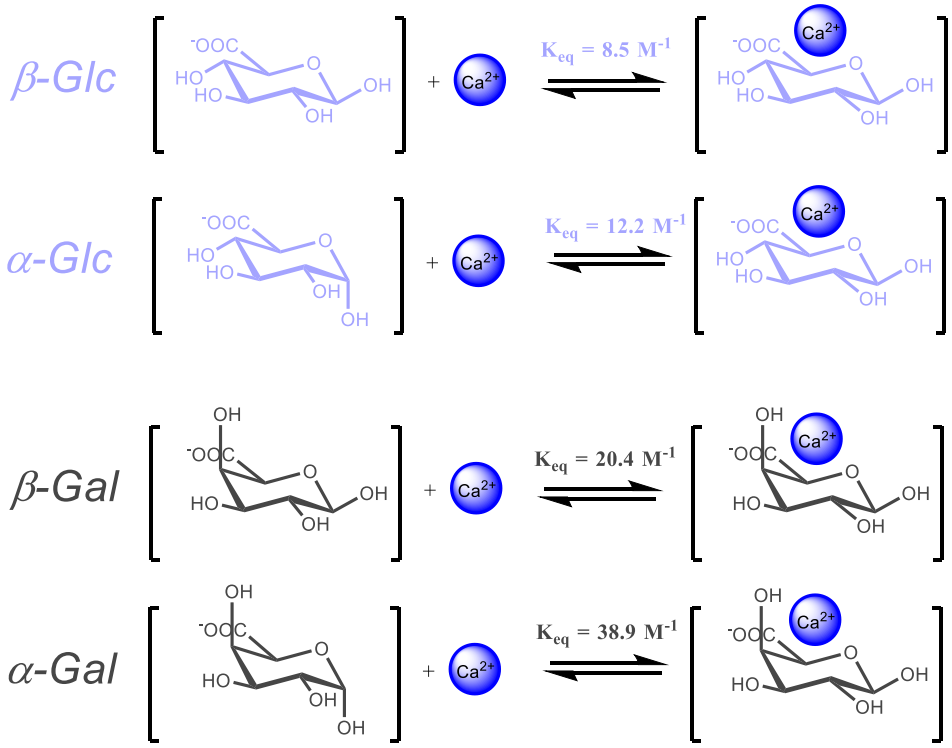

Figure 3.13 Stability constants for the Ca^{2+} complexes of **Gal** and **Glc** determined by Jaques *et al.*[22] The mode of coordination remains unspecified in each case.

As can be seen in Figure 3.13, disregarding the anomeric oxygen, the only stereochemical difference between **Glc** and **Gal** is that the hydroxyl group on C4 is equatorial in the former compound, but axial in the latter. Unsurprisingly therefore, many authors have attributed the stronger complexation of Ca^{2+} by **Gal** to binding modes that involve O4 in some manner.[5,20,75,88,*] However, evidence contrary to the involvement of O4 in galacturonate binding meant that the exact behaviour was disputed for some time.[1] For example, whilst not necessarily representative of complexation in solution, molecular structures derived from crystals of Ca-Na and Sr-Na double salts of *α*-D-galacturonic acid[89–92] do not show coordination between the metal ion and O4 – only the ring oxygen and a carboxylate oxygen. In contrast, the molecular structure of the crystalline adduct between $CaBr_2$ and *β*-**Glc** shows three independent binding modes that utilise in various combinations O1, O2, O4, O5 and O6, indicating a number of possible coordination modes with similar energy that could be accessible in solution (or possibly exist as a consequence of crystal packing requirements in the solid state).[93]

A series of NMR-based spectroscopic lanthanide-uronate experiments[27–32] has assisted in developing the understanding of the most likely cation coordination modes of **Gal** and **Glc**. Notably, Angyal *et al.*[83] and Izumi[94] both provided evidence to suggest that only the carboxylate and ring oxygens are involved in metal binding by *α*-**Gal** and *α*-**Glc**, and only the carboxylate oxygens are involved in metal binding by *β*-**Gal** and *β*-**Glc**, excluding entirely any contributions from O4. Angyal *et al.*[83] then proposed a theory that, whilst not involved directly in coordination, the orientation of the hydroxyl group on C4 is important for dictating the ease with which the carboxylate moiety can align with the plane of the ring oxygen for optimum binding of the cation. Hence, the equatorial position of O4 in **Glc** gives rise to a destabilising 1,3-parallel steric clash when the carboxylate is in the correct orientation for cation-coordination, whilst the axial position of the same group in **Gal** does not provide such a barrier and, consequently, facilitates stronger binding (see Figure 3.14). The cause of the greater metal-binding ability of *α*- over *β*-anomers in the **Gal** and **Glc** systems, was attributed to the greater ability of the axial O1 to donate electron density to the ring oxygen, and hence to the cation (see Figure 3.14).[83]

The predominance of the carboxylate binding in **Gal** and **Glc** may go some way to explaining the pH dependence on the strength of the binding.[75,88,99] For example, Anthonsen demonstrated that *α*H1 of Na-*α*-D-galacturonate shows a much larger change in chemical shift upon the addition of Eu^{3+} than does *α*-D-galacturonic acid (see Figure 3.15).[99] Similarly, the lack of involvement of other hydroxyl oxygens around the **Gal** and **Glc** rings offers a potential explanation as to why methyl glycosidation of the uronates does not appear to effect their metal binding abilities significantly.[5,14,20,79,95,96]

[*] The depiction by Fuks and Bünzli[88] of **Glc** and **Gal** binding metal ions in a $^1C_4$-manner rather than through the conventional $^4C_1$-arrangement seems to be very unlikely based on the very high energy associated with the former conformation. Such a theory has not gained widespread support.

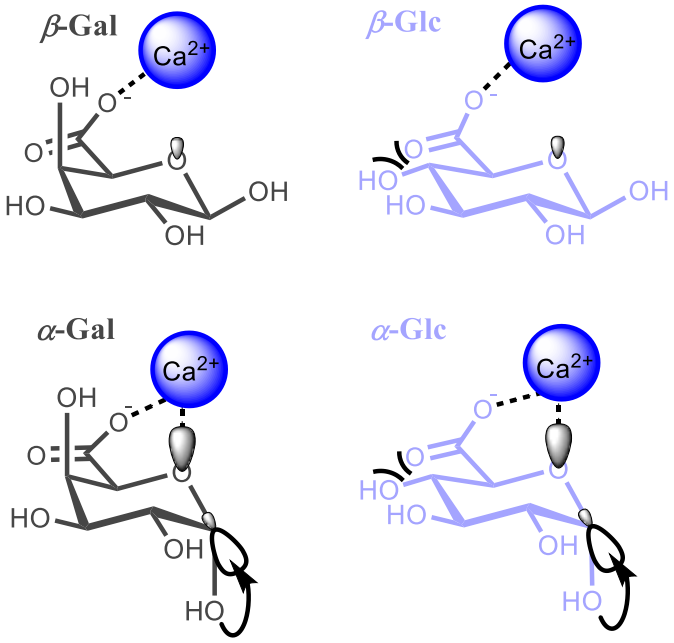

Figure 3.14 Probable binding modes of Ca^{2+} to **Gal** and **Glc**.[83]

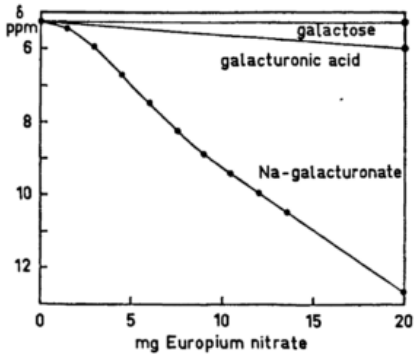

Figure 3.15 Changes to the chemical shift of αH1 in Na-α-D-galactopyranuronate, α-D-galactopyranuronic acid, and α-D-galactopyranose upon the addition of Eu^{3+}. Reproduced with from Anthonsen *et al*.[99] © Swedish Chemical Society 1972.

3.3.2.5 Binding of mono-uronates to d-block metals

Many authors such as Tajmir Rahni[97,100–104] and others[105–116] have sought to expand the range of metal ions examined for their ability to bind to mono-uronates beyond the s-block.[97,100–104,*] Of particular interest are d-block metals where, for example, the stability constants of Cu^{2+} with **Glc**, **Gal**, and **Man** have been shown to be around ten times greater than their Ca^{2+} equivalents.[21] Interestingly, authors cite fewer differences between the stability constants of **Gal** and **Glc** with (for example) Ni^{2+} or Co^{2+},[107] and there remains to be little evidence to suggest that binding occurs through the hydroxyl groups or ring oxygen

[*] Though, again, such studies have tended to focus on only **Glc** and **Gal**, rather than the algal-uronates

in such cases.[105] Independent computational investigations of mono-guluronate and di-guluronate units with various d-block metal ions indicated an affinity series of $Cu^{2+} > Co^{2+} > Zn^{2+} > Mn^{2+}$, which is in accordance with other carboxylate-metal stability trends.[80,117] Hence, it has been suggested that transition metal complexes of uronates are dominated by carboxylate-metal binding, with the higher strength being attributed to considerable covalent character arising from interactions with the cation d-orbitals.[117] Of course, the speciation behaviour of the d-block ions in aqueous solution must also be considered, and Angyal pointed out that (at pH 7) the dominant Cu^{2+} species in solution is likely to be $[Cu_2(OH)_2]^{2+}$, which may give rise to more complex binding modes than in the case of s-block ions. The case of Cu^{2+} is especially worthy of additional investigation, particularly because of the high affinity of alginates for this species (see Section 3.3.1.4) and also the extraordinary thermochemical behaviour exhibited by Cu(II)-uronate salts (see Chapters 4 and 5).

3.3.3 Probing saccharide-metal binding by NMR spectroscopy

As discussed in Section 3.3.1.1, contemporary understanding of the binding between a metal ion and a carbohydrate ligand owes much to the advent of nuclear magnetic resonance (NMR) spectroscopy. Chemists practising in the 1960s, who had been educated in classical carbohydrate analytical procedures, soon embraced the unparalleled sensitivity and richness of data offered by NMR spectroscopy, using the technique to great effect. Indeed, whilst ^{1}H and ^{13}C NMR spectroscopies are now employed routinely in metal-saccharide binding studies to observe signals from the composite nuclei of C-H bonds around the sugar, recent advances have now given researchers access to signals arising from hydroxyl protons[118–120] and, recently, even from the metal itself (with ^{43}Ca NMR spectroscopy being a notable example).[18,121,122,*] The work in this chapter, however, is limited to the more familiar NMR techniques, and, though a great deal of work has been carried out to investigate alginate-metal binding by solid- and gel-state NMR,[36,58,61–66] the discussions here are further narrowed to include only solution state studies. Within these restrictions, and bearing in mind the goal of understanding metal-mono-uronate interactions, there are a number of parameters that can be measured when conducting NMR-based spectroscopic investigations into metal-saccharide coordination:

I. Metal-induced changes to equilibria

As discussed in Chapter 2, monosaccharides reversibly adopt a number of different isomeric configurations when freely solvated in aqueous solutions. The position of the equilibrium between such configurations can offer insight into the differences in free energy of the two states when they are bound (or otherwise) to a metal ion. In this regard, it can be assumed that a shift in equilibrium upon the addition of a metal-ion is indicative of a more favourable binding interaction with the species that increases in concentration. Whilst mutarotation data was classically the method of choice for establishing the position of anomeric equilibria, ^{1}H NMR spectroscopy facilitates rapid measurement of such parameters by integration of

[*] It should be noted, however, that both hydroxyl-resonance and ^{43}Ca NMR spectroscopies still require quite specialised conditions and are not utilised in this study.

well-defined signals arising from protons in the different configurations.[14] Of interest to this chapter are the pyranose anomeric equilibria of mono-uronate compounds (particularly in the case of the algal uronates described in Chapter 2) in the presence of alkali and alkali earth metals.

II. Changes to chemical shift induced by diamagnetic cations

In the presence of an electric field (such as that surrounding a cation) the magnetic field around a nucleus is perturbed and hence, so too are the corresponding chemical shifts as measured by NMR spectroscopy. For protons, the Buckingham equation (expressed in general form as Equation 3.1)[123] has been proposed to predict the change in ^{1}H chemical shift ($\Delta\delta$) due to the interference of an electric field of magnitude E (where $E_{C\text{-}H}$ represents the component of E along the C-H bond):

$$\Delta\delta = A\Delta E_{C\text{-}H} + B\Delta E^2 \qquad \text{[Equation 3.1]}$$

Such a theoretical treatment has been used, with partial success, in discerning the binding of Ca^{2+} to **Glc** and **Gal**.[22] Furthermore, Angyal used the Buckingham formula extensively in his studies of polyols and sugars[12,14–16,124] and reported a large shift to higher frequencies (on the order of 0.3 ppm) for the central proton in an *ax-eq-ax* arrangement when bound to Ca^{2+}.[12] Modifications of Buckingham's work have also been made to enable the interpretation of $\Delta\delta$ values derived from ^{13}C NMR spectroscopy,[125,126] which again has found utility in the study of metal-saccharide binding.[17,22,127–130] However, difficulties have been reported in the determination of the precise geometry of Ca^{2+} coordination to **Glc** and **Gal** from $\Delta\delta(^{13}C)$ values in isolation,[22] largely owing to the influence of second order effects (discussed further in Appendix E).

III. Changes to chemical shift induced by paramagnetic cations

The changes in chemical shift ($\Delta\delta$) of either a ^{1}H or ^{13}C NMR spectroscopic signal are typically much larger for complexation with a paramagnetic cation relative to those of a diamagnetic cation.[131] As many lanthanides are paramagnetic, they can give rise to very large $\Delta\delta$ values – termed a lanthanide induced shift (LIS) - which in turn can be used to establish the geometry of ligand binding.[132] LIS values have found widespread utility in probing saccharide metal binding modes by NMR spectroscopy, including in the study of mono-uronates and their derivatives.[62,79,83,94–96,98,124] An observed LIS is governed by three interactions; an electric field influence (diamagnetic effect), a magnetic through-bond influence (contact effect), and a magnetic through-space influence (pseudo-contact effect).[132] The theory governing both the magnitude and direction of a LIS is somewhat involved, and interpretation of the resultant data can be both difficult and, in some cases, ambiguous. Furthermore, it is worth noting that, whilst lanthanides undoubtedly offer useful insight into potential binding modes displayed by a molecule, their typically 3+ charge does not necessarily make them good proxies for predicting the behaviour of divalent cations such as Ca^{2+}.[133]

IV. Measuring stability constants

Whilst in principle, changes to relevant chemical shifts and perturbations of anomeric equilibria should give sufficient data to calculate the stability constant of the metal-saccharide complex under investigation, the reality is much more complicated. Firstly, because the exchange between complexed and uncomplexed states of a metal and saccharide is extremely fast compared to the NMR spectroscopic timescale,[133,*] individually resolved peaks for both situations do not arise, rather an averaged signal is observed for the pair. As such, using $\Delta\delta$ to calculate a metal-sugar stability constant requires the extrapolation of a value for the "limiting shift" (the value of δ that corresponds to the fully complexed state), which is inherently subject to errors (such as the secondary binding modes that can be activated at higher metal concentrations).[1,7,14] Alternatively, methods for determining the stability constant of a metal-sugar complex by reference only to coordination-induced changes to the anomeric equilibria have also been utilised. In these cases, an assumption must be made that only one anomer is involved in binding, whilst the other does not interact with the metal ion.[14] For uronate-metal binding, such an assumption would surely be invalid, as the presence of the carboxylate group guarantees some degree of binding to every anomer present.

V. Selective line broadening

Aside from the intensity and positon of a peak in an NMR spectrum, the peak shape (specifically the half-width at half height, HWHH) can also give useful information about the chemical environment of the source nucleus. If a nucleus is in proximity to a paramagnetic field or is part of a molecule that has a large correlation time (for a large molecule or samples in a viscous solution), the resultant NMR spectroscopic signal may exhibit significant line broadening.[132] Such broadening is brought about by an increase in the transverse relaxation time (spin-spin relaxation) of a nucleus, and has interesting implications for the study of polyuronides. For example, the increase in viscosity of a sample of sodium alginate upon the addition of Ca^{2+} (or similar) causes line broadening of signals arising from nuclei in the vicinity of metal binding (owing to inhibition of molecular motion at that site).[62,64,65] For mono-uronates however, where changes to the tumbling of the saccharide upon metal binding are much less pronounced, line broadening through this mechanism does not appear to have been reported and is unlikely to be of interest for studies of coordination to alkali and alkali earth metals. For paramagnetic cation-monosaccharide binding, however, line broadening may be an insightful tool. Here, for example, Cu^{2+} ions may induce selective line broadening upon coordination to a sugar, without giving rise to very large and complex $\Delta\delta$ values.[105,132]

[*] Angyal determined that, under steady state conditions, the forward and backward rate of formation of a D-glucitol-Ca^{2+} complex is 108 M^{-1} s^{-1} at 40 °C.[133]

3.4 Summary of current understanding of metal-uronate interactions and chapter aims

Despite wide recognition that alginate is a unique bio-product possessing diverse applications in a range of sectors, the survey in Section 3.3.1.5 demonstrates that research into these areas has generated many uncertainties. Ultimately, many of the questions posed can be reduced to a single fundamental concern: what is the coordination environment of a metal-ion bound to an alginate chain? If the answer to such a query could be elucidated with respect to a range of different metal ions and **MM**/**GG**/**MG** arrangements, then suitable models could be developed to simulate, for example, the early stages and onset of gelation or the optimisation of desirable ion-exchange activities. For the particular application described in the latter half of this thesis (namely the thermolysis of kelp biomass), a knowledge of the binding site of a cation to a saccharide has been shown to be critical for understanding the thermodegradative routes taken by the carbohydrate. Indeed, Chapters 4 and 5 reveal that the entire thermal behaviour of alginate and alginate-rich kelp is dictated by the identity of the metal ion coordinated to the polymer, hence, a fundamental understanding of such complexation is critical.

As such, this chapter aims to re-dress one of the most neglected areas of research, namely the coordination of the monomeric units of alginate with different metal ions. The isolation and NMR spectroscopic characterisation of the elusive algal mono-uronates outlined in Chapter 2 will facilitate the study of metal binding behaviour by utilising the methods discussed in Section 3.3.3. In this regard, the key questions to be answered are:

- Which oxygen atoms of an algal mono-uronate molecule are involved in metal-coordination? Specifically, are the hydroxyl oxygens involved, or is binding restricted to carboxylate and rings oxygens?
- How important is the character of the cation to the nature of the coordination exhibited by algal mono-uronates? What are the differences across the s-block (including the metals to which alginate is most commonly bound in nature)? How does such behaviour contrast to d-block cations (for which alginate has a very high affinity)?
- How does the coordination behaviour of algal mono-uronates (**Gul** and **Man**) contrast with that of their more widely studied molecular cousins (**Glc** and **Gal**)?
- How is the binding between mono-uronates and a metal ion affected by the experimental conditions? Of particular relevance – what is the effect on metal complexation of lowering the pH of a uronate solution to the extent that the carboxylate moiety becomes protonated?

Whilst it is recognised that answering these questions will not be able prove the nature (or even existence) of the binding mode described by the classical Egg-Box model, it will provide currently lacking empirical evidence from which future theoretical studies can draw insight. Ultimately, when a full understanding of the metal binding behaviour of mono-uronates is achieved, then it is more likely that equivalent understanding can be gained for the polymer.

3.5 Results and discussion

3.5.1 Overview of experiments

Three sets of NMR-based spectroscopic experiments were carried out (summarised in Table 3.1) in order to identify the metal species with which algal mono-uronates (L-guluronate and D-mannuronate) complex and also to determine the mode of binding in such cases. Where appropriate, the related uronates (D-galacturonate and D-glucuronate) were studied in parallel to provide a point of comparison with the binding of the algal-derived saccharides. The selection of metal ions for Investigation A (see Section 3.5.2) was based in the first instance on those that are naturally found bound to alginate in kelps (specifically: Na^+, K^+, Mg^{2+}, Ca^{2+}, Sr^{2+}, and Ba^{2+}). These s-block metal ions, have also been extensively studied in other areas of alginate chemistry, including their influence on gelation behaviour, cation exchange, and (as is demonstrated in Chapters 4 and 5) thermochemistry. Within the range of selected metal ions, Ca^{2+} is often chosen as a probe cation for studying biological coordination environments owing to its high natural abundance and prevalence in many areas of biochemistry (including that of the uronides). Consequently, Investigation B concerns the use of Ca^{2+} to provide a more in-depth exploration of the binding mode of divalent cations to algal mono-uronates (see Section 3.5.3). Finally, because of the extraordinarily high affinity of alginates for Cu^{2+}, as well as the distinctive influence of this particular cation on uronide pyrolysis chemistry (see Chapters 4 and 5), Investigation C explores the uronate coordination behaviour of copper(II) alongside zinc(II) as a diamagnetic analogue (see Section 3.5.4).

Table 3.1 A summary of experimental investigations carried out in Chapter 3

	Investigation A	Investigation B	Investigation C
Purpose	To screen for complexation between mono-uronates and s-block metal ions	To more clearly elucidate the binding configuration of mono-uronates and divalent metal ions	To compare the uronate-binding behaviour of d-block metals
Metal(s) studied	Na^+, K^+, Mg^{2+} Ca^{2+}, Sr^{2+}, Ba^{2+}	Ca^{2+}	Cu^{2+}, Zn^{2+}
Nuclei studied	^1H	^{13}C, ^1H	^{13}C (Cu^{2+}) ^1H (Zn^{2+})
pH*	7.5 1.0	7.5	6.0 (Cu^{2+}) 1.0 (Zn^{2+})
[uronate] / M	0.043	0.260	0.260 (Cu^{2+}) 0.043 (Zn^{2+})
[metal] / M	1.0	0.0 – 1.3	0.052 (Cu^{2+}) 1.0 (Zn^{2+})
[metal] / [uronate]	23	0.0 – 5.0	1/500 (Cu^{2+}) 23 (Zn^{2+})

3.5.2 Investigation A: affinity of mono-uronates for s-block cations

3.5.2.1 General comments on Investigation A

The purpose of Investigation A was to gauge the differing affinities of mono-uronates for an array of relevant s-block metal ions. To this end, the ^{1}H NMR spectra of the sodium salts of L-guluronate (**Gul**), D-mannuronate (**Man**), D-glucuronate (**Glc**) and D-galacturonate (**Gal**) were recorded in D_2O solutions (295 K, pH* 7.5) containing 1.0 M aqueous metal chloride salts (with a "blank" experiment run in parallel containing only the uronate salt with no further additives).* Following the acquisition of the NMR spectra, the consequences of protonating the carboxylate moieties of the uronates on their ability to bind a cation was investigated by reducing the pH* of the solutions from 7.0 to 1.0, and re-acquiring the NMR spectra.†

The observable effect of the inclusion of the metal salts (and changes to pH*) to the resulting ^{1}H NMR spectra of the mono-uronates are to cause changes to the relative signal intensities (as the relevant saccharide configurational equilibria are perturbed) and to the chemical shifts (δ) of the protons (caused predominantly by the influence of the electric field of the cation), both of which are illustrated in Figure 3.16.

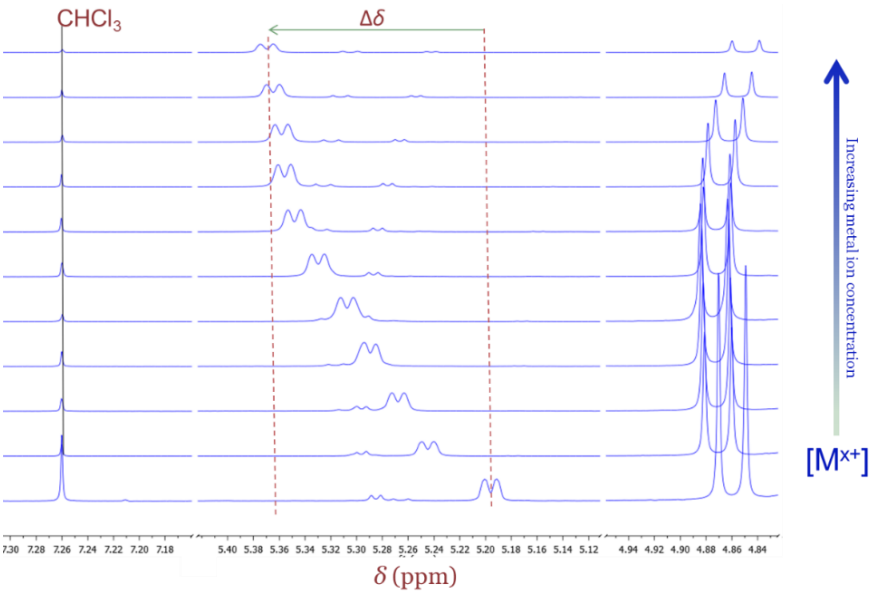

Figure 3.16 An example of the changes that can take place in the ^{1}H NMR spectra of mono-uronates upon increasing the concentration of metal ions (M^{x+}) in the solution. Changes to the relative chemical shift ($\Delta\delta$) and relative intensity of the peaks can both be seen prominently in this case.

* Whilst the blank experiment is often referred to as the "metal-free" scenario, this is something of a misnomer as any uronate salt will always require for a counteraction to be present, which, in the cases studied here, was Na^{+}. The additional metal chlorides are added in such a large excess, however, that the presence of the initial sodium may be assumed to be negligible.

† The term pH* was explained in Section 2.7.2.2 of Chapter 2, and is used to refer to the acidity of a D_2O solution as measured by a pH-probe calibrated in H_2O.

Naturally, Investigation A generated large quantities of data – not all of which is relevant to the discussions here (though Appendix E can be consulted for full tabulations and further explanations). Indeed, as the pyranose forms of the uronates dominate under the conditions studied, changes to the pyranose-furanose equilibria upon introduction of a metal ion are ignored (and the data in Appendix E demonstrates that such changes are largely very small anyway). Instead, the discussions focus on changes to the pyranose anomeric equilibria expressed as the ratio of α-anomer to β-anomer (α/β). Furthermore, the difference in the observed chemical shifts of the uronate protons in the metal-free and metal-containing solutions ($\Delta\delta_{obs}$) can be very insightful when considered as an absolute value (see Investigation B in Section 3.5.3 for example). However, for the purposes of screening for metal-uronate complexation (as in Investigation A), the differences in chemical shifts measured relative to another proton on the same ring ($\Delta\delta_{rel}$) are a more useful metric. The distinction between the different measures of "$\Delta\delta$" is elucidated fully in Appendix E (and full sets of data for both $\Delta\delta_{obs}$ and $\Delta\delta_{rel}$ are provided). For the following discussion, it is sufficient to note that when $\Delta\delta_{rel}$ values are either all zero (or close to zero) for a particular uronate anomer in the presence of a cation, no selective coordination between the metal and the hydroxyl groups around the monosaccharide ring is believed to be taking place. Given that $\Delta\delta_{rel}$ was found to be zero (or close to zero) in many of the cases considered in the following sections, only the most significant values are reported below.

3.5.2.2 Investigation A results for L-guluronate

As was discussed extensively in Chapter 2, the arrangement of hydroxyl groups in α-L-guluronic acid is highly destablising, owing particularly to a 1,3-diaxial clash (see Figure 3.17). Consequently, **Gul** exhibits the lowest α/β ratio of all of the four uronates studied: 0.21 when measured at pH* 7.5.[*] Figure 3.18 demonstrates the effect on this value of the addition of metal chloride salts (1.0 M) in to the uronate solution, and here it can be seen that Na^+, K^+, and Mg^{2+} have virtually no influence, with α/β ratios all staying within 0.05 of the metal-free case. Meanwhile, however, Ca^{2+}, Sr^{2+} and (to a lesser extent) Ba^{2+} all perturb the anomeric equilibrium dramatically in favour of the α-pyranose configuration, yielding α/β values of 1.50, 1.20, and 0.58, respectively. A decrease in the pH* to 1.0 at this stage (well below the pK_a of the uronic acids as shown in Chapter 2) decreases the energetic preference for α-**Gul** in the Ca^{2+} and Sr^{2+} solutions, has virtually no effect in the metal-free, Na^+, K^+, and Mg^{2+} solutions, and slightly increases the α/β ratio in the Ba^{2+} solution.

[*] This value is referred to as the "metal-free" case, and was measured for the uronate dissolved in D_2O without any additional metals added. The term "metal-free" is slightly misleading, as there is Na^+ present in the form of the uronate counter ion. As the added metals are in greater than 20-fold excess, the role of the Na^+ can be disregarded.

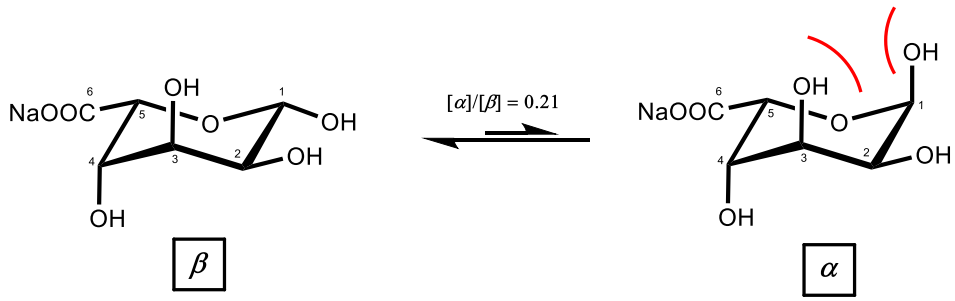

Figure 3.17 The anomeric equilibria found between pyranose anomers of sodium-L-guluronate in a D_2O solution (43 mM) at 295 K and pH* 7.5. The destabilising 1,3-diaxial clash of hydroxyl oxygens on the α-anomer is highlighted.

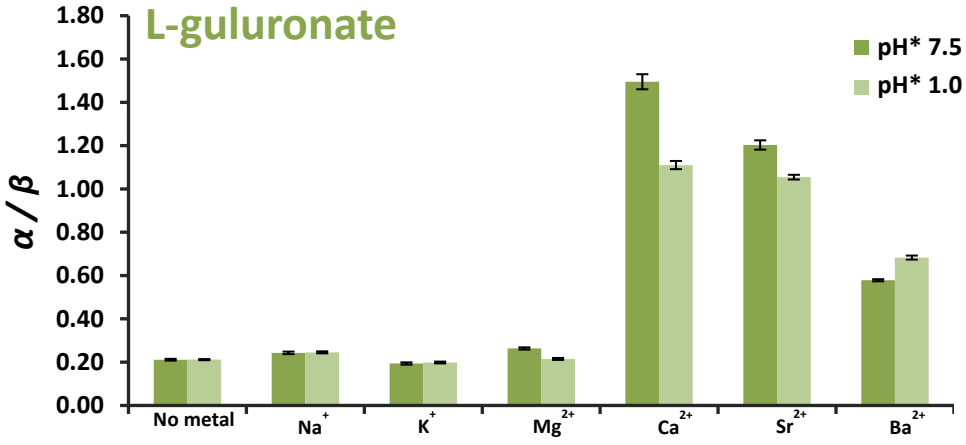

Figure 3.18 The α/β ratio of Na-L-gulopyranuronate recorded in 1.0 M solutions of different metal ions at 295 K and pH* 7.5 or 1.0.

Changes to the chemical shift of signals arising from the guluronate protons were also observed when comparing (at the same value of pH*) the metal-free and metal chloride solutions. For simplification (as mentioned in Section 3.5.2.1 and explained more fully in Appendix E) in for each added metal-ion the change in chemical shift for individual protons could be quoted relative to the change in chemical shift of a reference proton on the molecule in question – the so called $\Delta\delta_{rel}$ parameter. When $\Delta\delta_{rel}$ is considered for H1, H2, H3, and H5 relative to H4* of α- and β-L-guluronate in various metal solutions at pH* 7.5, the results can be seen in Table 3.2 (with a reminder of the uronate numbering system provided in Figure 3.19). The data in Table 3.2 displays very low values of $\Delta\delta_{rel}$ for the protons of α-**Gul** in the presence of Na^+, K^+, and Mg^{2+}, whilst additions of Ca^{2+}, Sr^{2+}, and Ba^{2+} give rise to much larger relative changes to chemical shift in the order $H_1 > H_2 \approx H_5 > H_3$. Meanwhile, β-**Gul** gives universally small values for $\Delta\delta_{rel}$ (< 0.10 ppm) for all protons (with the exception of H_1 and H_5 in the presence of Ba^{2+}).

* H4 is chosen as the reference proton as, in most cases, it has the largest shift to lower frequencies on the addition of metal chloride

The equivalent values of $\Delta\delta_{rel}$ for the protons of α- and β-**Gul** at pH* 1.0 are given in Table 3.3. It is interesting to note that, generally, the reduction in pH* reduces the magnitude of $\Delta\delta_{rel}$ in all cases, though not in a uniform manner. Hence, whilst the Ca^{2+} induced $\Delta\delta_{rel}$(α-**Gul**-H1) and $\Delta\delta_{rel}$(α-**Gul**-H5) values are reduced by 0.14 and 0.09 ppm, respectively on lowering the pH* from 7.5 to 1.0, $\Delta\delta_{rel}$(α-**Gul**-H2) and $\Delta\delta_{rel}$(α-**Gul**-H3) are only reduced by 0.04 and 0.03, respectively. Such differences cause a rearrangement of the order of $\Delta\delta_{rel}$ for α-**Gul** from $H_1 > H_2 \approx H_5 > H_3$ (at pH* 7.5) to $H_2 > H_1 > H_5 \approx H_3$ (at pH* 1.0). Similarly, the $\Delta\delta_{rel}$ values for β-**Gul**-H1 and β-**Gul**-H5 in the presence of Ba^{2+} and Sr^{2+} are considerably reduced at pH* 1.0. The implications of these results as evidence of the various binding modes active in α- and β-**Gul** are presented in Section 3.5.5.

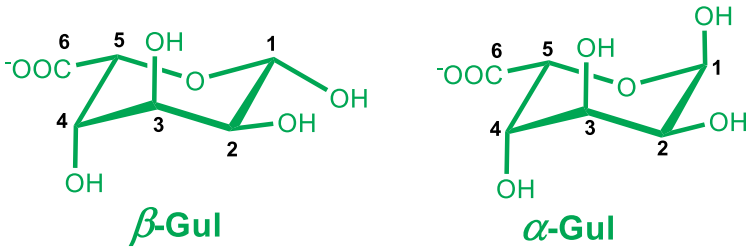

Figure 3.19 Atomic labels for β- and α-pyranose anomers of **Gul**

Table 3.2 $\Delta\delta_{rel}$ values for Na-L-guluronate in different metal chloride salts at pH* 7.5 (295 K, 400 MHz)

Solution	pH*		alpha pyranose						beta pyranose				
			Change in chemical shift (ppm) compared to metal-free solution relative to H4 ($\Delta\delta_{rel}$)										
			αH1	αH2	αH3	αH4	αH5		βH1	βH2	βH3	βH4	βH5
No metal	7.0		0.00	0.00	0.00	-	0.00		0.00	0.00	0.00	-	0.00
NaCl	7.0		0.04	0.03	0.04	-	0.04		0.01	0.01	0.02	-	0.02
KCl	7.0		0.03	0.02	0.03	-	0.01		0.01	0.01	0.01	-	0.01
$CaCl_2$	7.0		0.27	0.19	0.13	-	0.20		0.05	0.04	0.01	-	0.07
$SrCl_2$	7.0		0.28	0.20	0.14	-	0.22		0.07	0.06	0.03	-	0.08
$BaCl_2$	7.0		0.28	0.20	0.14	-	0.22		0.12	0.07	0.03	-	0.11
$MgCl_2$	7.0		0.06	0.00	0.02	-	0.04		0.01	0.00	0.01	-	0.02
$Ca(NO_3)_2$	7.0		0.24	0.15	0.09	-	0.19		0.05	0.04	0.02	-	0.06
CaI_2	7.0		0.28	0.21	0.15	-	0.21		0.09	0.06	0.05	-	0.10

Table 3.3 $\Delta\delta_{rel}$ values for Na-L-guluronate in different metal chloride salts at pH* 1.0 (295 K, 400 MHz)

Solution	pH*		alpha pyranose						beta pyranose				
			Change in chemical shift compared to metal-free solution relative to H4 ($\Delta\delta_{rel}$)										
			αH1	αH2	αH3	αH4	αH5		βH1	βH2	βH3	βH4	βH5
No metal	1.0		0.00	0.00	0.00	-	0.00		0.00	0.00	0.00	-	0.00
NaCl	1.0		0.02	0.02	0.02	-	0.02		0.00	-0.01	0.00	-	0.01
KCl	1.0		0.02	0.01	0.01	-	0.01		0.00	0.00	0.00	-	0.01
$CaCl_2$	1.0		0.13	0.15	0.10	-	0.11		0.01	0.00	0.02	-	0.01
$SrCl_2$	1.0		0.14	0.16	0.10	-	0.12		0.01	0.00	0.02	-	0.01
$BaCl_2$	1.0		0.15	0.15	0.10	-	0.14		0.04	0.01	0.01	-	0.04
$MgCl_2$	1.0		0.00	0.00	0.01	-	-0.02		-0.01	-0.01	-0.01	-	0.00

3.5.2.3 Investigation A results for D-mannuronate

The sodium salt of D-mannopyranuronate (see Figure 3.20) is unique within the mono-uronates to be the only molecule that has an inherent energetic preference for the *α*-anomer over the *β*-configuration (*α*/*β* = 2.63 under the metal-free conditions in Investigation A), a trait that was discussed in detail in Section 2.2.2 of Chapter 2. Upon the addition of a metal ion, the changes to the relative populations of the *α*- and *β*-D-mannopyranuronate forms (as displayed in Figure 3.21) are much more subtle than in the case of L-guluronate (see Section 3.5.2.2). Whilst addition of Na^{+}, Ca^{2+}, Sr^{2+}, and Mg^{2+}, appear to have virtually no impact on the *α*/*β* ratio, larger ions promote a slight increase in the proportion of the *β*-anomer present (with Ba^{2+} and K^{+} yielding *α*/*β* values of 1.36 and 1.77, respectively). A small increase in the proportion of mannofuranuronate upon the addition of Ca^{2+} (see Appendix E) is also noteworthy as the formation of Ca^{2+}-mannofuranose adducts have been identified elsewhere.[86]

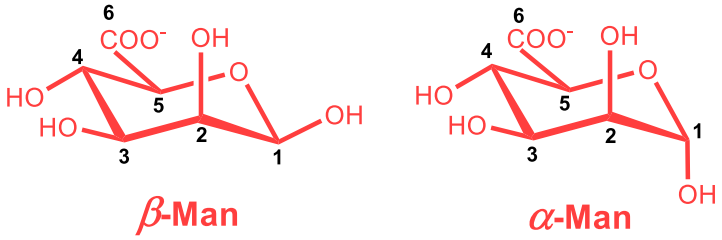

Figure 3.20 Atomic labels for *β*- and *α*-pyranose anomers of **Man**

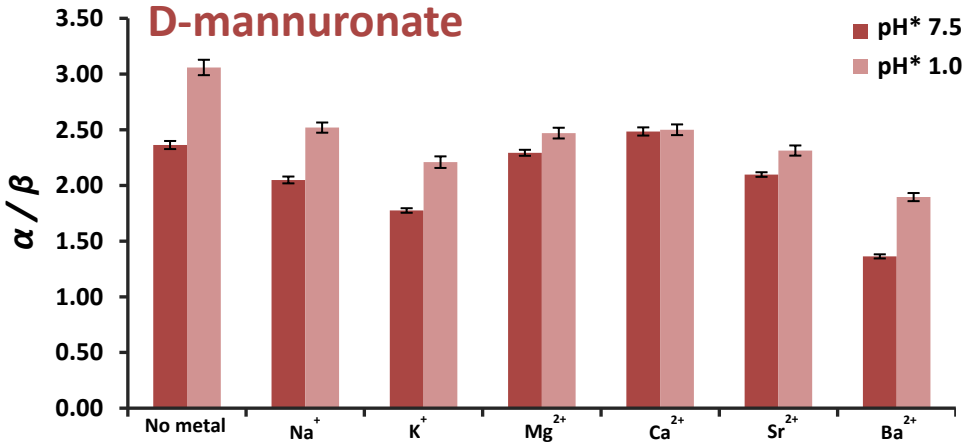

Figure 3.21 The *α*/*β* ratio of Na-D-mannopyranuronate recorded in 1.0 M solutions of different metal ions at 295 K and pH* 7.5 or 1.0.

With regards to the changes in chemical shift of the protons of *α*- and *β*-**Man** when metal ions are added to the solution, the effects were again more subtly than in the case of *α*-**Gul**. $\Delta\delta_{rel}$ for the protons of *α*- and *β*-**Man** (again relative to H4 in all cases) were quite small with very little difference between the two anomers in the cases of all of the metal ions screened (see Appendix E). Whilst slightly larger $\Delta\delta_{rel}$ values were observed for both anomers in the presence of Ca^{2+}, Sr^{2+}, and Ba^{2+} - this was only true for H1 and H5, not all of the ring protons.

The effect of lowering the pH* of the solution in order to protonate the mannuronate was also recorded. As noted in Section 2.4.2 of Chapter 2, the proportion of α-pyranose anomer increases slightly at lower pH values for mannuronate as the electron density around the ring is redistributed. The impact of including metal ions at pH* 1.0 is then to push the equilibrium back marginally towards formation of the β-anomer, with Ba^{2+} and K^{+} ions again being the most effective. Changes to $\Delta\delta_{rel}$ at pH* 1.0 are very small, and, whilst being detectably higher for the β-anomer (see Appendix E), accurate interpretation is somewhat limited by this fact.

Again, the implications of the results in this section for interpreting the various binding modes exhibited by α- and β-**Man** are discussed in Section 3.5.5.

3.5.2.4 Investigation A results for D-glucuronate

The s-block metal ion coordination to D-glucuronate has been reasonably well studied (see discussions in Section 3.3.2.4, the structure of **Glc** is provided in Figure 3.22 as a reminder). However, it was useful to examine the behaviour of **Glc** under the same conditions as **Man** and **Gul** in order to contextualise the results from Sections 3.5.2.2 and 3.5.2.3. In this regard Figure 3.23 illustrates the changes to the relative population of α- and β-pyranose anomers of **Glc** upon the addition of s-block metal ions. Here it can be seen that there is relatively little deviation from the α/β value of the metal-free conditions (α/β = 0.75) and those containing 1.0 M metal chloride, with the Ca^{2+}-rich solution giving rise to the largest (albeit still small) change (α/β = 1.03). Accordingly, the recorded values of $\Delta\delta_{rel}$ are all very small also (see Appendix E). When the pH* is decreased to 1.0 (which is accompanied by a change in α/β value to 0.95 in the metal-free case) the metallic cations studied were found to have an even smaller influence, barely perturbing the anomeric equilibrium and giving rise to $\Delta\delta_{rel}$ values of only 0.03 ppm or lower (see Appendix E).

3.5.2.5 Investigation A results for D-galacturonate

As with D-glucuronate, the larger number of studies carried out previously into the s-block metal-coordination behaviour of D-galacturonate makes it a useful comparator to study alongside the algal mono-uronates (a reminder of the structure of **Gal** is provided in Figure 3.24). Here, there are parallels to be drawn especially with the behaviour of L-guluronate. Sodium D-galactopyranuronate (which possesses an α/β ratio of 0.70 at pH* 7.5) does not appear to be affected significantly by the presence of excess Na^{+}, K^{+}, Mg^{2+} or, indeed, Ba^{2+} ions (see Figure 3.25). However, a considerable stabilisation of the α-pyranose anomer is detected upon inclusion of Ca^{2+} (α/β = 1.24), and, to a lesser extent Sr^{2+} (α/β = 1.02) in the analyte mixture. Whilst not as large as the changes detected in solutions of **Gul**, the affinity of α-**Gal** for (particularly) Ca^{2+} was described in the Section 3.3.2.4 of the literature review. It is noteworthy, in this regard, that upon lowering the pH* of the solution to 1.0, the energetic preference of α-**Gal** as Ca^{2+} is added is lost almost entirely (with the metal-free solution exhibiting an α/β ratio of 0.89, compared to 0.91 in the calcium-containing case).

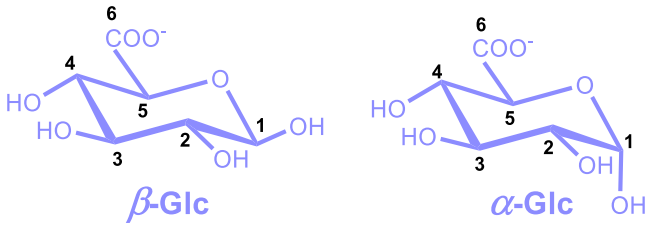

Figure 3.22 Atomic labels for *β*- and *α*-pyranose anomers of **Glc**

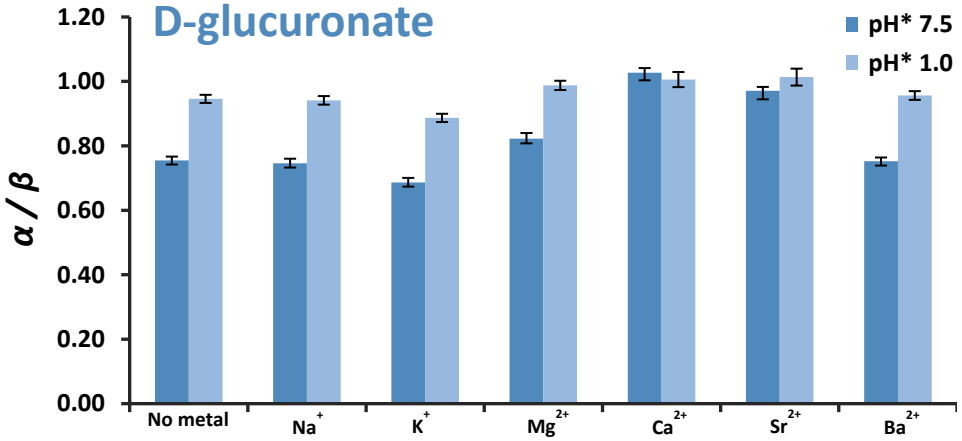

Figure 3.23 The *α*/*β* ratio of Na-D-glucopyranuronate recorded in 1.0 M solutions of different metal ions at 295 K and pH* 7.5 or 1.0.

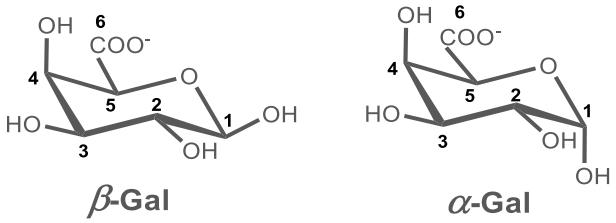

Figure 3.24 Atomic labels for *β*- and *α*-pyranose anomers of **Gal**

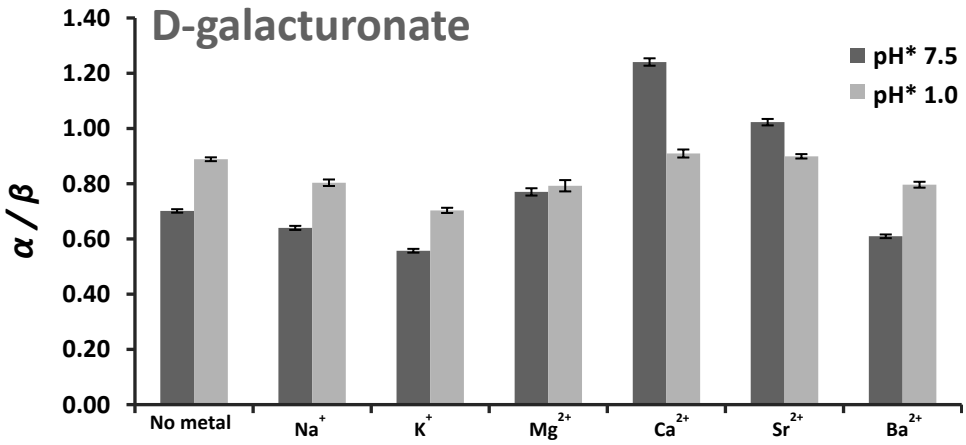

Figure 3.25 The *α*/*β* ratio of Na-D-galactopyranuronate recorded in 1.0 M solutions of different metal ions at 295 K and pH* 7.5 or 1.0

Turning to changes in chemical shift for **Gal** (reported in full in Appendix E), the $\Delta\delta_{rel}$ values provide an interesting contrast against those derived from **Gul** (see Section 3.5.2.2). Firstly, whilst α-**Gul** shows significant $\Delta\delta_{rel}$ values for H1, H2, H3, and H5 in the presence of (amongst other ions) Ca^{2+}, α-**Gal** only displays sizeable $\Delta\delta_{rel}$ values for H1 and H5 (and they are considerably smaller than their α-guluronate counterparts). Secondly, whilst the α-anomer of **Gul** generates large $\Delta\delta_{rel}$ values in the presence of Ca^{2+} (as well as Sr^{2+} and Ba^{2+}) and the β-anomer does not, the same is not true of **Gal**. Instead, α-**Gal** shows the larger $\Delta\delta_{rel}$ values compared to the β-**Gal**, but in going from Ca^{2+} to Sr^{2+} to Ba^{2+}, the two sets of data converge until (for Ba^{2+}) they are virtually identical. Thirdly, in all cases, as with **Gul**, **Gal** does not show significant values of $\Delta\delta_{rel}$ values for any proton in the presence of excess Na^{+}, K^{+} or Mg^{2+}. Finally, the $\Delta\delta_{rel}$ values for α- and β-**Gal** are reduced to near-zero on lowering the pH* to 1.0, whilst for α-**Gul** the decrease is not as drastic.

3.5.2.6 Investigation A - the impact of other anions on cation-uronate coordination

Additional experiments were carried out under the conditions defined for Investigation A (see Table 3.1), but where the cation remained the same (Ca^{2+}) and the anion was varied (Cl^{-}, NO_3^{-}, I^{-}). For **Gal**, **Glc**, **Man**, and **Gul**, the anions were found to change the α/β ratio (relative to the metal-free case) in the order $I^{-} > Cl^{-} > NO_3^{-}$ (see Figure 3.26). However, such variations in α/β ratio upon changing the anion were not nearly as drastic as changing the cation or pH* of the solutions of interest (see Sections 3.5.2.2 – 3.5.2.5).

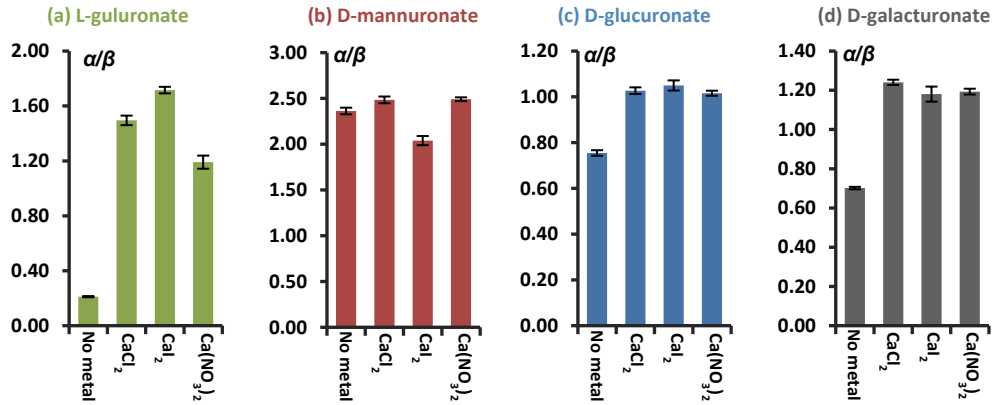

Figure 3.26 The α/β ratio of four sodium mono-uronates recorded in 1.0 M solutions of different calcium salts at 295 K and pH* 7.5.

3.5.2.7 Investigation A - the impact of ionic strength on metal-uronate binding

The role of the ionic strength of the uronate solutions was not explored extensively in this work as it has already been well documented that diluting a metal-saccharide solution decreases the degree of complexation.[77] However, an inherent flaw in the conditions utilised in Investigation A are that, to maintain a constant [metal]:[uronate] ratio in each experiment (1:23), the ionic strength of the solutions containing divalent cations (I = 6.09 M) were, by definition, far higher than those of the monovalent cations (I = 2.09 M). Consequently, an experiment was also conducted whereby the Ca^{2+} concentration was reduced from 1.0 M to 0.2 M (giving a lower [metal]:[uronate] ratio of 1:4.6) to give a solution of much lower ionic strength (I = 1.29 M). As suspected, where there had

previously been changes to the α/β ratio on inclusion of Ca^{2+}, such differences were now much smaller (see Figure 3.27) though still larger (in the case of **Gal** and **Gul**) than the impact of including monovalent cations as reported in Sections 3.5.2.2 – 3.5.2.5.

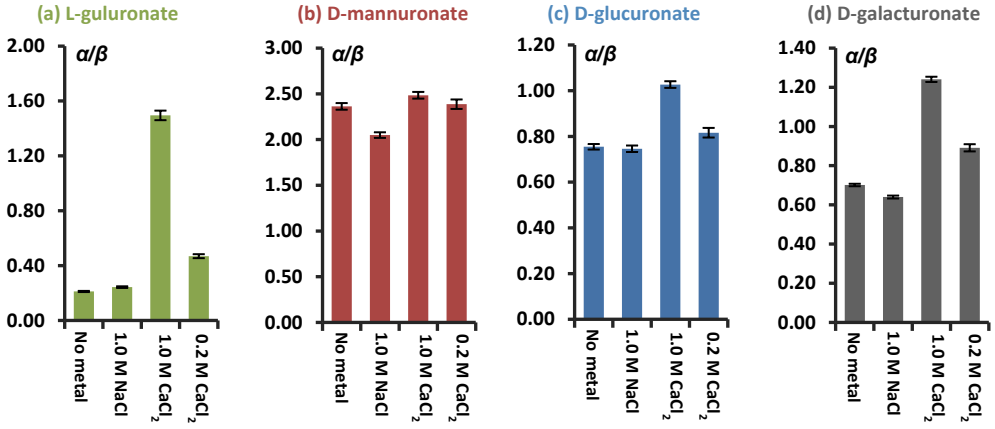

Figure 3.27 The α/β ratio of four sodium mono-uronates recorded in different concentration solutions of metal salts at 295 K and pH* 7.5.

3.5.3 Investigation B: ^{13}C and ^{1}H NMR spectroscopic study of mono-uronate coordination to Ca^{2+} ions

3.5.3.1 General comments on Investigation B

Investigation B was designed to offer a more in-depth analysis of the binding mode of Ca^{2+} to the algal mono-uronates. The experiments were based on similar NMR titrations to those conducted by Jaques *et al.* when investigating Ca^{2+} coordination to **Gal** and **Glc**.[22] By increasing the concentration of uronate in the analyte solution compared with Investigation A, ^{13}C NMR spectra could be recorded simultaneously with the corresponding ^{1}H spectral acquisition and, hence, data from both nuclei could be compared. The information of interest in Investigation B was the changes in chemical shift ($\Delta\delta$) as Ca^{2+} (in the form of concentrated aqueous $CaCl_2$) was added gradually to uronate solutions at pH* 7.5, which could then be plotted (see Figure 3.28 and Figure 3.29). As only one metal was under scrutiny in these experiments, there was no need to calculate $\Delta\delta_{rel}$ (as utilised for Investigation A in Section 3.5.2) and so Figure 3.28 and Figure 3.29 depict the absolute values of $\Delta\delta$ as they were measured from both the ^{13}C and ^{1}H NMR spectra (with positive values corresponding to a deshielding effect and negative to a shielding effect). From these plots (and by other arguments) it is possible to propose potential modes of metal coordination by the uronate molecule under investigation. Again, the discussion is only concerned with the α- and β-pyranose anomers of L-guluronate, D-mannuronate, and D-glucuronate, owing to their relevance to the metal coordination behaviour of polyuronides.*

* Whilst information regarding the coordination of Ca^{2+} to D-galacturonate would also have been helpful in this regard, this uronate was found, under the conditions studied, to precipitate from the analyte solution as the $CaCl_2$ concentration was increased, prohibiting analysis.

[blank page]

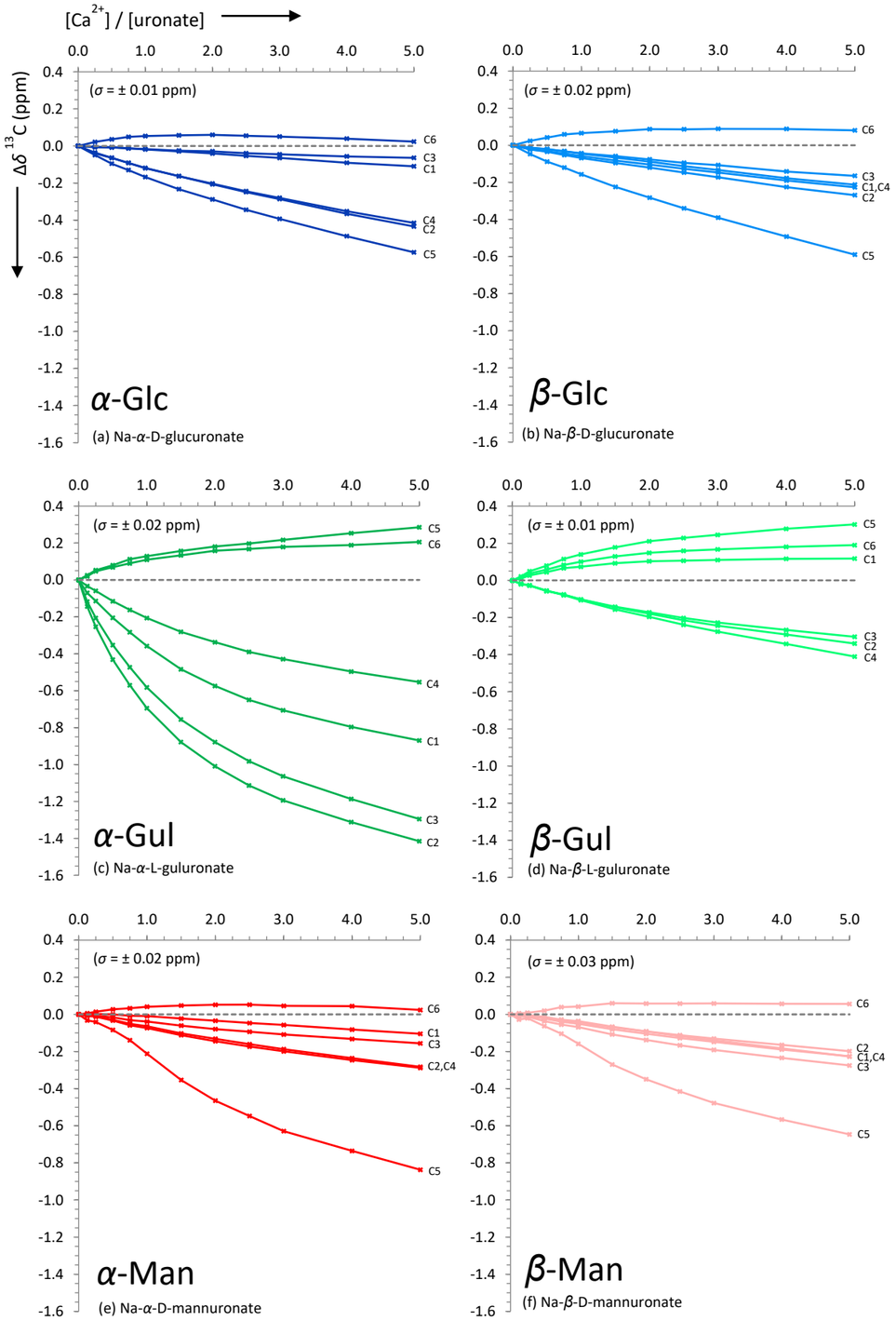

Figure 3.28 Change in chemical shifts, Δδ (ppm), of carbon signals in the ^{13}C NMR spectra of sodium uronates upon addition of aliquots of $CaCl_2$ in D_2O. Spectra recorded at 296 K, 400 MHz, D_2O (pH* = 7.5), [uronate] = 0.26 M. Each plot represents an average of two independent runs. Individual error bars are omitted for clarity but an average error, σ, is stated in parentheses for each plot.

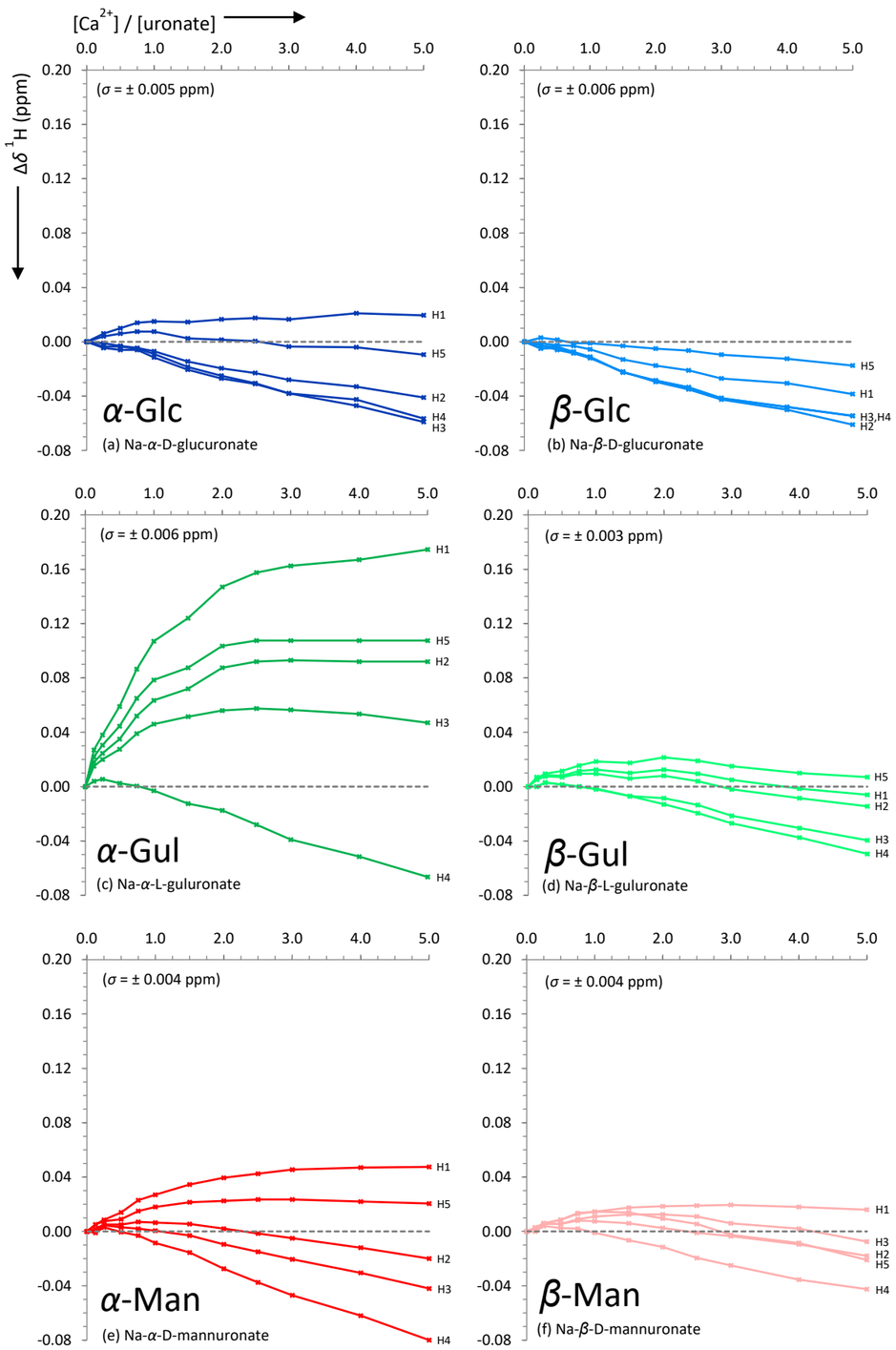

Figure 3.29 Change in chemical shifts, Δδ (ppm), of proton signals in the ^{1}H NMR spectra of sodium uronates upon addition of aliquots of $CaCl_2$ in D_2O. Spectra recorded at 296 K, 400 MHz, D_2O (pH* = 7.5), [uronate] = 0.26 M. Each plot represents an average of two independent runs. Individual error bars are omitted for clarity but an average error, σ, is stated in parentheses for each plot.

3.5.3.2 Investigation B results for L-guluronate

Differences in the behaviour of the two pyranose anomers of L-gulopyranuronate in the presence of Ca^{2+} first indicated in Investigation A (see Section 3.5.2.2) are illustrated clearly in the results of Investigation B (see Figure 3.28(c)-(d) and Figure 3.29(c)-(d)). Here it can be seen that the span of $\Delta\delta(^{13}C)$ values for *α*-**Gul** covers a window of 1.71 ppm, whilst that of *β*-**Gul** is only 0.71 ppm (at $[Ca^{2+}]/[\mathbf{Gul}] = 5.0$). Similarly, the range of $\Delta\delta(^{1}H)$ values for *α*-**Gul** spreads across 0.24 ppm, compared to only 0.06 ppm for *β*-**Gul** (at $[Ca^{2+}]/[\mathbf{Gul}] = 5.0$). Whilst C4, C5, C6, and H4 all display similar $\Delta\delta$ values upon the addition of Ca^{2+} in both *α*- and *β*-anomers, the large negative shifts of *α*C1 (-0.87 ppm), *α*C3 (-1.30 ppm) and *α*C2 (-1.42 ppm) and positive shifts of *α*H3 (0.05 ppm), *α*H2 (0.09 ppm), *α*H5 (0.11 ppm), and *α*H1 (0.17 ppm) contrast strongly with the equivalent *β*-shifts and, indeed, with all shifts in the **Glc** and **Man** experiments also (see Sections 3.5.3.3 and 3.5.3.4). One final additional observation is that $\Delta\delta$(C5) in the case of *α*- and *β*-**Gul** is a positive value (corresponding to a deshielding of that nucleus in both cases), whilst *α*- and *β*-**Man** and **Glc** show negative shifts for the same carbon atom. Though such a result makes **Gul** appear to be unique amongst the family of data acquired here, it should be noted that **Gal** has also be shown to have slightly positive values for $\Delta\delta$(C5) in the presence of Ca^{2+} in an independent investigation conducted by Jaques *et al*.[22] The implications of these results on the proposed binding modes of **Gul** to Ca^{2+} are discussed further in Section 3.5.5.

3.5.3.3 Investigation B results for D-mannuronate

The $\Delta\delta(^{13}C)$ and $\Delta\delta(^{1}H)$ values observed for D-mannopyranuronate in the presence of increasing $[CaCl_2]$ (see Figure 3.28(e)-(f) and Figure 3.29(e)-(f) show strong similarities with those of D-glucopyranuronate under the same conditions (see Section 3.5.3.4). Here, unlike in the case of *α*- and *β*-**Gul** (see Section 3.5.3.2), $\Delta\delta$(C5) is the most negatively shifted (-0.84 and -0.65 ppm for *α*- and *β*-**Man**, respectively) with the $\Delta\delta(^{13}C)$ measurements for C1, C2, C3, C4, and C6 being more tightly gathered at smaller shift values. Similarly, $\Delta\delta(^{1}H)$ values for H1-H5 are clustered more closely around 0 ppm than α-**Gul**, in a similar manner to *α*- and *β*-**Glc**, and *β*-**Gul**. Differences between the two pyranose anomers of **Man** are much subtler than in the case of **Gul**, with the $\Delta\delta(^{13}C)$ and $\Delta\delta(^{1}H)$ patterns being largely the same, but with marginally larger values for *α*-**Man** compared *β*-**Man**.

3.5.3.4 Investigation B results for D-glucuronate

The $\Delta\delta(^{13}C)$ and $\Delta\delta(^{1}H)$ values observed for *α*- and *β*-**Glc** in the presence of increasing $[Ca^{2+}]$ (see Figure(a)-(b) and Figure(a)-(b) are largely agreement with those derived in a similar experiment conducted by Jacques *et al*.[22] (with small differences being attributable to the differing ionic strengths employed in the two studies). Notably, the results for **Glc** show strong resemblances to those of *α*- and *β*-**Man** (see Section 3.5.3.3) and, to some degree, *β*-**Gul** (with the shifts of C5 being a clear exception). Furthermore, the difference between *α*- and *β*-**Glc** are, as with **Man**, very subtle, with the small difference in $\Delta\delta(^{1}H)$ values of *α*H1 (0.02) and *β*H1 (-0.04) offering the largest source of contrast.

3.5.4 Investigation C: binding of d-block metals to mono-uronates

3.5.4.1 General comments on Investigation C

As will be highlighted, the inclusion of d-block metals in the uronate binding experiments requires additional considerations to those required of the s-block metals in Investigations A and B. As a consequence, Investigation C was not as extensive as the former two studies, but sought only to gauge immediate similarities or differences between the interactions of uronates with cations possessing solely contracted s-character, and those with more complicated valence orbital structures. In this regard, Zn^{2+} and Cu^{2+} were selected for study, particularly because of the importance of these ions in the thermochemical experiments detailed in Chapters 4 and 5 of this thesis. The paramagnetic character and redox activity of Cu^{2+}, coupled with the speciation of Zn^{2+} at neutral pH values required for different approaches to be adopted for both metal ions, as is discussed in Section 3.3.3.

3.5.4.2 Binding of Zn^{2+} to mono-uronates

Experiments utilising Zn^{2+} were similar to those conducted in Investigation A, with the exception that the pH* of the analyte solutions was maintained at 1.0. The necessity to work at low pH is a consequence of the insolubility of zinc hydroxide salts formed at neutral pH* values. Hence, the $ZnCl_2$ concentration was kept at 1.0 M, and the uronate concentration at 43 mM, but a small addition of concentrated DCl was added to the D_2O solution to prevent precipitation prior to analysis. Upon allowing the $ZnCl_2$ solutions of **Gul**, **Man**, **Gal**, and **Glc** to reach equilibrium, it was found that the Zn^{2+} had little significant effect. The α/β values for all four uronates in the presence of Zn^{2+} (0.23, 2.64, 0.87, and 0.97 for **Gul**, **Man**, **Gal**, and **Glc**, respectively) were found to change only slightly from their metal-free values at the same pH* (0.21, 3.06, 0.89, and 0.95 for **Gul**, **Man**, **Gal**, and **Glc**, respectively), closely resembling the behaviour observed in the case of Mg^{2+} (see Section 3.5.2). Similarly, values of $\Delta\delta_{rel}$ for H1, H2, H3, and H5 (relative to H4 in all cases) were all zero or close to zero for all eight of the pyranuronate anomers studied (see Appendix E). Hence, in both regards to the chemical shift difference and changes to the anomeric equilibria, the effect of Zn^{2+} ions on all four uronates can viewed as being nearly identical to that of Mg^{2+} ions under the conditions studied.

3.5.4.3 Binding of Cu^{2+} to mono-uronates

The experiments into the binding of Cu^{2+} to mono-uronates were conducted in quite a different manner to those of Investigations B and C. First and foremost, the paramagnetic characteristics of Cu^{2+} prohibit the use of high concentrations of the metal (such as the 1.0 M utilised for metal chloride salts in Investigation A) for recording NMR spectra. Furthermore, the propensity of Cu^{2+} to undergo reduction to Cu^{+} in the presence of reducing sugars (such as mono-uronates) meant a pH* < 7.0 is required to ensure the metal-saccharide solution remains stable for long enough to conduct the experiment. As such, a replica of an experimental protocol developed by Synytsya *et al.* for the analysis of Cu^{2+}-galacturonate complexes was utilised here for the study of glucuronate, guluronate, and mannuronate.[105] Synytsya *et al.* utilised conditions of pH 5.5 (D_2O) and a [Cu^{2+}]/[uronate] ratio of 1:100 to demonstrate that only C6 and C5 of α- and β-**Gal** show specific line broadening (as explained in Section 3.3.3), whilst all proton peaks remain relatively unaffected. In the work conducted for this thesis, the experiment of Synytsya *et al.* was repeated (at pH* 6.00) and, whilst their original result for **Gal** was confirmed (see

Figure 3.30) the additional data collected here and presented in Figure 3.31 - Figure 3.33 also demonstrated that identical results are observable in the cases of all anomers of **Glc**, **Man**, and **Gul** under the same conditions.

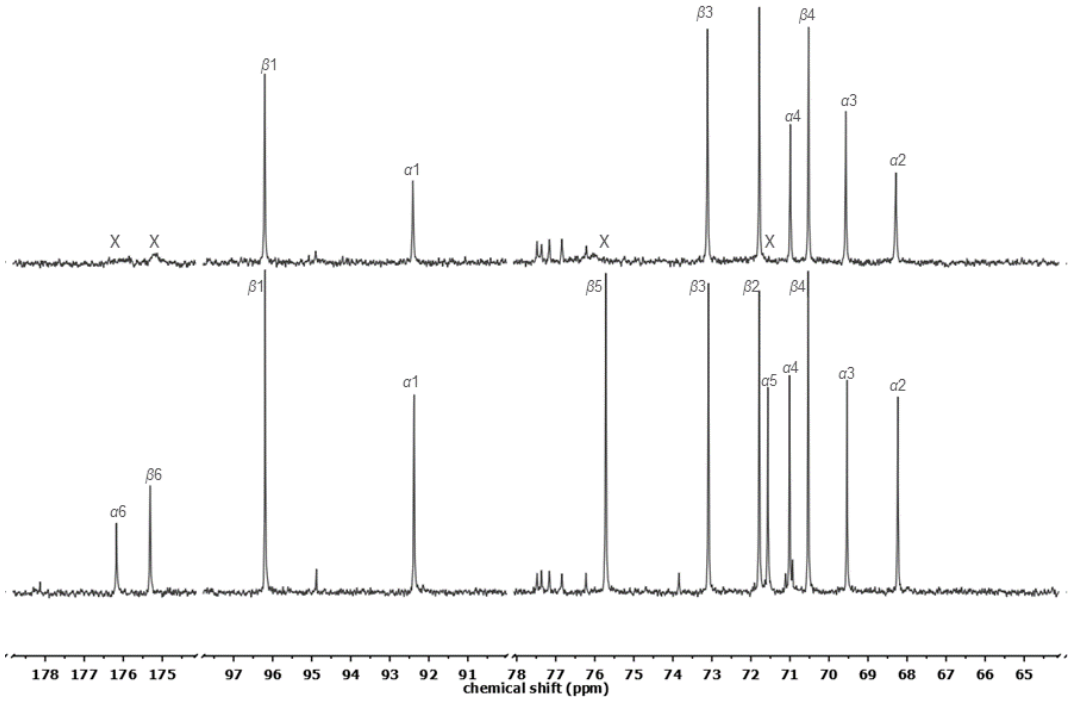

Figure 3.30 ^{13}C NMR spectra (400 MHz, D_2O) of Na-D-galacturonate in the presence of (top) and absence of (bottom) Cu^{2+} ions in a 1:500 [Cu^{2+}]/[uronate] ratio at 295 K and pH* 6.0. Peaks exhibiting significant line broadening are marked with an "X".

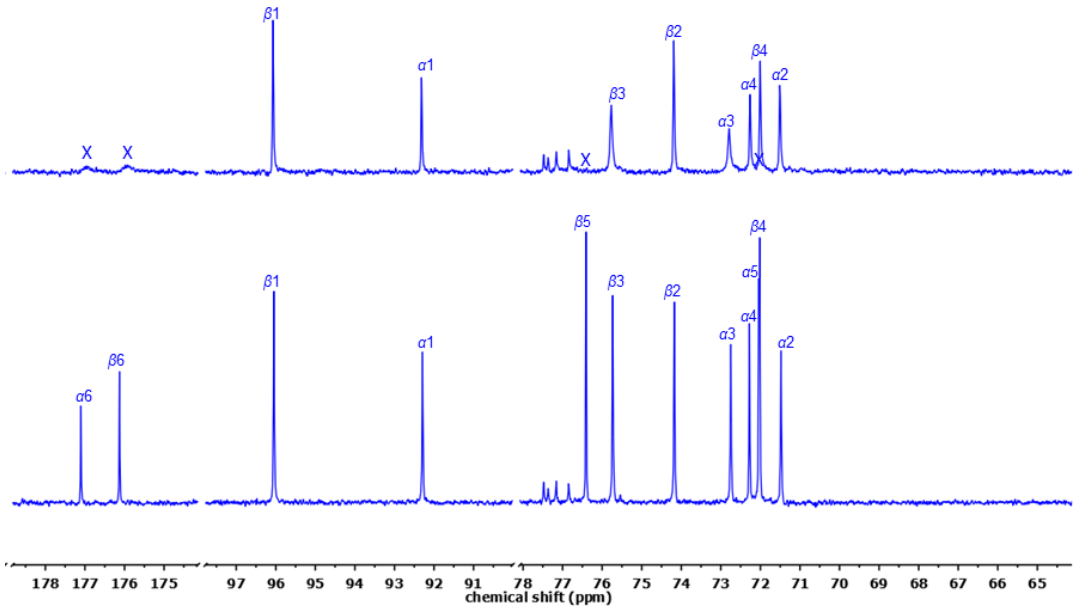

Figure 3.31 ^{13}C NMR spectra (400 MHz, D_2O) of Na-D-glucuronate in the presence of (top) and absence of (bottom) Cu^{2+} ions in a 1:500 [Cu^{2+}]/[uronate] ratio at 295 K and pH* 6.0. Peaks exhibiting significant line broadening are marked with an "X".

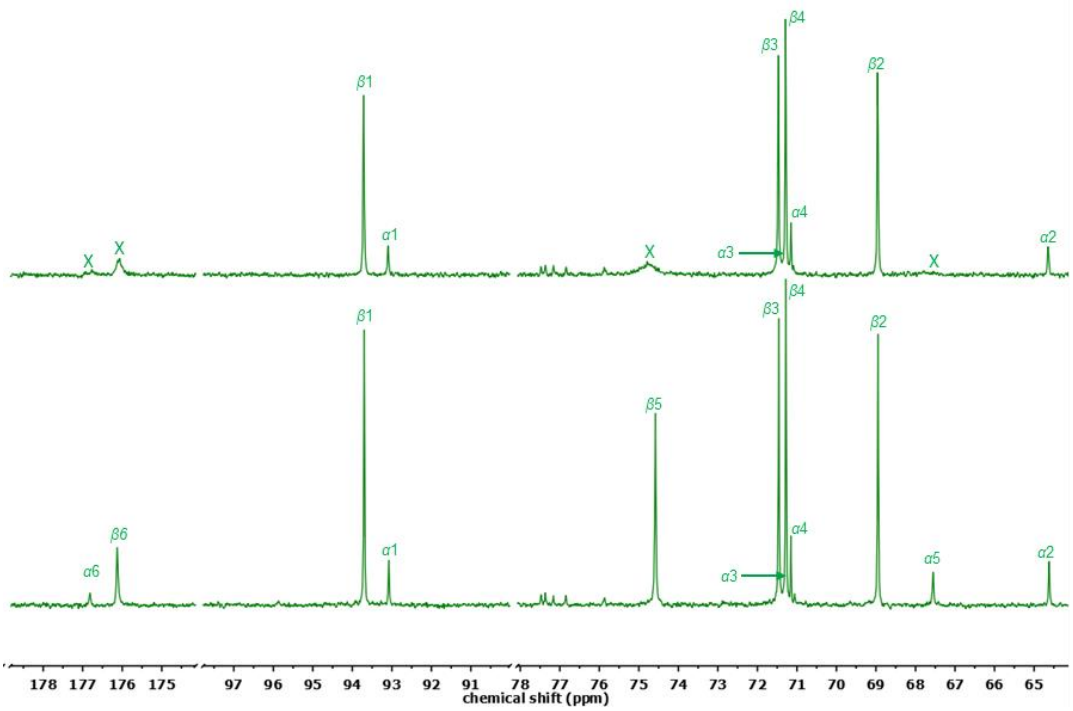

Figure 3.32 ^{13}C NMR spectra (400 MHz, D_2O) of Na-L-guluronate in the presence of (top) and absence of (bottom) Cu^{2+} ions in a 1:500 [Cu^{2+}]/[uronate] ratio at 295 K and pH* 6.0. Peaks exhibiting significant line broadening are marked with an "X".

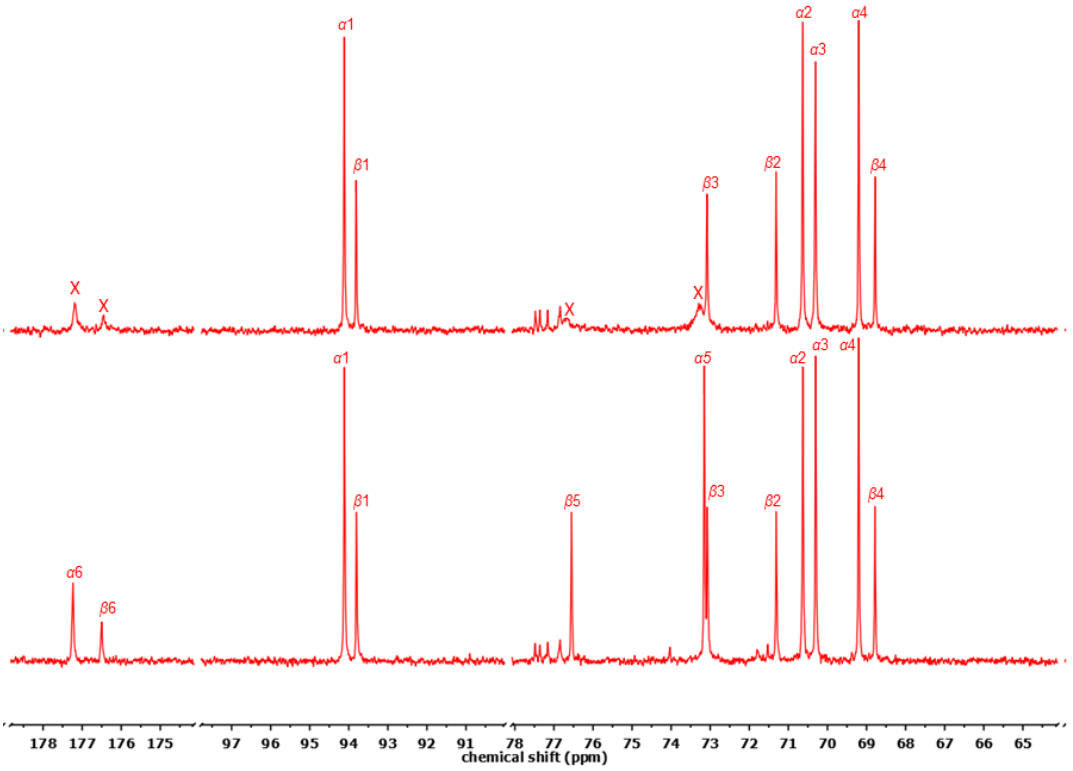

Figure 3.33 ^{13}C NMR spectra (400 MHz, D_2O) of Na-D-mannuronate in the presence of (top) and absence of (bottom) Cu^{2+} ions in a 1:500 [Cu^{2+}]/[uronate] ratio at 295 K and pH* 6.0. Peaks exhibiting significant line broadening are marked with an "X".

3.5.5 Synoptic discussion of the binding of s-block cations to mono-uronates

Whilst reviewing the results of Investigation A in Section 3.5.2, the most prominent observation is a clear affinity of *α*-**Gul** for the larger divalent cations: Ca^{2+}, Sr^{2+}, and Ba^{2+}. None of the other anomeric equilibria studied for **Man**, **Glc**, and **Gal** undergo nearly as significant a perturbation as that of **Gul** upon the inclusion of such divalent cations, which (in the case of Ca^{2+}) bring about a greater than three-fold increase in the number of *α*-pyranose molecules present in solution. Thus, it is concluded that *α*-**Gul** must display a binding mode that is unique amongst the eight uronate anomers studied, which upon complexation with Ca^{2+} (and similar cations) lowers the free energy of the molecule sufficiently to significantly alter the balance between *α*- and *β*-forms. In addition, the coordination mode of *α*-**Gul** is selective towards the larger of the divalent s-block cations (Ca^{2+}, Sr^{2+}, Ba^{2+}), with changes in the anomeric equilibria upon the inclusion of monovalent (Na^+ and K^+) and smaller divalent (Mg^{2+}) species being virtually undetectable.

Analysis of the NMR spectral data following Ca^{2+} titration from Investigation B (see Section 3.5.3) gives clear evidence that the unique coordination mode of *α*-**Gul** is comprised of the *ax-eq-ax* arrangement of hydroxyl groups found on C1, C2, and C3 (Figure 3.34), and is discussed in Sections 3.3.1.2 and 3.3.2.2. Whilst, in the absence of a cation, the 1,3-diaxial clash of hydroxyl oxygen atoms renders the *ax-eq-ax* motif particularly unstable, the screening of the dipolar charges by (for example) Ca^{2+} is sufficient to lower the free energy of the structure significantly.

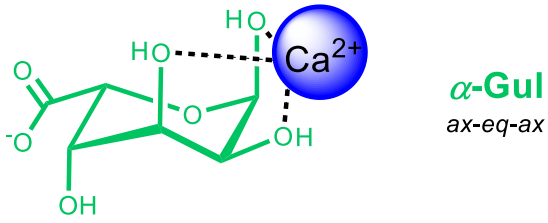

Figure 3.34 A possible neutral Ca^{2+}-coordination mode exhibited by ($^1C_4$)-*α*-L-gulopyranuronate involving the *ax-eq-ax* arrangement of hydroxyl groups.

With the Ca^{2+} coordinated in to the *ax-eq-ax* arrangement of hydroxyl groups, previous authors have demonstrated that C1, C2, and C3 would expected to be shielded, and H1, H2, and H3 deshielded compared to the unbound state, owing to the polarisation of the respective C-H bonds by the electric field of the cation (see Figure 3.35and discussions in Section 3.3.3). However, the results depicted in Figure 3.28(c)-(d) and Figure 3.29(c)-(d) do not fit perfectly with the shifts found in other Ca^{2+} complexes of *ax-eq-ax* containing molecules where, in *epi*-inositol for example, $\Delta\delta(^{13}C)$ are in the order C2 > C1 ≈ C3 and $\Delta\delta(^{1}H)$ are in the order H2 > H1 ≈ H3 (see Figure 3.4).[1,12,16] Similarly, the large deshielding of *α*H5 observed here *α*-**Gul** for would not be predicted by classical *ax-eq-ax* binding. These anomalies may be explained by considering the presence of a second coordination mode in the *α*-**Gul** system, probably involving the carboxylate moiety and ring oxygen (see Figure 3.36). It seems likely that such a secondary mode would be similar to that previously found in *α*-**Gal** (Section 3.3.2.4), as the two anomers possess the same relative orientation of functional groups on C1, C2, C4, and C5. Comparison of the $\Delta\delta_{abs}$ values of *α*-**Gal** in the

presence of Ca^{2+} (see Appendix E) indicate that binding involving the carboxylate and ring oxygens leads to deshielding of H1 and H5, which can also be observed in the *α*-**Gul** system. Hence, it can be concluded that Ca^{2+} binding is occurring in *α*-**Gul** with both *ax-eq-ax* arrangement of hydroxyl groups, and the carboxylate (and possibly ring oxygen).

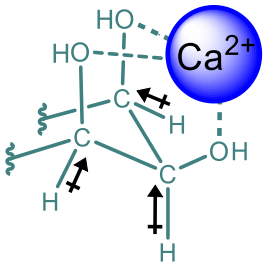

Figure 3.35 The polarisation of the C-H bonds when the electric field of a divalent cation is brought into the proximity of an *ax-eq-ax* arrangement of hydroxyl groups.

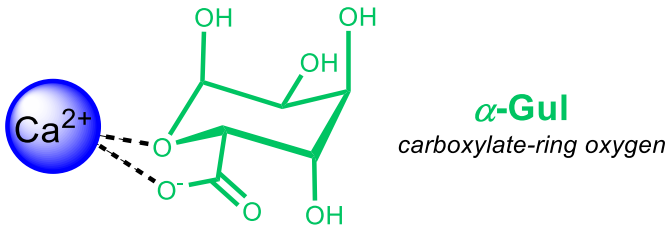

Figure 3.36 A second possible Ca^{2+}-coordination mode exhibited by ($^1C_4$)-*α*-L-gulopyranuronate involving the carboxylate and ring-oxygen

If the change in *α*/*β* ratio is used as the metric to determine the favourability of coordination between divalent cations and a monopyranuronate then, for L-guluronate, the affinity series is Ca^{2+} > Sr^{2+} > Ba^{2+} >> Mg^{2+}. Whilst Ca^{2+} may be regarded as being perfectly suited to binding to the *ax-eq-ax* arrangement, Mg^{2+} is either too small or too strongly solvated by H_2O to be able to coordinate. Meanwhile, it is tempting to say that the lower affinity of Ba^{2+} and Sr^{2+} to *α*-**Gul** is because they are too large, and have a lower charge density, and so cannot bind to the *ax-eq-ax* arrangement of hydroxyl groups. On further consideration, however, the smaller perturbation towards the *α*-anomer of **Gul** in the presence of Ba^{2+} may simply be because this metal ion can also coordinate to the *β*-anomer in a favourable manner too.* Additionally, **Man**, which showed very little response to the addition of metal ions, showed a tendency towards the formation of the *β*-anomer in the presence of Ba^{2+}. Hence, it might be concluded that the large size of Ba^{2+} facilitates binding with the wide, open faces of the pyranose rings of *β*-**Man** and *β*-**Gul**, specifically giving rise to interactions with *β*-**Gul**-O2 and *β*-**Gul**-O3, and *β*-**Man**-O1, *β*-**Man**-O2, and *β*-**Man**-O_{ring} (see Figure 3.37). In the case of *β*-**Man**, such a coordination mode (which features a *cis*-arrangement of hydroxyl oxygen atoms discussed in Section 3.3.1.2) also appears to show an affinity for the similarly large K^+, evidenced by a similar reduction in the *α*/*β* ratio in that case.

Evidence for a *β*-**Gul**-Ba^{2+} complex is also provided by the non-zero values of $\Delta\delta_{rel}$ observed in this case (see Table 3.2 in Section 3.5.2.2).

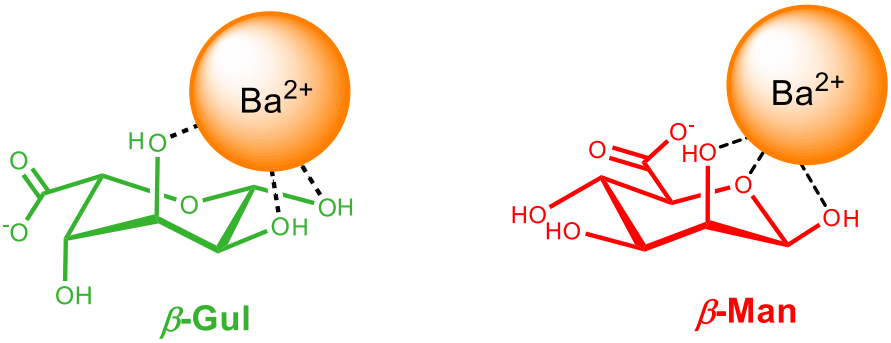

Figure 3.37 The possible affinity of larger cations (such as Ba^{2+}) for the cis-hydroxyl arrangements found in *β*-**Gul** (left) and *β*-**Man** (right).

Finally, considering the binding mode of Ca^{2+} to **Glc** and **Gal**, the results appear to be largely in accordance with the models discussed in Section 3.3.2.4. Hence, changes to the *α*/*β* ratios are consistent with slightly higher affinity of the *α*-pyranose anomers for Ca^{2+} in those two cases over their *β*-equivalents. Here, the *α*-pyranose anomers are believed to bind to the cation through the carboxylate oxygen and ring oxygen,* whilst the *β*-anomers coordinate through just the carboxylate† (see Figure 3.38). Furthermore, the $\Delta\delta_{rel}$ results for *α*- and *β*-**Man** are similar to those of **Glc** and **Gal**, leading to the conclusion that **Man** interacts with Ca^{2+} in a comparable fashion; through the carboxylate and ring oxygens in the *α*-anomer, and just the carboxylate in the *β*-form (see Figure 3.38). Finally, *β*-**Gul** may also be considered to be analogous to *β*-**Gal**, and so the two likely possess similar binding modes (as depicted for *β*-**Gul** in Figure 3.39).

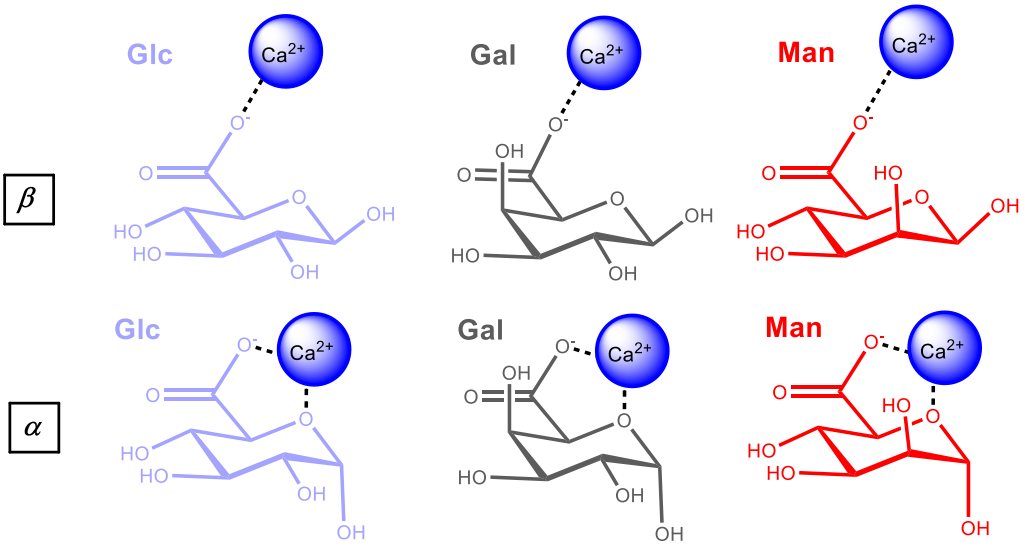

Figure 3.38 Coordination of Ca^{2+} (and other similar cations) by mono-uronates: **Glc**, **Gal**, and **Man** in their *α*- and *β*- forms. The denticity of the carboxylate binding cannot be specified at this stage.

* Evidenced by the larger, positive values of $\Delta\delta_{rel}$ for *α*-H1 and *α*-H5 than *α*-H2 and *α*-H3

† Evidence by the $\Delta\delta_{rel}$ values of *β*-H1 and *β*-H5, and *β*-H2 and *β*-H3 all being much more similar

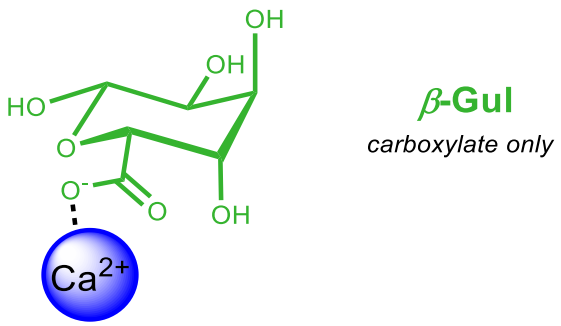

Figure 3.39 The likely coordination mode of *β*-**Gul** utilising only the carboxylate moiety. The denticity of the carboxylate binding cannot be specified.

3.5.6 Synoptic appraisal of the effect of environmental conditions on metal mono-uronate coordination

3.5.6.1 General comments on the role of environmental conditions in metal-uronate coordination

Whilst the metal and ligand are often the key protagonists in the formation of a coordination compound, it is also important to consider the influence of other environmental factors on the stability of such a complex. This sentiment is especially true in the case of metal uronates, where (as was demonstrated in Chapter 2) the degree of dissociation of the carboxylate group can be so critical in dictating the subsequent chemistry. Hence, the coordination chemistry results discussed in Sections 3.5.2 were also re-assessed with changes in the initial conditions (namely pH, ionic strength, and the identity of the counter anion), in order to gauge the effects of such changes.

3.5.6.2 The role of pH on metal-uronate coordination

The effects of decreasing the pH* from 7.5 to 1.0 when the uronate had been suspended in a 1.0 M solution of a given metal ion (as per Investigation A) was explored. The lower pH* value was sufficiently acidic to ensure that over 99% of the uronic carboxylic acid moieties in solution were protonated (as determined in Chapter 2) and, hence, such conditions should inhibit cation binding modes that feature the carboxylate functionality. Indeed, the effect of such protonation was to reduce the degree to which complexation occurred, evidenced by fewer deviations of the α/β ratio from the metal-free scenario (recorded at the same pH*) and smaller values for $\Delta\delta_{rel}$. Such results were unsurprising given the preliminary work of other authors in this area (see Section 3.3.2.4).[99] Interestingly, however, the dominance of the α-pyranose anomer of **Gul** in the presence of Ca^{2+}, Sr^{2+}, and Ba^{2+} remained even at low pH*, as too did the significant positive $\Delta\delta_{rel}$ values of α-H1, α-H2, and α-H3, signifying that the *ax-eq-ax* coordination mode was unaffected by the increase in $[H_3O^+]$.

3.5.6.3 The role of ionic strength on metal-uronate coordination

As part of this study, the role of ionic strength was not explored as exhaustively as other factors in the investigations described above. The results that were obtained were somewhat unsurprising and completely in accordance with the observations of other

authors.[76] Diluting the Ca^{2+}-uronate solutions generally caused a decrease in the values of the metrics that signify coordination (changes to α/β ratio and $\Delta\delta_{rel}$). Despite the dilution however, clear binding was still observable between the Ca^{2+} and α-**Gul**, with the same signifiers of *ax-eq-ax* coordination being present (such as the distinctive patterns of $\Delta\delta_{rel}$).

3.5.6.4 The role of the counter-anion on metal uronate coordination

Whilst changes to the Ca^{2+} counter anion (from Cl^- to I^- to NO_3^-) clearly had an impact on the metal-uronate coordination, the patterns of α/β ratio and $\Delta\delta_{rel}$ measurements remained consistent indicating that the cation binding mode remained constant. In the case of α-**Gul**, the magnitude of α/β ratio was found to be in the order CaI_2 > $CaCl_2$ > $Ca(NO_3)_2$, which may simply be a result of the differing activity of Ca^{2+} in concentrated solutions of those salts.[134]

3.5.7 Synoptic appraisal of the binding of d-block cations to mono-uronates

3.5.7.1 Binding of Zn^{2+} to mono-uronates

The experiments probing the coordination behaviour of Zn^{2+} with **Gul**, **Man**, **Gal**, and **Glc** were only conducted at pH* 1.0 owing to problems with solubility of the zinc species in solution at higher pH* values. Comparison with the equivalent s-block interactions with uronates at this lower pH* demonstrated a strong similarity between the behaviour of Zn^{2+} and that of Mg^{2+}. Similar α/β ratios between the Mg^{2+} and Zn^{2+} cases, and similar $\Delta\delta_{rel}$ values confirm that Zn^{2+} is either too small (and hence demanding too high a bite angle) or too strongly solvated to coordinate to the *ax-eq-ax* hydroxyl arrangement of α-**Gul**. Hence, it is likely that in all eight uronate anomers investigated, the Zn^{2+} coordination mode simply involves one (or both) of the carboxylate oxygens (see Figure 3.40).

3.5.7.2 Binding of Cu^{2+} to mono-uronates

Investigations of the response of mono-uronate to Cu^{2+} were quite different from those of the studies into Zn^{2+} or s-block metals, as they sought to observe selective line broadening as an indicator of binding (rather than $\Delta\delta_{rel}$ values or changes to the anomeric equilibrium). Cu^{2+} was the cation under investigation and, whilst the experimental procedure for was very different to the case of Zn^{2+}, the conclusions are largely the same. The selective line broadening of ^{13}C signals corresponding to C5 and C6 in all anomers of **Gul**, **Man**, **Gal** and **Glc** signify that binding of the Cu^{2+} in these cases is entirely through the carboxylate moieties. Whilst such results are not directly comparable with the Zn^{2+} experiments or, indeed, those of the s-block cations, the lack of line broadening in the signals corresponding the C atoms in the *ax-eq-ax* arrangement of hydroxyl groups in α-**Gul**, suggest that these ligands were not involved in Cu^{2+} binding. Hence, as with Zn^{2+}, it can be concluded that Cu^{2+} behaves in a similar manner to Mg^{2+} in coordinating to the uronates solely through the carboxylate moiety in all cases (see Figure 3.40).

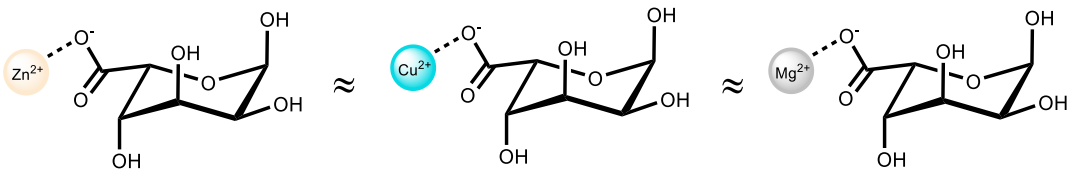

Figure 3.40 The similarity in uronate binding between Zn^{2+}, Cu^{2+}, and Mg^{2+}. The denticity of the carboxylate ligand cannot be specified.

3.5.8 Implications of studies concerning mono-uronates on the understanding of cation binding to alginates

Naturally, when attempting to extrapolate the results concerning the mono-uronates to gain an insight into the metal-binding of alginate, there are some important points to bear in mind. Significantly in this regard the *α*-L-gulopyranuronate unit (as depicted in Figure 3.41) appears in the polymer with O1 and O4 as ethereal oxygen atoms linked to the next unit in the chain, not as free hydroxyl groups as exist in the monosaccharide examined here. Studies elsewhere in the literature, however, indicate that such a difference is not of particular importance.[14] For example, Isbell prepared Ca^{2+} complexes of the methyl glycoside of *α*-D-gulopyranose as straightforwardly as the non-methylated saccharide.[76,77] Similarly, Grasdalen *et al.* also detected the *ax-eq-ax* coordination mode to be active in the Ln^{3+} complex of methyl *α*-D-gulopyranose,[79,98] and other authors found the methyl derivatives of sodium *α*-D-galactopyranuronate behave in a similar manner to the same sugar prior to glycosidation.[75,95,96] Hence it is conceivable that the binding modes proposed in Sections 3.5.5-3.5.7 for the mono-pyranuronates may well be the same as those exhibited by the polyuronates. Certainly, there is a good deal of similarity between the results presented in this thesis and those of Steginsky *et al.*, who recorded the $\Delta\delta(^1H)$ values of the proton signals of a polyguluronate chain upon titration with 0.0 – 5.0 equivalents of Ca^{2+}.[36] However, some authors have been sceptical that the binding modes exhibited in the monosaccharides are of any relevance to the behaviour of a polyuronide, citing the secondary structure of the polymer as being of far greater significance.[37,82] In this regard, it is wholly possible that cations do indeed interact with the *ax-eq-ax* arrangement of hydroxyl groups in an alginate chain, but that such coordination has little impact on the macroscopic properties of the polymer.

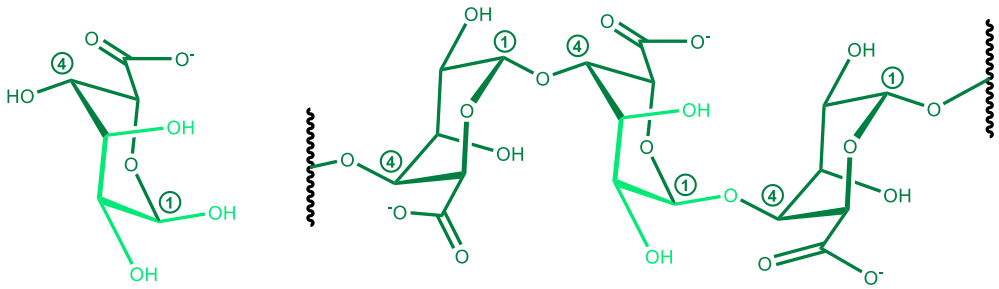

Figure 3.41 The *α*-L-gulopyranuronate unit as it appears as a free monomer (left) and when bound in an "Egg-Box" region of an alginate polymer (right). The *ax-eq-ax* site is highlighted by the lighter shade of green in both cases.

However, there are a number of insights that can be taken from the mono-uronate studies in Section 3.5.2.2 – 3.5.4 that will lead to a better understanding of metal-alginate coordination:

1) Firstly, the results of this chapter demonstrate that the argument of Plazinski and co-workers that neutral carbohydrate binding modes (namely the *ax-eq-ax* mode) are too weak to coordinate to a hydrated cation is untrue (see Section 3.3.2.2). For example, it has been demonstrated here that Ca^{2+} coordination may take place in *α*-D-gulopyranuronate by either the neutral *ax-eq-ax* binding mode, or by the ionic carboxylate, or by both.

2) Secondly, large differences between the behaviours of certain cations with mono-uronates are in good agreement with similar results reported for alginate polymers. For example, the ^{13}C NMR spectroscopic and small-angle X-ray scattering (SAXS) experiments performed by Wang *et al.* on alginate gels revealed disparity in the manner that Ca^{2+} and Cu^{2+} were bound to the polymer, with the former localised to guluronate sites and coordinated in the vicinity of all functional groups, and the latter bonded equally to guluronate and mannuronate residues through the carboxylate and well away from other oxygen atoms.[65,66] The results of Wang *et al.* are therefore commensurate with the differences in coordination chemistry observed between Ca^{2+} and Cu^{2+} in this thesis. Hence, where Wang *et al.* demonstrated that Ca^{2+} may interact with all of the neutral and ionic oxygen atoms around a L-guluronate ring in alginate, the same equivalent results were demonstrated here for Ca^{2+} and mono-*α*-L-guluronate. Furthermore, where Wang *et al.* demonstrated that Cu^{2+} interacts only with the carboxylate moiety of guluronate in alginate, the equivalent results were again demonstrated here for Cu^{2+} and mono-*α*-L-guluronate (see Figure 3.42). The differences between Ca^{2+} and Cu^{2+} are highlighted particularly because of the different thermochemical effects demonstrated by these ions in the thermochemical processing alginates and kelps (see Chapters 4 and 5, respectively). Furthermore, the very high affinity of kelps for Cu^{2+} ions (see Section 3.3.1.4) must be a consequence of the strong bond between the carboxylate moiety and the metal ion in question (rather than an affinity of the Cu^{2+} for the arrangement of hydroxyl groups provided by **GG** sites along the chain).

3) Finally, the extreme instability of the *α*-L-gulopyranuronate unit in the absence of a suitable cation (as observed in this chapter), continues to beg the question as to why such an energetically unfavourable moiety would be biosynthetically included in a molecule as ubiquitous as alginate if not to exploit some unique feature of its structure. Whilst the debate surrounding the Egg-Box model will continue for a long time to come, the results in this chapter will hopefully stimulate further fundamental consideration of the manner in which cations bind to simple mono-uronates in order to better inform future models.

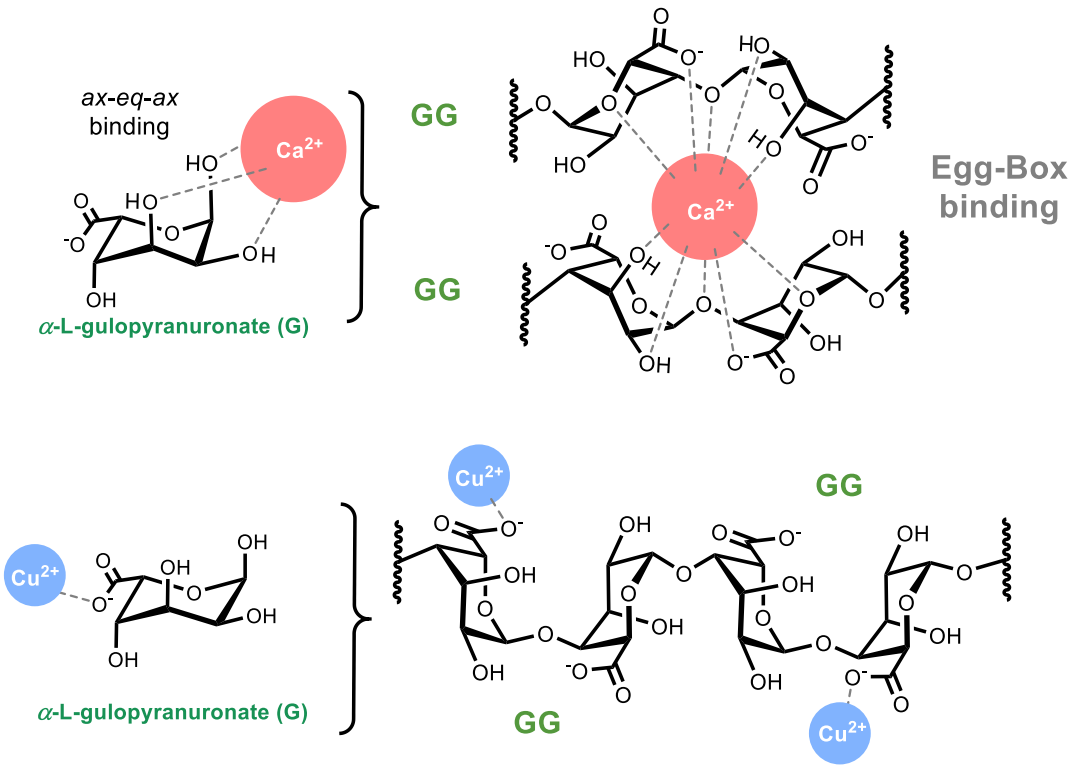

Figure 3.42 Possible differences between the binding of Ca^{2+} and Cu^{2+} to alginate chains, based on observed differences in their coordination to mono *α*-L-gulopyranuronate.

3.6 Summary, conclusions, and outlook

The results in this chapter represent the first systematic study of metal ion coordination with mono-uronates. Particularly notably, the data presented represent the first substantial NMR-based investigation of metal binding to the monomeric units of alginate. The key observations in this regard were that:

- **Gul** shows significant perturbations in its ^{1}H and ^{13}C NMR spectra upon the inclusion of Ca^{2+}, Sr^{2+}, and Ba^{2+}, that were not observed in the case of Na^{+}, K^{+}, and Mg^{2+} under the same conditions. The unparalleled increase in the *α*/*β* ratio of the pyranose anomers in the presence of the larger divalent cations indicates a relatively strong complexation of those ions (especially Ca^{2+}) with *α*-**Gul**. The Δ*δ* patterns observed in such cases (particularly a diagnostic deshielding of *α*-H1, -H2, and -H3 with simultaneous shielding of *α*-C1, -C2, and -C3) are indicative of binding to the *ax-eq-ax* arrangement of hydroxyl groups.
- The *ax-eq-ax* arrangement of hydroxyl groups in *α*-**Gul** is believed to be active in parallel with an additional coordination mode created by the carboxylate and ring oxygens. Upon lowering the pH of the solution the cation-complexing ability of the latter mode is greatly inhibited, whilst the former remains active (see Figure 3.43).

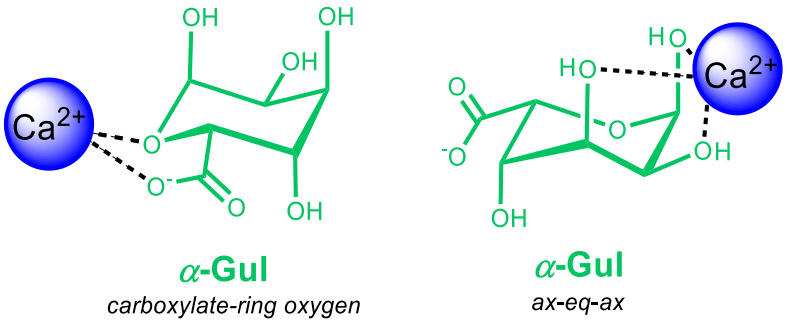

Figure 3.43 The two modes of Ca^{2+} coordination detected for *α*-**Gul**

- The remaining monopyranuronate anomers (**Gal**, **Glc**, **Man**, and *β*-**Gul**) bind to larger divalent cations simply through the carboxylate moiety (in the case of *β*-anomers) or a combined carboxylate/ring-oxygen coordination (in the case of *α*-anomers) (see Figure 3.44).

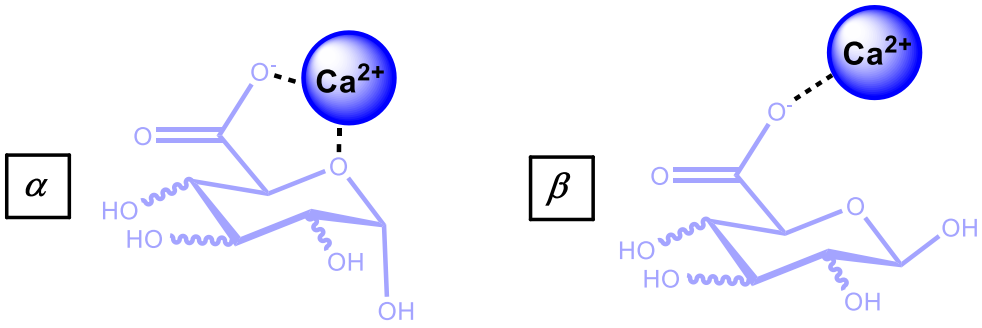

Figure 3.44 Modes of Ca^{2+} coordination proposed for *α*- and *β*-pyranuronate anomers

- Evidence for an additional neutral coordination mode in *β*-**Gul** and *β*-**Man** were also observed involving the *cis*-arrangement of hydroxyl oxygens on C1 and C2, active in the case of larger cations – particularly Ba^{2+} (see Figure 3.45).

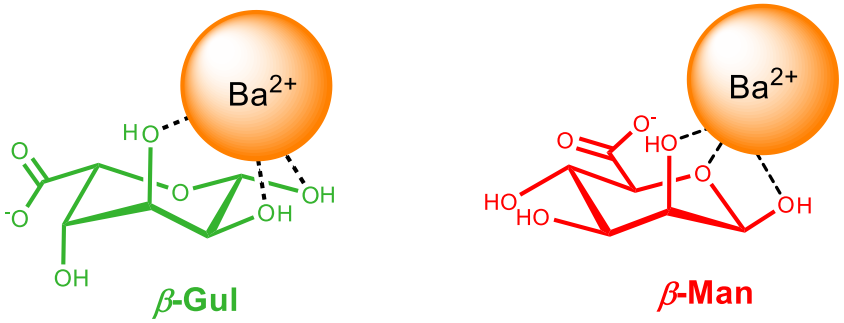

Figure 3.45 Additional mode of coordination of *β*-**Gul** and *β*-**Man** to large, divalent cations

- Finally, preliminary results for Cu^{2+} and Zn^{2+} indicate that the binding of divalent d-block metals to all mono-uronates probably occurs in same manner as the coordination of Mg^{2+} - utilising only the carboxylate moiety and no other oxygens on the saccharide ring (see Figure 3.46)

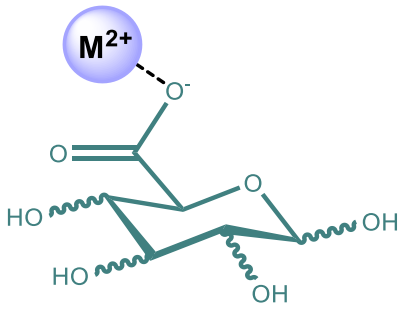

Figure 3.46 Generic binding mode of all mono-uronates to small divalent cations (M^{2+} = Mg^{2+}, Cu^{2+}, an Zn^{2+}). The denticity of carboxylate binding cannot be specified.

Whilst the results determined here are at odds with recent theoretical studies, they allow, for the first time a synoptic appraisal of the binding of cations by mono-uronates relative to each other. By taking into account the observations of Angyal, the previously established affinity series of Ca-uronate complexes (and those of other similar cations) may be expanded to include **Man** and **Gul**:

α-Gul > α-Gal > β-Gal ≈ β-Gul > α-Glc ≈ α-Man > β-Glc ≈ β-Man

This series is based on the principle that:

i. Mono-uronates with an axial hydroxyl group on O4 allow stronger cation coordination than those with an equatorial group.
ii. α-anomers facilitate stronger binding than β-anomers
iii. Mono-uronates with an additional neutral binding mode (created by an *ax-eq-ax* arrangement of oxygens) allow for stronger complexation than those uronates lacking such similar configuration of hydroxyl groups.

Though such an affinity series remains to be fully tested quantitatively, suggestions are made in Section 3.7.2 for how this might be achieved. Such studies would be particularly helpful as they could discern the relative contribution that each mode of coordination makes to the overall stability constant of the metal-uronate complexes.

Finally, it is clear that α-L-guluronate is unique amongst the mono-uronates in its cation complexing abilities with both neutral (*ax-eq-ax*) and anionic (carboxylate) binding modes being active simultaneously. However, as was discussed, the degree to which such behaviour is relevant to the macroscopic properties of alginate is yet to be discerned. Thus, whilst the results presented here do not confirm or refute any particular incarnation of the Egg-Box model of cation binding, they do provide a fundamental basis on which to build in future experimental and theoretical appraisals of metal coordination to mono-, oligo-, and poly-uronates.

3.7 Further work

3.7.1 The metal-binding properties of higher order uronides

Whilst the work in this chapter has focussed on algal mono-uronates, the information that could be extracted from the metal binding properties of the respective di-uronates is clearly vast. Indeed, as was demonstrated in Section 3.3.1.5, many computational studies of metal-alginate coordination take the di-uronate **MM**, **GG** units as their starting points.[62,71–73] Whilst the homo-dimers are arguably the most interesting candidates for further study (especially **GG**), there would also be merit to studying the hetero-dimeric **MG** and **GM** counterparts (see Figure 3.47). If the equivalent experiments to those conducted here for the monomeric units could be repeated, then such a study would go a long way to bridging the gap in understanding between mono-uronates and the physical properties of the polyuronides. Naturally, experiments on tri-, tetra-, penta-, and higher oligomers would be of interest, the opportunity to discern whether a Ca^{2+} ion would preferentially sit inside or outside of the **GG** cavity would be a truly enlightening development.

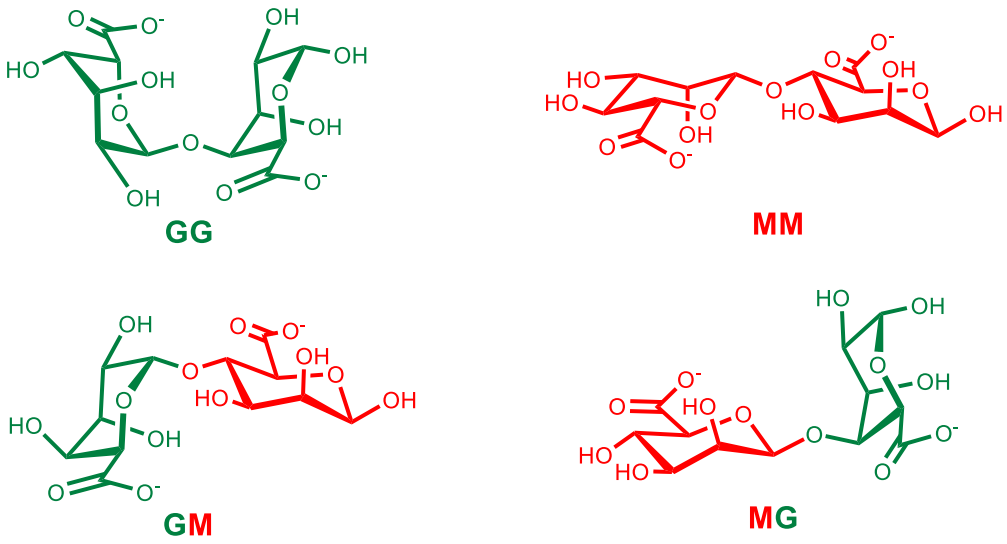

Figure 3.47 Disaccharide units of algal uronates of interest for further study

Of course, the importance of such di-uronate metal binding experiments has been widely recognised elsewhere (indeed Angyal described the potential value of such work almost 30 years ago).[1] However, whilst preliminary attempts to isolate the di-guluronate and di-mannuronate units in the preparation of this thesis (not reported here) were unsuccessful, other authors have noted the difficulty in achieving such a feat. For example, Gould *et al.*, in trying to prepare a strontium di-galacturonate compound were unable to avoid beta-elimination of their salt, yielding an unsaturated deoxy-saccharide.[135] Furthermore, the separation of such complicated mixtures of disaccharides would require more advanced chromatographic methods than those employed in Chapter 2 for the mono-uronates. In spite of the drawbacks, the development of automated synthetic carbohydrate

methodologies has led to a rise on commercial available oligosaccharides.[136–138,*] It is possible, therefore, that in a couple of years the necessary oligo-uronates will be available at an accessible price to facilitate the studies.

3.7.2 Quantitative assessments of metal-uronate binding

As was discussed in Section 3.3.3, measuring the stability constant of a Ca^{2+}-uronate complex by NMR spectroscopy presents difficulties, and was not attempted in this thesis.[14] Several other authors have reported methodologies that involve measuring the thermodynamic activity of the Ca^{2+} ion in uronate solution by means of an ion-selective electrode,[20–22,74] and, though preliminary efforts made during the preparation of this thesis were unsuccessful, further experiments in this regard are recommended. Naturally the highly complex equilibria that exist in solutions of mono-uronates complicate the ability to extract values for the strength of cation binding to a single anomer, but such endeavours are worth further perseverance in order to quantitatively validate the stability series proposed in Section 3.6. Similarly, the stoichiometry of metal-uronate binding might be established by constructing a Job's plot, though the high degree of speciation in the solutions would make interpretation of the data an extremely complicated task.[139]

3.7.3 Crystallisation of metal-uronate complexes

Whilst it is re-iterated that a molecular structure derived from crystalline material does not necessarily represent the form adopted by a complex when solvated in aqueous solution, such information can be insightful when attempting to determine likely metal-ion binding modes. Indeed, the relatively few crystal structures of metal mono-pyranuronate complexes that have been solved to-date[81,89–91,93,135,140] have all served to further discussion in this area in some form or another. Of particular importance would be a crystal structure containing a Ca^{2+}-*α*-L-gulopyranuronate unit, as this could provide more insightful information into the interaction of the cation with the neutral *ax-eq-ax* arrangement of hydroxyl groups. The molecular coordinates obtainable from such structures would, in-turn inform subsequent molecular modelling studies. Whilst attempts to grow metal-uronate crystals in the preparation of this thesis were largely unsuccessful (see further details in Appendix B), such experiments are worthy of further perseverance.

3.7.4 Advanced NMR spectroscopic assessments of metal-uronate binding

Naturally, continual developments in the field of NMR spectroscopy opens up wider experimental possibilities for the study of metal-uronate complexes beyond those reported in this chapter. Firstly, given the unprecedented clarity with which the NMR spectra of **Gul** and **Man** have now been determined (see Chapter 2) an improvement on the original experiments on Anthonsen *et al*. into the inclusion of Eu^{3+} in such spectra is now possible. Given how useful such lanthanide titrations have been for solving the coordination behaviour of **Gal** and **Glc**, it is hoped that similar insight could be gained for the algal uronates.

---

[*] See, for example, the work of Prof. Dr. P. H. Seeberger as presented in The Durham Lectures, 2013.

Furthermore, there is considerable scope for acquiring spectra beyond those of the ^{1}H and ^{13}C nuclei in the C-H bonds of saccharides. For example, authors have reported successful investigation of the ^{1}H resonance signals from the O-H protons in hydroxyl groups bound to a Ca^{2+} ion in a sugar complex.[118–120] More recently, Sipos and co-workers have exploited ^{43}Ca NMR spectroscopy to observe binding between that cation and glucose, sorbitol and heptagluconate ligands.[18,19,121,122] Of particular interest was a 2D ^{1}H-^{43}Ca HMBC experiment performed by those authors, where the correlation between a ^{1}H nucleus bonded to the carbon of the C-OH group and a coordinated $^{43}Ca^{2+}$ nucleus was observed directly (see Figure 3.48).

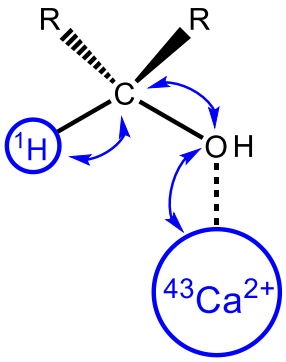

Figure 3.48 The through-bond correlation between ^{1}H-^{43}Ca nuclei in a Ca^{2+}-saccharide complex can be observed directly through new two-dimensional NMR spectroscoic methods.[19]

Finally, NMR spectroscopic methodologies have also been used to determine the extent to which metal ions catalyse the anomerisation of different uronate ions in solution. For example, Sn^{4+} was found to catalyse the interconversion of α- and β-pyran- and furanosides of D-galactouronate,[115] with Cu^{2+} being found to have a similar effect on D-glucuronate.[109] Performing similar experiments with the algal mono-uronates might give useful insight into, for example, the metal-mediated thermal degradation pathways available to such species.[141]

3.7.5 Metal-mediated transformations of uronates

Of course, the ability to drastically perturb the various uronate anomeric equilibria through the inclusion of a metal ion (especially in the case of L-guluronate) presents possibilities in the control uronate transformations. Whilst the role of metal-ions in the thermal degradation of uronates is explored extensively in Chapter 4 (and the hydrothermal degradation briefly in Appendix C) it is suffice to say that other authors have noted very large differences in the product slate of saccharide transformations in the presence of different metal ions.[141–146] It would be of interest to apply the understanding developed in this chapter to explaining differences in uronate chemical behaviour in the presence of metal-based catalysts[147,148] and, indeed, green, metal-rich solvents (such as seawater[149] or ionic liquids[142]). The different chemical degradation pathways that are triggered in uronates upon coordination to a metal ion will be a major theme in the remaining work of this thesis.

3.8 Materials and methods

3.8.1.1 General comments: Reagents and general conditions

All chemicals were purchased from Sigma Aldrich and used as received unless otherwise stated. D_2O (99.8 %) was bought from Apollo Scientific and used without further purification, and Norell® XR-55-7 NMR tubes (5.0 mm) were used throughout.

Stock solutions of sodium-L-guluronate, -D-mannuronate, -D-glucuronate, and -D-galacturonate were made up and exchanged with D_2O as described in Chapter 2, with their concentrations being determined according to the methods outlined in Appendix A.

D_2O solutions of NaCl, KCl, $CaCl_2$, $Ca(NO_3)_2$, $SrCl_2$, $BaCl_2$ (1.20 M or otherwise) were made up by dissolving the appropriate mass of the hydrated metal salt in D_2O, evaporating at 150 °C for 3 hours, and then re-dissolving the anhydrous salt in the required volume of fresh D_2O. A solution of $MgCl_2$ in D_2O (1.2 M) was made by dissolving the anhydrous metal salt directly into the required volume of liquid and then re-adjusting the pH* to 7.5 with small additions of DCl. A solution of CaI_2 in D_2O was made by dissolving the anhydrous metal salt directly into the required volume of liquid under an inert N_2 atmosphere, with no further adjustments. A solution of $ZnCl_2$ in D_2O (1.2 M) was made by first acidifying the solution to pH* 1.0 and then dissolving the anhydrous metal salt directly into the appropriate volume of liquid. A solution of $CuCl_2$ in D_2O (26 mM) was made by dissolving the appropriate volume of anhydrous metal salt directly into the required volume of liquid.

The pH* of solutions was measured by means of a Sigma-Aldrich® micro pH combination electrode (glass body, 183 mm L, 3.5 mm OD) connected to an Orion Star™ A111 pH-meter. As was explained in Chapter 2, the term pH* refers to the reading of the meter from a D_2O solution when the probe was calibrated in H_2O buffers. Whilst the pH* of metal-free solutions can be determined quite accurately (as in Chapter 2), those with extremely high ionic strengths can cause difficulties.[150,151] Hence, whilst the pH* values of the blank (metal-free) solutions were measured directly from the meter, the pH* of metal-rich solutions were double-checked with Fisherbrand™ pH-Fix Test Strips. In addition, preliminary experiments indicated that, for studies conducted at pH* 7.5, small variations of the pH (from pH* 6.0 to 9.0) had no measurable effects with regards to the relative shifts and peak ratios.

3.8.1.2 General comments: ^{1}H and ^{13}C NMR spectroscopy

All spectra for direct comparison were conducted under identical conditions, with a flame-sealed glass capillary (1.0 mm OD) containing $CHCl_3$ in $CDCl_3$ (5:95 vol.%) inserted co-axially into each analyte solution to provide a suitable external reference signal.[152,153] Data were acquired in all cases on a 400 MHz Bruker Avance NMR spectrometer at 295 ± 2 K according to the parameters described in Appendix D. Data processing was carried out in MestReNova 10.0.2-15465. Peak integration was performed manually on only clearly defined signals using the "sum" mode in MestreNova to generate the absolute integral without any additional correction. In cases where the centre of a peak was hard to determine in the 1D ^{1}H NMR spectrum due to overlap with neighbouring signals, a suitable cross peak in the ^{1}H-^{1}H COSY spectrum was used to determine the centroid positon. The ^{1}H and ^{13}C NMR

assignments of **Gul** and **Man** were as reported in Chapter 2, and those for **Gal** and **Glc** are given in Tables 3.4 and 3.5 based on the same arguments outlined in Chapter 2 Section 2.4.1. In addition to the 1D acquisitions, 2D NMR spectroscopic experiments (^{1}H-^{1}H COSY and ^{1}H-^{13}C HSQC) were performed at suitable intervals to confirm the identity of peaks following significant changes to the spectra and when interchange between signals had taken place. Further information regarding the manner in which NMR spectroscopic data was processed is provided in Appendix E.

Table 3.4 ^{1}H NMR assignments of sodium mono-uronate salts in D_2O (0.26 ± 0.02 M) at 400 MHz, pH* 7.0 – 7.2, and 295 ± 2 K (relative to $C\underline{H}Cl_3$ in $CDCl_3$, δ = 7.26 ppm).

δ (ppm) J (Hz)	**Na-D-glucopyranuronate**		**Na-D-galactopyranuronate**	
	α	**β**	**α**	**β**
δH1	**5.24, d**	**4.64, d**	**5.27, d**	**4.53, d**
$J_{1,2}$	3.8	8.0	3.5	7.9
δH2	**3.57, dd**	**3.28, m**[b]	**3.78, dd**	**3.46, dd**
$J_{1,2}$	3.8	n.d.	3.8	7.9
$J_{2,3}$	9.8	n.d.	10.4	9.9
δH3	**3.72, m**[c]	**3.51, *pt***[d]	**3.87, dd**	**3.65, dd**
$J_{2,3}$	n.d.	n.d	10.1	10.0
$J_{3,4}$	n.d.	n.d	3.5	3.5
δH4	**3.49, m**[d]	**3.51, m**[d]	**4.24, dd**	**4.17, dd**
$J_{3,4}$	n.d.	n.d.	3.6	3.5
$J_{4,5}$	n.d.	n.d.	1.5	1.2
δH5	**4.08, d**	**3.73, m**[c]	**4.37, d**	**4.02, d**
$J_{4,5}$	10.1	n.d.	1.3	1.4

Key: d = doublet, dd = doublet of doublets, *pt* = *pseudo*-triplet, m = multiplet, n.d. = not determined

[a] Scalar couplings (J) are quoted with a precision of ± 0.1 Hz.
[b] A complex multiplet owing to the strong coupling between βH3 and βH4 at pH* 7.0. At pH* 1.0, βH2 gives a doublet of doublets with $J_{1,2} = J_{2,3}$ = 9.1 Hz.
[c] αH3 and βH5 give overlapping signals that form a complex multiplet at pH* 7.0. At pH* 1.0, βH5 gives a doublet with $J_{4,5}$ = 9.6 Hz, and αH3 gives a *pseudo*-triplet with $J_{2,3} = J_{3,4}$ = 9.6 Hz.
[d] βH3, βH4, and αH4 overlap considerably, and cannot be resolved at pH* 7.0. βH3 gives a *pseudo*-triplet with $J_{2,3} = J_{3,4}$ = 9.6 Hz when the pH* of the solution is lowered to 1.0.

Table 3.5 ^{13}C NMR assignments of sodium mono-uronate salts in D_2O (0.26 ± 0.02 M) at 400 MHz, pH* 7.0 – 7.2, and 295 ± 2 K (relative to $C\underline{H}Cl_3$ in $CDCl_3$, δ = 7.26 ppm).

δ (ppm)	**Na-D-glucopyranuronate**		**Na-D-galactopyranuronate**	
	α	**β**	**α**	**β**
δC1	92.31	96.07	92.35	96.15
δC2	71.50	74.20	68.19	71.74
δC3	72.77	75.75	69.51	73.05
δC4	72.30	72.04	70.97	70.51
δC5	72.07	76.44	71.54	75.69
δC6	177.13	176.16	176.18	175.32

3.8.1.3 Investigation A

D_2O solutions of sodium uronate (100 μL, 260 mM, pH* 7.5) were combined with those of a chosen metal salt (500 μL, 1.2 M, pH* 7.5) and shaken together to yield the analyte solution (600 μL, 1.0 M metal, 43 mM uronate, pH* 7.5). After 12 hours at room temperature, the ^{1}H NMR spectrum was acquired at 400 MHz according to the procedure in Appendix D. The pH* of the solution was then reduced to 1.0 (such that > 99 % of the uronate carboxylate groups were protonated) by the addition of 25 μl of 2.5 M DCl. Whilst changes in concentration can affect the degree of complexation, preliminary experiments demonstrated that the addition of such small volumes of acid has a negligible impact. The acidified solution was allowed to stand for a further 12 hours, and the spectra were subsequently re-acquired.

Preliminary experiments (and literature examples)[76] indicated that the pyranose anomeric equilibrium settles very quickly after a metal ion has been added (on the order of minutes), with no further changes being detected on standing at pH* 7.5 for a number of months. On leaving the solutions to stand for 48 hours at pH* 1.0 however, the solutions of **Gul**, **Glc**, and **Man** begin to give rise to additional sets of smaller peaks their ^{1}H NMR spectra. These peaks correspond to the spontaneous lactonisation of the uronates in the acidified conditions (see Chapter 2 for an in-depth discussion). The lactone equilibrium forms at a much slower rate (days to weeks) than the anomeric equilibria (minutes) such that it may be neglected for the purposes of the discussions here.

3.8.1.4 Investigation B

D_2O solutions of **Gul**, **Man**, and **Glc** (500 μL, 260 mM, pH* 7.5) were titrated with small additions of D_2O solutions of $CaCl_2$ (6.5 M) to give [Ca^{2+}]:[uronate] ratios ranging from 0.0 to 5.0 as required. Following each addition, the solution was shaken, and allowed to stand at room temperature for a minimum of 1 hour prior to the ^{1}H and ^{13}C NMR spectra being acquired. As discussed in Section 3.8.1.3, the small changes in the concentration of the solution with the increasing volume were deemed to be negligible. The experiment could not be performed for **Gal** because, upon addition of $CaCl_2$ a white precipitate formed after a few hours, preventing suitable NMR spectra from being acquired.

3.8.1.5 Investigation C

Two completely independent experiments were conducted as part of Investigation C. The first, exploring the binding of Zn^{2+} ions, was essentially carried out according to the protocol described for s-block metal ions in Section 3.8.1.3. The only exception to the aforementioned procedure was that only the spectra at pH* 1.0 were acquired because higher pH* values gave rise to insoluble zinc precipitates.

The second experiment, concerning the complexation of Cu^{2+} ions with the mono-uronates was quite different to those described in Investigations A and B and followed the method described by Synytsya *et al*.[105] Here a sample of sodium uronate (500 μL, 260 mM, pH* 6.0) was subjected to analysis by ^{1}H and ^{13}C NMR spectroscopy both before and 12 hours after the addition of a solution of $CuCl_2$ (10 μL, 26 mM) corresponding to a [Cu^{2+}]/[uronate] ratio of 1:500.

3.9 Chapter acknowledgements

The Durham University NMR service are thanked for assistance in the preparation of the work in this chapter. Dr. Alan Kenwright is acknowledged particularly for helpful conversations.

3.10 Chapter references

1 S. J. Angyal, *Adv. Carbohydr. Chem. Biochem.*, 1989, **47**, 1–43.

2 C. H. Gill, *J. Chem. Soc.*, 1871, **24**, 269–275.

3 J. A. Rendleman, *Adv. Carbohydr. Chem.*, 1967, **21**, 209–271.

4 R. Codd, *Chem. Commun. (Camb).*, 2004, **8**, 2653–2655.

5 J. A. Rendleman, *Food Chem.*, 1978, **3**, 47–79.

6 J. A. Rendleman, *Food Chem.*, 1978, **3**, 127–162.

7 S. J. Angyal, *Chem. Soc. Rev.*, 1980, **9**, 415–428.

8 D. M. Whitfield, S. Stojkovski and B. Sarkar, *Coord. Chem. Rev.*, 1993, **122**, 171–225.

9 B. Gyurcsik and L. Nagy, *Coord. Chem. Rev.*, 2000, **203**, 81–149.

10 Y. E. Alekseev, A. D. Garnovskii and Y. Zhdanov, *Russ. Chem. Rev.*, 1998, **67**, 649–669.

11 S. John D., *Adv. Carbohydr. Chem. Biochem.*, 2013, **69**, 2–20.

12 S. J. Angyal and K. P. Davies, *J. Chem. Soc. D Chem. Commun.*, 1971, **10**, 500–501.

13 M. E. Evans and S. J. Angyal, *Carbohydr. Res.*, 1972, **25**, 43–48.

14 S. J. Angyal, *Aust. J. Chem.*, 1972, **25**, 1957–1966.

15 S. J. Angyal, *Pure Appl. Chem.*, 1973, **35**, 131–146.

16 S. J. Angyal, *Tetrahedron*, 1974, **30**, 1695–1702.

17 L. W. Jaques, E. B. Brown, J. M. Barrett and W. Brey WS Jr Weltner, *J. Biol. Chem.*, 1977, **252**, 4533–4538.

18 A. Pallagi, P. Sebők, P. Forgó, T. Jakusch, I. Pálinkó and P. Sipos, *Carbohydr. Res.*, 2010, **345**, 1856–1864.

19 A. Pallagi, Z. Csendes, B. Kutus, E. Czeglédi, G. Peintler, P. Forgo, I. Pálinkó and P. Sipos, *Dalt. Trans.*, 2013, **42**, 8460–8467.

20 R. O. Gould and A. F. Rankin, *J. Chem. Soc. D Chem. Commun.*, 1970, **8**, 489–490.

21 J. W. Haas, *Mar. Chem.*, 1986, **19**, 299–304.

22 L. W. Jaques, J. B. Macaskill and W. Weltner, *J. Phys. Chem.*, 1979, **83**, 1412–1421.

23 T. A. Davis, B. Volesky and A. Mucci, *Water Res.*, 2003, **37**, 4311–4330.

24 E. Stanford, *Chem. News.*, 1883, **47**, 254–256.

25 P. Gacesa, *Carbohydr. Polym.*, 1988, **8**, 161–182.

26 K. Y. Lee and D. J. Mooney, *Prog. Polym. Sci.*, 2012, **37**, 106–126.

27 E. D. T. Atkins, I. A. Nieduszynski, W. Mackie, K. D. Parker and E. E. Smolko, *Biopolymers*, 1973, **12**, 1879–1887.

28 E. D. T. Atkins, I. A. Nieduszynski, W. Mackie, K. D. Parker and E. E. Smolko, *Biopolymers*, 1973, **12**, 1865–1878.

29 E. Fourest and B. Volesky, *Appl. Biochem. Biotechnol.*, 1997, **67**, 215–226.

30 W. Mackie, R. Rizzo, F. Taravel and M. Vignon, *Int. J. Biol. Macromol.*, 1983, **5**, 329–341.

31 O. Smidsrød, A. Haug, S. G. Whittington, E. Sjöstrand and S. Svensson, *Acta Chem. Scand.*, 1972, **26**, 2563–2566.

32 G. T. Grant, E. R. Morris, D. A. Rees, P. J. C. Smith and D. Thom, *FEBS Lett.*, 1973, **32**, 195–198.

33 D. A. Rees, *Polysaccharide Shapes*, Springer Netherlands, Dordrecht, 1977.

34 R. Kohn, B. Larsen, L. J. Sæthre, E. Sjöstrand and S. Svensson, *Acta Chem. Scand.*, 1972, **26**, 2455–2468.

35 E. R. Morris, D. A. Rees, D. Thom and J. Boyd, *Carbohydr. Res.*, 1978, **66**, 145–154.

36 C. Steginsky, J. M. Beale, H. G. Floss and R. M. Mayer, *Carbohydr. Res.*, 1992, **225**, 11–26.

37 R. Kohn, *Pure Appl. Chem.*, 1975, **42**, 371–397.

38 A. Haug, J. Bjerrum, O. Buchardt, G. E. Olsen, C. Pedersen and J. Toft, *Acta Chem. Scand.*, 1961, **15**, 1794–1795.

39 A. Haug, O. Smidsrød, B. Larsen, S. Gronowitz, R. A. Hoffman and A. Westerdahl, *Acta Chem. Scand.*, 1965, **19**, 341–351.

40 O. Smidsrød and A. Haug, *Acta Chem. Scand.*, 1965, **19**, 329–340.

41 A. Haug, S. Myklestad, B. Larsen, O. Smidsrød, G. Eriksson, R. Blinc, S. Paušak, L. Ehrenberg and J. Dumanović, *Acta Chem. Scand.*, 1967, **21**, 768–778.

42 A. Haug, O. Smidsrød, B. Högdahl, H. A. Øye, S. E. Rasmussen, E. Sunde and N. A. Sørensen, *Acta Chem. Scand.*, 1970, **24**, 843–854.

43 G. Lunde, O. Smidsrød, A. Haug, J. Songstad and Å. Pilotti, *Acta Chem. Scand.*, 1972, **26**, 3421–3426.

44 O. Smidsrød, D.Sc. thesis, University of Trondheim, Trondheim: NTNF's Institutt for Marin Biokjemi, 1973.

45 F. Topuz, A. Henke, W. Richtering and J. Groll, *Soft Matter*, 2012, **8**, 4877–4881.

46 A. Penman and G. R. Sanderson, *Carbohydr. Res.*, 1972, **25**, 273–282.

47 W. S. J. Peschardt, United States Patent Office, US 2403547 A, 1946, 1–2.

48 M. Wilkinson, *Aquat. Conserv. Mar. Freshw. Ecosyst.*, 1992, **2**, 209–210.

49 K. Skja, in *Renewable Resources for Functional Polymers and Biomaterials: Polysaccharides, Proteins and Polyesters*, RSC, Cambridge, 2011, pp. 186–209.

50 K. G. Mandel, B. P. Daggy, D. A. Brodie and H. I. Jacoby, *Aliment. Pharmacol. Ther.*, 2000, **14**, 669–690.

51 S. S. Pedersen, A. Kharazmi, F. Espersen and N. Høiby, *Infect. Immun.*, 1990, **58**, 3363–3368.

52 D. W. Smith, *J. Chem. Educ.*, 1977, **54**, 540–542.

53 H. Irving and R. J. P. Williams, *J. Chem. Soc.*, 1953, 3192–3210.

54 Q. Yu, J. T. Matheickal, P. Yin and P. Kaewsarn, *Water Res.*, 1999, **33**, 1534–1537.

55 W. M. Antunes, A. S. Luna, C. Henriques and A. C. A. Da Costa, *Electron. J. Biotechnol.*, 2003, **6**, 175–184.

56 P. Lodeiro, B. Cordero, J. Barriada, R. Herrero and M. Sastredevicente, *Bioresour. Technol.*, 2005, **96**, 1796–1803.

57 R. Seale, E. R. Morris and D. A. Rees, *Carbohydr. Res.*, 1982, **110**, 101–112.

58 L. K. Jang, N. Harpt, D. Grasmick, L. N. Vuong and G. Geesey, *J. Phys. Chem.*, 1990, **94**, 482–488.

59 D. Thom, G. T. Grant, E. R. Morris and D. A. Rees, *Carbohydr. Res.*, 1982, **100**, 29–42.

60 D. A. Rees, *Pure Appl. Chem.*, 1981, **53**, 1–14.

61 D. Ramos, PhD thesis, University of Cincinnati, 1995.

62 C. DeRamos, A. Irwin, J. Nauss and B. Stout, *Inorg. Chim. Acta*, 1997, **256**, 69–75.

63 A. Elizabeth, PhD thesis, University of Cincinnati, 1997.

64 D. Lattner, H. C. Flemming and C. Mayer, *Int. J. Biol. Macromol.*, 2003, **33**, 81–88.

65 Z. Y. Wang, Q.-Z. Zhang, M. Konno and S. Saito, *Biopolymers*, 1993, **33**, 703–711.

66 Z. Y. Wang, J. W. White, M. Konno, S. Saito and T. Nozawa, *Biopolymers*, 1995, **35**, 227–238.

67 D. Filipiuk, L. Fuks and M. Majdan, *J. Mol. Struct.*, 2005, **744**–**747**, 705–709.

68 L. Fuks, D. Filipiuk and M. Majdan, *J. Mol. Struct.*, 2006, **792**–**793**, 104–109.

69 S. K. Papageorgiou, E. P. Kouvelos, E. P. Favvas, A. a Sapalidis, G. E. Romanos and F. K. Katsaros, *Carbohydr. Res.*, 2010, **345**, 469–473.

70 M. L. Dheu-Andries and S. Pérez, *Carbohydr. Res.*, 1983, **124**, 324–332.

71 I. Braccini and S. Pérez, *Biomacromolecules*, 2001, **2**, 1089–1096.

72 W. Plazinski and M. Drach, *J. Phys. Chem. B*, 2013, **117**, 12105–12112.

73 W. Plazinski and M. Drach, *Appl. Surf. Sci.*, 2012, **262**, 153–155.

74 R. Kohn, I. Furda, A. Haug and O. Smidsrød, *Acta Chem. Scand.*, 1968, **22**, 3098–3102.

75 T. Anthonsen, B. Larsen, O. Smidsrød, Å. Pilotti, S. Svensson and C.-G. Swahn, *Acta Chem. Scand.*, 1973, **27**, 2671–2673.

76 H. S. Isbell, *Bur. Stand. J. Res.*, 1930, **5**, 741–755.

77 H. S. Isbell, *Bur. Stand. J. Res.*, 1932, **8**, 1–8.

78 H. S. Isbell and W. W. Pigman, *J. Res. Natl. Bur. Stand.*, 1937, **18**, 141–194.

79 H. Grasdalen, T. Anthonsen, B. Larsen, O. Smidsrød, O. Dahl, O. Buchardt and G. Schroll, *Acta Chem. Scand.*, 1975, **29b**, 17–21.

80 W. Plazinski and M. Drach, *New J. Chem.*, 2015, **39**, 3987–3994.

81 F. Mo, T. J. Brobak and I. R. Siddiqui, *Carbohydr. Res.*, 1985, **145**, 13–24.

82 J. T. Triffitt, *Nature*, 1968, **217**, 457–458.

83 S. J. Angyal, D. Greeves and L. Littlemore, *Carbohydr. Res.*, 1988, **174**, 121–131.

84 C. H. S. Wong, F. M. Siu, N. L. Ma and C. W. Tsang, *J. Mol. Struct. Theo. Chem.*, 2001, **536**, 227–234.

85 J. K. Dale, *J. Am. Chem. Soc.*, 1929, **51**, 2788–2795.

86 D. C. Craig, N. C. Stephenson and J. D. Stevens, *Carbohydr. Res.*, 1972, **22**, 494–495.

87 D. Powell, E. R. Morris, M. J. Gidley and D. A. Rees, *J. Mol. Biol.*, 1982, **155**, 517–531.

88 L. Fuks and J. C. G. Bünzli, *Helv. Chim. Acta*, 1993, **76**, 2992–3000.

89 J. Hjortås, B. Larsen, S. Thanomkul, I. Szabo-Lin, C. Guthenberg and B. Mannervik, *Acta Chem. Scand.*, 1974, **28b**, 689–689.

90 S. Thanomkul, J. A. Hjortås and H. Sørum, *Acta Crystallogr. Sect. B Struct. Crystallogr. Cryst. Chem.*, 1976, **32**, 920–922.

91 S. E. B. Gould, R. O. Gould, D. A. Rees and W. E. Scott, *J. Chem. Soc. Perkin Trans. 2*, 1975, **3**, 237–242.

92 H. S. Isbell and H. L. Frush, *J. Res. Natl. Inst. Stand. Technol.*, 1944, **32**, 77–94.

93 L. DeLucas, C. E. Bugg, A. Terzis and R. Rivest, *Carbohydr. Res.*, 1975, **41**, 19–29.

94 K. Izumi, *Agric. Biol. Chem.*, 1980, **44**, 1623–1631.

95 B. J. Kvam, H. Grasdalen, O. Smidsrød, T. Anthonsen and R. Kivekäs, *Acta Chem. Scand.*, 1986, **40b**, 735–739.

96 H. Grasdalen, T. Anthonsen, B. Larsen, O. Smidsrød, O. Dahl, O. Buchardt and G. Schroll, *Acta Chem. Scand.*, 1975, **29b**, 99–108.

97 L. Fuks, D. Filipiuk and W. Lewandowski, *J. Mol. Struct.*, 2001, **563**–**564**, 587–593.

98 H. Grasdalen, T. Anthonsen, O. Harbitz, B. Larsen, O. Smidsrød, C.-O. Pontchour, P. Phavanantha, S. Pramatus, B. N. Cyvin and S. J. Cyvin, *Acta Chem. Scand.*, 1978, **32a**, 31–39.

99 T. Anthonsen, B. Larsen, O. Smidsrød, M. J. Tricker and S. Svensson, *Acta Chem. Scand.*, 1972, **26**, 2988–2989.

100 H. A. Tajmir-Riahi, *Carbohydr. Res.*, 1983, **122**, 241–248.

101 H. A. Tajmir-Riahi, *Carbohydr. Res.*, 1984, **125**, 13–20.

102 H. A. Tajmir-Riahi, *J. Inorg. Biochem.*, 1985, **24**, 127–136.

103 H. A. Tajmir-Riahi, *Inorg. Chim. Acta*, 1986, **119**, 227–232.

104 H. A. Tajmir-Riahi, *J. Inorg. Biochem.*, 1986, **26**, 23–33.

105 A. Synytsya, M. Urbanová, V. Setnička, M. Tkadlecová, J. Havlíček, I. Raich, P. Matějka, A. Synytsya, J. Čopíková and K. Volka, *Carbohydr. Res.*, 2004, **339**, 2391–2405.

106 G. M. Escandar and L. F. Sala, *J. Chem. Educ.*, 1997, **74**, 1329–1332.

107 G. M. Escandar, L. F. Sala and M. Gonzalez Sierra, *Polyhedron*, 1994, **13**, 143–150.

108 G. M. Escandar and L. F. Sala, *Can. J. Chem.*, 1992, **70**, 2053–2057.

109 I. Cook, R. Magee, R. Payne and B. Ternai, *Aust. J. Chem.*, 1986, **39**, 1307–1314.

110 R. Aruga, *Bull. Chem. Soc. Jpn.*, 1981, **54**, 1233–1235.

111 Z. Cetin, C. Kantar and M. Alpaslan, *Environ. Toxicol. Chem.*, 2009, **28**, 1599–1608.

112 P. Selvarengan, J. D. Kubicki, J.-P. Guégan and X. Châtellier, *Chem. Geol.*, 2010, **273**, 55–75.

113 E. Ferrari, R. Grandi, S. Lazzari and M. Saladini, *J. Inorg. Biochem.*, 2005, **99**, 2381–2386.

114 H. Sterk, M. Braun, O. Schmut and H. Feichtinger, *Carbohydr. Res.*, 1985, **145**, 1–11.

115 A. Rotondo, E. Rotondo, G. A. Casella and G. Grasso, *Dalt. Trans.*, 2008, **2**, 596–601.

116 G. Micera, A. Dessí, H. Kozłowski, B. Radomska, J. Urbanska, P. Decock, B. Dubois and I. Olivier, *Carbohydr. Res.*, 1989, **188**, 25–34.

117 P. Agulhon, V. Markova, M. Robitzer, F. Quignard and T. Mineva, *Biomacromolecules*, 2012, **13**, 1899–1907.

118 M. C. R. Symons, J. Benbow and H. Pelmore, *J. Chem. Soc. Faraday Trans. 1 Phys. Chem. Condens. Phases*, 1982, **78**, 3671–3677.

119 M. C. R. Symons, J. Benbow and H. Pelmore, *J. Chem. Soc. Faraday Trans. 1 Phys. Chem. Condens. Phases*, 1984, **80**, 1999–2016.

120 S. Bekiroglu, PhD thesis, Swedish University of Agricultural Sciences, Uppsala, 2003.

121 A. Pallagi, C. Dudás, Z. Csendes, P. Forgó, I. Pálinkó and P. Sipos, *J. Mol. Struct.*, 2011, **993**, 336–340.

122 D. L. Bryce, *Dalt. Trans.*, 2010, **39**, 8593–8602.

123 A. D. Buckingham, *Can. J. Chem.*, 1960, **38**, 300–307.

124 S. J. Angyal, *Carbohydr. Res.*, 1973, **26**, 271–273.

125 J. Batchelor, *J. Am. Chem. Soc.*, 1975, **97**, 3410–3415.

126 J. Batchelor, J. Feeney and G. C. Roberts, *J. Magn. Reson.*, 1975, **20**, 19–38.

127 K. Zhuo, Y. Wang, Y. Zhao, Q. Liu and J. Wang, *Spectrochim. Acta Part A Mol. Biomol. Spectrosc.*, 2008, **71**, 100–104.

128 K. Zhuo, H. Liu, X. Zhang, Y. Liu and J. Wang, *Carbohydr. Res.*, 2008, **343**, 2428–2432.

129 M. F. Czarniecki and E. R. Thornton, *Biochem. Biophys. Res. Commun.*, 1977, **74**, 553–558.

130 T. Kondoh, A; Oi, *Z. Naturforsch.*, 1997, **52a**, 351–357.

131 D. Parker, *Chem. Soc. Rev.*, 2004, **33**, 156–165.

132 M. Martin, G. Martin and J. J. Delpeuch, in *Practical NMR Spectroscopy*, Heyden, London, 1980, pp. 396–409.

133 J. Beattie and M. Kelso, *Aust. J. Chem.*, 1981, **34**, 2563–2568.

134 J. Burgess, in *Metal ions in solution*, Ellis Horwood Limited, Chichester, 1978, pp. 38–74.

135 S. E. B. Gould, R. O. Gould, D. A. Rees and A. W. Wight, *J. Chem. Soc., Perkin Trans. 2*, 1976, **4**, 392–398.

136 Q. Zhang, E. R. van Rijssel, H. S. Overkleeft, G. A. van der Marel and J. D. C. Codée, *European J. Org. Chem.*, 2016, **14**, 2393–2397.

137 M. T. C. Walvoort, H. van den Elst, O. J. Plante, L. Kröck, P. H. Seeberger, H. S. Overkleeft, G. A. van der Marel and J. D. C. Codée, *Angew. Chemie Int. Ed.*, 2012, **51**, 4393–4396.

138 Q. Zhang, E. R. van Rijssel, M. T. C. Walvoort, H. S. Overkleeft, G. A. van der Marel and J. D. C. Codée, *Angew. Chemie Int. Ed.*, 2015, **54**, 7670–7673.

139 J. S. Renny, L. L. Tomasevich, E. H. Tallmadge and D. B. Collum, *Angew. Chemie Int. Ed.*, 2013, **52**, 11998–12013.

140 H. R. Tang, P. S. Belton, S. C. Davies and D. L. Hughes, *Carbohydr. Res.*, 2001, **330**, 391–399.

141 H. B. Mayes, M. W. Nolte, G. T. Beckham, B. H. Shanks and L. J. Broadbelt, *ACS Catal.*, 2015, **5**, 192–202.

142 S. Bali, M. Tofanelli, R. D. Ernst and E. M. Eyring, *Biomass and Bioenergy*, 2012, **42**, 224–227.

143 A. Saddawi, J. Jones and A. Williams, *Fuel Process. Technol.*, 2012, **104**, 189–197.

144 K. R. Enslow and A. T. Bell, *ChemCatChem*, 2015, **7**, 479–489.

145 K. R. Enslow and A. T. Bell, *Catal. Sci. Technol.*, 2015, **5**, 2839–2847.

146 H. Lönnberg and A. Vesala, *Carbohydr. Res.*, 1980, **78**, 53–59.

147 F. van der Klis, A. E. Frissen, J. van Haveren and D. S. van Es, *ChemSusChem*, 2013, **6**, 1640–1645.

148 S. Rautiainen, P. Lehtinen, J. Chen, M. Vehkamäki, K. Niemelä, M. Leskelä and T. Repo, *RSC Adv.*, 2015, **5**, 19502–19507.

149 W. Hongsiri, B. Danon and W. de Jong, *Ind. Eng. Chem. Res.*, 2014, **53**, 5455–5463.

150 A. K. Covington and M. Whitfield, *Pure Appl. Chem.*, 1988, **60**, 865–870.

151 Y. Marcus, *Pure Appl. Chem.*, 1989, **61**, 1133–1138.

152 H. E. Gottlieb, V. Kotlyar and A. Nudelman, *J. Org. Chem.*, 1997, **62**, 7512–7515.

153 G. R. Fulmer, A. J. M. Miller, N. H. Sherden, H. E. Gottlieb, A. Nudelman, B. M. Stoltz, J. E. Bercaw and K. I. Goldberg, *Organometallics*, 2010, **29**, 2176–2179.

Chapter 4

Chapter 4

The metal-mediated thermolysis of alginates and related uronides*

4.1 Chapter abstract

The work in this chapter is aimed at discerning the role of metal ions in the pyrolysis of alginates, with a view ultimately to exploiting such knowledge in the thermochemical treatment of macroalgal biomass. Both pyrolysis-gas chromatography mass spectrometry (Py-GCMS) and thermogravimetric analysis (TGA) were employed in order to probe the thermochemistry of alginic acid (**HAlg**) and various metal alginates (**MAlg**, where M = Na^+, Ca^{2+}, Mg^{2+}, Sr^{2+}, Ba^{2+}, Co^{2+}, Ni^{2+}, Zn^{2+}, and Cu^{2+}) for mutual comparison under helium across a range of temperatures. Here, the alkali and alkali earth metals were found to increase the stability of the alginate polymer by the highest amounts, inhibiting the onset of rapid pyrolysis relative to **HAlg** by around 40 °C. Meanwhile, the d-block metals inhibited rapid pyrolysis to a lesser extent, and Cu(II) was actually found to promote it. Similarly, the s-block metals yielded high levels of char and small oxygenate molecules (particulalrly acetol and diacetyl), whilst the d-block ions promoted char degradation and gave a distribution of products more akin to that of **HAlg** (rich in 2-furaldehyde, 2-FF). Additional evidence from the solid-state characterisation of chars was utilised to inform tentative mechanistic interpretations of the thermo-analytical results. Particularly, the low-temperature formation of Cu^0 from **Cu(II)Alg** is offered as evidence of a *Hofer-Moest* type decarboxylation mechanism possibly being active. Further investigations of related uronides (pectin and mono-uronic acids) yielded similar results to those of the alginates, indicating the wide applicability of the conclusions. Indeed, the work demonstrates that the thermal behaviour of a metal-bound uronide is a function of the identity of the cation

* The preliminary results that ultimately gave rise to this chapter were published as a communication in 2013. Later experiments were, however, conducted with greater scope and detail and served to largely supersede the earlier work. The original paper is reproduced in Appendix T for reference, as some limited discussion is made in this Chapter of the kinetic analyses contained within it.

to a greater extent than the stereochemistry of its constituent units. Finally, tentative mass balances are provided for the pyrolysis of **H-**, **Na-**, **Ca-**, and **Cu(II)-Alg** at 500 °C. Here, the high levels of char, CO_2, and H_2O arising from alginates were recognised as being unappealing for industrial-scale pyrolysis, though the selective, low temperature release of 2-FF was identified as being a major attribute in the case of both **Cu(II)Alg** and **HAlg**.

4.2 Chapter Introduction and context

The experiments and discussions in Chapters 2 and 3 have served to introduce and extend the rich chemistry of algal mono-uronides. Building upon this work, Chapter 4 takes as its focus the pyrolysis of alginates (linear co-polymers of L-guluronate and D-mannuronate, see Figure 4.1). Having recognised differences in the metal coordination behaviour of uronic acids earlier in the thesis, the present chapter will seek to define and rationalise observed trends in uronide thermochemistry. Given the ultimate aim of this dissertation to examine and explain how metal binding properties of uronides dictate the pyrolysis of their parent biomass, Chapter 4 serves as a "model compound" study to underpin the investigations in Chapter 5 on the thermochemistry of whole seaweeds. Given the complexity associated with carbohydrate pyrolysis reactions, the first half of this chapter is dedicated to an extensive literature review on that topic. As there have been very few studies of uronide thermochemistry in the past, the review will first deal with the pyrolysis of neutral carbohydrates (which have been investigated in more detail), which provide valuable insight into the mechanisms generally associated with saccharide thermolysis. The review will then discuss the relevant thermochemical studies concerning uronides and metal-bound uronides, in order to establish the context for the experimental work in the latter half of the chapter.

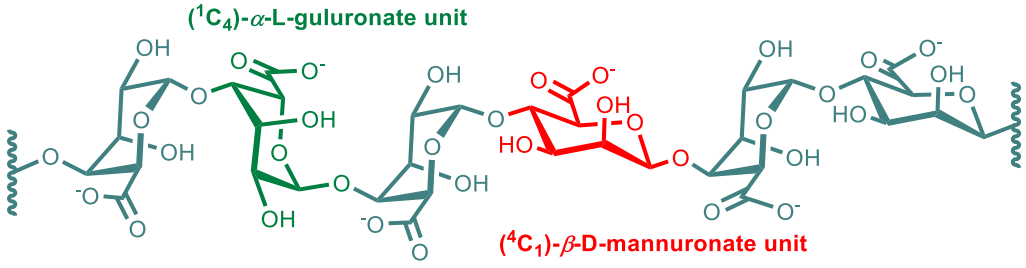

Figure 4.1 Alginate and its constituent monosaccharides

4.3 Background

4.3.1 The pyrolysis of saccharides and the pyrolysis of biomass

Since the days of our early ancestors, human beings have been fascinated by the thermochemistry of biomass. Whilst originally humans sought to derive heat from the combustion of such feedstocks, nowadays our requirements or more nuanced, and we recognise that there is significant value to be found in the compounds formed from thermal decomposition in and of themselves (see Chapter 1). Of course, the signature product distribution of a piece of biomass is intrinsically linked to its individual chemical components, and so the vast complexity of the pyrolysis process can be significantly

reduced by consideration of these isolated compounds, of which carbohydrates typically form the largest fraction. If we consider, for example, an orange peel, the thermochemical signatures of the constituent carbohydrates (depicted in Figure 4.2) can be identified when the whole biomass is subjected to the same pyrolysis conditions (as per the experiments of Kim *et al.* shown in Figure 4.3).[1]

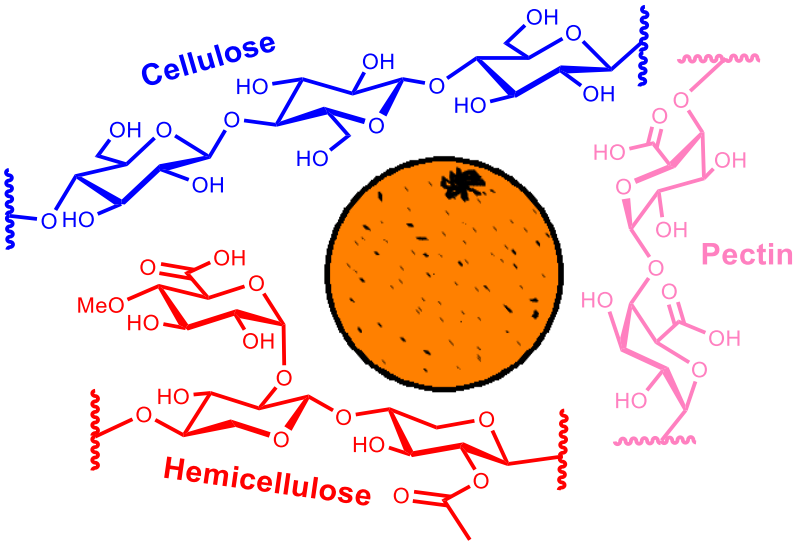

Figure 4.2 Biomass (such as citrus peel) contains a variety of polysaccharides

In studying Figure 4.3 it is interesting to note the vastly different thermolysis profiles of the three carbohydrates (cellulose, pectin, and hemicellulose), despite them possessing close chemical similarity. Each artefact in the thermograms corresponds to a thermochemical event, and relating these effects to the polysaccharide structure will be a key theme within this chapter.

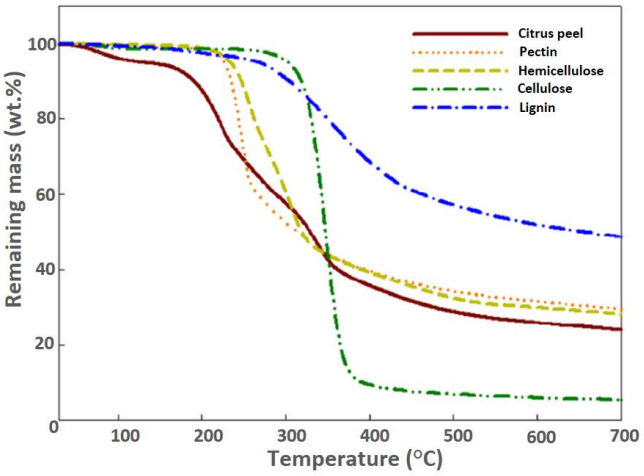

Figure 4.3 Thermogravimetric analysis of citrus peel and its biochemical components under N_2 (re-printed with permission from Kim *et al.*© Springer Science and Business Media, New York, 2014).[1]

As work is on-going to find a feedstock possessing all of the necessary characteristics defined in Chapter 1 to be a suitable candidate for pyrolysis on an industrial scale, so too is there a demand to understand on the molecular scale the behaviour of biomass-derived carbohydrates. The following sections will summarise existing knowledge, particularly highlighting gaps in current understanding. Ultimately, the findings will be exploited for the purpose of thermally upgrading uronide-rich biomass (namely kelp) in Chapter 5.

4.3.2 Background to the pyrolysis of non-uronide carbohydrates

4.3.2.1 An introduction to carbohydrate thermochemistry

As discussed in Section 4.3.1 and (more fully) in Chapter 1, the utilisation of carbohydrate-rich biomass for the generation of fuels and chemicals has been a major incentive for the study of saccharide thermochemistry. It is worth recognising, however, the multitude of other motivations that have driven scientists to pursue an understanding of carbohydrate thermolysis, including within the fields of food chemistry, tobacco research, fire control and forensics, catalyst synthesis, and the development of heat-resistant materials. Hence, whilst many papers amongst the reference list of this chapter originate from a seemingly disparate array of publications, most are linked by a common goal – to understand and influence the mechanisms underpinning the thermal degradation of carbohydrates. Yet, despite the wealth of research that has been carried out in order to achieve this aim, the scientific community is far from a position of consensus regarding the thermolytic pathways of even the simplest saccharides. This unsettled situation is doubtless a product of the complexity of carbohydrate thermochemistry (with sometimes many hundreds of products forming through a multitude of competing reactions)[2] coupled to differing experimental approaches (where even small changes in starting parameters delivers drastically different results).[3] Consequently, there is still much uncertainty concerning, for example, the effect of the degree of polymerisation (DP) of a saccharide on thermolysis reactions or, notably, the influence(s) of coordinated metal ions. There are, however, a number of areas of substantial agreement, and the following sections (4.3.2.1 - 4.3.2.4) will aim to highlight these especially in an attempt to inform later discussions on the thermochemical behaviour of less-well studied carbohydrate classes (namely the uronides).

Whilst most research targeted at the thermal conversion of biomass is concerned with the thermochemistry of *poly*saccharides (the native state of most carbohydrates in plant matter), there is undoubtedly merit in devoting time to the consideration of the behaviour of constituent *mono*saccharides.[4,5] In this regard, the degree of similarity between the thermal behaviour of monomeric and polymeric saccharides (including their thermogravimetric profiles and product distributions) can be indicative of certain thermolysis mechanisms. For example, where there is close agreement between the pyrolysis traits of both mono- and poly-saccharide, it might be assumed that, in the initial heating stages, the polymer is simply reverting to its constituent monomer units. Conversely, where significant differences appear, the glycosidic bonds that link the polysaccharide chain can be considered to be directing the pyrolysis of the polymer along

an alternate pathway. Consequently, and in accordance with the philosophy described in Chapters 1 – 3 of this thesis, the behaviour of mono-uronates will be considered in detail to then provide insight into their polymeric counterparts (see Section 4.3.3).

4.3.2.2 The pyrolysis of monosaccharides

With an overwhelming interest in the pyrolysis behaviour of cellulose (see Section 4.3.2.3), *β*-D-glucopyranose (see Figure 4.4) has tended to dominate thermochemical investigations of monosaccharides and, consequently, reviews of the field (by Moldoveanu[2] and Antal[6] for example) tend to focus on this molecule above others. The thermochemistry of D-glucose is, however, fairly representative of the behaviour of most aldohexopyranoses,[2,7,8*] and an extensive review of all members of that class would not be fruitful here. Instead, only the salient points of the pyrolysis of *β*-D-glucose are considered in order to inform later discussions on the pyrolysis of polysaccharides and, ultimately, uronides.

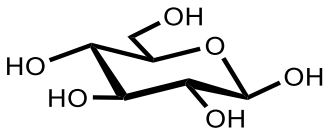

($^4C_1$)-*β*-D-glucopyranose

Figure 4.4 D-glucose: the fundamental building block of all cellulosic biomass

Following loss of the water of hydration, the first step in the thermal degradation of *β*-D-glucose is melting, occurring at approximately 153 – 156 °C.[9] Further heating induces oligomerisation within the sample, giving rise to a slow loss of mass owing to the elimination of water prior to the onset of rapid pyrolysis at around 200 °C.[9] Rapid pyrolysis proceeds in D-glucose until around 350 °C and a typical distribution of the major volatile organic products liberated during this period is depicted in Figure 4.5 (omitting char, water, and CO).[2] Whilst the same degradation compounds are often reported in studies by various authors,[2,5,10,11] the relative distribution can vary quite widely between accounts. Mettler *et al.*[5] and Mayes *et al.*[10] described only modest 2-furaldehyde (2-FF) yields compared to Moldoveanu,[2] yet the former authors mutually disagree with regards to the relative proportions of char and glycoaldehyde produced. Such inconsistencies between studies highlight the difficulties associated with working in the complex field of pyrolysis chemistry – where small changes to parameters (in both the sample and the thermo-analytical methodology) can have drastic impacts on the reported results.[3] There is clearly an advantage in testing a number of variables within the same study, where self-consistency can be assured, as external comparisons can be fraught with difficulty.[†]

---

[*] With differences in product slates largely being centred around the stereochemistry of the evolved anhydrosugars.

[†] Indeed, for the sake of this introduction, the data for the diagrams is taken from a single study by Moldoveanu.[2]

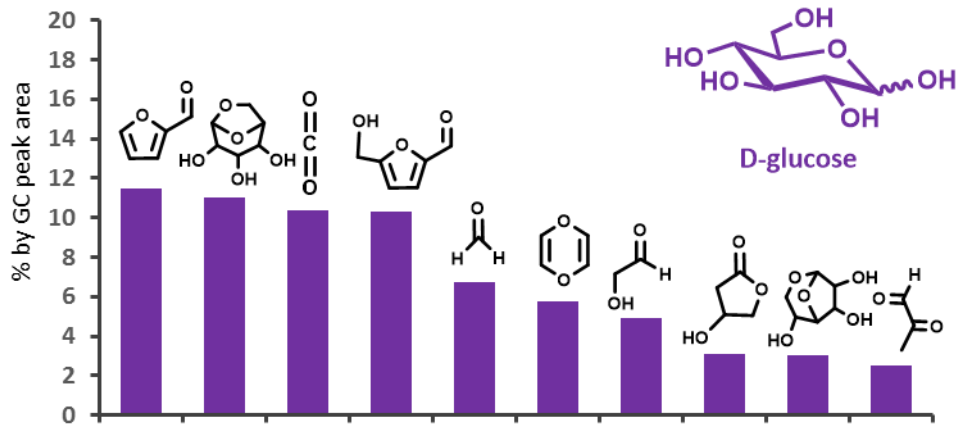

Figure 4.5 The product distribution of the pyrolysis of D-glucose at 900 °C (data taken from the work of Moldoveanu).[2]

Naturally, there has been much debate about the fragmentation pathways pursued by glucose during pyrolysis, with three mechanisms believed to be the most prevalent: retro-aldolisation, dehydration, and Grob fragmentation* (see Figure 4.6).[4,10–20] By combination of these primary degradation mechanisms with requisite ring-opening, ring-flipping, tautomerisation, and cyclisation steps, the final degradation products are reached (as illustrated by the work of Vinu and Broadbelt summarised in Figure 4.7).[12] A recent, comprehensive series of investigations by John B. Paine III and co-workers employed isotopic labelling methods to elucidate which mechanistic routes dominate glucose thermolysis.[14–17] In some cases the results were highly surprising, such as the overwhelming (> 90 %) incorporation of C1 to C5 into the resulting 2-furaldehyde (2-FF) through the elimination (*via* Grob fragmentation) of C6 as formaldehyde (see Figure 4.8),[6,15] despite the cleaved C5-C6 linkage being the strongest C-C or C-O bond in the D-glucose molecule.[13]

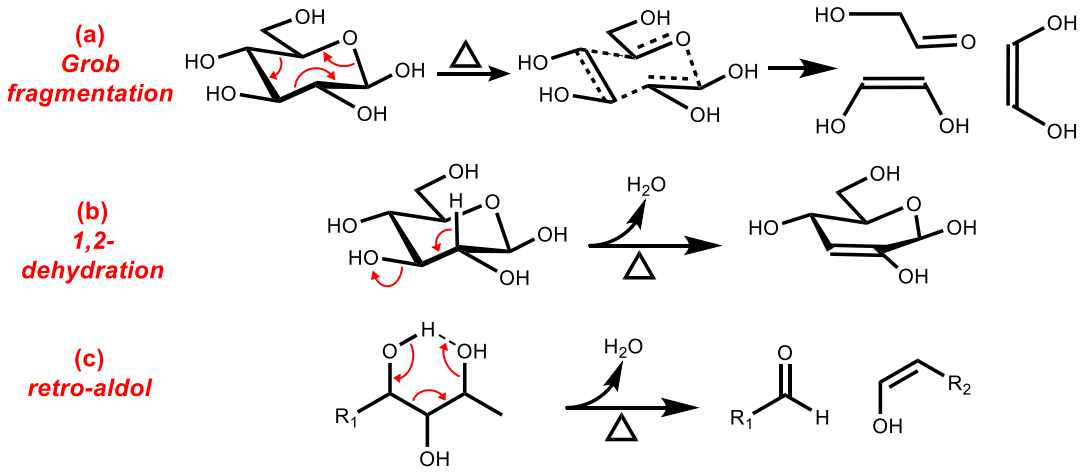

Figure 4.6 Mechanisms of a) Grob fragmentation, b) 1,2-dehydration, and c) retro-aldol reactions in saccharide pyrolysis

* It is worth highlighting that it is possible for all three mechanisms to occur for the glucose molecule in either cyclic or open chain configurations, though the relative rates for such transformations may differ.[10]

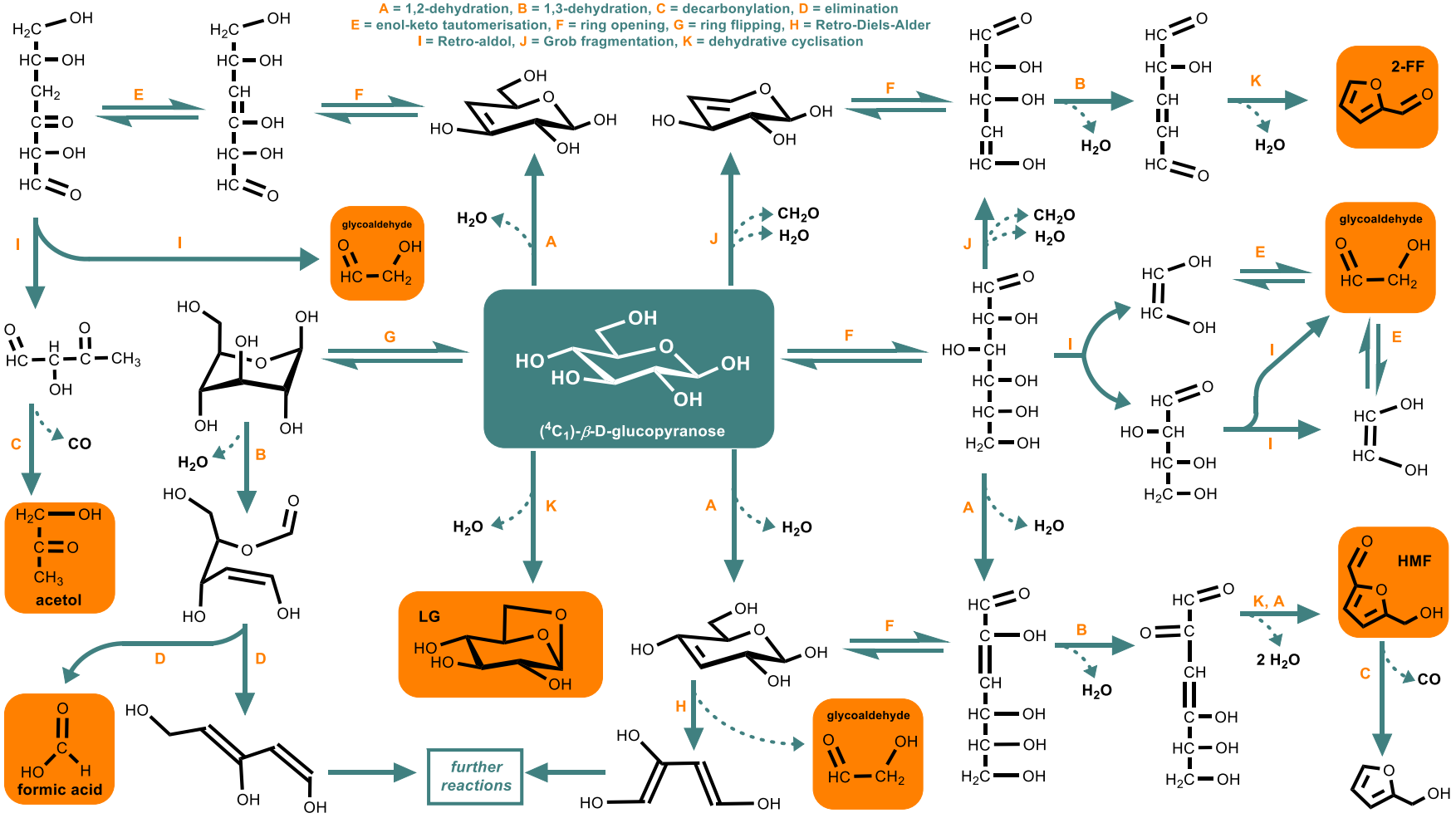

Figure 4.7 Dominant reaction pathways in the pyrolysis of D-glucose (redrawn from Vinu and Broadbelt with permission from The RSC)[12]

Whilst D-glucose is often depicted in the $^4C_1$-*β*-pyranose form, it is worth bearing in mind that (as was discussed in Chapter 2) such aldohexoses participate in a number of configurational equilibria in aqueous solution. A few investigations have been conducted in order to probe the relevance of such configurational isomerism in the pyrolysis of glucose. For example, computational work by Broadbelt *et al.* demonstrated that, at 500 °C, key thermolytic pathways (such as the formation of 1,6-anhydro-*β*-pyranose (levoglucosan, LG)) are much higher in energy for *α*-D-glucopyranose than the *β*-counterpart, despite empirically-derived product yields for both isomers being nearly identical (see Figure 4.9).[10] The authors attributed this result to the rapid interconversion between the various configurations that occur in the molten (or *condensed*)[21] phase of saccharides such as glucose under pyrolysis conditions. This anhydrous isomerism has profound implications for our ability to control the mechanistic pathways of carbohydrate pyrolysis.[22] Indeed, very recent work by Wong *et al.* demonstrated that, by altering the substituent on the glycosidic oxygen (essentially "pinning" the initial stereochemical configuration by prohibiting anomerisation), the LG yield increases from 2 to 90 wt.%.[23]

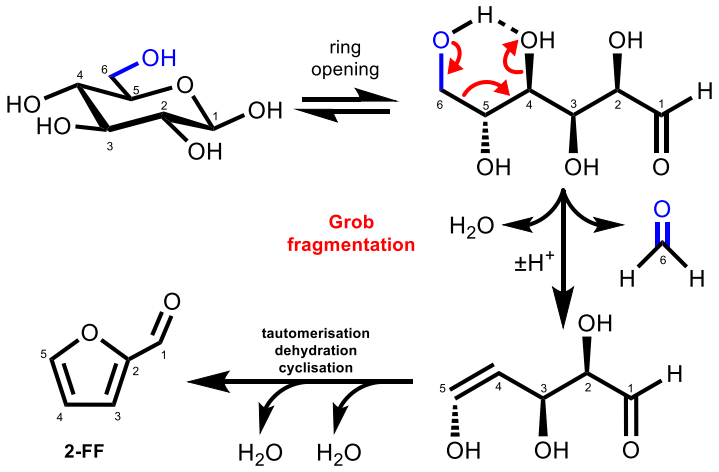

Figure 4.8 The formation of 2-FF from D-glucose through elimination of C6 as CH_2O[15]

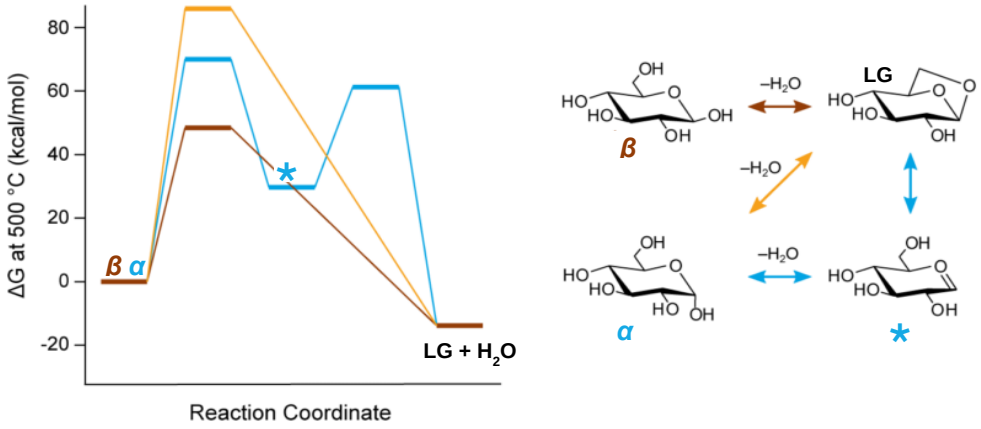

Figure 4.9 The conversion of *α*- and *β*- D-glucopyranose to levoglucosan (LG) (adapted with permission from Broadbelt *et al.*)[10] *

* http://pubs.acs.org/doi/abs/10.1021/sc500113m

Finally, whilst hexose degradation is often characterised by high yields of hydroxymethylfuraldehyde (HMF)[2,5,10], aldopentopyranoses have a much higher selectivity for 2-FF (see exemplar product slate for xylose in Figure 4.10).[2] Subsequent theoretical work by Wang *et al.* has demonstrated that the preference for HMF over 2-FF in hexoses arises because of the strong C5-C6 bond (absent in pentoses) remaining intact.[8]

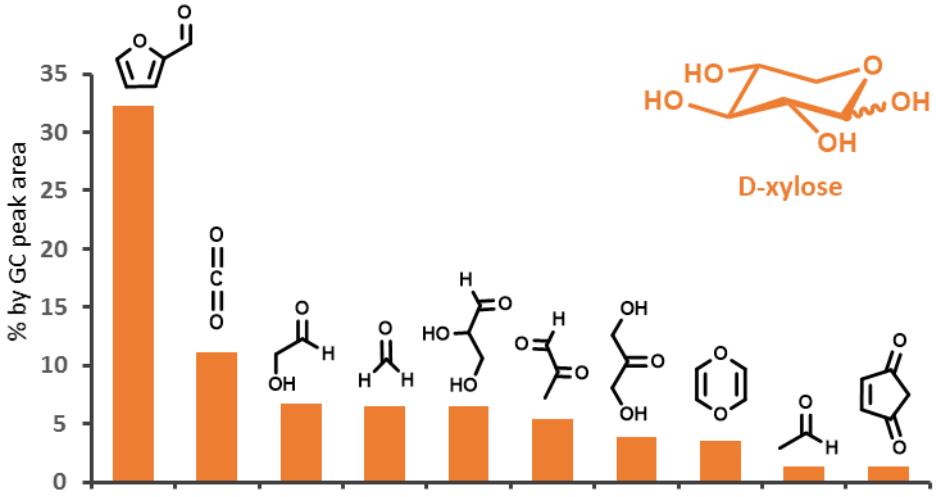

Figure 4.10 The product distribution of the pyrolysis of D-xylose at 900 °C (data taken from the work of Moldoveanu).[2]

4.3.2.3 The pyrolysis of polysaccharides

The field of polysaccharide pyrolysis is unsurprisingly dominated by investigations into the thermochemical behaviour of cellulose (the most abundant biopolymer on the planet)[24] and a number of review articles have been produced reflecting that fact.[6,12,18,25–28] Of course, the ubiquity of cellulose within nature owes much to the inherent stability of the structure, which consists of hydrogen bonded chains of (1-4)-linked $^4C_1$-*β*-D-glucopyranose units (see Figure 4.11). The durability afforded by the rigid cellulose architecture also confers a somewhat surprising thermal resistance to the polysaccharide. Indeed, compared to other biomass derived polysaccharides (including xylan for example) cellulose undergoes degradation at a very high temperature (> 300 °C) and across a notably narrow thermal window (reflecting the rapidity of pyrolysis) as evinced by the work of Kim *et al.* (see Figure 4.3).[1]

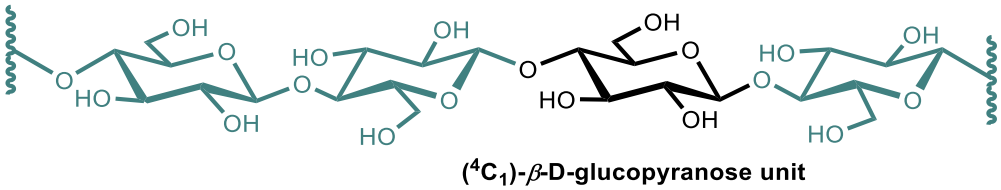

Figure 4.11 The structure of cellulose

Naturally, as researchers have attempted to develop kinetic models of cellulose thermolysis, the question of what chemical changes are occurring within the sample during the initial heating stage (prior to catastrophic degradation) was (and is) much debated, culminating in the formulation of the widely-acclaimed *Broido-Shafizadeh* model (summarised in Figure 4.12).[29–31] The authors of the model coined the phrase "active cellulose" as a somewhat pragmatic term to describe the saccharide matrix following a set of unspecified and unconfirmed depolymerisation reactions and inter/intra-molecular rearrangements. To-date the nature (or even existence) of active cellulose is still one of the most hotly contested questions within the field of analytical pyrolysis.[12,29,32–34]

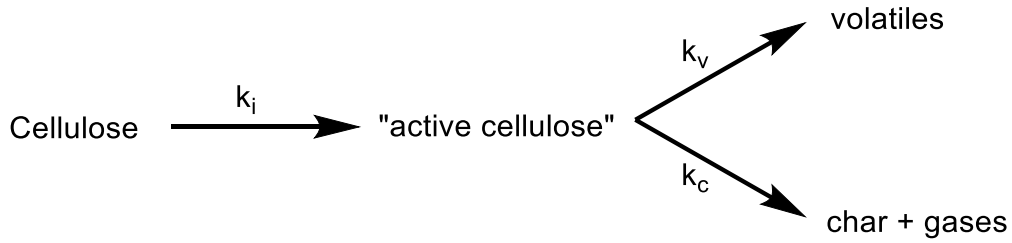

Figure 4.12 The *Broido-Shafizadeh* model of cellulose pyrolysis[29–31]

Whilst the intermediate(s) of cellulose pyrolysis (including active cellulose) remain to be clarified, the final product distribution is much better documented. Allowing for variations between sample condition and experimental configurations, investigations typically report cellulose pyrolysates to comprise: 60 wt.% 1,6-anhydro-*β*-D-glucopyranose (levoglucosan, LG, depicted in Figure 4.13), 10 – 20 wt.% small oxygenates,[*] 5 – 10 wt.% pyrans and furans,[†] 10 wt.% CO_2 and CO, and 10 wt.% char.[2,5,11,28] There is clear distinction between the product array for cellulose and those for glucose reported in Section 4.3.2.2, with the overwhelming selectivity towards LG formation from the polymer being the most readily recognisable. Mettler *et al.*[5] (amongst others)[35,36] have performed experiments on cellulose samples of varying DP to explore the connection between the monomeric and polymeric forms of glucose. The authors concluded that the inability of the latter to access an open chain configuration (owing to the glycosidic linkages) inhibits the formation of the wider distribution of compounds produced by the monomer. The exact mechanism of glycosidic cleavage and LG formation has, however been the principle subject of a good many papers.[10,12,13,28,32,37–42] The potential pathways (as summarised in Figure 4.14) are: heterolytic glycosidic bond scission (ionic pathway), homolytic glycosidic bond cleavage (radical pathway), simultaneous cleavage/LG formation (concerted mechanism), and cleavage by adventitious water (hydrolysis).[39] Many authors tend to conclude that the concerted route is the most likely origin of LG,[12,38,40] and Mettler *et al.* have argued that homolytic glycosidic bond fission is responsible for the formation of furanic molecules (such as hydroxymethylfuraldehyde, HMF).[40] Furthermore, within this paradigm of cellulose

[*] Including pyruvaldehyde, glycoaldehyde, and formic acid

[†] Including HMF, 2-furancarboxaldeyde, and 1,5-anhydro-4-deoxy-D-glycero-hex-1-en-3-ulose

decomposition, the smaller oxygenate products are believed to arise from mid-chain fragmentation through, for example, retro-Diels-Alder chemistry (see Figure 4.15 and discussion in Section 4.3.2.2).[2,12]

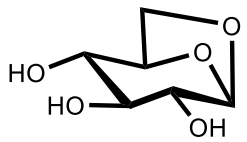

1,6-anhydro-β-D-glucopyranose
(levoglucosan, LG)

Figure 4.13 Levoglucosan (LG); the principle pyrolysis product of cellulose

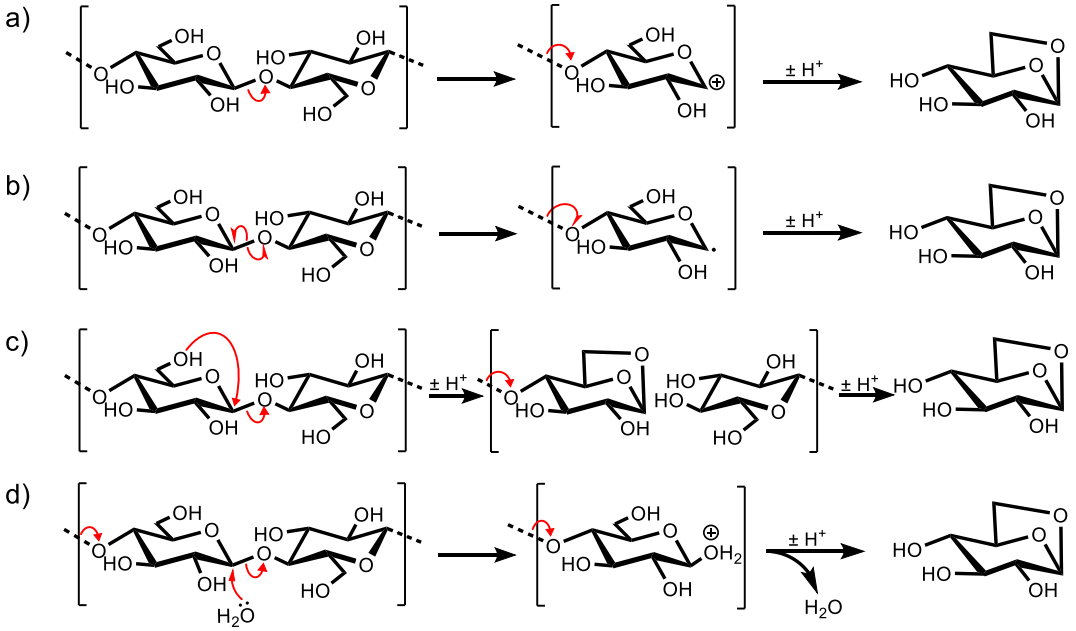

Figure 4.14 Mechanism of LG formation from cellulose *via* a) heterolytic, b) homolytic, c) concerted, and d) hydrolytic glycosidic bond cleavage.[39]

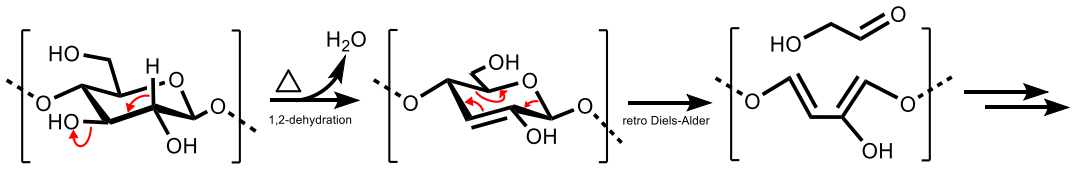

Figure 4.15 Glycoaldehyde formation from cellulose by mid-chain dehydration and retro-Diels-Alder reactions[2,12]

Interestingly, when considering the wider field of polysaccharide pyrolysis, a number of authors have independently concluded that the stereochemistry of glycosidic bonds has a negligible impact on the subsequent thermochemical behaviour of glucans, with α- and β-orientated 1,3-, 1,4-, and 1,6-linkages degrading in a similar fashion.[4,40,43] Far more important than the nature of the glycosidic linkage in dictating thermochemistry, is the substituent on C5. Hence the pyrolysis chemistry of xylan, which may simplistically be considered as the pentose equivalent of cellulose,* features a $-CH_2$ rather than $-CHCH_2OH$ on C5 (see Figure 4.16) and, in further contrast, polyuronides (see Section 4.3.3.3) possess a $-CHCOO^-$ moiety. Such substitutions have profound effects on both the observed thermogravimetric behaviour and the distribution of the pyrolysate of the saccharide. Hence, xylan demonstrates a considerably lower pyrolysis onset temperature (see Figure 4.3), lower yields of anhydrosugars, and much higher production of char, CO_2, and 2-FF than cellulose.[27,44–47]

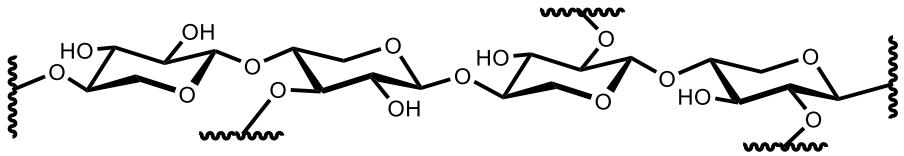

Figure 4.16 Xylan: a xylose-based polysaccharide that can simplistically be considered to be a C5-equivalent of cellulose.

Finally, it is worth considering the multitude of extraneous factors that have been found to influence polysaccharide thermochemistry, beyond the chemical structure of the carbohydrate in question. Primary amongst such parameters is the heating rate of the sample, where slower rates have repeatedly been demonstrated to maximise char yield.[21,28,41,48–51] Similarly, the pyrolysis-product spectrum of a compound can be quite dramatically altered according to the sample dimension.[48] Mettler *et al.* have pioneered the technique of "thin-film" pyrolysis in order to gain a further understanding of the role that mass transport and inhomogeneous heat transfer play in explaining such phenomenon.[48] Furthermore, the effects of endemic moisture within the sample, the swelling of the sample, and the crystallinity of the sample have all (amongst others) been addressed in the literature.[3,6,10,39,52,53] Whilst a discussion of all such effects is not required here, it is worth noting that one of the most drastically influential additional factors on pyrolysis is the presence of metal ions, which is considered in detail in the following section.

4.3.2.4 The role of metal ions in the pyrolysis of saccharides

The presence of even small (<< 1 wt.%) quantities of inorganic material in a sample of carbohydrate (be it impurity or additive) can have dramatic implications for subsequent thermochemical behaviour, far outweighing stereochemical differences between the saccharides.[43] The varied effect(s) of metal ions have been demonstrated by a multitude of authors, and the desire to obtain a more detailed understanding of these phenomena has

* In fact, xylan (which is a principal constituent of hardwood hemicellulose) comprises 1,4-linked β-D-xylopyranose with occasional branched units of 4-O-methyl-α-D-glucuronic acid, α-D-glucuronic acid, and α-L-arabinofuranose.[27]

become a key question in the field of thermochemistry in recent years (featuring prominently in the list comprised by Mettler *et al.* of the top ten fundamental challenges facing pyrolysis research).[21] Majoritively, the impetus for pursuing this topic has been to determine whether removing metal ions from carbohydrate-rich biomass (demineralising) prior to pyrolysis is of overall benefit to thermal processing,[54,55] though some investigators have also been motivated by the notion of purposefully doping in non-native metal ions (impregnation) in order to enhance certain thermolytic behaviours (a topic explored in the context of macroalgae in Chapter 5, and more generally in Appendix P).[56,57]

The binding between neutral carbohydrates and coordinated cations (discussed extensively in Chapter 3) is typically very weak, which initially led authors to presume that, during pyrolysis, the predominant role of the metal ions is to catalyse secondary reactions between the evolving products.[27] However, distinctive artefacts in the thermogravimetric traces of, for example, metal-bound cellulose are a clear indication that such coordination can also drastically influence the primary degradation of the carbohydrate.[4,56–58] Deconvoluting the influence of metal ions on primary and secondary thermochemical mechanisms remains as a key challenge within this area (see Figure 4.17).

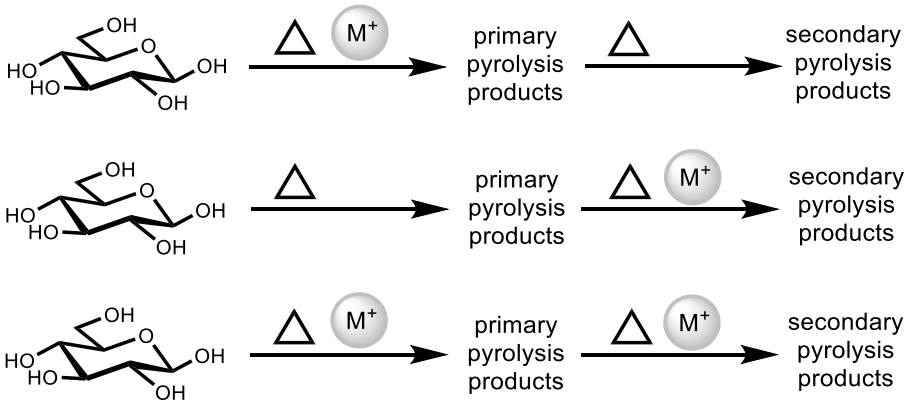

Figure 4.17 The stages at which metal ions may influence pyrolysis product formation

Unsurprisingly, cellulose and glucose have been the protagonists in the majority of investigations seeking to understand the influence of metal ions in the pyrolysis of (respectively) poly- and mono-saccharides, and so make for excellent case studies. In this regard, alkali and alkali-earth metals, whilst not drastically altering either the pyrolysis onset temperature or the identity of the reaction products from cellulose, do significantly perturb the relative distributions of formed compounds.[58] Hence, the presence of s-block cations have been demonstrated to invoke a three-fold reduction in cellulosic LG yield,[27] and five-fold increase in the residual char.[56] Indeed, an increase in the formation of smaller molecules and char at the expense of anhydrosugars is characteristic of the action of metal ions in the pyrolysis of all glucan-based mono- and polysaccharides.[27,54–64] Furthermore, though much less well-studied, the presence of metal ions have been reported to have similar effects on the thermochemistry of xylans, with Mg^{2+} and Ca^{2+} promoting dehydration reactions that ultimately result in a three-fold increase in char and five-fold increase in 2-furaldehyde.[45,59]

The observed changes in thermochemical behaviour of a saccharide instigated by the coordination of metal ions naturally begs questions of the underlying mechanisms. Here, the group of Linda Broadbelt have used an impressive array of analytical, theoretical, and microkinetic methods to probe the multifarious thermolytic pathways encountered in a model Na^+-glucose system.[61–63,65] Their work has revealed that of the reactions depicted in Figure 4.7 (and many more besides) Na^+ catalyses around 70 %, inhibits 25 %, and has no effect on the remainder. As cations were already known to catalyse ring-opening reactions,[66] Broadbelt et al. were somewhat surprised to note that in-fact the rate of the LG formation mechanism was accelerated to a much higher degree (over 50 times compared to the metal free scenario) in a manner seemingly inconsistent with the measured decrease in yield of this product.[10,61] The authors were able to rationalise the observation, however, by noting that the Lewis acidic Na^+ significantly promoted dehydration reactions (see Figure 4.18), which compete with LG formation to yield unsaturated bonds that ultimately form char and/or furanic species.[17,59,67]

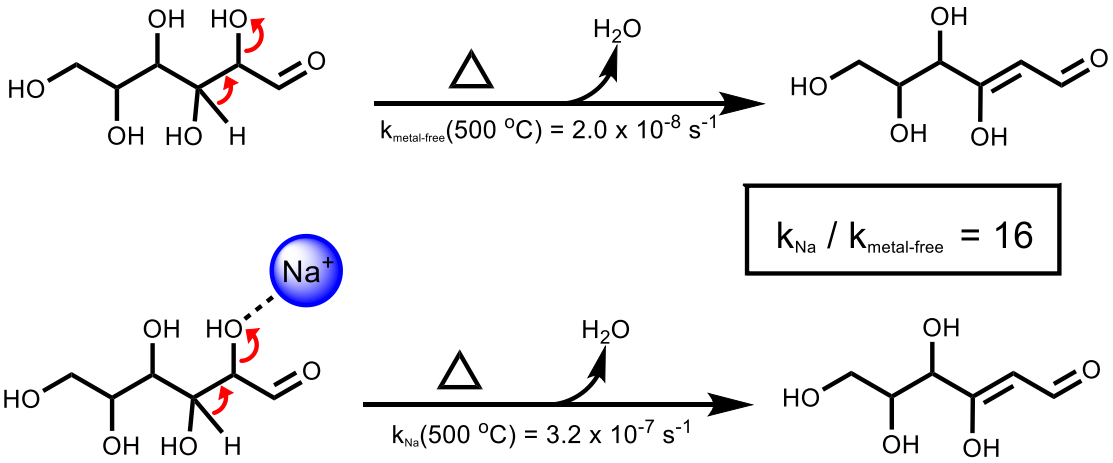

Figure 4.18 The increase in rate of pyrolytic 1,2-dehydration reactions in open-chain glucose upon the addition of a Na^+ ion.[61]

Being less abundant within biomass, d-block metals have not received the same level of scrutiny with regards to their influence on saccharide pyrolysis behaviour as have their counterparts in the s-block, resulting in a more fragmentary understanding. Zn^{2+}, Ni^{2+}, Fe^{3+}, and Co^{2+} have all been shown to increase char yields in cellulose pyrolysis, but such effects are heavily dominant on the initial loading of the metal into the saccharide sample.[56,57,64,68] Ni^{2+} and Cu^{2+} have been cited as predominantly influencing secondary reaction mechanisms with,[59] for example, the decrease in LG yield from Cu^{2+}-impregnated cellulose (which was far smaller than the equivalent decrease by the action of an s-block metal)[60] has been attributed to an accelerated decomposition of LG to levoglucosenone (see Figure 4.19).[68] Such behaviour is quite contrary to the action of Ni^{2+} on xylan, where catalysis of primary degradation mechanisms such as depolymerisation and dehydration reactions were reported to increase the 2-furaldehyde yield by a factor of almost 50.[57,59] Such complexity,

depending on both the identity of the saccharide and the metal, currently prevents any universal conclusions from being made on the role of d-block elements in carbohydrate thermolysis.

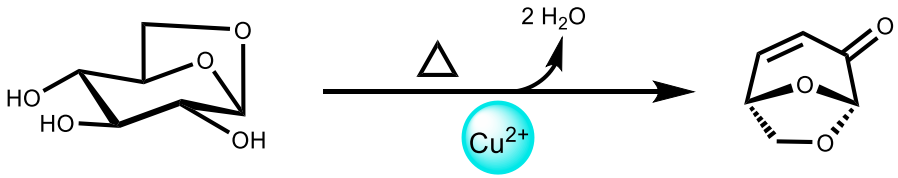

Figure 4.19 Cu(II)-catalysed conversion of LG to levoglucosenone[68]

In summary, therefore, metal ions can be seen to have both extensive and varied consequences on the pyrolysis of neutral saccharides. These effects, have been found to be replicated in studies of biomass containing both the carbohydrate and metal-ions in question (see mini-review in Appendix P). The following section explores the pyrolysis of uronides (a historically overlooked topic) both under metal-free, and metal-bound states. The discussions in the preceding sections on neutral carbohydrates will serve as a useful point of comparison to support the discussions.

4.3.3 Background to the pyrolysis of uronides

4.3.3.1 An introduction to uronide thermochemistry

Uronide thermochemistry has not been afforded the same level of scrutiny that have glucose-based carbohydrates, particularly with regards to a rigorous analysis of the pyrolysis product slate. The perceived niche appeal of uronide-based biomass (such as macroalgae) for thermochemical applications is almost certainly the root cause for the lack of development in this field, and the greatest drivers for research until now have predominantly arisen from the tobacco industry.[50,69–72*] In the context of pyrolysis for biofuels, interest in uronides has centred around the notable (if minor) role of the decarboxylation of D-glucuronic acid branches on the *β*-D-xylopyranose backbone of xylan (a principle constituent of hemicellulose), which is often cited as being the first step in the degradation of lignocellulosic feedstocks (see Figure 4.20).[8,27,45,47,73,74] This decarboxylation is said to account for the very low onset temperature (see Figure 4.3) and early exothermicity exhibited by xylan-rich hemicellulose.[74] Despite widespread interest, very little research has been undertaken to probe the thermal behaviour of biomass in which uronides form the principle constituent(s), and where such low temperature phenomena as observed in xylan might be expected to dominate the course of pyrolysis, accompanied by the rapid release of CO_2.

*The tobacco industry has long been interested in the thermal degradation of pectinous material, though associated studies are often conducted under necessarily esoteric conditions (typically a puffing, oxidative atmosphere), which are of little relevance to the anaerobic environment encountered in the pyrolysis of biomass.

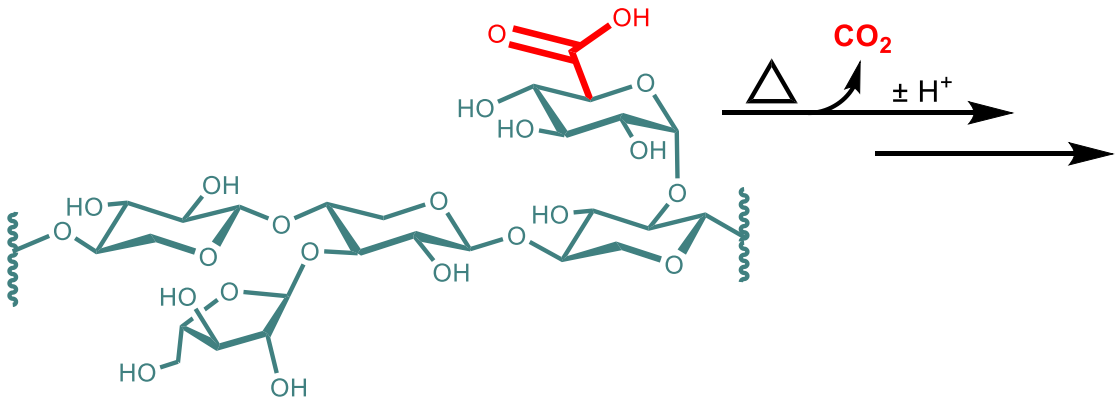

Figure 4.20 Decarboxylation of branched glucuronide units is believed to be the first step in the pyrolysis of xylan-based hemicellulose and, hence, woods.[45]

The notion that decarboxylation is the initial step in anhydrous uronide pyrolysis was first proposed by Arthur Perlin, who studied the degradation of a range of mono- and poly-uronic acids and salts at 255 °C under N_2.[75] Perlin's resourceful methodology provided evidence, albeit indirectly, that around 90 mol.% of the CO_2 derived from alginic acid originated from decarboxylation of the initial -COOH moiety. Whilst this hypothesis has remained largely unchallenged since its inception in 1952, recent theoretical work has indicated that other thermally-activated degradation pathways in polyuronides may occur before, or in place of, decarboxylation.[76] Indeed, the mechanism of anhydrous thermal decarboxylation of carboxylate moieties is surprisingly poorly understood and is further confounded by the fact that any thermal behaviour is intrinsically tied to the identity of the bound counteraction (see Appendix Q for a detailed discussion). As such, the presence of metal ions in uronide-rich biomass can have profound implications for pyrolysis, and a systematic appraisal of such phenomena forms the impetus of the work reported in this chapter. Accordingly, the following sections will briefly summarise existing literature concerning the pyrolysis of mono- and poly-uronides, and the role of metal ions in such reactions.

4.3.3.2 The pyrolysis of mono-uronides

It is irrefutable that the thermochemistry of the aldohexuronic acids has been much less well explored than other aldoses, and, where work does exist, it is certainly not in the level of detail of, for example, the microkinetic analyses of Broadbelt *et al.* (discussed in Section 4.3.2).[61–63,65] Indeed, to-date, only two studies concerning Py-GC analysis of any mono-uronic acid have been conducted (both focussing on D-glucuronic acid).[2,25] The results of one of these works (by Moldoveanu) are displayed in Figure 4.21 and depict the yields of various compounds at 900 °C.[2] The differences between Figure 4.21 and the analogous figures for D-glucose and D-xylose (Figure 4.5 and Figure 4.10 respectively) are immediately apparent, with the product slate of D-glucuronic acid being dominated by the formation of a lactone. The ready formation of the lactone (the precise identity of which will be discussed later in this chapter) therefore forms an interesting analogy with the behaviour

exhibited by glucan-based saccharides, which degrade to levoglucosan in high yields (see Sections 4.3.2.2 and 4.3.2.3 and Figure 4.22). The thermal liberation of lactones from other mono-uronic acids is yet to be demonstrated.

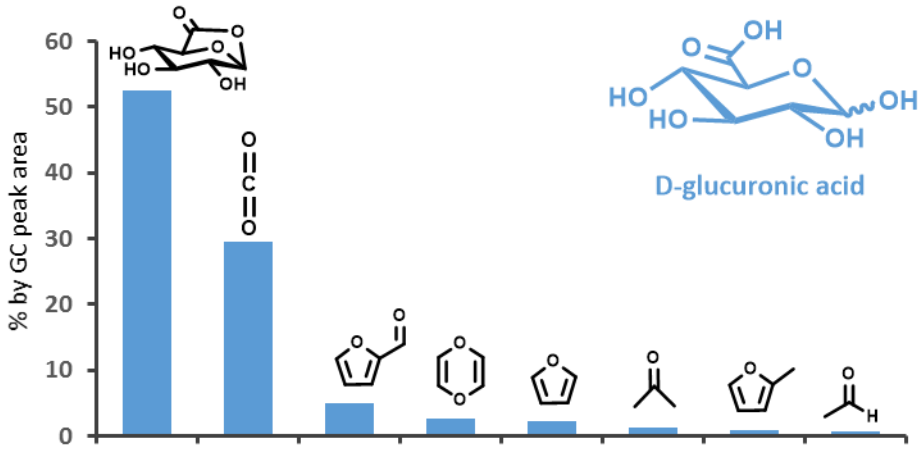

Figure 4.21 The product distribution of the pyrolysis of D-glucuronic acid at 900 °C (data taken from the work of Moldoveanu).[2]

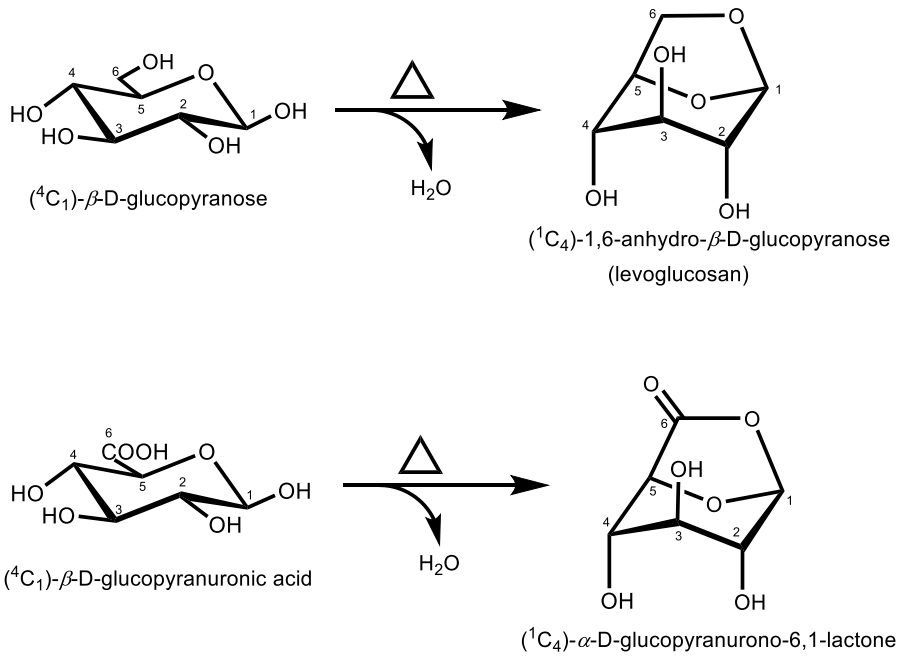

Figure 4.22 Moldoveanu identified a potential parallel between the thermolytic formation of levoglucosan from glucose and of a 6,1-lactone from glucuronic acid.[2]

4.3.3.3 The pyrolysis of polyuronides

Limited work has been carried out to investigate the pyrolysis behaviour of both pectin (derived from citrus peel)[18,76–80] and alginic acid (derived from macroalgae).[18,26,50,81–84] A defining feature of the thermolysis of polyuronic acids is the remarkably low onset temperature, some 150 °C below cellulose for example.[50] Previous studies have also universally identified CO_2 and 2-furfural as the major reaction products in the case of both pectin and alginic acid, but do not offer fully quantitative information regarding the yields of such compounds.[2,18,77–79,82,85,86] It is easy to imagine, therefore, that such polyuronides follow a pyrolysis pathway whereby decarboxylation generates a C5-backbone, which then degrades in a similar fashion to xylan, with the liberation of 2-FF (see Section 4.3.2.3 and Figure 4.23).[26] Certainly, this chapter will attempt to provide further evidence to better assess such a claim. These few results therefore offer promise in terms of the low pyrolysis temperature required to degrade polyuronides and the highly selective product stream. However, previous studies have also demonstrated an extreme sensitivity towards the nature of the carboxylate group, including the degree of esterification,[78,79] and, most notably, the identity of the bound counteraction (discussed in the following Section).

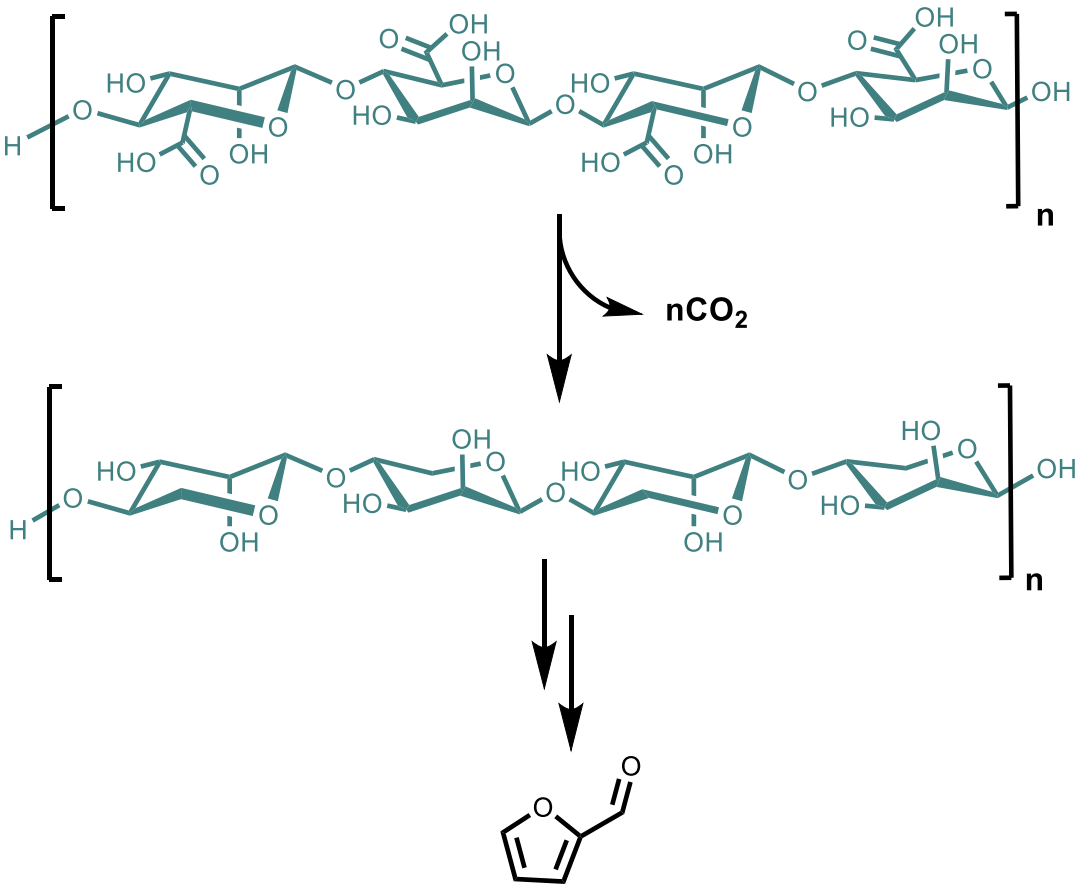

Figure 4.23 A potential route of 2-furaldehyde (2-FF) formation from polyuronides *via* the decarboxylative formation of a polypentose.

4.3.3.4 The role of metal ions in the pyrolysis of uronides

In Section 4.3.2.4, the dramatic impact of small quantities of metal ions on the pyrolysis of neutral mono- and poly-saccharides was discussed. Given such remarkable deviations from the natural course of pyrolysis in carbohydrates, even with very small metal loadings, it is worth considering the case of uronate salts, for which a (typically metal) countercation is necessarily present in stoichiometric quantities. Accordingly, investigators have devoted effort to elucidating the role of cations in the pyrolysis of uronides (especially alginates), covering metals from across the periodic table including: Na,[72,75,82,83,87–91]Ca,[82,92] Ba,[75,86,93] Al,[94] Cu,[86,90] Zn,[86,91,95,96] Mn,[88] Co,[88] Ni,[90] and Fe,[89] amongst others.[97–100] Over the course of the preparation of this thesis, the groups of Xia[86,92,96] and Liu[88–91,93–95] have been particularly productive in terms of their investigations of the pyrolysis behaviour of metal alginates with a view, in their case, to developing flame retardant fibres. However, whilst the output of these groups has been plentiful, their studies are somewhat deficient in areas such as the characterisation of starting materials, quantitative analyses of the product streams, and rigorous control of variables. Indeed, across the field, the level of detail in published data is far below the level of detail and rigour that can be found in the studies of glucan-based carbohydrates discussed in Section 4.3.2. Consequently, steadfast conclusions on the role of metal ions in the thermal degradation of mono- or poly-uronides are difficult to draw at this stage. Certainly, s-block ions (namely Na^+) have been demonstrated to strongly inhibit the production of 2-FF relative to the H^+ form,[72,82] seemingly in contrast to their d-block counterparts (though a current lack of fully quantitative date makes such a comparison difficult).[86,88–96] Furthermore, Na^+ and Ca^{2+} have been observed to retard uronide thermolysis behaviour and promote char formation,[72,82,83] whilst the equivalent influence of d-block metals is much less reported. Hence, there are a good many question still to be answered on the role of metal ions in uronide pyrolysis before the rich-mechanistic insight discerned in recent years for glucose and glucan-based saccharides can be realised. Working towards a detailed model of metal-mediated uronide pyrolysis is, however, vital if the thermal upgrading of uronide-rich biomass (including macroalgae) is to be truly understood and optimised.

4.4 Summary of current knowledge and chapter aims

Whilst carbohydrate pyrolysis may at first appear a daunting subject matter, researchers have come a long way in defining the myriad of thermally activated degradative pathways pursued by glucan-based saccharides. The same cannot be said of uronides however, where even a mass balance of pyrolysis products is a long way from being realised. To complicate matters, the thermochemistry of uronides is intrinsically linked to the identity of the countercation, multiplying the levels of complexity manifold. Whilst efforts have been made to start to interrogate such chemistry, experiments have tended to be both sporadic in their choice of parameters and phenomenological in their analyses, giving rise to a demand for a more systematic approach.

The importance of garnering an understanding of metal-mediated pyrolysis is especially pertinent given recent interest in the thermochemical conversion of macroalgae biomass to fuels and chemicals. As has been highlighted elsewhere in this thesis, brown seaweeds

are rich in both alginate and metal ions and, hence, the thermochemical implications of combining these two constituents is of great importance. Given the ultimate ambition of this thesis in advancing the development of the thermal utilisation of kelp, the present chapter will particularly focus on alginic acid and its associated salts. Accordingly, the specific aims of the following work are:

- To conduct a systematic and self-consistent evaluation of the role of metal ions in the pyrolysis of alginates, both in terms of their kinetic effect and influence on the product distribution.
- To probe the underlying mechanisms of uronide pyrolysis, especially the role that decarboxylation and lactone-formation play in dictating the product spectrum
- To offer a critical appraisal of the degree to which metal ions help or hinder pyrolysis from the point view of the thermochemical upgrading of uronide-rich biomass.

Naturally, in pursuing these questions, it will be necessary to draw upon the findings of Chapters 2 and 3, particularly with regards to the metal-binding, anomerisation, and lactonisation behaviour of mono-uronates. Unfortunately, the absence of well-defined solid samples of algal mono-uronic acids (or salts thereof) renders thermochemical investigation of these compounds impossible for the time being. As such, two commercially available mono-uronates (D-galacturonic and D-glucuronic acids) can be used as the most closely-related alternatives. Finally, whilst experimental work will focus predominantly on alginates, the pyrolysis of pectin (and related pectinates) will also be considered in order to gauge the wider applicability of the elucidated conclusions.

4.5 Results

4.5.1 General comments on the experimental strategy employed in the thermal analysis of alginates and related uronides

The complexity of the pyrolysis process of carbohydrates requires for several analytical techniques to be employed in tandem, each targeted at different observable thermochemical traits. It is strongly advised that Appendix L be consulted for an in-depth introduction to such techniques, and the more subtle aspects of their operation and interpretation. The most common thermoanalytical tool, thermogravimetric analysis (TGA) was used in almost all of the cases described below, and provides information on the kinetics of the pyrolysis process by following the sample mass with temperature. Several on-line analyses can be employed to monitor the volatilised material (including TGA-mass spectrometry (TGA-MS)) and off-line analyses of the remaining char (powder X-ray diffraction (PXRD) and Fourier transform infra-red spectroscopy (FTIR)). Beyond TGA, micropyrolysis coupled to gas chromatography-mass spectrometry (Py-GCMS) was invaluable to the work in this chapter. Py-GCMS facilitates access to much higher heating rates than conventional thermogravimetric apparatus as well as unprecedented levels of insight into the myriad of small organic compounds liberated during thermolysis. For the purpose of this thesis, great efforts were made in order to quantify product yields where

possible, which required for both careful characterisation of the starting materials and calibration of the analytical equipment. Such an approach is far from commonplace within thermoanalytical studies, and Appendix L should again be consulted for more in-depth discussion of the requisite method development. Naturally, owing to restrictions of both time and equipment, not all techniques could be employed in all cases, and samples were selected based upon their displaying of contrasting or interesting thermal behaviour.

In the following discussions alginic acid is abbreviated to **HAlg** and corresponding alginate salts to **MAlg** (where M is the identity of the metal in question). Similarly, D-galacturonic acid and galacturonate salts are referred to as either **HGal** or **MGal**, and D-glucuronic acid and glucuronate salts as **HGlc** and **MGlc**. Finally, pectin (as a polymer of principally D-galacturonic acid units) is abbreviated to **HPec** and pectinate salts as **MPec**. The structures of the **HAlg**, **HPec**, **HGal** and **HGlc** used in the experiments are depicted in Figure 4.24 for reference.

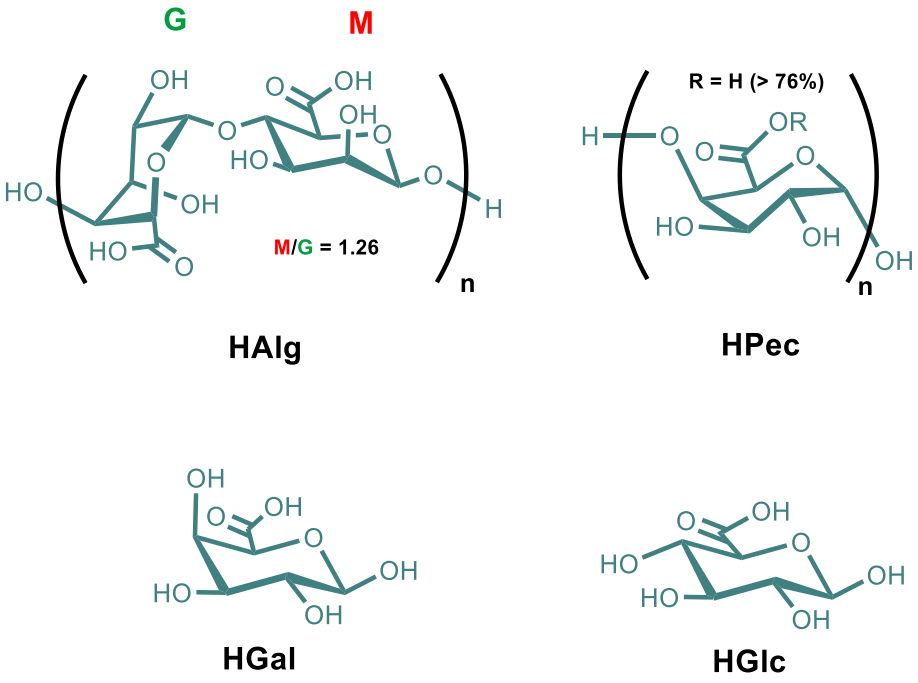

Figure 4.24 Structures of the polyuronides (alginic acid (**HAlg**) and pectin (**HPec**) and mono-uronides (galacturonic acid (**HGal**) and glucuronic acid (**HGlc**)) used in the thermochemical experiments detailed below.

4.5.2 Compositional- and thermal-analysis of alginic acid and alginate salts

4.5.2.1 Characterisation of alginic acid and alginate salts

The composition of commercial **NaAlg** along with the alginic acid and other alginate species derived from it were determined by a combination of combustion (CHN) and inductively coupled plasma-mass spectrometric (ICP-MS) analyses. The absorbed moisture within the samples (established from TGA) was also accounted for, thereby yielding an accurate formula unit for each compound (reported in Table 4.1) from which a molecular weight

could be calculated. The mannuronate:guluronate (**M**:**G**) ratio of the polymer was established to be 1.26 ± 0.02, and additional detail regarding its composition is reported in Appendix J. The solid-state Fourier transform infra-red (FTIR) spectra of the alginates were found to be in accordance with those reported in the literature.[101,102] The wavenumbers of diagnostic vibrational modes for each alginate are reported in Table 4.1 and the full spectra provided in Appendix G.

Table 4.1 Results from the solid-state characterisation of alginic acid and alginates by FTIR

Cation	Calculated formula	Characteristic vibrational frequencies (cm^{-1})			
		ν(OH)	$\nu(COO)_{asym}$	$\nu(COO)_{sym}$	ν(C-O)
H^+	$C_6H_8O_6.(0.7\ H_2O)$	3385	1723	1637	1028
Na^+	$C_6H_7O_6Na.(1.5\ H_2O)$	3254	1597	1408	1025
Mg^{2+}	$C_6H_7O_6Mg_{0.5}.(2.6\ H_2O)$	3283	1600	1419	1036
Ca^{2+}	$C_6H_7O_6Ca_{0.5}.(1.7\ H_2O)$	3218	1589	1412	1025
Sr^{2+}	$C_6H_7O_6Sr_{0.5}.(2.6\ H_2O)$	3218	1589	1408	1025
Ba^{2+}	$C_6H_7O_6Ba_{0.5}.(1.1\ H_2O)$	3229	1582	1408	1028
Co^{2+}	$C_6H_7O_6Co_{0.5}.(1.7\ H_2O)$	3216	1582	1460	1027
Ni^{2+}	$C_6H_7O_6Ni_{0.5}.(1.8\ H_2O)$	3237	1585	1411	1024
Cu^{2+}	$C_6H_7O_6Cu_{0.5}.(1.4\ H_2O)$	3249	1588	1399	1030
Zn^{2+}	$C_6H_7O_6Zn_{0.5}.(1.8\ H_2O)$	3238	1592	1410	1026

4.5.2.2 TGA analysis of alginic acid and metal alginate salts

Dynamic thermogravimetric analysis (TGA) was conducted on samples of the metal alginates under a flow of He and at a heating rate of 10 °C min^{-1}. After correcting for initial moisture content and smoothing the data as per the methods outlined in Appendix L, the TGA and corresponding derivative-TGA (DTG) traces were plotted (shown for **HAlg**, **NaAlg**, **CaAlg** and **Cu(II)Alg** in Figure 4.25) and characteristic thermal parameters were assigned for each (see Table 4.2 and explanations below). All alginates were found to follow three broadly-defined degradation regimes, which are generically recognised in the thermolysis of most organic polymers:

I. **Drying (*T* = Ambient → *T* ≈ 110 °C)**
   The hygroscopic alginate polymers typically contain 5 – 20 wt.% loosely bound water molecules (*moisture*), which is readily desorbed upon heating above ambient temperature. This stage is not discussed in the results as an isothermal drying period was added to the start of the TGA run to drive off the water and correct the starting masses to a moisture-free value (see further explanation in Appendix L).

II. Rapid pyrolysis (T ≈ 150 - 210 °C → T ≈ 270 - 450 °C)

From about 150 – 210 °C (depending on the heating rate and sample in question) the alginates undergo rapid pyrolysis, in which up to 60 wt.% of the starting mass is volatilised over a very narrow thermal window. The term T_i is used to refer to the temperature of initiation of rapid pyrolysis and T_f to refer to the final temperature. Other important metrics include $\Delta M(T_i - T_f)$, which is the mass loss across the period of rapid pyrolysis, and T_{max1} and T_{max2}, which signify temperatures of maximal mass loss rate (in turn denoted Rate[T_{max1}] and Rate[T_{max2}]). For consistency, each of the thermal parameters have rigorous definitions, elaborated in Appendix L. The rapid pyrolysis stage will be the focal point of the discussions in Section 4.6.

III. Secondary degradation (T > 450 °C)

A region of much slower mass loss following rapid pyrolysis in which slow, secondary degradations and the char structure evolves (see Section 4.5.2.5). Less attention is devoted to this region in the following discussions.

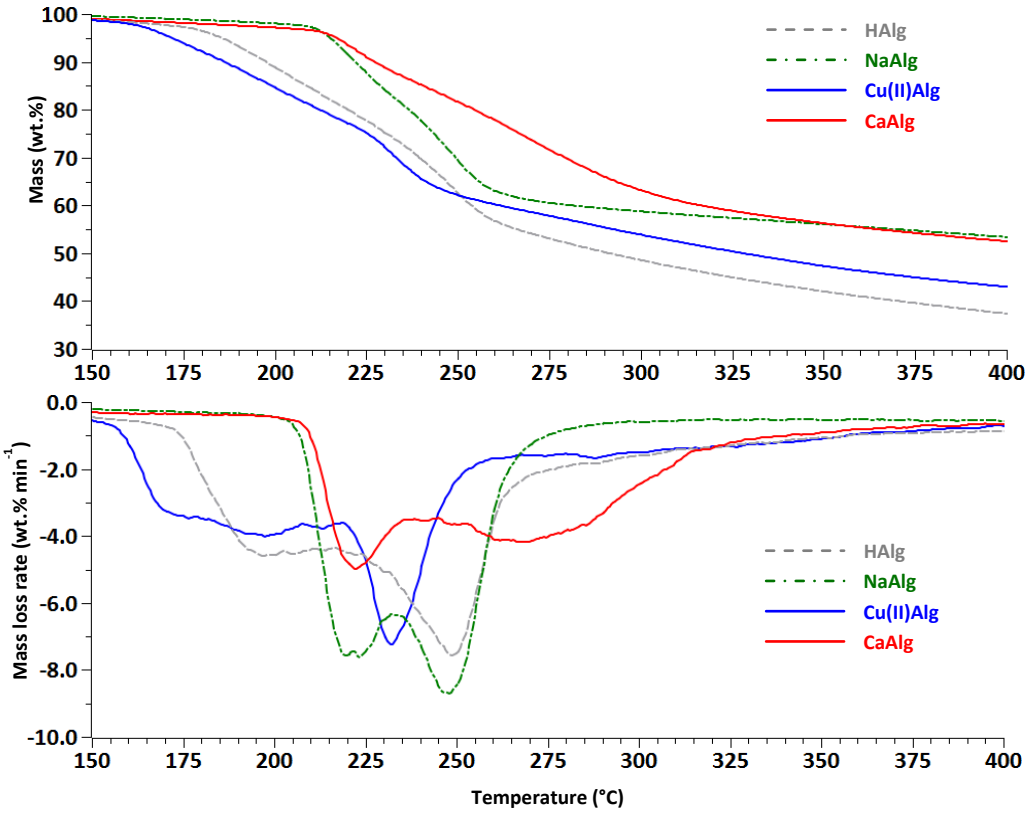

Figure 4.25 TGA (top) and DTG (bottom) plots of the period of rapid pyrolysis of **H-**, **Na-**, **Cu(II)-** and **Ca-Alg** when heated at 10 °C min^{-1} under He.

In addition to the thermal events described in Table 4.2, the alkali earth metal alginates all show thermogravimetric events between 450 – 550 °C, though with mass loss rates of 0.6 – 0.8 wt.% min^{-1} they are not classed as being *rapid* pyrolysis. Despite such events being relatively slow, they are important in determining the composition of the char (see Section 4.5.2.5). Finally, it is worth highlighting that the period of rapid pyrolysis for Na^+ is so fast and narrow that the T_{max} events can sometimes be seen to coalesce into a single peak, accompanied by an extreme intumescence (see Section 4.5.2.5).

Table 4.2 Characteristic thermal parameters in the rapid pyrolysis of alginic acid and associated alginates (heated at 10 °C min^{-1} under He).

Cation	T_i (°C)	T_f (°C)	$\Delta M(T_i - T_f)$ (wt.%)	T_{max1} (°C)	Rate[T_{max1}] (wt.% min^{-1})	T_{max2} (°C)	Rate[T_{max2}] (wt.% min^{-1})
H^+	173 ± 3	357 ± 5	56 ± 1	195 ± 3	-4.8 ± 0.5	249 ± 3	-7.4 ± 0.5
Na^+	206 ± 3	274 ± 5	39 ± 3	218 ± 4	-8.3 ± 1.0	245 ± 5	-9.1 ± 0.5
Mg^{2+}	200 ± 3	369 ± 14	48 ± 4	249 ± 3	-5.4 ± 0.5	-	-
Ca^{2+}	211 ± 3	340 ± 5	39 ± 1	222 ± 3	-4.8 ± 0.5	269 ± 3	-4.3 ± 0.5
Sr^{2+}	212 ± 3	323 ± 5	34 ± 1	222 ± 3	-5.1 ± 0.5	267 ± 4	-3.8 ± 0.5
Ba^{2+}	212 ± 3	311 ± 5	30 ± 1	221 ± 3	-4.1 ± 0.5	259 ± 3	-4.1 ± 0.5
Co^{2+}	198 ± 3	361 ± 5	41 ± 1	214 ± 3	-4.0 ± 0.5	451 ± 3[a]	-1.8 ± 0.5[a]
Ni^{2+}	203 ± 3	452 ± 5	59 ± 1	246 ± 3	-4.0 ± 0.5	389 ± 3	-2.3 ± 0.5
Cu^{2+}	164 ± 5	360 ± 8	51 ± 1	200 ± 4	-3.9 ± 0.5	237 ± 6	-7.1 ± 0.5
Zn^{2+}	195 ± 3	360 ± 6	40 ± 2	209 ± 3	-3.8 ± 0.5	421 ± 3[b]	-1.3 ± 0.5[b]

[a] T_{max2} for Co(II)-alginate occurs during a secondary period of rapid pyrolysis from 375 ± 3 to 485 ± 6 °C, after which stage the mass lost since the initiation of rapid pyrolysis is 56 ± 2 wt.%.

[b] T_{max2} for Zn(II)-alginate occurs during a secondary period of rapid pyrolysis from 368 ± 3 to 458 ± 3 °C, after which stage the mass lost since the initiation of rapid pyrolysis is 51 ± 1 wt.%.

4.5.2.3 TGA-kinetic analysis of alginic acid and Cu(II)-alginate

By performing the dynamic TGA experiment of the type described in Section 4.5.2.2 over a range of heating rates, a lumped kinetic model may be applied in order to discern the Arrhenius parameters for the rapid pyrolysis of the alginates. This approach was the subject of a publication prepared in the exploratory phases of this thesis. The key results are reproduced in Table 4.3, but Appendix T (containing a reprint of the original manuscript) should be consulted for a full discussion.

Table 4.3 A summary of kinetic parameters calculated for **HAlg** and **Cu(II)Alg** under rapid pyrolysis conditions (taken from the paper presented in Appendix T)

Sample	T_{max1}		T_{max2}	
	lnA	E_A (kJ mol^{-1})	*lnA*	E_A (kJ mol^{-1})
Alginic acid	36 ± 4	174 ± 10	55 ± 5	269 ± 20
Cu(II)-alginate	24 ± 3	123 ± 8	52 ± 5	248 ± 20

4.5.2.4 TGA-MS analysis of alginic acid and alginate salts

By coupling a mass spectrometer to the TGA apparatus, time-resolved data may be obtained relating to the volatile material evolved from the thermolysis process. In reality, the experimental setup in the present case was mostly restricted to observations of CO_2 and H_2O release. The evolution of CO_2 was found to correspond largely with the key temperatures of fast pyrolysis of the alginate sample, namely the T_i and T_{max} values (see Figure 4.26a). Similarly, H_2O release was found to follow approximately the same pattern as CO_2 (see Figure 4.26b) - though very small traces of water were also found to be liberated at temperatures preceding the onset of rapid pyrolysis. The release of 2-FF could also be observed by monitoring characteristic ions m/z 96 and 95, though the compound was only faintly detectable in the cases of **HAlg** and **Cu(II)Alg**. For **HAlg**, 2-FF was released between 175 – 350 °C, peaking at 250 °C, and for **Cu(II)Alg** between 200 – 350 °C, peaking at 230 °C.

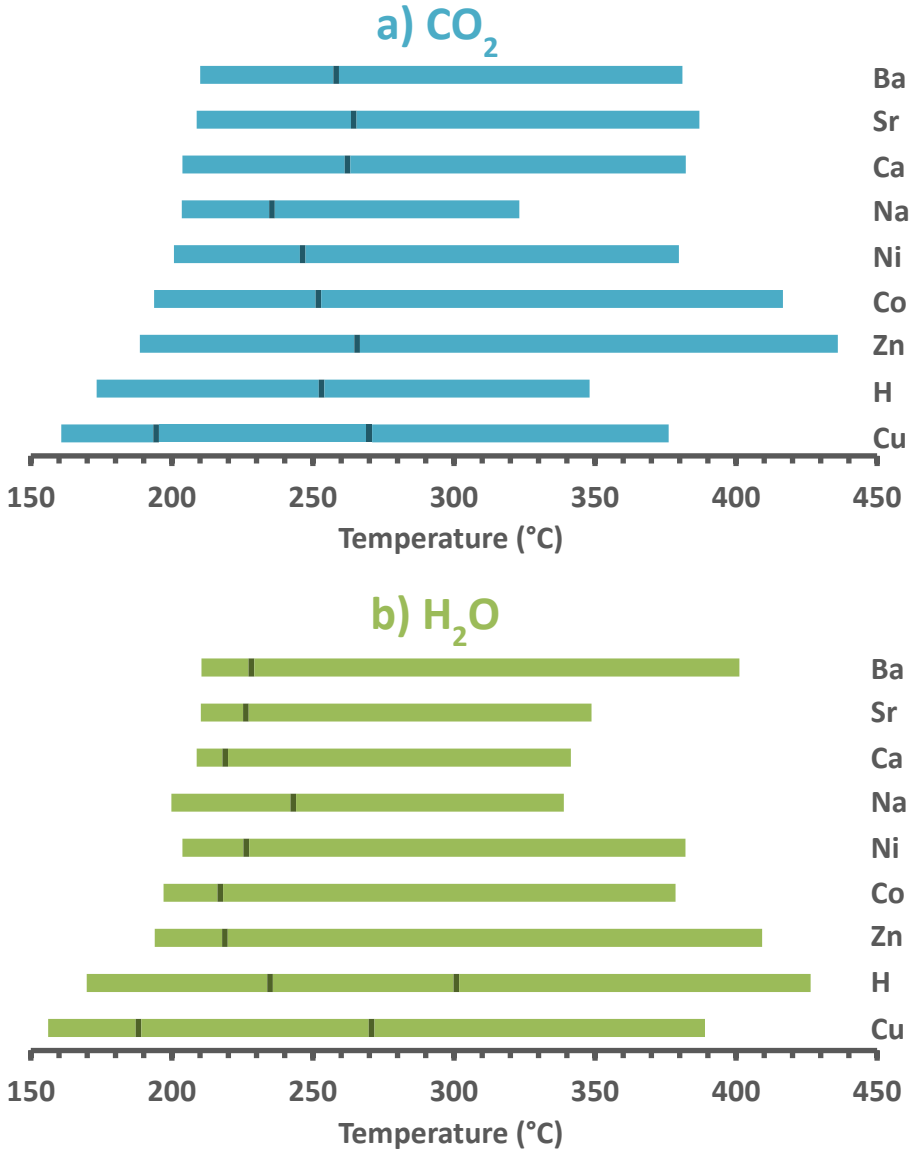

Figure 4.26 Periods of release of (a) CO_2 and (b) H_2O during the rapid pyrolysis of alginic acid and various alginates (determined by TGA-MS). The vertical black mark denotes temperatures at which maximal levels of the gases were generated.

By applying the technique outlined in Appendix L, it was also possible to quantify the water of pyrolysis* from the TGA-MS trace for m/z = 18. At 500 °C, the water of pyrolysis was found to be 24 ± 6 wt.% for **HAlg**, 37 ± 6 wt.% for **NaAlg**, 28 ± 6 wt.% for **CaAlg**, and 32 ± 6 wt.% for **Cu(II)Alg**. These values for the yield of water arising from the pyrolysis of the uronides can subsequently be included attempts to calculate a pyrolysis mass balance (see Section 4.5.2.8).

4.5.2.5 Analysis of alginate by TGA, XRD, and FTIR

The residual solid matter remaining after pyrolysis is known as char (though it is important to also specify the final temperature at which the char has been obtained). Figure 4.27 depicts the moisture corrected wt.% of material remaining following pyrolysis in He up to 500 °C for a range of alginates. Also shown in Figure 4.27 is the yield of "metal-corrected char", which is the remaining weight of material minus the mass of any metal ions in the sample (i.e. the organic fraction of the char).

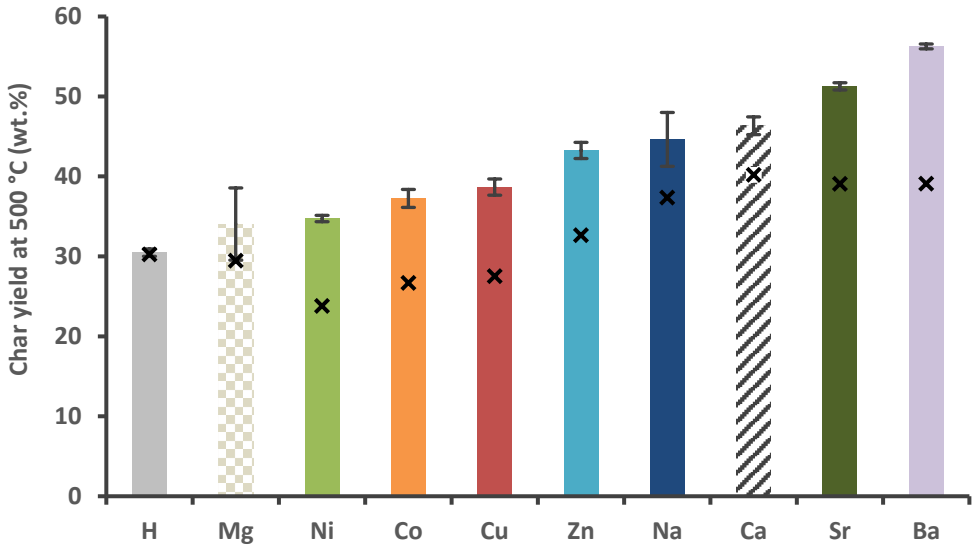

Figure 4.27 The yield of char of various alginates heated to 500 °C at 10 °C min^{-1} under He (calculated on a moisture-free basis). The "**X**" symbol marks the yield of char with the mass of metal known to be in the sample deducted (and hence represents the organic-only fraction of the char).

In order to study the char structure further, **CaAlg** and **Cu(II)Alg** were selected for a series of isothermal experiments. Here, the alginates were ramped (at 10 °C min^{-1}) to a specified temperature (T_{iso}) and held for 60 minutes. The residual solid was then subjected to analysis by both Fourier transform infra-red spectroscopy (FTIR) and powder X-ray diffraction (PXRD). The results of such experiments across a range of values of T_{iso} are displayed in Figure 4.28 and Figure 4.29. The peaks in the PXRD patterns of **Cu(II)Alg** char correspond

* This is the water released from the thermolytic cleavage of C-OH bonds within the alginate polymers, and does not include the moisture initially bound within the sample.

to the formation of Cu^0, whilst in corresponding analysis of **CaAlg** peaks can be seen at 600 °C arising from $CaCO_3$, and at 800 °C from $CaO/Ca(OH)_2$.

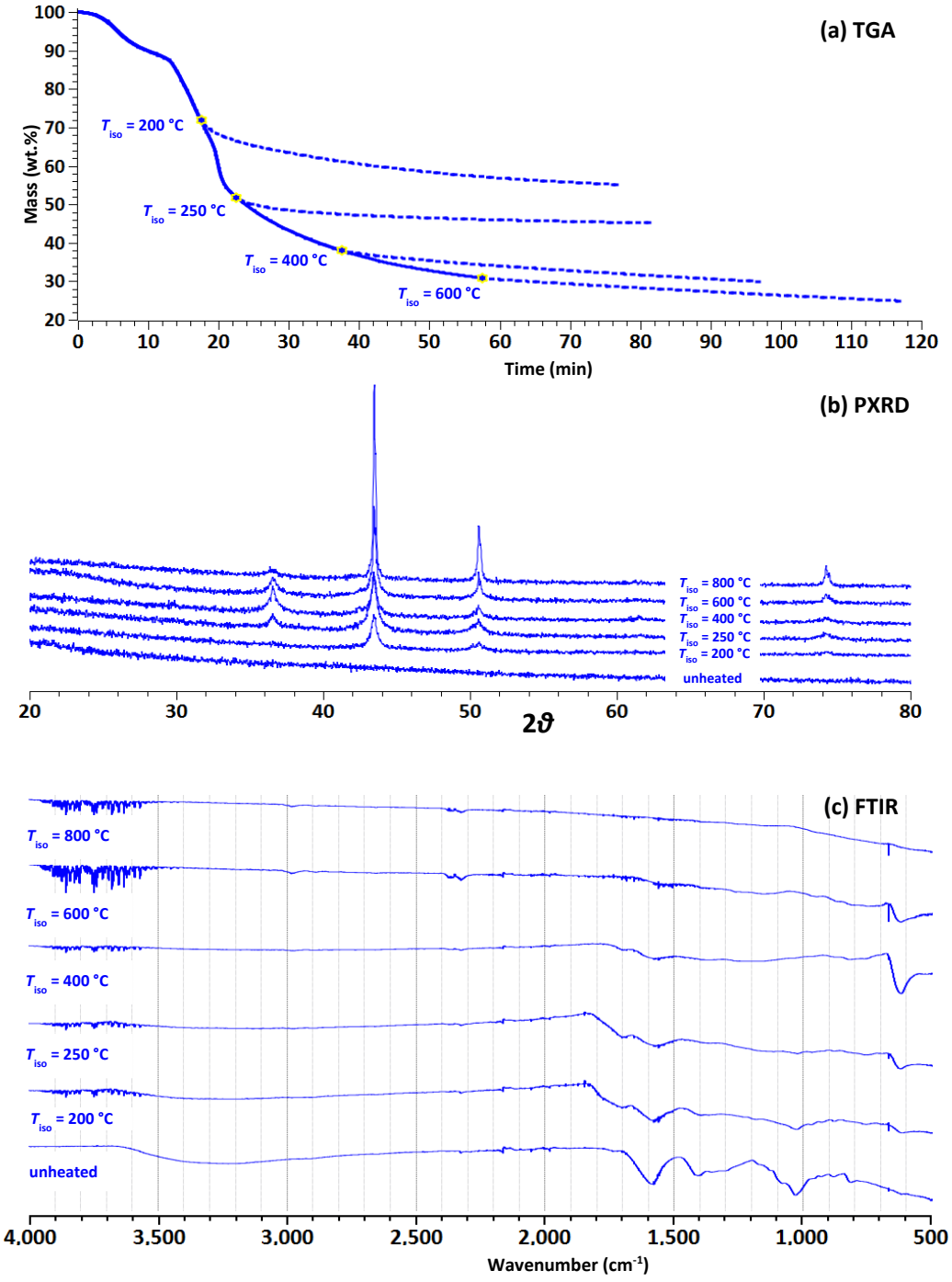

Figure 4.28 Analysis of the char of Cu(II)-alginate subjected to heating for 60 minutes under He at various isothermal temperatures (T_{iso}). (a) TGA (yellow stars mark the start of the isothermal heating at T_{iso}), (b) PXRD analysis of char obtained from heating at T_{iso}, and (c) FTIR analysis of char obtained from heating at T_{iso}.

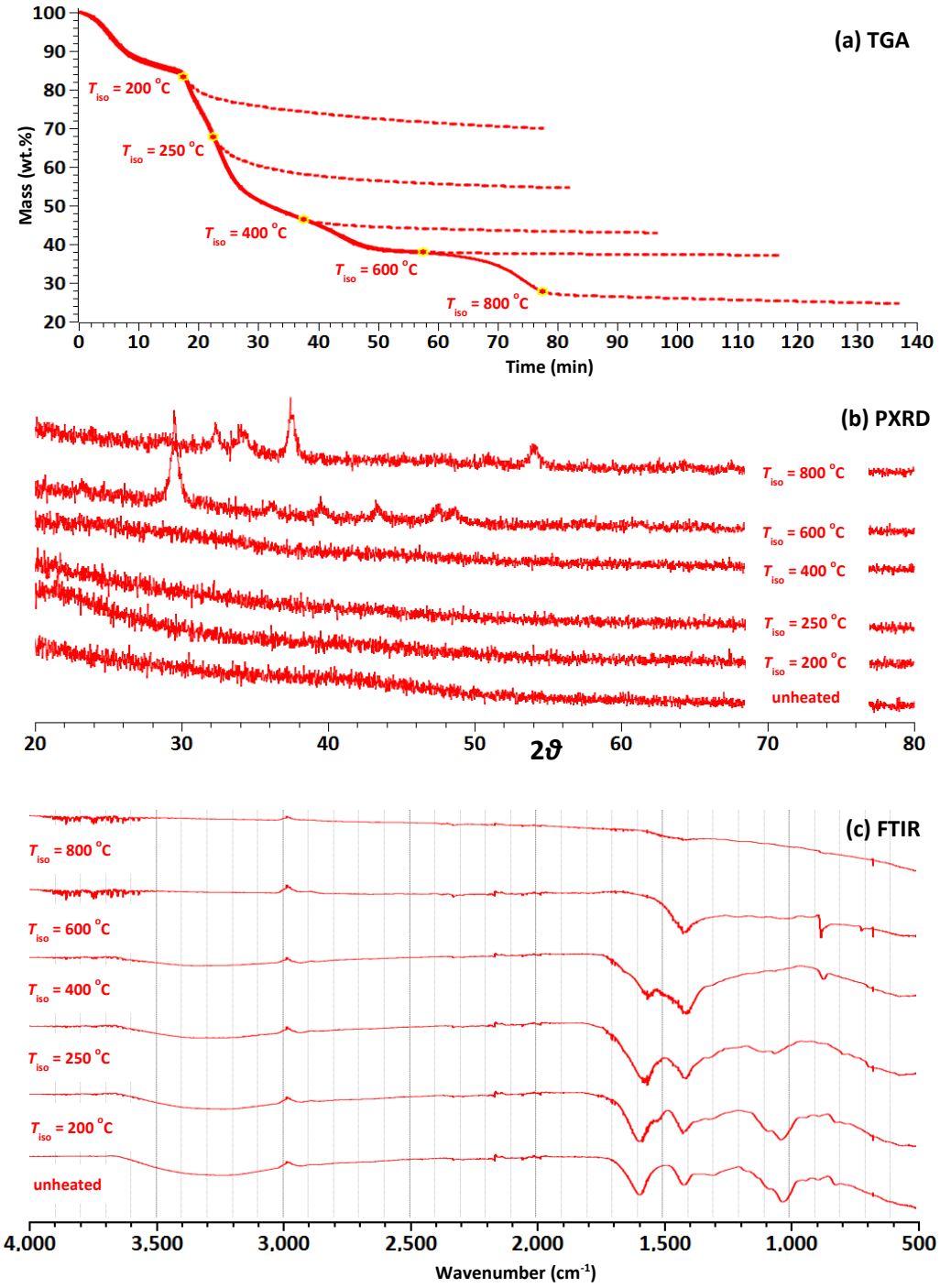

Figure 4.29 Analysis of the char of Ca-alginate subjected to heating for 60 minutes under He at various isothermal temperatures (T_{iso}). (a) TGA (yellow stars mark the start of the isothermal heating at T_{iso}), (b) PXRD analysis of char obtained from heating at T_{iso}, and (c) FTIR analysis of char obtained from heating at T_{iso}.

Char collected after heating **NaAlg** to 900 °C at 10 °C min^{-1} under He was also subjected to analysis by PXRD, which clearly revealed the formation of crystalline Na_2CO_3 in the sample. Preliminary experiments involving the isothermal heating of **NaAlg** at various temperatures (though under an atmosphere of N_2) demonstrated a drastic intumescence.[*] Here, the char was found to swell to many times the original volume at the point of rapid pyrolysis (see Figure 4.30), before collapsing above 600 °C (accompanied by a mass loss step of approximately 15 - 20 wt.%). Na_2CO_3 was not detected prior to the collapse of the expanded char structure. The origins of such swelling of pyrolysed samples of **NaAlg** are considered in Section 4.6.2.2.

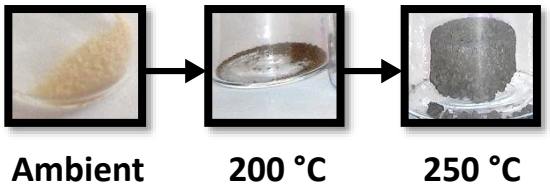

Figure 4.30 Swelling of samples of **NaAlg** observed upon isothermal heating under N_2

Finally, samples of alginic acid and Sr-, Ba-, Mg-, Co(II)-, Zn(II)-, and Ni(II)-alginates were all heated to 900 °C at 10 °C min^{-1} under He, and also analysed by PXRD. Clear peaks corresponding to Ni^0, Co^0, and ZnO were found in the chars of their respective alginates, and preliminary experiments indicated that such species began to form at temperatures between 400 °C – 600 °C. Broad peaks were detected in the X-ray diffraction patterns of Mg-, Sr-, and Ba-alginate chars, but they were not sufficiently well resolved to allow unambiguous assignment. No diffraction peaks were detected in the chars of alginic acid at any temperature.

4.5.2.6 Py-GCMS analysis of alginic acid and alginate salts

By capturing pyrolysate material on a chemical trap and subsequently desorbing this condensate into the injection port of a GCMS, the myriad of volatile organic compounds formed in a pyrolysis reaction can be separated and characterised. Such a procedure is the fundamental premise behind Py-GCMS (explained more fully in Appendix L). For alginates, typically around 40-60 compounds were detected for Py-GCMS analysis at 500 °C for 20 seconds under He (15 mL min^{-1}).[†,‡] The GC peak area of each compound in the chromatogram gives a semi-quantitative indication of the yield, and may be compared to the total peak area to obtain a *selectivity by GC peak area*. In order to simplify the

[*] Indeed, such intumescence was observed in all uronide samples containing Na^+ or K^+ and could, on occasion, be catastrophic. In one such experiment, the swelling of the char was sufficiently forceful so as to push open the furnace chamber, admitting oxygen and igniting the remaining material.

[†] Note that the heating rate in Py-GCMS experiments (typically 1.2×10^6 °C min^{-1}) was far higher than for TGA (typically 10 °C min^{-1}) and so the period required to reach the target temperature is negligible in the former case.

[‡] The reaction was demonstrated to be complete after 20 seconds, with no new compounds being liberated at longer residence times.

interpretation of such vast quantities of data, the compounds were classified and grouped according to classes of common chemical motifs, and the total GC peak area for each class was subsequently calculated (the grouping criteria can be found in Appendix M, and full compound lists for **H-**, **Na-**, **Ca-**, and **Cu(II)-Alg** are reported in Appendix O). The selectivity by GC peak area for **H-**, **Na-**, **Ca-**, **Mg-**, **Cu(II)-**, **Zn(II)-**, **Ni(II)-**, and **Co(II)-Alg** at 500 °C for each compound class are shown in Figure 4.31 (where **O** = small aliphatic and oxygenate molecules, **Ar** = aromatic or cyclohexene derivatives, **CP**= cyclopentene derivatives, **FN** = furanone derivatives, **FR** = furan derivatives, **FF** = furfural derivatives, and **U** = unknown). It is worth noting at this stage that, though trace levels of other furfural-derivatives were detected, the **FF**-class was overwhelmingly dominated by 2-furaldehyde (2-furfural, 2-FF) in all cases. Furthermore, traces of uronolactones were detected in the pyrolysis of both **HAlg** and **Cu(II)Alg**, but were not included in the total GC peak area calculations (see Section 4.5.5 and Appendix L for further results and discussions on this matter).

Whilst the selectivity by GC peak area offers a semi-quantitative interpretation of the composition of the volatilised compounds, absolute yields may only be determined through full quantification of the starting material and calibration of the GCMS for the species in question. As 2-FF was identified as a key pyrolysis product for alginic acid and a number of other alginates, a fully quantitative assessment of the formation of the compound was deemed to be advantageous. Accordingly, the yield of 2-FF (expressed as a mol.% per uronate unit of the alginate) is shown in Figure 4.32 for **HAlg** and corresponding alginates pyrolysed at temperatures between 200 – 500 °C. Furthermore, for **HAlg** and **Cu(II)Alg**, additional plots are provided (Figure 4.33) depicting the relationship between the selectivity for 2-FF (by total GC peak area) and the absolute yield of the compound at various temperatures across the quoted range.

Finally, by summing the total peak area and dividing by the amount of organic material that was pyrolysed,[*] an indication of the total yield of volatile material may be realised. In order to allow straightforward comparison between samples, the total GC peak area was normalised against that of **HAlg** at 500 °C. It is informative to plot the normalised total GC peak area alongside the mass of organic material remaining following pyrolysis (see examples for **HAlg** and **Cu(II)Alg** in Figure 4.34, and for the other alginates in Appendix O). Quantifying the organic material typically yielded sizeable errors due to the tiny masses involved combined with drifting in the calibration of the high-precision analytical balance over long periods of time.

[*] Organic material is defined as:

(mass of material) – (mass of initial moisture content + mass of metal content)

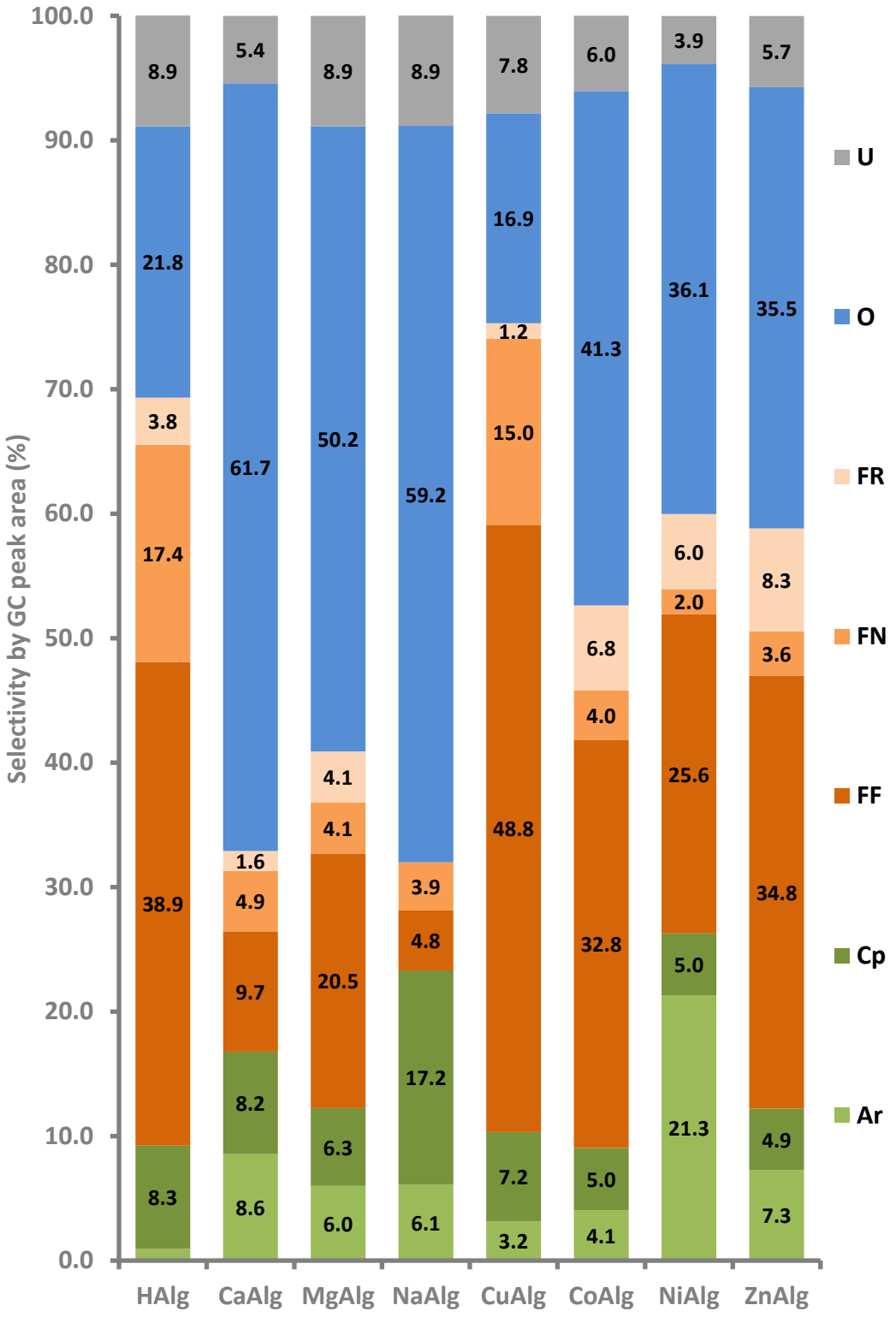

Figure 4.31 Selectivity by GC peak area (%) of product fractions in the Py-GCMS (500 °C, 20 °C ms^{-1}, 20 s, He 15 ml min^{-1}) analysis of alginic acid and alginate salts. Product fraction codes are: **U** = unknown, **O** = aliphatics and small oxygenates, **FR** = furan-derivatives, **FN** = furanone-derivatives, **FF** = furfural-derivatives, **Cp** = cyclopentene-derivatives, **Ar** = aromatic and cyclohexene-derivatives. The size of each fraction is also expressed numerically as a % by GC peak area. Error bars are not shown, but were typically less than ± 10 % of the displayed value.

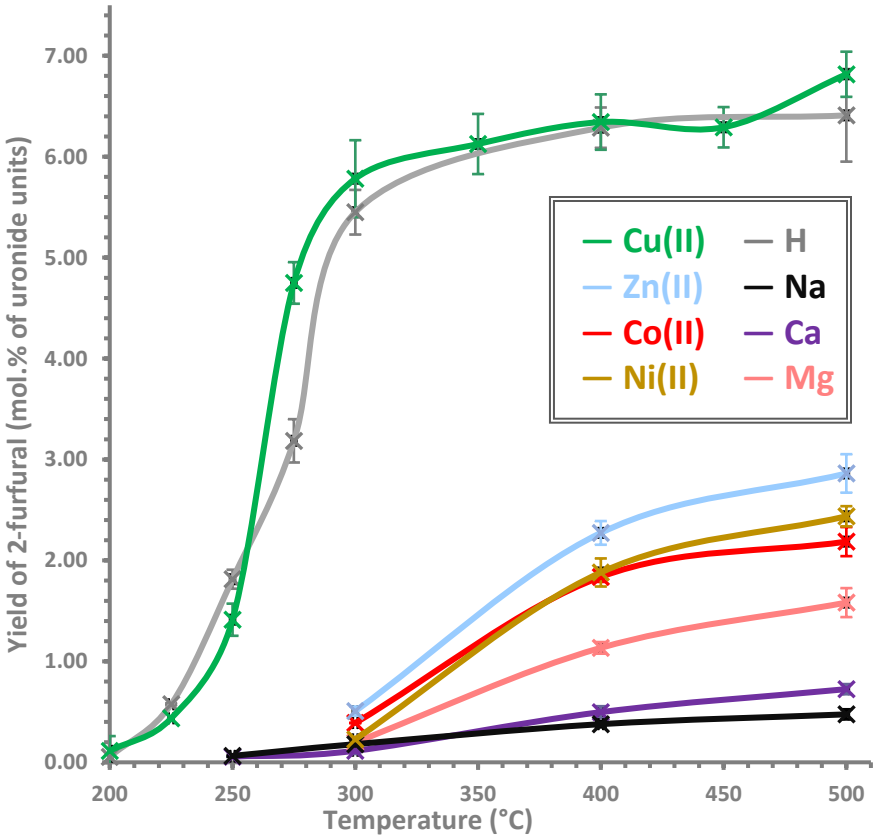

Figure 4.32 Yield of 2-furaldehyde (2-furfural, 2-FF) per uronate unit of alginic acid and metal alginates pyrolysed at various temperatures (20 °C ms^{-1}, 20 s, He 15 mL min^{-1}).

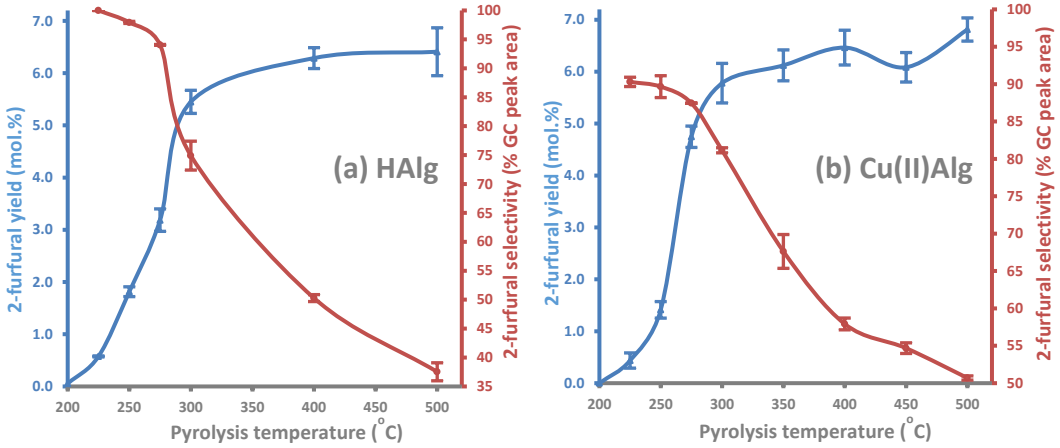

Figure 4.33 **Yield** (mol.% per unit of uronate) and **selectivity** (% by GC peak area) of 2-furaldehyde (2-furfural, 2-FF) from (a) **HAlg** and (b) **Cu(II)Alg** pyrolysed at various temperatures (20 °C ms^{-1}, 20 s, He 15 mL min^{-1}).

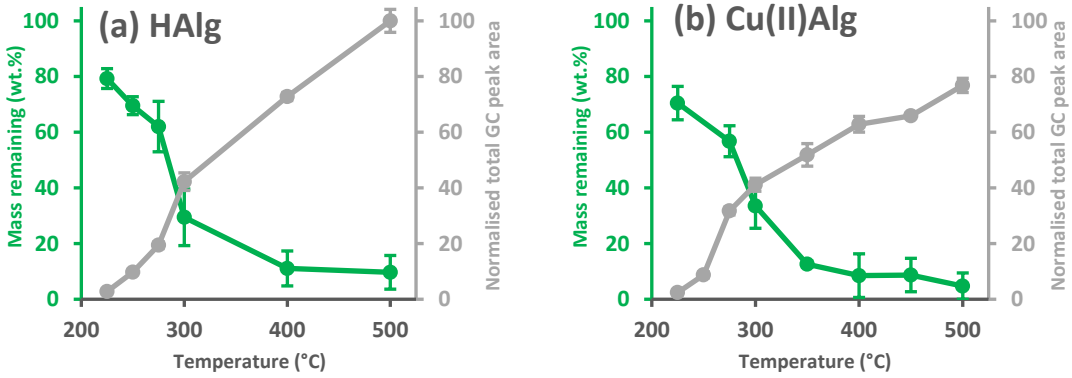

Figure 4.34 Plots of **remaining organic mass** and **total GC peak areas** (normalised against **HAlg** at 500 °C) for (a) **HAlg** and (b) **Cu(II)Alg** pyrolysed at various temperatures under He.

4.5.2.7 Py-FGA analysis of alginic acid and alginate salts

Whilst Py-GCMS captures the majority of condensable volatile organic species that are liberated during alginate pyrolysis, the non-condensable gases or *fixed gases* (namely CO_2 and CO) pass straight through the trap. Coupling a second gas chromatograph equipped with a thermal conductivity detector (GC-TCD) to the pyrolyser unit facilitates analysis of the fixed gases in a technique known as Py-FGA. Appendix L provides further detail on the function and operation of the Py-FGA, and how it can be calibrated to quantify yields of both CO_2 and CO from the pyrolysis of alginates. The yields of both gases from the rapid pyrolysis of **HAlg**, **NaAlg**, **CaAlg**, and **Cu(II)Alg** are reported in Table 4.4. Unfortunately, an equivalent method for quantifying the water released during pyrolysis could not be established in time to form part of this analysis, though a value could be estimated from TGA-MS data (see Section 4.5.2.4).

Table 4.4 Results for the Py-FGA analysis of alginic acid and various alginates performed at 500 °C (20 °C ms^{-1}, 20 s, He 15 mL min^{-1})

Sample	Yield (wt.%)		Molecules per uronate unit	
	CO_2	CO	CO_2	CO
Alginic acid	23.3 ± *0.7*	4.9 ± *0.1*	0.93 ± *0.03*	0.31 ± *0.03*
Cu(II)-alginate	29.9 ± *2.7*	6.4 ± *0.1*	1.19 ± *0.11*	0.40 ± *0.03*
Na-alginate	34.3 ± *0.4*	6.0 ± *0.2*	1.36 ± *0.03*	0.37 ± *0.03*
Ca-alginate	30.4 ± *1.8*	3.1 ± *0.1*	1.21 ± *0.07*	0.19 ± *0.03*

4.5.2.8 Attempts to construct a tentative mass balance for the thermolysis of alginic acid and alginate salts

Following the work in the Sections 4.5.2.3 – 4.5.2.7, it was possible to attempt to construct a tentative mass balance for the flash pyrolysis of **HAlg**, **NaAlg**, **CaAlg**, and **Cu(II)Alg** at 500 °C. The precise details of the mass balance calculation are described in Appendix L, but in brief, the various contributory factors are (expressed as a wt.% of a moisture- and metal-free sample):

I. **Yield of 2-FF:** calculated from Py-GCMS
II. **Yield of CO_2:** calculated from Py-FGA
III. **Yield of CO:** calculated from Py-FGA
IV. **Yield of H_2O:** calculated indirectly from TGA-MS
V. **Yield of volatile organic material:** estimated from the assumption that all compounds in the Py-GCMS analysis have the same response factor as 2-FF.
VI. **Yield of organic char:** calculated by weighing the sample before and after Py-GCMS analysis, correcting for moisture content, and deducting the mass of the residual metal within the char.

The results of the mass balance analysis are depicted in Figure 4.35.

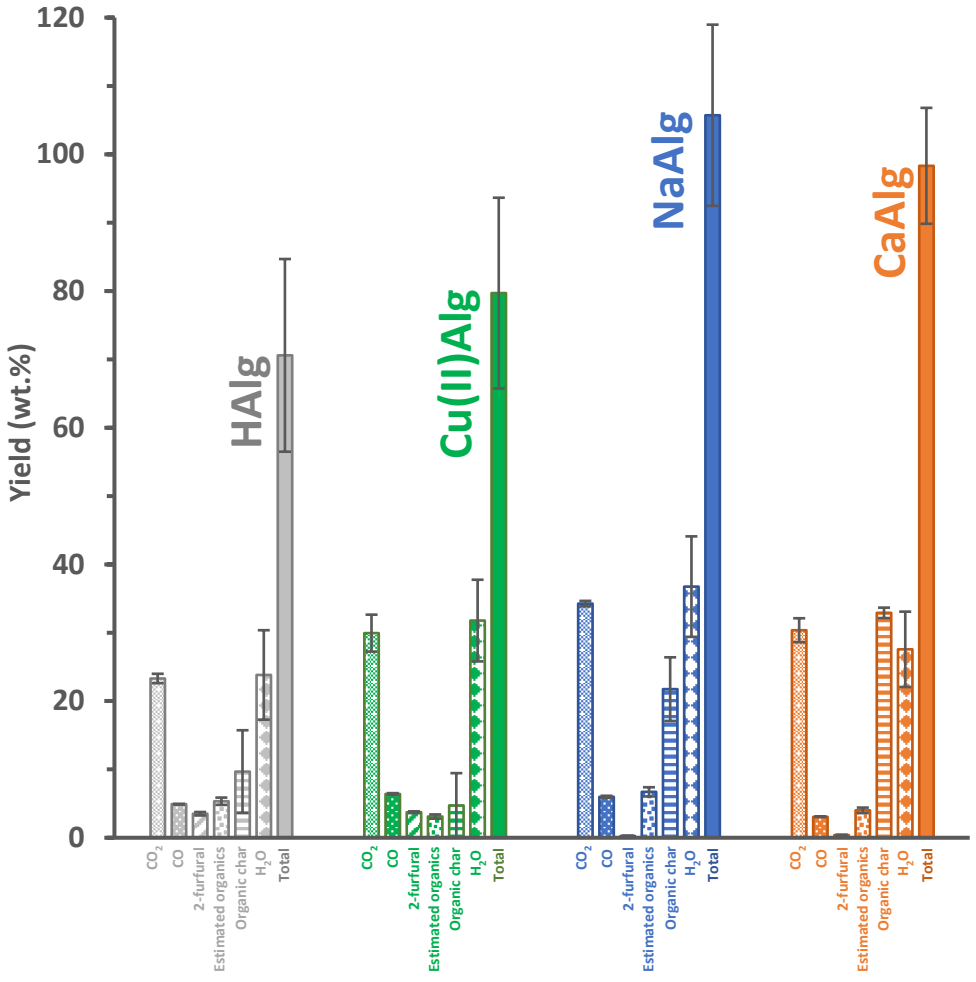

Figure 4.35 Tentative mass balance for the rapid pyrolysis (500 °C) of alginic acid and related alginate salts.

4.5.3 Compositional- and thermal-analysis of pectin and pectinates

4.5.3.1 Characterisation of pectin and various pectinates

The elemental compositions of commercial pectin (**HPec**),* and derivative metal-pectinate salts (**NaPec**, **CaPec**, and **Cu(II)Pec**) were determined by a combination of combustion (CHN) and inductively coupled plasma-mass spectrometric (ICP-MS) analyses (see Table 4.5). The adsorbed moisture within the samples (established from TGA) was also accounted for. Because the precise degree of esterification was not discerned, an accurate formula unit could not be calculated for either pectin or related pectinate salts. The solid-state Fourier transform infra-red (FTIR) spectra of **HPec** and the pectinates were found to be in accordance with those reported in the literature.[103–105] The wavenumbers of diagnostic vibrational modes for each sample are reported in Table 4.5 and the full spectra provided in Appendix G.

Table 4.5 Results from the solid-state characterisation of pectin and pectinates

Cation	Elemental (wt.%)				Characteristic vibrational frequencies (cm^{-1})			
	C	H	M	H_2O	ν(OH)	$\nu(COO)_{asym}$	$\nu(COO)_{sym}$	ν(C-O)
H^+	37.66	5.13	1.40	11.4	3372	1733	1604	1011
Na^+	29.63	4.31	7.95	17.4	3274	1597	1407	1012
Ca^{2+}	31.90	4.66	2.76	13.6	3242	1588	1416	1007
Cu^{2+}	28.77	4.78	9.38	17.4	3209	1584	1399	1009

4.5.3.2 TGA analysis of pectin and various pectinates

The thermograms for **H-**, **Na-**, **Ca-** and **Cu(II)-Pec** yielded by heating the samples under a He atmosphere at 10 °C min^{-1} were recorded and analysed as described in Section 4.5.2.2. As the characteristic stages of pyrolysis of the pectin-derived samples were found to be the same as found for the alginates, the key pyrolysis parameters (T_i, T_{max}, T_f, and so on) were defined as previously (see Section 4.5.2.2), and are reported in Table 4.6.

Table 4.6 Characteristic thermal parameters in the rapid pyrolysis of pectin and associated pectinates (heated at 10 °C min^{-1} under He).

Cation	T_i (°C)	T_f (°C)	$\Delta M(T_i - T_f)$ (wt.%)	T_{max1} (°C)	Rate[T_{max1}] (wt.% min^{-1})	T_{max2} (°C)	Rate[T_{max2}] (wt.% min^{-1})
H^+	203 ± 5	352 ± 5	56 ± 1	233 ± 5	-14.0 ± 1.0	298 ± 5	-2.1 ± 0.5
Na^+	210 ± 5	289 ± 5	41 ± 1	244 ± 5	-15.9 ± 1.0	-	-
Ca^{2+}	219 ± 5	350± 6	38 ± 1	255 ± 6	-5.8 ± 0.5	-	-
Cu^{2+}	178 ± 10	353 ± 5	50 ± 4	226 ± 5	-5.0 ± 0.5	251 ± 6	-9.0 ± 1.0

* According to the manufacturer (*Sigma Aldrich*) the pectin was composed of > 75 wt.% galacturonic acid units, with the remainder assumed to be galacturonic acid methyl esters.

4.5.3.3 TGA-MS analysis of pectin and various pectinates

Repeated TGA-MS analyses of pectinate salts were not possible, and so accurate values for the temperatures CO_2 and H_2O release are not quoted as in the case of alginates. It is worth mentioning however, that the profiles of evolution of CO_2, H_2O, and (in the case of **HPec** and **Cu(II)Pec**) 2-FF were largely synchronous with the TGA data reported in Table 4.6.

4.5.3.4 Py-GCMS analysis of pectin and various pectinates

The samples of **HPec** and associated salts were subject to a similar Py-GCMS investigation as to that reported for alginates in Section 4.5.2.6, albeit at a lower temperature of 300 °C (20 °C ms^{-1}, 20 s, He 15 mL min^{-1}). The selectivity by GC peak area for the various compound classes following pyrolysis under such conditions are shown in Figure 4.36. As per the equivalent alginates, the salts of **HPec** and **Cu(II)Pec** were found to exhibit high selectivities towards the formation of 2-FF, and the yield of this product was therefore quantified precisely (see Figure 4.37).*

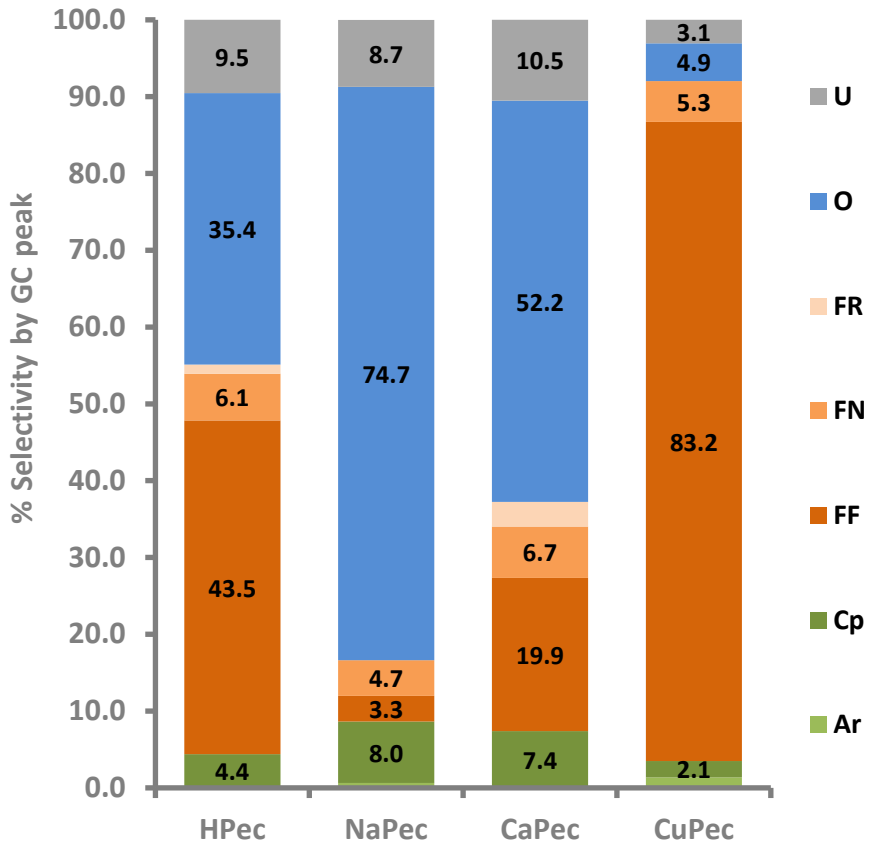

Figure 4.36 Selectivity by GC peak area (%) of product fractions in the Py-GCMS (300 °C, 20 °C ms^{-1}, 20 s, He 15 ml min^{-1}) analysis of pectin and pectinate salts. Product fraction codes are: **U** = unknown, **O** = aliphatics and small oxygenates, **FR** = furan-derivatives, **FN** = furanone-derivatives, **FF** = furfural-derivatives, **Cp** = cyclopentene-derivatives, **Ar** = aromatic and cyclohexene-derivatives. The size of each fraction is also expressed numerically as a % by GC peak area. Error bars are not shown, but were typically less than ± 10 % of the displayed value.

* Note that the yield of 2-FF in the case of pectinates in quoted as a mol.% of the carbon in the sample as an accurate formula unit was not determined in these cases.

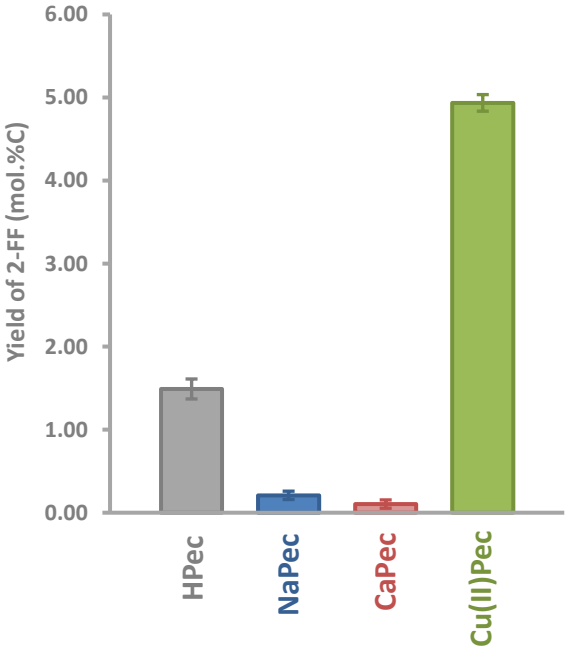

Figure 4.37 Yield of 2-FF derived from the rapid pyrolysis of pectin and related pectinate salts at 300 °C (20 °C ms^{-1}, 20 s, He 15 mL min^{-1}) expressed as a mol.% of the carbon in the sample.

4.5.4 Compositional- and thermal-analysis of mono-uronic acids and their salts

4.5.4.1 Characterisation of mono-uronic acids and their salts

The composition of commercial D-galacturonic and D-glucuronic acids, alongside their prepared metal-uronate salts (Na^+, Ca^{2+}, and Cu^{2+}) was determined by a combination of combustion (CHN) and inductively coupled plasma-mass spectrometric (ICP-MS) analyses. The adsorbed moisture within the samples (established from TGA) was also accounted for to yield an accurate molecular formula for each compound (reported in Table 4.7 and Table 4.8). The ^{1}H NMR spectra of the uronate salts were as expected from the work in Chapter 3 and identical to their parent uronic acid following the exchange for H^+ of the metal cation over a resin. It should be stressed that, whilst the free acids (**HGlc** and **HGal**) were used in anomerically pure forms (*β*-pyranose and *α*-pyranose respectively), the salts (which were left in aqueous solution as a necessary part of their preparation) were comprised of mixtures of the two anomers.

The solid-state Fourier transform infra-red (FTIR) spectra of the uronates were found to be in accordance with those reported in the literature.[106–109] The wavenumber of diagnostic vibrational modes for each sample are reported in Table 4.7 and Table 4.8 and the full spectra provided in Appendix G.

Table 4.7 Results from the solid state characterisation of D-glucuronic acid and corresponding D-glucuronate salts

Cation	Calculated formula	Characteristic vibrational frequencies (cm^{-1})			
		ν(OH)	$\nu(COO)_{asym}$	$\nu(COO)_{sym}$	ν(C-O)
H^+	$C_6H_{10}O_7.(0.2\ H_2O)$	3384	1705	1485^{Sh}	1019
Na^+	$C_6H_9O_7Na.(0.4\ H_2O)$	*multiple*	1586	1473	1018
Ca^{2+}	$C_6H_9O_7Ca_{0.5}.(0.6\ H_2O)$	3262	1594	1425	1015
Cu^{2+}	$C_6H_9O_7Cu_{0.5}.(1.6\ H_2O)$	3287	1584	1425	1018

Sh = shoulder

Table 4.8 Results from the solid state characterisation of D-galacturonic acid and corresponding D-galacturonate salts

Cation	Calculated formula	Characteristic vibrational frequencies (cm^{-1})			
		ν(OH)	$\nu(COO)_{asym}$	$\nu(COO)_{sym}$	ν(C-O)
H^+	$C_6H_{10}O_7.(1.2\ H_2O)$	3337	1707	1439	1024
Na^+	$C_6H_9O_7Na.(0.7\ H_2O)$	*multiple*	1599	1413	1024
Ca^{2+}	$C_6H_9O_7Ca_{0.5}.(1.0\ H_2O)$	3272	1596	1421	1013
Cu^{2+}	$C_6H_9O_7Cu_{0.5}.(1.9\ H_2O)$	3305	1590	1410	1016

4.5.4.2 TGA analysis of mono-uronic acids and their salts

The thermogravimetric profiles of mono-uronates were not as easily characterised as those of the polyuronides (alginates and pectinates), because the phases of decomposition were much less distinct. As such, the TGA profiles for the H-, Na-, Ca-, and Cu(II)-forms of **Glc** and **Gal** are shown in Figure 4.38 and Figure 4.39, respectively, for direct comparison.

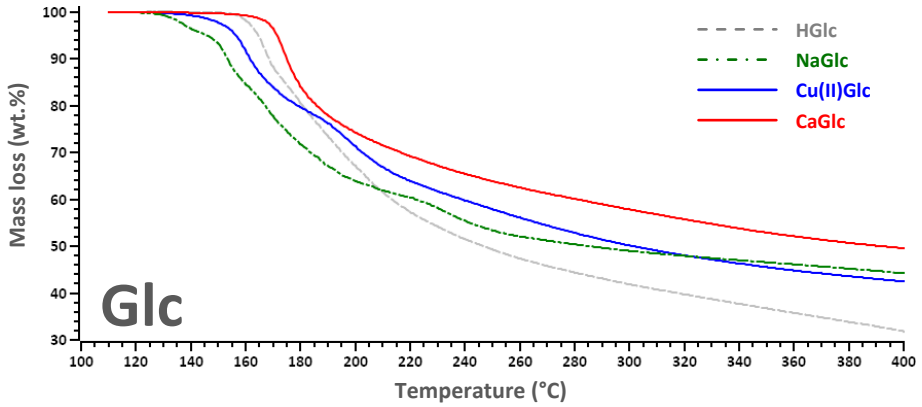

Figure 4.38 The TGA profile of the thermolysis of **H-**, **Na-**, **Ca-**, and **Cu(II)-Glc** heated under a flow of He at 10 °C min^{-1}.

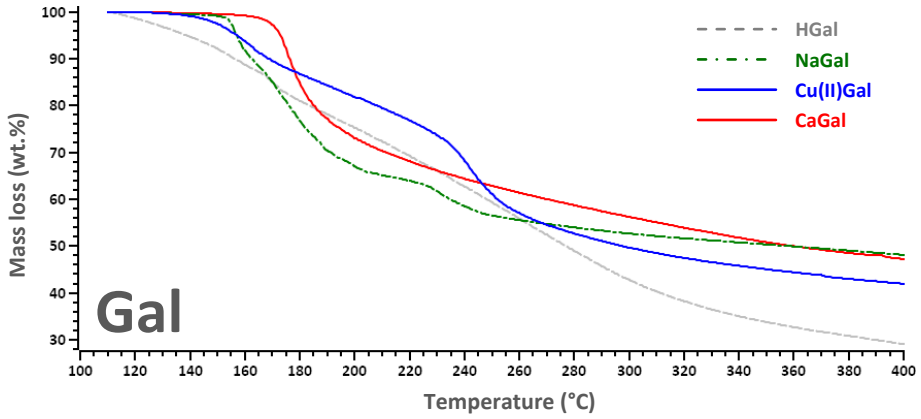

Figure 4.39 The TGA profile of the thermolysis of **H-**, **Na-**, **Ca-**, and **Cu(II)-Gal** heated under a flow of He at 10 °C min^{-1}.

4.5.4.3 Py-GCMS analysis of mono-uronic acids and their salts

Py-GCMS analyses of the mono-uronic acids and their salts were undertaken in a similar manner to that described for the alginates in Section 4.5.2.6. The selectivities by GC peak area for **HGlc**, **HGal**, and their Na^+, Ca^{2+}, and Cu^{2+} salts pyrolysed at 500 °C (20 °C ms^{-1}, 20 s, He 15 mL min^{-1}) are shown in Figure 4.40. It is very important to highlight that, overwhelmingly, the main product of pyrolysis of **HGlc** was, in fact, an anhydrosugar (a uronolactone) that was, for reasons explained in Section 4.5.5, excluded from the selectivity calculations. Disregarding such lactone formation, the free acids and Cu^{2+} salts of the mono-uronates showed the highest selectivity for 2-FF, and so this product was quantified more precisely (see Figure 4.41).

4.5.5 Results for the detection of anhydrosugars by Py-GCMS analysis of mono- and poly-uronides

In Section 4.3 the importance of anhydrosugar formation during the pyrolysis of carbohydrates was introduced. Anhydrohexose compounds, however, have extremely high boiling points and, as explained in Appendix L cannot be considered to be "volatile" pyrolysis products. Consequently, whilst the Py-GCMS apparatus used in this thesis does allow for the *detection* of anhydrosugars, quantification is not usually possible. In this regard, the pectins, galacturonates, and most alginates and glucuronates analysed were not found to yield detectable levels of anhydrosugars upon pyrolysis. An exception to this statement was the overwhelming levels of an anhydrosugar found in the GCMS trace from the pyrolysis of solid samples of *β*-D-glucuronic acid (see Figure 4.42). The selectivity (by GC peak area) could not be calculated for the anhydrosugar, because it was not quantitatively desorbed from the pyrolyser trap (hence why it was excluded from analysis in Section 4.5.4.3, though it was estimated to account for at least 80 % of the GC peak area). Subjecting D-glucofuranurono-6,3-lactone (GlcLac) to the same Py-GCMS analysis as **HGlc**, yielded an identical signal in terms of both retention time, peak shape, and MS-fragmentation pattern (shown in Figure 4.42). Hence, the anhydrosugar detected in the pyrolysis of **HGlc** was assigned to being from the family of bicyclic 6,3-uronolactones discussed in Chapter 2. A lactone signal was also seen (but at a much lower intensity compared to **HGlc**) in the pyrogram of **Cu(II)Glc**. Finally, two small signals possessing the

same MS-fragmentation pattern as GlcLac (though appearing at different retention times) were also detected in each of the chromatograms arising from **HAlg** and **Cu(II)Alg**, though they were of low intensity relative to the noise.

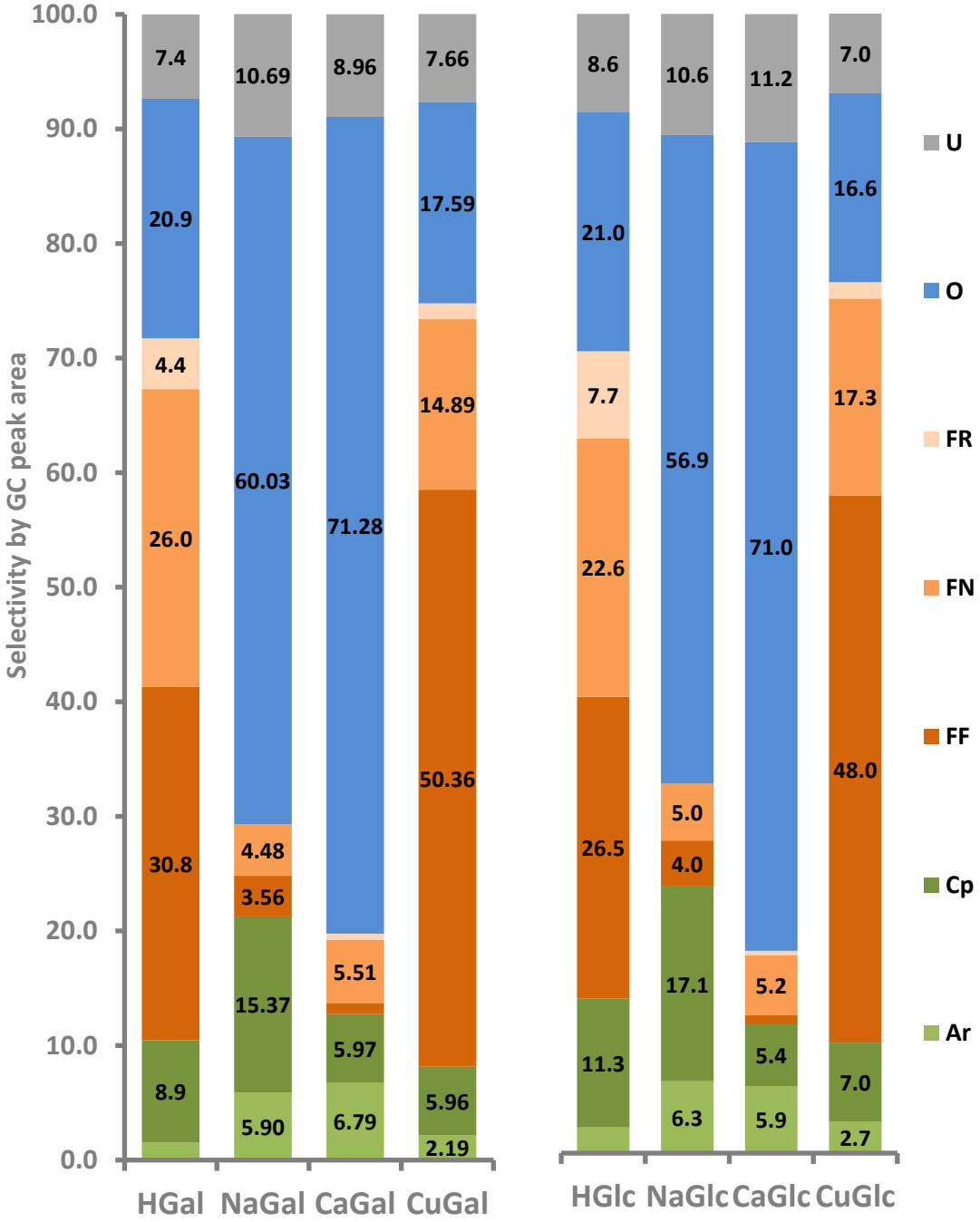

Figure 4.40 Selectivity by GC peak area (%) of product fractions in the Py-GCMS (500 °C, 20 °C ms^{-1}, 20 s, He 15 ml min^{-1}) analysis of mono-uronic acids and metal salts. Product fraction codes are: **U** = unknown, **O** = aliphatics and small oxygenates, **FR** = furan-derivatives, **FN** = furanone-derivatives, **FF** = furfural-derivatives, **Cp** = cyclopentene-derivatives, **Ar** = aromatic and cyclohexene-derivatives. The size of each fraction is also expressed numerically as a % by GC peak area. Error bars are not shown, but were typically less than ± 10 % of the displayed value.

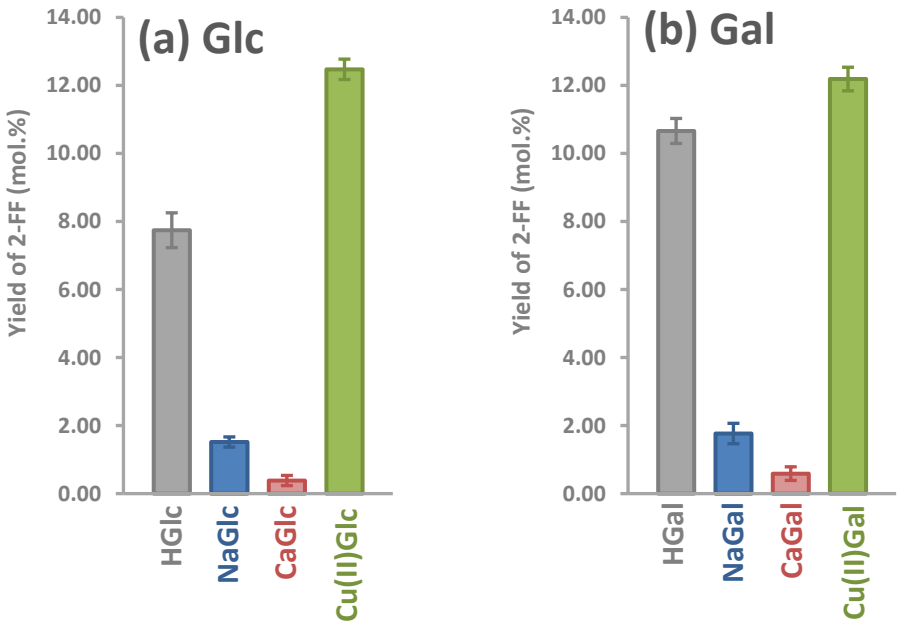

Figure 4.41 Comparison of the yields of 2-FF derived from the rapid pyrolysis of a) mono-glucuronic, and b) mono-galacturonic acids and related salts at 500 °C (20 °C ms^{-1}, 20 s, He 15 mL min^{-1}).

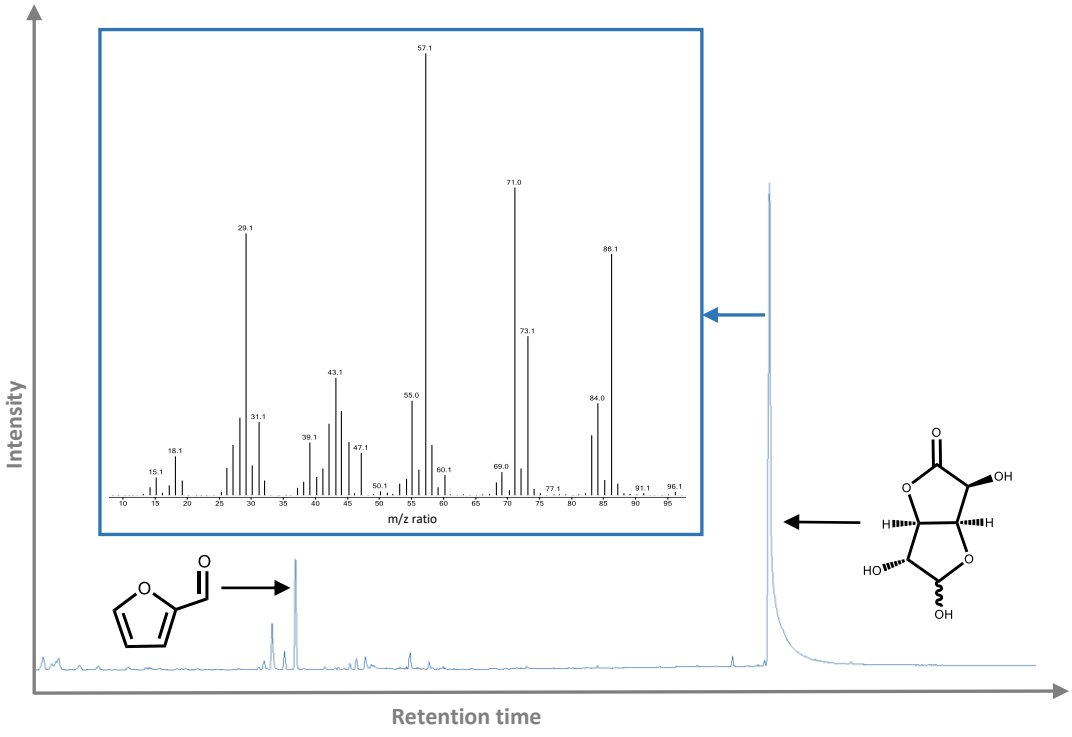

Figure 4.42 Py-GCMS trace from the analysis of **HGlc** at 500 °C (20 °C ms^{-1}, 20 s, He 15 mL min^{-1}). The mass spectrum of the peak assigned to D-glucofuranurono-6,3-lactone is inset.

4.5.6 The Py-GCMS analysis of Reductic acid (2,3-dihydroxycyclopent-2-en-1-one)

Reductic acid (2,3-dihydroxycyclopent-2-en-1-one) (see Figure 4.43) is an important degradation product of uronic acids in the hydrothermal environment (as discussed in Appendix C). In order to gauge similarities between the mechanisms of thermal and hydrothermal degradation of uronides, reductic acid was subject to Py-GCMS analysis at 500 °C (20 °C ms^{-1}, 20 s, He 15 ml min^{-1}). The principal products (as determined by GC peak area) of the thermolysis of reductic acid were found to be 4-cyclopentene-1,3-dione (≈ 20 %) and cyclopentane-1,2-dione (≈ 35 %), as depicted in Figure 4.43. Hence, if reductic acid was an intermediate in the pyrolysis of uronides, it would be expected that the two diagnostic compounds in Figure 4.43 would be detected in the subsequent pyrograms.

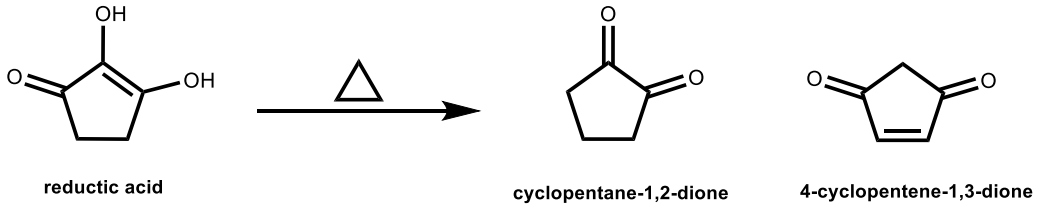

Figure 4.43 Products from the flash pyrolysis of reductic acid at 500 °C

4.6 Discussion of results from the thermal analysis of alginates and related uronides

4.6.1 The metal-free pyrolysis of alginic acid and related uronides

4.6.1.1 General comments on the metal-free pyrolysis of alginic acid

The thermal degradation of alginic acid (**HAlg**) as followed by TGA (see Figure 4.25) is best contextualised by comparison with that of cellulose (reported previously by other authors – see Figure 4.2 at the start of this Chapter).[1] In this regard, **HAlg** requires a markedly low temperature to initiate rapid pyrolysis (T_i = 173 ± 3 °C) compared to cellulose (T_i ≈ 300 °C), although the thermal window over which the former degrades is much wider (indicating a slower mass loss rate) than the latter. Furthermore, **HAlg** gives rise to a more convoluted DTG profile (with T_{max} peaks at both 195 ± 3 °C and 249 ± 3 °C) indicating greater complexity in the degradative pathway (potentially dependant on a stepwise mechanism).

Following the period of rapid pyrolysis, the mass balance (as measured at 500 °C) for alginic acid (see Figure 4.35) indicates that the most abundant products by weight are CO_2 (23.3 ± 0.68 wt.%) and H_2O (23.8 ± 6.5 wt.%),* with the equivalent of 0.93 ± 0.03 and 2.3 ± 0.6 molecules of each released respectively per unit of uronate in the polymer. TGA-MS analysis (see Figure 4.26) indicated that the CO_2 and H_2O evolution profiles essentially

* It should be noted that there are considerable shortcomings in the attempted mass balance reported here. See Appendix L for further details.

mirrored the shape of the corresponding thermogram (though very small traces of H_2O were also detected in the temperatures preceding T_i). Furthermore, CO was also found to be a significant product of pyrolysis (4.9 ± 0.1 wt.%) with 0.31 ± 0.03 molecules being liberated per uronate unit. Overwhelmingly, however, the single largest destination for the majority of the carbon in alginic acid appears to be the solid char remaining at the end of the thermolysis reaction. Such char, whilst only representing 9.67 ± 6.05 wt.% of the products,[*] has been measured by Coburn to comprise around 90 wt.% carbon, and very little oxygen.[50] Work in the group of Prof. James Clark has demonstrated that, by 500 °C, this char is rich in unsaturated carbon-carbon bonds, and has lost virtually all of the starting –COOH moieties.[81]

From the point of view of industrial-scale pyrolysis, however, it is the condensable "pyrolysis oil" that garners the most interest, and the results of the Py-GCMS analysis can give an indication of the likely composition of such a fraction in the case of **HAlg**. In this regard, the mass balance in Figure 4.35 indicates that, in fact, the yield of condensable organic compounds from the thermolysis of alginic acid at 500 °C is quite low (8.85 ± 0.78 wt.%). Despite this setback, it appears also that the same fraction is very rich in 2-furaldehyde (2-FF) with a selectivity (by GC peak area) of 37.53 ± 1.56 %, representing an absolute yield of 6.41 ± 0.46 mol.%. Indeed, Figure 4.31 demonstrates the dominance of furan-based products in the pyrolysate of alginic acid, an observation also noted by authors of similar studies.[82,89,94]

Both Py-GCMS (see Figure 4.32) and TGA-MS analyses indicate that 2-FF is released across a narrow window, starting at 175 °C (by TGA-MS) or 200 °C (by Py-GCMS),[†] and being virtually complete by 300 - 350 °C. Ross *et al.* reported a decrease in 2-FF yield from **HAlg** at temperatures approaching 500 °C, though data presented in Figure 4.32 implies that this yield in-fact remains almost constant at elevated temperatures, albeit with diminishing selectivity as secondary products begin to be liberated (see Figure 4.33).[82] Furthermore, data in Figure 4.35 indicate that such secondary products are volatilised predominantly between 350 °C – 500 °C, possibly as a result of char degradation. Whilst these additional products are too numerous to discuss individually (consult the full list in Appendix O), it is worth highlighting the furanone compound class, which is generated in reasonably high proportions, and may be closely mechanistically linked to 2-FF formation (see Section 4.6.1.3). Finally, it is worthy of note that similarly high selectivity towards 2-FF formation was found to be generic to all of the uronic acids studied, including **HGlc**, **HGal** and **HPec** in

[*] "Char" here refers to the char measured by weighing the solid before and after thermolysis on the micropyrolyser (with a heating rate of 20 °C ms^{-1}). This particular method of char quantification has a very large error associated with it, and the true value is likely to lie towards the upper end of the quoted limits (see Appendix L for further discussion).

[†] The discrepancy in the observed temperatures measured for the onset of 2-FF release by the two techniques (TGA-MS and Py-GCMS) is a consequence of the two very different heating rates employed. Hence, for TGA-MS, the sample was heated at 10 °C min^{-1} compared to the 20 °C ms^{-1} employed in Py-GCMS.

addition to **HAlg** (see Figure 4.36 and Figure 4.40, respectively). The similarities and differences in the thermal behaviour of such uronides will be the basis of discussion in Section 4.6.1.2.

4.6.1.2 The influence of stereochemistry and degree of polymerisation on the metal-free pyrolysis of alginic acid and related uronides

Discussions throughout Section 4.3.2 highlighted the contrasting thermal behaviour between mono- and poly-saccharides, generating an impetus to investigate the equivalent correlations in the case of mono- and poly-uronides. Ideally, to explore such relationships for alginic acid, well-defined solid samples of the composite monomers (*β*-D-mannuronic and *α*-L-guluronic acids) would be required, however such compounds are not currently available (as explained in Chapter 2). Consequently, *α*-D-galacturonic (*α*-**HGal**) and *β*-D-glucuronic acids (*β*-**HGlc**) were therefore substituted as closely related alternatives (see Figure 4.44. Whilst similarities were found between the thermochemical behaviour of *α*-**HGal** and *β*-**HGlc**, mutual differences between them, as well as with alginic acid (**HAlg**) and also pectin (**HPec**) were clear, and will be explored in the following section.

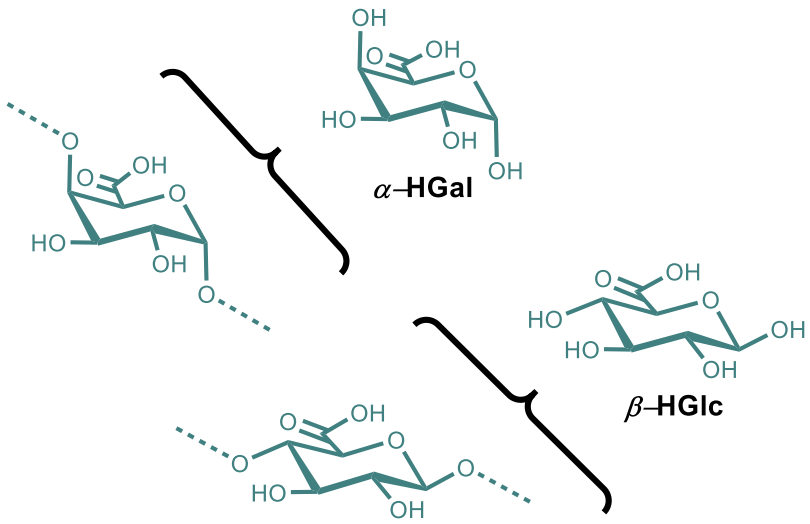

Figure 4.44 *α*-D-galacturonic (*α*-**HGal**) and *β*-D-glucuronic acids (*β*-**HGlc**) were studied as model compounds for the thermochemical behaviour of polyuronides.

From thermogravimetric analysis, the mono-uronic acids were found to undergo rapid pyrolysis at much lower temperatures (see Figure 4.38 and Figure 4.39) than their polymeric counterparts (see Figure 4.25. *α*-**HGal**, for example, began degradation from as early as 110 °C (immediately following the isothermal drying period included in the run) and **HGlc** at around 154 °C, in contrast to **HAlg** and **HPec** (for which T_i = 173 ± 3 and 203 ± 5 °C respectively). The lower onset temperature for the mono-uronic acids may be due to a multitude of reasons. One possible explanation is that the monosaccharide particles melt (or at least begin to sinter) at comparatively low temperatures (*α*-**HGal** at 110 °C and *β*-**HGlc** at 165 °C),[110,111] at which point decarboxylation may take place more readily as proton mobility is increased (see discussions in Appendix Q). Alternatively, the phenomena may be a result of intramolecular dehydrations within the monosaccharides, again facilitated by lower melting temperatures (as is seen in glucose and related carbohydrates).[6] In either

case, from a kinetic point of view, there are clearly large contrasts in the mass loss profiles of mono- and poly-meric uronic acids.

With regards to product formation, the most readily apparent difference between **HAlg**, **HPec**, *α*-**HGal**, and *β*-**HGlc** is the identification of an anhydrosugar generated in high yields uniquely from the latter compound. The anhydrosugar in question was identified as D-glucofuranurono-6,3-lactone (GlcLac), and it clearly dominated the Py-GCMS trace of **HGlc** (see Figure 4.42). It is important to highlight that the assignment made here of the anhydrosugars as being GlcLac is in contradiction to that proposed by Moldoveanu in a similar analysis, where the author claimed that D-glucopyranurono-6,1-lactone was formed instead (See Figure 4.45). The distinction is not merely semantic, as the appearance of GlcLac demonstrates that *β*-D-glucopyranuronic acid behaves in a contrasting manner to *β*-D-glucopyranose, which forms a 6,1-bicyclic anhydrosugar (levoglucosan) during thermolysis (quite unlike D-glucofuranurono-6,3-lactone). The production of GlcLac also signifies strong similarities between the anhydrous pyrolysis and the hydrothermolysis of **HGlc**, as it was demonstrated in Chapter 2 that D-glucofuranurono-6,3-lactone forms readily at elevated temperatures from aqueous solutions of glucuronic acid. Correspondingly, **HGal**, which forms no lactones under hydrothermal conditions, does not succumb to lactonisation under the anhydrous pyrolysis conditions studied either. Finally, it is interesting to note that **HAlg** gives rise to seemingly only trace levels of detectable anhydrosugars (conceivably the mannuronic and guluronic equivalents of GlcLac characterised in Chapter 2), and **HPec** generates none at all.

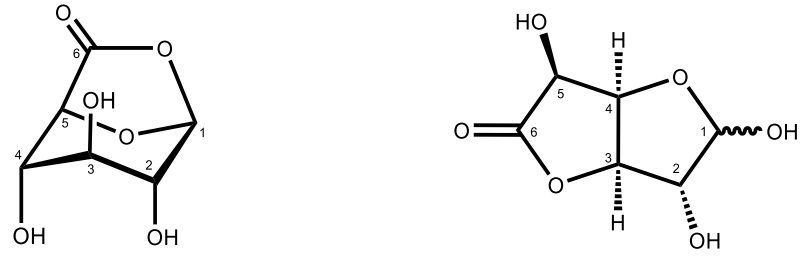

Figure 4.45 The identity of the lactone formed by **HGlc** upon pyrolysis according to Moldoveanu (left) and this study (right).[2]

Of course, where *α*-**HGal**, *β*-**HGlc**, **HPec**, and **HAlg** differ in terms of their abilities to yield anhydrosugars, they are unified in their high selectivities towards the formation of 2-FF. Indeed, at 500 °C, **HGal** generates a very high yield of 2-FF (10.66 ± 0.34 mol.%), as does **HGlc** (7.74 ± 0.51 mol.%) (see Figure 4.41), with the product accounting for 29.27 ± 0.97 % and 26.48 ± 1.53 % of the respective GC-peak areas (see Figure 4.40). The slightly lower yield of 2-FF from *β*-**HGlc** compared to *α*-**HGal** could, therefore, reflect the tendency of the former compound to form GlcLac in preference to furaldehyde. It is also interesting to note that, whilst the absolute yields of 2-FF are higher for the monosaccharides than in the case of **HAlg** (see Section 4.6.1.1), the selectivities (by GC peak area) of *β*-**HGlc** and *α*-**HGal** for the furaldehyde are lower. This discontinuity reflects the fact that other volatile compounds are present in greater proportions in the pyrolysate of the mono-uronic acids,

particularly from the **FN** class (furanone-derivative) (see Figure 4.40). A mechanistic interpretation of these results, and others, is provided in the following section.

Finally, it is of interest to compare the formation of 2-FF from the two polyuronide compounds studied, **HAlg** and **HPec**. At 300 °C, **HAlg** demonstrates a considerably higher yield (4.54 ± 0.18 and 1.49 ± 0.12 mol.%C for **HAlg** and **HPec**, respectively) and selectivity (74.91 ± 2.50 and 38.18 ± 2.95 % by GC peak area for **HAlg** and **HPec**, respectively) for 2-FF. The cause of the difference is not fully understood, and further work will be required to discern a mechanistic explanation. Intriguingly, the difference in 2-FF formation by **HAlg** compared to **HPec** is in contrast to the behaviour of the Cu(II)-salts of the respective polymers, with **Cu(II)Alg** and **Cu(II)Pec** generating equally high yields and selectivities of 2-FF (see Section 4.6.2.6). Suggestions as to how such effects could be exploited in the context of industrial pyrolysis are made in Section 4.6.4.

4.6.1.3 Tentative mechanistic interpretation of the metal-free pyrolysis of alginic acid and related uronides

A mechanistic interpretation of the formation of all of the compounds identified throughout the Py-GCMS analysis of alginic acid and related uronic acids is, of course, not feasible. However, a few selected cases are discussed below, with the prevalence of 2-furaldehyde (2-FF) in the product-stream making it an obvious choice for particular attention. Naturally, in the absence of additional data (such as isotopic labelling studies or corroborating theoretical work) the proposed pathways can only be purely speculative, but based (in part) on mechanisms familiar within the field of carbohydrate thermochemistry (see Section 4.3.2).

The formation of 2-FF from a polyuronide requires for (in some combination): decarboxylation (see Figure 4.46a), cleavage of the O1-C4 glycosidic bond (see Figure 4.46b), elimination of two water molecules (see Figure 4.46c), and recyclisation between the ring oxygen and C2 (see Figure 4.46d). Whilst Figure 4.46 depicts such mechanistic steps individually, there is also a chance that one or more occur simultaneously. One possible single-step mechanism is depicted in Figure 4.47. Whilst elegant, evidence for the idealised "single-step" mechanism is not well supported by the TGA and TGA-MS data for alginic acid in Sections 4.5.2.2. Such results indicate at least two individual mass loss events during the rapid pyrolysis stage (defined by T_{max1} and T_{max2}), with CO_2 and H_2O release peaking during the first event, and 2-FF release peaking during the second. This sequence indicates that decarboxylation and dehydration occur whilst the glycosidic bond remains intact, until a threshold temperature (well above 200 °C). Indeed, it is possible that the combined dehydration/decarboxylation steps are mutually autocatalytic, with hydroxyl groups accepting carboxylic acid protons, and thereby promoting elimination of both CO_2 and H_2O (see Figure 4.48). The low temperature, synchronous dehydration/decarboxylation of alginic acid would inevitably lead to unsaturation within the remaining structure, which may in turn facilitate unusually high levels of char formation *via* cross-linking of the polymers at temperatures below those required for glycosidic bond scission (see Figure 4.49).

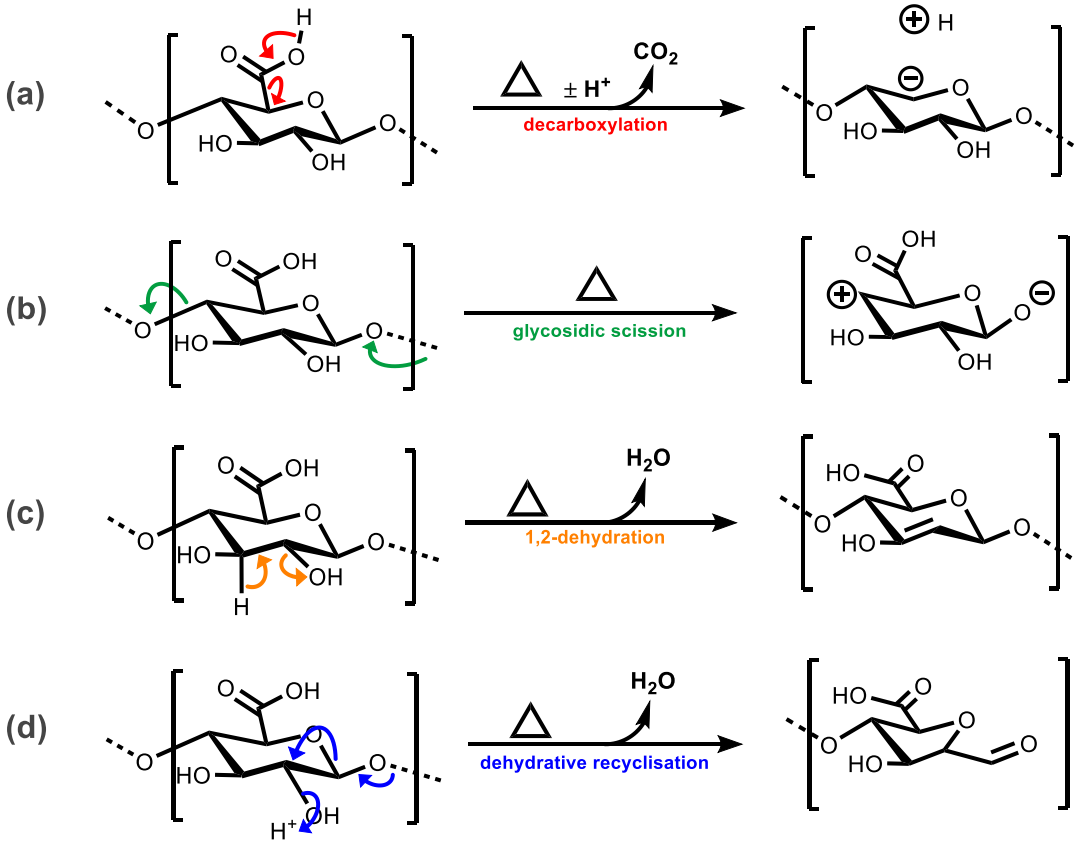

Figure 4.46 Necessary mechanistic steps in the formation of 2-FF from a polyuronic acid (such as **HAlg** or **HPec**)

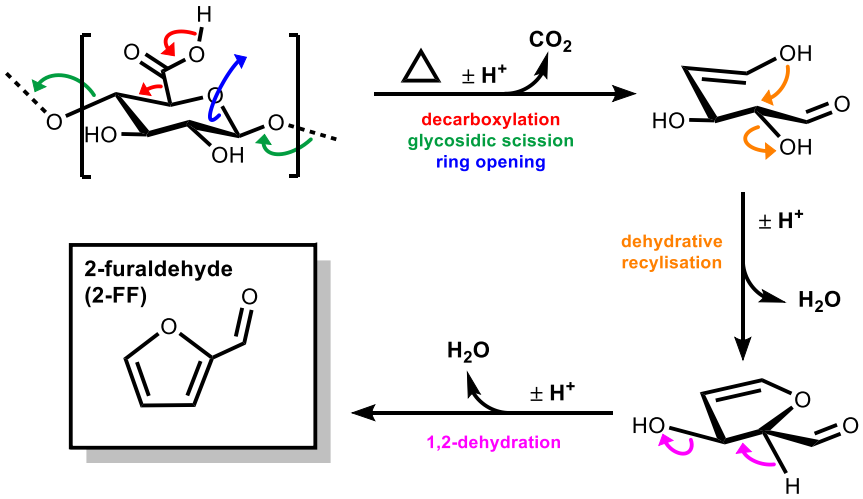

Figure 4.47 An idealised mechanism for the formation of 2-FF from polyuronic acid (such as **HAlg** or **HPec**)

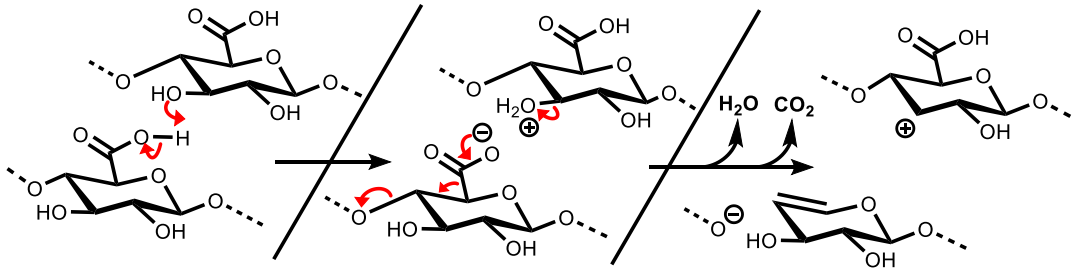

Figure 4.48 Elimination of H_2O and CO_2 from a polyuronic acid (such as **HAlg** or **HPec**) by an autocatalytic mechanism

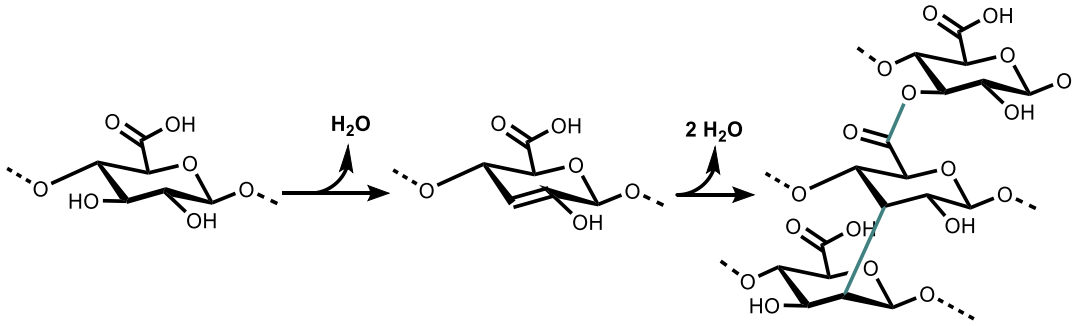

Figure 4.49 Low-temperature cross-linking of polyuronate polymer chains as a possible mechanism for the high levels of char formation[43]

Where 2-FF comprises the most significant product of the volatile organic phase of uronides bearing a free-acid group, they are usually accompanied by the formation of compounds bearing a furanone-motif. The furanone-derived molecules are interesting as their occurrence possibly signifies a competitive but closely-related pathway to the formation of 2-FF. For example, a speculative mechanism might include a cyclising deformylation at C1 in place of a dehydration, as illustrated in Figure 4.50. Such a mechanism would explain why the relative proportions of furanone molecules compared to furaldehyde species is higher in mono-uronides than their polymeric counterparts, as the readily opened ring structure of monosaccharides more easily facilitates elimination of the C1 carbon. Elucidating further the conditions that favour furanone formation over 2-FF might provide valuable insight into the overall mechanism of uronide thermolysis, and additional work is recommended in Section 4.8.1.2. On a related note, the pyrolysis of uronides did not give rise to peaks associated with the formation of reductic acid, despite this compound featuring prominently in the analogous hydrothermal degradation of the uronides - see Appendix C. The formation of carbocyclic reductic acid (as opposed to furan-based ring) signifies that an entirely different mechanism is active when thermolysis is carried out in H_2O, highlighting the requirement for further work to discern the role of water in controlling the thermal degradation pathways available to uronides.

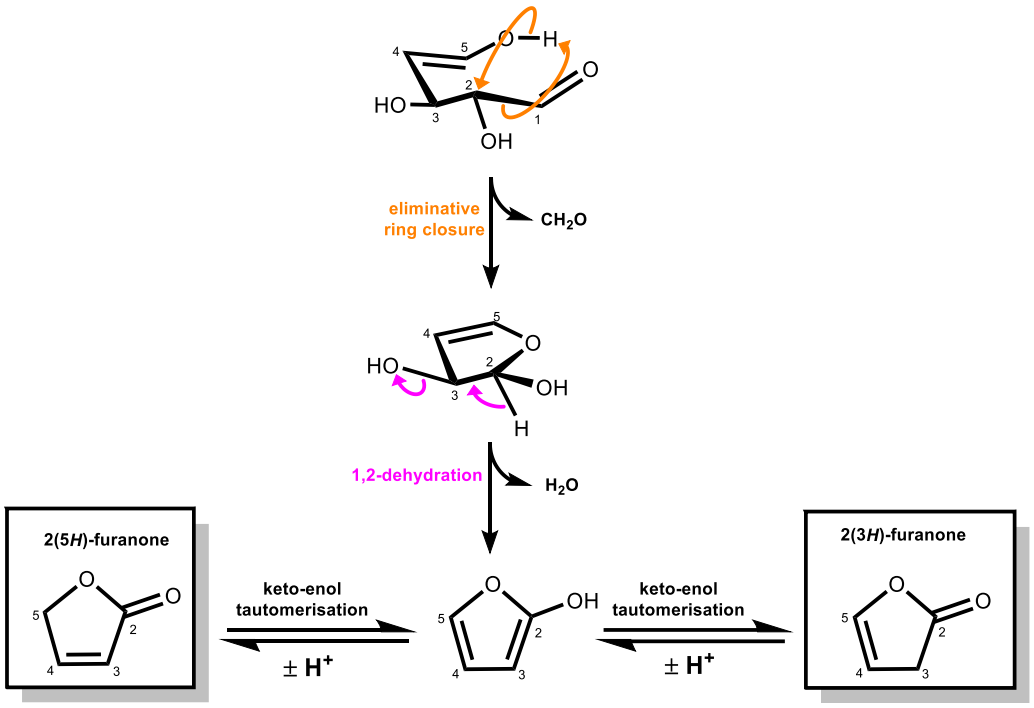

Figure 4.50 A potential mechanism for the formation of furanone compounds following initial decomposition of a polyuronic acid (such as **HAlg**)

Finally, it is worth commenting briefly on the potentially differences in mechanism between the (nominally) anhydrous pyrolysis of uronides conducted here, and the equivalent hydrothermolysis (discussed briefly in Chapter 2). In this regard, the formation of intramolecular esters between the uronic carboxylic acid moiety and hydroxyl groups (*lactonisation*) provides an edifying case study. **HGlc** and **HGal** display similar behaviour in the pyrolysis environment as in the hydrothermal experiments described in Chapter 2, with the former readily giving rise to bicyclic furanurono-6,3-lactones and the latter being stereochemically forbidden from behaving in the same manner. Interestingly however, whilst both L-guluronic and D-mannuronic acids do display a tendency to lactonise under the conditions specified in Chapter 2, their polymeric counterpart (alginic acid) did not reveal significant peaks corresponding to uronolactone formation upon pyrolysis. Hence, it can be assumed that early rupture of the glycosidic bond is essential for the formation of a uronolactone (provided that the uronide in question possesses the necessary stereochemistry in the first place). The impact of metal ions on the corresponding lactonisation behaviour is considered in more detail in Section 4.6.2.8.

4.6.2 The metal mediated pyrolysis of alginates and related uronates

4.6.2.1 General comments on the metal-mediated pyrolysis of alginates and related uronates

The results presented in Section 4.5 demonstrate that the effect on thermal behaviour of binding a metallic countercation to alginate (or a related uronate) can be both dramatic and varied. Indeed, for all of the metals studied (Na^{+}, Mg^{2+}, Ca^{2+}, Sr^{2+}, Ba^{2+}, Co^{2+}, Ni^{2+}, Zn^{2+},

and Cu^{2+}), differences in the kinetics of thermolysis and selectivity towards various product fractions (volatile organic compounds, permanent gases, and char) were all noted relative to alginic acid. Such effects will be discussed in detail below, though it is worth highlighting a couple of overarching trends in the first instance. The differences in the thermal behaviours of metal alginates are perhaps most readily highlighted by comparison of T_i (the temperature marking the initiation of rapid pyrolysis), as plotted in Figure 4.51. Here it can be seen that Cu^{2+} (T_i = 164 ± 5 °C) appears to stand alone from the other metals in its ability to promote the onset of rapid pyrolysis at a temperature below that of **HAlg** (T_i = 173 ± 3 °C).

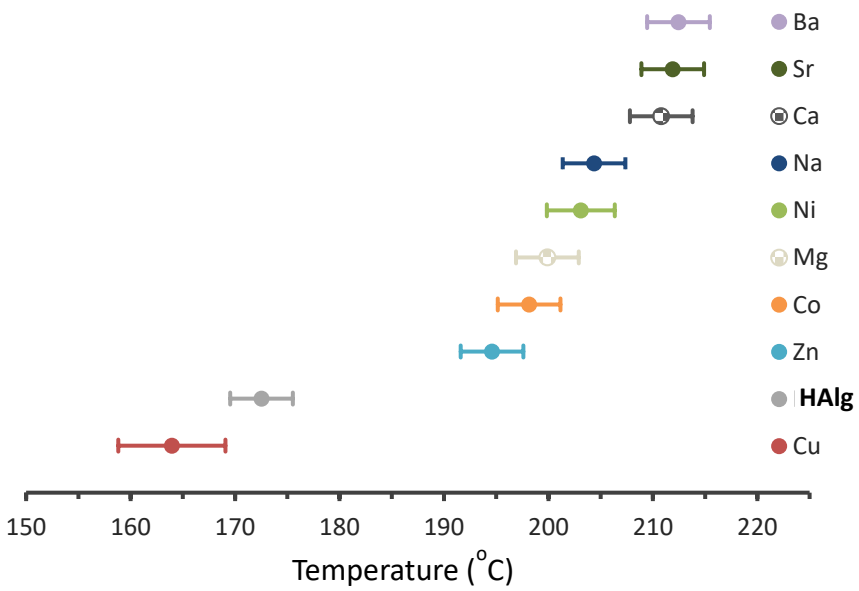

Figure 4.51 The values of T_i measured for **HAlg** and a variety of metal alginates when heated at 10 °Cmin^{-1} under He.

The relative stabilities of the alginate salts can therefore be summarised as below:*

(least stable) ⟶ *(most stable)*

$$\mathbf{Cu^{2+} < H^{+} << Zn^{2+} < Co^{2+} < Mg^{2+} < Ni^{2+} < Na^{+} < Ca^{2+} \approx Sr^{2+} \approx Ba^{2+}}$$

Such a trend has marked similarities with those observed in the thermal behaviour of metal carboxylate species (such as oxalates and related oxysalts, as discussed extensively in Appendix Q), where Cu^{2+} also appears to considerably decrease thermal stability in stark contrast to alkali and alkali earth metals.

Aside from the differences to the degradation kinetics, it is also interesting to observe the effect of the aforementioned metal ions on the char yield arising from alginate pyrolysis. Whilst superficially it can be observed that all metal alginates have higher relative residual

* The H-, Na-, Ca-, and Cu(II)-pectinates studied were also found to conform to the same trend

mass at 500 °C than does alginic acid (see Figure 4.52), if the weight of the metal component of the sample is deducted (known from elemental analysis of the starting material) a more informative picture of the char yield is realised. This *metal-corrected char yield* is indicative of how much organic material remains unvolatilised from the original sample, and is marked with an "X" in Figure 4.52.

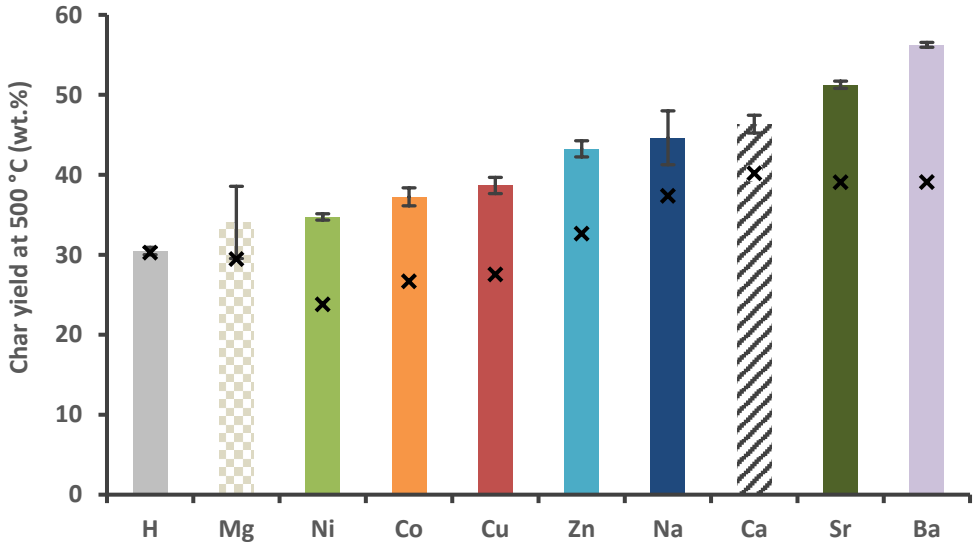

Figure 4.52 The char yield of alginic acid and various metal alginates following heating to 500 °C at 10 °Cmin^{-1} under He. The "X" in each case signifies the organic char yield, which is calculated by correcting for the mass of the metal ions in the original sample.

From studying the data presented in Figure 4.52, a relative order can be established for the amount of organic matter remaining for each alginate following pyrolysis:

(lowest char) ⟶ *(highest char)*

$$Cu^{2+} \approx Ni^{2+} \approx Co^{2+} < H^{+} \approx Zn^{2+} \approx Mg^{2+} << Na^{+} < Ca^{2+} \approx Sr^{2+} \approx Ba^{2+}$$

Such a trend strongly indicates that d-block metals appear to play a role in impeding formation of the carbonaceous alginate char, again in contrast to the s-block ions that appear to have the opposite effect. Of course, the fate of the metals within the char structure may go some way to explaining such observations. Here, the PXRD analysis described in Section 4.5.2.5 reveals that d-block metal alginates seemingly give rise to metal and/or metal oxide deposits at relatively low temperatures, whilst the s-block ions yield carbonates, which were not detected until temperatures >> 500 °C. Again, there are parallels that can be drawn between the thermal behaviour of metal alginates and that of metal carboxylate salts, which show similar trends in terms of the fate of the metal ions (see Appendix Q for a full discussion of the latter compounds).

Finally, one of the most striking areas of contrast between the thermal behaviour of metal alginates at 500 °C can be seen in Figure 4.31, which compares the selectivity (by GCMS peak area) of the various fractions of volatile organic compounds detected during pyrolysis.

The distributions of, for example, small oxygenated compounds in the case of alkali and alkali earth metal alginates are radically different to the furaldehyde-rich pyrolysate of d-block metal alginates. The disparity in selectivities is most notable when comparing the greater than 14-fold increase in the yield of 2-FF from **Cu(II)Alg** (6.82 ± 0.22 mol.%) compared from **NaAlg** (0.48 ± 0.06 mol.%).[*] Naturally, there are many more nuanced differences to be found in the vast collection of Py-GCMS data (presented in full in Appendix O), and, indeed, in all of the alginate thermochemical data reported in Section 4.5.2. Collation of all of the branches of thermochemical evidence can then be utilised to inform a speculative mechanistic appraisal of metal-mediated alginate thermolysis (presented in Section 4.6.2.8). Ultimately, the (somewhat subjective) question of whether metal ions are a help or hindrance to uronide pyrolysis is addressed in Section 4.6.4.

4.6.2.2 The role of monovalent s-block metals in the pyrolysis of alginates

Monovalent s-block metals (specifically Na^+) are of particular interest when considering alginate thermochemistry as it is to these ions that the polymer is most commonly found to be bound in nature (see Chapter 5). It is striking, therefore, how the thermolysis profile of **NaAlg** differs from that of the free acid-form, with the onset temperature for rapid pyrolysis (T_i) being increased by some 30 - 40 °C in the presence of Na^+ (from 173 ± 3 °C to 206 ± 3 °C). The contrast can be further appreciated by studying the shape of the thermogravimetric traces (see Figure 4.25), which demonstrate that, despite the higher onset temperature, **NaAlg** thermally degrades with much greater rapidity than does **HAlg** with, for example, the mass loss rate at T_{max1} increasing from -4.8 wt.% min^{-1} (**HAlg**) to -8.3 wt.% min^{-1} (**NaAlg**). In some cases, such as experiments performed at higher heating rates or under conditions of less efficient heat transfer,[†] the two DTG peaks observed in the thermogram of **NaAlg** (signified by T_{max1} and T_{max2}) can coalesce into a single event exhibiting an extremely high mass loss rate of >> -10 wt.% min^{-1} (see Appendix T and examples in the literature).[83,84,87] TGA-MS experiments (see Figure 4.26) demonstrate that the period of rapid mass loss is accompanied by an equally high rate of release of H_2O and CO_2.

The combination of delayed onset and high mass loss rate observed in the pyrolysis of **NaAlg** may go some way to explaining the surprising behaviour of the resulting char, which demonstrates extreme intumescence during the period of rapid pyrolysis (see Figure 4.30). It is possible, therefore, that the Na^+ ion stabilises the alginate against pyrolysis until a suitably high temperature that the polymer has softened considerably. At T_i, the rapid release of H_2O and CO_2 within the soft polymer matrix could explain the expansion witnessed for **NaAlg** but not seen in alginates decomposing at lower temperatures (**Cu(II)Alg** and **HAlg** for example) or at lower mass loss rates (**CaAlg**, **SrAlg**, and **BaAlg** for example) (see Figure 4.53). The swollen char remains stable until around 600 °C, after which point it collapses, accompanied by the formation of crystalline Na_2CO_3. Other

[*] The values for yield of 2-FF are quoted in mol.% per mono-uronate unit of the polymer.

[†] Less efficient heat transfer could be brought about by an increase in sample mass or particle size, or by changes to the TGA apparatus (including the furnace or type of sample pan).

authors have also noted the unusual intumescence of Na-uronides and the formation of expanded, yet highly stable, chars matrices, and this topic is suggested for further investigation in Section 4.8.1.4.[72,84]

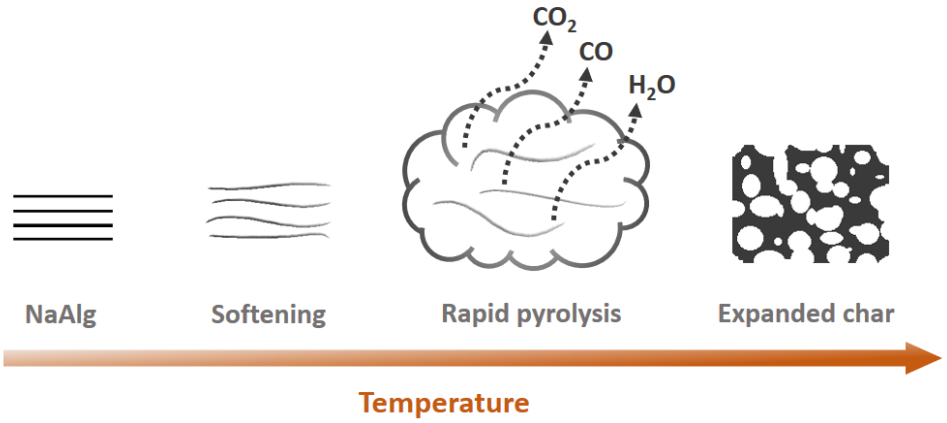

Figure 4.53 A possible model for the formation of expanded char in the pyrolysis of **NaAlg**

With regards to the products released during pyrolysis of alginates, the tentative mass balance depicted in Figure 4.35 demonstrates that, at 500 °C the sodium-coordinated alginate is predominantly decomposed into CO_2 (34.3 ± 0.4 wt.%), H_2O (36.7 ± 7.3 wt.%) and organic char (21.7 ± 4.7 wt.%). The yields of CO_2 and H_2O are therefore the highest of those measured, with 1.36 ± 0.03 and 3.57 ± 0.71 molecules of each being released, respectively, per uronate unit of the polymer. The higher levels of organic char (greater than twice as much as, for example, **HAlg** under the same conditions) might be attributable to the formation of the stabilised structure discussed above. However, the char of **NaAlg** cannot be as carbon-rich as that of **HAlg**, as presumably such a situation would manifest a considerable decrease in the yields of volatile organic species, which does not appear to be the case. Indeed, Py-GCMS experiments (whilst only semi-quantitative) demonstrate that **NaAlg** generates around 80 % of the normalised GC total peak area relative to **HAlg**. Despite the similar yields, however, Figure 4.31 shows how different the relative compositions of the two sets of pyrolysates are. In this regard, **NaAlg** can be seen to generate much higher levels of small oxygenated molecules, including acetol, diacetyl, and methyl pyruvate (see Figure 4.54), which form 21.69 ± 0.16, 7.37 ± 0.08, and 6.58 ± 0.26 % of the total GC peak area, respectively. Conversely, that data in Figure 4.31 (in Section 4.5.2.6) illustrates the very low selectivity of **NaAlg** towards furaldehyde-based molecules under pyrolysis conditions, in contrast to other alginate salts and **HAlg**. Indeed, Figure 4.32 demonstrates that yield of 2-FF originating from **NaAlg** is the lowest for any of the metals alginate studied. Further analysis (see Appendix O) also confirms that **NaAlg** does not give significant yields of any volatile organic species until well above 250 °C (under the flash pyrolysis conditions in the Py-GCMS unit).

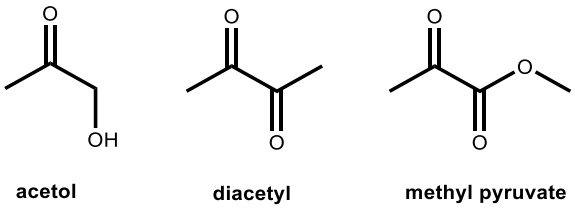

Figure 4.54 Principle volatile organic products liberated by **NaAlg** at 500 °C

Finally, it is worth noting that, whilst this section has been dedicated to the thermochemistry of **NaAlg**, preliminary results indicated that the equivalent potassium salt, **KAlg**, displayed clear similarities, particularly with regards to the TGA profile and char properties. However, difficulties in the preparation and characterisation of **KAlg** prohibited the full suite of thermal methods from being implemented within the available time, and further work is recommended to confirm fully the degree of apparent similarity with **NaAlg**.

4.6.2.3 The role of divalent s-block metals in the pyrolysis of alginates

As was noted in Section 4.6.2.1, the TGA analysis of **Ca-**, **Sr-**, and **Ba-Alg** revealed that their respective cations stabilise the uronide polymer against rapid pyrolysis, all displaying onset temperatures higher than any of the other metals studied (T_i = 208 – 215 °C) including Na^+ (see Section 4.6.2.2). In contrast to Na^+, however, pyrolysis for the divalent s-block alginates proceeds very slowly, indicating that these cations significantly retard the decomposition and volatilisation of alginate. Further evidence of this retardation effect can be garnered by considering the mass remaining at 500 °C, which again is higher for Ca-, Sr-, and Ba-alginate than any other metal (see Figure 4.27). Notably, however, the three alginates all appear to act in a roughly similar manner, all exhibiting near-identical temperatures and mass loss rates during significant degradative events (see Table 4.2) and (once the mass of metal in the starting material has been corrected for) all giving near-identical organic char yields. The remarkably similar behaviour of all three alginates is therefore evidence of a common degradative mechanism existing between them (discussed further in Section 4.6.2.8).

In order to provide a point of reference for the thermal behaviour of **Cu(II)Alg** (discussed in Section 4.6.2.5), **CaAlg** was subjected to more in-depth analysis, particularly exploring the structure of the residual char at various temperatures. The results of these experiments (presented in Figure 4.29) demonstrated that absorbances in the FTIR assigned to the vibrations of the -COO^- moiety (1589 and 1412 cm^{-1})[101,102] remained virtually unchanged within the char until at least 400 °C, suggesting that decarboxylation of the Ca^{2+}-bound uronide had not occurred. In the temperatures leading up to 600 °C, the same peaks were found to disappear, accompanied by a small mass loss event and formation of $CaCO_3$ within the residual material. Contrastingly, the absorbances at 1025 cm^{-1} (C-O stretches) and 1080 cm^{-1} (OCO_{ring} vibration),[101,102] were significantly reduced in intensity at temperatures between 200 - 250 °C, indicating that extensive dehydration and possibly glycosidic-bond rupture occurred during that stage. The stabilisation of divalent s-block metal alginates against decarboxylation is a theme that will be returned to again in the mechanistic discussion of Section 4.6.2.8.

The products arising from the pyrolysis of **CaAlg** at 500 °C are best summarised by reference to the mass balance in Figure 4.35. Here it can be seen that, whilst yields of CO_2 (30.36 ± 1.75 wt.%), H_2O (27.57 ± 5.51 wt.%), and CO (3.06 ± 0.02 wt.%) are comparable to those from **NaAlg** and **Cu(II)Alg**, the yield of organic char from **CaAlg** is considerably larger (32.90 ± 0.76 wt.%).[*] Accordingly, the normalised total GC peak area from **CaAlg** at 500 °C (a semi-quantitative measure of the quantity of organic volatile material released during pyrolysis, see Appendix L) is significantly diminished, being around half that of **HAlg**. Of the volatile organic compounds that are released, Figure 4.31 illustrates the high selectivity towards small oxygenated species (according to their % by GC peak area), including: acetone (8.06 ± 0.07), diacetyl (5.19 ± 0.03), acetic acid (5.46 ± 0.41), acetol (10.32 ± 0.05), and acetoin (6.57 ± 0.59), amongst many others (see Appendix O). Comparatively, yields of 2-FF are very low for **CaAlg** (0.72 ± 0.05 mol.% and 7.97 ± 0.11 % by GC peak area at 500 °C), as shown in Figure 4.32. Preliminary Py-GCMS experiments conducted on samples of **SrAlg** and **BaAlg**, whilst not assessed quantitatively, indicated strong similarities in their product spectrum relative to those from **CaAlg**.

Interestingly, whilst the discussion in this section has focussed on the thermal behaviour of the heavier Group II alginates, Mg-bound alginate (**MgAlg**) displayed a number of significant differences. For example, relative to **CaAlg**, **MgAlg** demonstrated a lower onset temperature for rapid pyrolysis (see Figure 4.51 and Table 4.2), a smaller yield of organic char (see Figure 4.52), and a volatile organic product distribution richer in 2-FF and lower in small oxygenated molecules (see Figure 4.31). Indeed, the behaviour of **MgAlg** across all of these thermochemical experiments is much more akin to the d-block metals discussed in Section 4.6.2.4 than the s-block ions presented in this section. Suggestions as to the mechanistic origins of the differences in thermolysis behaviour between Mg^{2+} and the heavier s-block alginates are subsequently made in Section 4.6.2.8.

4.6.2.4 The role of d-block metals in the pyrolysis of alginates

It can be readily observed, when reviewing the results of the thermochemical experiments in Section 4.5, that **Cu(II)Alg** appears to behave in a radically different manner to the other d-block alginates studied (namely **Co(II)-**, **Ni(II)-**, and **Zn(II)-Alg**). Consequently, the next section (Section 4.6.2.5) is dedicated entirely to discussions on Cu(II)-mediated decomposition of alginates, and the matter is not considered here. With regards to Co(II)-, Ni(II)- and Zn(II)-alginates, there is a good degree of similarity between their thermochemical behaviours (see Table 4.2 and Figure 4.31), and clear distinctions from their s-block metal counterparts (discussed previously in Section 4.6.2.2 and 4.6.2.3). For example, the d-block metals (T_i = 198 ± 3 °C, 203 ± 3 °C, and 195 ± 3 °C for **Co(II)-**, **Ni(II)-**, and **Zn(II)-Alg** respectively) clearly inhibit the onset of rapid pyrolysis compared to **HAlg** (T_i = 173 ± 3 °C), but not quite as severely as the heavier divalent s-block metals (T_i ≈ 212 °C). A distinct feature of the ensuing thermodegradative profile of the d-block alginates is that they exhibit a secondary period of rapid pyrolysis, albeit with around half of the mass loss

[*] Note that the organic char yield measured for CaAlg from Py-GCMS analysis is slightly lower than that obtained from TGA owing to differences in the heating rate of the two techniques.

rate found in the initial stage.* The secondary stage of rapid pyrolysis for **Co(II)-**, **Ni(II)-**, and **Zn(II)-Alg** (characterised by T_{max2} temperatures of 451 ± 3 °C, 389 ± 3 °C, and 421 ± 3 °C respectively) is conceivably a consequence of degradation of the char structure formed in the first period. Hence, this secondary stage might be evidence that the char formed initially by the d-block alginates is inherently unstable (in contrast to those of the s-block alginates) or that the metals themselves go some way to promoting the char degradation at higher temperatures or, indeed, a combination of both of these factors. Either way, the d-block metals (especially Ni^{2+}) give rise to reduced levels of organic char than **HAlg**, and much less than that of the s-block alginates (see Figure 4.52). Furthermore, preliminary experiments also indicated that crystalline deposits of Ni^0, Co^0 and ZnO found to form from the thermolysis of their parent alginates, do not appear until after the secondary period of rapid pyrolysis has taken place.

With regards to the products of pyrolysis, **Co(II)-**, **Ni(II)-**, and **Zn(II)-Alg** all display considerable similarities. For example, all three metals induce formation of approximately similar yields of 2-FF from the alginate polymer (2.19 ± 0.14 mol.%, 2.44 ± 0.1 mol.%, and 2.86 ± 0.19 mol.% at 500 °C for Co(II), Ni(II), and Zn(II) respectively) and over a similar temperature profile (see Figure 4.32). These yields of 2-FF (2-3 mol.% at 500 °C) are markedly reduced compared to the equivalent values for **Cu(II)Alg** and **HAlg** (6-7 mol.% at 500 °C), but a considerable increase relative to **NaAlg** and **CaAlg** (<< 1 mol.% at 500 °C). As a consequence of their predisposition towards 2-FF formation, the **FF**-class (furfural-derivatives) dominates the Py-GCMS peak area of the d-block metal alginates, and, indeed, all three show mutually similar distributions across all of the other classes too (see Figure 4.31).† The most distinct deviation from this rule can be found in the greatly increased formation of aromatic compounds (particularly toluene and xylene) in the case of **Ni(II)Alg** over **Zn(II)-** and **Co(II)-Alg**. The origin of the aromatics from **Ni(II)Alg** is, as yet, unknown, but may be related to the enhanced levels of char degradation exhibited by the compound, as discussed above.

Taking all of the evidence in this section into account, the d-block metals (excluding Cu^{2+}) may be considered to induce thermochemical behaviour in alginates that is intermediate between s-block ions and the (metal-free) H^+ form. It is argued in Section 4.6.2.8 that such behaviour can be explained by reference to the reduction potential of the metal ions in question, and certainly the appearance of metallic Ni and Co in the char of **Ni(II)Alg** and **Co(II)Alg** gives credence to this hypothesis. The question remains, however, why does **Cu(II)Alg** behave in such a radically different manner to its d-block counterparts, and that question is addressed in part in the following section.

---

* For **Ni(II)Alg**, the slower secondary stage of rapid pyrolysis overlaps with the fast first stage, and it has not been possible to deconvolute the two to provide a clear onset temperature for the former event. The two stage are better separated in the cases of **Co(II)Alg** and **Zn(II)Alg** and hence secondary stage onset temperatures can be easily measured.

† It should also be pointed out that **Ni(II)Alg** exhibits the highest normalised total peak area (see Appendix O) compared to **Co(II)Alg** and **Zn(II)Alg**, hence the enhanced aromatic molecules are known to be forming in addition to (and not at the expense of) the other classes.

4.6.2.5 The role of Cu^{2+} in the pyrolysis of alginates

Whilst the thermochemistry of **Co(II)-**, **Ni(II)-**, and **Zn(II)-Alg** were discussed simultaneously in Section 4.6.2.4, the analogous behaviour of **Cu(II)Alg** is sufficiently different so as to warrant a detailed analysis in its own right. In this regard, the first observation to mark out Cu^{2+} as being unique in its influence on the thermal behaviour of alginate, compared to other d-block metals (and, indeed, any of the metals studied in this chapter), is the remarkably low temperature required to initiate rapid pyrolysis (T_i). For **Cu(II)Alg**, T_i is 164 ± 5 °C and, as can be seen in Figure 4.51, Cu^{2+} is therefore the only metal ion to induce a lower onset for pyrolysis of the alginate polymer relative to the free acid form (T_i for **HAlg** = 173 ± 3 °C). The shape of the thermolysis profile for **Cu(II)Alg** (Figure 4.25) then broadly follows that of **HAlg** (albeit slightly offset towards lower temperatures), displaying two significant thermal events, T_{max1} (200 ± 4 °C) and T_{max2} (237 ± 6 °C), with the second significantly more rapid than the first (Rate[T_{max1}] = -3.9 ± 0.5 wt.% min^{-1}, Rate[T_{max2}] = -7.1 ± 0.5 wt.% min^{-1}). Simultaneous TGA-MS experiments (see Figure 4.26) indicate that the profiles of CO_2 and H_2O formation roughly trace the same bimaximal profile, but that the release of 2-furaldehyde (2-FF) is more associated with T_{max2}.

In order to gain a further understanding of the changes occurring within the **Cu(II)Alg** matrix during the period of rapid pyrolysis, a series of TGA experiments was conducted with an isothermal heating period at temperatures before, during, and after the thermal events described above. Following the experiments, the char was recovered from the TGA apparatus and analysed by FTIR and PXRD (see Section 4.5.2.5). These experiments revealed that absorbances in the FTIR of **Cu(II)Alg** assigned to vibrations of the carboxylate moiety (1588 and 1399 cm^{-1}) significantly decrease in intensity by 200 °C, with the synchronous appearance of a broad peak at 1700 cm^{-1}, signifying decarboxylation and the formation of new double bonds.[81] Furthermore, the period up to 200 °C also led to the reduction in signal intensity from absorbances at 1025 cm^{-1} (C-O stretches) and 1080 cm^{-1} (OCO_{ring} vibration),[101,102] indicating dehydration and rupture of the glycosidic bond. As the temperature is increased further, all of the signals begin to reduce in intensity until, by 600 °C, the spectrum is virtually featureless. Simultaneously, peaks corresponding to Cu^0 appear in the PXRD of the **Cu(II)Alg** chars from as low as 200 °C, growing significantly in both strength and definition to 250 °C, and then steadily thereafter. The results from the isothermal studies of **Cu(II)Alg** are therefore in stark contrast to the equivalent experiments performed for **CaAlg** (also reported in Section 4.5.2.5).[*] The appearance of Cu^0 at very low temperatures in the char of **Cu(II)Alg** signifies a reduction of the Cu^{2+} starting state. Whilst it remains possible that the Cu^0 forms through a reaction of Cu^{2+} with the residual carbonaceous char or liberated CO,[112,113] it is argued in Section 4.6.2.8 that the observed reduction is part of the primary degradation mechanism of **Cu(II)Alg** (with strong similarities to other Cu(II)-carboxylate salts, as described in Appendix Q).

[*] For the Ca^{2+}-coordinated polymer, the FTIR signals found in the starting material persisted to much higher temperatures, and crystalline material (in the form of $CaCO_3$) was not detected until 600 °C.

With regards to the products of pyrolysis, and particularly the tentative mass balance at 500 °C depicted in Figure 4.35, **Cu(II)Alg** also displayed several notable features. Whilst the yields of CO_2 (29.9 ± 2.7 wt.%), H_2O (31.8 ± 5.9 wt.%), and CO (6.4 ± 0.1 wt.%) were not too dissimilar from those from **NaAlg** and **CaAlg** (with all three being slightly higher than **HAlg**) the yield of organic char (21.7 ± 4.7 wt.%) was significantly reduced compared to alginic acid and the s-block alginates. Arguably, however, the most interesting result of the mass balance calculations for **Cu(II)Alg** is the yield of 2-FF, as derived from Py-GCMS analysis. Here it can be seen that Cu^{2+}-bound alginate demonstrates a very high selectivity for 2-FF formation in both absolute (6.82 ± 0.22 mol.%, see Figure 4.32) and relative (47.14 ± 0.91 % by GC peak area, see Figure 4.31) terms, slightly higher than those exhibited by metal-free alginic acid. Impressively, this relatively high-yielding release of 2-FF by **Cu(II)Alg** reaches a maximum value at around 300 °C,[*] by which stage other metal-alginates have barely begun to liberate the compound (see Figure 4.32). Indeed, data in Figure 4.33 demonstrates that, at temperatures exceeding 300 °C, the selectivity for 2-FF from **Cu(II)Alg** (by GC peak area) actually begins to decrease as secondary products are generated from degradation of the remaining material (see Figure 4.34). Such secondary products (listed in full in Appendix O) include 2-(5*H*)-furanone (and associated tautomers), diacetyl, and 1,2-cyclopentanedione (see Figure 4.55).

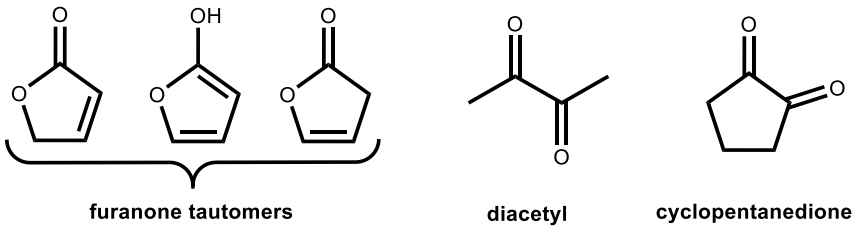

Figure 4.55 Significant secondary volatile organic products yielded from the pyrolysis of **Cu(II)Alg** at 500 °C.

In Chapter 3, a set of experiments was performed in order to demonstrate the close binding between Cu^{2+} and the uronide carboxylate moiety. It is therefore reasonable to assume that the thermochemical behaviour arising from **Cu(II)Alg** described in this section has its origins in that Cu^{2+}-carboxylate coordinative interaction. The potential mechanistic implications of the presence of Cu^{2+} in the alginate matrix are analysed in Section 4.6.2.8, and the potential relevance to the industrial-scale pyrolysis of uronide-rich biomass is discussed in Section 4.6.4.

4.6.2.6 The influence of stereochemistry on the metal-mediated pyrolysis of alginates and related uronates

The work in Chapter 3 elucidated significant differences in the metal binding behaviour of various mono-uronates depending on their stereochemistry. It might be a reasonable, therefore, to assume some degree of difference in the product yields from the pyrolysis of the metal-uronide compounds studied based on the identity of the parent uronic acid.

[*] The release of 2-FF by Cu(II)Alg appears to occur at a slightly higher temperature in the Py-GCMS than in the TGA-MS. However, such an observation is consistent with the heating rate being many orders of magnitude higher in the former technique compared to the latter.

However, such a hypothesis does not appear to be born out. For example, the yield of 2-FF for **Cu(II)Pec** at 300 °C (4.93 ± 0.10 mol.%C)* is virtually identical to that derived from **Cu(II)Alg** under the same conditions (4.81 ± 0.32 mol.%C). The same can also be said of the equivalent Na- and Ca-compounds. In a similar vein, Chapter 5 presents data from the pyrolysis of seven alginate polymers, all with different stereochemical compositions (with differing ratios of mannuronate:guluronate units (**M**:**G**)), but all of which behave in a nearly identical manner (when bound to the same counter cation). Finally, as can be seen in Figure 4.41, the yields of 2-FF for salts of mono-D-galacturonate and mono-D-glucuronate differed only when the coordinated metal ion was varied (from Na^+ to Ca^{2+} and Cu^{2+}), and not significantly when the uronate was changed.†

When all of the results above are viewed in context, the potential role of stereochemistry in influencing the pathway of metal-mediated uronide thermal decomposition is somewhat relegated. Indeed, even when stereochemistry was found to play a key role in dictating the thermolysis behaviour of the free acids (see, for example, the differences between **HGal** and **HGlc** or between **HPec** and **HAlg** reported in Section 4.6.1.2), the same was not true of the metal salts. Indeed, the experiments in this chapter prove that the identity of the metal ion in a uronide complex is far more influential on the subsequent thermochemical behaviour than the stereochemistry of the uronate unit to which it is bound. Hence, it can be assumed that the coordinated counter-cation dictates a set of thermochemical mechanistic steps that are common across all uronates, a notion discussed further in Section 4.6.2.8.

4.6.2.7 The influence of degree of polymerisation on the metal-mediated pyrolysis of alginates and related uronates

Whilst the work presented here does not rigorously probe the influence of the degree of polymerisation on subsequent pyrolysis behaviour of uronides as such a study would require a set of well-defined mono-, oligo, and poly-meric uronides. However, acknowledging the fact that such compounds were not available for study, taking the results from the pyrolysis of monomeric Na-, Ca-, and Cu(II)- salts of glucuronate and galacturonate and comparing them to the equivalent polyuronides is the next best option. The first observation, in this regard, is that the absence of the glycosidic bond in the mono-uronate salts facilitates the onset of rapid pyrolysis of **MGlc** and **MGal** at lower temperatures that the equivalent **MAlg** (as can be seen by comparing the TGA traces in Figure 4.38 and Figure 4.39 with those of Figure 4.25). With regards to the formation of 2-furaldehyde, the mono-uronates generally display approximately two-fold higher yields than their polymeric alginate counterparts (see Figure 4.41). There are also clear differences in the distribution of the various classes of products for **MGal** and **MGlc**

* The yields of products must be expressed in mol.%C for pectin and pectinate salts because a standard formula unit could not be defined for these compounds in the same manner as the alginate and mono-uronate salts.

† Interestingly, the presence of a metal ion in the uronate salt also appears to heavily supress the tendency of **HGlc** to form the uronolactone, GlcLac (discussed in Section 4.6.1.2). **HGal**, on the other hand, does not form a uronolactone in either the free-acid or salt form.

compared to **MAlg**, but an in-depth analysis is beyond the scope of these discussions. Instead, it is sufficient to note that the glycosidic bond in polyuronates serves to stabilise the polymer and influence the favourability of certain pyrolytic pathways, including inhibiting the release of 2-FF. Further work is recommended in Section 4.8.1.2 to gain a more finely tuned understanding of these important effects.

4.6.2.8 Tentative mechanistic interpretation of the metal-mediated pyrolysis of alginates and related uronates

Having provided possible mechanistic interpretations of the observed thermochemical behaviour of mono- and poly-uronic acids (see Section 4.6.1.3), the aim of this section is to further rationalise the role played by metal ions in such processes. As before, it is not possible to fully explain the myriad of complex observations reported throughout Section 4.6.2, but some key trends are deserving of particular attention, and are discussed below.

Firstly, the trend in the temperature (T_i) at which rapid pyrolysis is instigated for alginates (and, indeed, pectinates) was highlighted in Section 4.6.2.1, and indicated that all of the metal ions studied (except Cu^{2+}) serve to increase the thermal stability of the polymer. The trend was likened to those previously derived in the literature for metal carboxylate salts (including malonates and oxalates - described in detail in Appendix Q). In order to understand the trend in alginate T_i values, it is worth re-calling from Section 4.3.3.1 that the low-temperature pyrolysis behaviour of polyuronic acids is believed to originate from their ability to decarboxylate. It might therefore be reasonable to assume that the thermal stability of a metal-uronate is based around the influence of the coordinated cation on decarboxylation. Most metal ions act to inhibit decarboxylation (see Appendix Q) according to the following approximate order:

(*increasing stability against decarboxylation)* ⟶

$H^+ \approx Cu^{2+} < Co^{2+} \approx Ni^{2+} \approx Zn^{2+}$ < alkali metals ≈ alkali earth metals

Whilst there is no established consensus for the cause of the instability of copper(II) carboxylates, one might assume that relatively easy reduction of the Cu^{2+} species has a part to play (see the table of reduction potentials in Appendix Q for reference). Hence, it is possible that Cu^{2+} facilitates a *Hofer-Moest* type decarboxylation in **Cu(II)Alg**, whereby the metal acts as a sink for the $2e^-$ liberated by rupture of the C-C bond (see Figure 4.56a).[114] Indeed, Stapley and BeMiller have demonstrated that just such a mechanism is active in the electrolytic degradation of D-glucuronic acid, albeit in an aqueous environment and with a Pt anode performing the role of the Cu^{2+} ion.[115] Furthermore the formal $2e^-$ reduction undertaken by Cu^{2+} according to the *Hofer-Moest* mechanism would also explain the observed formation of crystallites of Cu^0 within the char matrix of **Cu(II)Alg** at temperatures above 200 °C. Naturally, there are other variations on the *Hofer-Moest* mechanism that could be active, particularly the possibility of a homolytic scission of the carboxylate C-C bond leading to formation of a radical (see Figure 4.56b). In both hetero- and homo-lytic pathways, the ring-oxygen atom (adjacent to the site of decarboxylation) would serve to stabilise the resultant carbocation/radical by donating electron density to the electron deficient carbon atom (see Figure 4.57) and making both options feasible.[116] Evidence for homolytic thermal decarboxylation in other Cu(II)-carboxylates has been provided by

observations of a stepwise reduction of Cu^{2+} ($Cu^{2+} \rightarrow Cu^{+} \rightarrow Cu^{0}$) during thermolysis (see Appendix Q), though further work would be required to identify such behaviour in **Cu(II)Alg** (see Section 4.8.1.5). Despite the mechanistic uncertainty, it is clear that Cu(II)-promoted cleavage of the carboxylate C-C bond in alginates (be it homolytic or heterolytic) gives rise to a high-energy species in which further degradative steps would be expected to follow quickly. Accordingly, alginates bound to metal ions with more negative reduction potentials (Ni^{2+}, Zn^{2+}, and Co^{2+} for example), which less readily mediate decarboxylation, exhibit higher rapid pyrolysis onset temperatures. Similarly, alkali and alkali earth metals, which cannot exhibit redox chemistry under the conditions described, inhibit decarboxylation (and hence degradation of the alginate polymer backbone) to the maximal degree.

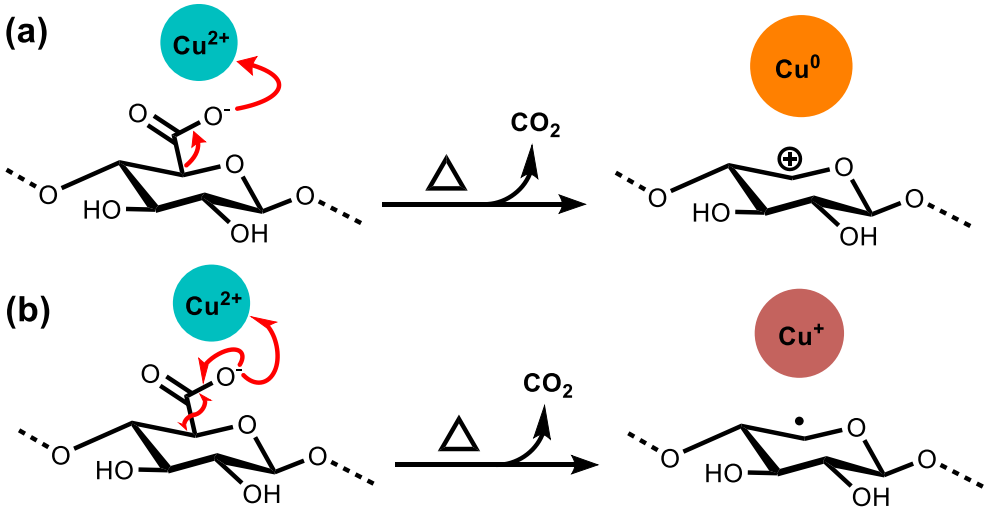

Figure 4.56 Thermally-induced Cu(II)-mediated decarboxylation of a polyuronate by (a) a (heterolytic) *Hofer-Moest* mechanism, or (b) a (homolytic) radical mechanism

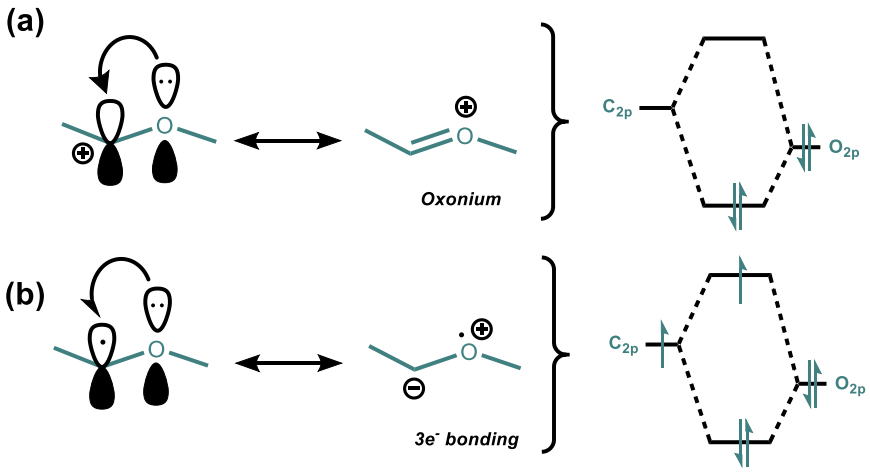

Figure 4.57 The stabilising influence of oxygen lone pair electrons on an adjacent carbon centre following decarboxylation by (a) heterolytic, or (b) homolytic bond cleavage

Considering this mechanism of metal-mediated uronide decarboxylation further, it is possible to explain some of the trends reported in Sections 4.6.2.2 - 4.6.2.5, pertaining to the pyrolytic formation of volatile organic species. Of particular note throughout those sections was the variation in the degree of selectivity towards the formation of 2-furaldehyde (2-FF) by different metal alginates. In all cases, with the exception of Cu^{2+}, every metal studied was found to decrease the yield of 2-FF relative to the parent **HAlg**, according to the observed trend:

(*Lowest yield of 2-FF)* ⟶ (*Highest yield of 2-FF)*

$$\mathbf{Na^{+} \approx Ca^{2+} < Mg^{2+} < Co^{2+} \approx Ni^{2+} < Zn^{2+} < H^{+} \approx Cu^{2+}}$$

The result is perhaps surprising given that, in studies by other authors under aqueous conditions, alkali, alkali earth, and d-block metals were all found to catalyse the conversion of various carbohydrates to 2-FF.[117–120] The question may therefore be asked, why does Cu^{2+} appear to stand alone in slightly increasing the yield of 2-FF from alginate relative to alginic acid (with even greater improvement observed for the Cu(II)-salts of pectinate, D-galacturonate, and D-glucuronate)? In this regard, it is conceivable that, following the Cu^{2+}-mediated *Hofer-Moest* mechanism described above, the remaining C5 backbone of the decarboxylated uronide is well-suited to form 2-FF after relatively few steps (see Figure 4.58). However, for different metal alginates, as the temperature required to facilitate decarboxylation increases, alternative reactions (particularly the cleavage of the glycosidic bond) begin to dominate, with the formation of a very different set of products. The extreme case of such *inhibited decarboxylation* is typified by **NaAlg**, which shows severely supressed yields of 2-FF, but an abundant array of small oxygenate molecules instead. A possible mechanism for the formation of one such small oxygenate, acetol, from **NaAlg** is provided in Figure 4.59, and demonstrates the consequences of preserving the carboxylate C-C bond to temperatures above the point of glycosidic scission.

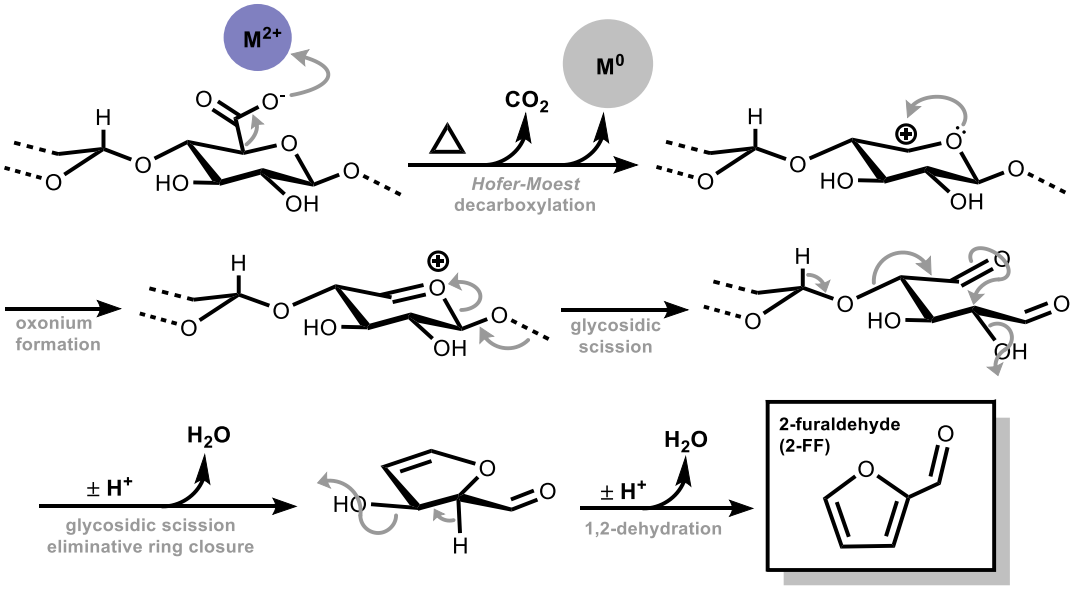

Figure 4.58 Formation of 2-furaldehyde (2-FF) from a polyuronate (such as alginate or pectinate) *via* a metal-mediated *Hofer-Moest* decarboxylation

The fate of the carboxylate moiety in the mechanism depicted in Figure 4.59 is the generation of sodium glyoxalate, which would likely react further to form a more stable sodium oxysalt (such as sodium oxalate for example).[121] The degradation of the stabilised sodium oxysalt at significantly elevated temperatures (> 600 ˚C) may account for the sudden formation of Na_2CO_3 under such conditions (see Appendix Q), as exemplified in Figure 4.60.[122]

Of course, whilst the reasons behind the contrast between Cu^{2+} and Na^+ in their effect on alginate thermolysis is easy to speculate on, extrapolating the hypothesis to the subtler differences between (for example) Ca^{2+} and Mg^{2+} or Co^{2+} and Zn^{2+} is much more difficult. Such explanations would require a detailed knowledge of how each metal ion catalyses or inhibits various competing pathways (decarboxylation, dehydration, glycosidic bond cleavage, ring opening, chain cross-linking, and so on), which is currently lacking. As such, the theoretical and microkinetic analysis of uronide thermolysis is highlighted as an area of priority for further investigations (see Section 4.8.1.2).

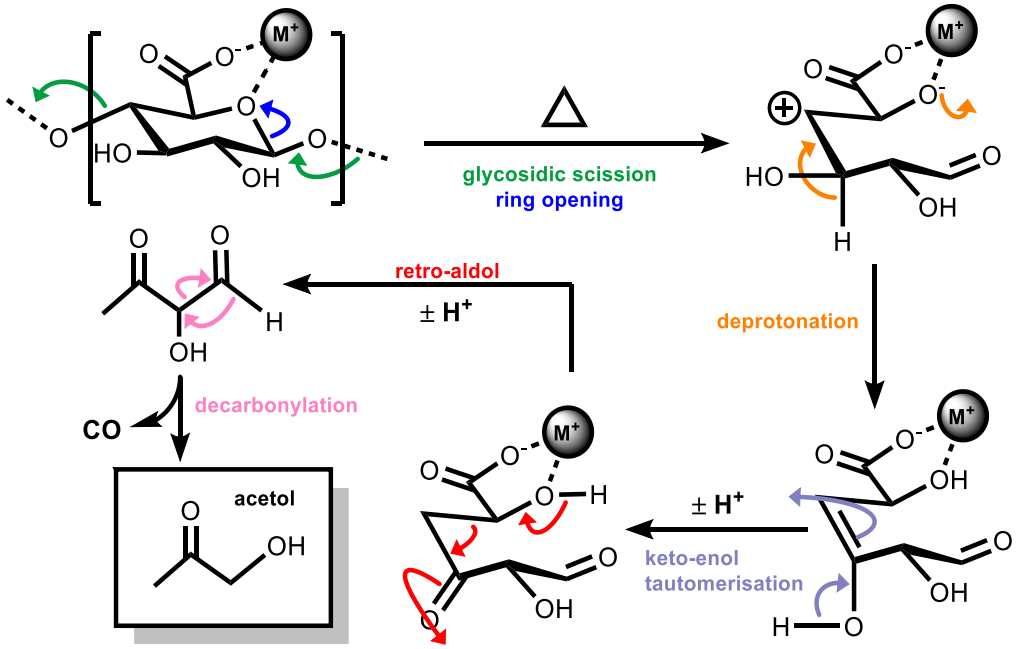

Figure 4.59 The pyrolytic formation of acetol from a polyuronide with a stabilised carboxylate moiety (such as **NaAlg**).

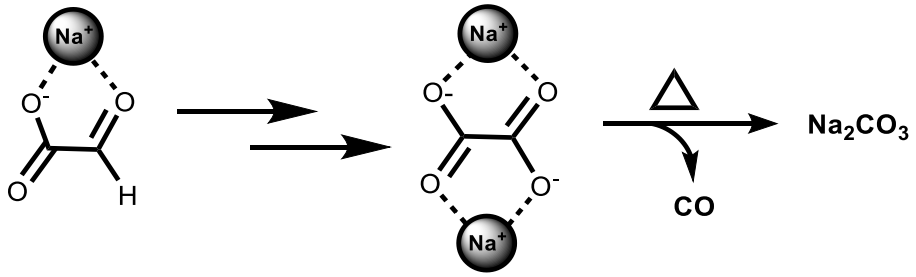

Figure 4.60 The formation of a stable sodium oxysalt (sodium oxalate for example) from sodium glyoxalate,[121] and subsequent decomposition to Na_2CO_3[122]

Finally, it is worth commenting on the mechanistic role of metal ions in the formation of uronolactones. The formation, or lack thereof, of uronolactones from polyuronides and their salts was a key result in this chapter, particularly because similar anhydrosugar formation is known to dominate the pyrolysis chemistry of, for example, cellulose (see Section 4.3.2.3). As **HAlg**, **HPec**, and **HGal** were not found to yield appreciable levels of the corresponding uronolactones (see Section 4.5.5), it is unsurprising that their metal salts did not either. More interesting, however, is the observation that coordination to Na^{+}, Ca^{2+}, or Cu^{2+} was found to prevent or diminish (in the latter case) the formation of GlcLac from mono-D-glucuronate. The explanation to this scenario can be found by recalling the results of Chapter 2, where uronolactone formation was shown to be prohibited in the aqueous environment upon neutralisation of the –COOH moiety. Hence, it can be concluded that the ring-closing esterification (and associated elimination of water) only occurs for uronic acids in the free acid form, and not when coordinated to a metal ion (see Figure 4.61).

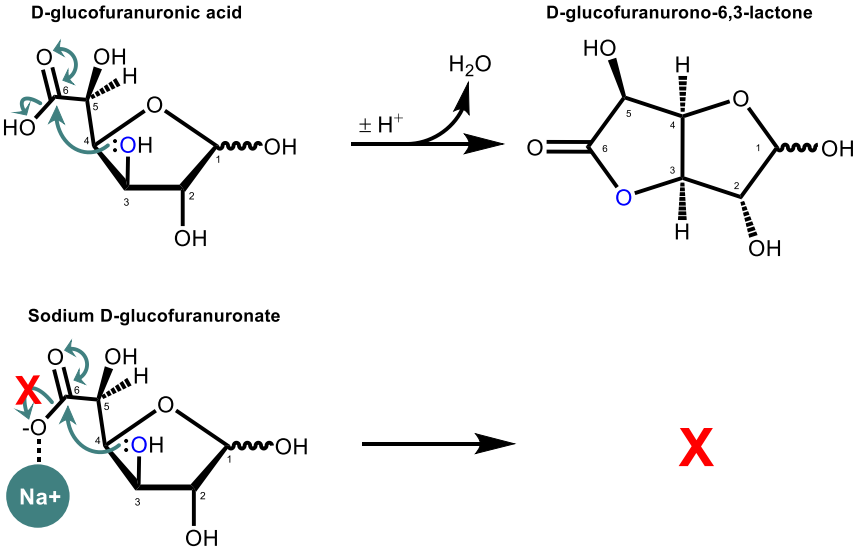

Figure 4.61 Metal-uronates (bottom) cannot undergo lactone formation *via* dehydrative cyclisation as the free-acid can (top)

Whilst there are a multitude of additional observations made throughout this chapter that warrant significantly greater mechanistic interpretation, such discussions are reserved for later work. Instead, it is more fruitful at this point to direct the discussion towards an appraisal of the practical significance of the results of this chapter, to which Section 4.6.4 is dedicated.

4.6.3 The role of additional variables in the pyrolysis of alginic acid, alginates, and related uronides

This chapter has focussed predominantly on the effect of varying the bound metal ion on the subsequent thermal behaviour of a uronide. However, in constructing such experiments, there are a vast number of additional variables that could have been investigated. Whilst these additional parameters were not studied systematically here, anecdotal consideration of their influence are summarised below for the purpose of informing future work:

- **The role of sample dimension**
  Sample dimension has been demonstrated elsewhere to be a key parameter in micropyrolysis, influencing both mass and heat transport.[3,21,48] Experiments described in Appendix L revealed that, for pyrolysis on the scale utilised in this chapter (10^{-4} – 10^{-2} g, 100 – 250 μm), small changes in either mass or particle size did not significantly affect the results of subsequent TGA or Py-GCMS studies.

- **The role of sample preparation**
  It is not common practice in the literature to discuss the physical "formulation" of a sample for analytical pyrolysis in any great detail, though such considerations might be important.[6] For example, a sample that has been centrifuged and air-dried, whilst identical in chemical formula, may differ considerably from a sample that has been filtered and vacuum-dried. Such differences in preparative methods were not investigated systematically here, though samples were treated in as consistent a manner as possible. However, in an interesting preliminary experiment, a commercial sample of **HAlg**, that was nominally identical to that used elsewhere in this chapter, was found to give an approximately 30 % increased yield 2-FF at 500 °C. The cause of the increase remains unclear, but it would be of interest to further define the parameters associated with the physical state of uronide samples arising from their preparation method, and understand the subsequent influences on thermochemistry.

- **The role of counter-anion**
  Though less frequently studied, anions as well as cations have been found to influence carbohydrate thermochemistry.[60,123] Naturally, the preparation of metal uronate samples required for a suitable metal salt to be included in the synthesis, with a sacrificial counter anion (see Sections 4.9.1.1). Whilst the counter anion is, in theory, removed in the washing process, a preliminary experiment was conducted to ensure that its identity was not of consequence to the subsequent thermolysis in the case of alginates. Here, it was found that changing the counter-anion from Cl^- to NO_3^- did not have an observable effect in either Py-GCMS or TGA experiments.

- **The role of thermal parameters**
  The versatility of the TGA and Py-GCMS apparatus allows for a great deal of variation in the thermal parameters used in a pyrolysis experiment. For example, the heating rate, residence time, ramp programme, and transfer-line temperatures can all be altered as required.[3] Some discussion of the rationale behind the chosen values for such parameters used in this chapter are provided in Appendix L. Of all of these thermal parameters, the heating rate is often cited as being the most critical.[41,50,124] Whilst changes to heating rate were not investigated systematically, some comparison can be made between the TGA experiments (heating rate = 10 °C min^{-1}, slow pyrolysis) and accompanying Py-GCMS experiments (heating rate = 120000 °C min^{-1}, flash pyrolysis). The most significant difference between the

slow and flash pyrolysis conditions appeared to be the amount of char generated from each experiment, with a much smaller yield in the latter case than the former. However, when the Py-GCMS experiment was repeated with the slow TGA heating rate, the same distribution of volatile organic products was found to form from **HAlg**, **Cu(II)Alg**, **CaAlg**, and **NaAlg**, albeit in much reduced yields. Hence, it can be generalised (pending a more detailed investigation) that a reduced heating rate favours alginate char formation, but without significantly affecting the mechanisms that lead to the release of volatile organic species. Similar observations have been reported in studies of the thermal degradation of various other carbohydrates.[41,50,125]

- **The role of pyrolysis environment**
  In conjunction with the thermal parameters (see above) the TGA and Py-GCMS apparatus also allow for considerable control of the environment in which the sample is pyrolyzed. For example, the atmosphere (air, He, N_2, H_2O, or vacuum) and flow (static or dynamic) may be altered to give vastly different results.[50,84] In the work conducted here, high purity helium was used to provide an inert gas flow (15 – 30 mL min^{-1}), with little variation. Preliminary experiments discussed in Appendix L indicated that exchanging the pyrolysis atmosphere for N_2 had little influence on the thermolysis of alginates below 300 °C, but at elevated temperatures, trace O_2 could cause catastrophic differences to arise. The presence of H_2O in the pyrolysis environment is a factor that is highlighted particularly for additional research in Section 4.8.1.7.

4.6.4 Synoptic appraisal of the thermolysis of uronides and their suitability for large-scale thermochemical treatment

The work in this chapter has sought to establish fundamental insight into the thermal degradative pathways of mono- and poly-uronides. Ultimately, however, the work was carried out in order to better establish how uronide-rich biomass may be upgraded through thermochemical processing. As such, it is worth reflecting at this stage as to which, if any, of the results in this chapter would be of benefit in an industrial pyrolysis process. In this regard, the mass balance derived for alginic acid (and its Na^+, Ca^{2+}, and Cu^{2+} salts) is especially helpful as, for the first time, it offers a quantitative (if approximate) overview of the likely solid, liquid, and gaseous yields to arise from pyrolysis. Taking the mass balance into account however, it is discouraging to see that around half of the mass of the uronide polymer is lost worthlessly as either CO_2 or H_2O in all cases. The next largest product fraction is the organic char, and, whilst the extremely high carbon content offers intrinsic value to the char, it is largely considered to be one of the least desirable products of pyrolysis. Hence, on first inspection, the pyrolysis of uronides does not appear to offer much in the way of tantalising industrial opportunity.

However, when the results reported in this chapter are inspected in more detail, there is some scope for optimism. Firstly, the extremely low degradation temperature of polyuronides – such as alginic acid, is remarkable within the field of biomass-derived polysaccharide thermolysis. Indeed, whilst **HAlg** was demonstrated here to have volatilised

around 50 wt.% of its mass by 300 °C, similar studies elsewhere indicate that cellulose is only just beginning to enter the rapid pyrolysis phase at this temperature. More impressive still are the high levels of 2-furaldehyde (2-FF) liberated between 200 - 300 °C by **HAlg** and **Cu(II)Alg**, with 2-FF having been highlighted as potentially lucrative biofuel and platform commodity chemical.[126,127] Of course, whilst yields of < 7 mol.% might sound reasonably modest, one must remember that within pyrolysis chemistry (especially relating to saccharides) the number of different volatile organic products generated is frequently in the range 50 – 100. Indeed, it is often stated that the key to the commercialisation of biomass pyrolysis is high product selectivity,[6] and, in this regard, **HAlg** and **Cu(II)Alg** show considerable promise. Both compounds supply 2-FF in appreciable yields with extremely high selectivity (> 80 % of the GC peak area) at a comparatively low temperature. Furthermore, it is also extremely encouraging to note that the effects are not unique to alginates, but appear to be universal to all mono- and poly-uronides, including pectin – a key component of promising biomass feedstocks such as citrus peel.[76,128,129]

Naturally, whilst the degradative pathways of the organic polymer are the primary focus when considering the large-scale pyrolysis of uronides, it is also important to bear in mind the fate of the metal ion. Some authors have noted that metal-rich material does not lend itself well to the industrial pyrolysis process because, at higher temperatures, the inorganic matter can slag or foul the reactor.[130,*] However, at lower temperatures, the inorganic material would be expected to remain embedded in the char matrix and be less problematic for the reactor system. Indeed, recent work by a number of investigators has sought to synthesise metal nanoparticles through the pyrolysis of a modified metal alginate.[131–134] The utility of resulting carbon-supported metals have been demonstrated in a range of catalytic processes,[132] indicating that the Cu^0, Ni^0, Co^0 and ZnO crystallites that were found to form in the chars of their parent alginates in work in this chapter may also possess value in their own right.

Of course, in the context of the pyrolysis of alginate-rich biomass (such as macroalgae), it is important to remember that **HAlg** and (for example) **Cu(II)Alg** do not represent the native state of the saccharide, which is much more likely to be found in the **NaAlg** or **CaAlg** form. Hence, in order to derive the benefits of H^+ or Cu^{2+}, it would be required to either acid wash the biomass (to yield **HAlg**), or perform an ion exchange in Cu(II)-rich solution (to yield (**Cu(II)Alg**). Such pre-treatments (especially the latter) form the basis of work in Chapter 5.

4.7 Summary and conclusions

This chapter aimed to screen the effects of various metal ions on the pyrolysis behaviour of alginates (and related-uronides). In this regard the following findings were made:

- Uronides decompose in quite a different manner to neutral polysaccharides (such as cellulose). Uronide thermolysis is initiated at a low temperature (<< 300 °C), but gives rise to comparatively high levels of char, CO_2, and H_2O.

[*] Slagging and fouling are two closely related mechanisms of inorganic material depositing within a thermochemical reactor, causing blockages and a potentially catastrophic loss in heating efficiency.

- Binding a metal ion to an alginate tends to increase the pyrolysis onset temperature (with the exception of Cu^{2+}) compared to the free-acid form. The following stability series was discererned for different meal alginates relative to **HAlg**:

(least stable) ⟶ *(most stable)*

$$\mathbf{Cu^{2+} < H^{+} << Zn^{2+} < Co^{2+} < Mg^{2+} < Ni^{2+} < Na^{+} < Ca^{2+} \approx Sr^{2+} \approx Ba^{2+}}$$

- The bound metal ion can significantly alter the yield of various products arising from the pyrolysis of alginate, according to the summarised results in Table 4.9. Again, Cu^{2+} can be seen to influence pyrolysis in a different manner to the other metal ions, increasing the yield of 2-FF, and decreasing the yield of small oxygenated molecules (such as acetol).

Table 4.9 A summary of the effect of various metal ions on the pyrolysis behaviour of alginate at 500 °C relative to alginic acid

Metal ion	Selectivity to small oxygenates	Selectivity to 2-FF	Pyrolysis onset temp	CO_2 Yield	CO Yield	H_2O Yield	Char Yield
Cu^{2+}	Decrease	Increase	Decrease	Increase	Increase	Increase	Decrease
Na^{+}	Very large increase	Very large decrease	Large increase	Increase	Increase	Increase	Large increase
Mg^{2+}	Large increase	Decrease	Large increase	N.D.	N.D.	N.D.	No change
Ca^{2+}	Very large increase	Large decrease	Very large increase	Increase	Decrease	Increase	Very large increase
Co^{2+} Ni^{2+} Zn^{2+}	Increase	Small decrease	Large increase	N.D.	N.D.	N.D.	Decrease

N.D = not determined

- Cu^{0} was found to form in chars of **Cu(II)Alg** at temperatures > 200 °C. Synchronous disappearance of peaks in the FTIR relating to the vibrational modes of the uronide carboxylate moiety was taken as evidence that a Cu(II)-mediated thermal decarboxylation (a *Hofer-Moest* decarboxylation) mechanism was taking place. The mechanism could be used to rationalise the elevated formation of 2-FF from the **Cu(II)Alg**, highlighting how other metals (such as Ca^{2+}) would inhibit such thermolytic pathways by stabilising the carboxylate against decarboxylation.

- Small variations were detected between the pyrolysis behaviour of **HAlg** *versus* **HPec**, and **HGal** *versus* **HGlc**. However, binding a metal ion to the uronides (Na^{+}, Ca^{2+} or Cu^{2+}) had a similar influence in all cases – notably that Cu^{2+} increased the yield of 2-FF, whilst the s-block metals tended to encourage the formation of small oxygenated molecules.

- Some similarities were found between the pyrolysis and hydrothermolysis of uronides (such as the ability of **HGlc** to form GlcLac), but there were also noticeable differences (such as the absence of reductic acid formation in the anhydrous case).

Hence, in summary, it can be concluded that uronides generally have quite unfavourable pyrolysis traits (high yields of char, CO_2, and H_2O, and low yields of liquid hydrocarbons), but the selection of counter cation can cause significant changes to these results. Cu^{2+} increases the yield and selectivity for 2-FF from **Alg** (and **Pec**, **Gal**, and **Glc**), conceivably by promoting a low temperature, metal-mediated decarboxylation. This mechanism appears to be general to all uronides, and is active regardless of the stereochemistry of the composite mono-uronide unit. In Chapter 5, the application of these results will be tested by applying the findings to the pyrolysis of samples of alginate-rich kelps.

4.8 Future work

4.8.1 Key questions and proposed strategies for future investigations

Whilst best efforts were made to ensure that the work in this chapter was as comprehensive as possible, inevitably many questions remain to be answered. A few of those outstanding issues are highlighted here, as well as suggestions as to how they may be tackled by future researchers.

4.8.1.1 How can the mass balance of uronide pyrolysis be improved?

The mass balance presented in Section 4.5.2.8 was the best that could be delivered with the available resources, however, there are clear areas for improvement. For example, the H_2O yield was calculated from TGA data, which will inevitably be different from that derived from the much more rapid heating afforded by Py-GCMS. An improved method of calibrating the Py-FGA apparatus to account for H_2O generated in the micropyrolyser should improve matters (see Appendix L). Furthermore, the inability to quantify the yield of uronolactones and related anhydrosugars could be improved by advanced calibration methods (described in more detail in Appendix L). Finally, errors in the reported char yield could be considerably reduced by minimising the time between weighing the sample before and after pyrolysis, and by accounting for small losses in moisture from the quartz reactor tube upon heating. Taking all of the above into account, the large errors associated with the calculated mass balance could be significantly diminished with the addition of a few extra experimental precautions.

4.8.1.2 How can the distribution of volatile organic products arising from uronide pyrolysis be better understood?

The complex (but repeatable) patterns in the distribution of various fractions of volatile organic products gave considerable scope for speculative mechanistic discussions on uronide thermolysis (see Sections 4.6.1.3 and 4.6.2.8). However, a more systematic theoretical approach, replicating the equivalent experiments of Broadbelt *et al.* in their analysis of the pyrolysis of glucose (see Section 4.3.2.2) could yield more concrete

conclusions.[10,11,19] Specific questions to study by computational methods might include the influence of inhibiting decarboxylation in uronides upon heating, or the reasons behind slight changes in preferences for the formation of furanone- over furfural-based compounds.

4.8.1.3 How applicable are the findings of this study to other uronides?

Part of the aim of this chapter was to discern the extent to which the pyrolysis of alginic acid (and alginates) is representative of the pyrolysis of all mono- and poly-uronides. Whilst the similarities between, for example, alginate and pectin, were very clear, there were also notable contrasts with the mono-uronic acids. In order to gain a better understanding of the relationship between mono- and poly-uronide thermolysis, a series of additional experiments is recommended with systematic variation of the degree of polymerisation (DP). Such experiments have been shown to be incredibly insightful in the context of the pyrolysis of glucans (see Section 4.3.2.3).[5,36] Naturally, for investigations into the pyrolysis of kelp, it would ideal if the mono-, oligo, and poly-saccharides under scrutiny were algal-uronides (see Figure 4.62), though such compounds are not currently readily available. However emerging automated carbohydrate synthetic methodologies may facilitate such work in the near future.[135–137]

($^1C_4$)-α-L-gulopyranuronic acid ($^4C_1$)-β-D-mannopyranuronic acid

Figure 4.62 Mono- (n = 1) and oligo- (2 ≥ n ≤ 20) guluronic and mannuronic acids could provide valuable insight into the pyrolysis behaviour of their respective polymeric forms

4.8.1.4 Why is char formation so prevalent in uronide thermolysis and what is the underlying structure?

As was discussed in Section 4.6.1.1, char is the ultimate destination of the majority of carbon in the pyrolysis of alginic acid. As the least valuable product fraction, it would be beneficial to gain a better understanding of the mechanisms behind the formation of char, and particularly to try and understand why yields of char are so high for **HAlg** compared to, for example, cellulose. Further solid state characterisation could be helpful in this regard, including solid-state NMR (SSNMR), %CHN analysis, and Raman spectroscopy. Detailed char characterisation remains to be problematic in pyrolysis research more generally, and will be a good topic for future review.

4.8.1.5 What are the intermediate stages leading to the formation of the observed crystallites in the chars of metal alginates?

One of the most interesting results of Chapter 4, was the identification (by PXRD) of crystalline metals and metal oxysalts within the char matrix of alginates. In Section 4.6.2.8, speculative explanations were provided that rationalised the appearance of such crystallites in the context of the alginate degradation mechanism. However, there is clearly more to be understood. For example, it is ambiguous as to whether Cu^{2+} ions undergo a multistep reduction ($Cu^{2+} \rightarrow Cu^{+} \rightarrow Cu^{0}$) or a single 2e- process ($Cu^{2+} \rightarrow Cu^{0}$). Furthermore, a quantitative assessment of the proportion of Cu^{2+} that is reduced is also lacking. Similarly, it is hoped that the cause behind the extreme intumescence observed in pyrolysed samples of **NaAlg** may be better understood. The high thermal stability of sodium-uronide chars has also been a point of discussion for other authors,[72,84] and remains an outstanding area of uncertainty. Techniques such as X-ray photo-electron spectroscopy (XPS) or solid-state NMR (SSNMR) may be helpful in furthering the understanding of the fate of the cation in the pyrolysis of metal-bound uronides.

4.8.1.6 What is the role of additional metals in the pyrolysis of uronides?

The s- and d-block metal alginates studied in this chapter were selected based on their relevance to the pyrolysis of macroalgae (see Chapter 5). However, there are of course a number of other candidates that would provide helpful insights. For example, a trend behind reduction potential and alginates carboxylate stability was proposed, and hence may be tested further by selecting more readily reduced metal ions. Here, Pd^{2+} has been shown to form Pd^{0} nanoparticles during the pyrolysis of alginate-rich seaweed,[132] though the corresponding thermal behaviour of **Pd(II)Alg** has not been studied in detail. Furthermore, references to the thermolysis of **Ag(I)Alg**, **Au(I)Alg**, **Pt(II)Alg** and **Hg(II)Alg** are scant in the literature, but deserving of further attention given the strongly oxidising nature of their bound cations. Similarly, very little work has been carried out on the thermochemical properties of trivalent metal ions (particularly those of environmental significance such as Fe^{3+} and Al^{3+}), though preliminary efforts in this regard are discussed in Appendix K.

4.8.1.7 How can the uronide pyrolysis environment be best controlled for further optimisation of the process?

As discussed in Section 4.6.3, of the huge number of possible variables in thermochemical experiments, few were explored in detail here (with the emphasis instead on the chemistry of the starting material). The heating rates, residence time, particle size, sample mass, pyrolysis atmosphere and so on were all selected based on brief preliminary experiments and work in the literature.[3] Of course, such shortcomings leave scope for further optimisation and investigation of thermal parameters in uronide pyrolysis. Of particular interest, is the role played by water in the pyrolysis environment. Other authors have speculated that adventitious water can influence glycosidic scission and proton mobility in the condensed phase of pyrolysis, which could have drastic consequences for subsequent degradation mechanisms (see Figure 4.63).[39] As such, a series of systematic experiments would be of interest whereby the amount of moisture present during heating is carefully controlled.

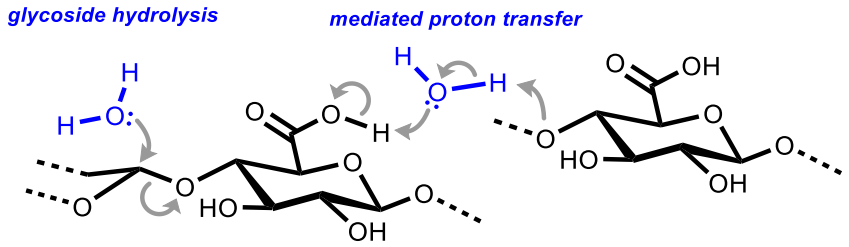

Figure 4.63 Possible roles played by adventitious water in the pyrolysis of a polyuronides (such as alginic acid or pectin).

4.8.1.8 Are the findings in this chapter of practical significance to the pyrolysis of uronide-rich biomass?

Of course, the premise of this chapter lies in the assumption that the findings of purified uronides (such as alginate) are translatable to the thermochemical treatment of promising biomass candidates (such as kelps). Some authors have warned against an over-reliance on "model compound"-based studies in pyrolysis research, arguing that their findings can be far removed from the complex thermochemical environment encountered in multi-component biomass mixtures.[138] As such, it is imperative that the conclusions arising from this chapter be robustly tested in the context of the pyrolysis of whole biomass material; a goal that is the motivation for the work carried out in Chapter 5.

4.9 Materials and methods

4.9.1 Preparation and characterisation of uronides for thermal analysis

4.9.1.1 Preparation of alginic acid and various metal alginates from commercial sodium alginate

Sodium alginate (**NaAlg**) was purchased from Sigma Aldrich as a yellow granular powder and used as received. According to the manufacturer, the alginate was extracted from *Macrocystis pyrifera* (Lot# MKBG5630V) with a quoted M_w of 120 - 190 kDa. The **M**:**G** ratio was determined to be 1.25 by the methods described in Appendix J (slightly lower than the quoted value of 1.56). Alginic acid (**HAlg**) and metal alginates (**MAlg**) were all derived from the common **NaAlg** sample according to the methods outlined in the remainder of this section. All other chemicals were purchased from Sigma Aldrich and used as received, unless specified otherwise.

HAlg was prepared by neutralisation of **NaAlg** as defined in Equation 4.1. In a typical preparation, **NaAlg** (500 mg) was suspended in HCl (50 mL, 0.05 M) and shaken for 1 hour. Variations in time (up to 12 hours) and HCl concentration (up to 0.1 M) did not give rise to significant differences in the thermochemical behaviour of the resulting **HAlg**. Following the neutralisation, the white **HAlg** suspension was isolated by centrifugation (5 minutes, 3000 rpm) and washed with HCl (5 mL, 0.05 M), H_2O (2 × 25 mL). The final set of washings was determined to be free of Cl^- by testing with $AgNO_3$. After drying at 70 °C in air for 24 hours, samples were ground by pestle and mortar to fit through a 60-mesh sieve (250 μm). Finally, the samples were re-equilibrated with atmospheric moisture prior to thermochemical analysis.

$$NaAlg + HCl \longrightarrow HAlg + NaCl \qquad \textbf{[Equation 4.1]}$$

All metal alginates studied (with the exception of **MgAlg** – see below) were prepared by ion exchange with the **NaAlg**, as defined in Equation 4.2. **NaAlg** (500 mg) was suspended in a solution containing the relevant metal chloride (25 mL, 1.0 M) as a 10-fold excess. The pH of the solutions was not adjusted, but was not found to be below 5 (and hence well above the pK_a of the alginate carboxylate moiety). The reaction mixture was shaken for 12 hours, prior to isolation of the metal alginate by centrifugation (5 minutes, 3000 rpm) and washing with deionised H_2O (4 × 25 mL). The final set of washings was determined to be free of Cl^- by testing with $AgNO_3$. After drying at 70 °C in air for 24 hours, samples were ground by pestle and mortar to fit through a 60-mesh sieve (250 μm). Finally, the samples were re-equilibrated with atmospheric moisture prior to thermochemical analysis.

$$x\,NaAlg + M^{x+}Cl_x \longrightarrow M^{x+}Alg_x + x\,NaCl \qquad \textbf{[Equation 4.2]}$$

MgAlg cannot be prepared in the same manner as other metal alginates owing to its solubility in aqueous solutions. Instead, **MgAlg** was prepared from the parent **NaAlg** by first neutralising to yield **HAlg** (see procedures above) and then reacting the alginic acid with $Mg(OH)_2$, as defined in Equations 4.1 and 4.3. **HAlg** (500 mg) was suspended with $Mg(OH)_2$ (70 mg, 1.2×10^{-3} moles) in deionised H_2O (10 mL) and the mixture shaken vigorously for 24 hours. The cloudy solution was clarified by centrifugation (5 minutes, 3000 rpm) prior to the addition of ice cold acetone (40 mL) to precipitate the **MgAlg** as a white gelatinous mass. The **MgAlg** was recovered by centrifugation (5 minutes, 3000 rpm) and subsequently washed with more acetone (2 × 40 mL). After drying at room temperature in air for 14 hours and then at 70 °C for 24 hours, the **MgAlg** was ground and passed through a 60-mesh sieve (250 μm). Finally, the sample was re-equilibrated with atmospheric moisture prior to thermochemical analysis.

$$2HAlg + Mg(OH)_2 \longrightarrow MgAlg_2 + 2H_2O \qquad \textbf{[Equation 4.3]}$$

4.9.1.2 Characterisation of alginic acid and metal alginates

The elemental composition of the synthesised alginic acid and alginate salts (including %CHN, %metal, and $\%H_2O$) was achieved by a combination of combustion analysis, inductively-coupled plasma optical emission spectroscopy (ICP-OES), and thermogravimetric analysis (TGA). The precise experimental details of these methods, including the procedure required to digest the samples for analysis by ICP-OES, are provided in Chapter 5, Section 5.8.2.2. Additional characterisation of the alginate samples was conducted by Fourier transform infra-red spectroscopy (FTIR) on a PerkinElmer Spectrum Two spectrometer equipped with a Universal Attenuated Total Reflectance (UATR) accessory. The monomer sequence of the alginate (including the ratio of mannuronate:guluronate, **M**:**G**) was determined according to standard NMR protocols, described in Appendix J.

4.9.1.3 Preparation of metal pectinates from commercial pectin

Pectin (**HPec**) was purchased from Sigma Aldrich as a fine off-white powder and used as received. According to the manufacturer, the pectin was extracted from citrus peel with and had a quoted composition of ≥ 74.0 % polygalacturonic acid units. All metal pectinate salts were derived from a common **HPec** sample according to the following procedures.

Sodium pectinate (**NaPec**) was first prepared by neutralisation of **HPec**, as defined in Equation 4.4). **HPec** (5.0 g) was suspended in deionised H_2O (500 mL) and NaOH (0.5 M) was added slowly until the solution was neutral and the solid was fully dissolved. **NaPec** was precipitated as a white solid by the addition of ice cold EtOH (500 mL). The gelatinous **NaAlg** was recovered on a Büchner funnel and washed with EtOH (2 × 200 mL) prior to drying at room temperature in air for 14 hours, and then at 70 °C for 24 hours. The **NaPec** was ground to pass through a 60-mesh sieve (250 μm) and then re-equilibrated with atmospheric moisture prior to thermochemical analysis.

$$HPec + NaOH \longrightarrow NaPec + H_2O \qquad \textbf{[Equation 4.4]}$$

Calcium and copper(II)-pectinates (**CaPec** and **Cu(II)Pec**) were synthesised by ion exchange with **NaPec**, as defined in Equation 4.5. **NaPec** (500 mg) was suspended in a solution containing the relevant metal chloride (25 mL, 1.0 M) as a 10-fold excess. The pH of the solutions was not adjusted, but was not found to be below 5 (and hence well above the pK_a of the alginate carboxylate moiety). The reaction mixture was shaken for 12 hours, prior to isolation of the metal pectinate by centrifugation (5 minutes, 3000 rpm) and washing with deionised H_2O (4 × 25 mL). The final set of washings was determined to be free of Cl^- by testing with $AgNO_3$. After drying at 70 °C in air for 24 hours, samples were ground by pestle and mortar to fit through a 60-mesh sieve (250 μm). Finally, the **CaPec** and **Cu(II)Pec** samples were re-equilibrated with atmospheric moisture prior to thermochemical analysis.

$$2NaPec + MCl_2 \longrightarrow MPec_2 + 2NaCl \qquad \textbf{[Equation 4.5]}$$

4.9.1.4 Characterisation of pectin and metal pectinate salts

Elemental analysis of the pectin and pectinate salts (including %CHN, %metal, and $\%H_2O$) was achieved according to the same methods as those listed for alginates in Section 4.9.1.2. Additional characterisation of the pectin samples was conducted by Fourier transform infra-red spectroscopy (FTIR) on a PerkinElmer Spectrum Two spectrometer equipped with a Universal Attenuated Total Reflectance (UATR) accessory.

4.9.1.5 Preparation of mono-uronate salts from commercial uronic acids

α-D-galacturonic acid monohydrate (**HGal**) and β-D-glucuronic acid (**HGlc**) were purchased from Sigma Aldrich and used as received. Na^+, Ca^{2+}, and Cu^{2+} salts of D-galacturonate and D-glucuronate were prepared by neutralisation of the respective acids, according to Equations 4.6 – 4.11. **HGal** (160 mg, 0.77 mmol) or **HGlc** (150 mg, 0.77 mmol) were dissolved in deionised water (1.5 mL) to yield 0.5 M solutions. The aqueous uronic acids were then shaken with either $Cu_2(OH)_2CO_3$ (40 mg, 0.19 mmol, $CaCO_3$ (38 mg, 0.38 mmol), or Na_2CO_3 (40 mg, 0.38 mmol) (all slightly below the stoichiometrically required amounts)

for 12 hours at room temperature. Following the reaction, any remaining solid was removed by filtration by passing the resulting solutions through a syringe filter (0.45 μm). The uronate salts were precipitated as white (Na^+ and Ca^{2+}) or pale green (Cu^{2+}) powders by the addition of a ten-fold excess of ice cold acetone. The samples were collected by centrifugation (3000 rpm, 20 mins) and then washed with acetone (2 × 10 mL). After drying in air at room temperature for 24 hours and again for 3 hours at 70 °C, the uronate salts were re-weighed to confirm near quantitative yields in all cases. Further grinding of the samples was not necessary prior to thermochemical experiments as they were already in a finely powdered form.

$$HGal + Na_2CO_3 \longrightarrow NaGal + H_2O + CO_2 \quad \textbf{[Equation 4.6]}$$

$$2HGal + Cu(II)_2(OH)_2CO_3 \longrightarrow Cu(II)Gal_2 + H_2O + CO_2 \quad \textbf{[Equation 4.7]}$$

$$2HGal + CaCO_3 \longrightarrow CaGal_2 + H_2O + CO_2 \quad \textbf{[Equation 4.8]}$$

$$HGlc + Na_2CO_3 \longrightarrow NaGlc + H_2O + CO_2 \quad \textbf{[Equation 4.9]}$$

$$2HGlc + Cu(II)_2(OH)_2CO_3 \longrightarrow Cu(II)Glc_2 + H_2O + CO_2 \quad \textbf{[Equation 4.10]}$$

$$2HGlc + CaCO_3 \longrightarrow CaGlc_2 + H_2O + CO_2 \quad \textbf{[Equation 4.11]}$$

4.9.1.6 Characterisation of mono-uronate salts

Elemental analysis of the uronic acids and their salts (including %CHN, %metal, and $\%H_2O$) was achieved according to the same methods as those listed for alginates in Section 4.9.1.2. Further solid-state characterisation of the uronate samples was conducted by Fourier transform infra-red spectroscopy (FTIR) on a PerkinElmer Spectrum Two spectrometer equipped with a Universal Attenuated Total Reflectance (UATR) accessory. In order to confirm that the Cu^{2+} had not oxidised the reducing end of the uronate ligand during the preparation, **Cu(II)Gal** and **Cu(II)Glc** were dissolved in D_2O (10 mg per 600 μL), shaken with 100 mg of cation-exchange resin (Amberlite® IR 120 – D^+ form), and the solutions studied by ^1H NMR spectroscopy. The Na^+ and Ca^{2+} uronate salts were similarly subjected to analysis by ^1H NMR to confirm their high purity by reference to the spectra obtained in Chapter 3.

4.9.2 Thermal analysis of uronide materials

4.9.2.1 Thermogravimetric analysis (TGA)

A detailed discussion of the experimental parameters relating to thermogravimetric analysis (TGA) and derivative thermogravimetric analysis (DTG) is provided in Appendix L. TGA/DTG analyses were carried out on a Perkin Elmer Pyris 1 analyser. The sample (ranging in mass from 5 to 50 mg depending on the experiment) was loaded into a ceramic crucible and heated from room temperature to 900 °C at a rate of 10 °C min^{-1} under a He

atmosphere (with a flow of 30 mL min^{-1}). An isothermal drying period of 10 minutes at 100 °C was included in most runs, and the data subsequently corrected to reflect the mass lost as moisture during this stage.

4.9.2.2 Preparation and analysis of char samples

Char samples derived from different metal alginates suitable for various forms of solid-state analysis were prepared by isothermal TGA. The alginate samples were loaded into the TGA apparatus and heated according to the procedure described in Section 4.9.2.1. At a specified target temperature (T_{iso}), an isothermal period of 60 minutes was employed to allow the maturation of crystalline material within the sample. Following the isothermal period, the furnace was cooled to room temperature, opened, and the residual char gathered from the sample pan. Preliminary experiments were also conducted in which the sample was heated at 10 °C min^{-1} to 900 °C without an isothermal period, or heated under N_2 instead of He. The resulting sooty powders were further ground and sieved (60 mesh, 250 μm) onto a poly(methyl methacrylate) disc coated in a thin layer of petroleum jelly. The char sample was then subject to analysis by X−ray powder diffraction (PXRD) on a Bruker D8 Advance diffractometer utilising Cu Kα radiation (λ = 1.5406 Å) at scattering angles (2θ) from 20° to 80° with a step size of 0.02°. Peak assignment was carried out through comparison with data from the Crystallographic Open Database (COD) and diagnostic peak patterns are reported in Appendix F for reference. Additional characterisation of the char samples was conducted by Fourier transform infra-red spectroscopy (FTIR) on a PerkinElmer Spectrum Two spectrometer equipped with a Universal Attenuated Total Reflectance (UATR) accessory.

4.9.2.3 Pyrolysis-gas chromatography mass spectrometry (Py-GCMS)

The complexity of the pyrolysis-gas chromatography mass spectrometry (Py-GCMS) experiments required a significant level of method development, discussed at length in Appendix L. The final parameters used in the experiments are also provided in Appendix L along with their rationalisation, though a brief overview is also reported here. Micropyrolysis was conducted on a CDS 5200 Pyroprobe coupled to an Agilent 7820A gas chromatograph and Agilent 5977E mass selective detector.

Latter experiments were also carried out in which the Pyroprobe was coupled to a CDS 5500 permanent gas analyser equipped with a thermal conductivity detector unit. In a typical experiment, a finely ground sample was packed with quartz wool into a short length of quartz tube, with weighing before and after to determine the mass of pyroysable material (between 100 – 250 μg). Once loaded into the Pyroprobe and purged with an inert gas (He), pyrolysis was conducted at 20 °C ms^{-1} up to a target temperature, which was maintained for 20 seconds. Volatilised organic material was condensed on a Tenax® trap, before being desorbed into the GC inlet *via* a transfer line heated at 300 °C. A Thermo Scientific TraceGold TG-1701MS (60 m × 250 μm × 0.25 μm) column was employed to separate the components of the pyrolysate under a constant flow of He (0.68 mL min^{-1}) and pre-programmed temperature profile: 40 °C (hold 2 mins), heat at 10 °C min^{-1} to 250 °C (hold 10 mins). Following ionisation (70 eV) and detection (1.6 – 300 amu, 781 units s^{-1}), identification of the products was carried out by comparison with a commercial standard

(Sigma Aldrich, used as received) where possible, or by reference to a spectral library.* Finally, the sample was re-weighed following pyrolysis in order to facilitate a calculation of conversion. Details of the calibrations required to quantify yields of significant pyrolysis products (namely 2-furaldehyde, CO_2 and CO) are provided in Appendix L.

4.10 Chapter acknowledgements

Doug Carswell is thanked especially for carrying out many of the TGA and TGA-MS experiments detailed in this chapter. Drs. Ben Smith and Li Li are gratefully acknowledged for help in setting up and operating the Py-GCMS and fixed gas analyser. Malcolm Brown and Aaron Richardson of the Durham University Glassblowing Workshop are thanked for preparation of quartz tubing for Py-GCMS experiments, as is Gary Oswald for guidance on using the X-ray diffractometer. Dr. Emily Unsworth, Judith Magee, Dr. Hilary Redden, Blanca Cota Ka, and staff of the Durham University Geography Department are all acknowledged for providing advice and assistance with the digestion and elemental analysis of samples. Dr. Unsworth is also recognised for generously allowing time for access to her high precision analytical balance.

4.11 Chapter references

1 Y. M. Kim, H. W. Lee, S. Kim, C. Watanabe and Y. K. Park, *BioEnergy Res.*, 2015, **8**, 431–439.

2 S. C. Moldoveanu, in *Techniques and Instrumentation in Analytical Chemistry*, 2010, Vol. 28, pp. 419–470.

3 F. Ronsse, D. Dalluge, W. Prins and R. C. Brown, *J. Anal. Appl. Pyrolysis*, 2012, **95**, 247–256.

4 P. R. Patwardhan, J. a. Satrio, R. C. Brown and B. H. Shanks, *J. Anal. Appl. Pyrolysis*, 2009, **86**, 323–330.

5 M. S. Mettler, A. D. Paulsen, D. G. Vlachos and P. J. Dauenhauer, *Green Chem.*, 2012, **14**, 1284–1288.

6 M. J. Antal, in *Advances in Solar Energy*, Springer New York, Boston, MA, 1983, pp. 61–111.

7 D. R. Budgell, E. R. Hayes and R. J. Helleur, *Anal. Chim. Acta*, 1987, **192**, 243–253.

8 S. Wang, B. Ru, H. Lin and Z. Luo, *Bioresour. Technol.*, 2013, **143**, 378–383.

9 F. örsi, *J. Therm. Anal.*, 1973, **5**, 329–335.

*Reductic acid is not currently commercially available and so was synthesised, purified, and characterised according to the method in Appendix C in order to be used as a standard reference material.

10 H. B. Mayes, M. W. Nolte, G. T. Beckham, B. H. Shanks and L. J. Broadbelt, *ACS Sustain. Chem. Eng.*, 2014, **2**, 1461–1473.

11 X. Zhou, M. W. Nolte, H. B. Mayes, B. H. Shanks and L. J. Broadbelt, *Ind. Eng. Chem. Res.*, 2014, **53**, 13274–13289.

12 R. Vinu and L. J. Broadbelt, *Energy Environ. Sci.*, 2012, **5**, 9808–9826.

13 S. Wang, X. Guo, T. Liang, Y. Zhou and Z. Luo, *Bioresour. Technol.*, 2012, **104**, 722–728.

14 J. B. Paine, Y. B. Pithawalla, J. D. Naworal and C. E. Thomas, *J. Anal. Appl. Pyrolysis*, 2007, **80**, 297–311.

15 J. B. Paine, Y. B. Pithawalla and J. D. Naworal, *J. Anal. Appl. Pyrolysis*, 2008, **83**, 37–63.

16 J. B. Paine, Y. B. Pithawalla and J. D. Naworal, *J. Anal. Appl. Pyrolysis*, 2008, **82**, 42–69.

17 J. B. Paine, Y. B. Pithawalla and J. D. Naworal, *J. Anal. Appl. Pyrolysis*, 2008, **82**, 10–41.

18 S. C. Moldoveanu, in *Techniques and Instrumentation in Analytical Chemistry*, Elsevier, Amsterdam, 1998, Vol. 20, pp. 217–315.

19 X. Zhou, M. W. Nolte, B. H. Shanks and L. J. Broadbelt, *Ind. Eng. Chem. Res.*, 2014, **53**, 13290–13301.

20 Y. Zhang, C. Liu and H. Xie, *J. Anal. Appl. Pyrolysis*, 2014, **105**, 23–34.

21 M. S. Mettler, D. G. Vlachos and P. J. Dauenhauer, *Energy Environ. Sci.*, 2012, **5**, 7797–7809.

22 A. Broido, Y. Houminer and S. Patai, *J. Chem. Soc. B Phys. Org.*, 1966, **11**, 411–414.

23 L. Chen, J. Zhao, S. Pradhan, B. E. Brinson, G. E. Scuseria, Z. C. Zhang and M. S. Wong, *Green Chem.*, 2016, **18**, 5438–5447.

24 D. Klemm, B. Heublein, H. P. Fink and A. Bohn, *Angew. Chemie Int. Ed.*, 2005, **44**, 3358–3393.

25 H. R. Schulten, U. Bahr and W. Görtz, *J. Anal. Appl. Pyrolysis*, 1981, **3**, 137–150.

26 H. R. Schulten, U. Bahr and W. Görtz, *J. Anal. Appl. Pyrolysis*, 1982, **3**, 229–241.

27 F. X. Collard and J. Blin, *Renew. Sustain. Energy Rev.*, 2014, **38**, 594–608.

28 D. Shen, R. Xiao, S. Gu and K. Luo, *RSC Adv.*, 2011, **1**, 1641–1660.

29 J. Lédé, *J. Anal. Appl. Pyrolysis*, 2012, **94**, 17–32.

30 F. Shafizadeh and Y. L. Fu, *Carbohydr. Res.*, 1973, **29**, 113–22.

31 A. G. W. Bradbury, Y. Sakai and F. Shafizadeh, *J. Appl. Polym. Sci.*, 1979, **23**, 3271–3280.

32 G. Varhegyi, E. Jakab and M. J. Antal, Jr., *Energy & Fuels*, 1994, **8**, 1345–1352.

33 S. Matsuoka, H. Kawamoto and S. Saka, *J. Anal. Appl. Pyrolysis*, 2014, **106**, 138–146.

34 S. Xin, H. Yang, Y. Chen, M. Yang, L. Chen, X. Wang and H. Chen, *J. Anal. Appl. Pyrolysis*, 2015, **116**, 263–271.

35 J. C. Degenstein, P. Murria, M. Easton, H. Sheng, M. Hurt, A. R. Dow, J. Gao, J. J. Nash, R. Agrawal, W. N. Delgass, F. H. Ribeiro and H. I. Kenttämaa, *J. Org. Chem.*, 2015, **80**, 1909–1914.

36 B. Zhang, E. Leng, P. Wang, X. Gong, J. Zhang, Y. Zhang and M. Xu, *J. Anal. Appl. Pyrolysis*, 2015, **114**, 119–126.

37 S. Wu, D. Shen, J. Hu, H. Zhang and R. Xiao, *J. Anal. Appl. Pyrolysis*, 2016, **119**, 147–156.

38 H. B. Mayes and L. J. Broadbelt, *J. Phys. Chem. A*, 2012, **116**, 7098–7106.

39 X. Zhang, W. Yang and C. Dong, *J. Anal. Appl. Pyrolysis*, 2013, **104**, 19–27.

40 M. S. Mettler, S. H. Mushrif, A. D. Paulsen, A. D. Javadekar, D. G. Vlachos and P. J. Dauenhauer, *Energy Environ. Sci.*, 2012, **5**, 5414–5424.

41 Y. Lin, J. Cho, G. a Tompsett, P. R. Westmoreland and G. W. Huber, *J. Phys. Chem. C*, 2009, **113**, 20097–20107.

42 Y. Zhang, C. Liu and X. Chen, *J. Anal. Appl. Pyrolysis*, 2015, **113**, 621–629.

43 G. R. Ponder, G. N. Richards and T. T. Stevenson, *J. Anal. Appl. Pyrolysis*, 1992, **22**, 217–229.

44 S. D. Stefanidis, K. G. Kalogiannis, E. F. Iliopoulou, C. M. Michailof, P. Pilavachi and A. Lappas, *J. Anal. Appl. Pyrolysis*, 2014, **105**, 143–150.

45 P. R. Patwardhan, R. C. Brown and B. H. Shanks, *ChemSusChem*, 2011, **4**, 636–643.

46 F. Shafizadeh, G. D. McGinnis and C. W. Philpot, *Carbohydr. Res.*, 1972, **25**, 23–33.

47 K. Werner, L. Pommer and M. Broström, *J. Anal. Appl. Pyrolysis*, 2014, **110**, 130–137.

48 A. D. Paulsen, M. S. Mettler and P. J. Dauenhauer, *Energy & Fuels*, 2013, **27**, 2126–2134.

49 G. Várhegyi, M. J. Antal, E. Jakab and P. Szabó, *J. Anal. Appl. Pyrolysis*, 1997, **42**, 73–87.

50 S. Coburn, PhD thesis, University of Greenwich, UK, 2006.

51 J. Zhang, M. W. Nolte and B. H. Shanks, *ACS Sustain. Chem. Eng.*, 2014, **2**, 2820–2830.

52 G. Várhegyi, P. Szabó, W. S. L. Mok and M. J. Antal, *J. Anal. Appl. Pyrolysis*, 1993, **26**, 159–174.

53 Z. Wang, A. G. McDonald, R. J. M. Westerhof, S. R. A. Kersten, C. M. Cuba-Torres, S. Ha, B. Pecha and M. Garcia-Perez, *J. Anal. Appl. Pyrolysis*, 2013, **100**, 56–66.

54 D. J. Nowakowski and J. Jones, *J. Anal. Appl. Pyrolysis*, 2008, **83**, 12–25.

55 A. Trendewicz, R. Evans, A. Dutta, R. Sykes, D. Carpenter and R. Braun, *Biomass and Bioenergy*, 2015, **74**, 15–25.

56 F. X. Collard, A. Bensakhria, M. Drobek, G. Volle and J. Blin, *Biomass and Bioenergy*, 2015, **80**, 52–62.

57 F. X. Collard, J. Blin, A. Bensakhria and J. Valette, *J. Anal. Appl. Pyrolysis*, 2012, **95**, 213–226.

58 P. R. Patwardhan, J. A. Satrio, R. C. Brown and B. H. Shanks, *Bioresour. Technol.*, 2010, **101**, 4646–4655.

59 A. Khelfa, A. Bensakhria and J. V. Weber, *J. Anal. Appl. Pyrolysis*, 2013, **101**, 111–121.

60 G. N. Richards and G. Zheng, *J. Anal. Appl. Pyrolysis*, 1991, **21**, 133–146.

61 H. B. Mayes, M. W. Nolte, G. T. Beckham, B. H. Shanks and L. J. Broadbelt, *ACS Catal.*, 2015, **5**, 192–202.

62 X. Zhou, H. B. Mayes, L. J. Broadbelt, M. W. Nolte and B. H. Shanks, *AIChE J.*, 2016, **62**, 766–777.

63 X. Zhou, H. B. Mayes, L. J. Broadbelt, M. W. Nolte and B. H. Shanks, *AIChE J.*, 2016, **62**, 778–791.

64 N. Shimada, H. Kawamoto and S. Saka, *J. Anal. Appl. Pyrolysis*, 2008, **81**, 80–87.

65 H. B. Mayes, J. Tian, M. W. Nolte, B. H. Shanks, G. T. Beckham, S. Gnanakaran and L. J. Broadbelt, *J. Phys. Chem. B*, 2013, **118**, 131217085854005.

66 Y. Yu, D. Liu and H. Wu, *Energy & Fuels*, 2014, **28**, 245–253.

67 Y. Zhang and C. Liu, *J. Anal. Appl. Pyrolysis*, 2014, **110**, 297–304.

68 P. Rutkowski, *J. Anal. Appl. Pyrolysis*, 2012, **98**, 86–97.

69 S. Zhou, Y. Xu, C. Wang and Z. Tian, *J. Anal. Appl. Pyrolysis*, 2011, **91**, 232–240.

70 D. Zhao, Y. Dai, K. Chen, Y. Sun, F. Yang and K. Chen, *J. Anal. Appl. Pyrolysis*, 2013, **102**, 114–123.

71 H. S. Shim, M. R. Hajaligol and V. L. Baliga, *Fuel*, 2004, **83**, 1495–1503.

72 B. E. Waymack, J. L. Belote, V. L. Baliga and M. R. Hajaligol, *Fuel*, 2004, **83**, 1505–1518.

73 W. F. Degroot, W. P. Pan, M. D. Rahman and G. N. Richards, *J. Anal. Appl. Pyrolysis*, 1988, **13**, 221–231.

74 X. Zhou, W. Li, R. Mabon and L. J. Broadbelt, *Energy Technol.*, 2016, **8801**, 1–29.

75 A. S. Perlin, *Can. J. Chem.*, 1952, **30**, 278–290.

76 J. Aburto, M. Moran, A. Galano and E. Torres-García, *J. Anal. Appl. Pyrolysis*, 2015, **112**, 94–104.

77 A. Ohnishi, E. Takagi and K. Katŏ, *Carbohydr. Res.*, 1978, **67**, 281–288.

78 R. E. Aries, C. S. Gutteridge, W. a. Laurie, J. J. Boon and G. B. Eijkel, *Anal. Chem.*, 1988, **60**, 1498–1502.

79 S. Ge, Y. Xu, Z. Tian, S. She, L. Huang, Z. Zhang, Y. Hu, J. Weng, M. Cao and L. Sheng, *J. Therm. Anal. Calorim.*, 2015, **120**, 1399–1405.

80 S. C. Moldoveanu and V. David, in *Journal of Chromatography Library*, Elsevier, Amsterdam, 2002, vol. 65, pp 847–917.

81 P. S. Shuttleworth, V. Budarin, R. J. White, V. M. Gun'ko, R. Luque and J. H. Clark, *Chem. Eur. J.*, 2013, **19**, 9351–9357.

82 K. Anastasakis, A. Ross and J. Jones, *Fuel*, 2011, **90**, 598–607.

83 J. P. Soares, J. E. Santos, G. O. Chierice and E. T. G. Cavalheiro, *Eclética Química*, 2004, **29**, 57–64.

84 A. Ross, C. Hall, K. Anastasakis, A. Westwood, J. Jones and R. J. Crewe, *J. Anal. Appl. Pyrolysis*, 2011, **91**, 344–351.

85 S. C. Moldoveanu, in *Techniques and Instrumentation in Analytical Chemistry*, Elsevier, Amsterdam, 2010, vol. 28, pp. 471–526.

86 J. Zhang, Q. Ji, F. Wang, L. Tan and Y. Xia, *Polym. Degrad. Stab.*, 2012, **97**, 1034–1040.

87 D. Li, L. Chen, X. Yi, X. Zhang and N. Ye, *Bioresour. Technol.*, 2010, **101**, 7131–7136.

88 Y. Liu, J. C. Zhao, C. J. Zhang, Y. Guo, P. Zhu and D. Y. Wang, *J. Mater. Sci.*, 2016, **51**, 1052–1065.

89 Y. Liu, J. S. Wang, P. Zhu, J. C. Zhao, C. J. Zhang, Y. Guo and L. Cui, *J. Anal. Appl. Pyrolysis*, 2016, **119**, 87–96.

90 Y. Liu, J. C. Zhao, C. J. Zhang, Y. Guo, L. Cui, P. Zhu and D. Y. Wang, *RSC Adv.*, 2015, **5**, 64125–64137.

91 Y. Liu, J. Zhao, C. Zhang, H. Ji and P. Zhu, *J. Macromol. Sci. Part B*, 2014, **53**, 1074–1089.

92 J. Zhang, Q. Ji, X. Shen, Y. Xia, L. Tan and Q. Kong, *Polym. Degrad. Stab.*, 2011, **96**, 936–942.

93 Y. Liu, C. J. Zhang, J. C. Zhao, Y. Guo, P. Zhu and D. Y. Wang, *Carbohydr. Polym.*, 2016, **139**, 106–114.

94 Y. Liu, Z. Li, J. Wang, P. Zhu, J. Zhao, C. Zhang, Y. Guo and X. Jin, *Polym. Degrad. Stab.*, 2015, **118**, 59–68.

95 Y. Liu, X. R. Zhao, Y. L. Peng, D. Wang, L. Yang, H. Peng, P. Zhu and D. Y. Wang, *Polym. Degrad. Stab.*, 2016, **127**, 20–31.

96 G. Tian, Q. Ji, D. Xu, L. Tan, F. Quan and Y. Xia, *Fibers Polym.*, 2013, **14**, 767–771.

97 A. A. Said and R. M. Hassan, *Polym. Degrad. Stab.*, 1993, **39**, 393–397.

98 A. A. Said, M. M. M. Abd El-Wahab and R. M. Hassan, *Thermochim. Acta*, 1994, **233**, 13–24.

99 I. Zaafarany, *J. King Abdulaziz Univ.*, 2010, **22**, 193–202.

100 M. P. Segato and É. T. G. Cavalheiro, *J. Therm. Anal.*, 2007, **87**, 737–741.

101 S. K. Papageorgiou, E. P. Kouvelos, E. P. Favvas, A. a Sapalidis, G. E. Romanos and F. K. Katsaros, *Carbohydr. Res.*, 2010, **345**, 469–473.

102 D. Filipiuk, L. Fuks and M. Majdan, *J. Mol. Struct.*, 2005, **744**–**747**, 705–709.

103 N. Wellner, M. Kačuráková, A. Malovíková, R. H. Wilson and P. S. Belton, *Carbohydr. Res.*, 1998, **308**, 123–131.

104 A. Assifaoui, C. Loupiac, O. Chambin and P. Cayot, *Carbohydr. Res.*, 2010, **345**, 929–933.

105 A. Synytsya, *Carbohydr. Polym.*, 2003, **54**, 97–106.

106 H. A. Tajmir-Riahi, *Carbohydr. Res.*, 1983, **122**, 241–248.

107 H. A. Tajmir-Riahi, *J. Inorg. Biochem.*, 1985, **24**, 127–136.

108 H. A. Tajmir-Riahi, *Carbohydr. Res.*, 1984, **125**, 13–20.

109 A. Synytsya, M. Urbanová, V. Setnička, M. Tkadlecová, J. Havlíček, I. Raich, P. Matějka, A. Synytsya, J. Čopíková and K. Volka, *Carbohydr. Res.*, 2004, **339**, 2391–2405.

110 R. L. Whistler and M. L. Wolfrom, *Volume 2. Reactions of carbohydrates*, Academic Press, New York, 1963.

111 C. A. Marsh, in *Glucuronic Acid Free and Combined*, Elsevier, 1966, pp. 3–136.

112 E. A. Goldstein and R. E. Mitchell, *Proc. Combust. Inst.*, 2011, **33**, 2803–2810.

113 J. J. Byerley and E. Peters, *Can. J. Chem.*, 1969, **47**, 313–321.

114 J. A. Stapley and J. N. BeMiller, *Carbohydr. Res.*, 2007, **342**, 407–418.

115 J. A Stapley and J. N. BeMiller, *Carbohydr. Res.*, 2007, **342**, 610–613.

116 L. Somsák and R. J. Ferrier, *Adv. Carbohydr. Chem. Biochem.*, 1991, **49**, 37–92.

117 W. Hongsiri, B. Danon and W. de Jong, *Ind. Eng. Chem. Res.*, 2014, **53**, 5455–5463.

118 B. Danon, G. Marcotullio and W. de Jong, *Green Chem.*, 2014, **16**, 39–54.

119 C. Rong, X. Ding, Y. Zhu, Y. Li, L. Wang, Y. Qu, X. Ma and Z. Wang, *Carbohydr. Res.*, 2012, **350**, 77–80.

120 K. R. Enslow and A. T. Bell, *ChemCatChem*, 2015, **7**, 479–489.

121 G. Mattioda and Y. Christidis, in *Ullmann's Encyclopedia of Industrial Chemistry*, Wiley-VCH Verlag GmbH & Co. KGaA, Weinheim, Germany, 2000.

122 D. Dollimore and D. L. Griffiths, *J. Therm. Anal.*, 1970, **2**, 229–250.

123 U. Vaid, S. Mittal and J. Nagendra Babu, *React. Funct. Polym.*, 2015, **97**, 48–55.

124 T. R. Carlson, J. Jae, Y. C. Lin, G. a. Tompsett and G. W. Huber, *J. Catal.*, 2010, **270**, 110–124.

125 T. R. Carlson, G. A. Tompsett, W. C. Conner and G. W. Huber, *Top. Catal.*, 2009, **52**, 241–252.

126 J. P. Lange, E. van der Heide, J. van Buijtenen and R. Price, *ChemSusChem*, 2012, **5**, 150–166.

127 J. J. Bozell and G. R. Petersen, *Green Chem.*, 2010, **12**, 539–554.

128 C. M. Santos, J. Dweck, R. S. Viotto, A. H. Rosa and L. C. de Morais, *Bioresour. Technol.*, 2015, **196**, 469–479.

129 J. W. Kim, S. H. Park, J. Jung, J. K. Jeon, C. H. Ko, K. E. Jeong and Y. K. Park, *Bioresour. Technol.*, 2013, **136**, 431–436.

130 A. Ross, K. Anastasakis, M. Kubacki and J. Jones, *J. Anal. Appl. Pyrol.*, 2009, **85**, 3–10.

131 S. Rajeshkumar, C. Malarkodi, G. Gnanajobitha, K. Paulkumar, M. Vanaja, C. Kannan and G. Annadurai, *J. Nanostructure Chem.*, 2013, **3**, 44.

132 H. L. Parker, J. R. Dodson, V. L. Budarin, J. H. Clark and A. J. Hunt, *Green Chem.*, 2015, **17**, 2200–2207.

133 S. Baskoutas, P. Giabouranis, S. N. Yannopoulos, V. Dracopoulos, L. Toth, A. Chrissanthopoulos and N. Bouropoulos, *Thin Solid Films*, 2007, **515**, 8461–8464.

134 Z. Schnepp, S. C. Wimbush, S. Mann and S. R. Hall, *CrystEngComm*, 2010, **12**, 1410–1415.

135 Q. Zhang, E. R. van Rijssel, H. S. Overkleeft, G. A. van der Marel and J. D. C. Codée, *Euro. J. Org. Chem.*, 2016, **2016**, 2393–2397.

136 Q. Zhang, E. R. van Rijssel, M. T. C. Walvoort, H. S. Overkleeft, G. A. van der Marel and J. D. C. Codée, *Angew. Chemie Int. Ed.*, 2015, **54**, 7670–7673.

137 M. T. C. Walvoort, H. van den Elst, O. J. Plante, L. Kröck, P. H. Seeberger, H. S. Overkleeft, G. A. van der Marel and J. D. C. Codée, *Angew. Chemie Int. Ed.*, 2012, **51**, 4393–4396.

138 A. V. Bridgwater, *Biomass and Bioenergy*, 2012, **38**, 68–94.

Chapter 5

Chapter 5

The metal-mediated thermolysis of alginate-rich kelp biomass

5.1 Chapter abstract

In this chapter, samples of alginate-rich kelps are enriched with Cu^{2+} ions (for which they have a very high affinity) in order to take advantage of the favourable thermochemical influences of that metal, and diminish the deleterious effects of s-block species found within the native biomass. A combined approach utilising thermogravimetric analysis (TGA) and pyrolysis-gas chromatography mass spectrometry (Py-GCMS) was employed to discern the impact of Cu^{2+} ions during the pyrolysis of the biomass. It was found that Cu(II)-treated kelps initiated rapid pyrolysis at lower temperature than their untreated counterparts, by an average of 40 °C. Furthermore, Cu(II)-treatment of *Ascophyllum nodosum* (**A.nod**) gave rise to yields of 2-furaldehyde (2-FF) of 3.10 ± 0.26 mol.%C, an approximate eight-fold increase on the result from the untreated biomass. At 300 °C, the improvement was even larger (almost a 16-fold increase), and the results were found to be repeatable across all five of the kelp samples tested. Meanwhile, treating the seaweed in a solution of Ca^{2+} was not found to effect pyrolysis appreciably compared to the untreated cases.

In addition to investigating whole samples of kelp, the individual alginates were extracted from each of the species tested, and pyrolysed as a Na^{+}, Ca^{2+}, and Cu^{2+} salt. Here it was shown that the thermolysis behaviour of the alginates depended only on the identity of the bound counter cation, and not the differing **M**:**G** ratio. Analysis of other components of the biomass (such as the residue remaining after alginate extraction) confirmed that around 90 – 95 % of the 2-FF formed from the pyrolysis of Cu(II)-treated kelp originated from the alginate fraction, conceivably following the same *Hofer-Moest* type decarboxylation exhibited by **Cu(II)Alg** in Chapter 4. As the improvement in the yield of 2-FF was found to be generic for all alginate-rich kelps following a treatment in Cu^{2+}, a proposal is made for integrating the findings into a phytoremediative, seaweed-based thermal biorefinery.

5.2 Chapter introduction and context

The earlier chapters of this thesis explored fundamental behaviours of algal mono- and poly-uronides, particularly their thermo- and coordination- chemistries. Naturally, however, questions remain as to the relevance of studies of such "model compounds" in the utilisation of whole seaweed as a feedstock for thermochemical production of fuels and commodity chemicals. The present chapter seeks to address those queries, namely by utilising the results of Chapters 2, 3, and 4 to rationalise phenomena observed during the thermal degradation of alginate-rich kelp biomass. Particularly, evidence is sought as to whether the distinctive influence of Cu^{2+} ions on the pyrolysis of alginates (detailed in Chapter 4) is observable when the same polyuronide is nested within an algal biomass matrix. For completeness, the role played by Cu^{2+} ions on non-uronide components of the kelp biomass will also be explored. Consequently, this chapter will provide a case study with which to review the validity of employing a model compound approach in thermochemical studies of kelp biomass, and will offer a judgement as to the most appropriate direction for future research. Finally, the chapter will address the viability of combining the metal-binding properties of alginates (explored in Chapter 3) and their thermochemical traits (discussed in Chapters 2 and 4) in a kelp biorefinery featuring a coupled phytoremediation-thermal upgrading approach.

5.3 Literature background

5.3.1 Metals and the pyrolysis of kelp biomass

5.3.1.1 An introduction to the pyrolysis of kelp

An exhaustive review of the literature surrounding the thermochemical upgrading of kelp was carried out and published during the early stages of this doctoral project (reproduced for reference in Appendix S).[1] The article discussed the suitability of kelp (and other types of seaweed biomass) for a range of thermochemical technologies (hydrothermal liquefaction, gasification, catalytic pyrolysis, amongst others) and contains more detail than is relevant here. Hence, the main points of the review (especially those relating to pyrolysis) are summarised here (though the reader is urged to refer to Appendix S, and the references contained within it to gain a deeper insight in the routes available for the upgrading of kelp biomass).

- **What is kelp biomass?**
  Kelps are *phaeophyceae* (brown seaweeds) that are common to the shores of Northern Europe. They consist of a flat, flexible thallus (body) comprised of fronds, a stipe, and a holdfast to anchor the alga in position in the absence of a network of roots (see Figure 5.1). Kelp are distinct from terrestrial biomass because of their high growth rates (around 1 kg of carbon per square meter per year),[2,3] extreme size (growing up to 60 - 80 m in length),[3,4] and non-lignocellulosic biochemical composition. Indeed, despite being very rich in carbohydrates, cellulose only accounts for around 5 - 10 wt.% of the dry weight of most kelp, with other saccharides laminarin, fucoidan, and D-mannitol – see Figure 5.2) being present in similar proportions, depending upon the time of year.[5]

However, the most prolific constituent of kelp biomass is alginate, the linear copolymer of (1→4)-linked *β*-D-mannuronate (**M**) and *α*-L-guluronate (**G**) discussed extensively in Chapters 1 – 4 of this thesis (see Figure 5.3). Alginate forms up to 40 wt.% of the dry weight of kelp biomass, existing in the cell walls and occupying the space between the cellulose microfibrils to confer flexibility upon the parent alga (see Figure 5.1). The anionic nature of alginate also demands for the presence of counter-cations, explaining (to a large degree) why dry kelp biomass contains around 10 wt.% metal ions (mostly Na^+ and K^+),[5,6] incredibly high relative to most terrestrial feedstocks.

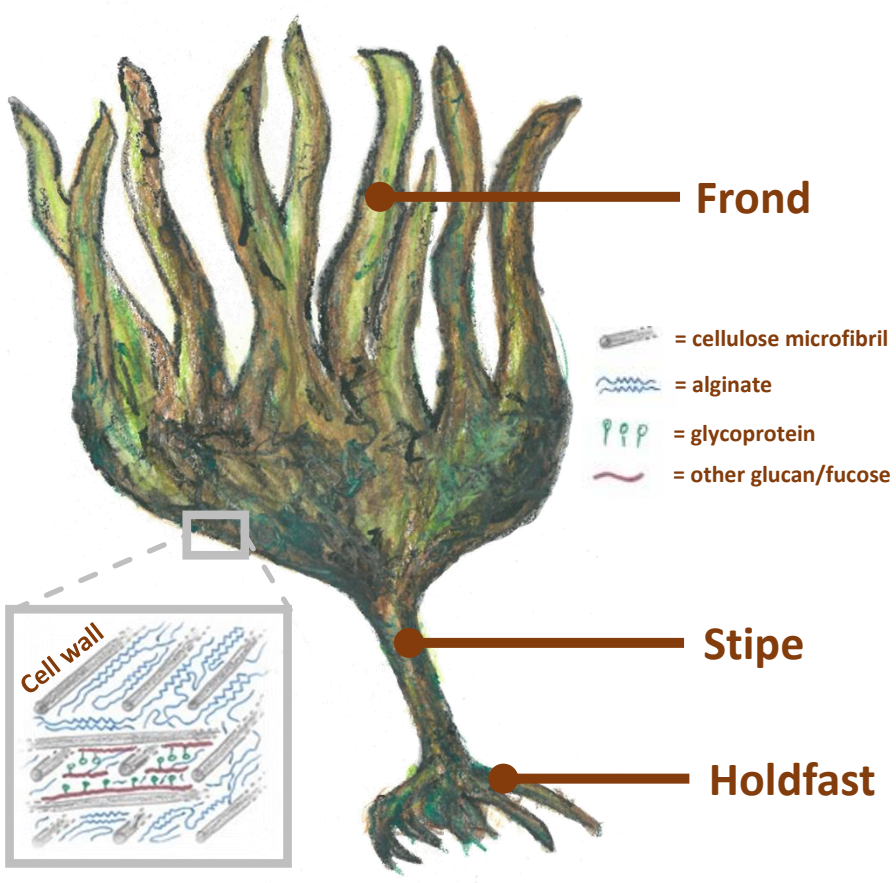

Figure 5.1 The structure of a typical kelp specimen, including the cell wall composition. Kelp image reproduced with permission from the original drawing by Natalie Patel. Cell wall diagram redrawn with permission from Michel *et al.*[7] © CNRS (2010).

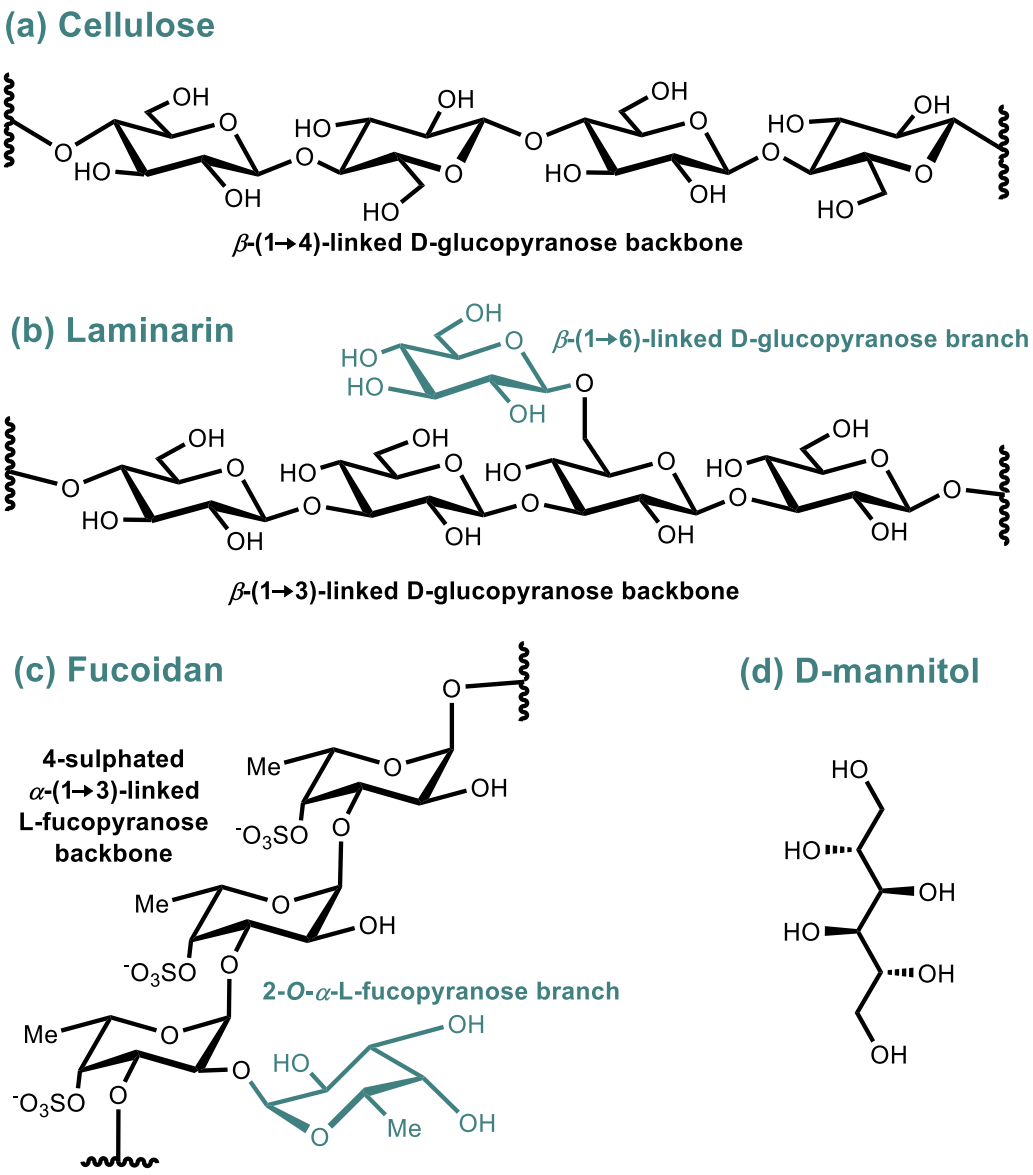

Figure 5.2 Typical structures of secondary carbohydrates in kelps.[8] (a) cellulose (a glucan),[4] (b) laminarin (a glucan),[9,10] (c) fucoidan (a fucose),[10,11] and (d) D-mannitol (a free sugar).[4]

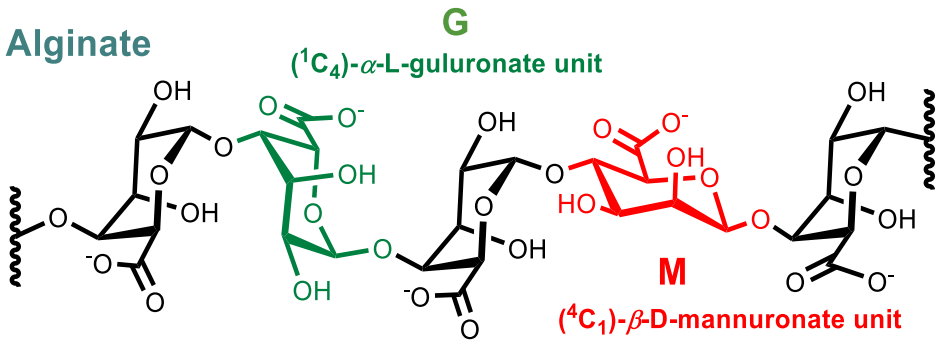

Figure 5.3 Alginate and its constituent monosaccharide units.

- **What happens when kelp biomass is pyrolysed?**
  To some degree the answer to this question is still unclear, as few dedicated studies have attempted to answer it. Andy Ross and co-workers made some headway in their analysis of the pyrolysis of individual components of kelp biomass (namely mannitol, laminarin, fucoidan, and alginic acid)* at varying temperatures.[12] The array of products found to be liberated by such carbohydrates is depicted in Figure 5.4, with the formation of furan- and furaldehyde- derivatives being particularly notable. Furthermore, Ross *et al.* noted the relatively low temperatures required to bring about the pyrolysis of kelps (compared to lignocellulosic biomass) as being advantageous for their pyrolysis.[4,13] Despite Ross' work, there is relatively little information available on how the micropyrolysis and model-compound studies translate into obtainable yields of bio-oil, -gas, and -char. Whilst some authors have reported high liquid yields from kelp biomass under pyrolysis conditions (around 40 wt.%), the organic phase (in which the most lucrative products reside) only account for around 4 – 16 wt.% of the fraction.[14,15] Yields of bio-char can be very high, up to 60 wt.% of the products,[14] which, whilst being the lowest value pyrolysis product, may find use as a soil remediating agent.[16,17] Finally, studies have also reported that the bio-gas derived from the pyrolysis of kelp is quite rich in H_2 (up to 5 vol.%) though high temperatures (> 500 °C) are required to reach such yields, with CO_2 dominating at lower degrees of heating.[14,15]

Hence, whilst the review article in Appendix S concluded that the pyrolysis of kelp biomass shows advantageous traits, there remain to be significant technological hurdles that must be tackled before the process is commercially viable. Indeed, the concerns that lead Morgan and Smith to conclude, in 1978, that it is "unlikely that simple pyrolysis [of macroalgae] would be an economic prospect in the foreseeable future", have yet to be overcome, even by more recent efforts.[18–23] It therefore appears that "simple" pyrolysis may not be a successful tactic, and the addition of pyrolysis-modifying reagents may be necessary. Here, Lee *et al.* have met with some success in their endeavours to pyrolyse *Laminaria japonica* in the presence of zeolites.[24] However, as was discussed in Chapter 1, co-mixing solid catalysts in pyrolysis generally gives a very poor contact between the additive and the reacting biomass particle, with impregnation of catalytically active species in the biomass matrix being a much more effective strategy (see Appendix P). With this in mind, Section 5.3.1.2 considers the routes to which the intrinsic metal ions profile of macroalgae can be controlled, and Section 5.3.1.3 reflects upon the implications for subsequent pyrolysis.

* Alginic acid (**HAlg**) is, of course, not a constituent of raw algal biomass, as the polymer is found naturally in the form of a metal alginate salt (**MAlg**). The distinction is not merely semantic, as the identity of the bound cation is vital to subsequent thermochemical behaviour.

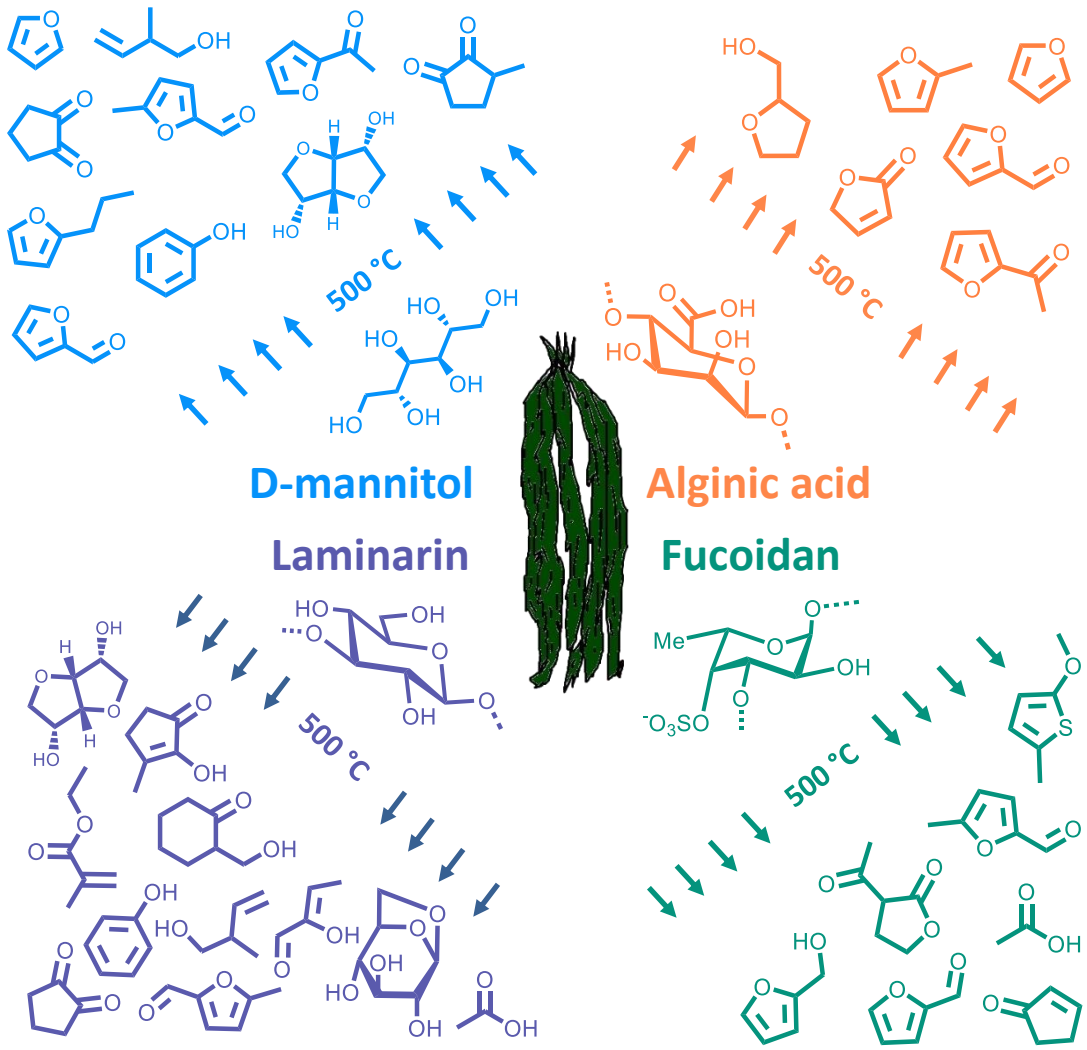

Figure 5.4 Pyrolysis of carbohydrates commonly found in kelp at 500 °C under He (data taken from the work of Ross *et al.*)[12]

5.3.1.2 Indigenous and artificially-incorporated metals in alginate-rich kelp

The extraordinarily high metal content of seaweed has been highlighted as one of the key differences of the feedstock compared to most terrestrial biomass. The abundance of metal ions is, to a large extent, a consequence of the high loading of anionic alginate within the algal biomass matrix, meaning that cations are resistant to removal by washing in water alone. Of course, the abundance of the metal ions within the kelp vary by season, species, geographical location and environmental, but tend to peak when the alginate-content is at its maximal value.

The composition of the metal profile within alginate-rich kelps is a product of two factors: the concentration of different metal ions in the local environment,* and the relative affinity of the alginate for those particular metal species. As such, the vast majority of metal ions found in kelp (> 90 wt.%) are Na^+ and K^+, reflecting the extremely high abundance of these species in seawater. Similarly, Ca^{2+} and Mg^{2+} are the most significant divalent metals. However, over years of research, authors have attempted to establish an affinity series for alginates (and, hence, alginate-rich kelps), whereby different metal ions might be selectively exchanged for those already bound. The series, first proposed by Haug *et al.*,[25,26] is presented in Figure 5.5.

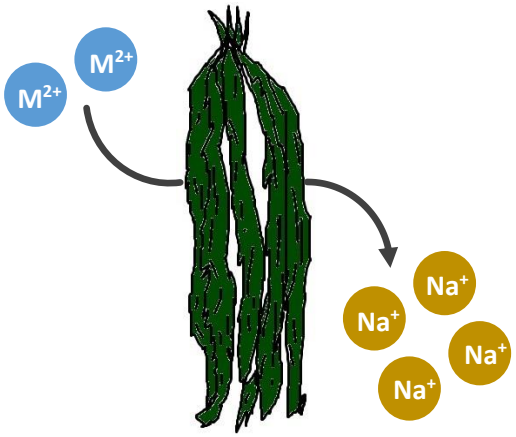

Affinity series: $Pb^{2+} > Cu^{2+} > Cd^{2+} > Ba^{2+} > Sr^{2+} > Ca^{2+} > Co^{2+} > Ni^{2+} > Mn^{2+} > Mg^{2+}$

Figure 5.5 Exchanging native Na^+ for divalent metal ions in alginate-rich seaweeds[25,26]

From Figure 5.5, it can be seen that Cu^{2+} is towards the high-affinity end of the series, with most alginates showing a 200 – 300 fold preference for the metal ion over Na^+.[27] This result is in contrast to Ca^{2+}, which shows only a 10 – 20 fold enhanced preference compared to Na^+ (though this figure is more heavily dependent on the **M**:**G** ratio of the alginate than in the case of Cu^{2+}).[27] Chapter 3 attempted, in part, to explain the origins of the enhanced preference of alginates for Cu^{2+} over Ca^{2+}. Here it was argued that, as Cu^{2+} ions are too small to fit into so-called "egg-box" binding pockets along the polyuronide (see Figure 5.6), the metal ion simply forms a strong (non-stereospecific) ionic interaction with the carboxylate moiety. It is this Cu^{2+}-carboxylate bond that subsequently delivers the enhanced affinity over Ca^{2+}. Hence, despite Ca^{2+} fitting perfectly in the "egg-box" sites created by **GG** dimers along the alginate chain (see Figure 5.6), such stereospecific coordination cannot compensate for the weaker binding of the cation to the carboxylate moiety, ultimately yielding a much lower stability constant for the **CaAlg** salt.

* For example, during the preliminary stages of this thesis, *L. digitata* collected from Marsden Bay (South Shields, UK) was found to be around 100-times enriched in Al^{3+} than was expected. This large increase in Al^{3+} was a consequence of the harvesting site being 16 miles downstream from an industrial aluminium smelting facility, and 2 miles away from the Port of the Tyne, both of which would give rise to enhanced levels of the metal ion in the seawater.

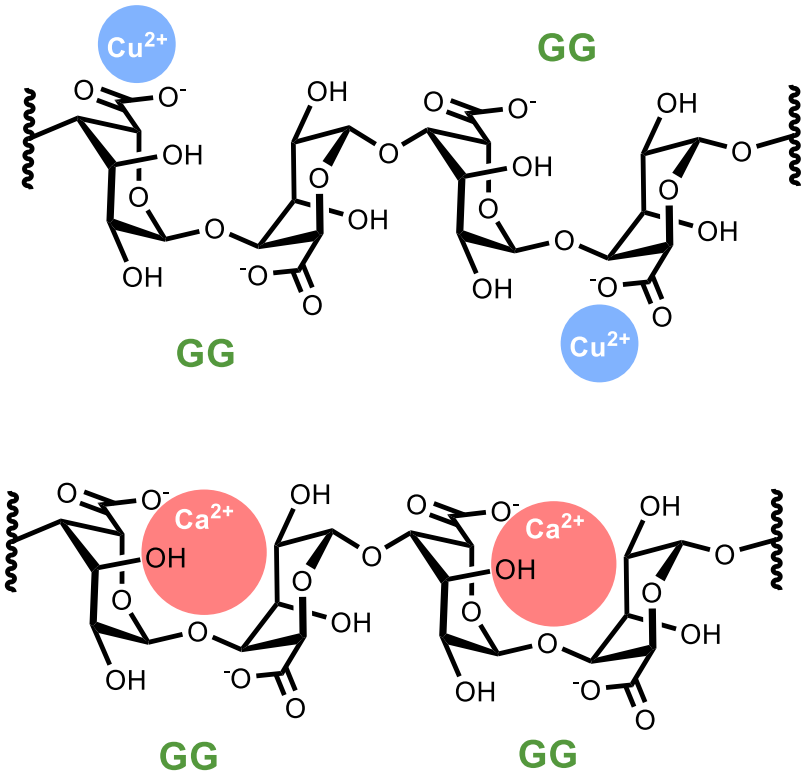

Figure 5.6 The difference in alginate binding behaviour of Cu^{2+} (top) and Ca^{2+} (bottom) based on the arguments presented in Chapter 3

Regardless of the molecular origins of the affinity series, the ability of alginates (and hence kelp) to exchange environmentally benign metals (Na^{+}, K^{+}, Mg^{2+}, *etc.*) for toxic species (Cd^{2+}, Cu^{2+}, Pb^{2+}, *etc.*) has been recognised as a potential route to the bioremediation of polluted water streams.[10,28–35] With this in mind, Section 5.3.1.3 provides a discussion of the likely impacts on subsequent thermal processing of the presence of metal-ions (both native and non-native) within kelp biomass.

5.3.1.3 Implications of the presence of metals ions on the pyrolysis of alginate-rich kelp

The ability of alginate-rich seaweed to sequester metal-ions in high abundance (see Section 5.3.1.2), and the strong influence exerted by such ions in the pyrolysis of biomass feedstocks generally (see Appendix P), gives a good justification for investigating the roles of the same metal ions in the pyrolysis of kelps. In this regard, only two studies have been conducted to explore the impact that naturally occurring metal ions have on the pyrolysis of brown algae; by Ross[13] and by Choi,[36] and by their respective co-workers. Both sets of authors used an acidic pre-treatment to remove the metallic constituents from *Laminaria* specimens prior to pyrolysis, and both noted considerable improvements to the properties of the bio-oil and -char derived from the process. In their work, Ross *et al.* described an increase in the yield of 2-furaldehyde (2-furfural, 2-FF), which they attributed to conversion of **NaAlg** to **HAlg** within the kelp, prior to pyrolysis (consistent with results in Chapter 4 of this thesis, and elsewhere,[37] that demonstrate the role played by Na^{+} in inhibiting the formation of 2-FF by alginate thermolysis, see Figure 5.7). Similarly, Choi *et al.* recorded significant swelling of

untreated *Laminaria japonica* during pyrolysis, causing blockages in their reactor system. Such behaviour is reminiscent of the extreme expansion observed for samples of **NaAlg** described in Chapter 4. Accordingly, the acid-washing employed by Choi and co-workers, significantly diminished the swelling of the seaweed, and improved the processability of the feedstock, (again, presumably by converting the **NaAlg** into **HAlg**, see Figure 5.7). However, both sets of authors conceded that their respective experimental approaches did not enable them to absolutely confirm the origins of the observed effects, which may well have arisen from other changes within the biomass (aside from metal removal) following the harsh acid pre-treatment.

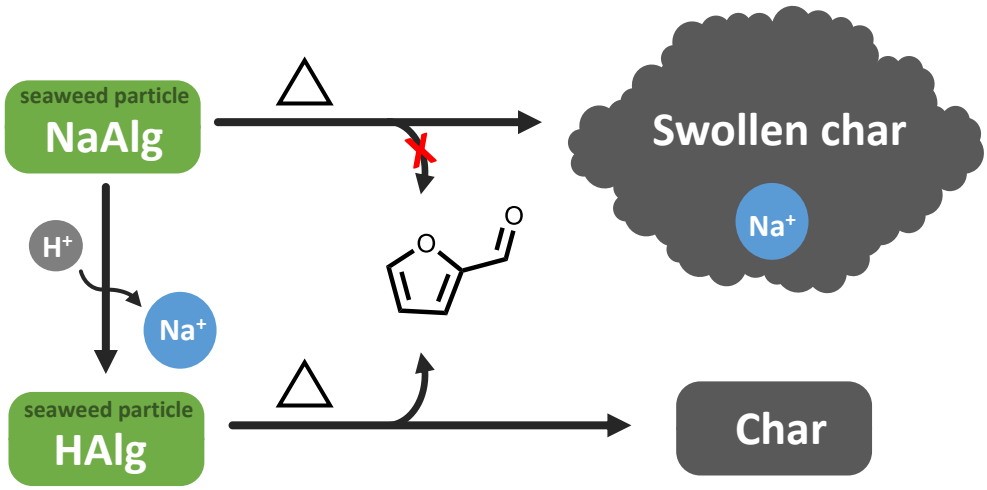

Figure 5.7 The conversion of NaAlg to HAlg by acid washing kelp, and the subsequent impact on pyrolysis behaviour[13,36]

Despite there being clear advantages to including an acidic pre-treatment in the preparation of kelp biomass, such a step would add considerable expense to any commercial thermochemical process.[13,36] It may be, therefore, that the removal of metal-ions prior to pyrolysis, as explored by Ross *et al.* and Choi *et al.*, may not work out to be economically feasible. Conversely, there have been no reports to-date of macroalgae being deliberately enriched in a selected metal ion in order to enhance certain desirable thermochemical traits, as has been achieved for terrestrial feedstocks.[38–44] In this regard, it may be possible to exploit the unique, selective biosorption properties of alginates within the kelp-biomass matrix to dope in (in high abundance) a favourable metal ion. Based on the results of Chapter 4, and, indeed, on the affinity series shown in Section 5.3.1.2, Cu^{2+} seems to be the optimum candidate for such experiments, striking a balance between having high binding affinity, and desirable influence on alginate pyrolysis (decreasing the pyrolysis onset temperature, and increasing selectivity towards the formation of 2-FF). The experiments conducted in this chapter will be devoted to investigating this tandem "metal-exchange – pyrolysis" approach to the thermolysis of kelps.

5.4 Chapter aims and approach

The literature overview provided in Section 5.3.1.3 has highlighted a gap in current understanding of the role of intrinsic metal ions in the pyrolysis of kelp biomass. Whilst the limited studies that have been conducted have concluded that removal of metal-ions from the seaweed prior to thermal processing is the most desirable option, no work has been undertaken to attempt to include metal ions that may have a more positive influence during pyrolysis. As such, Cu^{2+} was highlighted as a good candidate for such studies, as alginate-rich kelps have a naturally high affinity for this ion, and it is known (from Chapter 4) to convey favourable thermochemical properties. With this in mind, the aims of this chapter are:

- To enrich samples of alginate-rich kelp with Cu^{2+} ions
- To measure a set of diagnostic thermochemical properties, including kinetic parameters (the onset temperature of rapid pyrolysis, maximal pyrolysis rates, *etc.*) and yields of products (such as 2-FF, fixed gases, char, *etc.*)
- To compare the effects of Cu(II)-treatment with the untreated case, and a case where the kelp has been treated with a divalent metal species that is expected not to convey favourable thermochemical properties (such as Ca^{2+})
- To discern the fate of Cu^{2+} ions during the pyrolysis of kelp, and propose a mechanism for its observed effects
- To offer a critical appraisal as to the whether or not the Cu(II)-treatment of kelps would be of overall benefit to their pyrolysis on an industrial scale, and highlight areas for future research.

In attempting to achieve the above aims, there are two significant problems faced by earlier researchers in the field that will need to be overcome:

- **Problem 1:** Pre-treating kelp can lead to many changes within the biomass matrix, making it difficult to pin-point the origins of subsequent differences in thermochemical behaviour. Interpretation of the results may be restricted to purely phenomenological discussions.

- **Problem 2:** The highly variable nature of biomass generally (and kelp especially) means that results can be quite specific to the particular batch of feedstock used. As such, there is trepidation about the universal applicability of experiments utilising only sample of biomass.

In order to overcome both of these problems, a novel methodology will be developed in which the kelp biomass is fractionated into alginate and alginate-extracted components, for individual testing in conjunction with the whole, unfractionated biomass. By conducting the same metal-treatment procedures on all fractions of the biomass, the origin of observed differences in pyrolysis behaviour should be more readily discerned. With a fundamental understanding of the role of Cu^{2+}, the formulated conclusions should be widely applicable to all similar kelps, and not just the individual batches tested.

5.5 Results and discussion

5.5.1 Overview of results and discussions

As a key aim of this thesis is to understand the role of uronides in the pyrolysis of seaweeds, five-alginate rich kelps were selected for study. In each of these cases, aside from simply analysing the biomass as a whole, various fractions were also extracted and studied with a view to being able to trace the origin of observed thermochemical traits (see Figure 5.8). Hence, the alginate from each seaweed was studied individually, as too was the alginate-extracted algal-residue (**AE-AR**),[*] which is the structural biomass matrix remaining following the removal of soluble carbohydrates and other easily dissolved components. The kelp samples were also doped with either Cu^{2+} or Ca^{2+} to observe the effects on subsequent thermochemistry.[†] Additionally, the experiments on Cu(II)- and Ca-enriched kelps were also complimented by experiments on the Cu(II)- and Ca-exchanged alginates and Cu(II)- and Ca-enriched **AE-AR**.

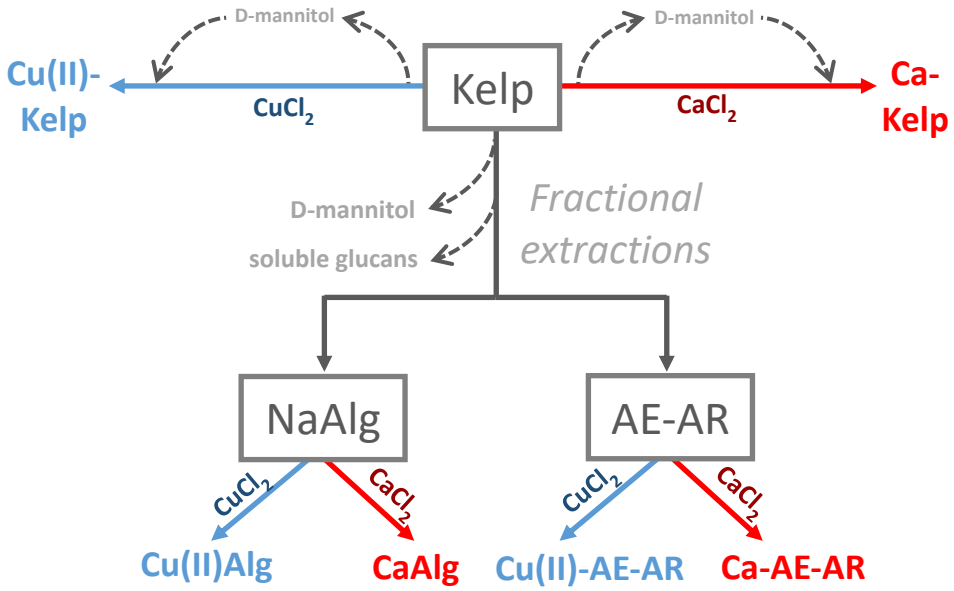

Figure 5.8 A summary of the preparative routes to the various types of biomass sample studied in this chapter, including whole kelp, alginates (**Alg**), and alginate-extracted algal-residues (**AE-AR**), all in various states of metal enrichment.

Following the preparation of the various types of modified-kelp sample, extensive efforts were made to quantify the biochemical and inorganic composition of the kelp specimens as much as possible. The results from these analyses are reported in Section 5.5.2.2 and

[*] In the context of industrial alginate production, the **AE-AR** would be recognised as "kelp slag",[118] though the latter term is not employed here.

[†] Following the metal-enrichment step, D-mannitol (which is easily removed by the process) was added back into the kelp to keep the organic composition of the biomass as close to the starting state as possible.

5.5.2.3. After the starting materials were sufficiently well-defined, the thermochemical investigations were instigated, and are reported in Section 5.5.3. Where possible, the nature of the thermochemical studies was kept similar to those reported for the model uronide compounds in Chapter 4 (and additional information regarding their design and undertaking is provided in Appendix L). Hence, a combination of thermogravimetric analysis (TGA) and pyrolysis-gas chromatography mass-spectrometry (Py-GCMS) was employed to obtain data on both the kinetics and products of kelp thermolysis. As in Chapter 4, where possible, efforts were made to generate quantitative results, particularly with regards to the liberation of 2-furaldehyde (2-furfural, 2-FF) by the various specimens. The multitude of experiments conducted across the many types of sample allowed for an overarching appraisal of the role of the selected metal-ions in the thermolysis of kelps (see Section 5.5.4), and facilitated discussions regarding the implications of the results for the industrial-scale thermal-upgrading of brown seaweed biomass (see Section 5.5.5).

5.5.2 Characterisation and metal-exchange of macroalgal biomass

5.5.2.1 General comments on the characterisation and metal-exchange of macroalgal biomass

In order to exploit the cation-exchange properties of alginates (discussed in Section 5.3.1.2), it was desirable to use samples of macroalgae that were rich in the polysaccharide. As such, five species of kelp all known to produce alginate abundantly were chosen: *Laminaria digitata* (**L.dig**), *Laminaria hyperborea* (**L.hyp**), *Saccharina latissima* (**S.lat**), *Fucus vesiculosus* (**F.ves**), and *Ascophyllum nodosum* (**A.nod**). The algae were harvested from Boulmer beach in Northumberland (UK) in late January, at which point in the seasonal calendar literature studies indicated that stocks of alginate would be highest (see photograph in Figure 5.9).[5,6]

Figure 5.9 Kelp (*Laminaria digitata*) pictured prior to harvesting

After the raw macroalgae had been dried, ground and sieved, the biochemical composition of each of the samples was characterised, and are reported in Section 5.5.2.2. The seaweed biomass was then separated into two fractions: *alginate* and an *alginate-extracted algal-residue* (**AE-AR**) (as explained in Section 5.5.1), which were both subjected to additional characterisations (reported in Sections 5.5.2.4 and 5.5.2.5, respectively). Finally, all three types of sample (the whole seaweed biomass, the alginate, and the **AE-AR**) underwent a metal-exchange treatment with either Ca^{2+} or Cu^{2+} (as explained in Section 5.5.1). Subsequent characterisation of the Ca- and Cu(II)-treated samples are discussed in Sections 5.5.2.3 (macroalgae), 5.5.2.4 (alginates), and 5.5.2.5 (**AE-AR**).

5.5.2.2 Characterisation of untreated macroalgal biomass

As was discussed in the preceding section, five samples of alginate-rich kelp were utilised in this work: *Laminaria digitata* (**L.dig**), *Laminaria hyperborea* (**L.hyp**), *Saccharina latissima* (**S.lat**), *Fucus vesiculosus* (**F.ves**), and *Ascophyllum nodosum* (**A.nod**). The kelps were freshly harvested, with the exception of **S.lat**, which had been recently beach-cast. Once collected, the samples were prepared according to the methods described in Section 5.8.1.1, and were dried as soon as possible to minimise chemical and biological degradation. After shredding, the macroalgae were frozen for 1 - 3 days prior to further processing. Upon re-thawing, careful effort was made not to lose any leachate. At this stage, drying the samples to a constant weight removed around 80 wt.% of their mass, leaving behind the "dry mass". In-fact, this dry mass still contains considerable levels (≈ 5 – 10 wt.%) of residual moisture absorbed within the structure (as demonstrated in Figure 5.10). Following grinding of the biomass samples to a uniform size distribution, they were analysed to determine their elemental composition (wt.%CHNS and wt.%metals). The results for these elemental analyses are reported in Appendix I for each of the seaweeds in question. However, additional fractionation of the algal biomass facilitated a quantitative biochemical profile of the samples to be prepared (see Figure 5.10), vital for understanding the pyrolysis studies in Section 5.5.3.

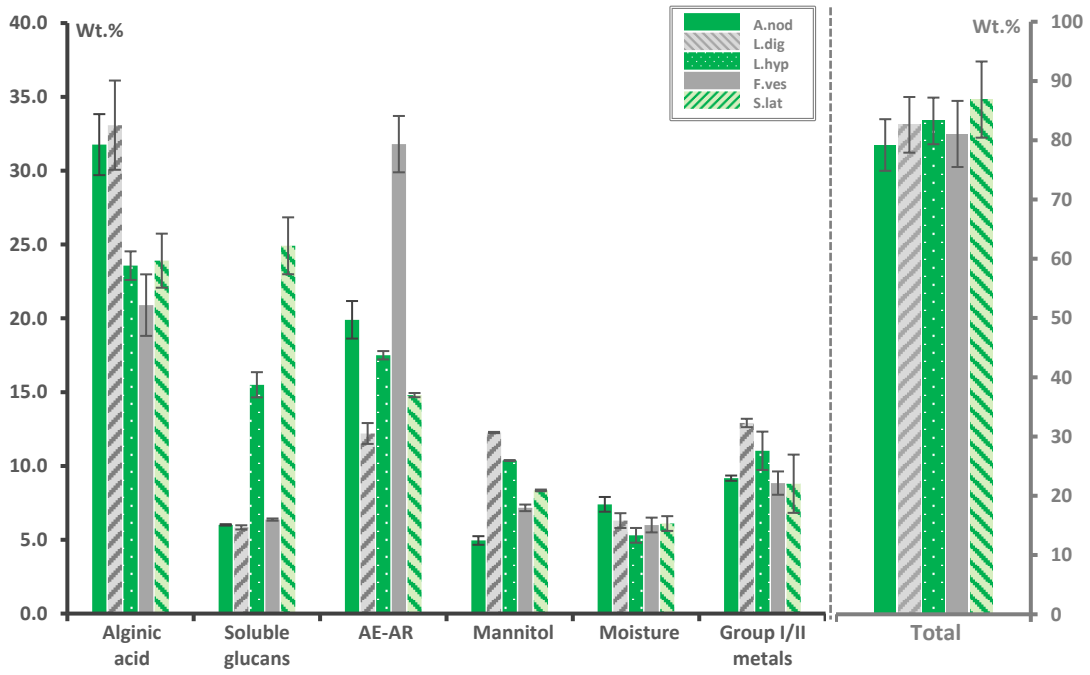

Figure 5.10 Composition of the five species of kelp studied in this chapter

The first point to note about the data in Figure 5.10 is that the values depicted are in excellent agreement with those determined by previous authors in similar studies.[5,6,45,46] Hence, the results of the biological characterisation presented here are consistent with those expected, after allowing for species, season and geographical location. Accordingly, the stocks of mannitol within the five harvested kelps were found to be low (5 - 12 wt.%), as were soluble glucans (5 – 15 wt.%), which is expected owing to the reduction of the reserves of these compounds over the preceding winter months.[45] The exception appears to be **S.lat**, which showed relatively high levels of soluble glucans, conceivably as a consequence of this sample having been beach-cast and hence susceptible to degradation of its structural carbohydrates. Further attempts to identify the soluble glucans in the kelps were unsuccessful, though NMR spectroscopic analysis of the fractions indicated laminarin and fucoidan* were, as expected, prominent constituents.[9,47–49] Very small quantities of uronic acids were detected in the soluble glucan fractions, which may have been glucuronic acid from the fucoidan,[50] or simply contamination by small amounts of short-chain alginates.

Significantly, from the point of view of the subsequent thermal analysis in this chapter, alginic acid was found to be highly abundant in all five of the kelp samples studied, with the polysaccharide accounting for around 20 – 35 wt.% of the dry-mass. **L.dig** and **A.nod** were found to be particularly rich in alginic acid, and are subject to special attention in the later parts of this chapter. Other authors have noted differences in the alginate content in the stipes of algal specimens compared to their fronds, but no such distinction was made in this work as material from several samples of varying shape and size was processed together to give a representative homogenised feedstock.[6] Of course, whilst the value for the "alginic acid" content of the kelp is reported in Figure 5.10, in reality the polysaccharide exists in the deprotonated (alginate) form when found in nature. The high proportion of s-block ions measured within the kelps therefore reflect the fact that these metals act as the counter cations to the anionic alginate polymer. The metal profile of the seaweeds was unsurprisingly dominated by Na^+ and K^+, which, in roughly equimolar proportions, account for 80 – 90 % of the metal species detected in the samples (by mole and by mass). The remaining metals were a mixture of Ca^{2+}, Mg^{2+} and Sr^{2+}, with Cu^{2+} and other d-block cations being below the limits required for accurate determination by ICP-OES. As with the other fractions shown in Figure 5.10, this metal profile is in good agreement with studies by previous authors.[5,46]

Following removal of all the extractable fractions of the kelp biomass an insoluble residue remains (referred to as the *alginate-extracted algal-residue*, **AE-AR**). The nature of this insoluble material is discussed in more detail in Section 5.5.2.5, but it mainly consists of proteins, polyphenols, and structural carbohydrates.[5] When the various fractions (alginic acid, soluble glucans, mannitol, **AE-AR**, metals, and moisture) are summed together, they account for around 80 – 85 wt.% of the macroalgal biomass. The remaining mass balance is likely to be formed of other inorganic anions (chlorides, iodides, phosphates), lipids, polyphenols, soluble amino acids, and carbohydrates that were not adequately detected by the analytical techniques employed.[4,5,45,49]

* Evidence for fucoidan, a sulphate polysaccharide, was also provided by the 2 – 3 wt.% sulphur detected in the kelps (see Appendix I).

5.5.2.3 Characterisation of metal-exchanged macroalgal biomass

Having carried out a thorough biochemical compositional analysis in Section 5.5.2.2, the macroalgae samples **L.dig**, **L.hyp**, **S.lat**, **F.ves**, and **A.nod**, were all subjected to a metal-exchange treatment by soaking in 1.0 M $CaCl_2$ or $CuCl_2$. The resulting Cu(II)- and Ca-exchanged kelp samples (denoted **Cu(II)-L.dig**, **Ca-L.dig**, *etc*.) were then analysed prior to utilisation in thermochemical experiments of Section 5.5.3. Preliminary investigations (and literature studies)[51,52] indicated that the metal-exchange procedure would result in removal of some of the soluble organic constituents of the seaweed biomass. Whilst it was not possible to account for all of these losses, the D-mannitol fraction was quantitatively replaced in order to maintain as much similarity with the untreated biomass as possible. Elemental analysis (detailed in full in Appendix I) demonstrated complete loss of all other metal species from the kelp samples, and significant enrichment of either Ca^{2+} or Cu^{2+} in their respective cases.[*] A slight enhancement in wt.%C and wt.%H was noted in most cases too, likely in response to the decrease in the total wt.%metals. Crucially, however the ratio of (wt.%C):(wt.%H) remained virtually constant for the kelps studied upon metal exchange, especially in the cases of **A.nod** and **L.dig** (which form the focus of Section 5.5.3). Hence (following the replenishment of their D-mannitol contents) the Ca- and Cu(II)-exchanged samples of **A.nod** and **L.dig** can largely be considered to be compositionally analogous to their untreated counterparts in all but metal profile.

5.5.2.4 Characterisation and metal-exchange of extracted alginates

Two different types of uronide-extraction methodologies were utilised over the course of the study, both are described in detail in Section 5.8.1. The first was aimed at completely removing alginic acid (**HAlg**) from the biomass, in order to accurately quantify it (see Section 5.5.2.2) and to generate an *alginate-extracted algal-residue* (**AE-AR**) for further study (see Section 5.5.2.5). The second extraction procedure, whilst being milder and much less efficient, yielded samples of sodium alginate (**NaAlg**) with a higher purity and a lower degree of degradation. The alginate fraction from the second extraction procedure forms the basis of discussions here and throughout the thermochemical experiments described in Section 5.5.3.

The **NaAlg** samples extracted from **L.dig** (**NaAlg-DIG**), **L.hyp** (**NaAlg-HYP**), **S.lat** (**NaAlg-LAT**), **F.ves** (**NaAlg-VES**), and **A.nod** (**NaAlg-NOD**) were all converted into their Ca- or Cu(II)-forms (abbreviated in accordance with the same conventions as the **NaAlg** samples) by the ion-exchange procedure described in Section 5.8.1.4. In addition to the freshly extracted alginates, two batches of commercial **NaAlg** (one from Sigma Aldrich and one from BDH) were also utilised in this work. The **NaAlg** supplied by Sigma Aldrich (which was studied extensively in Chapter 4) had originally been extracted from *Macrocystis pyrifera* by the manufacturer and is denoted **NaAlg-SIG**, whilst the sample from BDH was derived from *Laminaria hyperborea* and is denoted **NaAlg-BDH**. The Ca- and Cu(II)-exchanged variants of **NaAlg-SIG** and **NaAlg-BDH** were prepared in the same manner as those from the other seaweeds (and are abbreviated according to the same convention).

[*] Whilst the results demonstrated complete loss of the starting metals and enhancement of the levels of the dopant metal (either Ca^{2+} or Cu^{2+}), they were not of sufficient quality to prove whether or not the exchange was quantitative, which remains a point for future investigation.

The **Na-**, **Ca-** and **Cu(II)-Alg** samples were subjected to elemental analysis and examination by Fourier-transform infra-red (FTIR) spectroscopy. The results of such analyses were in accordance with those previously described in Chapter 4, confirming that the desired alginate salt had been prepared (data reported in Appendix G and H for reference). The alginates were also analysed by nuclear magnetic resonance (NMR) spectrocopy in order to determine the monomer sequence of the polymer, particularly the ratio of mannuronate:guluronate units (**M**:**G** ratio – see Figure 5.11). In this regard, values of **M**:**G** were determined for **NaAlg-DIG** (**M**:**G** = 1.34 ± 0.02), **NaAlg-HYP** (**M**:**G** = 1.13 ± 0.02), **NaAlg-LAT** (**M**:**G** = 0.95 ± 0.02), **NaAlg-VES** (**M**:**G** = 0.78 ± 0.02), **NaAlg-NOD** (**M**:**G** = 1.86 ± 0.02), **NaAlg-SIG** (1.25 ± 0.02), and **NaAlg-BDH** (0.53 ± 0.02), with more detailed measurements being reported in Appendix J. This even distribution of **M**:**G** values across the range 0.53 – 1.86 gives ample scope for determining whether the mannuronate:guluronate ratio is of significance to the alginate thermal behaviour discussed in Section 5.5.3.

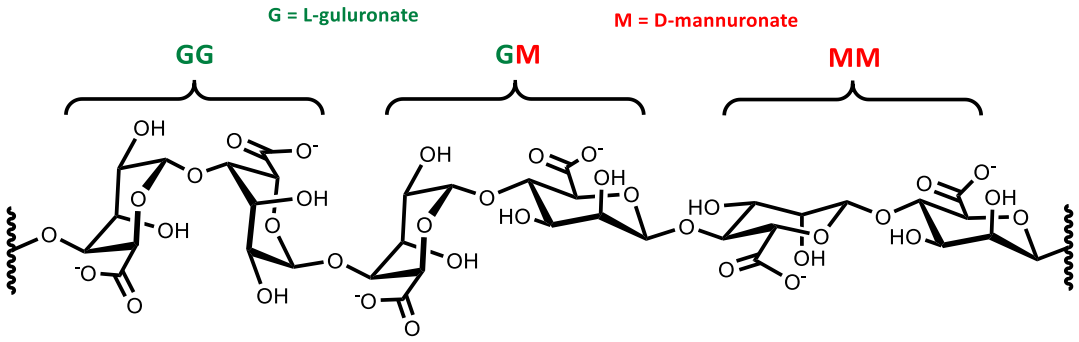

Figure 5.11 The structure of alginate, highlighting **G** and **M** regions

5.5.2.5 Characterisation and metal-exchange of alginate-extracted algal-residue (AE-AR)

Following the various procedures employed to fully extract alginate (in the alginic acid form) from the macroalgal biomass, a solid fibrous material is found to remain, referred to here as the *alginate-extracted algal-residue* (**AE-AR**).* Recognising that this insoluble **AE-AR** material is relatively ill-defined, it was decided to study its thermochemical properties, in order to compare with the more well-recognised components of algal-biomass (such as alginate, laminarin, and mannitol).[12] Digestion and subsequent carbohydrate analysis of the fraction indicated that 30 – 45 wt.% of the **AE-AR** was comprised of insoluble glucans – most likely cellulosic polysaccharides. Further investigations indicated that the residue had a uronic acid components of 2 – 5 wt.%, which could signify the presence of small amounts of hemicellulose, fucoidan, or traces of unextracted alginate.[45,50,53] Elemental analysis of the **AE-AR** revealed a two to three-fold enrichment in the wt.%N in the samples compared to the parent kelp biomass, indicating an enhanced protein content in the residues. A semi-quantitative metal-analysis also showed that the **AE-AR** contained only Na^+ and (to a lesser extent) Ca^{2+}, which is unsurprising given that the alginate-extraction procedure required for treatment with salts of those cations at various stages (see 5.8.1.5).

* Of course, it should also be pointed out that the other soluble kelp fractions (such as mannitol and laminarin) have been separated from the biomass by the time the AE-AR is isolated.

The **AE-AR** fractions were subjected to the same metal-exchange process as the macroalgae and extracted alginates (described in Sections 5.5.2.3 and 5.5.2.4, respectively). Here, the residues were soaked in either $CaCl_2$ or $CuCl_2$ before being dried and re-analysed (see results in Appendix I). As anticipated, the Na^+ was completely removed from the samples, and increased levels of either Ca^{2+} or Cu^{2+} were observed in their respective cases. Furthermore, consistency in the wt.%N and ratio of (wt.%C):(wt.%H) before and after the metal-exchange were good indications that the treatment did little to affect the organic constituents of the sample (unsurprisingly given the poor solubility of such components). Hence, the **AE-AR** for each seaweed (denoted **AE-AR-DIG**, **AE-AR-NOD**, *etc.*) were ready for thermochemical analysis (see Section 5.5.3), along with their Cu(II)- and Ca-exchanged counterparts (abbreviated to **Cu(II)-AE-AR-DIG**, **Ca-AE-AR-DIG**, *etc.*).

5.5.3 Thermal analysis of macroalgal biomass

5.5.3.1 General comments on the thermal analysis of macroalgal biomass

In order to study the role played by various metal-ions in the pyrolysis of kelps, a series of thermochemical experiments was undertaken. These were essentially comprised of two different experimental approaches: thermogravimetric analysis (TGA) and pyrolysis-gas chromatography mass spectrometry (Py-GCMS), the results of which are reported in Sections 5.5.3.2 and 5.5.3.4 – 5.5.3.7, respectively. TGA yields a plot of sample mass with increasing temperature (and hence an impression of the kinetics of the biomass degradation), where Py-GCMS gives an insight into the identity and quantity of volatile organic compounds liberated from the reaction. There are significant differences between the two techniques (with, for example, the heating rate of Py-GCMS being orders of magnitude greater than for TGA), though, as a first approximation, the two types of measurement are quite complimentary (see Appendix L for a detailed discussion). An additional set of experiments was also carried out to investigate the properties of the chars of algal samples with and without a Cu^{2+} pre-treatment (see Section 5.5.3.3). Here powder X-ray diffraction (PXRD) and Fourier transform infrared spectroscopy (FTIR) were used to study the chars *ex situ*, following an isothermal TGA experiment. In all cases (TGA, TGA-FTIR, TGA-PXRD, and Py-GCMS) identical conditions were used to those employed in the model compound studies of Chapter 4.

Of course, the thermochemical experiments were not just conducted on whole kelp biomass, but also on the alginate and alginate-extracted algal-residues (**AE-AR**) as well. Such an approach, which is rationalised fully in Section 5.5.1, facilitated the assignment of certain thermochemical behaviours observed in the whole kelp biomass to a particular component(s) within the matrix (see Section 5.5.3.5). One such observed behaviour was the selective release of 2-furaldehyde (2-furfural, 2-FF) by samples of Cu(II)-treated kelps (see Section 5.5.3.4), a phenomenon for which it was desirable to obtain fully quantitative data (see Section 5.5.3.6). Quantitation is not common-place in Py-GCMS analysis, and (again) the reader is advised to refer to Appendix L for a discussion of the experimental precautions necessary to facilitate such work. Efforts were also made to quantify the release of CO_2 and CO, which account for significant proportions of the products yielded by pyrolysed kelp (see Section 5.5.3.7).

Finally, the time consuming and inherently data-rich experiments attempted in this chapter meant that is was desirable to restrict the number of samples for processing. As such, the results are largely focussed on the two most alginate-rich seaweeds, **L.dig** and **A.nod**, though references are made to the equivalent results from **L.hyp**, **S.lat**, and **F.ves** where appropriate.

5.5.3.2 Thermogravimetric analysis (TGA) of algal biomass before and after metal-exchange

Thermogravimetric analysis (TGA) was conducted under N_2 with a heating rate of 10 °C min^{-1} on samples of whole macroalgae in both native and metal-exchanged states. In addition, the **NaAlg** extracted each alga was studied under the same conditions, along with the **CaAlg** and **Cu(II)Alg** equivalents. Finally, the alginate-extracted algal-residue (**AE-AR**) from each species was investigated, with the Ca- and Cu(II)-treated forms again being studied for comparison. The data from all of these thermogravimetric experiments is depicted in Figure 5.12 (macroalgae), Figure 5.13 (alginates), and Figure 5.14 (algal-residues), with "average" curves being highlighted in each case.[*] The first derivative of the TGA plots (known as the DTG) are also depicted (along with analogous "average" DTG plots), as this allows for easy comparison of more subtle changes in the individual thermogravimetric curves.

As expected from the discussions in Chapter 4, and elsewhere,[4,12,54] the TGA results demonstrate that, with increasing temperature, the selected kelps decompose in three broadly defined stages:

I. Drying (*T* = Ambient → *T* ≈ 110 °C)

Water comprises around 80 wt.% of the wet mass of freshly harvested kelp samples, and even after several days of desiccation at 60 °C, the samples still hold around 5 – 10 wt.% moisture. At elevated temperatures, this loosely bound water is volatilised (in a reversible manner), with the amount of moisture lost being dependent on the relative humidity of the initial sample preparation environment. As such, low-temperature drying-phenomena are of relatively little interest in the study of the irreversible pyrolysis observed at higher temperatures. Consequently, an isothermal drying period was included at the start of each TGA run to drive off the loosely-bound water and correct the sample starting mass to a moisture-free value (see further explanation in Appendix L).

[*] Average thermogravimetric curves are formed by calculating the arithmetic mean of the values from of the individual contributory curves at a given temperature. Such a method is useful for amalgamating the information from several similar curves (for example, all of the **NaAlg** samples) into a more succinct form. The use of average TGA curves is appropriate in this case as samples of the same type were mostly found to possess extremely similar thermolysis characteristics. The individual TGA and DTG profiles that contribute to the average curves are still depicted (albeit unlabelled) in Figure 5.12 - Figure 5.14 to demonstrate the level of spread in thermal behaviour for each type of sample.

II. Rapid pyrolysis (T ≈ 150 - 210 °C → T ≈ 350 - 400 °C)

From about 150 – 210 °C (depending on the heating rate and sample in question) the macroalgae undergo rapid pyrolysis, in which 40 - 50 wt.% of the starting mass is volatilised over a very narrow thermal window. The term T_i is used to refer to the temperature of initiation of rapid pyrolysis and T_f to refer to the final temperature. Other important metrics include: $\Delta M(T_i - T_f)$, which is the mass loss across the period of rapid pyrolysis, and T_{max1} and T_{max2}, which signify temperatures of maximal mass loss rate (in turn denoted Rate[T_{max1}] and Rate[T_{max2}]). Values for these thermal parameters (which are rigorously defined in Appendix L) are reported in Table 5.1, expressed as an average (± standard deviation) for each type of sample studied. As the rapid pyrolysis period corresponds to the point at which the majority of potentially valuable volatile compounds are liberated, it will be the focal point of discussions in the rest of Section 5.5.3.

III. Secondary degradation (T > 450 °C)

A region of much slower mass loss follows rapid pyrolysis in which secondary degradations occur and the char structure evolves. As the focus of this chapter is the formation of volatile chemicals during the period of rapid pyrolysis, much less attention is devoted to high temperature degradation steps in the discussion.

Table 5.1 Characteristic thermal parameters from the rapid pyrolysis of macroalgal biomass heated at 10 °C min^{-1} under He (standard deviations in parentheses)

Sample	Treatment	T_i (°C)	T_f (°C)	$\Delta M(T_i - T_f)$ (wt.%)	T_{max1} (°C)	Rate[T_{max1}] (wt.% min^{-1})	T_{max2} (°C)	Rate[T_{max2}] (wt.% min^{-1})
Macroalgae	**Untreated**	210 (5)	349 (18)	36 (3)	248 (6)	-4.6 (1.0)	294 (3)	-2.8 (0.4)
	Ca^{2+}-treated	207 (2)	392 (13)	46 (6)	243 (4)	-4.2 (0.9)	344 (3)	-2.9 (0.8)
	Cu^{2+}-treated	170 (11)	400 (6)	53 (5)	203 (7)	-3.8 (0.6)	286 (3)	-4.0 (0.8)
Alginates	**Na^{+}-bound**	206 (3)	280 (3)	42 (1)	220 (2)[a]	-8.6 (0.6)	240 (7)[a]	-9.6 (1.1)
	Ca^{2+}-bound	209 (4)	342 (11)	40 (2)	247 (7)[b]	-5.3 (0.8)[b]	-	-
	Cu^{2+}-bound	171 (8)	360 (11)	50 (2)	197 (1)	-4.6 (0.6)	241 (4)	-6.7 (0.5)
Alginate-extracted algal residues (AE-AR)	**Untreated**	236 (5)	409 (20)	42 (15)	316 (21)	-5.0 (3.0)	-	-
	Ca^{2+}-treated	234 (17)	433 (12)	51 (11)	344 (3)	-6.6 (3.4)	-	-
	Cu^{2+}-treated	193 (25)	401 (12)	45 (7)	271 (12)	-3.6 (0.7)	-	-

[a] In some cases for **NaAlg**, T_{max1} and T_{max2} coalesce into a single event

[b] **CaAlg-SIG** and **CaAlg-BDH** both showed an additional T_{max} event to that listed in the table, though this additional feature was not apparent on the average curve of all **CaAlg** samples

[blank page]

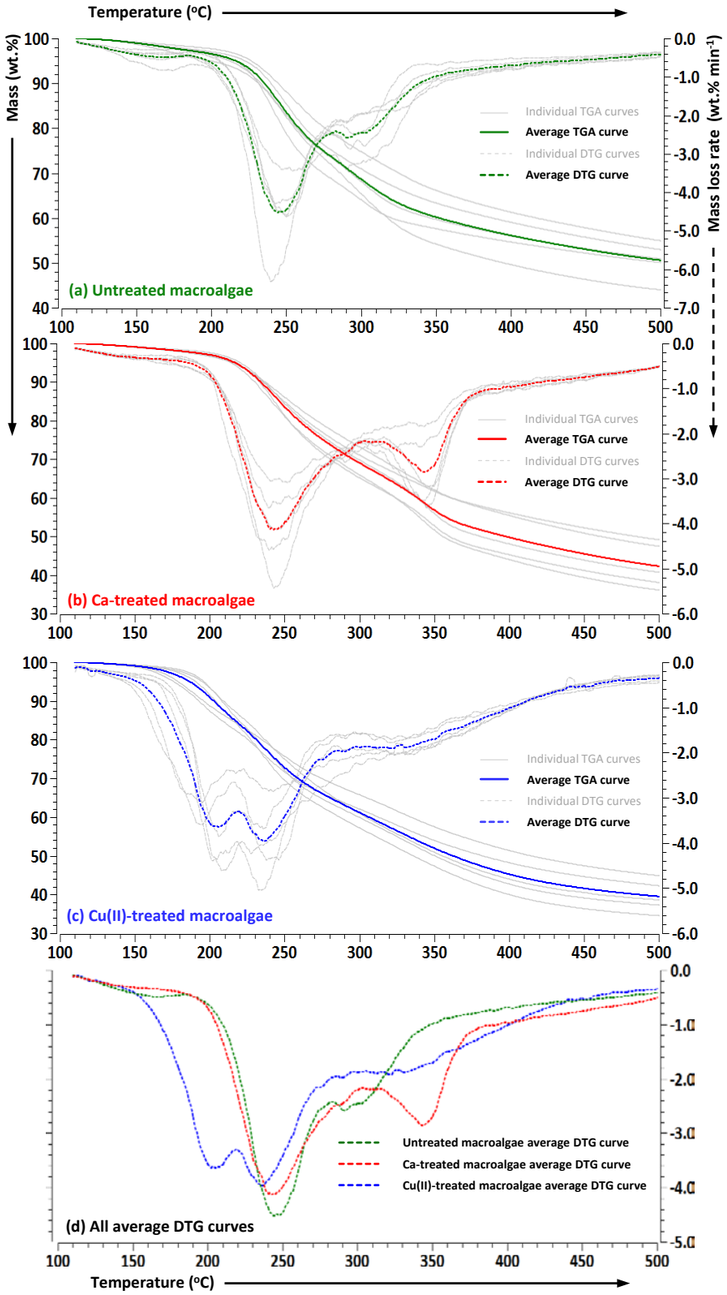

Figure 5.12 Average TGA (—) and DTG (---) traces of (a) untreated, (b) Ca-treated, and (c) Cu(II)-treated samples of macroalgae heated at 10 °C min^{-1} under He. The faint grey lines represent traces from the individual samples to indicate the degree of variation from the average. Plot (d) shows all three average DTG traces overlaid for comparison.

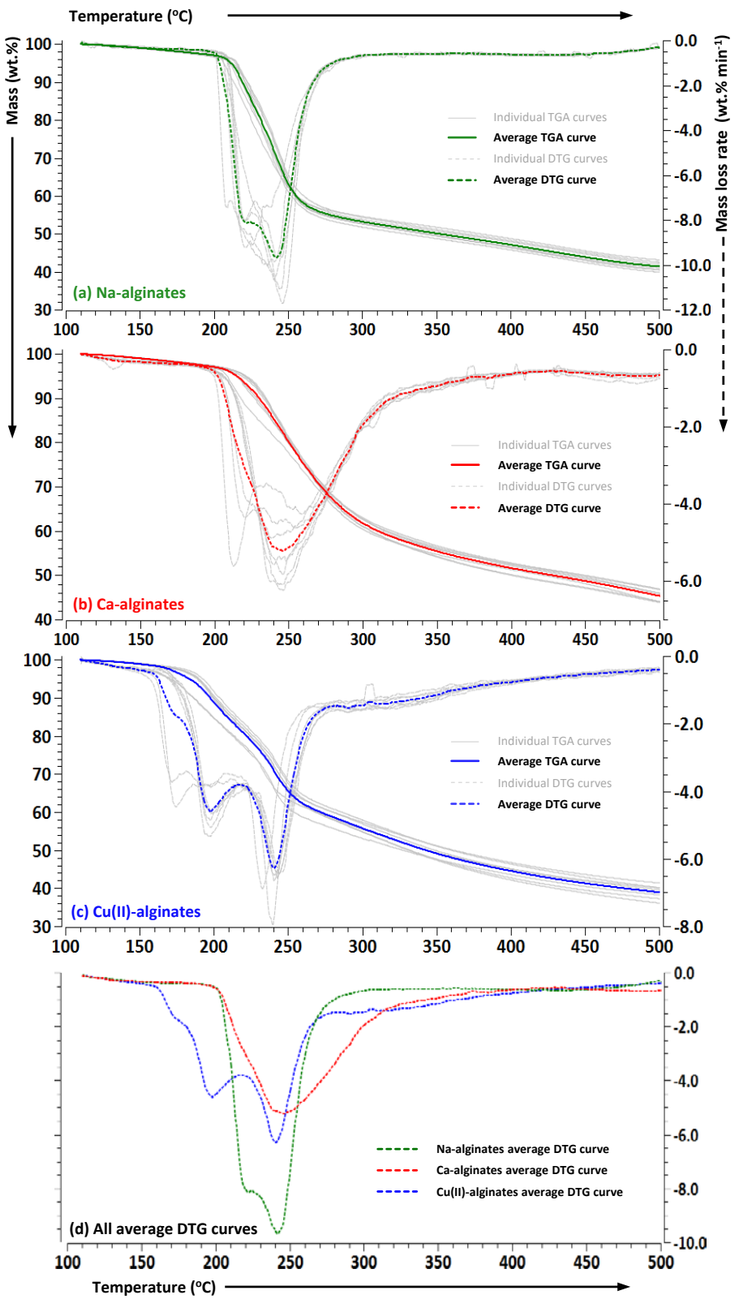

Figure 5.13 Average TGA (—) and DTG (---) traces of (a) **NaAlg**, (b) **CaAlg**, and (c) **Cu(II)Alg** samples heated at 10 °C min^{-1} under He. The faint grey lines represent traces from the individual samples to indicate the degree of variation from the average. Plot (d) shows all three average DTG traces overlaid for comparison.

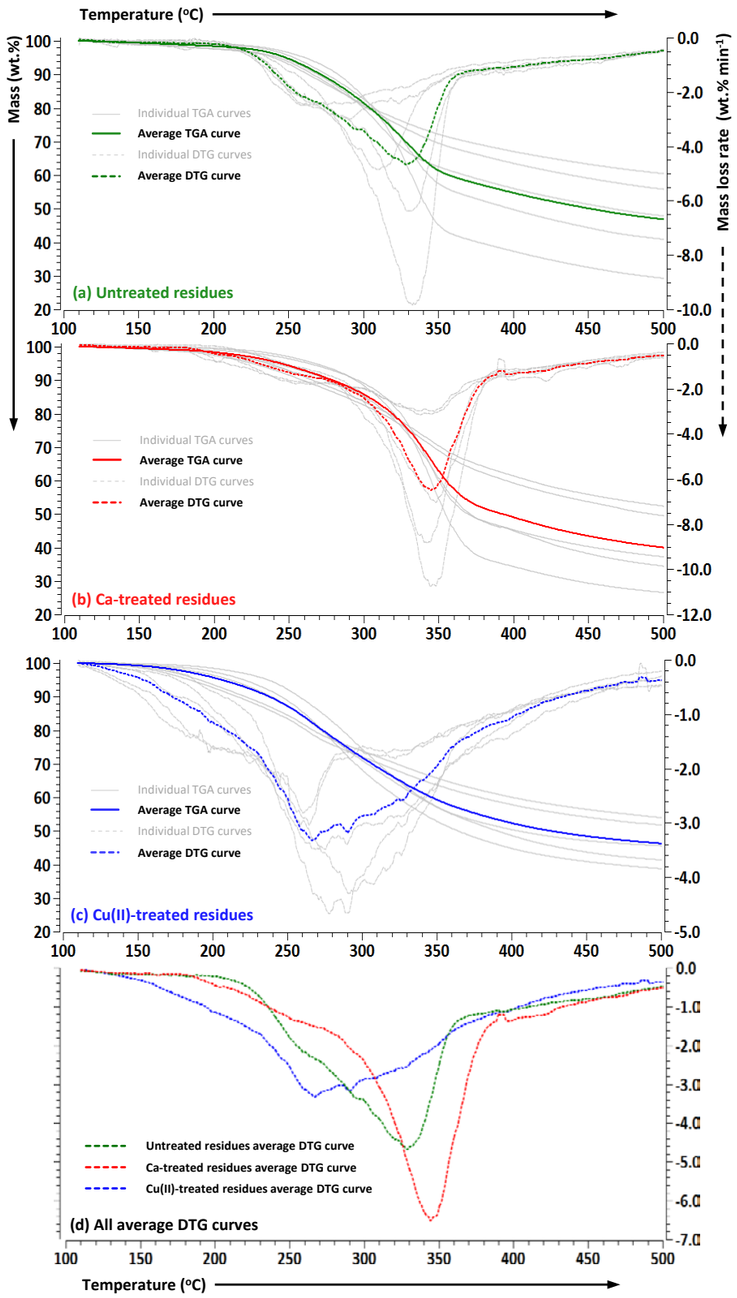

Figure 5.14 Average TGA (—) and DTG (---) traces of (a) **AE-AR**, (b) **Ca-AE-AR**, and (c) **Cu-AE-AR** samples heated at 10 °C min^{-1} under He. The faint grey lines represent traces from the individual samples to indicate the degree of variation from the average. Plot (d) shows all three average DTG traces overlaid for comparison.

When viewed together, Figure 5.12 – Figure 5.14 clearly demonstrate the individual contributions made by alginate and **AE-AR** to the overall shape of the TGA profile originating from samples of whole (unfractionated) macroalgae. For example, the average DTG curve for untreated macroalgae (see Figure 5.12a) is clearly a weighted convolution of the average DTG curves for **NaAlg** (see Figure 5.13a) and **untreated**-**AE-AR** (see Figure 5.14a). Similar statements can also be made of the Ca- and Cu(II)-treated macroalgae (see Figure 5.12 - Figure 5.14, subplots b and c). Generally, the rapid pyrolysis of the alginates occur at a lower temperature than the **AE-AR**, regardless of the identity of the bound cation. Hence, **NaAlg**, **CaAlg**, and **Cu(II)Alg** all demonstrate T_i values that are around 20 - 30 °C lower than the equivalent **Na-AE-AR**, **Ca-AE-AR** and **Cu(II)-AE-AR** samples, and T_{max1} values that are 70 – 100 °C lower. Furthermore, the deviation of **AE-AR** samples from the average TGA and DTG curves is much larger than in the case of the alginates, which behave in a very reproducible manner, dependant only on the identity of the bound cation (as discussed below). When viewed collectively, the results from the thermogravimetric analysis therefore indicate that alginate decomposition gives rise to consistent, low temperature thermolysis behaviour in macroalgae, whereas the differing composition of the **AE-AR** leads to more variable behaviour between species at higher temperatures.

Regarding the impact of the metal ions on the TGA profiles of macroalgae, alginates, and **AE-AR**, Figure 5.12d, Figure 5.13d, and Figure 5.14d are useful points of reference. These figures clearly demonstrate that the Cu(II)-promoted onset of rapid pyrolysis reported for **Cu(II)Alg** in Chapter 4 is translated to Cu(II)-treated macroalgae, which has an average T_i value around 40 °C lower than those of the untreated and Ca-treated samples. Interestingly, the **Cu(II)-AE-AR** samples also show a notable shift to degradation at lower temperatures (see Figure 5.14d), though not quite as drastically as in the case of **Cu(II)Alg** (see Figure 5.13d). Mutual differences between the untreated and Ca-treated macroalgae TGA curves are, on the other hand, more subtle. Indeed, until about 270 °C, the two curves are virtually identical (see Figure 5.12d), with a notable divergence at higher temperatures as the Ca^{2+} ions retard the degradation of the **AE-AR** (see Figure 5.14d). The similarity between untreated macroalgae and the Ca-treated macroalgae below 270 °C is a little surprising, given how differently **NaAlg** behaves compared to **CaAlg** (see Figure 5.13d), with a much higher value for Rate[T_{max1}] being exhibited by the former compound (-8.6 ± 0.6 wt.% min^{-1}) than the latter (-5.3 ± 0.8 wt.% min^{-1}). Hence, it seems that the high mass loss rate associated with **NaAlg** samples (discussed at length in Chapter 4) is suppressed to some degree when the compound is embedded within an algal biomass matrix.

Finally, it is worth noting that the presence of both Ca^{2+} and Cu^{2+} appears to decrease the level of char remaining following rapid pyrolysis (see the values of $\Delta M(T_i - T_f)$ in Table 5.1 for example. However, closer inspection indicates that the ability of the two metals to bring about the reduction in char relative to the untreated sample, is a product of different effects. In the case of Ca-treated macroalgae, the Ca^{2+} enhances the degree of degradation of only the **AE-AR** whereas, for Cu(II)-treated macroalgae, the Cu^{2+} enhances the degree of

degradation of both the **AE-AR** and alginate fractions. Naturally, additional information into the role of the metal ions in biomass thermolysis can be derived by *ex situ* analysis of the residual char following the completion of a TGA experiment. Such a methodology was used to good effect in the study of metal alginates in Chapter 4, and forms the basis of the following section.

5.5.3.3 Solid-state analysis of chars derived from algal biomass and Cu-treated algal biomass

Following on from the TGA experiments described in Section 5.5.3.2, it was decided to analyse the char samples arising from both untreated samples of macroalgae (specifically **A.nod** and **L.dig**) and their Cu(II)-treated counterparts (**Cu(II)-A.nod** and **Cu(II)-L.dig**). To this end, the relevant biomass was heated to 250 °C at 10 °C min^{-1} under N_2 and held for 60 minutes, to allow for the maturation of crystallites in the sample. Following the heating programme, the char was removed and studied by both Fourier transform infra-red spectroscopy (FTIR) and powder X-ray diffraction (PXRD). The results of both sets of analyses from before and after the thermolysis reaction are shown in Figure 5.15 and Figure 5.16.

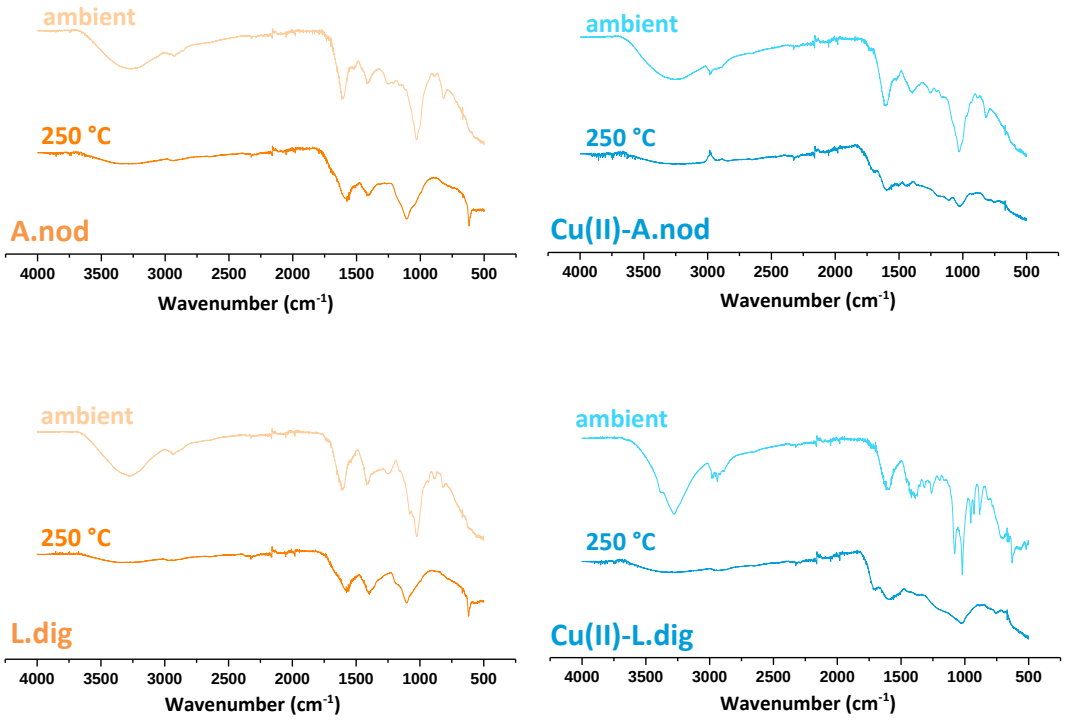

Figure 5.15 FTIR analysis of the chars of **A.nod** (top) and **L.dig** (bottom) in untreated (left) and Cu(II)-exchanged (right) states, following heating for 60 minutes under He at 250 °C.

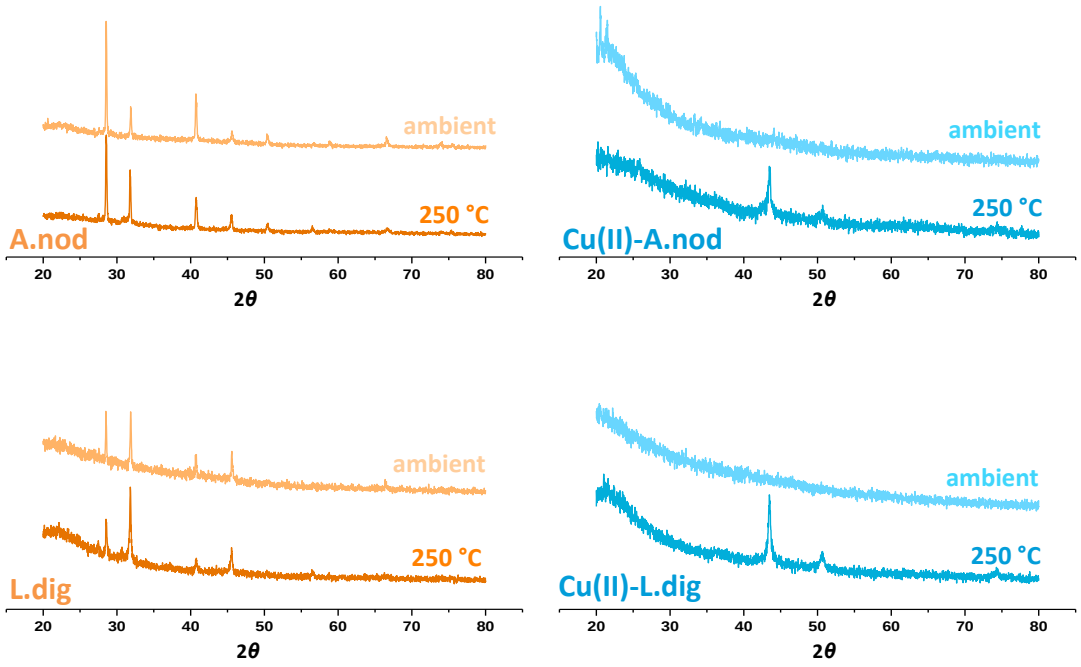

Figure 5.16 PXRD analysis of the chars of **A.nod** (top) and **L.dig** (bottom) in untreated (left) and Cu(II)-exchanged (right) states, following heating for 60 minutes under He at 250 °C.

The task of interpreting the FTIR analysis of kelp samples is simplified greatly by reference to the work of McCormack *et al.*,[55] who assigned and catalogued a large number of characteristic stretching frequencies from for a variety of species. For untreated **A.nod** and **L.dig**, the FTIR spectrum is dominated by the absorbances of monovalent metal alginates (**NaAlg** and **KAlg**), which can be confirmed by reference to the exemplar spectra in Appendix G. Particularly, the peaks at around 1600 and 1410 cm^{-1} correspond to the asymmetric and symmetric vibrational modes of the alginate carboxylate moiety.[56] In addition, a small peak at around 1240 cm^{-1} is believed to originate from an asymmetric S=O stretch, conceivably arising from fucoidan, whilst a shoulder at 1530 cm^{-1} is characteristic of a protein amide band.[55] The broad peak at 3250 cm^{-1} is attributable to bound water within the biomass, and the strong peak at 1030 cm^{-1} is assigned to C-O stretches in C-O-C and C-O-H moieties (principally from the alginate, but also from other carbohydrates in the biomass).[57] The equivalent analysis of ambient temperature samples of **Cu(II)-A.nod** and **Cu(II)-L.dig** (see Figure 5.15) show a good degree of similarity with the untreated samples (albeit with a slight shift in carboxylate peak position in accordance with the coordination of a divalent cation).[56] Both Cu(II)-treated samples also show additional fine structure, which, whilst prominent, cannot currently be assigned unambiguously.

By subjecting the untreated and Cu(II)-treated kelp samples to the isothermal heating regime described above, changes to the FTIR spectrum are observed (see Figure 5.15). In all cases, loss of the broad peak at around 3250 cm^{-1} is consistent with the dehydration behaviour described in Section 5.5.3.2. Untreated **A.nod** and **L.dig** show broadening of the peak at 1030 cm^{-1}, which also shifts to higher wavenumbers (around 1100 cm^{-1}). This observation could be caused by the scission and rearrangement of C-O bonds within the sample, likely signalling the cleavage of glycosidic linkages or elimination of hydroxyl groups

as water.[57] Furthermore, the reduction in intensity of the peak at 1240 cm^{-1} is consistent with the early degradation of fucoidan within the samples.[12,23] Otherwise, the main peaks of the **L.dig** and **A.nod** samples are largely unchanged at 250 °C, with the alginate carboxylate moieties clearly remaining in-tact. The behaviour of the untreated macroalgal samples is therefore in contrast with the Cu-exchanged biomass, which show more drastic variations in the FTIR spectra of their chars upon heating. For instance, both **Cu-L.dig** and **Cu-A.nod** demonstrate widespread loss of both resolution and intensity to all peaks across the 500 – 1700 cm^{-1} window. Particularly notable is the coalescence and reduction in intensity of the carboxylate stretches (at 1588 and 1399 cm^{-1}), consistent with Cu(II)-mediated decarboxylation of the alginate. Furthermore, the appearance of a new peak at 1700 cm^{-1} (which was absent in the untreated macroalgae) can be assigned to the formation of new C=C bonds within the char (in accordance with the arguments from similar analyses of **Cu(II)Alg** in Chapter 4).

Analysis of the same chars by PXRD is a somewhat more straightforward, yet equally informative, exercise. Unsurprisingly, untreated **L.dig** and **A.nod** give rise to diffraction peaks corresponding to NaCl and KCl (see Appendix F), which are presumably deposited on the surface of the biomass following the evaporation of seawater. Heating the kelps to 250 °C leaves the NaCl and KCl peaks unaltered (see Figure 5.16). **Cu(II)-A.nod** and **Cu(II)-L.dig**, on the other hand, show no peaks corresponding to crystalline material at ambient temperature, but evidence of Cu^0-formation after heating at 250 °C (see Figure 5.16). The observation is consistent with the formation of Cu^0 from **Cu(II)Alg** under similar conditions, as reported in Chapter 4.

The TGA and char analysis detailed here, and in the previous sections, indicate a number of similarities between the thermal behaviour of pure **Cu(II)Alg** (discussed extensively in Chapter 4) and that of Cu(II)-treated kelps. In order to investigate such phenomena further, the following sections will explore the products of algal pyrolysis, particularly the release of volatile organic compounds at different temperatures by means of pyrolysis gas-chromatography mass-spectrometry (Py-GCMS).

5.5.3.4 Semi-quantitative Py-GCMS analysis of algal biomass before and after metal-exchange

The first set of measurements that may be derived from Py-GCMS analysis at a given temperature is the conversion (the difference in sample weight before and after pyrolysis) and normalised* total GC peak area (which provides a semi-quantitative indication of the yield of volatile organic compounds from the biomass). The result for these two measurements recorded for **L.dig**, **Ca-L.dig**, and **Cu(II)-L.dig** at 300 and 500 °C are shown in Figure 5.17a. Similarly, the equivalent results for **A.nod**, **Ca-A.nod**, and **Cu(II)-A.nod** are shown in Figure 5.17b. From Figure 5.17, the role of the Cu^{2+} ion in promoting the

* "Normalisation", in this regard, is a two-step process. Firstly, the total GC peak arising from a particular sample is divided by the (moisture-corrected) starting mass. This value is then subsequently re-calculated as a percentage of the largest obtained result, which in this case was obtained from **Cu(II)-L.dig** at 500 °C.

volatilisation of organic compounds from macroalgal biomass at lower temperatures can be clearly seen. Hence, at 300 °C, **Cu(II)-L.dig** generated around twice the amount of volatile organic species relative to **L.dig**, **Cu(II)-A.nod** gave around three times as much as **A.nod**. Meanwhile, the Ca-treated samples, whilst exhibiting similar degrees of conversion to the Cu-treated seaweeds, show reduced tendencies to generate volatile organic compounds, likely liberating CO_2 and H_2O instead. However, comparing the Py-GCMS results at 300 °C with those at 500 °C, there are clear contrasts. For example, the higher temperature experiments give rise to much smaller differences in normalised total GC peak area for the metal-treated seaweeds compared to their untreated counterparts. This greater similarity in the normalised total GC peak area between the variously treated samples is indicative that, by 500 °C, thermolysis reactions are initiated in components of the biomass that are much less influenced by the presence of metal ions.

Naturally, much more information can be extracted from the Py-GCMS experiments than simply conversion and total GC peak area. As was demonstrated extensively in Chapter 4 (and explained in detail in Appendix L), the selectivity (expressed as a % of the total GC peak area) of a pyrolysed analyte for various classes of products (defined in Appendix M) can also be an insightful tool for exploring differences in thermal behaviour. In this regard, plots of the % selectivity (by total GC peak area) at 500 °C are shown Figure 5.18 for **L.dig**, **Ca-L.dig**, **Cu(II)-L.dig**, **A.nod**, **Ca-A.nod**, and **Cu(II)-A.nod**.[*] Analysis of Figure 5.18 reveals the drastic influence exerted by Cu^{2+} ions within the macroalgal biomass upon pyrolysis. Particularly noticeable is the increased selectivity (by GC peak area) in the cases of **Cu(II)-A.nod** and **Cu(II)-L.dig** for the "**F**"-type molecules, which contain a furan ring (namely furfural-derivatives (**FF**), furan-derivatives (**FR**), and furanone-derivatives (**FN**)). Hence, the selectivity (by GC peak area) for furan-based molecules increases from around 20 % for **A.nod** and **L.dig**, to 60 % following exchange of their native metal ions for Cu^{2+}. Especially remarkable, in this regard, is the sizeable increase in the formation of 2-furaldehyde (2-furfural, 2-FF) and 5-methyl-2-furaldehyde (5-methylfurfural, 5-MeFF) brought about by the Cu(II)-treatment. Indeed, the selectivity (by GC peak area) towards 2-FF undergoes a four- and seven-fold increase for **Cu(II)-L.dig** (*versus* **L.dig**) and **Cu(II)-A.nod** (*versus* **A.nod**), respectively, warranting a more in-depth quantitative analysis of these phenomena in Section 5.5.3.6. A further observation made from studying Figure 5.18, is the appearance of appreciable levels (≈ 3 - 5 % by GC peak area) of levoglucosenone (LGO) in Cu(II)-rich samples, where previously none had been detected. The growth in selectivity towards 2-FF (and other furan-based molecules) and LGO in **Cu(II)-L.dig** and **Cu(II)-A.nod** appears to occur largely at the expense of the formation of compounds in the "**O**"-class (aliphatics and small oxygenates). For example, the higher levels of acetol, acetic acid, and diacetyl, which are detected in the pyrolysate of untreated kelps, are reduced to vanishingly low amounts following exchange with Cu^{2+}.

[*] As with the analyses in Chapter 4, anhydrosugars are excluded from the selectivity calculations as a result of their poor volatility and hence inaccurate detection. Further discussion on this topic is provided in Appendix L.

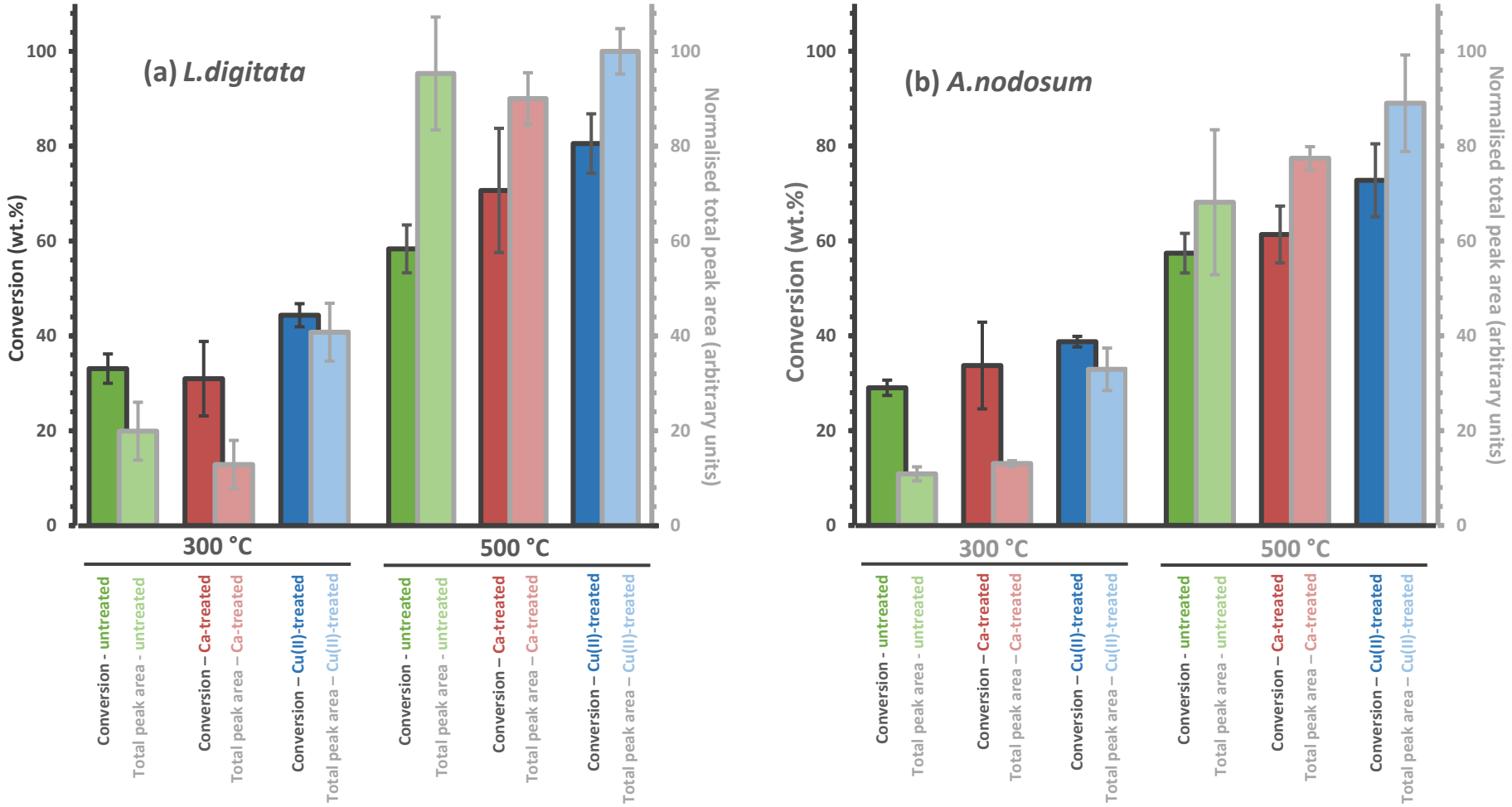

Figure 5.17 Results from the Py-GCMS analysis of **untreated**, **Ca-treated** and **Cu(II)-treated** samples of **(a) L.dig**, and **(b) A.nod** at 300 °C and 500 °C (20 °C ms^{-1}, 20 s, He 15 mL min^{-1}). **Conversion** is represented by the darker colouring, and **normalised total peak area** by the lighter colouring.

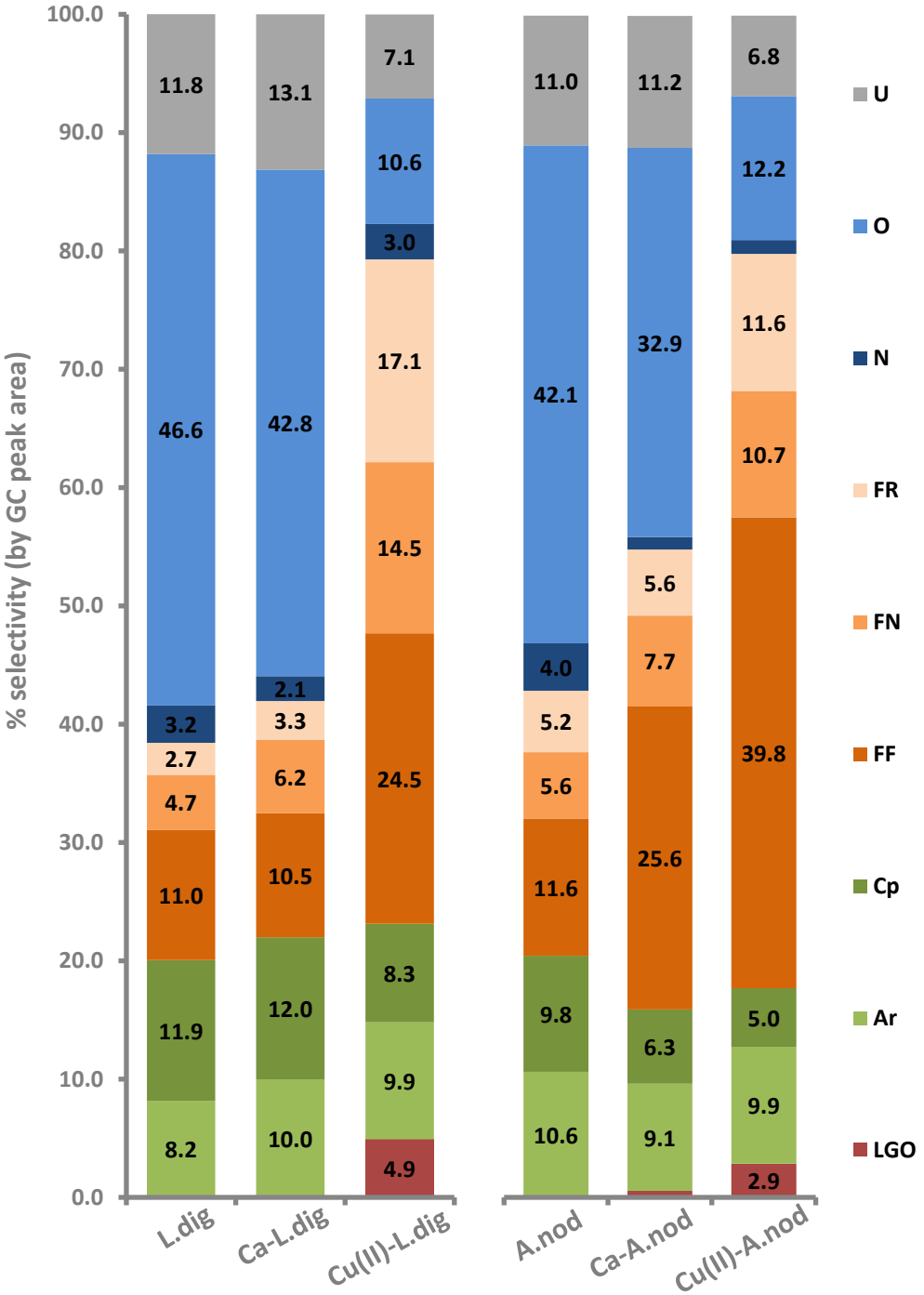

Figure 5.18 Selectivity by GC peak area (%) of product fractions in the Py-GCMS (500 °C, 20 °C ms^{-1}, 20 s, He 15 mL min^{-1}) analysis of kelps and metal-treated kelps. Product fraction codes are: **U** = unknown, **O** = aliphatics and small oxygenates, **N** = containing a heteroatom **FR** = furan-derivatives, **FN** = furanone-derivatives, **FF** = furfural-derivatives, **Cp** = cyclopentene-derivatives, **Ar** = aromatic and cyclohexene-derivatives, **LGO** = levoglucosenone. The size of each fraction is also expressed numerically as a % by GC peak area. Error bars are not shown, but were typically less than ± 10 % of the displayed value.

It is interesting, therefore, to contrast the impact of Cu^{2+} on **A.nod** and **L.dig** to that of Ca^{2+}, with the relevant selectivities (by GC peak area) for various pyrolysate compounds again being shown in Figure 5.18. For **Ca-A.nod** and **Ca-L.dig**, the differences in product distribution relative to their untreated kelp samples are much more subtle than for **Cu(II)-A.nod** and **Cu(II)-L.dig**. Whilst **Ca-A.nod** does show a doubling in selectivity (by GC peak area) towards **FF**-class molecules (especially 2-FF and 5-MeFF), the value still remains below half of that generated by **Cu(II)-A.nod**. Furthermore changes to the **FN**- and **FR**-classes are less noticeable for **Ca-A.nod**, as are differences across all classes in **Ca-L.dig**, which gives a very similar product distribution to untreated **L.dig**.

Given the dramatic influence played by Cu^{2+} ions in altering the distribution of pyrolysis products in the cases of Cu(II)-treated **A.nod** and **L.dig**, further investigations were carried out to determine which fractions of the biomass key products originated from. These additional experiments utilised the both the extracted alginates and **AE-AR** fractions of the kelp species, and are discussed in the following section.

5.5.3.5 Establishing the origin of pyrolysis products in Cu(II)-treated macroalgae

In Section 5.3.1.3 it was hypothesised that exchanging the native metal ions in alginate-rich macroalgal biomass for Cu^{2+} would lead to an increase in the formation of 2-FF. The argument was based, in-part, on the dramatic increase in yield observed in **Cu(II)Alg**, relative to **NaAlg** and **CaAlg** (measured in Chapter 4). The results in Section 5.5.3.4 appear to verify the prediction, showing an increase in selectivity (by GC peak area) of the algal biomass upon treatment with Cu^{2+} ions. However, in order to prove the hypothesis absolutely, further analysis is required to discern the origin of the 2-FF from within the biomass, and to confirm whether or not it ultimately derives from alginate or elsewhere. In order to achieve this aim, the samples of **Cu(II)Alg** prepared from the **A.nod** and **L.dig** biomass were analysed by Py-GCMS and compared to samples of the associated Cu(II)-treated alginate-extracted algal-residue (**Cu(II)-AE-AR**) and Cu(II)-treated seaweed. For these experiments, a qualitative assessment of the pyrograms was deemed to be sufficient, which are shown for **Cu(II)-L.dig**, **Cu(II)-AE-AR-DIG**, and **Cu(II)Alg-DIG** in Figure 5.19 and for **Cu(II)-A.nod**, **Cu(II)-AE-AR-NOD**, and **Cu(II)Alg-NOD** in Figure 5.20.

Analysis of the data in Figure 5.19 and Figure 5.20 indicates that the **Cu(II)-AE-AR** is responsible for a far wider range of the products found in the pyrolysate of the Cu(II)-treated kelp biomass than are the **Cu(II)Alg** samples. Indeed, the contribution of **Cu(II)Alg** appears to largely be 2-FF and small amounts of 2-(*5H*)-furanone, whilst, for both kelps, the **Cu(II)-AE-AR** liberates the same two compounds, in addition to acetic acid, toluene, 5-MeFF and levoglucosenone (LGO) (amongst many others). Of course, the raw pyrograms in Figure 5.19 and Figure 5.20 cannot provide a conclusive account of the relative contributions of **Cu(II)Alg** and **Cu(II)-AE-AR** towards the final yield of 2-FF from the kelp biomass, without additional mathematical interpretation. To this end, the proceeding Section provides a fully quantitative assessment of the yields of 2-FF originating from kelp biomass, and each of its individual fractions.

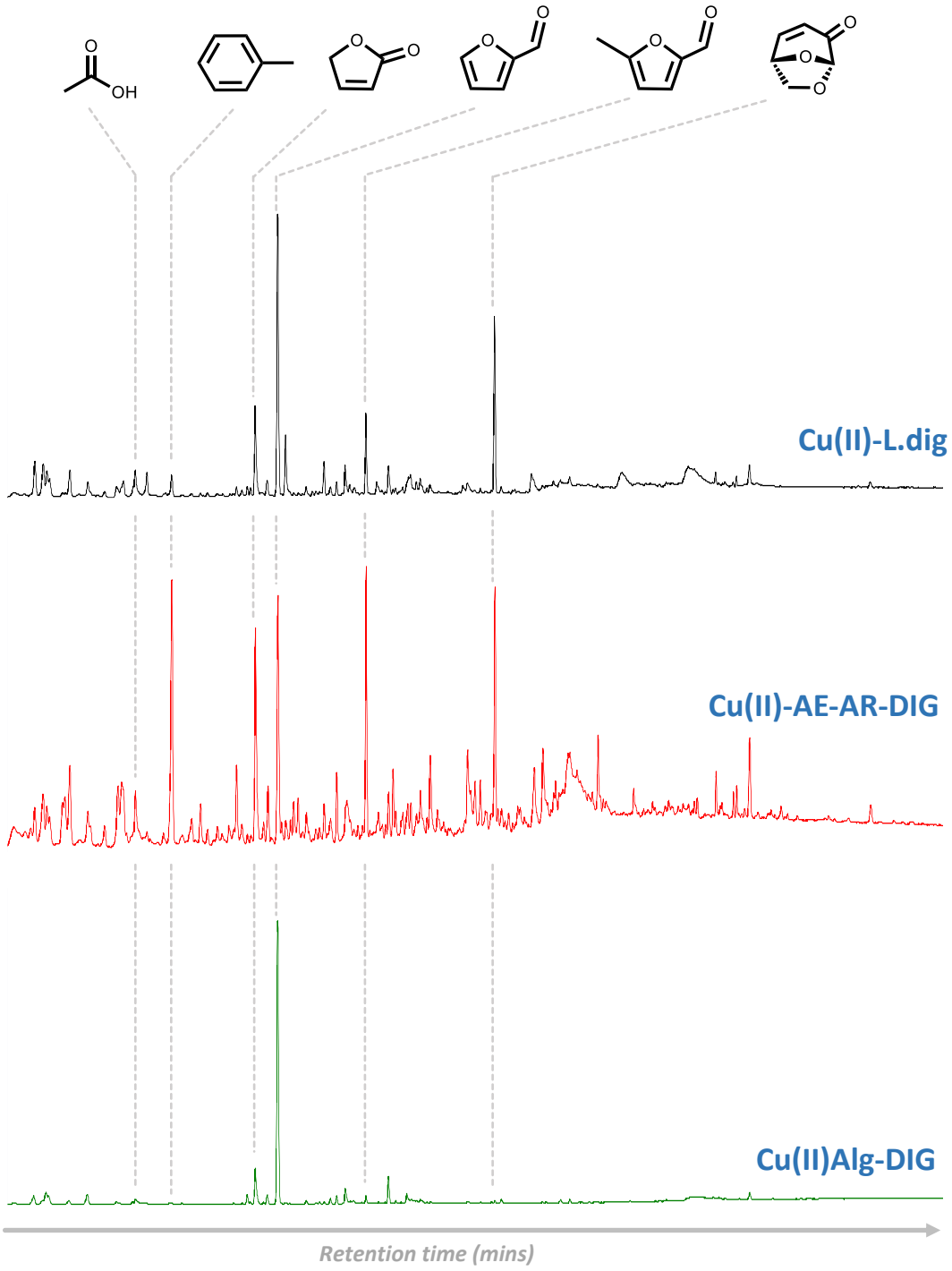

Figure 5.19 Chromatograms (5 – 30 minutes) from the Py-GCMS analysis of various Cu(II)-enriched fractions of **L.dig** at 500 °C (20 °C ms^{-1}, 20 s, He 15 mL min^{-1}). The presence of various pyrolysis products are shown for Cu(II)-treated **L.dig** (top), Cu(II)-treated alginate-extracted **L.dig** residue (middle), and Cu(II)-alginate from **L.dig** (bottom). The plots do not enable a quantitative comparison in this raw state and so the intensity scale is omitted.

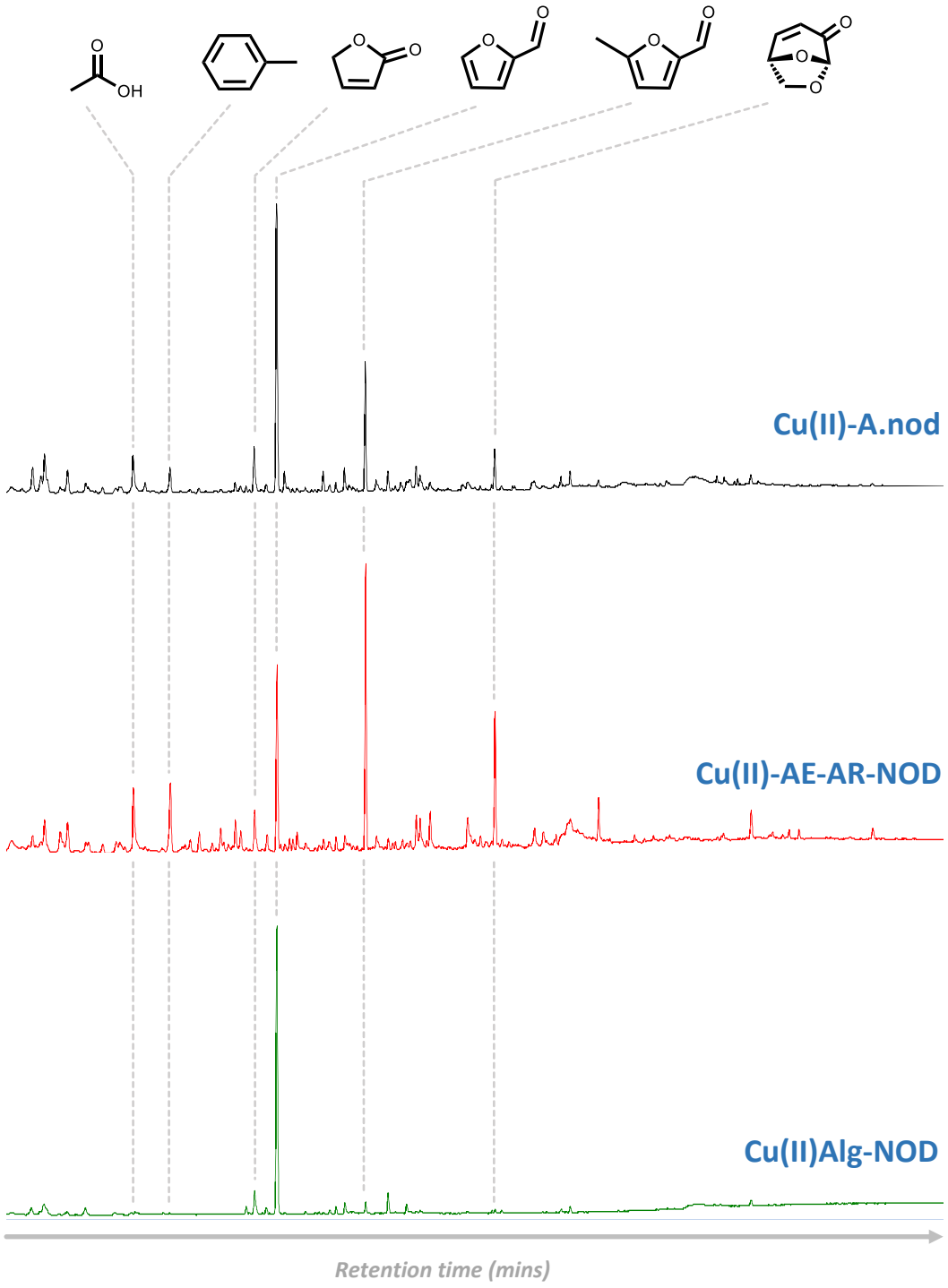

Figure 5.20 Chromatograms (5 – 30 minutes) from the Py-GCMS analysis of various Cu(II)-enriched fractions of **A.nod** at 500 °C (20 °C ms^{-1}, 20 s, He 15 mL min^{-1}). The presence of various pyrolysis products are shown for Cu(II)-treated **A.nod** (top), Cu(II)-treated alginate-extracted **A.nod** residue (middle), and Cu(II)-alginate from **A.nod** (bottom). The plots do not enable a quantitative comparison in this raw state and so the intensity scale is omitted.

5.5.3.6 Quantitative assessment of the yield of 2-furfural (2-FF) from algal biomass before and after metal-exchange

Whilst qualitative (or even semi-quantitative) analysis by Py-GCMS is relatively straightforward, a fully quantitative analysis of the products liberated during pyrolysis requires for additional experimental precautions to be put in place (see details in Appendix L). As such, not all compounds released by samples of macroalgae and metal-exchanged macroalgae could be subjected to a full quantification, but 2-furfural (2-FF) was selected as an exceptional case. Hence, the yields of 2-FF under flash pyrolysis conditions at 500 °C for **L.dig**, **Ca-L.dig**, **Cu(II)-L.dig**, **A.nod**, **Ca-A.nod**, and **Cu(II)-A.nod** were determined and are shown in Figure 5.21. From Figure 5.21, it is clear to see the effect that Cu^{2+} ions play in promoting the formation of 2-FF from the algal biomass, with yields of the compound increasing by a factor of around four and eight for **Cu(II)-L.dig** and **Cu(II)-A.nod**, respectively (relative to the untreated biomass). No such increase was observed in the Ca-treated samples, which only showed very modest changes in the case of both **Ca-L.dig** and **Ca-A.nod**.

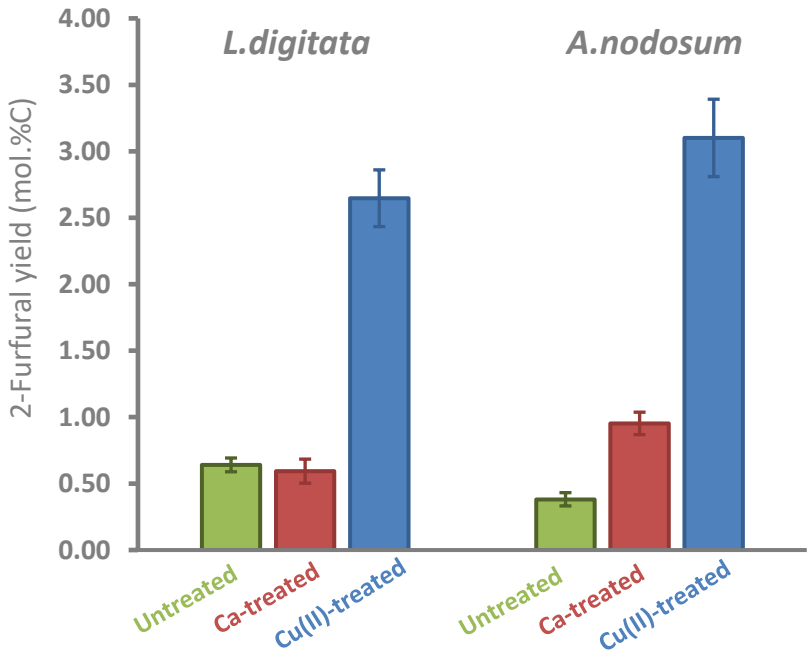

Figure 5.21 Yields of 2-furfural (2-FF) measured for the pyrolysis of **untreated**, **Ca-treated** and **Cu(II)-treated** **L.dig** and **A.nod** at 500 °C (20 °C ms^{-1}, 20 s, He 15 mL min^{-1}). The yields are expressed as a mol.% of the starting carbon content of the sample.

The results presented in Section 5.5.3.5 indicated that the Cu^{2+}-promoted the formation of 2-FF in both the **Cu(II)Alg** and **Cu(II)-AE-AR** fractions of **A.nod** and **L.dig**. In order to quantify the contribution of both the alginate and **AE-AR** fractions to the total yield of 2-FF in Cu(II)-treated macroalgae, an experiment was carried out to determine the absolute amount of 2-FF released in each case. Here it was found that **Cu(II)Alg** liberated around 10 times the quantity of 2-FF than the **Cu(II)-AE-AR**, which, when accounting for the relative proportions of both fractions within the seaweeds (see Figure 5.10 and discussions in Section 5.5.2.2), means that 90 – 95 % of the 2-FF liberated by **Cu(II)-L.dig** and **Cu(II)-A.nod** is a consequence of the thermolysis of alginate.

Once it had been established that the **Cu(II)Alg** was the source of the vast majority of 2-FF in the pyrolysis of Cu(II)-treated macroalgae, the results of Chapter 4 could be utilised to further optimise the reaction. In Chapter 4, it was concluded that 300 °C was the ideal pyrolysis temperature for deriving 2-FF from **Cu(II)Alg**, with higher temperatures delivering an increasingly poor selectivity for only a modest improvement in yield. As such, a second set of Py-GCMS experiments was conducted on the Cu(II)-treated seaweeds, with pyrolysis taking place at 300 °C. The results are reported in Table 5.2, along with a calculation of the ratio of the yield of 2-FF arising from metal-treated biomass samples relative to their untreated form. Here it was found that around 60 – 65 % of the 2-FF yielded at 500 °C by **Cu(II)-A.nod** and **Cu(II)-L.dig** could be recovered at 300 °C, which is lower than the 85 % recovery possible from pure **Cu(II)Alg** under the same conditions (as determined in Chapter 4). This slightly diminished recovery of 2-FF when **Cu(II)Alg** is embedded within the algal biomass matrix could possibly be improved by further optimisation of the pyrolysis temperature in the 300 – 400 °C window, a task reserved for future work. Never-the-less, the experiments at 300 °C revealed that the Cu(II)-treatment leads to a ten- to fifteen-fold increase in 2-FF yield compared to untreated **A.nod** and **L.dig**, far higher than the increase obtained from the Ca-treatment (three-fold at best). The relatively high selectivities (by GC peak area) for **Cu(II)-A.nod** (46.2 ± 2.3 %) and **Cu(II)-L.dig** (28.4 ± 1.8 %) at 300 °C are also encouraging, especially as the other prominent products released at this temperature (LGO and 5-MeFF) are relatively valuable compounds too. Furthermore, similar experiments conducted on other macroalgae species (**L.hyp**, **S.lat**, and **F.ves**) revealed an eight-fold increase in 2-FF yield following exchange of their metal ions with Cu^{2+}, and similar selectivities towards the compound (by GC peak area) as **Cu(II)-A.nod** and **Cu(II)-L.dig**. The implications for industrial pyrolysis of the improved 2-FF yield and selectivity in Cu(II)-treated macroalgae are considered in Section 5.5.5.

Table 5.2 The yield of 2-furfural (2-FF) measured from the pyrolysis of variously metal-treated kelp samples at 300 °C (20 °C ms^{-1}, 20 s, He 15 mL min^{-1}). The yields are expressed as mol.% of the starting carbon content of the sample.

Sample	Species	Treatment	Yield of 2-FF (mol.%C)		2-FF yield ratio (metal-treated/ untreated)
			Untreated	Metal- treated	
Macroalgal biomass	***L. digitata***	**Ca^{2+}-treated**	0.18 ± 0.03	0.15 ± 0.03	**0.83 ± 0.22**
	L. digitata	**Cu^{2+}-treated**	0.18 ± 0.03	1.71 ± 0.14	**9.64 ± 1.89**
	A. nodosum	**Ca^{2+}-treated**	0.12 ± 0.01	0.36 ± 0.03	**2.94 ± 0.36**
	A. nodosum	**Cu^{2+}-treated**	0.12 ± 0.01	1.89 ± 0.26	**15.58 ± 2.51**
	S. latissima	**Cu^{2+}-treated**	0.19 ± 0.01	1.38 ± 0.04	**7.19 ± 0.45**
	L. hyperborea	**Cu^{2+}-treated**	0.15 ± 0.02	1.21 ± 0.13	**8.11 ± 1.40**
	F. vesiculosus	**Cu^{2+}-treated**	0.11 ± 0.01	0.86 ± 0.04	**8.01 ± 0.45**

Finally, it is worth mentioning that, whilst not studied quantitatively, the Cu(II)-alginates of **L.hyp**, **S.lat**, and **F.ves** were all subjected to pyrolysis at 500 °C, under the same conditions as **Cu(II)Alg-DIG** and **Cu(II)Alg-NOD**. The pyrograms in all cases were essentially superimposable relative to each other (as were those arising from commercial samples, **Cu(II)Alg-SIG** and **Cu(II)Alg-BDH**), indicating that variation in the constitution of the alginates between different species (especially the varying **M**:**G** ratios found in Appendix J) is not particularly significant in determining 2-FF yield. It is quite possible that, upon a fully quantitative analysis of the extracted alginates, more subtle difference may become apparent, though such investigations are again reserved for future work.*

5.5.3.7 Quantitative assessment of the yield of bio-oil, -gas, and -char from macroalgae before and after metal-exchange: towards a full mass balance

In Chapter 4, a full mass balance was presented to quantitatively account for all of the products of pyrolysis arising from key model compounds. Unfortunately, such a feat was not possible in the present chapter owing to restrictions on time and equipment availability. However, several positive steps were made towards achieving the desired mass balance for samples of **A.nod**, **L.dig**, and their Cu(II)-treated counterparts, and they are discussed here.

Firstly, the Py-GCMS apparatus was coupled to a fixed-gas analyser (FGA) in order to determine yields of non-condensable gaseous products, specifically CO_2 and CO. The results from the Py-FGA experiments are reported in Table 5.3 for untreated and Cu(II)-treated **A.nod** and **L.dig**, and they reveal a notable discrepancy between the release of the two gases. The liberation of CO_2 appears to be largely unaffected by the presence of Cu^{2+} ions, whereas the yield of CO is almost doubled when the cation is present. In Chapter 4, it was reported that the yield of CO remains virtually constant in going from **NaAlg** to **Cu(II)Alg**, and so the observed increase in the release of the gas in the Cu(II)-treated kelps must be attributable to fractions other than the alginate. The dramatic increase in CO upon addition of Cu^{2+} to the biomass is, however, surprising as the metal ion has generally been found to suppress the formation of this gas.[58,59] In truth, there are number of gaseous equilibria likely to be active during the pyrolysis, the water-gas-shift (Equation 5.1) (which is known to be catalysed at low temperatures by Cu^0)[60] and the Sabatier reaction (Equation 5.2).[61] Whilst attempts were made to quantify the yield of CH_4, which would help to identify the role of either reactions in determining the gaseous products, the fixed-gas analyser was not set up in time for such experiments to take place.

$$CO + H_2O \rightleftharpoons CO_2 + H_2 \qquad \text{[Eq. 5.1]}$$

$$CO_2 + 4H_2 \rightleftharpoons CH_4 + H_2O \qquad \text{[Eq. 5.2]}$$

* Indeed, small quantities of **CaAlg** and **NaAlg** prepared from all of the individual kelp species were also subjected to analysis by Py-GCMS, and, from a qualitative perspective, also proved to be indistinguishable from the commercial samples **CaAlg-SIG** and **NaAlg-SIG**.

Furthermore, it would also be of interest to quantify the release of H_2 from the seaweed samples, from the point of view of preparing syngas for the Fischer-Tropsch process. d-block metals have been shown to increase the yield of H_2 in the pyrolysis of cellulosic feedstocks,[44,62,63] and it seems likely that the same might be true for Cu(II)-treated kelps, especially given the role of Cu^0 in catalysing the water-gas-shift.[60]

Table 5.3 The yields of non-condensable gases (CO and CO_2) from the pyrolysis of **A.nod** and **L.dig** at 500 °C (20 °C ms^{-1}, 20 s, He 15 mL min^{-1}) before and after Cu(II)-treatment. The yields are expressed as both a wt.% of the (moisture-corrected) starting mass, and as a mol.% of the starting carbon content of the sample.

Sample	Yield (wt.%)		Yield (mol.%C)	
	CO_2	CO	CO_2	CO
A.nod	13.4 ± *0.4*	2.4 ± *0.2*	10.3 ± *0.3*	3.1 ± *0.2*
Cu(II)-A.nod	14.4 ± *0.2*	4.3 ± *0.5*	10.1 ± *0.2*	4.7 ± *0.5*
L.dig	12.7 ± *0.4*	1.6 ± *0.2*	11.4 ± *0.5*	2.2 ± *0.2*
Cu(II)-L.dig	13.9 ± *0.4*	2.9 ± *0.2*	11.0 ± *0.3*	3.5 ± *0.2*

With regards to the other fractions of the kelp pyrolysate, the results are less complete. Preliminary TGA-MS experiments (not reported) indicated that untreated kelp samples released substantial amounts of H_2O when pyrolysed at 10 °C min^{-1} to 500 °C, estimated to be about 40 wt.%. Along with the char (again, approximately 40 wt.%) and yield of fixed gases yields (around 15 wt.%, see above), the expected yield of condensable hydrocarbon compounds (which would comprise the bio-oil in a larger scale experiment) is expected to be very small (around 5 wt.%). By using the calibration from the quantitative analysis of 2-FF and applying it to the remaining peaks in the pyrograms, an approximate appraisal of the total volatile organic yields can be determined, found to be in the range 4 – 6 wt.%.* These low yields of organic bio-oil are on a par with those derived in the upscaled experiments of Morgan and Smith on the alginate-rich *Fucus serratus*.[15] Whilst further work is required to fully elucidate a mass balance for all of the fractions in the pyrolysis of kelps, it can be seen that the high yields of "liquid products" reported by some authors (in the range 30 – 40 wt.%) are likely to be heavily dominated by water.[19,20]

Unfortunately, the acquired data were not sufficiently extensive or reliable to discern the role of Cu^{2+} in influencing the yields of solid, liquid, and gas fractions in the pyrolysis of kelps, beyond what has already been discussed. However, it is anticipated that the greater degrees of conversion observed for Cu(II)-treated kelps (and, hence, lower yields of char) would lead to higher liquid fractions overall, though further wok is required to prove such a hypothesis (see Section 5.7.2.2).

* This calculation requires for the assumption that all of the compounds have the same GCMS response factor as 2-FF, which is clearly inaccurate, though suitable for a first approximation.

5.5.4 Synoptic assessment on the impact of metal-exchange in the thermolysis of macroalgal biomass

The discussions in Section 5.5.3 detail the multifarious effects on kelp thermochemical behaviour following exchange of the indigenous metal ions with Cu^{2+}. Taking all of the TGA and Py-GCMS experiments into account, the following section will offer a synoptic appraisal of the pyrolysis of Cu(II)-exchanged macroalgae. However, in addition to merely summarising the results, this section will seek to contextualise them by comparison with studies of the pyrolysis of alginates (see especially Chapter 4) and with studies of other metal-treated biomass conducted elsewhere (see Appendix P for a mini-review of this topic). In each case, the main observation is quoted, and further discussion follows thereafter:

- **Cu^{2+} ions decrease the onset temperature for rapid pyrolysis**

Section 5.5.3.2 revealed that Cu^{2+} had the effect of lowering the onset temperature of kelp degradation, relative to the untreated sample. Diagnostic signatures in the DTG of the macroalgae were assigned to individual components of the biomass, and here it was shown that Cu^{2+} predominantly influences the pyrolysis of the alginate fraction, with the *alginate-extracted algal-residue* (AE-AR) decreasing in decomposition temperature more marginally. These results are consistent with the large decrease in T_i reported for **Cu(II)Alg** in Chapter 4, and attributed to a Cu^{2+}-mediated decarboxylation mechanism. The less significant impact of Cu^{2+} on the **AE-AR** is unsurprising as the cupric ion has been demonstrated to have only a minor influence in the primary thermolysis of cellulose.[64] Hence, whilst appreciable decreases in pyrolysis onset temperature have been recorded for Cu(II)-impregnated lignocellulosic biomass, such effects arise from reactions of Cu^{2+} with uronic acids in the hemicellulose rather than with neutral polysaccharides.[59,64,65]

- **Cu^{2+} ions increase the yield of 2-furfural**

In Section 5.5.3.6 it was shown that Cu^{2+}-treated algal biomass gives a higher yield of 2-FF than in the untreated case. Further fractionation of the kelp confirmed that > 90 % of this 2-FF originated from the alginate in the sample, rather from other components. Depending on the species of seaweed, the ratio of 2-FF yield for Cu(II)-treated *versus* untreated macroalgae at 300 °C was found to be around 9 – 15 times, somewhat lower than the 30-fold enhancement observed for **Cu(II)Alg** compared to **NaAlg** under the same conditions. It is possible, therefore, that the 2-FF volatilised from the alginate is consumed in secondary reactions as it percolates through the biomass matrix.[66] Never the less, the extremely low temperature means that the Cu(II)-promoted formation of 2-FF from kelp is impressive compared to similar effects observed in studies with terrestrial biomass. For example, an enhancement of five-times the yield of 2-FF was recorded for poplar wood loaded with 40 wt.% $ZnCl_2$ at 350 °C, and of nine-times for corncob with 20 wt.% $ZnCl_2$ loading at 400 °C.[38] A fruitful comparison could also be made with the results of Ross *et al.*, who developed a method of pre-treating kelp by acid prior to pyrolysis.[13] Here, the authors demonstrated an increase in selectivity (by GC peak area) for 2-FF upon replacement of the alkali and alkali earth metals with H^+. It would certainly be of interest to conduct a quantitative comparison between the acid-treatment (from Ross' work) and Cu(II)-treatment (presented in this thesis) in the future.

- **Cu^{2+} induce additional changes to the pyrolysis product slate of macroalgae**

Beyond increasing the yield of 2-FF, the Cu^{2+} gave rise to elevated levels of 5-MeFF and LGO, and nearly doubled the amount of CO released. All three of these observations were attributable to the interactions of the metal ions with components of the kelp besides alginate. For example, the increase in 5-methylfurfural can be considered to arise from Cu^{2+} interacting with components in the **AE-AR**, as well as with laminarin and fucoidan.[12] Similarly, the increase in LGO is a well-documented consequence of d-block metal-mediated decomposition of the glucan-rich phases of biomass.[38,40,67–70] Meanwhile, the promoted formation of CO (which is not observed in the pyrolysis of isolated **Cu(II)Alg**) could well be a consequence of secondary reactions of Cu^{2+} or Cu^{0} with the char, which is also found to decrease in yield for Cu(II)-treated kelps. The results are in agreement with the works of previous authors, who suggested that the d-block metals (such as Cu^{2+}) are more influential in affecting secondary reactions of neutral components of the biomass.[64]

- **Cu^{2+} ions give rise to the formation of Cu^{0} nanoparticles in the char**

The appearance of Cu^{0} in the Cu(II)-treated kelp biomass at 250 °C was already anticipated, as the equivalent observation was also recorded during the pyrolysis of isolated **Cu(II)Alg** (see Chapter 4, Section 4.5.2). Furthermore, the appearance of nanocrystalline Cu^{0} and Ni^{0} in the pyrolysis of cellulosic biomass also renders the observations presented here somewhat unsurprising.[41,42,69–73] However, the unprecedentedly low temperature at which the formation of zero-valent copper has been recorded in the present case is quite remarkable. As described in Appendix Q, the mechanism of converting M^{2+} to M^{0} in biomass has been hypothesised to proceed *via* an amorphous $M_xO_yH_z$ phase, followed by reduction of MO by carbon or CO (see Figure 5.22a).[41] Whilst such a mechanism is credible at higher temperatures (> 350 °C), there is scant evidence for its plausibility below 300 °C. As such, it seems that the *Hofer-Moest* decarboxylative mechanism presented in Chapter 4 (see Figure 5.22b) still remains as the most likely route for the reduction of Cu^{2+} to Cu^{0}, though further evidence would still be required to prove this conjecture. Regardless of the mechanism, the reduction of M^{2+} by alginate-rich seaweed biomass has been expounded as a useful method towards the preparation of catalytic nanoparticles, including Au^{0},[74] Pd^{0},[75] ZnO,[76] and more complex metal oxides.[77]

- **Ca^{2+} played a much less influential role than Cu^{2+} in the thermolysis of kelp**

Experiments on Ca-exchanged macroalgae were also reported in this chapter, to act as a comparison with the Cu(II)-treated equivalents. Such "control" investigations were important in order to prove that the changes observed in the Cu^{2+} case were not merely a generic effect of treating the kelp biomass in a solution of *any* divalent metal salt. In this regard, very few significant changes were observed between the untreated and Ca-treated kelp samples, with the their TGA and Py-GCMS profiles remaining remarkably similar (especially at temperatures ≤ 300 °C).

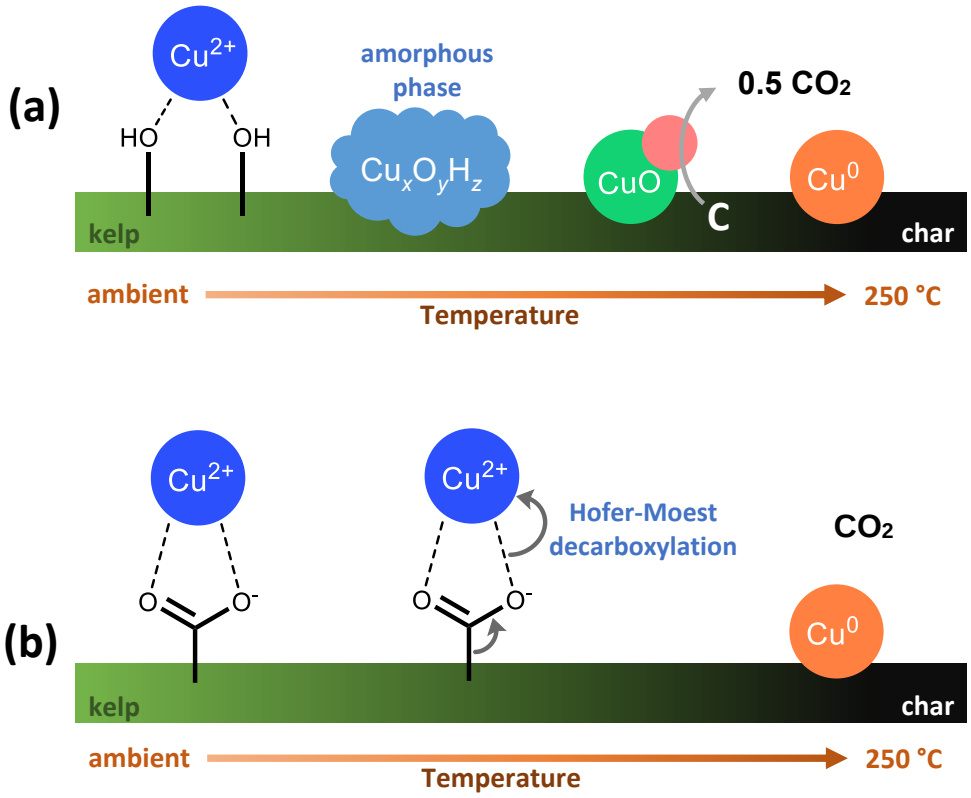

Figure 5.22 Possible routes for the thermally driven formation of Cu^0 from Cu^{2+} in kelp biomass based on (a) conversion to an amorphous copper (hydr)oxide phase followed by carbothermal reduction, and (b) a Hofer-Moest decarboxylation.

- **The effect of Cu^{2+} ions is universal across all species of alginate-rich kelp**
  Across the five species of kelp studied the same thermochemical observations were recorded upon treatment with Cu^{2+} ions (albeit to different degrees), despite their containing varying levels and types of alginate. Interestingly, all of the isolated alginates, regardless of **M**:**G** ratio, showed nearly identical TGA and Py-GCMS traces, dependant only on the identity of the bound cation (Na^+, Ca^{2+}, and Cu^{2+}). Whilst the sample size is still relatively small, such results are encouraging as they indicate a possible universality of the mechanism of degradation of Cu(II)-treated alginate-rich kelps, the implications of which are explored more deeply in Section 5.5.5.

5.5.5 Implications of metal-exchange on the industrial pyrolysis of macroalgal biomass: a perspective

Of course, for any bioresource-based technology to succeed, it must hold commercial potency. Whilst this thesis in no way aims to make an economic assessment of the results contained within it, the following section reviews the findings of the present chapter, and explores their relevance to potential industrial processes based around the thermal conversion of kelp.

The first point to note, therefore, is that the results in Sections 5.5.3.7 are consistent with the formation of very low yields of liquid hydrocarbons forming from the pyrolysis of kelp biomass, as has been found elsewhere (see Appendix S). However, it has also been demonstrated that the composition of this hypothetical bio-oil fraction can be significantly altered by incorporation of Cu^{2+} into the parent biomass, particularly to favour the formation of 2-FF. 2-FF has been highlighted as a key target for biomass conversion technologies,[78,79] as have similar furan derivatives that would also appear in the kelp bio-oil, in addition to LGO (a lucrative compound in its own right).[80] Hence, whilst yields of 2-FF of around 2 wt.%C might seem modest in absolute terms, the extremely low temperatures at which such values can be reached (300 °C) are very encouraging, compared to the more drastic heating required to derive similar products from terrestrial biomass.[81,82,*] It is possible, therefore, that the overall low hydrocarbon yields, would be compensated to some degree by the high selectivity towards favourable products, and significantly reduced processing temperatures required for them to form. Hence, it is viable that a low temperature pyrolysis step might be employed in advance of additional processing, such as gasification, to process the remaining fractions of the biomass (see below).[22,83]

Some authors have argued that, to supplement the cost of pyrolysis, a pre-extraction step should be included prior to thermal processing, in which valuable kelp bio-products are isolated and sold on.[23,84–87] Hence, fucoidan,[23] D-mannitol,[52] laminarin,[51] or even low-levels of lipids,[88] could all be easily removed from harvested biomass, whilst the Cu^{2+} remained bound to the alginate within the kelp, which could then be pyrolysed as before. Naturally, the fate of this Cu^{2+} could also add value to the upgrading process, with the formation of Cu^0 within the char phase being potentially useful for a number of reasons:

- The starting, toxic, aqueous Cu^{2+} ions are concentrated into the form of Cu^0 supported on carbon, a benign and much more easily handled material. Recovery of the metal from the char could be a valuable endeavour, and render the carbon suitable for use as a fertiliser or solid fuel[17,85]
- The Cu^0 supported on the carbonaceous char may have a multitude of applications as a low grade heterogeneous catalyst.[75,89,90]
- The Cu^0 particles may catalyse additional degradation of the char upon further processing, conceivably giving an enhanced yield of H_2 under gasification or microwave-mediated gasification conditions.[63,69,71–73,91] It is also possible that the Cu(II)-enriched seaweed could be co-fed with an additional feedstock (waste polystyrene[92] or rice husk[93] for example) to enhance the degradation of the secondary material at higher temperatures.
- Metal-enriched seaweed chars have also found utility as supercapacitors and in electrocatalysis[94,95]

[*] Lower pyrolysis temperatures are of course favourable for their associated lower energy cost, as well as the protection afforded to the reactor from the reduction of volatilised inorganic species, which cause slagging, fouling, and corrosion.[4,119]

Combining all of the above discussions, it is possible to propose a conceptual scheme for a biorefinery based upon the upgrading of kelp from the remediation of Cu^{2+}-polluted waste water (see Figure 5.23).

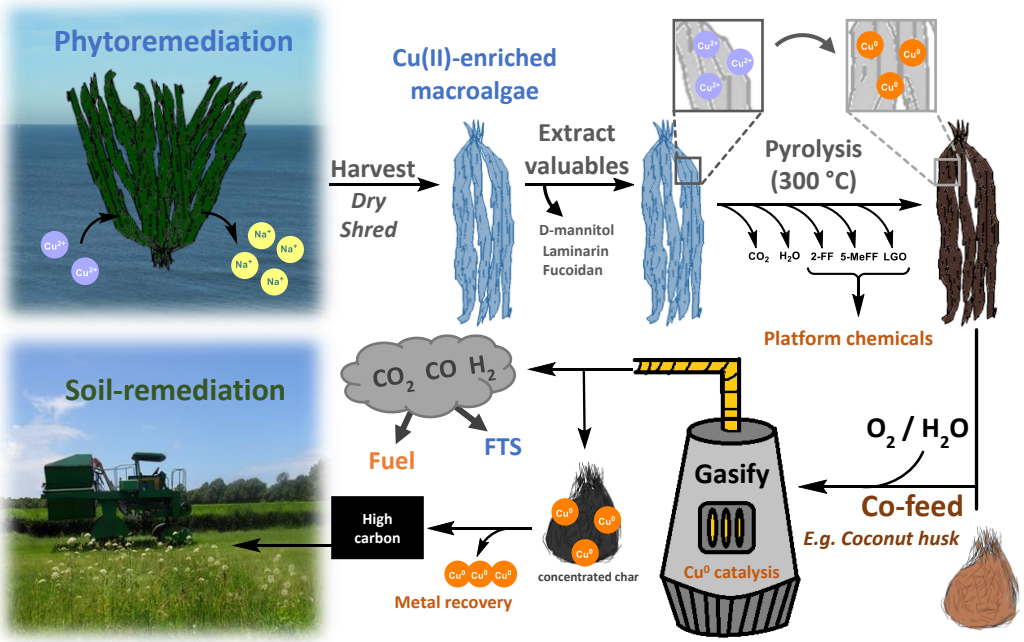

Figure 5.23 A conceptual phytoremediative kelp-based thermal biorefinery.

Naturally, the state of the work described in this chapter is a long way off the realisation of the biorefinery described in Figure 5.23, but it does provide scope for the development of the technology. Particularly, the results in this chapter (and Chapter 4) indicate that the impact of Cu^{2+} ions on thermochemistry are fairly universal across all mono- and poly-uronic acids, indicating that the processing techniques need not be restricted to kelp, but could extend to other uronide-rich, readily available biomass feedstocks, such as orange peel waste.[96–98]

5.6 Summary and conclusions

This Chapter built upon the discussions in Chapters 2, 3, and 4 concerning the metal-coordination and thermochemical behaviour of algal uronides. In this regard, five species of alginate-rich, brown seaweeds were treated in solutions of Cu^{2+} and Ca^{2+} to observe the effect of metal-exchange on subsequent pyrolysis reactions. The most important results to arise from these experiments were:

I. **Introducing Cu^{2+} ions decrease the onset temperature to initiate rapid pyrolysis in kelps by an average of around 40 °C.**

II. **Introducing Cu^{2+} ions increases the selectivity towards furan-derived products in the pyrolysate of kelps, at the expense of small oxygenated molecules.**

III. **Introducing Cu^{2+} ions increases the yield of 2-furfural (2-FF) from the pyrolysis of kelp by a factor of 7 – 15 (300 °C) and 4 – 8 (500 °C). The highest yield of 2-FF (3.10 ± 0.29 mol.%C) was derived from Cu(II)-treated A.nod at 500 °C.**

IV. **Cu^{2+} ions give rise to the formation of Cu^0 nanoparticles in the kelp bio-char.**

V. **Introducing Cu^{2+} ions increases the yield of levoglucosenone (LGO), 5-methyl-2-furfural (5-MeFF), and CO arising from kelp biomass during pyrolysis.**

VI. **Introducing Ca^{2+} ions played a much less influential role than Cu^{2+} in the thermolysis of kelp, changing the kinetic and product profiles to a much smaller degree (especially at temperatures ≤ 300 °C).**

VII. **The effect of Cu^{2+} ions is universal across all species of alginate-rich kelp.**

VIII. **No significant differences were observed in the pyrolysis of 7 different samples of Na-, Ca-, and Cu(II)Alg, derived from different seaweeds and with different M:G ratios.**

Observations (I) - (III) were all demonstrated to arise because of the influence of Cu^{2+} ions on the thermal degradation of alginate, with over 90 % of the 2-FF originating from that source. In this regard, points (I) – (III) are fully consistent with the results of Chapter 4, as is the formation of Cu^0 in the biochar indicated by point (V). However, it was also acknowledged that there are alternative routes for the reduction of Cu^{2+} to Cu^0 beyond the *Hofer-Moest* decarboxylation proposed in the previous chapter. Point (IV) provides evidence of the interaction of Cu^{2+} ions with components of the kelp besides alginate, conceivably the structural or soluble glucans that reside within the biomass matrix. Point (VI) provides further evidence for the conclusions of points (I) – (V), by demonstrating that the observed effects of treating the kelp with Cu^{2+} ions are a consequence of the action of those Cu^{2+} ions, and not simply a generic consequence that would accompany any metal-treatment.

Finally, points (VII) and (VIII) indicate that the results of this study should be applicable to any alginate-rich seaweed, regardless of the composition of the alginate within the kelp. In this regard, the model-compound approach adopted earlier in this thesis has, to some extent, been vindicated, as it has allowed for a rational and generally applicable conclusion to be asserted concerning the metal-mediated pyrolysis of kelps. The universal applicability of the effects of the Cu(II)-treatment enabled the conceptualisation of a phytoremediative kelp-based thermal biorefinery, the development of which could form the focus of future investigations.

5.7 Further work

5.7.1 Overview of proposed further work

The pinnacle of this chapter was the proposal of a phytoremediative kelp-base thermal biorefinery, and it was suggested that further work should be focussed on development of

this concept. As such, the further work described in this section is largely focussed on the design of experiments that would help to develop the technology (see Section 5.5.5).

5.7.2 Scaling up the metal-mediated pyrolysis of kelp

5.7.2.1 Pyrolysis reactions on a gram-scale

The micropyrolysis experiments performed in this Chapter are not necessarily representative of a large scale thermochemical reactor, where heat and mass transfer could be expected to be dramatically different. A number of authors have sought to explore the differences comparing upscaled reactions (on a gram/kilogram scale) with their micropyrolysis experiments, with a notable example being the pyrolysis of Zn^{2+}-impregnated corncob.[38–40] Recently, a number of experiments have sought to explore the pyrolysis of seaweeds (*Laminaria japonica*,[19,20] *Sargassum natans*,[99] and *Ulva lactuca*[100]) on the 10 - 100 g scale, and proven to be very insightful. As such, work undertaken in the preparation of this thesis* has also be aimed at building a prototype pyrolyser capable of 1 g – 10 g reactions (see in Figure 5.24). As yet, the reactor has not been utilised for the pyrolysis of macroalgae, but such experiments are anticipated in the near future.

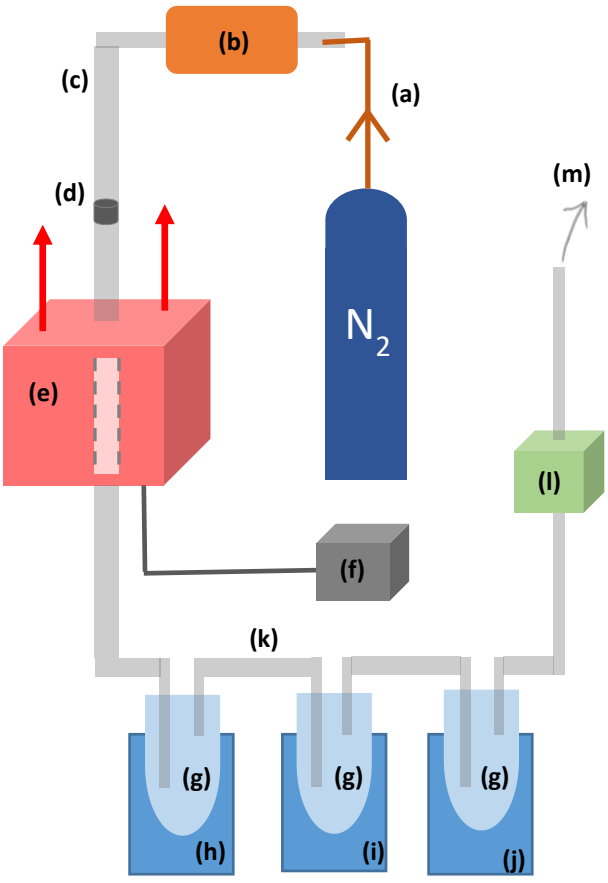

a) **Inert gas supply**
b) **Gas pre-heater**
c) **Quartz reactor**
d) **Quartz frit (feedstock bed)**
e) **Moveable vertical furnace**
f) **Temp. controller**
g) **Condenser flask**
h) **Ice bath**
i) **Dry ice bath**
j) **Liquid nitrogen bath**
k) **Condenser line**
l) **Flowmeter**
m) **Vent / Analysis**

Figure 5.24 A design for a multigram-scale pyrolysis reactor

* In collaboration with Dr. Li Li

5.7.2.2 Scaling up the analysis: a full mass balance

Scaling up the pyrolysis reactor design would, hopefully, give rise to quantifiable amounts of bio-oil, bio-gas, and bio-char. As such, the mass balance that proved to be elusive in the preparation of this chapter would be much more easily accessible, especially given the minimisation of errors associated with handling biomass on the microgram scale. In addition to simply quantifying the yields of various fractions of product, the upscaled procedure would also allow for a more thorough analysis of their properties. For example, aside from simply performing GC analysis on the bio-oil, it could also be analysed for calorific value, viscosity, acidity, stability, and so on, as has been achieved elsewhere.[19,20,99,100] In addition, isolation of the char and gas fractions would facilitate more detailed analysis of their nature and composition.

5.7.2.3 Utilising in-tact and fresh kelps

The seaweed preparation methodology used in this chapter (see Section 5.8.1) was more intensive than might be expected for an industrial pyrolysis unit. In future experiments, rather than using powdered kelp that had been treated in a solution of the desired dopant metal, it might be more informative to use biomass that had been soaked (or even grown) in the metal-rich water, and then pyrolysed as either whole fronds, or with minimal shredding. Again, such reactions would require a larger apparatus than the TGA or Py-GCMS techniques used here, but would reveal how removal of steps such as grinding (and especially freezing)[36] alter subsequent analysis.

5.7.2.4 Integrating the pre-extraction step

In contrast to the reduced levels of pre-treatment described in Section 5.7.2.3, it would also be of interest to study the effect of some additional steps, namely the extraction of various high-value compounds. Authors have noted that rhamnose-based carbohydrates[84,85] laminarin,[51] mannitol,[52] and fucoidan,[23] are all potentially lucrative and easily extractable targets from kelp. Naturally, it is anticipated that different pre-treatment methods would have varying impacts on proceeding pyrolysis,[23] though the degradation of the alginate would still likely dominate the thermochemical profile.

5.7.3 Integrating advanced thermal technologies into the metal-mediated pyrolysis of kelps

5.7.3.1 Microwave reactions

Very little work has been carried out on the integration of microwave heating into the thermal conversion of macroalgal biomass, though the few studies conducted so far have been extremely positive (see further discussions in the paper contained in Appendix S).[101–103] Intrinsic metal ions have been found to increase the absorption of microwaves by biomass, increasing the energy efficiency of the thermolysis process,[63,104] as such, the technology might be especially suitable for the metal-treated kelp samples described in this chapter.

5.7.3.2 Gasification

Following the pyrolysis of the macroalgae described in this chapter, a carbon-rich char remains that would be suitable for further processing by gasification. Again, work is now on-going at Durham University to pursue this aim, which will be facilitated by modification of the Py-GCMS apparatus to enable the injection of steam and pressurised reactive gases into the pyrolysis chamber. *In situ* generated Cu^0 and Ni^0 nanoparticles have been shown to enhance the yields of H_2 in the gasification of wood-chips, plastic pellets, and cellulosic biomass,[69,71,72,91] so it might be expected that the Cu^0 formed in the pyrolysis of Cu(II)-treated macroalgae would have the same effect. Additionally, a coupled microwave-gasification approach may also be successful.[63]

5.7.3.3 Additional biomass feedstocks and opportunities for co-feeding

Research by Kawamoto *et al.* has demonstrated that the low temperature degradation of hemicellulose can activate the thermolysis of other, more stable components of the biomass (such as lignin).[105] It is possible, therefore, that the low temperature pyrolysis of alginates within the kelp biomass could be to activate lignin-rich co-feedstocks. Limited work has been carried out into co-feeding kelp during the pyrolysis of rice husk,[93] and polystyrene,[92] but such studies did not integrate the metal-exchange technique demonstrated in this thesis.

In addition, the favourable pyrolysis traits exhibited by Cu(II)-treated macroalgae, may also be preserved in other uronide-rich biomass. Indeed, it was demonstrated in Chapter 4 that pectin (a polyuronide of D-galacturonic acid) behaved in a similar manner to alginate. As such, it might be anticipated that Cu(II)-treated citrus peels, which are naturally rich in pectin and often cited as a readily available pyrolysis feedstock,[96–98] would behave in a similar manner to the kelp studied here.

5.7.4 Additional points for further investigation

5.7.4.1 Exploring the thermochemical impact of additional metal-ions

The choice of Cu^{2+} as the metal ion with which the algal biomass was doped in this chapter, was based not only the predicted favourable thermochemical influence of the metal, but also of the fact that alginate (and hence kelp) possesses a high affinity for the species.[35,106] Hence, considering the affinity series discussed in Section 5.3.1.2, it would also be of interest to investigate the effects of macroalgae enriched in other toxic metal species (namely Pb^{2+} and Cd^{2+}, which are readily absorbed by kelps).[34,107] Alternatively, it might be advantageous to explore the possibility of recovering precious metals by coupling bioremediation to the thermochemical upgrading in kelps. For instance, Au^0 and Pd^0 nanoparticles have already been found to form during the pyrolysis of kelps enriched in those metal cations, though the corresponding influence on the thermal degradation of the kelp biomass was not reported.[74,75] Finally, it would be of interest to investigate the pyrolysis of macroalgal biomass that had been used in the remediation of water polluted with non-metallic contaminants (nitrates and phosphate for example), which seaweeds also have a high affinity for.[108] In all cases, finding a use for the pollutant-enriched chars would be key for the commercialisation of the process, be it as a low-grade heterogenous catalyst or as a fertiliser.

5.7.4.2 Additional mechanistic questions for investigation

Clearly, in the pyrolysis of a complicated feedstock such as macroalgae, it is not possible to discern the origin of every pyrolysis product. However, some observations remained to be particularly intriguing. Amongst these was the doubling in yield of CO found when the kelp biomass was enriched in Cu^{2+} ions, despite evidence in the literature against such an occurrence. A greater understanding of the interactions between Cu^{2+} and, for instance, D-mannitol, fucoidan, or laminarin, could be of assistance in this regard. Furthermore, questions remain as to the mechanism of formation of Cu^{0} within the biomass, particularly the intermediate states adopted by the metal as it is reduced from the starting Cu^{2+} state. Additional analysis of char samples by X-ray photoelectron spectroscopy (XPS) would be necessary to gain further insight into the reaction.[42,67,72]

5.7.4.3 Additional optimisations

The Cu(II)-treatment utilised in this chapter was expected to give a maximal loading of Cu^{2+} within the algal biomass matrix, however, other authors have noted that varying metal loadings can lead to drastically different effects in subsequent thermochemical experiments.[38,40,58,62,72] As such, it is recommended that a more systematic approach be undertaken, particularly exploring the effect of Cu^{2+} doping at levels that might be more relevant to the metal ion concentrations found in polluted waste-water streams. As might be expected, further optimisations of the pyrolysis temperature, heating rate, and pyrolysis atmosphere may also prove to be advantageous to the overall yields of desirable products.[109]

5.8 Materials and methods

5.8.1 Preparation of macroalgal biomass, extracted alginates, and algal residues

5.8.1.1 Sampling and initial preparation of macroalgal biomass

Samples of five species of brown macroalgae were collected from Boulmer beach, Northumberland, UK (55°25'07.2"N 1°34'51.3"W) on 22nd January 2015, when alginate contents were predicted to be high.[5,6] The selected species were *Laminaria digitata* (**L.dig**), *Laminaria hyperborea* (**L.hyp**), *Saccharina latissima* (**S.lat**), *Fucus vesiculosus* (**F.ves**), and *Ascophyllum nodosum* (**A.nod**).[*] All samples were harvested directly from their growth site with the exception of **S.lat**, which was freshly beach cast. In transit and prior to processing, the biomass was stored in the dark and in seawater at 4 °C. The kelps were separated into their individual species, and 5 to 8 whole specimens of each were processed together according to the following method: Within 24 hours of harvesting, macroalgae were rinsed for 30 seconds with tap-water to remove salts, sand, and attached epiphytes. The clean biomass was shredded to pieces of approximately 2 cm^2 in size and weighed and transferred to a glass evaporating dish to obtain the *wet mass*. Samples were then frozen at -18 °C for 1-3 days, before being thawed and dried at 60 °C under a flow of air until a

[*] Taxonomic identification was kindly provided by Dr. Hilary Redden

constant weight was recorded, giving the *dry mass*. When dry, the macroalgae were immediately ground in a NutriBullet™ (600 W) food-processor for 30 seconds and passed through a 60-mesh (250 μm) sieve. The matter retained on the sieve was re-ground for a further 30 seconds, followed by further sieving. This process was repeated until 99 wt.% of the material had passed through the sieve, with the remaining 1 wt.% being disposed of. The collected sieved material was returned to storage at -18 °C until required.

5.8.1.2 Preparation of Ca- and Cu-exchanged macroalgal biomass

The naturally occurring metal ions in the samples of macroalgae were replaced with either Ca^{2+} or Cu^{2+} by means of ion-exchange, according to the following method: macroalgal biomass (500 mg), prepared as in Section 5.8.1.1, was suspended in a solution of either $CaCl_2$ or $CuCl_2$ (25.0 mL, 1.0 M) as required and shaken for 20 hours. The slurry was centrifuged (3000 rpm, 15 min) and washed with deionised H_2O (25 mL) five times. Preliminary experiments revealed that the washing procedure resulted in near quantitative removal of D-mannitol from the biomass and so this sugar was replaced by re-suspending the seaweed in 1.0 mL of deionised water containing the necessary quantity of D-mannitol (as determined by the method outlined in Section 5.8.2.5) and shaking for a further 20 hours. Finally, the ion-exchanged, D-mannitol-replenished biomass was dried at 60 °C for 24 hours and re-ground to pass through a 60-mesh (250 μm) sieve with a pestle and mortar. The degree of ion-exchange was determined by ICP analysis (see 5.8.2.1).

5.8.1.3 Extraction of Na-alginates (NaAlg) from macroalgal biomass

An alginate extraction employing mild conditions was utilised in order to obtain purified, undegraded samples of sodium alginate (**NaAlg**) from each of the collected macroalgal species, suitable for thermochemical study.[34] Macroalgal biomass (500 mg), prepared as in Section 5.8.1.1, was suspended in aqueous formaldehyde (2.5 mL, 5 vol.%) and shaken for 6 hours. The macroalgae was washed with HCl (3 × 50 mL, 0.2 M) and deionised H_2O (1 × 50 mL) with separation by centrifugation (3000 rpm, 15 min) each time. The biomass was re-suspended in NaOH (0.04 M, 50 mL) and shaken for 12 hours prior to recovery of the alginate-rich supernatant by centrifugation (3000 rpm, 15 min). Following neutralisation to pH 7.0 ± 0.1 with HCl (0.2 M), the alginate solution was reduced *in vacuo* (40 °C, 40 mbar) to approximately 25 mL and precipitated by shaking with an equal volume of EtOH for 30 mins. The fibrous **NaAlg** precipitate was recovered by centrifugation (3000 rpm, 15 min) before washing with aqueous EtOH (1 × 50 mL, 60 vol.%), absolute EtOH (3 × 50mL), and finally absolute Et_2O (1 × 50 mL) with separation by centrifugation (3000 rpm, 15 min) each time. The samples were air-dried at room temperature for 24 hours and at 60 °C for a further 24 hours prior to weighing. Between 60 – 140 mg of white, fluffy **NaAlg** was obtained for each macroalga. Prior to use, the **NaAlg** samples were re-dissolved in deionised H_2O (1.0 mL per 100 mg of **NaAlg**) and re-dried at 60 °C for 24 hours to give a brittle sample suitable for study *via* the thermochemical techniques outlined in Sections 5.8.3.

The mannuronate:guluronate (**M**/**G**) ratio of the alginates were analysed by ^{1}H NMR spectroscopy according to the method of Grasdalen[110,111] with modifications by Davies *et al.*[31] The methodology and full results of such analyses are reported in Appendix J.

5.8.1.4 Preparation of Ca- and Cu(II)-alginates (CaAlg, Cu(II)Alg) from extracted Na-alginate (NaAlg)

The Na^+ ions in **NaAlg** were replaced with either Ca^{2+} or Cu^{2+} by ion-exchange, according to the following method. **NaAlg** (60 mg), prepared as in Section 5.8.1.3, was suspended in a solution of either $CaCl_2$ or $CuCl_2$ (3.0 mL, 1.0 M) as required and shaken for 20 hours. The alginate was centrifuged (3000 rpm, 15 min) and washed with deionised H_2O (25 mL) five times prior to being dried at 60 °C for 24 hours and re-ground with a pestle and mortar to pass through a 60-mesh sieve (250 μm). The degree of ion-exchange was determined by ICP analysis (see Section 5.8.2.1). **Ca-** and **Cu(II)-Alg** were also prepared from commercial **NaAlg** samples (obtained from Sigma Aldrich and BDH) in the same manner.

5.8.1.5 Preparation of alginate-extracted algal-residue (AE-AR) from macroalgal biomass

The *alginate-extracted algal-residue* (**AE-AR**) is the fibrous solid material remaining following the extraction of **NaAlg** and other water soluble components (D-mannitol, laminarin, pigments, amino acids, free metal salts etc.) from the kelp biomass.[5,8] The **AE-AR** from five different species of macroalgae were prepared according to sequential extraction procedure detailed below. In each case, 1.0 g of the biomass was used (prepared according to the method in Section 5.8.1.1), with recovery of the solid from successive supernatants being achieved *via* centrifugation (3000 rpm, 5 min):

I. Warm neutral wash: 3 × $CaCl_{2(aq)}$ (25.0 mL, 0.18 M), 50 °C; stirred (500 rpm, 3 hours)

II. Warm water wash: 1 × deionised H_2O (25.0 mL), 50 °C; stirred (500 rpm, 3 hours)

III. Cold acid wash: 3 × $HCl_{(aq)}$ (25.0 mL, 0.05 M), room temperature; stirred (500 rpm, 3 hours)

IV. Cold water wash: 1 × deionised H_2O (25.0 mL), room temperature; stirred (500 rpm, 3 hours)

V. Warm alkali wash: 3 × $Na_2CO_{3(aq)}$ (25.0 mL, 0.28 M), 50 °C; stirred (500 rpm, 3 hours)

VI. Warm water wash: 1 × deionised H_2O (25.0 mL), 50 °C; stirred (500 rpm, 3 hours)

VII. Cold water wash: 2 × deionised H_2O (25.0 mL), room temperature; shaken (10 min)

VIII. Aqueous ethanol wash: 2 × $EtOH_{(aq)}$ (50 vol.%), room temperature; shaken (10 min)

IX. Ethanol wash: 2 × EtOH (100 vol.%), room temperature; shaken (10 min)

X. Ether wash: 1 × Et_2O (100 vol.%), room temperature; shaken (10 min)

Following the final ether wash, the **AE-AR** was air-dried at room temperature for 10 hours and subsequently at 60 °C for 24 hours before being ground to fit through a 60-mesh (250 μm) sieve.

5.8.1.6 Preparation of Ca- and Cu(II)-exchanged alginate-extracted algal-residues (Ca-AE-AR, Cu(II)-AE-AR)

The metal ions remaining bound within the alginate-extracted algal-residue (**AE-AR**) prepared in Section 5.8.1.5 were replaced with either Ca^{2+} or Cu^{2+} by ion-exchange, according to the following method: Algal residue (60 mg) was suspended in a solution of either $CaCl_2$ or $CuCl_2$ (3.0 mL, 1.0 M) and shaken for 20 hours. The slurry was centrifuged (3000 rpm, 15 min) and washed with deionised H_2O (25 mL) five times before being air-dried at room temperature for 24 hours and at 60 °C for a further 24 hours. Finally, the metal-exchanged algal residues were ground to fit through a 60-mesh (250 μm) sieve.

5.8.2 Characterisation of macroalgal biomass, extracted alginates, and algal residues

5.8.2.1 Elemental analysis of macroalgae and associated biomass fractions[*]

Macroalgae and metal-treated macroalgae (prepared in Section 5.8.1.1 and Section 5.8.1.2 respectively) along with their associated fractions (alginates and alginate-extracted algal residues) were all analysed to discern their elemental composition according to the following methods:

%CHN was determined by combustion analysis on an Exeter Analytical, CE-440 Elemental Analyser. Around 1 mg of accurately weighed sample was loaded into a tin capsule and combusted in pure oxygen in a horizontal furnace at 975 °C to determine the quantity of CO_2 and H_2O released. Calibration was achieved by utilising a standard sample of acetanilide (Exeter Analytical), and 4-bromobenzoic acid (Elemental Microanalysis) was run periodically to ensure consistent instrument performance. The reported %H was corrected to account for the moisture already present in the sample prior to combustion.

%S was determined by combustion analysis performed by MEDAC Ltd. (Surrey, UK) on a FlashEA® 1112 Elemental Analyser. A similar procedure was used to that described for the %CHN analysis detailed above.

%metal was determined by inductively-coupled plasma optical emission spectroscopy (ICP-OES). Samples were first digested and made up to an appropriate concentration in HNO_3 (1.6 M) according to the methods outlined in Section 5.8.2.2. ICP-OES was then conducted on a JobinYvon Horiba Ultima2 Spectrometer in the radial torch configuration, and with a sequential monochromator. Calibration of signal intensity and wavelength were achieved by use of analytical standards of the appropriate metal nitrate salt (Fluka), with allowances for the high Na^+ content of samples where necessary. A sample of commercial algal material (International Atomic Energy Agency Environment Laboratories, Material IAEA-413) was digested and analysed in the same manner to confirm the reliability of the procedures.

[*] Dr. Emily Unsworth is thanked especially for performing the many measurements of %CHN and %metal and for providing advice on sample preparation

%moisture was determined using the TGA apparatus described in Section 5.8.3.1. Here, approximately 10 mg of powdered algal biomass was evenly loaded into a ceramic sample pan and heated at from room temperature to 110 °C at 10 °C min^{-1} under a flow of dry air (30 mL min^{-1}). The sample was held at 110 °C for 15 minutes and the %moisture was defined as the %mass lost from the start of the experiment until the completion of the isothermal period.

%ash was determined from the same experimental setup as %moisture (see above). After the %moisture had been determined at 110 °C, the sample was further heated (again at 10 °C min^{-1}) to a temperature of 550 °C, where it was held for 15 minutes. The %ash was defined as the %mass remaining following the isothermal period at 550 °C.

5.8.2.2 Digestion of macroalgae and associated biomass fractions prior to analysis by ICP-OES[*]

Prior to the ICP-OES analysis detailed in Section 5.8.2.1, all of the biomass studied in this chapter (whole macroalgae, alginates, algal-residues *etc.*) was digested on a SCP Science DigiPREP LS according to the standardised protocol of the United States Environmental Protection Agency (Method EPA3051B). Samples of dry algal biomass (10 – 100 mg) were weighed accurately into a Teflon™ vial. Hydrogen peroxide (30 % w/v, 4 mL) was added in 1 mL aliquots, before the gradual addition of 16 mL *aqua regia* (HCl (12.0 M): HNO_3 (15.7 M), 4:1 v/v). The digestate slurry was gradually heated to a point of steady reflux, which was sustained for 300 minutes. After cooling, the contents of the vials were evaporated to dryness at (60 ^oC), before being redissolved in HNO_3 (5 mL, 1.6 M) by sonicating the mixture for 1 minute and then shaking for 16 hours. Any solid material remaining following the dissolution period was removed by centrifugation on an IKA mini-G for (6000 rpm, 15 minutes), prior to dilution to an appropriate concentration for analysis with HNO_3 (1.6 M).

It was clear that, in some cases, the DigiPREP digestion method was not sufficiently harsh to completely destroy the biomass organic matrix, and so a second protocol was trialled with heating in *aqua regia* at 200 °C in a sealed Carius tube. Whilst being more expensive, dangerous, and time consuming, the latter method gave complete degradation of the untreated kelp biomass, with no solid material remaining at the end. Following analysis by ICP-OES (see Section 5.8.2.1), there were no significant differences recorded for the %metal content of samples prepared by either the DigiPREP or Carius tube digestion methods for untreated kelp samples. However, for Ca- and Cu(II)-treated kelps, there was noticeably more solid material remaining following the DigiPREP digestion than in the untreated case, giving rise to the possibility that not all metal ions had been quantitatively transferred to the aqueous phase. Unfortunately, the full Carius digestion procedure could not be carried out for the metal-treated kelp samples, and so the results of the ICP-OES analysis may only be viewed as being a qualitative representation of the %metal content (see Appendix I).

---

[*] Dr. Hilary Redden and staff of the Durham University Geography Department are thanked especially for assisting with the digestion of samples on the DigiPrep.

5.8.2.3 Biochemical component analysis of macroalgal biomass by sequential fractionation

In order to quantitatively determine the biochemical composition of the harvested macroalgal biomass, sequential neutral ($CaCl_2$), acidic (HCl), and alkaline (Na_2CO_3) extractions were undertaken to isolate fractions for further analysis. The extraction procedure, which combines elements from a number of similar literature procedures,[5,8,47,112,113] is outlined in Figure 5.25 and explained in detail below.

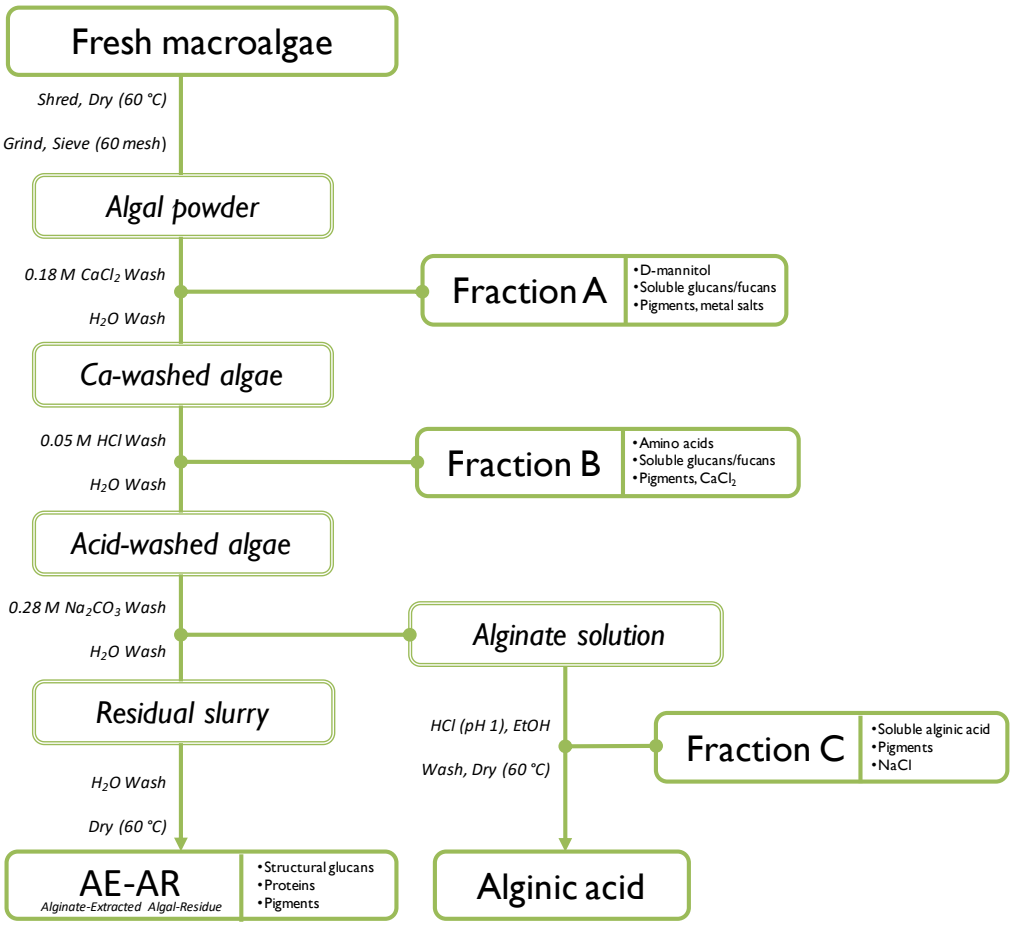

Figure 5.25 The sequential fractionation procedure used to isolate various biochemical components of macroalgal biomass for further analysis. The predominant components of each fraction are described where possible.

The procedure described requires a starting mass of 1.0 g of **algal powder** (as prepared from fresh macroalgae in Section 5.8.1.1) with recovery of the solid from successive supernatants being achieved *via* centrifugation (3000 rpm, 5 min) each time:

Neutral extraction of **algal powder**

- 3 × $CaCl_{2(aq)}$ (25.0 mL, 0.18 M), 50 °C, stirred (500 rpm, 3 hours)
- 1 × deionised H_2O (25.0 mL), 50 °C, stirred (500 rpm, 3 hours)

*The liquids were pooled to give **Fraction A** and the solid **Ca-washed algae** used in the acid extraction below.*

Acid extraction of **Ca-washed algae**

- 3 × $HCl_{(aq)}$ (25.0 mL, 0.05 M), room temperature, stirred (500 rpm, 3 hours)
- 1 × deionised H_2O (25.0 mL), room temperature, stirred (500 rpm, 3 hours)

*The liquids were pooled to give **Fraction B** and the solid **acid-washed algae** used in the alkali extraction below.*

Alkali extraction of **acid-washed algae**

- 3 × $Na_2CO_{3(aq)}$ (25.0 mL, 0.28 M), 50 °C, stirred (500 rpm, 3 hours)
- 1 × deionised H_2O (25.0 mL), 50 °C, stirred (500 rpm, 3 hours)

*The liquids were pooled to give the **alginate solution**, from which **alginic acid** was precipitated as below. The solid **alginate-extracted algal-residue** (**AE-AR**) was washed as below.*

Precipitation of **alginic acid** from **alginate solution**

- A 20 mL aliquot of the 100 mL **alginate solution** was neutralised with HCl (2.0M, 5.0 mL) and shaken until effervescence ceased. Further HCl (2.0 M, 1.0 mL) was added to convert the **alginate** to **alginic acid**.
- An equal volume of EtOH was added to fully precipitate the **alginic acid** as an off-white gel.

*The liquids were pooled to give **Fraction C** and the gelatinous **alginic acid** separated and washed as below.*

Washing **alginic acid**

- 2 × EtOH (100 vol.%), room temperature, shaken (10 min)
- 1 × Et_2O (100 vol.%), room temperature, shaken (10 min)

*the washed **alginic acid** was air-dried at room temperature for 10 hours and subsequently at 60 °C for 24 hours.*

Washing the ***alginate-extracted algal-residue*** (**AE-AR**)

- Cold water wash: 2 × deionised H_2O (25.0 mL), room temperature, shaken (10 min)
- Aqueous ethanol wash: 2 × $EtOH_{(aq)}$ (50 vol.%), room temperature, shaken (10 min)
- Ethanol wash: 2 × EtOH (100 vol.%), room temperature, shaken (10 min)
- Ether wash: 1 × Et_2O (100 vol.%), room temperature, shaken (10 min)

*the washed **alginate-extracted algal-residue** (**AE-AR**) was air-dried at room temperature for 10 hours and subsequently at 60 °C for 24 hours.*

Onward analysis of extracted fractions

- **Fractions A**, **B**, and **C** were analysed for D-mannitol (see Section 5.8.2.5), soluble glucans (see Section 5.8.2.6) and uronic acids (See Section 5.8.2.7)
- Following washing and drying, the solid **alginic acid** and **AE-AR** fractions were weighed and their moisture contents determined by heating for 1 hour at 110 °C.
- The **AE-AR** fraction from each sample was further digested (see Section 5.8.2.4) to facilitate analysis of the glucan and uronic acid contents.

Mass balance for the biochemical composition of macroalgal biomass

Each of the quantified constituents of the biomass was expressed as a wt.% of the whole macroalgae according to the following formulae. The wt.% of each individual constituent can be summed together to give a mass balance that should equal 100 wt.%:

$$\text{Moisture (wt.\%)} = \frac{\text{mass of moisture lost by macroalgae at 110 °C over 60 minutes}}{\text{starting mass of macroalgae (mg)}} \times 100$$

$$\text{Metals (wt.\%)} = \frac{\text{mass of all metal ions mesured in the samples by ICP-OES (mg)}}{\text{starting mass of macroalgae (mg)}} \times 100$$

$$\text{Mannitol (wt.\%)} = \frac{\text{mannitol quantified in Fraction A (mg)} + \text{mannitol quantified in Fraction B (mg)}}{\text{starting mass of macroalgae (mg)}} \times 100$$

$$\text{Alginic acid (wt.\%)} = \frac{\text{mass of dry alginic acid (mg)} + \text{ glucans quantified in Fraction C (mg)}}{\text{starting mass of macroalgae (mg)}} \times 100$$

$$\text{Soluble glucans (wt.\%)} = \frac{\text{glucans quantified in Fraction A (mg)} + \text{glucans quantified in Fraction B (mg)}}{\text{starting mass of macroalgae (mg)}} \times 100$$

$$\text{AE-AR (wt.\%)} = \frac{\text{Alginate-extracted algal-residue (AE-AR) quantified from each species (mg)}}{\text{starting mass of macroalgae (mg)}} \times 100$$

Theoretical mass balance:

Moisture (wt.%) + metals (wt.%) + alginic acid (wt.%) + mannitol (wt.%) + soluble glucans (wt.%) + AE-AR (wt.%) = 100 wt.%

5.8.2.4 Digestion and analysis of carbohydrates in alginate-extracted algal-residues (AE-AR)

In order to analyse the carbohydrates comprising the alginate-extracted algal-residue (**AE-AR**) it was first necessary to partially digest the sample according to the methods of Schiener *et al.*[5] and Sluiter *et al.*[114], with quantification of the released glucose or uronic acids being achieved *via* standard sulphuric acid assays (see Sections 5.8.2.6 and 5.8.2.7 respectively). In a typical procedure, dry **AE-AR** (10 mg) was suspended in H_2SO_4 (280 μL, 13.5 M) in a 15 mL glass autoclave liner, sonicated for 5 minutes to disperse the particles, and stood in a water bath at 30 °C for 1 hour. Upon cooling the mixture over ice, deionised H_2O was added to bring the volume up to 5.0 mL. The solutions were then heated to 120 °C in a sealed autoclave and stirred (500 rpm, 15 minutes). Repeating the experiment with

a longer period of heating (up to 60 minutes) did not yield significantly different results. Upon cooling, aliquots were taken from the digestate, spun in an IKA® mini-G centrifuge (6000 rpm, 5 minutes) to separate insoluble material, and diluted by 10- or 100-fold with deionised H_2O to provide solutions suitable for analysis by the methods outlined in Sections 5.8.2.6 and 5.8.2.7. A blank experiment in which no **AE-AR** was included was also conducted by the same methods, and used to provide the background readings in the experiments described below.

5.8.2.5 Quantification of D-mannitol in solutions

The quantity of D-mannitol in solutions was ascertained by ^{1}H NMR spectroscopy. In a typical procedure, an accurately measured aliquot of the solution to be tested was shaken for 2 hours with Amberlite® IR120 (H^+) ion exchange resin (200 mg resin / 10 mL of solution). The resin was removed by filtration and rinsed with deionised water (3 × 5.0 mL). The collected aqueous fractions were then pooled and reduced to dryness *in vacuo* (40 °C, 40 mbar). The dried material was dissolved in D_2O (1.0 mL) and reduced to dryness twice more, before finally being re-dissolved in D_2O (1.0 mL, spiked with a known quantity of acetone as an internal standard). In some cases, it was necessary to spin solutions in an IKA® mini-G centrifuge (6000 rpm, 5 mins) to separate insoluble material prior to analysis by ^{1}H NMR. The ^{1}H NMR spectrum was recorded on a Bruker Avance 400 MHz spectrometer at 298 K (according to the parameters in Appendix D). Quantification of the D-mannitol was achieved by first integrating appropriate peaks against the acetone signal (δ = 2.05 ppm) and then by comparing their area with a calibration line derived from standard solutions of D-mannitol, ranging from 0.0 - 20.0 mg /mL D_2O. The final value of the %mannitol in the sample was calculated from the average of at least two readings derived from individually prepared analyte solutions.

5.8.2.6 Quantification of glucans in solutions

The quantity of glucans in solutions was determined by means of a standard phenol-H_2SO_4 assay.[115] In general, aqueous phenol (0.5 mL, 0.3 M) was added to 2.0 mL of the solution to be studied (or some dilution made up to 2.0 mL by deionised H_2O) in a glass test tube. H_2SO_4 (5.0 mL, 18.4 M) was added quickly by the action of an Eppendorf® Variable Volume pipette, causing instantaneous boiling of the solution. Upon cooling for exactly 60 minutes, the absorbance at 485 nm of 200 μL of the solution was measured by a 96-well Thermo Scientific Multiskan™ GO Microplate Spectrophotometer. Quantification was achieved by comparison with a calibration line derived from standard solutions of D-glucose in deionised H_2O (0 – 100 μg / mL) and from an average of a minimum of three readings.

5.8.2.7 Quantification of uronic acids in solutions

The quantity of uronic acids in solutions was determined by means of a 3-phenylphenol-H_2SO_4 assay developed by van den Hoogan *et al*.[116] In general, Portions (40 μL) of each analyte were added separately to a standard 96-well microtitre plate. H_2SO_4 (200 µL, 18.4 M) containing $Na_2[B_4O_5(OH)_4]$ (20 nM) was added to each well and the microtitre plate heated to 80 °C for exactly 60 minutes. After cooling to ambient temperature, the background absorbance at 540 nm was measured on a Thermo Scientific Multiskan™ GO Microplate Spectrophotometer. 3−Phenylphenol (0.10 g, 0.60 mmol) was dissolved in

Me_2SO (1.0 mL) and added to H_2SO_4 (4.9 mL, 15.0 M) just before use. A portion (40 µL) of the 3−phenylphenol/Me_2SO/H_2SO_4 solution was added to each analyte and the microtitre plate was shaken for 15 minutes prior to a second reading of the absorbance at 540 nm. Quantification was achieved my comparison with calibration lines derived from standard solutions of D-glucuronic and D-galacturonic acid in deionised H_2O (0 – 200 μg / mL). As different uronic acids are known to respond variously with H_2SO_4-based colourometric assays (see Appendix A),[117] only a range of possible values for the %uronic acid in the sample could be reported.

5.8.3 Thermal analysis of macroalgae and associated biomass

5.8.3.1 Thermogravimetric analysis (TGA) of macroalgae and associated biomass

A detailed discussion of the experimental parameters relating to thermogravimetric analysis (TGA) and derivative thermogravimetric analysis (DTG) is provided in Appendix L. TGA/DTG analyses were carried out on a Perkin Elmer Pyris 1 analyser. The sample (ranging in mass from 5 to 50 mg depending on the experiment) was loaded into a ceramic crucible and heated from room temperature to 900 °C at a rate of 10 °C min^{-1} under a He atmosphere (with a flow of 30 mL min^{-1}). An isothermal drying period of 10 minutes at 100 °C was included in most runs, and the data subsequently corrected to reflect the mass lost as moisture during this stage.

5.8.3.2 Preparation and analysis of char samples from macroalgal biomass

Samples of char derived from untreated and metal-treated specimens of macroalgal biomass were prepared by TGA, and subjected to various forms of *ex-situ* solid-state analysis. The seaweed was loaded into the TGA apparatus and heated according to the procedure described in Section 5.8.3.1. At 250 °C, an isothermal period of 60 minutes was employed to allow the maturation of crystalline material within the sample. Following the isothermal period, the furnace was cooled to room temperature, opened, and the residual char gathered from the sample pan. The resulting sooty powders were further ground and sieved (60 mesh, 250 μm) onto a poly(methyl methacrylate) disc coated in a thin layer of petroleum jelly. The char sample was then subject to analysis by X−ray powder diffraction (PXRD) on a Bruker D8 Advance diffractometer utilising Cu Kα radiation (λ = 1.5406 Å) at scattering angles (2θ) from 20° to 80° with a step size of 0.02°. Peak assignment was carried out through comparison with data from the Crystallographic Open Database (COD) and diagnostic peak patterns are reported in Appendix F for reference. Additional characterisation of the char samples was conducted by Fourier transform infra-red spectroscopy (FTIR) on a PerkinElmer Spectrum Two spectrometer equipped with a Universal Attenuated Total Reflectance (UATR) accessory.

5.8.3.3 Pyrolysis-gas chromatography mass spectrometry (Py-GCMS)

The complexity of the pyrolysis-gas chromatography mass spectrometry (Py-GCMS) experiments required a significant level of method development, discussed at length in Appendix L. The final parameters used in the experiments are also provided in Appendix L along with their rationalisation, though a brief overview is also reported here. Micropyrolysis was conducted on a CDS 5200 Pyroprobe coupled to an Agilent 7820A gas

chromatograph and Agilent 5977E mass selective detector. Latter experiments were also carried out in which the Pyroprobe was coupled to a CDS 5500 permanent gas analyser equipped with a thermal conductivity detector unit. In a typical experiment, a finely ground sample was packed with quartz wool into a short length of quartz tube, with weighing before and after to determine the mass of pyroysable material (between 100 – 250 μg). Once loaded into the Pyroprobe and purged with an inert gas (He), pyrolysis was conducted at 20 °C ms^{-1} up to a target temperature, which was maintained for 20 seconds. Volatilised organic material was condensed on a Tenax® trap, before being desorbed into the GC inlet *via* a transfer line heated at 300 °C. A Thermo Scientific TraceGold TG-1701MS (60 m × 250 μm × 0.25 μm) column was employed to separate the components of the pyrolysate under a constant flow of He (0.68 mL min^{-1}) and pre-programmed temperature profile: 40 °C (hold 2 mins), heat at 10 °C min^{-1} to 250 °C (hold 10 mins). Following ionisation (70 eV) and detection (1.6 – 300 amu, 781 units s^{-1}), identification of the products was carried out by comparison with a commercial standard (Sigma Aldrich, used as received) where possible, or by reference to a spectral library.* Finally, the sample was re-weighed following pyrolysis in order to facilitate a calculation of conversion. Details of the calibrations required to quantify yields of significant pyrolysis products (namely 2-furaldehyde, CO_2 and CO) are provided in Appendix L.

5.9 Chapter acknowledgements

In this chapter, gratitude is owed particularly to Dr. Hilary Redden for her extensive assistance with the identification, harvesting, and handling of seaweed biomass. Doug Carswell is thanked for conducting a significant number of the TGA experiments. Drs. Ben Smith and Li Li are gratefully acknowledged for help in setting up and operating the Py-GCMS and fixed gas analyser. Malcolm Brown and Aaron Richardson of the Durham University Glassblowing Workshop are thanked for preparation of quartz tubing for Py-GCMS experiments, as is Gary Oswald for guidance on using the X-ray diffractometer. Dr. Emily Unsworth, Judith Magee, Dr. Hilary Redden, Blanca Cota Ka, and staff of the Durham University Geography Department are all acknowledged for providing advice and assistance with the digestion and elemental analysis of samples. Dr. Unsworth is also recognised for generously allowing time for access to her high precision analytical balance. Finally, the staff of MEDAC Ltd. (Surrey, UK) are thanked for determining the %S in macroalgal samples.

5.10 Chapter references

1 J. S. Rowbotham, P. Dyer, H. Greenwell and M. Theodorou, *Biofuels*, 2012, **3**, 441–461.

2 K. Gao and K. R. McKinley, *J. Appl. Phycol.*, 1994, **6**, 45–60.

* Reductic acid is not currently commercially available and so was synthesised, purified, and characterised according to the method in Appendix C in order to be used a standard reference material.

3 M. Song, H. Duc Pham, J. Seon and H. Chul Woo, *Renew. Sustain. Energy Rev.*, 2015, **50**, 782–792.

4 A. Ross, J. Jones, M. Kubacki and T. Bridgeman, *Bioresour. Technol.*, 2008, **99**, 6494–6504.

5 P. Schiener, K. D. Black, M. S. Stanley and D. H. Green, *J. Appl. Phycol.*, 2015, **27**, 363–373.

6 W. A. P. Black, *J. Mar. Biol. Assoc. United Kingdom*, 1950, **29**, 45–72.

7 G. Michel, T. Tonon, D. Scornet, J. M. Cock and B. Kloareg, *New Phytol.*, 2010, **188**, 67–81.

8 L. E. Rioux, S. L. Turgeon and M. Beaulieu, *Carbohydr. Polym.*, 2007, **69**, 530–537.

9 S. U. Kadam, B. K. Tiwari and C. P. O'Donnell, *Int. J. Food Sci. Technol.*, 2015, **50**, 24–31.

10 T. A. Davis, B. Volesky and A. Mucci, *Water Res.*, 2003, **37**, 4311–4330.

11 M. T. Ale and A. S. Meyer, *RSC Adv.*, 2013, **3**, 8131–8141.

12 K. Anastasakis, A. ROSS and J. Jones, *Fuel*, 2011, **90**, 598–607.

13 A. Ross, K. Anastasakis, M. Kubacki and J. Jones, *J. Anal. Appl. Pyrol.*, 2009, **85**, 3–10.

14 Y. J. Bae, C. Ryu, J. K. Jeon, J. Park, D. J. Suh, Y. W. Suh, D. Chang and Y. K. Park, *Bioresour. Technol.*, 2011, **102**, 3512–3520.

15 P. J. Morgan and K. Smith, *Analyst*, 1978, **103**, 1053–1060.

16 M. I. Bird, C. M. Wurster, P. H. de Paula Silva, A. M. Bass and R. de Nys, *Bioresour. Technol.*, 2011, **102**, 1886–1891.

17 M. I. Bird, C. M. Wurster, P. H. De Paula Silva, N. A. Paul and R. De Nys, *GCB Bioenergy*, 2012, **4**, 61–69.

18 J. W. Choi, J. H. Choi, D. J. Suh and H. Kim, *J. Anal. Appl. Pyrolysis*, 2015, **112**, 141–149.

19 H. V. Ly, S. S. Kim, H. C. Woo, J. H. Choi, D. J. Suh and J. Kim, *Energy*, 2015, **93**, 1436–1446.

20 H. V. Ly, S. S. Kim, J. H. Choi, H. C. Woo and J. Kim, *Energy Convers. Manag.*, 2016, **122**, 526–534.

21 K. Kebelmann, A. Hornung, U. Karsten and G. Griffiths, *J. Anal. Appl. Pyrolysis*, 2013, **104**, 131–138.

22 Y. Uemura, R. Matsumoto, S. Saadon and Y. Matsumura, *Fuel Proc. Technol.*, 2015, **138**, 133–138.

23 J. Choi, J. W. Choi, D. J. Suh, J. M. Ha, J. W. Hwang, H. W. Jung, K. Y. Lee and H. C. Woo, *Energy Convers. Manag.*, 2014, **86**, 371–378.

24 H. W. Lee, J. K. Jeon, S. H. Park, K. E. Jeong, H. J. Chae and Y. K. Park, *Nanoscale Res. Lett.*, 2011, **6**, 500–507.

25 A. Haug, J. Bjerrum, O. Buchardt, G. E. Olsen, C. Pedersen and J. Toft, *Acta Chem. Scand.*, 1961, **15**, 1794–1795.

26 R. Kohn, *Pure Appl. Chem.*, 1975, **42**, 371–397.

27 A. Haug, O. Smidsrød, B. Larsen, S. Gronowitz, R. A. Hoffman and A. Westerdahl, *Acta Chem. Scand.*, 1965, **19**, 341–351.

28 Q. Yu, J. T. Matheickal, P. Yin and P. Kaewsarn, *Water Res.*, 1999, **33**, 1534–1537.

29 W. M. Antunes, A. S. Luna, C. A. Henriques and A. C. A. Da Costa, *Electron. J. Biotechnol.*, 2003, **6**, 174–184.

30 P. Lodeiro, B. Cordero, J. Barriada, R. Herrero and M. Sastredevicente, *Bioresour. Technol.*, 2005, **96**, 1796–1803.

31 T. A. Davis, F. Llanes, B. Volesky, G. Diaz-Pulido, L. Mccook and A. Mucci, *Appl. Biochem. Biotechnol.*, 2003, **110**, 75–90.

32 T. A. Davis, F. Llanes, B. Volesky and A. Mucci, *Environ. Sci. Technol.*, 2003, **37**, 261–267.

33 T. A. Davis, J. P. Pinheiro, H. Grasdalen, O. Smidsrød and H. P. van Leeuwen, *Environ. Sci. Technol.*, 2008, **42**, 1673–1679.

34 T. A. Davis, M. Ramirez, A. Mucci and B. Larsen, *J. Appl. Phycol.*, 2004, **16**, 275–284.

35 E. Fourest and B. Volesky, *Appl. Biochem. Biotechnol.*, 1997, **67**, 215–226.

36 J. M. M. Adams, A. Schmidt and J. A. Gallagher, *J. Appl. Phycol.*, 2015, **27**, 985–991.

37 A. Ross, C. Hall, K. Anastasakis, A. Westwood, J. Jones and R. J. Crewe, *J. Anal. Appl. Pyrolysis*, 2011, **91**, 344–351.

38 Q. Lu, C. Q. Dong, X. M. Zhang, H. Y. Tian, Y. P. Yang and X. F. Zhu, *J. Anal. Appl. Pyrolysis*, 2011, **90**, 204–212.

39 S.-J. Oh, S.-H. Jung and J.-S. Kim, *Bioresour. Technol.*, 2013, **144**, 172–178.

40 Q. Lu, Z. Wang, C. Q. Dong, Z. F. Zhang, Y. Zhang, Y. P. Yang and X. F. Zhu, *J. Anal. Appl. Pyrolysis*, 2011, **91**, 273–279.

41 Y. Richardson, J. Motuzas, A. Julbe, G. Volle and J. Blin, *J. Phys. Chem. C*, 2013, **117**, 23812–23831.

42 W. J. Liu, K. Tian, H. Jiang, X. S. Zhang, H. S. Ding and H. Q. Yu, *Environ. Sci. Technol.*, 2012, **46**, 7849–7856.

43 B. B. Jiu, B. X. Li and Q. J. Yu, *J. Anal. Appl. Pyrolysis*, 2015, **112**, 270–275.

44 K. Bru, J. Blin, A. Julbe and G. Volle, *J. Anal. Appl. Pyrolysis*, 2007, **78**, 291–300.

45 D. Manns, A. L. Deutschle, B. Saake and A. S. Meyer, *RSC Adv.*, 2014, **4**, 25736–25746.

46 J. M. M. Adams, A. Ross, K. Anastasakis, E. M. Hodgson, J. A. Gallagher, J. Jones and I. S. Donnison, *Bioresour. Technol.*, 2011, **102**, 226–234.

47 N. P. Chandia, B. Matsuhiro, J. S. Ortiz and A. Mansilla, *J. Chil. Chem. Soc.*, 2005, **50**, 501–504.

48 Y. Date, K. Sakata and J. Kikuchi, *Polym. J.*, 2012, **44**, 888–894.

49 E. Percival, *Br. Phycol. J.*, 1979, **14**, 103–117.

50 B. Larsen, A. Haug and T. J. Painter, *Acta Chem. Scand.*, 1966, **20**, 219–230.

51 W. A. P. Black, W. J. Cornhill, E. T. Dewar and F. N. Woodward, *J. Appl. Chem.*, 1951, **1**, 505–517.

52 W. A. P. Black, E. T. Dewar and F. N. Woodward, *J. Appl. Chem.*, 2007, **1**, 414–424.

53 A. J. Mian and E. Percival, *Carbohydr. Res.*, 1973, **26**, 133–146.

54 D. Li, L. Chen, S. Chen, X. Zhang, F. Chen and N. Ye, *Fuel*, 2012, **96**, 185–191.

55 S. H. S. Shekhar, G. Lyons, C. McRoberts, D. McCall, E. Carmichael, F. Andrews and R. McCormack, *J. Appl. Phycol.*, 2011, **24**, 1141–1157.

56 S. K. Papageorgiou, E. P. Kouvelos, E. P. Favvas, A. Sapalidis, G. E. Romanos and F. K. Katsaros, *Carbohydr. Res.*, 2010, **345**, 469–473.

57 S. Xin, H. Yang, Y. Chen, M. Yang, L. Chen, X. Wang and H. Chen, *J. Anal. Appl. Pyrolysis*, 2015, **116**, 263–271.

58 P. T. Williams and P. A. Horne, *Renew. Energy*, 1994, **4**, 1–13.

59 S. E. Kinata, K. Loubar, M. Paraschiv, A. Bouslamti, C. Belloncle and M. Tazerout, *J. Anal. Appl. Pyrolysis*, 2013, **104**, 210–217.

60 A. A. Gokhale, J. A. Dumesic and M. Mavrikakis, *J. Am. Chem. Soc.*, 2008, **130**, 1402–1414.

61 B. Hou, Y. Huang, X. Wang, X. Yang, H. Duan and T. Zhang, *AIChE J.*, 2016, **62**, 2879–2892.

62 F. X. Collard, J. Blin, A. Bensakhria and J. Valette, *J. Anal. Appl. Pyrolysis*, 2012, **95**, 213–226.

63 S. Zhang, Q. Dong, L. Zhang and Y. Xiong, *Bioresour. Technol.*, 2015, **191**, 17–23.

64 H. Yuan, S. Xing, Huhetaoli, T. Lu and Y. Chen, *J. Anal. Appl. Pyrolysis*, 2015, **112**, 325–332.

65 V. A. Beliy and E. V. Udoratina, *Cent. Eur. J. Chem.*, 2014, **12**, 1294–1303.

66 A. D. Paulsen, M. S. Mettler and P. J. Dauenhauer, *Energy & Fuels*, 2013, **27**, 2126–2134.

67 S. Eibner, F. Broust, J. Blin and A. Julbe, *J. Anal. Appl. Pyrolysis*, 2015, **113**, 143–152.

68 Q. Fu, D. Argyropoulos, D. Tilotta and L. Lucia, *J. Anal. Appl. Pyrolysis*, 2008, **81**, 60–64.

69 G. N. Richards and G. Zheng, *Energy & Fuels*, 1995, **9**, 136–140.

70 G. N. Richards and G. Zheng, *J. Anal. Appl. Pyrolysis*, 1991, **21**, 133–146.

71 T. G. Devi, M. P. Kannan and G. N. Richards, *Fuel*, 1990, **69**, 1440–1447.

72 Y. Richardson, J. Blin, G. Volle, J. Motuzas and A. Julbe, *Appl. Catal. A Gen.*, 2010, **382**, 220–230.

73 Y. Shen, C. Areeprasert, B. Prabowo, F. Takahashi and K. Yoshikawa, *RSC Adv.*, 2014, **4**, 40651–40664.

74 S. Rajeshkumar, C. Malarkodi, G. Gnanajobitha, K. Paulkumar, M. Vanaja, C. Kannan and G. Annadurai, *J. Nanostructure Chem.*, 2013, **3**, 44–51.

75 H. L. Parker, J. R. Dodson, V. L. Budarin, J. H. Clark and A. J. Hunt, *Green Chem.*, 2015, **17**, 2200–2207.

76 S. Baskoutas, P. Giabouranis, S. N. Yannopoulos, V. Dracopoulos, L. Toth, A. Chrissanthopoulos and N. Bouropoulos, *Thin Solid Films*, 2007, **515**, 8461–8464.

77 Z. Schnepp, S. C. Wimbush, S. Mann and S. R. Hall, *CrystEngComm*, 2010, **12**, 1410–1415.

78 J. J. Bozell and G. R. Petersen, *Green Chem.*, 2010, **12**, 539–554.

79 J.-P. Lange, E. van der Heide, J. van Buijtenen and R. Price, *ChemSusChem*, 2012, **5**, 150–166.

80 M. De bruyn, J. Fan, V. L. Budarin, D. J. Macquarrie, L. D. Gomez, R. Simister, T. J. Farmer, W. D. Raverty, S. J. McQueen-Mason and J. H. Clark, *Energy Environ. Sci.*, 2016, **9**, 2571–2574.

81 S. D. Stefanidis, K. G. Kalogiannis, E. F. Iliopoulou, C. M. Michailof, P. a. Pilavachi and A. a. Lappas, *J. Anal. Appl. Pyrolysis*, 2014, **105**, 143–150.

82 D. Shen, R. Xiao, S. Gu and K. Luo, *RSC Adv.*, 2011, **1**, 1641–1660.

83 Q. Chen, J. Zhou, B. Liu, Q. Mei and Z. Luo, *Chinese Sci. Bull.*, 2011, **56**, 1449–1456.

84 R. S. Baghel, N. Trivedi, V. Gupta, A. Neori, C. R. K. Reddy, A. Lali and B. Jha, *Green Chem.*, 2015, **17**, 2436–2443.

85 K. Kebelmann, PhD Thesis, Aston University, United Kingdom, 2013.

86 F. M. Kerton, Y. Liu, K. W. Omari and K. Hawboldt, *Green Chem.*, 2013, **15**, 860–871.

87 M. Chakraborty, C. Miao, A. McDonald and S. Chen, *Fuel*, 2012, **95**, 63–70.

88 T. Suganya and S. Renganathan, *Bioresour. Technol.*, 2012, **107**, 319–326.

89 J. R. Dodson, V. L. Budarin, A. J. Hunt, P. S. Shuttleworth and J. H. Clark, *J. Mater. Chem. A*, 2013, **1**, 5203–5207.

90 M. B. Gawande, A. Goswami, F.-X. Felpin, T. Asefa, X. Huang, R. Silva, X. Zou, R. Zboril and R. S. Varma, *Chem. Rev.*, 2016, **116**, 3722–3811.

91 C. Lin and H. Chen, *Energy & Fuels*, 2014, **28**, 3178–3184.

92 K. Kositkanawuth, PhD Thesis, The University of Texas at Arlington, USA, 2012.

93 S. Wang, Y. Hu, Q. Wang, S. Xu, X. Lin, H. Ji and Z. Zhang, *J. Therm. Anal. Calorim.*, 2016, **126**, 1689–1702.

94 E. Raymundo-Piñero, M. Cadek and F. Béguin, *Adv. Funct. Mater.*, 2009, **19**, 1032–1039.

95 D. Mondal, M. Sharma, C. Wang, Y. Lin, H. Huang, A. Saha, S. K. Nataraj and K. Prasad, *Green Chem.*, 2016, **18**, 2819–2826.

96 C. M. Santos, J. Dweck, R. S. Viotto, A. H. Rosa and L. C. de Morais, *Bioresour. Technol.*, 2015, **196**, 469–479.

97 Y. M. Kim, H. W. Lee, S. Kim, C. Watanabe and Y.-K. Park, *BioEnergy Res.*, 2015, **8**, 431–439.

98 J. W. Kim, S. H. Park, J. Jung, J. K. Jeon, C. H. Ko, K. E. Jeong and Y. K. Park, *Bioresour. Technol.*, 2013, **136**, 431–436.

99 S. Wang, Q. Wang, X. Jiang, X. Han and H. Ji, *Energy Convers. Manag.*, 2013, **68**, 273–280.

100 T. N. Trinh, P. A. Jensen, K. Dam-Johansen, N. O. Knudsen, H. R. Sørensen and S. Hvilsted, *Energy & Fuels*, 2013, **27**, 1399–1409.

101 N. Ferrera-Lorenzo, E. Fuente, J. M. Bermúdez, I. Suárez-Ruiz and B. Ruiz, *Bioresour. Technol.*, 2014, **151**, 199–206.

102 W. Jun, C. Mingqiang, L. Shaomin, C. Minggong, F. Min, S. Qianqian, and Wang Guangce, in *2011 International Conference on Materials for Renewable Energy & Environment*, IEEE, 2011, vol. 1, pp. 772–776.

103 V. L. Budarin, Y. Zhao, M. J. Gronnow, P. S. Shuttleworth, S. W. Breeden, D. J. Macquarrie and J. H. Clark, *Green Chem.*, 2011, **13**, 2330–2333.

104 N. Xiao, H. Luo, W. Wei, Z. Tang, B. Hu, L. Kong and Y. Sun, *J. Anal. Appl. Pyrolysis*, 2015, **112**, 173–179.

105 H. Kawamoto, T. Watanabe and S. Saka, *J. Anal. Appl. Pyrolysis*, 2015, **113**, 630–637.

106 M. Patrón-Prado, B. Acosta-Vargas, E. Serviere-Zaragoza and L. C. Méndez-Rodríguez, *Water, Air, Soil Pollut.*, 2009, **210**, 197–202.

107 D. M. Vieira, A. C. A. da Costa, C. A. Henriques, V. L. Cardoso and F. Pessoa de Franca, *Electron. J. Biotechnol.*, 2007, **10**, 368–375.

108 A. Cole, Y. Dinburg, B. S. Haynes, Y. He, M. Herskowitz, C. Jazrawi, M. Landau, X. Liang, M. Magnusson, T. Maschmeyer, A. F. Masters, N. Meiri, N. Neveux, R. de Nys, N. Paul, M. Rabaev, R. Vidruk-Nehemya and A. K. L. Yuen, *Energy Environ. Sci.*, 2016, **9**, 1828–1840.

109 F. Ronsse, D. Dalluge, W. Prins and R. C. Brown, *J. Anal. Appl. Pyrolysis*, 2012, **95**, 247–256.

110 H. Grasdalen, *Carbohydr. Res.*, 1983, **118**, 255–260.

111 H. Grasdalen, B. Larsen and O. Smidsrød, *Carbohydr. Res.*, 1979, **68**, 23–31.

112 B. Larsen, D. M. S. A. Salem, M. A. E. Sallam, M. M. Mishrikey and A. I. Beltagy, *Carbohydr. Res.*, 2003, **338**, 2325–2336.

113 C. S. Lobban, D. J. Chapman and B. P. Kremer, *Experimental Phycology: A Laboratory Manual*, Cambridge University Press, Cambridge, 1988.

114 A. Sluiter, B. Hames, R. O. Ruiz, C. Scarlata, J. Sluiter and D. Templeton, *Biomass Anal. Technol. Team Lab. Anal. Proced.*, 2004, **2011**, 1–14.

115 M. DuBois, K. A. Gilles, J. K. Hamilton, P. A. Rebers and F. Smith, *Anal. Chem.*, 1956, **28**, 350–356.

116 B. M. van den Hoogen, P. R. van Weeren, M. Lopes-Cardozo, L. M. van Golde, A. Barneveld and C. H. van de Lest, *Anal. Biochem.*, 1998, **257**, 107–111.

117 A. Haug, B. Larsen, O. Fykse, A. Block-Bolten, J. M. Toguri and H. Flood, *Acta Chem. Scand.*, 1962, **16**, 1908–1918.

118 T. Jin, H. Wang, J. Wang and H. Mou, *J. Appl. Phycol.*, 2015, **27**, 1327–1336.

119 D. J. Lane, P. J. van Eyk, P. J. Ashman, C. W. Kwong, R. de Nys, D. A. Roberts, A. J. Cole and D. M. Lewis, *Energy & Fuels*, 2015, **29**, 2542–2554.

Chapter 6

Chapter 6

Summary, appraisal, and outlook

6.1 Chapter overview and summary

This chapter will draw the preceding work together, highlighting key findings and areas of overlap between (see Section 6.2). Having summarised the experimental findings of the thesis, Section 6.3 will provide a synoptic appraisal of the generalised conclusions that may be drawn, as well as the degree to which the adopted experimental strategy has been successful. Finally, a perspective on the priority areas for future research is provided in Section 6.4.

The following general conclusions are reached:

- Metal ions influence the pyrolysis behaviour of alginates by coordinating to their carboxylate moieties and subsequently inhibiting or promoting decarboxylation.

- Evidence for stereospecific interactions of metal ions with hydroxyl groups within alginates were found, but not shown to be of significance to subsequent pyrolysis behaviour.

- The findings of the alginate pyrolysis studies are directly transferable to those involving kelp, with pre-treatment in Cu^{2+} giving similar favourable results (such as decreasing the pyrolysis onset temperature and increasing the selective formation of useful products) in the uronide model compounds as in the biomass.

6.2 Thesis summary and key findings

6.2.1 Summary of the contents of each chapter

This thesis aimed to employ a model compound approach to study and optimise the metal-mediated thermolysis of kelps. The coordination- and thermo-chemistry of alginate (the principal constituent of kelp) and its constituent monosaccharides (D-mannuronic and L-guluronic acids) were studied alongside related uronides (pectin, D-glucuronic acid, and D-galacturonic acid), depicted in Figure 6.1. Prior to summarising the results from the above investigations, a brief precis of each chapter and its contents is presented:

- **Chapter 1** introduces the thermochemical upgrading of macroalgae, highlighting challenges for current research. The strategy of using metal complexes of mono- and poly-uronides as model compounds is laid out.
- **Chapter 2** details the isolation and characterisation (by NMR spectroscopy) of monosaccharides that comprise alginate. The chapter explores the effect of heat, and pH on the saccharides, particularly their ability to form uronolactones.
- **Chapter 3** explores the metal-binding properties of the mono-uronate salts prepared in Chapter 2, with a view to probing the widely known "Egg-Box" model of cation-alginate binding.
- **Chapter 4** investigates the impact of the bound counter-cation on the thermochemical behaviour of a range of algal (and non-algal) mono- and poly-uronides.
- **Chapter 5** studies the impact of the metal ions probed in Chapters 2 and 4 on the subsequent thermochemical behaviour of alginate-rich kelp biomass. Cu^{2+} ions were utilised to attempt to enhance the thermal degradation of kelps.

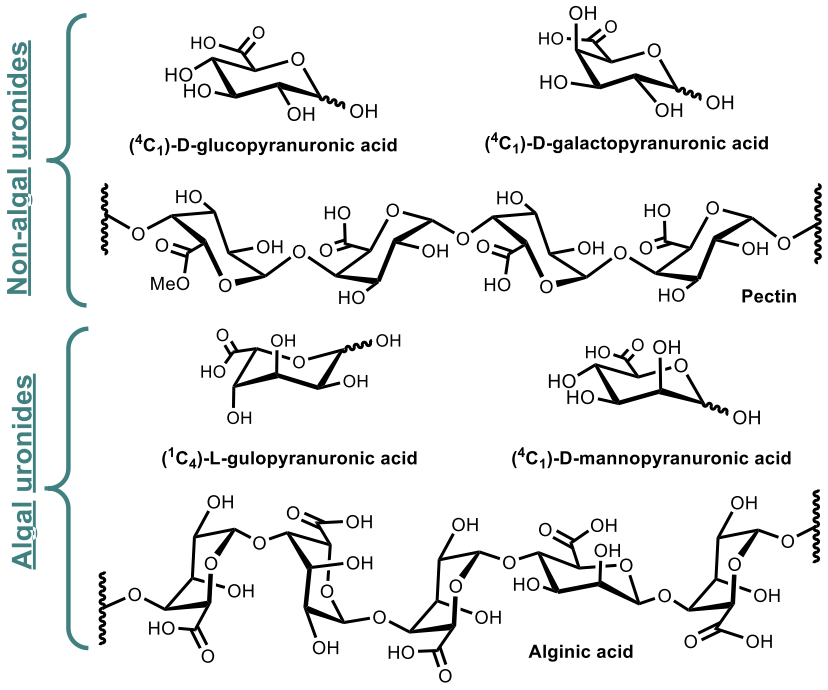

Figure 6.1 A summary of the uronides studied in this thesis.

6.2.2 Summary of key findings

6.2.2.1 The isolation and solution-state characterisation of algal mono-uronates

- ***Key finding*: The various anomers of algal mono-uronates have varying stabilities, and possess different values of pK_a**

In Chapter 2, a strategy for the isolation of solutions of D-mannuronate and L-guluronate was developed based on the hydrolysis of alginate. Whilst low yielding, the technique enabled the preparation of purified solutions of algal mono-uronates, which in turn enabled the clearest and most comprehensive NMR spectroscopic analysis of the compounds to-date. Previous ambiguities from the literature were clarified, and the instability of the structure of $^1C_4$-α-L-gulopyranuronate was demonstrated by reference to its relatively low abundance in solution. Studies under different pH conditions showed very little perturbation of the various configurational equilibria, but did reveal slight differences in pK_a of the different saccharide anomers, something suggestive of slight differences in electron distribution around the various sugar rings (see Figure 6.2).

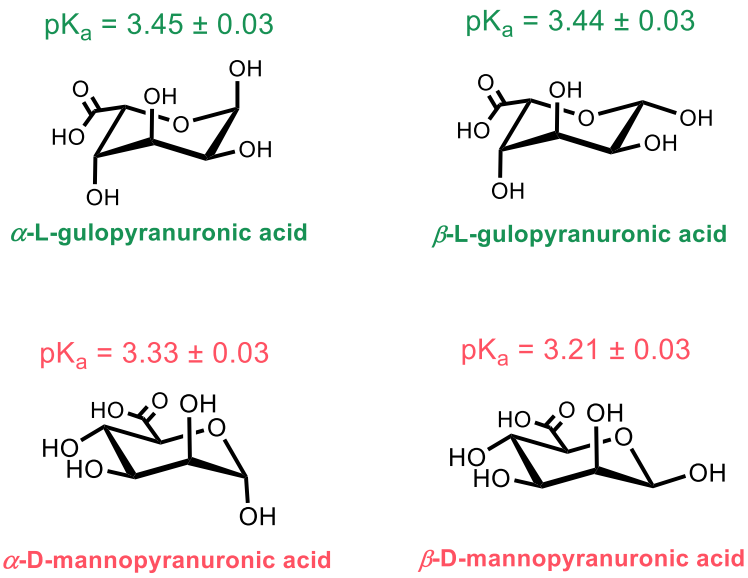

Figure 6.2 The pK_a values determined experimentally for algal mono-uronic acids.

6.2.2.2 The thermal and hydrothermal lactonisation of mono- and poly-uronides

- **Key finding: The stereochemistry, degree of polymerisation, and nature of the bound counter-cation are all important for dictating whether a uronolactone will form under hydrothermolysis/pyrolysis conditions (summarised in Figure 6.4).**

It was predicted that bicyclic furanurono-6,3-lactones (see Figure 6.3) would form from the pyrolysis of uronides, in an analogous manner to levoglucosan arising from the pyrolysis of glucans. Two sets of investigations were undertaken: one (in Chapter 2) under

hydrothermal conditions with NMR spectroscopic characterisation (on mono-uronic acids **HGul**, **HMan**, **HGlc**, and **HGal**) and the other (in Chapter 4) utilising Py-GCMS (on mono-uronic acids **HGlc** and **HGal**, and polyuronides **HAlg** and **HPec**). The NMR-based spectroscopic studies revealed that, upon heating, **HMan** was reversibly converted to the corresponding uronolactone to roughly the same extent as **HGlc**. **HGul** formed uronolactones to a lesser degree than **HMan**/**HGlc**, and **HGal** was stereochemically forbidden from forming any uronolactones. Accordingly, during pyrolysis, **HGlc** formed uronolactones extensively, whilst **HGal** did not (with **HMan** and **HGul** being unavailable for testing). Though Py-GCMS could not provide a quantitative analysis of the formation of uronolactones, **HAlg** clearly gave rise to only trace levels, whilst **HPec** gave none. In all cases, no uronolactones were detected when uronides were heated as their Na^+ salts. The various factors contributing to whether a selected uronide will form a uronolactone under thermolysis conditions are summarised in Figure 6.4

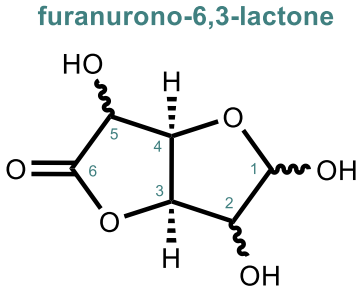

Figure 6.3 The structure of the bicyclic lactones formed from uronic acids upon heating.

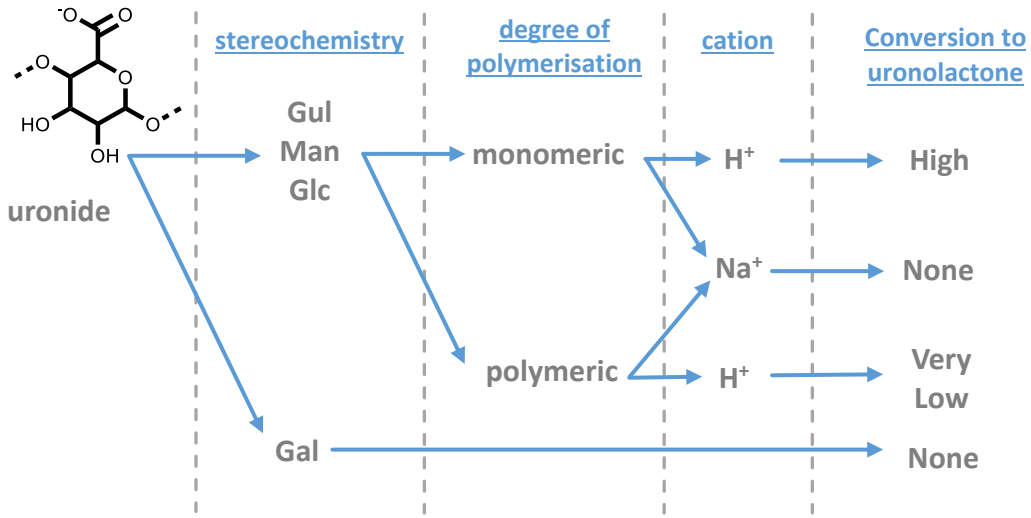

Figure 6.4 Schematic review of the factors influencing the formation of uronolactones by the pyrolysis of uronides.

6.2.2.3 The interaction of s- and d-block metals with algal mono-uronates

- **<u>Key finding:</u> Mono-uronates coordinate to metal ions through their carboxylate moiety (and possibly ring oxygen). *α*-L-gulopyranuronate also binds to larger divalent cations through an *axial-equatorial-axial* array of hydroxyl groups.**

The work conducted in Chapter 3 probed differences in the metal-binding properties of algal (and non-algal) mono-uronate salts, to provide fundamental insight into the coordination of metals by alginate, and hence within kelp. The samples of **NaGul** and **NaMan** prepared and characterised in Chapter 2, were exposed to a variety of mono- and di-valent s- and d-block metal ions. Evidence of metal-uronate binding was provided from changes in the anomeric equilibria observed upon introduction of the metal ion; the corresponding variation in ^{1}H and ^{13}C NMR chemical shifts gave an indication as to the mode of coordination. Here it was shown that the *α*-anomer of L-gulopyranuronic acid has a particular affinity for large divalent cations (Ca^{2+}, Sr^{2+}, and Ba^{2+}), something attributed to access to an *ax-eq-ax* arrangement of hydroxyl groups (see Figure 6.5) found only within that anomer (of the four uronates investigated). However, the studies also showed that smaller cations (Mg^{2+}, Zn^{2+}, and Cu^{2+}) show little affinity for the same *ax-eq-ax* arrangement of *α*-L-gulopyranuronate, with coordination likely occurring solely through the carboxylate (see Figure 6.5).

Investigations utilising mono-uronates are, of course, not necessarily translatable to the binding of polyuronides, and hence the results neither confirm nor refute the so-called "classical Egg-Box model" (a widely-cited view of metal-alginate binding that has been challenged in recent years). However, whilst the ability of Ca^{2+} to occupy "Egg-Box" binding sites along the alginate polymer still remains to be demonstrated, the results of the mono-uronate studies indicate that Cu^{2+} cannot occupy such sites (see Figure 6.5).

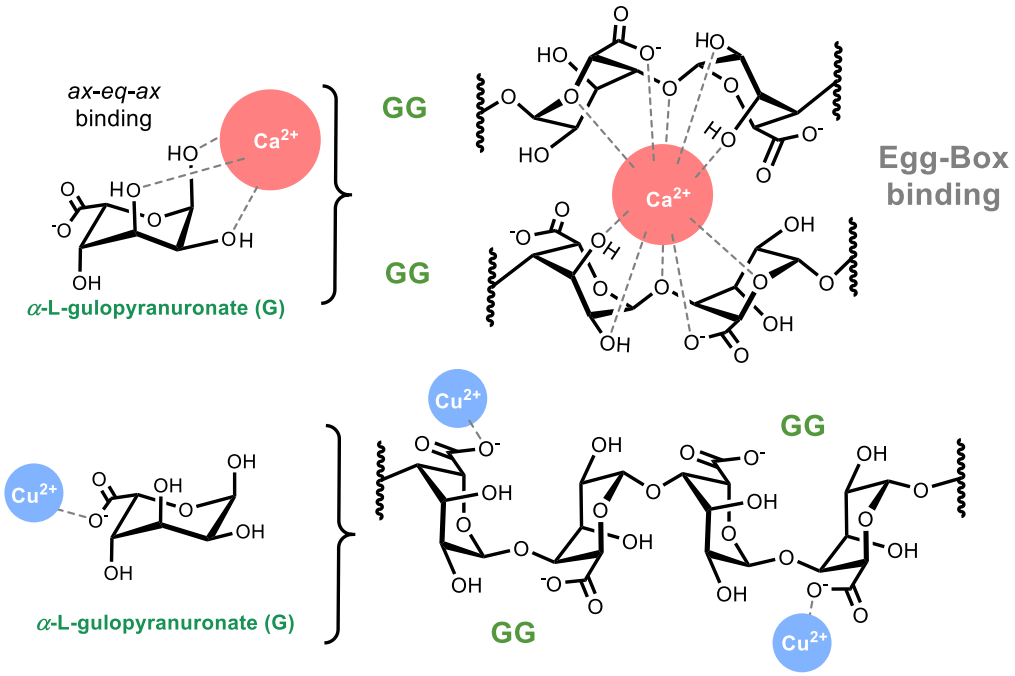

Figure 6.5 The binding of Ca^{2+} (top) and Cu^{2+} (bottom) to mono-*α*-L-gulopyranuronate, and predicted models for their coordination to alginate.

6.2.2.4 The impact of s-block and d-block metal ions on the pyrolysis of alginates

- **<u>Key finding:</u> Cu^{2+} promotes low temperature alginate decomposition and formation of 2-furfural through a metal-mediated decarboxylation. Other metal ions tend to inhibit such effects.**

The impact of a variety of s- and d-block metals on the pyrolysis of alginates was studied in Chapter 4, using a range of thermoanalytical techniques. A summary of the results, where the impact of the metal ion is quoted relative to the parent **HAlg,** can be found in Table 6.1. From Table 6.1, and other data in Chapter 4, the following series can be deduced for the thermal stability conferred to the alginate polymer by the cation:

(least stable) ⟶ *(most stable)*

$$Cu^{2+} < H^{+} << Zn^{2+} < Co^{2+} < Mg^{2+} < Ni^{2+} < Na^{+} < Ca^{2+} \approx Sr^{2+} \approx Ba^{2+}$$

Table 6.1 A summary of the effect of various metal ions on the pyrolysis behaviour of alginate at 500 °C relative to alginic acid, summarised from the results of Chapter 4.

Metal ion	Selectivity to small oxygenates	Selectivity to 2-FF	Pyrolysis onset temp	CO_2 Yield	CO Yield	H_2O Yield	Char Yield
Cu^{2+}	Decrease	Increase	Decrease	Increase	Increase	Increase	Decrease
Na^{+}	Very large increase	Very large decrease	Large increase	Increase	Increase	Increase	Large increase
Mg^{2+}	Large increase	Decrease	Large increase	N.D.	N.D.	N.D.	No change
Ca^{2+}	Very large increase	Large decrease	Very large increase	Increase	Decrease	Increase	Very large increase
Co^{2+} Ni^{2+} Zn^{2+}	Increase	Small decrease	Large increase	N.D.	N.D.	N.D.	Decrease

N.D. = not determined

The alginate stability trend discerned here has strong similarities with those derived in the literature for other metal carboxylates. Hence, it was proposed that the relatively high reduction potential of Cu^{2+} ions induces a metal-mediated decarboxylation (so-called *Hofer-Moest* decarboxylation). Such a mechanistic model was used to rationalise the selectivity of the pyrolysis reaction to various products, including the desirable compound 2-FF. Hence, low temperature decarboxylation (mediated by Cu^{2+} for example) promotes formation of 2-FF, whilst inhibited decarboxylation (mediated by Ca^{2+} for example) allows for alternative thermolytic pathways to be activated, giving rise to a different array of products (see Figure 6.6). Additional evidence from analysis of the pyrolysis chars at different temperatures gave evidence in support of the *Hofer-Moest* mechanism, particularly the formation of crystalline Cu^{0}.

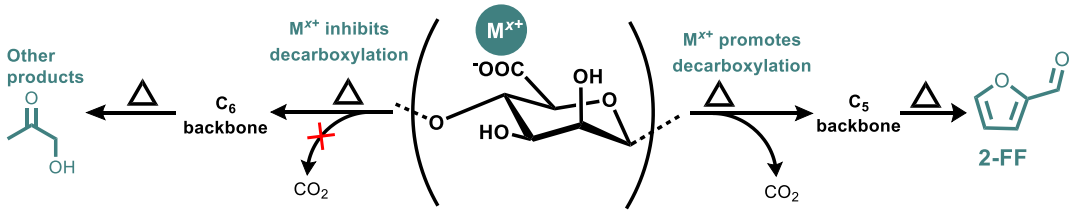

Figure 6.6 A summary of the different impact of metals ions (M^{x+}) on the subsequent pyrolysis products of alginate, based on whether the cation inhibits or promotes decarboxylation.

6.2.2.5 The impact of metal ions on the pyrolysis of uronides generally

- **<u>Key finding:</u> The effect of changing the stereochemistry of the particular uronide being pyrolysed has a less drastic impact on the subsequence thermal degradation behaviour than changing the bound metal ion.**

The applicability of the conclusions reported in Section 6.2.2.4 were tested by subjecting a range of other uronides (alginates with varying **M**:**G** ratio, pectinate salts, mono-D-glucuronate and -D-galacturonates) to similar pyrolysis experiments. It was found that the suite of liberated pyrolysis products was dictated, first and foremost, by the identity of the bound metal cation. Whilst there were slight differences between the thermochemical behaviour of, for example, **Cu(II)Alg** *versus* **Cu(II)Pec**, or **Cu(II)Gal** *versus* **Cu(II)Glc**, such variations were much more subtle than the effect brought about by changing the metal ion bound to each of the uronides. A particularly interesting demonstration of this effect was reported in Chapter 5, where a qualitative analysis of seven alginates extracted from a variety of different kelps (with **M**:**G** ratios ranging from 0.53 – 1.86) revealed no significant changes in their thermochemical behaviour when they were all bound to the same metal ion (Cu^{2+}, Ca^{2+}, or Na^{+}). Hence, in all of the uronides tested (regardless of their stereochemistry), the Cu^{2+} salt was found to yield more 2-FF than the free acid, whilst the Na^{+} and Ca^{2+} salts gave significantly less.

6.2.2.6 The impact of metal ions on the pyrolysis of alginate-rich kelp biomass

- **<u>Key finding:</u> Cu^{2+} and Ca^{2+} have a similar effect on the pyrolysis behaviour of whole alginate-rich kelp as they have when coordinated to a uronide.**

Samples of kelp were enriched in Ca^{2+} and Cu^{2+} and their subsequent thermochemical behaviour probed, revealing extensive differences between the two treatments. Cu(II)-bound biomass displayed a significantly reduced pyrolysis onset temperature and an increased yield of 2-FF, whereas the Ca^{2+}-enriched materials gave results similar to those of the untreated biomass (containing predominantly Na^{+} and K^{+}). Analysis of the char formed from the Cu(II)-treated kelp showed synchronous formation of Cu^{0} and loss of carboxylate functionalities during pyrolysis, an indication that the *Hofer-Moest* decarboxylation proposed for the uronide model compounds was also active within the complete biomass matrix. Surveying the results as a whole allowed for the conceptualisation of a phytoremediative kelp-based thermal biorefinery in which the high affinity of alginate-rich seaweed for Cu^{2+} is coupled to the beneficial influence of that metal ion during pyrolysis.

6.3 Conclusions from key findings

6.3.1 What is the relevance of the Egg-Box model of metal-uronide coordination to subsequent pyrolysis behaviour?

The Egg-Box model is the dominant theory of alginate-cation coordination, and posits that metal ions coordinate not only to the carboxylate moiety, but also to the *ax-eq-ax* (axial-equatorial-axial) arrangement of hydroxyl groups around the ring of the composite *α*-L-guluronate units. This thesis considers the role that differing coordination behaviour would have on subsequent pyrolysis reactions, and several key findings can be drawn together to draw a conclusion:

1) **The axial-equatorial-axial arrangement of hydroxyl groups in mono-*α*-L-guluronate interacts with large divalent cations (Ca^{2+}, Sr^{2+}, Ba^{2+}), but not mono-valent (Na^{+}, K^{+}) or smaller divalent cations (Mg^{2+}, Zn^{2+}, Cu^{2+}).**

2) **The carboxylate (and possibly ring oxygen) of mono-*α*-L-guluronate interacts with all of the cations listed in point (1).**

3) **Varying the number of Egg-Box sites in an alginate (by changing the M:G ratio) does not give rise to substantially different pyrolysis behaviour.**

4) **The pyrolysis characteristics of NaAlg and MgAlg are more similar to CaAlg than to Cu(II)Alg.**

5) **Cu(II)Alg promotes a metal-mediated decarboxylation of alginate, whereas the other metal ions inhibit such a mechanism**

<u>Conclusion:</u> The thermal degradation pathways followed by metal alginates are dictated by the ability of the bound metal ion to promote decarboxylation. The effect of the coordination of hydroxyl groups around the uronide ring did not give detectable differences to subsequent pyrolysis behaviour.

<u>Implications:</u> The results imply that the choice of metal ion is more important than the stereochemistry of the polyuronide in dictating final pyrolysis behaviour. Hence, when selecting uronide-rich biomass for thermochemical upgrading, controlling the metal profile of the feedstock is of more importance than optimising the composition of the polyuronides within it.

6.3.2 What can be learned about the thermolysis of kelp from fundamental studies of mono- and poly-uronides?

A secondary aim of this thesis was to establish the validity of using uronides as model compounds to gain fundamental insight into the thermolysis of kelp, in an analogous fashion to the use of glucans in the thermolysis of terrestrial, cellulosic biomass feedstocks. The key findings of previous sections can be drawn together to provide a conclusion on this topic:

- **Studying uronides in their isolated state avoids the confounding influences brought about by the pyrolysis of other components within the biomass**

- **Uronides generally possess several undesirable thermochemical characteristics (high yield of char, H_2O, and CO_2, low yield of liquid hydrocarbons, *etc.*).**

- **Cu^{2+} significantly improves the pyrolysis behaviour of alginates, decreasing the onset temperature, char yield, and promoting the low temperature release of 2-FF**

- **Similar improvements to those observed in alginate thermolysis following coordination to Cu^{2+} were also seen in kelp after the same treatment.**

- **The observed influences of Cu^{2+} on kelp could be rationalised through the fundamental mechanistic insight gained from the model compound studies.**

- **Other uronides (such as pectin) show similar results to alginate, with regards to the effect of Na^{+}, Ca^{2+}, and Cu^{2+}**

<u>Conclusion</u>: The model compound study was largely successful. Rather than screening hundreds of samples of biomass, the underlying chemistry could be elucidated to formulate general rules. Such a strategy enables a more rational approach to the optimisation of the thermal processing of biomass.

<u>Implications</u>: The results imply that biomass rich in alginate (or uronides generally) should be suitable for use as feedstocks in a coupled phytoremediative/thermochemical biorefinery. However, caution should be exercised as the results of the model compound studies may become increasingly removed from reality when the process is scaled-up.

6.4 Outlook and priorities for future research

6.4.1.1 Improving the availability of model-compounds

One of the key aims of this thesis was to gain a fundamental insight into the pyrolysis of uronides, to ease the analytical complexities of studying the equivalent behaviour in whole kelp. However, the research was hampered, to some degree, by the lack of availability of purified solid samples of algal mono-uronic acids (**HMan** and **HGul**), and their oligomeric counterparts. Whilst the compounds did become available through chemical vendors during the preparation of this thesis, their price remained prohibitively high. Some success was

achieved in Chapter 2 in preparing the two algal mono-saccharides, though a failure to crystallise them prevented analysis outside of the solution state. As such, a highly desirable experiment, namely the Py-GCMS analysis of HMan and HGul could not be carried out as had been planned, and readily available HGal and HGlc were used as alternatives. If, in the future, the role of the glycosidic bond is to be well understood in uronide thermolysis (as has been achieved in cellulose research), it is imperative that algal mono- and oligo-uronic acids become more widely accessible to researchers (see Figure 6.7).

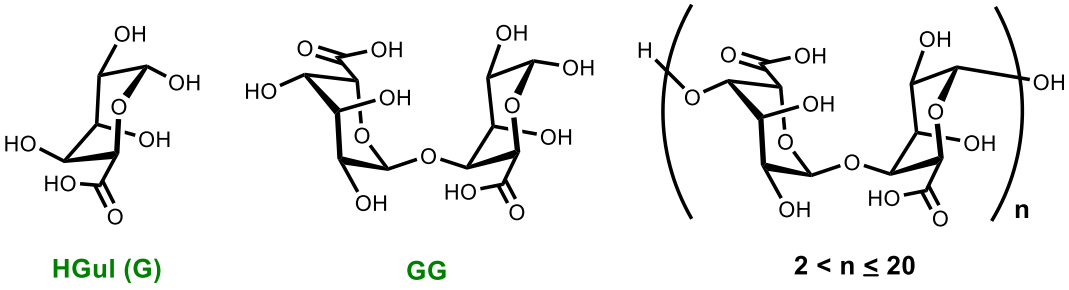

Figure 6.7 Mono-, di-, and oligo-uronic acids of particular interest for future research

In addition to understanding pyrolysis behaviour, access to algal oligo-uronides would be of value to studies probing the metal coordination of alginates. As was demonstrated in Chapter 3, studying mono-uronates by NMR spectroscopy provided fresh insight into previously held views of uronide-metal binding, and challenged the results of recent computational studies. Investigating oligo-uronates (and especially the L-guluronate – L-guluronate dimer, **GG**, shown in Figure 6.7 and its coordination to Ca^{2+}) by similar NMR spectroscopic methods (as well as additional ^{43}Ca NMR spectroscopy studies) would be especially enlightening for further examining the validity of the widely applied "Egg-Box" model. Such knowledge could have implications for applications far beyond pyrolysis, such as in the fields of food technology or drug delivery. It is hoped that recent, rapid advancements in automated oligo-saccharide synthesis may bring the desired uronides to a point where they can be affordably obtained, in reasonable quantities, by researchers without a specialism in preparative carbohydrate chemistry.

6.4.1.2 Furthering fundamental understanding of the thermolysis of mono-, oligo-, and poly-uronic acids and their metal salts

Following the work in this thesis, there are several outstanding issues that could be addressed without much further methodological development. For example, there were reservations in Chapter 4 about the large errors associated with the pyrolysis mass balance of **HAlg**, **NaAlg**, **CaAlg**, and **Cu(II)Alg**, though simple measures were described that could improve the situation. Hence, quantitation of many other volatile organic compounds could be achieved by applying the same methods as those utilised for 2-FF. The yield of H_2O, CH_4 and H_2 should all be obtainable by further work conducted with the pyrolysis-fixed gas analyser equipment. A fuller, quantitative impression of uronide thermochemistry should also facilitate computational studies of the type that are now commonplace in cellulose research, but absent for alginates. Computational studies will, in turn, help to validate the thermolytic mechanisms hypothesised in the second half of Chapter 4.

In addition to the mass balance, it is clearly desirable to gain a fuller understanding of the nature and formation of polyuronide chars. The char represents the sink for most of the carbon atoms in the pyrolysis of polyuronides and minimising its formation will be a key challenge for future researchers. Unfortunately, the underlying reason that char formation is so much more prolific in the pyrolysis of polyuronides compared to neutral polysaccharides (such as cellulose) is not currently clear. Furthermore, questions remain about the interaction of metal ions with the char:

- why does Na^+ cause such dramatic swelling of the char?
- How do d-block metals decrease the yield of char?
- What is the oxidation state of copper and nickel in the char prior to their deposition as Cu^0 and Ni^0?

It is hoped that these questions, and others, may be answered by the application of techniques such as X-ray photoelectron spectroscopy (XPS) and solid-state NMR (SSNMR), in addition to a more detailed set of FTIR studies to those already undertaken in this thesis.

Finally, several fundamental questions remain regarding the role of water in the thermolysis of uronides. The first questions surround nominally anhydrous pyrolysis experiments, where adventitious water may play a critical role in facilitating ion mobility, or hydrolysing glycosidic bonds. Even in very dry samples, water was detected as a significant pyrolysis product, giving rise to the possibility that the compound may mediate subsequent degradative steps of the uronide. However, by deliberately adding water to the reaction to achieve either gasification or hydrothermal liquefaction conditions, it is possible that the thermolysis of uronides may be optimised further. Particularly, decarboxylation should be more readily achievable in an aqueous environment (where proton mobility is more facile) and Appendix C describes preliminary measures to develop such experiments further.

6.4.1.3 Scaling up the pyrolysis of kelp

Though micropyrolysis experiments (of the type employed in this thesis) can give impressive insights into thermochemical reactions, they do have significant shortcomings. In this regard, the tiny quantities of sample that must be utilised (due to the limitations of the commercial instrument) give rise to gross errors in any subsequent attempts to calculate a mass balance. To minimise such errors, and also probe more deeply the impacts of heat and mass transfer on the yield of target compounds (such as 2-FF) arising from kelp, it is recommended that gram-scale experiments be conducted in future. Such experiments would deliver appreciable yields of products that could be handled and analysed for both composition and physical characteristics. Equipped with the data from the larger scale experiments, researchers will be in a much better placed position to assess the viability of the industrialisation of the pyrolysis of kelp. Hence, it is concluded that a combined approach of fundamental micropyrolysis and model-compound studies, coupled with incremental scaling-up, will give the best route to potentially realising a phytoremediative kelp-based biorefinery, of the type proposed in this thesis.

6.5 Final comments

Optimising the thermal processing of carbohydrate-rich biomass ultimately requires an intimate knowledge of the chemistry of the constituent saccharides. In the case of macroalgae and alginates, this means an understanding of the coordination behaviour of the many different candidates of metallic counter-cation. Carbohydrate coordination chemistry and carbohydrate thermochemistry are, individually, very specialised areas of research, and knitting together these fields was a particular challenge encountered in this thesis. The difficulties are exacerbated by the fact that the carbohydrates in question are, in themselves, fairly niche, with the composite monosaccharides being both scarcely researched and difficult to obtain. Furthermore, investigations into algal-uronides (both their coordination chemistry and thermochemistry) have, in the past, tended to be quite sporadic, with a lack of the kind of systematic appraisal that will ultimately be required to address many of the complex research problems described in the preceding chapters. As such, perhaps one of the most significant achievements of this thesis is the bringing together of the previously disparate literature from studies relating to the above topics (spanning over a century of research) in a manner where it can be surveyed holistically. Whilst, in many ways, this thesis has provided only glimpses of insight into the pyrolysis of metal-bound uronides (and, hence, kelps), it is hoped that the accompanying literature reviews and methodological developments will provide a foundation for future researchers at Durham, and elsewhere, to advance this highly complex and interdisciplinary field.

Appendices

Appendices A – O

Additional results and methodology

Appendix A - Determining the concentration of uronic acids in aqueous and deuterated-aqueous solutions

Appendix B - Attempts to grow crystals of mono-uronate salts

Appendix C - A note on the hydrothermolysis of uronides

Appendix D - NMR spectrometers: typical experimental parameters

Appendix E - Metal-uronate NMR spectroscopic experiments: additional theory, tabulated supplementary data, and error analysis

Appendix F - Characteristic peaks used to confirm the identification of crystalline materials via Powder X-ray diffraction (PXRD) analysis

Appendix G - Raw data from the FTIR analysis of alginates and related uronides

Appendix H - Results from the elemental analysis of alginates and related uronides

Appendix I - Results from the elemental analysis of kelps, and related biomass

Appendix J - Analysis of the **M**:**G** ratio of extracted alginates by ^{1}H NMR spectroscopy

Appendix K - A note on the preparation and pyrolysis of Fe(III)Alg

Appendix L - Thermoanalytical methods utilised in the study of uronides and uronide-rich biomass

Appendix M - Glossary of compounds detected in the Py-GCMS analysis of uronides and uronide-rich biomass

Appendix N - Detection and identification of compounds in Py-GCMS

Appendix O - Additional Py-GCMS data for uronides and uronide-rich biomass

Appendix A - Determining the concentration of uronic acids in aqueous and deuterated-aqueous solutions

A.1 Introduction

To facilitate the experiments detailed in Chapter 2 and 3, methods were required to accurately determine the concentration of D-galacturonate (**Gal**), D-glucuronate (**Glc**), D-mannuronate (**Man**), and L-guluronate (**Gul**) in aqueous and deuterated-aqueous solutions. This Appendix details the development and implementation of two methods, which could, where necessary, be cross-checked against each other:

I. **UV spectrophotometric method:** based on the change in absorption at 485nm of a solution containing uronic acid(s) following reaction with phenol and hot, concentrated sulphuric acid
II. **^{1}H NMR spectrometric method:** based the change in integral ratio between a reference signal and peaks arising from a uronic acid in the 400 MHz ^{1}H NMR spectrum

A.2 Determination of uronic acid concentration by the UV phenol-sulphuric acid method of Dubois *et al.*[1]

A.2.1 Background to the UV phenol-sulphuric acid method of quantifying uronic acids

Whilst a number of colourometric assays exist within carbohydrate chemistry to determine the concentration of aqueous solutions of saccharides,[2] by far the simplest and most widely utilised is the so-called "phenol-sulphuric acid method" developed in the 1950's by Dubois *et al*.[1] The principle behind many colourometric carbohydrate assays, including the method of Dubois *et al.*, is based on the rapid dehydration and degradation of saccharides in the presence of hot, strong acid to yield furan derivatives (such as furfural and hydroxymethylfurfural) that subsequently undergo condensation reactions in the presence of phenolic or other aromatic compounds (including phenol, resorcinol, anthrone, and carbazole) to generate a chromophore (see Figure A.1).

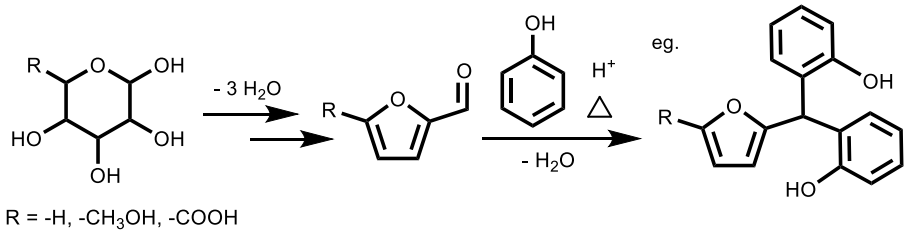

Figure A.1 Dehydration, degradation, and phenolic condensation of hexoses and pentoses to yield chromophores for quantition *via* UV spectrophotometric analysis

By comparison of the absorbance of the analyte solution at a particular wavelength (480 – 490 nm in the case of the phenol-sulphuric acid assay) with a calibration curve established from samples of known concentrations, the relative amount of the saccharide under investigation can be determined. Unfortunately, uronic acids do not undergo acid-catalysed degradation in a uniform manner with respect to each other and, as such, do not respond to the phenol-sulphuric acid assay in the same way.[1,3,4] Indeed, in theory, to account for the discrepancies in reactivity, an individual calibration curve should be drawn up for each uronic acid under investigation. Whilst establishing calibrations for standards of **Glc** and **Gal** is straight forward (see Figure A.2) as the two sugars are commercially available, the absence of well-defined solid samples of the algal-uronates, **Man** and **Gul**, means that a similar plot cannot easily be constructed for these latter species. Fortunately, early alginate pioneers Haug and Larsen conducted a detailed study to quantitatively determine the different sensitivities of each uronic acid to a variety of common assays (referred to here as the *Relative Response Factor*, $RRF_{x/y}$, of the two uronates (x/y) being compared).[4,†] The $RRF_{x/y}$ values for **Gal**, **Glc**, **Man**, and **Gul** in the phenol-sulphuric acid assay as determined from Haug and Larsen's measurements are reported in Table A.1.

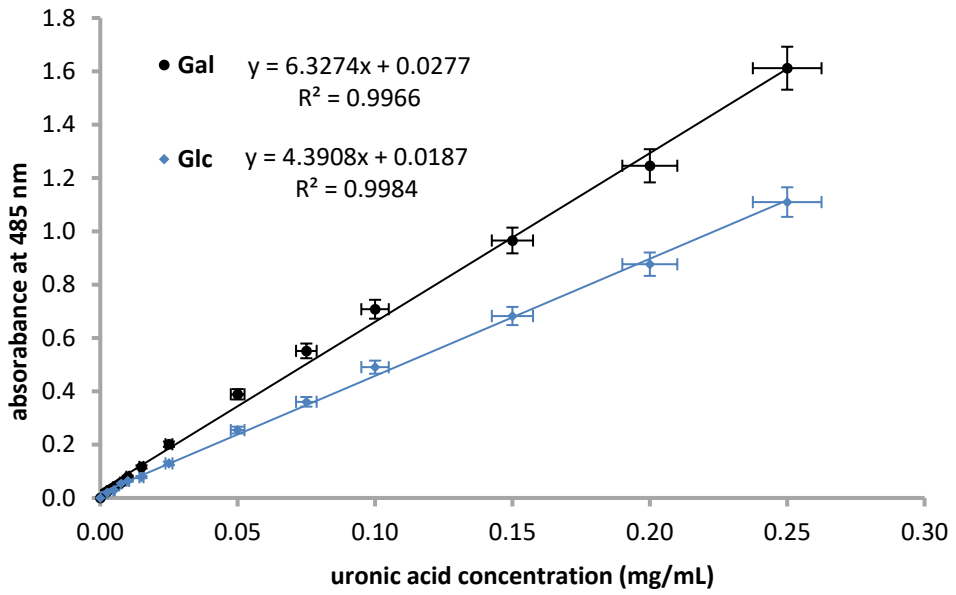

Figure A.2 Absorbance (at 485 nm) of solutions of galacturonate (**Gal**) and glucuronate (**Glc**) of differing concentrations following reaction with phenol-sulphuric acid. Error bars shown at ± 5 %. (Plotted from data obtained in this thesis).

The reproducibility of Haug and Larsen's work can be demonstrated by comparing their values for $RFF_{Gal/Glc}$ and $RFF_{Glc/Gal}$ (1.42 and 0.70 respectively) with those determined from Figure A.2 (1.44 and 0.69 respectively) from measurements made in this thesis. The good agreement between the two sets of measurements validates the use of $RFF_{Gal/Y}$ and

[†] Though Haug and Larsen did not explicitly state the $RRF_{x/y}$ values for uronates in the phenol-sulphuric acid method, the values may be derived indirectly from the gradients of the lines plotted in their work.

$RFF_{Glc/Y}$ to establish the concentration of **Gul** and **Man** *via* the phenol-sulphuric acid from calibrations plots made using **Gal** and **Glc** (such as that depicted in Figure A.2). Hence, even in the absence of suitable solid standards of **Man** and **Gul**, the phenol-sulphuric acid method is still a viable method of quantification of these two sugars.

Table A.1 The Relative response factors ($RRF_{x/y}$) of different uronates in the phenol-sulphuric acid method, as measured by Haug and Larsen[4]

Uronates being compared (x/y)			Relative response factor ($RRF_{x/y}$) in phenol-sulphuric acid assay
x	**/**	**y**	
Gal	**/**	**Glc**	**1.42**
Gal	**/**	**Man**	**1.82**
Gal	**/**	**Gul**	**1.07**
Glc	**/**	**Gal**	**0.70**
Glc	**/**	**Man**	**1.27**
Glc	**/**	**Gul**	**0.75**

With the accuracy of the assay typically found to be in the region of ± 5 – 10 %, the phenol-sulphuric acid method was deemed to be a good first approximation for determining the concentration of unknown samples of aqueous **Gal**, **Glc**, **Man** and **Gul**. However, owing to the laborious nature of the method and the high risk of random experimental error, coupled with the practical difficulties of handling large quantities of boiling, concentrated sulphuric acid, a secondary method of analysis was established for "fine-tuning" solutions to the correct concentration. This secondary method is the ^1H spectrometric technique detailed in Section A.3.

A.2.2 Materials and methods for UV phenol-sulphuric acid methodology[1]

The presence of lactones in aqueous samples of uronic acids may interfere with quantitative colourometric analysis, and it is important to first destroy them by neutralisation of the solution.[5,4] When a suitable uronic acid solution had been prepared, a 2.0 mL aliquot (or some dilution made up to 2.0 mL by deionised H_2O) was taken and aqueous phenol (0.5 mL, 0.3 M) was added in a glass test tube. H_2SO_4 (5.0 mL, 18.4 M) was added quickly by the action of an Eppendorf® Variable Volume pipette (500 – 5000 μL), causing instantaneous boiling of the solution. Browning of the solution was indicative of the presence of uronic acids, which could be further quantified by UV-VIS spectrophotometry as follows: Upon cooling for exactly 60 minutes, the absorbance at 485 nm of 200 μL of the solution was measured by a 96-well Thermo Scientific Multiskan™ GO Microplate Spectrophotometer. Quantification was achieved by comparison with a calibration line derived from standard solutions of 0 – 200 μg D-glucuronic acid (Sigma) / mL deionised H_2O and 0 – 200 μg D-galacturonic acid (Sigma) / mL deionised H_2O, with the varying sensitivities of different uronic acids being corrected for according to the work of Haug and Larsen (see Section A.2.1).[4]

A.3 Determination of uronic acid concentration by ^{1}H NMR spectroscopy

A.3.1 Background to the ^{1}H NMR spectrometric quantification of uronic acids

Whilst the phenol-sulphuric acid assay provides a convenient method of establishing the concentration of a completely unknown aqueous (or deuterated-aqueous) solution of uronic acid, when "fine-tuning" of the concentration is required (for example, when diluting stock solutions to exactly 50.0 mg uronic acid/mL D_2O), a method based on quantitative ^{1}H NMR spectroscopy was employed. Here, well-defined signals in the 400 MHz ^{1}H NMR spectrum of a uronic acid were integrated against a standard signal from $C\underline{H}Cl_3$. To avoid contaminating the uronic acid sample with standard, a flame-sealed capillary tube was prepared containing $CDCl_3$ spiked with 5 vol.% $CHCl_3$, which was then inserted into the tube coaxially. A similar method was employed by Koch in the quantification of Al in tea leaves by ^{27}Al NMR spectroscopy.[6] Here Koch demonstrated that an accurate knowledge of the ^{27}Al content within the reference capillary (or ^{1}H content in these experiments) is not required, so long as the same solution is used each time.[6] Hence, by making up standard solutions of known concentrations of **Glc**, and by transferring the same reference capillary tube between the samples for the acquisition of each spectra, a calibration plot could be drawn up (see Figure A.3). The average response for a single uronide proton environment summed across all its anomeric forms (i.e. α-pyranose proton(average signal) + β-pyranose(average signal) + α-furanose(average signal) + β-furanose(average signal)) was measured relative to the signal of the standard reference solution. Quantitation was found to be unaffected by changes to the position of the anomeric equilibria as well as to the pD of the solution, with signals arising from neat **HGlc** solutions (pD 1.0) lying on the same calibration line as **NaGlc** signals in NaOD (pD 7.0).

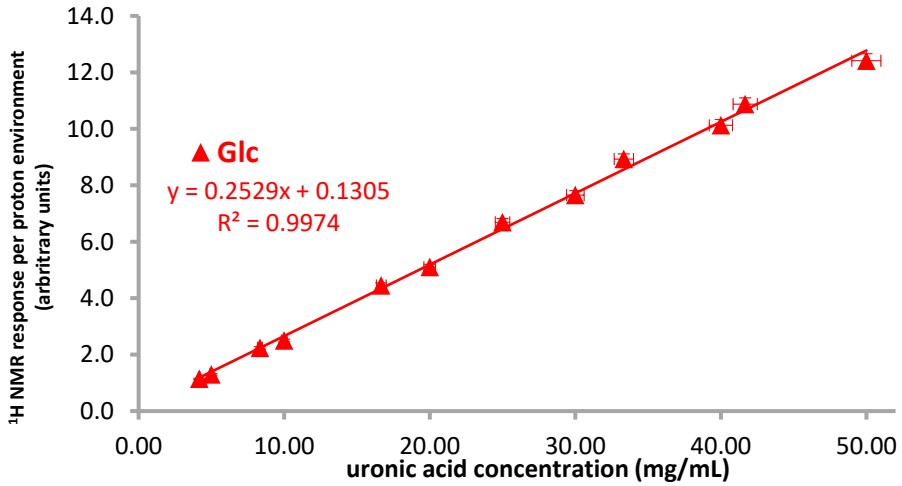

Figure A.3 ^{1}H NMR spectroscopic response (400 MHz, 298 K) per uronic acid proton environment in solutions of different concentration measured relative to a $C\underline{H}Cl_3$ reference peak. Error bars shown at ± 2 %. (Plotted from data obtained in this thesis).

The error in the determined uronic acid concentration as determined by this NMR spectroscopic method are much smaller than in the case of the phenol-sulphuric acid procedure detailed previously. The values of the integrals for each of the measured proton environments typically agreed to within ± 2 % of each other. A similar error was associated with the forumlation and subsequent dilution of the initial stock solution of **Glc**. Consequently, all points in the calibration were found to lie on the line of best fit after the addition of ± 2 % vertical and horizontal error bars.

A.3.2 Materials and methods for ^{1}H NMR spectrometric methodology

A stock solution containing Na-D-glucuronate in D_2O (Apollo Scientific) of concentration 50.0 mg/mL was made up by first dissolving D-glucuronic acid (Sigma) in D_2O, neutralising with NaOD (0.1 and 0.01 M) and then making up to the required volume. Serial dilutions of the stock solution were used to produce the necessary samples for construction of a calibration plot, with 600 μL of each being transferred to a Norell® XR-55-7 NMR tube (5.0 mm). Stock solutions of other concentrations were also made up in a similar manner in order to establish the repeatability of the method. A reference solution of 5 vol.% $CHCl_3$ in $CDCl_3$ (Apollo scientific) was transferred to a glass capillary (1.0 mm OD), which was subsequently flame sealed. The capillary containing the reference solution was inserted co-axially into the calibrant solution and the ^{1}H NMR spectrum recorded on a 400 MHz spectrometer using with the parameters listed in Appendix D. The reference capillary was recovered, cleaned with D_2O, added to the next calibrant solution, and the process repeated. The ^{1}H NMR resonances were referenced against the resultant $C\underline{H}Cl_3$ signal (δ = 7.260 ppm)[7] and assigned according to arguments in Chapter 2. Well-resolved peaks were integrated against the reference signal and normalised (as outlined in Section) to yield a calibration plot (see Figure A.3). The reference capillary was subsequently transferred to a solution with unknown uronic acid molarity, the ^{1}H NMR spectrum recorded under the same conditions as the calibration, and the integration procedure repeated in order to establish the concentration. The process was used for D_2O solutions of **Gal**, **Glc**, **Man**, and **Gul** with fresh D-glucuronic acid calibration plots being constructed as required. Values for the concentration of uronic acid solutions determined are subsequently quoted to within ± 5 %.

A.4 References

1 M. DuBois, K. A. Gilles, J. K. Hamilton, P. A. Rebers and F. Smith, *Anal. Chem.*, 1956, **28**, 350–356.

2 S. Cui and Y. Brummer, in *Food Carbohydrates*, CRC Press, 2005, pp. 68–104.

3 R. W. Scott, W. E. Moore, M. J. Effland and M. A. Millett, *Anal. Biochem.*, 1967, **21**, 68–80.

4 A. Haug, B. Larsen, O. Fykse, A. Block-Bolten, J. M. Toguri and H. Flood, *Acta Chem. Scand.*, 1962, **16**, 1908–1918.

5 J. D. Blake and G. N. Richards, *Carbohydr. Res.*, 1968, **8**, 275–281.

6 K. R. Koch, *Analyst*, 1990, **115**, 823-825.

7 H. E. Gottlieb, V. Kotlyar and A. Nudelman, *J. Org. Chem.*, 1997, **62**, 7512–7515.

Appendix B – Attempts to grow crystals of mono-uronate salts

B.1 Introduction

Crystalline metal mono-uronate salts could be extremely interesting pyrolysis model compounds, because the metal-saccharide interactions in such samples are well-defined. Whilst crystal structures have been published for metal-uronate salts, they are not as readily available as might be assumed.[1–5] Hence, preliminary work was undertaken in this thesis to grow crystals of mono-uronates (and particularly algal mono-uronates) bound to metal ions that may be of interest to pyrolysis research.

Obtaining suitable crystals to enable study of the metal mono−uronide systems in the solid state is a non–trivial exercise for a number of reasons:

1 The crystals form as very thin, long needles, necessitating slow growth to obtain sample large enough to diffract along all three axes.[2,3,5]

2 As reducing sugars, uronic acids are susceptible to Fehling's–type oxidation when in the presence of redox active metals such as Cu^{2+} and Fe^{3+}.[6]

3 Often adventitious sodium induce crystallisation of a sodium uronate salt in preference to the desired metal uronate.[3]

To combat such difficulties, efforts were focussed in the first instance on the crystallisation of cadmium(II) α−D−galacturonate ($CdGal_2$). Cadmium(II) is not susceptible to reduction by the aldehyde form of the saccharides, and has a sufficiently large atomic scattering factor to overcome the problem of the (potentially) thin dimensions of the crystal. Galacturonate is also known to bind strongly to divalent metal ions, and was the cheapest and most readily available mono-uronate for initial testing.

B.2 The crystal structure of $Cd_{0.6}Na_{1.4}H_{0.4}Gal_3.3H_2O$

Through the partial neutralisation of D−galacturonic acid with cadmium carbonate, crystalline cadmium sodium α−D−galacturonate trihydrate ($Cd_{0.6}Na_{1.4}H_{0.4}Gal_3.3H_2O$) was prepared (see Figure B.1) It can be seen from the formula unit that, despite efforts to exclude sodium ions from the crystallisation process, the compound still precipitates as a double salt owing to the decrease in solubility afforded by complexation of the Na^+ ion. Similar difficulties were recorded in the preparation of the calcium sodium and strontium sodium double salts, reported elsewhere.[2–4] The relevant crystal data for $Cd_{0.6}Na_{1.4}H_{0.4}Gal_3.3H_2O$ are given in Table B.1.

Table B.1 Relevant crystallographic data for $Cd_{0.6}Na_{1.4}H_{0.4}Gal_3.3H_2O$

Empirical formula	$C_{18}H_{39.4}Cd_{0.6}Na_{1.4}O_{27}$	ρ_{calc}mg/mm^3	1.745
Formula weight	787.52	m/mm^{-1}	0.542
Temperature/K	120.0	F(000)	815.0
Crystal system	hexagonal	Crystal size/mm^3	0.06 × 0.02 × 0.01
Space group	$P6_3$	2Θ range for data collection	3.39 to 54.828°
a/Å	13.449(5)	Reflections collected	14683
b/Å	13.449(5)	Independent reflections	2471[R(int) = 0.0449]
c/Å	9.566(3)	Data/restraints/parameters	2471/5/163
α/°	90	Goodness-of-fit on F^2	1.118
β/°	90	Final R indexes [I>=2σ (I)]	R_1 = 0.0340, wR_2 = 0.0880
γ/°	120	Final R indexes [all data]	R_1 = 0.0345, wR_2 = 0.0883
Volume/Å^3	1498.4(12)	Largest diff. peak/hole / e Å^{-3}	0.39/-0.28
Z	2	Flack parameter	0.01(2

$Cd_{0.6}Na_{1.4}H_{0.4}Gal_3.3H_2O$ represents the first molecular structure of a d−block metal interacting with a uronate moiety. However, no significant differences are seen between this structure and that of previously prepared alkali/alkali earth metal galacturonate salts.[2,3] The cadmium structure crystallises in the $P6_3$ space group and is an isomorphous replacement of the equivalent strontium/calcium sodium double salts (with only slight differences in the unit cell parameters owing to the difference in ionic radii of the metal centres). Hence, a full discussion of the geometrical features of the structure are not warranted here. Attempts to crystallise other metal-uronates using the same experimental conditions were, unfortunately, not met with similar success.

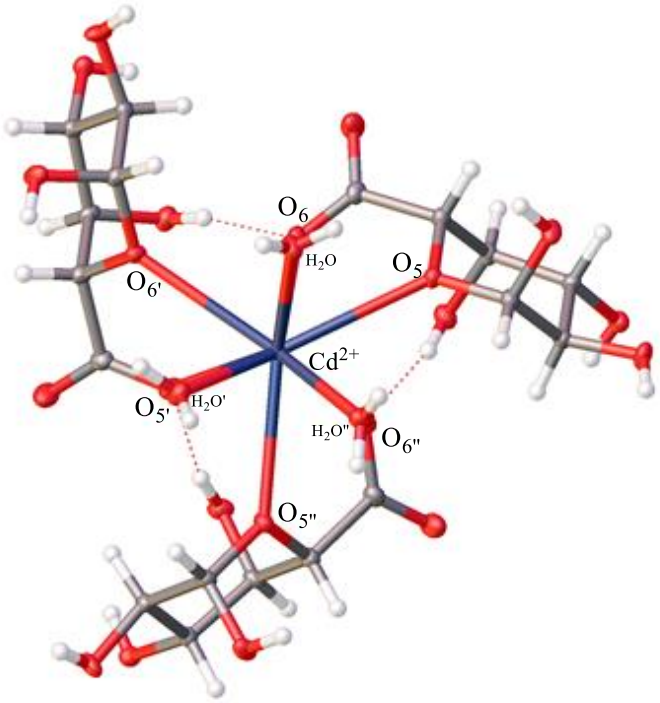

Figure B.1 The view down 001 plane of crystalline $Cd_{0.6}Na_{1.4}H_{0.4}Gal_3.3H_2O$

B.3 Materials and methods

Cadmium carbonate (99.999% trace metals) and D−galacturonic acid were purchased from Sigma Aldrich and used as received. D−Galacturonic acid (0.20 g, 1.03 mmol) was dissolved in distilled, deionised H_2O (2.0 mL). The D−galacturonic acid solution (0.30 mL, 0.52 M) was then added to an excess of cadmium carbonate (0.052 g, 0.30 mmol) and the vessel shaken vigorously for 3 hours. The solution was then filtered through a TITAN2 0.2 μm micro−syringe filter. The cadmium galacturonate solution was then diluted with about half the volume of ethanol and allowed to stand for two weeks. A small number of very fine crystalline needles were formed. Subsequent analysis by single crystal X−ray diffraction revealed that these crystals corresponded to the cadmium sodium galacturonate double salt: $C_{18}H_{39.4}Cd_{0.6}Na_{1.4}O_{27.}$

Owing to the thin, needle−like shape of crystalline samples of cadmium sodium α−D−galacturonate, synchrotron radiation was necessitated in order to obtain diffraction data of a suitable quality. Single crystal X−ray diffraction was therefore carried out on samples of cadmium sodium α−D−galacturonate at 120 K on a CrystalLogic 3−circle kappa−diffractometer using beamline Il9 of the Diamond Light Source (Rutherford Appleton Laboratory, Oxford). X−rays were monochromated *via* a Si(111) double−crystal and measurement was conducted through a Rigaku Saturn 724+ CCD detector. Data was processed using CrystalClear−SM Expert2.0 (Rigaku, 2009),APEX2 (Bruker) and the structure was solved using SHELXTL and OLEX2 software.[7] Heavy atoms were first located by direct methods and the refinement carried out on F^2 by full matrix least squares techniques with non−hydrogen atoms being treated anisotropically and hydrogen atoms riding in idealised positions on their parent atoms.

Further characterisation was not carried out on the $Cd_{0.6}Na_{1.4}H_{0.4}Gal_3.3H_2O$ owing to a lack of sample. Dr. Andrei Batsanov if thanked for collecting and refining the crystal data.

B.4 References

1 J. Hjortås, B. Larsen, S. Thanomkul, I. Szabo-Lin, C. Guthenberg and B. Mannervik, *Acta Chem. Scand.*, 1974, **28b**, 689–689.

2 S. Thanomkul, J. A. Hjortås and H. Sørum, *Acta Crystallogr. Sect. B Struct. Crystallogr. Cryst. Chem.*, 1976, **32**, 920–922.

3 S. E. B. Gould, R. O. Gould, D. A. Rees and W. E. Scott, *J. Chem. Soc. Perkin Trans. 2*, 1975, 237–242.

4 H. S. Isbell and H. L. Frush, *J. Res. Natl. Inst. Stand. Technol.*, 1944, **32**, 77–94.

5 F. Mo, T. J. Brobak and I. R. Siddiqui, *Carbohydr. Res.*, 1985, **145**, 13–24.

6 S. Deiana, C. Gessa, P. Piu and R. Seeber, *J. Inorg. Biochem.*, 1990, **40**, 301–307.

7 O. V. Dolomanov, L. J. Bourhis, R. J. Gildea, J. A. K. Howard and H. Puschmann, *J. Appl. Crystallogr.*, 2009, **42**, 339–341.

Appendix C – A note on the hydrothermolysis of uronides

C.1 Introduction

Whilst the focus of this thesis has been the anhydrous thermolysis of uronides, the solution-state algal mono-uronates prepared in Chapter 2, and the aqueous coordination chemistry explored in Chapter 3, could both find future application in the study of alginate hydrothermolysis. This appendix describes the isolation and purification of reductic acid, a key degradation product of uronides when treated under hydrothermal conditions.

C.2 Background

Whilst there have been many studies of the hydrothermal chemistry of uronides, a full review cannot provided here (though it is suggested as a future topic of interest). Instead, it is noteworthy to briefly highlight the conclusions of Bornik *et al.*,[1] who summarised the most likely routes of hydrothermolysis of a mono-uronic acid according to the scheme in Figure C.1.

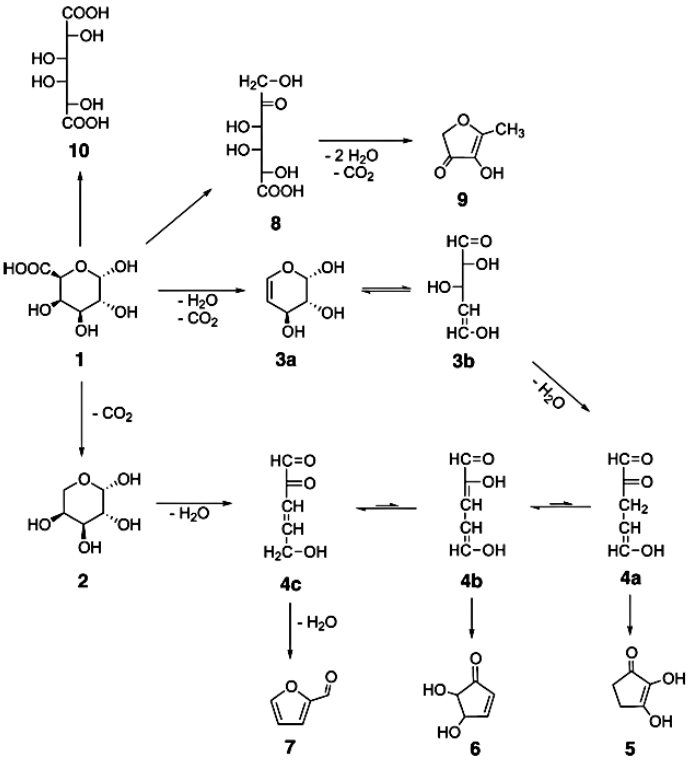

Figure C.1 Degradation pathways of D-galacturonic acid (1) under acidic, hydrothermal conditions. Decarboxylation to L-arabinose (2) or eliminative decarboxylation to 4,5-unsaturated 4-deoxy-L-arabinose (3) to 2-ketoglutaraldehyde (4) leading to reductic acid (5), 4,5-dihydroxy-2-cyclopenten-1-one (6), and 2-furfural (7). Isomerization to D-tagaturonic acid (8) and formation of norfuraneol (9) or galactaric acid (10). Reproduced, with permission, from Bornik *et al.*[1] © 2013 American Chemical Society

From Figure C.1 it can be seen that, in contrast to the anhydrous pyrolysis of uronic acids (where 2-furfural is the most favourable degradation product), in the hydrothermal environment, a number of thermolytic pathways are available, one of which leads to the formation of reductic acid. Hence, it was decided to synthesise this compound, not only to use as a reagent in pyrolysis reactions (see Chapter 4), but also as a preliminary measure towards the future study of the hydrothermolysis of algal mono- and poly-uronides.

As a final point to note, succinic acid was found to be a common contaminant in the algal mono-uronates synthesised in Chapter 2. There is literature to support the notion that this succinic acid was formed by the oxidation of reductic acid (proceeding *via* 2-*α*-ketoglutaric acid, and then to succinic acid *via* an oxidative decarboxylation).[2] Whilst the contamination was a source of annoyance in this thesis, succinic acid is another potentially lucrative platform chemical that could be derived from alginate-rich kelp, and therefore worthy of further investigation.

C.3 Isolation and characterisation of reductic acid

Reductic acid (2,3-dihydroxycyclopent-2-en-1-one) is a known degradation product of mono-uronic acids[1] and was prepared, using a method adapted from that of Goldstein,[3] in order to study its properties and to use as an analytical standard. Alginic acid (11.25 g, 65 mmol equivalents of mono-uronic acids) was split equally into nine glass liners of a Baskerville 10-well autoclave. Degassed deionised H_2O was used to make up H_3PO_4 (45 mL, 1.8 M) and added in 5 mL portions to each of the wells. The autoclave purged with N_2 for 30 mins prior sealing and heating to 135 °C, inducing an increase of pressure to 3 bar. Over the course of the 5 hour reaction, the pressure was seen to increase to 6 bar owing to decarboxylation of the uronides. The products of all of the wells were pooled in 50 mL centrifuge tubes and the resulting deep yellow liquor was separated from the black char by centrifugation (3000 rpm, 30 mins). The char was washed with hot (80 °C) deionised H_2O (3 X 80 mL) with recovery of the liquid fraction being achieved by centrifugation (3000 rpm, 30 mins) each time. The washings were combined and $CaCO_3$ added over a period of 24 hours to bring the solution to neutrality, with separation of the resulting $Ca_3(PO_4)_2$ by filtration. The $Ca_3(PO_4)_2$ was washed with deionised H_2O (2 X 125 mL) to bring the total volume of product solution up to approximately 500 mL. Amberlite® IR120 (H^+) ion exchange resin (25 ml) that had previously been washed with HCl (3.0 M) and deionised H_2O until free of Cl^- ions, was added to the yellow solution to remove remaining Ca^{2+} ions. Reduction *in vacuo* (40 °C, 40 mbar) yielded a thick syrup that was redissolved in hot (60 °C) EtOH (10 mL). Upon cooling, ice cold Et_2O (100 mL) was added to yield a dull grey solid that was removed by filtration. The solid was washed with more ice cold Et_2O (2 X 50 mL) and the solutions pooled and concentrated to a thick yellow syrup *in vacuo* (40 °C, 800 mbar then 40 mbar). Ice cold Et_2O (10 mL) was added to yield a crude fraction of crystals that were separated by filtration and recrystallised by re-dissolving in hot EtOH and storing at 5 °C. The pale yellow, diamond shaped crystals were separated by filtration, washed with ice cold acetone (2 X 25 mL) and dried at 40 °C for 24 hours to give the pure reductic acid (approximately 300 mg, 2.6 mmol) with an isolated yield of around 4.0 mol.%. The isolated yield, characterisations, and molecular structure of the obtained reductic acid were all in good agreement with those reported by other authors.[3–6]

^{1}H NMR (400 MHz, D_2O): δ single peak (s, -CH2-) measured at 2.52 ppm (pH* = 0.86), 2.52 ppm (pH* = 2.67), 2.44 ppm (pH* = 4.52), 2.30 ppm (pH* = 8.76), and 2.30 ppm (pH* = 12.42). Derived $pK_a(1) = 4.8$.

^{13}C NMR (400 MHz, D2O, pH* = 4.52): δ 187.6 (-C=O), 130.9 (-C-OH), 26.7(-CH2-)

^{13}C NMR-DEPT (400 MHz, D2O, pH* = 4.52): δ 26.7 (-CH2-)

ESI-MS m/z: $[M - H^+]$ Calcd for $C_5H_5O_3^-$ = 113.1; Found = 113.1.

CHN: Anal. calcd for $C_5H_6O_3$: C, 52.63; H, 5.30. Found: C, 52.74; H, 5.36.

FTIR: 3302 cm^{-1} (O-H stretch), 1680 cm^{-1} (αβ-unsaturated C=O stretch)

UV: λ_{max} (H_2O / PO_4^{3-} buffer, pH 3.0) = 263 nm

XRD: Structure refined with R1 = 5.7 %, in good agreement with data published by Semmingsen *et al.*[6] Selected bond lengths shown in Figure C.2 and key refinement parameters shown in Table C.1. Data collected and refined by Dr. Andrei Batsanov.

Table C.1 Crystallographic parameters from reductic acid

Empirical formula	**$C_5H_6O_3$**
Formula weight	114.10
Temperature/K	120
Crystal system	monoclinic
Space group	$P2_1/n$
a/Å	7.1410(5)
b/Å	8.6456(5)
c/Å	7.8843(5)
α/°	90
β/°	95.2156(18)
γ/°	90
Volume/Å^3	484.75(5)
Z	4
ρ_{calc}g/cm^3	1.563
μ/mm^{-1}	0.131
F(000)	240.0
Crystal size/mm^3	0.322 × 0.246 × 0.122
Radiation	MoKα (λ = 0.71073)
2Θ range for data collection/°	7.01 to 54.99
Index ranges	-9 ≤ h ≤ 9, -11 ≤ k ≤ 11, -10 ≤ l ≤ 10
Reflections collected	5386
Independent reflections	1115 [R_{int} = 0.0587, R_{sigma} = 0.0387]
Data/restraints/parameters	1115/0/97
Goodness-of-fit on F^2	1.087
Final R indexes [I>=2σ (I)]	R_1 = 0.0567, wR_2 = 0.1467
Final R indexes [all data]	R_1 = 0.0578, wR_2 = 0.1483
Largest diff. peak/hole / e Å^{-3}	0.66/-0.33

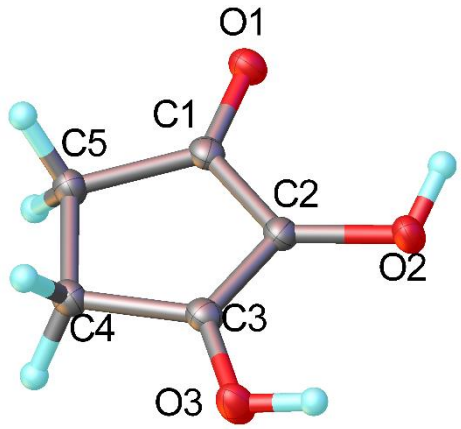

Selected bond lengths

O1-C1: 1.2502(17) Å

O2-C2: 1.3620(16) Å

O3-C3: 1.3214(17) Å

C1-C2: 1.4243(19) Å

C1-C5: 1.5072(17) Å

C2-C3: 1.3642(18) Å

C3-C4: 1.4902(18) Å

C4-C5: 1.5364(18) Å

Figure C.2 The crystal structure, and selected bond lengths, of reductic acid, as isolated in this thesis

C.4 References

1 M. A. Bornik and L. W. Kroh, *J. Agric. Food Chem.*, 2013, **61**, 3494–3500.

2 T. Reichstein and R. Oppenauer, *Helv. Chim. Acta*, 1933, **16**, 988–998.

3 S. Goldstein, US2854484 A, United States Patent Office, 1958.

4 M. Bornik, PhD Thesis, Technischen Universität Berlin, Germany, 2012.

5 I. F. Trotter, H. W. Thompson and F. Wokes, *Biochem. J.*, 1948, **42**, 601–602.

6 D. Semmingsen, J. Seita, A. Holm, O. O. Orazi, G. Schroll, D. H. Williams and A. M. Pilotti, *Acta Chem. Scand.*, 1977, **31b**, 81–85.

Appendix D - NMR spectrometers: typical experimental parameters

D.1 Typical NMR spectrometer acquisition parameters

Bruker Avance-400 MHz

Experiment	^{1}H	$^{13}C^{*}$	^{1}H-^{1}H COSY
RF pulse energy (MHz)	400.13	100.62	400.13 X 400.13
Temperature (K)	295 ± 2	295 ± 2	295 ± 2
Number of scans	8	1024	1
Pulse width (μs)	10.0	8.00	10.0
Spectral width (Hz)	8000	24000	variable
Acquisition time (s)	4.09	1.36	Total time = 2.19 s
Relaxation delay (s)	1.00	2.00	

Varian Inova-500 MHz

Experiment	^{1}H	^{1}H-^{1}H COSY
RF pulse energy (MHz)	499.61	499.61 X 499.61
Temperature (K)	variable	variable
Number of scans	16-32	1
Pulse angle (°)	37.8	37.8
Spectral width (Hz)	10000	1400 X 1400
Acquisition time (s)	4.00	0.19
Relaxation delay (s)	0.00	1.00

Varian VNMRS-600 MHz

Experiment	^{1}H	^{1}H pure shift	$^{13}C^{*}$	^{1}H-^{1}H COSY	^{1}H-^{13}C HSQC	^{1}H-^{13}C HMBC
RF pulse energy (MHz)	599.61	599.61	150.78	599.61 X 599.61	599.61 X 150.78	599.61 X 150.78
Temperature (K)	295 ± 2	295 ± 2	295 ± 2	295 ± 2	295 ± 2	295 ± 2
Number of scans	8	2	896	1	2	2
Pulse width (μs)	4.25	8.50	4.88	8.50	8.50	8.50
Spectral width (Hz)	10000	7000	38000	6000 X 6000	6000 X 21000	6000 X 36000
Acquisition time (s)	3.9	1.00	1.00	0.85	0.15	0.43
Relaxation delay (s)	10.0	1.00	3.00	0.40	1.00	0.70

Varian VNMRS-700 MHz

Experiment	^{1}H	^{1}H pure shift	$^{13}C^{*}$	^{1}H-^{1}H COSY	^{1}H-^{13}C HSQC
RF pulse energy (MHz)	699.74	699.74	175.97	699.74 X 699.74	699.74 X 175.96
Temperature (K)	295 ± 2	295 ± 2	295 ± 2	295 ± 2	295 ± 2
Number of scans	4	2	2000	1	2
Pulse width (μs)	3.27	9.80	4.95	9.80	9.80
Spectral width (Hz)	11000	7700	45000	4800 X 4800	4800 X 35000
Acquisition time (s)	3.90	1.02	2.94	0.15	0.15
Relaxation delay (s)	10.00	2.00	3.00	1.00	1.00

* All one-dimensional ^{13}C experiments were proton decoupled

D.2 Advanced NMR methodologies

In addition to routine 1-D and 2-D ^{1}H and ^{13}C NMR experiments, work in Chapter 2 used parameters that were developed in-house by Dr Juan A Aguilar Malavia:

- **Pure shift**[1] experiments were employed to make ^{1}H NMR data easier to interpret by collapsing the homonuclear couplets, meaning each signal is rendered a singlet. The PSYCHE pulse sequence was utilised to provide good sensitivity and tolerance towards strong coupling.

- **Comprehensive sensing**[2] was used to reduce the time required to acquire 2D experiments (particularly the ^{1}H-^{13}C HSQC), without a reduction in resolving power. Here, the time required to acquire the ^{1}H-^{13}C spectrum was reduced from 106 minutes to just 14, by sampling the chemical shift incoherently and reconstructing the result. Specifically, the classic Nyquist-Shannon sampling method was replaced with a random one in the form of a Poisson distribution. The results were processed replacing the usual 'discrete double Fourier transform', required by the Nyquist-Shannon sampling procedure with an L1-minimizing algorithm (Iterative Soft Thresholding, IST). [2]

I am especially grateful to Juan for his time and expertise in developing, applying, and explaining these methods.

D.3 References

1 M. Foroozandeh, R. W. Adams, N. J. Meharry, D. Jeannerat, M. Nilsson and G. A. Morris, *Angew. Chemie Int. Ed.*, 2014, **53**, 6990–6992.

2 J. A. Aguilar, R. Belda, A. Botana and A. M. Kenwright, *RSC Adv.*, 2016, **6**, 83380–83385.

Appendix E – Metal-uronate NMR spectroscopic experiments: additional theory, tabulated supplementary data, and error analysis.

E.1 Absolute ($\Delta\delta_{obs}$) and relative ($\Delta\delta_{rel}$) changes in chemical shift of ^{1}H signals in the NMR spectra of mono-uronates in aqueous solutions containing metal ions.

E.1.1 Further explanation of the absolute ($\Delta\delta_{obs}$) and relative ($\Delta\delta_{rel}$) changes in chemical shift

The experiments conducted in Chapter 3 of this thesis were aimed, in part, at discerning the site of metal binding to uronate monomers through measuring changes to the chemical shift ($\Delta\delta$) of both ^{1}H and ^{13}C signals upon the addition of a metal ion. Here, the $\Delta\delta$ value for a particular nucleus (**n**) following the addition of a metal salt to the solution is defined as:

$$\Delta\delta(\mathbf{n}) = \delta(\mathbf{n})_{\text{in the presence of metal salt}} - \delta(\mathbf{n})_{\text{in metal-free solution}}$$

Changes to δ(**n**) arise as the binding cation distorts the electron cloud surrounding the **n**. However, the observed change in chemical shift ($\Delta\delta_{obs}$) of **n** upon the addition of a metal salt is, in actuality, a sum of the varying shielding ($\Delta\delta_{shield}$) and deshielding ($\Delta\delta_{deshield}$) influences exerted on that nucleus:

$$\Delta\delta_{obs} = \Sigma(\Delta\delta_{shield}) + \Sigma(\Delta\delta_{deshield})$$

Burgess and others have discussed the influences of inorganic species on the magnitudes of $\Delta\delta_{shield}$ and $\Delta\delta_{deshield}$ in the ^{1}H NMR spectrum of H_2O,[1,2] and we may adapt such treatments for the consideration of cation-uronate coordination. Hence, upon including a metal salt in a uronate solution, $\Delta\delta_{shield}$ and $\Delta\delta_{deshield}$ influences would arise from:

- Binding of the metal cation to a specific arrangement of saccharide oxygen atoms causing changes to the electron distribution around the carbohydrate ring by through-bond induction.
- Binding of the metal cation to a specific arrangement of saccharide oxygen atoms causing changes to the electron distribution around the carbohydrate ring by through-space polarisation (Buckingham effect).[3]
- A “bulk” effect arising from the electric field of anions and cations in the vicinity of, but not bound to, the saccharide (analogous to a change in the dielectric constant of the solvent).[4]
- Interruption to the hydrogen bonding network of water molecules surrounding the saccharide.[1,2]

Hence, whilst we may only be interested in the effect of the cation on the uronate in question, it should be remembered that $\Delta\delta_{obs}$ will contain additional contributions from, for example, polarisation of bonds brought about by the presence of the counter-anion or other (non-bonded) cations. Furthermore, the magnitude of $\Delta\delta_{shield}$ and $\Delta\delta_{deshield}$ arising from site-specific binding of a particular cation will vary with the nature of the cation in question. Such confounding influences can make $\Delta\delta_{obs}$ difficult to interpret, especially when comparing the effect of metals with different valencies (as they necessarily require the inclusion of different ratios of counter-anions).[1,2]

One remedy to simplify the situation is to measure the magnitude of $\Delta\delta_{obs}$ for a particular proton (H*X*) relative to that of another proton on the same molecule (H*Y*). Such a treatment gives rise to the parameter known as $\Delta\delta_{rel}$, defined as:

$$\Delta\delta_{rel} = \Delta\delta_{obs}(HX) - \Delta\delta_{obs}(HY)$$

For the work presented in Chapter 3, the reference proton (H*Y*) was chosen as H4. Whilst the choice of reference proton may seem somewhat arbitrary, it was based simply on the empirical observation that, in all pyranose anomers of **Gal**, **Glc**, **Man** and **Gul**, H4 usually gave rise to the largest negative (deshielding) $\Delta\delta_{obs}$ values (see structures in Figure E.1).

On its own, $\Delta\delta_{rel}$ is not a particularly useful parameter with which to analyse the coordination mode of a particular cation to a particular saccharide; for this the original $\Delta\delta_{obs}$ values must be consulted. However, $\Delta\delta_{rel}$ does facilitate rapid screening of metal-uronate interactions by application of the following assumption:

If the $\Delta\delta_{rel}$ values for all protons on a uronate anomer in the presence of a selected cation are zero (or close to zero) then it can be assumed that the metal ion is not selectively binding to a particular arrangement of hydroxyl oxygens around the saccharide ring.

Hence, in essence the $\Delta\delta_{rel}$ parameter allows us to ignore the “bulk” effects that may be present in the NMR spectra upon the inclusion of a metal salt and rapidly look across the tables of chemical shift data to identify interactions of interest. The tabulated forms of both $\Delta\delta_{obs}$ and $\Delta\delta_{rel}$ for all protons in all pyranose anomers of **Gal**, **Glc**, **Gul**, and **Man** under many different conditions are given in Section E.1.2.

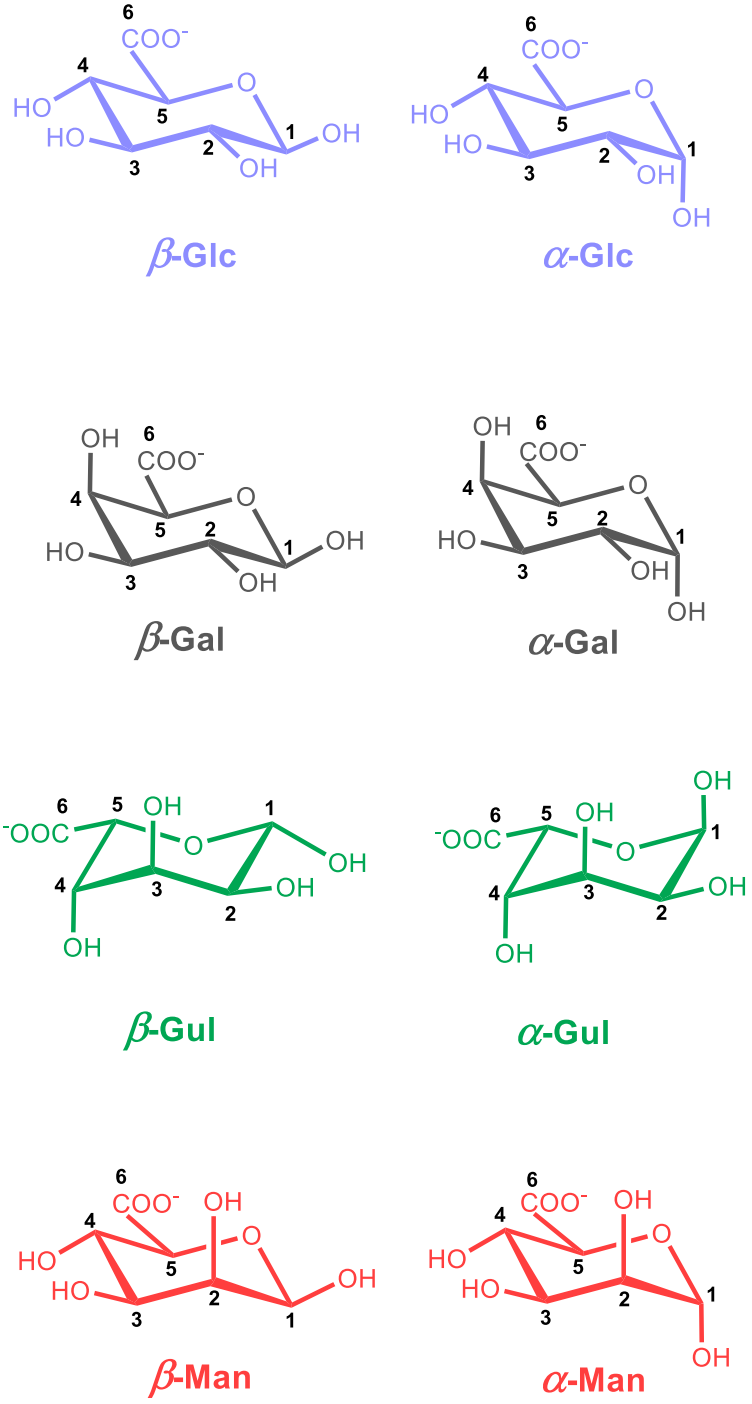

Figure E.1 The structure of mono-pyranuronates and their numbering conventions

E.1.2 Tabulated values of $\Delta\delta_{obs}(^1H)$ and $\Delta\delta_{rel}(^1H)$ for different uronates in the presence of varying metal salts and pH* values

Table E.1 $\Delta\delta_{obs}$ and $\Delta\delta_{rel}$ values for Na-D-glucuronate in metal chloride salts at pH* 7.5

Solution	pH*	alpha pyranose					beta pyranose				
		Absolute change in chemical shift compared to metal-free solution ($\Delta\delta_{obs}$)									
		αH1	αH2	αH3	αH4	αH5	βH1	βH2	βH3	βH4	βH5
No metal	7.5	0.00	0.00	0.00	0.00	0.00	0.00	0.00	0.00	0.00	0.00
1.0 M NaCl	7.5	-0.04	-0.05	-0.06	-0.06	-0.06	-0.04	-0.05	-0.05	-0.05	-0.04
1.0 M KCl	7.5	-0.06	-0.06	-0.07	-0.07	-0.06	-0.05	-0.07	-0.06	-0.06	-0.05
1.0 M $CaCl_2$	7.5	0.00	-0.06	-0.08	-0.07	-0.03	-0.06	-0.08	-0.08	-0.08	-0.03
1.0 M $SrCl_2$	7.5	-0.04	-0.09	-0.12	-0.11	-0.08	-0.09	-0.11	-0.11	-0.11	-0.07
1.0 M $BaCl_2$	7.5	-0.08	-0.12	-0.14	-0.13	-0.12	-0.09	-0.12	-0.13	-0.13	-0.08
1.0 M $MgCl_2$	7.5	-0.07	-0.08	-0.10	-0.09	-0.07	-0.07	-0.09	-0.08	-0.09	-0.05
1.0 M $Ca(NO_3)_2$	7.5	0.07	0.00	0.00	0.00	0.05	0.00	-0.01	0.00	0.00	0.03
1.0 M CaI_2	7.5	-0.06	-0.12	-0.15	-0.13	-0.10	-0.06	-0.14	-0.09	-0.14	-0.04
		Change in chemical shift compared to metal-free solution relative to H4 ($\Delta\delta_{rel}$)									
		αH1	αH2	αH3	αH4	αH5	βH1	βH2	βH3	βH4	βH5
No metal	7.5	0.00	0.00	0.00	-	0.00	0.00	0.00	0.00	-	0.00
1.0 M NaCl	7.5	0.02	0.02	0.01	-	0.01	0.02	0.00	0.00	-	0.02
1.0 M KCl	7.5	0.01	0.01	-0.01	-	0.00	0.01	0.00	0.00	-	0.01
1.0 M $CaCl_2$	7.5	0.08	0.02	-0.01	-	0.05	0.03	0.00	0.00	-	0.05
1.0 M $SrCl_2$	7.5	0.06	0.02	-0.01	-	0.03	0.02	0.00	0.00	-	0.04
1.0 M $BaCl_2$	7.5	0.05	0.01	-0.01	-	0.01	0.03	0.01	0.00	-	0.05
1.0 M $MgCl_2$	7.5	0.02	0.00	-0.01	-	0.01	0.02	-0.01	0.01	-	0.04
1.0 M $Ca(NO_3)_2$	7.5	0.07	0.00	0.00	-	0.06	0.00	-0.01	0.00	-	0.03
1.0 M CaI_2	7.5	0.03	0.01	-0.01	-	0.01	0.04	0.00	0.02	-	0.05

Table E.2 $\Delta\delta_{obs}$ and $\Delta\delta_{rel}$ values for Na-D-glucuronate in metal chloride salts at pH* 1.0

Solution	pH*	alpha pyranose					beta pyranose				
		Absolute change in chemical shift compared to metal-free solution ($\Delta\delta_{obs}$)									
		αH1	αH2	αH3	αH4	αH5	βH1	βH2	βH3	βH4	βH5
No metal	1.0	0.00	0.00	0.00	0.00	0.00	0.00	0.00	0.00	0.00	0.00
1.0 M NaCl	1.0	-0.04	-0.05	-0.05	-0.05	-0.05	-0.04	-0.05	-0.04	-0.05	-0.03
1.0 M KCl	1.0	-0.05	-0.06	-0.07	-0.06	-0.06	-0.05	-0.06	-0.05	-0.06	-0.04
1.0 M $CaCl_2$	1.0	-0.08	-0.08	-0.10	-0.09	-0.11	-0.08	-0.09	-0.08	-0.10	-0.08
1.0 M $SrCl_2$	1.0	-0.11	-0.11	-0.13	-0.12	-0.14	-0.11	-0.12	-0.11	-0.13	-0.11
1.0 M $BaCl_2$	1.0	-0.13	-0.13	-0.15	-0.14	-0.16	-0.13	-0.14	-0.13	-0.15	-0.12
1.0 M $MgCl_2$	1.0	-0.08	-0.08	-0.10	-0.08	-0.11	-0.07	-0.09	-0.07	-0.10	-0.07
1.0 M $ZnCl_2$	1.0	-0.08	-0.09	-0.11	-0.10	-0.13	-0.08	-0.10	-0.09	-0.11	-0.10
		Change in chemical shift compared to metal-free solution relative to H4 ($\Delta\delta_{rel}$)									
		αH1	αH2	αH3	αH4	αH5	βH1	βH2	βH3	βH4	βH5
No metal	1.0	0.00	0.00	0.00	-	0.00	0.00	0.00	0.00	-	0.00
1.0 M NaCl	1.0	0.01	0.00	-0.01	-	0.00	0.02	0.01	0.02	-	0.02
1.0 M KCl	1.0	0.01	0.00	-0.01	-	0.00	0.02	0.00	0.01	-	0.02
1.0 M $CaCl_2$	1.0	0.01	0.01	-0.01	-	-0.02	0.02	0.01	0.03	-	0.03
1.0 M $SrCl_2$	1.0	0.01	0.00	-0.01	-	-0.02	0.02	0.01	0.03	-	0.03
1.0 M $BaCl_2$	1.0	0.01	0.00	-0.01	-	-0.02	0.02	0.01	0.02	-	0.03
1.0 M $MgCl_2$	1.0	0.00	0.00	-0.01	-	-0.02	0.03	0.01	0.03	-	0.03
1.0 M $ZnCl_2$	1.0	0.02	0.01	-0.01	-	-0.03	0.03	0.01	0.03	-	0.01

Table E.3 $\Delta\delta_{obs}$ and $\Delta\delta_{rel}$ values for Na-D-galacturonate in metal chloride salts at pH* 7.5

Solution	pH*		alpha pyranose						beta pyranose				
Absolute change in chemical shift compared to metal-free solution ($\Delta\delta_{obs}$)													
			αH1	**αH2**	**αH3**	**αH4**	**αH5**		**βH1**	**βH2**	**βH3**	**βH4**	**βH5**
No metal	**7.5**		0.00	0.00	0.00	0.00	0.00		0.00	0.00	0.00	0.00	0.00
1.0 M NaCl	**7.5**		-0.04	-0.06	-0.05	-0.06	-0.04		-0.02	-0.06	-0.03	-0.06	-0.03
1.0 M KCl	**7.5**		-0.04	-0.06	-0.06	-0.07	-0.05		-0.03	-0.07	-0.04	-0.07	-0.03
1.0 M $CaCl_2$	**7.5**		0.11	-0.05	-0.05	-0.07	0.06		0.02	-0.05	-0.03	-0.07	0.05
1.0 M $SrCl_2$	**7.5**		0.05	-0.10	-0.10	-0.12	0.00		-0.01	-0.08	-0.07	-0.13	0.00
1.0 M $BaCl_2$	**7.5**		0.01	-0.12	-0.13	-0.16	-0.04		0.00	-0.10	-0.10	-0.16	0.00
1.0 M $MgCl_2$	**7.5**		-0.01	-0.09	-0.07	-0.08	-0.01		-0.05	-0.10	-0.05	-0.09	-0.03
1.0 M $Ca(NO_3)_2$	**7.5**		0.15	0.00	0.01	0.00	0.12		0.05	0.01	0.01	-0.01	0.07
1.0 M CaI_2	**7.5**		0.02	-0.15	-0.13	-0.16	-0.02		0.01	-0.12	-0.06	-0.12	-0.01
Change in chemical shift compared to metal-free solution relative to H4 ($\Delta\delta_{rel}$)													
			αH1	**αH2**	**αH3**	**αH4**	**αH5**		**βH1**	**βH2**	**βH3**	**βH4**	**βH5**
No metal	**7.5**		0.00	0.00	0.00	-	0.00		0.00	0.00	0.00	-	0.00
1.0 M NaCl	**7.5**		0.03	0.01	0.01	-	0.02		0.04	0.00	0.03	-	0.04
1.0 M KCl	**7.5**		0.02	0.01	0.01	-	0.02		0.04	0.00	0.03	-	0.03
1.0 M $CaCl_2$	**7.5**		0.18	0.01	0.02	-	0.13		0.09	0.02	0.04	-	0.12
1.0 M $SrCl_2$	**7.5**		0.17	0.02	0.03	-	0.12		0.11	0.04	0.05	-	0.13
1.0 M $BaCl_2$	**7.5**		0.17	0.04	0.03	-	0.12		0.16	0.06	0.06	-	0.16
1.0 M $MgCl_2$	**7.5**		0.07	-0.01	0.01	-	0.07		0.03	-0.02	0.03	-	0.05
1.0 M $Ca(NO_3)_2$	**7.5**		0.15	0.00	0.01	-	0.12		0.05	0.02	0.01	-	0.07
1.0 M CaI_2	**7.5**		0.18	0.01	0.03	-	0.14		0.17	0.04	0.10	-	0.15

Table E.4 $\Delta\delta_{obs}$ and $\Delta\delta_{rel}$ values for Na-D-galacturonate in metal chloride salts at pH* 1.0

Solution	pH*		alpha pyranose						beta pyranose				
Absolute change in chemical shift compared to metal-free solution ($\Delta\delta_{obs}$)													
			αH1	**αH2**	**αH3**	**αH4**	**αH5**		**βH1**	**βH2**	**βH3**	**βH4**	**βH5**
No metal	**1.0**		0.00	0.00	0.00	0.00	0.00		0.00	0.00	0.00	0.00	0.00
1.0 M NaCl	**1.0**		-0.04	-0.06	-0.05	-0.05	-0.04		-0.03	-0.06	-0.03	-0.05	-0.02
1.0 M KCl	**1.0**		-0.04	-0.06	-0.05	-0.06	-0.05		-0.03	-0.07	-0.03	-0.05	-0.02
1.0 M $CaCl_2$	**1.0**		-0.04	-0.08	-0.07	-0.08	-0.08		-0.05	-0.09	-0.05	-0.08	-0.05
1.0 M $SrCl_2$	**1.0**		-0.07	-0.12	-0.11	-0.12	-0.10		-0.08	-0.13	-0.09	-0.12	-0.08
1.0 M $BaCl_2$	**1.0**		-0.08	-0.15	-0.13	-0.15	-0.12		-0.07	-0.14	-0.11	-0.15	-0.09
1.0 M $MgCl_2$	**1.0**		-0.08	-0.10	-0.09	-0.09	-0.09		-0.06	-0.11	-0.06	-0.09	-0.06
1.0 M $ZnCl_2$	**1.0**		-0.07	-0.12	-0.11	-0.12	-0.15		-0.08	-0.13	-0.08	-0.12	-0.10
Change in chemical shift compared to metal-free solution relative to H4 ($\Delta\delta_{rel}$)													
			αH1	**αH2**	**αH3**	**αH4**	**αH5**		**βH1**	**βH2**	**βH3**	**βH4**	**βH5**
No metal	**1.0**		0.00	0.00	0.00	-	0.00		0.00	0.00	0.00	-	0.00
1.0 M NaCl	**1.0**		0.01	-0.01	0.00	-	0.01		0.02	-0.01	0.02	-	0.03
1.0 M KCl	**1.0**		0.01	0.00	0.00	-	0.01		0.03	-0.01	0.02	-	0.03
1.0 M $CaCl_2$	**1.0**		0.04	0.00	0.01	-	0.00		0.03	-0.01	0.03	-	0.03
1.0 M $SrCl_2$	**1.0**		0.05	0.00	0.01	-	0.02		0.04	-0.01	0.03	-	0.04
1.0 M $BaCl_2$	**1.0**		0.07	0.00	0.02	-	0.03		0.07	0.01	0.04	-	0.06
1.0 M $MgCl_2$	**1.0**		0.01	-0.01	0.00	-	0.00		0.03	-0.02	0.03	-	0.03
1.0 M $ZnCl_2$	**1.0**		0.05	0.00	0.01	-	-0.03		0.04	-0.01	0.04	-	0.02

Table E.5 $\Delta\delta_{obs}$ and $\Delta\delta_{rel}$ values for Na-L-guluronate in metal chloride salts at pH* 7.5

Solution	pH*	alpha pyranose					beta pyranose				
		Absolute change in chemical shift compared to metal-free solution ($\Delta\delta_{obs}$)									
		αH1	**αH2**	**αH3**	**αH4**	**αH5**	**βH1**	**βH2**	**βH3**	**βH4**	**βH5**
No metal	**7.5**	0.00	0.00	0.00	0.00	0.00	0.00	0.00	0.00	0.00	0.00
1.0 M NaCl	**7.5**	-0.03	-0.04	-0.04	-0.07	-0.04	-0.05	-0.05	-0.04	-0.06	-0.05
1.0 M KCl	**7.5**	-0.05	-0.06	-0.05	-0.08	-0.06	-0.06	-0.06	-0.06	-0.07	-0.06
1.0 M $CaCl_2$	**7.5**	0.17	0.09	0.02	-0.10	0.10	-0.02	-0.03	-0.07	-0.08	-0.01
1.0 M $SrCl_2$	**7.5**	0.12	0.04	-0.02	-0.16	0.05	-0.05	-0.06	-0.09	-0.12	-0.04
1.0 M $BaCl_2$	**7.5**	0.07	-0.01	-0.07	-0.20	0.02	-0.03	-0.08	-0.12	-0.16	-0.04
1.0 M $MgCl_2$	**7.5**	-0.02	-0.08	-0.07	-0.09	-0.04	-0.09	-0.09	-0.09	-0.10	-0.08
1.0 M $Ca(NO_3)_2$	**7.5**	0.22	0.13	0.08	-0.01	0.17	0.05	0.04	0.02	0.00	0.06
1.0 M CaI_2	**7.5**	0.08	0.00	-0.05	-0.21	0.00	-0.09	-0.12	-0.14	-0.18	-0.08
		Change in chemical shift compared to metal-free solution relative to H4 ($\Delta\delta_{rel}$)									
		αH1	**αH2**	**αH3**	**αH4**	**αH5**	**βH1**	**βH2**	**βH3**	**βH4**	**βH5**
No metal	**7.5**	0.00	0.00	0.00	-	0.00	0.00	0.00	0.00	-	0.00
1.0 M NaCl	**7.5**	0.04	0.03	0.04	-	0.04	0.01	0.01	0.02	-	0.02
1.0 M KCl	**7.5**	0.03	0.02	0.03	-	0.01	0.01	0.01	0.01	-	0.01
1.0 M $CaCl_2$	**7.5**	0.27	0.19	0.13	-	0.20	0.05	0.04	0.01	-	0.07
1.0 M $SrCl_2$	**7.5**	0.28	0.20	0.14	-	0.22	0.07	0.06	0.03	-	0.08
1.0 M $BaCl_2$	**7.5**	0.28	0.20	0.14	-	0.22	0.12	0.07	0.03	-	0.11
1.0 M $MgCl_2$	**7.5**	0.06	0.00	0.02	-	0.04	0.01	0.00	0.01	-	0.02
1.0 M $Ca(NO_3)_2$	**7.5**	0.24	0.15	0.09	-	0.19	0.05	0.04	0.02	-	0.06
1.0 M CaI_2	**7.5**	0.28	0.21	0.15	-	0.21	0.09	0.06	0.05	-	0.10

Table E.6 $\Delta\delta_{obs}$ and $\Delta\delta_{rel}$ values for Na-L-guluronate in metal chloride salts at pH* 1.0

Solution	pH*	alpha pyranose					beta pyranose				
		Absolute change in chemical shift compared to metal-free solution ($\Delta\delta_{obs}$)									
		αH1	**αH2**	**αH3**	**αH4**	**αH5**	**βH1**	**βH2**	**βH3**	**βH4**	**βH5**
No metal	**1.0**	0.00	0.00	0.00	0.00	0.00	0.00	0.00	0.00	0.00	0.00
1.0 M NaCl	**1.0**	-0.04	-0.04	-0.04	-0.06	-0.04	-0.05	-0.05	-0.04	-0.05	-0.04
1.0 M KCl	**1.0**	-0.05	-0.06	-0.06	-0.07	-0.06	-0.06	-0.06	-0.06	-0.06	-0.05
1.0 M $CaCl_2$	**1.0**	0.01	0.04	-0.01	-0.12	0.00	-0.09	-0.09	-0.08	-0.10	-0.09
1.0 M $SrCl_2$	**1.0**	-0.02	0.00	-0.06	-0.16	-0.03	-0.11	-0.12	-0.10	-0.12	-0.11
1.0 M $BaCl_2$	**1.0**	-0.04	-0.05	-0.10	-0.19	-0.06	-0.10	-0.13	-0.14	-0.15	-0.11
1.0 M $MgCl_2$	**1.0**	-0.10	-0.10	-0.09	-0.10	-0.12	-0.10	-0.10	-0.10	-0.10	-0.10
1.0 M $ZnCl_2$	**1.0**	-0.10	-0.11	-0.11	-0.12	-0.15	-0.12	-0.13	-0.12	-0.12	-0.13
		Change in chemical shift compared to metal-free solution relative to H4 ($\Delta\delta_{rel}$)									
		αH1	**αH2**	**αH3**	**αH4**	**αH5**	**βH1**	**βH2**	**βH3**	**βH4**	**βH5**
No metal	**1.0**	0.00	0.00	0.00	-	0.00	0.00	0.00	0.00	-	0.00
1.0 M NaCl	**1.0**	0.02	0.02	0.02	-	0.02	0.00	-0.01	0.00	-	0.01
1.0 M KCl	**1.0**	0.02	0.01	0.01	-	0.01	0.00	0.00	0.00	-	0.01
1.0 M $CaCl_2$	**1.0**	0.13	0.15	0.10	-	0.11	0.01	0.00	0.02	-	0.01
1.0 M $SrCl_2$	**1.0**	0.14	0.16	0.10	-	0.12	0.01	0.00	0.02	-	0.01
1.0 M $BaCl_2$	**1.0**	0.15	0.15	0.10	-	0.14	0.04	0.01	0.01	-	0.04
1.0 M $MgCl_2$	**1.0**	0.00	0.00	0.01	-	-0.02	-0.01	-0.01	-0.01	-	0.00
1.0 M $ZnCl_2$	**1.0**	0.02	0.01	0.01	-	-0.03	0.00	0.00	0.00	-	-0.01

Table E.7 $\Delta\delta_{obs}$ and $\Delta\delta_{rel}$ values for Na-D-mannuronate in metal chloride salts at pH* 7.5

Solution	pH*	alpha pyranose					beta pyranose				
		Absolute change in chemical shift compared to metal-free solution ($\Delta\delta_{obs}$)									
		αH1	αH2	αH3	αH4	αH5	βH1	βH2	βH3	βH4	βH5
No metal	7.5	0.00	0.00	0.00	0.00	0.00	0.00	0.00	0.00	0.00	0.00
1.0 M NaCl	7.5	-0.05	-0.04	-0.05	-0.07	-0.05	-0.03	-0.03	-0.02	-0.06	-0.04
1.0 M KCl	7.5	-0.06	-0.05	-0.06	-0.08	-0.07	-0.04	-0.05	-0.05	-0.08	-0.06
1.0 M $CaCl_2$	7.5	0.03	-0.03	-0.06	-0.11	0.01	0.01	-0.03	-0.02	-0.06	-0.01
1.0 M $SrCl_2$	7.5	-0.02	-0.08	-0.10	-0.15	-0.05	-0.03	-0.07	-0.06	-0.10	-0.05
1.0 M $BaCl_2$	7.5	-0.06	-0.11	-0.13	-0.16	-0.09	-0.02	-0.08	-0.08	-0.11	-0.07
1.0 M $MgCl_2$	7.5	-0.07	-0.06	-0.08	-0.10	-0.06	-0.06	-0.07	-0.05	-0.11	-0.03
1.0 M $Ca(NO_3)_2$	7.5	0.09	0.03	0.01	-0.03	0.08	0.04	0.03	0.03	0.00	0.03
1.0 M CaI_2	7.5	-0.02	-0.09	-0.14	-0.19	-0.06	0.01	-0.08	-0.03	-0.17	0.00
		Change in chemical shift compared to metal-free solution relative to H4 ($\Delta\delta_{rel}$)									
		αH1	αH2	αH3	αH4	αH5	βH1	βH2	βH3	βH4	βH5
No metal	7.5	0.00	0.00	0.00	-	0.00	0.00	0.00	0.00	-	0.00
1.0 M NaCl	7.5	0.02	0.03	0.02	-	0.02	0.04	0.03	0.04	-	0.03
1.0 M KCl	7.5	0.02	0.03	0.02	-	0.01	0.04	0.03	0.02	-	0.02
1.0 M $CaCl_2$	7.5	0.14	0.08	0.05	-	0.12	0.08	0.04	0.04	-	0.05
1.0 M $SrCl_2$	7.5	0.12	0.07	0.04	-	0.10	0.08	0.04	0.05	-	0.06
1.0 M $BaCl_2$	7.5	0.10	0.05	0.03	-	0.07	0.10	0.03	0.04	-	0.04
1.0 M $MgCl_2$	7.5	0.04	0.04	0.03	-	0.04	0.05	0.04	0.05	-	0.07
1.0 M $Ca(NO_3)_2$	7.5	0.12	0.06	0.04	-	0.10	0.04	0.03	0.03	-	0.04
1.0 M CaI_2	7.5	0.17	0.10	0.05	-	0.14	0.18	0.09	0.14	-	0.17

Table E.8 $\Delta\delta_{obs}$ and $\Delta\delta_{rel}$ values for Na-D-mannuronate in metal chloride salts at pH* 1.0

Solution	pH*	alpha pyranose					beta pyranose				
		Absolute change in chemical shift compared to metal-free solution ($\Delta\delta_{obs}$)									
		αH1	αH2	αH3	αH4	αH5	βH1	βH2	βH3	βH4	βH5
No metal	1.0	0.00	0.00	0.00	0.00	0.00	0.00	0.00	0.00	0.00	0.00
1.0 M NaCl	1.0	-0.04	-0.04	-0.04	-0.05	-0.04	-0.02	-0.03	-0.02	-0.06	-0.02
1.0 M KCl	1.0	-0.06	-0.06	-0.07	-0.06	-0.06	-0.04	-0.05	-0.04	-0.08	-0.02
1.0 M $CaCl_2$	1.0	-0.08	-0.08	-0.10	-0.09	-0.09	-0.04	-0.06	-0.04	-0.10	-0.05
1.0 M $SrCl_2$	1.0	-0.11	-0.11	-0.13	-0.13	-0.12	-0.07	-0.09	-0.08	-0.13	-0.07
1.0 M $BaCl_2$	1.0	-0.13	-0.14	-0.16	-0.16	-0.13	-0.07	-0.11	-0.10	-0.15	-0.06
1.0 M $MgCl_2$	1.0	-0.09	-0.08	-0.10	-0.10	-0.09	-0.06	-0.07	-0.06	-0.11	-0.06
1.0 M $ZnCl_2$	1.0	-0.08	-0.09	-0.10	-0.13	-0.13	-0.07	-0.09	-0.07	-0.13	-0.10
		Change in chemical shift compared to metal-free solution relative to H4 ($\Delta\delta_{rel}$)									
		αH1	αH2	αH3	αH4	αH5	βH1	βH2	βH3	βH4	βH5
No metal	1.0	0.00	0.00	0.00	-	0.00	0.00	0.00	0.00	-	0.00
1.0 M NaCl	1.0	0.01	0.01	0.01	-	0.01	0.04	0.03	0.03	-	0.04
1.0 M KCl	1.0	0.00	0.00	-0.01	-	0.00	0.04	0.03	0.04	-	0.05
1.0 M $CaCl_2$	1.0	0.01	0.02	0.00	-	0.01	0.05	0.04	0.05	-	0.05
1.0 M $SrCl_2$	1.0	0.02	0.02	0.00	-	0.02	0.06	0.04	0.05	-	0.06
1.0 M $BaCl_2$	1.0	0.03	0.02	0.00	-	0.02	0.08	0.04	0.04	-	0.08
1.0 M $MgCl_2$	1.0	0.01	0.02	0.00	-	0.01	0.05	0.04	0.06	-	0.05
1.0 M $ZnCl_2$	1.0	0.05	0.04	0.03	-	0.00	0.06	0.04	0.06	-	0.04

E.2 Changes to mono-uronate configurational equilibria upon the introduction of metal salts

E.2.1 Calculating the position of uronate configurational equilibria and the associated errors

In the discussions below, the following abbreviations are used:

%P = the mol% of pyranose species in solution

%F = the mol% of furanose species in solution

%αP = the mol% of α-pyranose species in solution

%βP = the mol% of β-pyranose species in solution

α/β = the ratio of %αP:%βP

%αF = the mol% of α-furanose species in solution

%βF = the mol% of β-furanose species in solution

σ%αP = the error in %αP

σ%βP = the error in %βP

σ%F = the error in %F

And, hence, the following relationships are also assumed to be true:

%αP + %βP = %P

%αF + %βF = %F

%P + %F = 100 %

Whilst previous reports rely solely on the ratio of anomeric ^{1}H NMR signals to determine α/β, the spectra acquired in the preparation of this thesis were well enough resolved to utilise signals arising from other protons too. Hence, for each well-resolved signal arising from a proton on a particular conformer, a value for the mol% of that conformer in the solution could be obtained. For example, the integral of the signal of H1 of an α-pyranose conformer measured against a standard reference peak ($\int\alpha$P(H1)), could subsequently be translated into a mol% value (%αP(1)) according to Equation (E.1):

$$\%\alpha\mathrm{P}(1) = \frac{\int \alpha\mathrm{P}(\mathrm{H1})}{\left(\frac{\int \alpha\mathrm{P}(\mathrm{H1}) + \int \alpha\mathrm{P}(\mathrm{H2}) + \ldots \int \alpha\mathrm{P}(\mathrm{H}i)}{i}\right) + \left(\frac{\int \beta\mathrm{P}(\mathrm{H1}) + \int \beta\mathrm{P}(\mathrm{H2}) + \ldots \int \beta\mathrm{P}(\mathrm{H}j)}{j}\right) + \int \alpha\mathrm{F}(\mathrm{H}) + \int \beta\mathrm{F}(\mathrm{H})} \mathrm{X}\ 100 \qquad \text{[Eq. E.1]}$$

Where $\int\beta$P(H1), $\int\beta$P(H2), and $\int\beta$P(H*j*) represent the integral of signals arising from the *β*-pyranose anomer, and *α*F(H) and *β*F(H) represent the integral of single signals arising from the *α*- and *β*-furanose anomers.

Integrating other signals from the same *α*-anomer ($\int\alpha$P(H2), $\int\alpha$P(H3), …$\int\alpha$P(H*i*)) in an analogous fashion to $\int\alpha$P(H1), gives a total of *i* repeat measurements for %*α*P (%*α*P(1), (%*α*P(2)…(%*α*P(*i*)). Averaging %*α*P(1)-(*i*) to give a mean value for %*α*P helps to reduce errors from small variations in the peak areas, baseline, spectral distortions, and so on. However, in order to minimise errors in %*α*P arising from minor fluctuations in temperature, pH, concentrations, ionic strength, *etc.* the entire set of experiments were repeated. The repeat run gave rise to a second set of values for %*α*P: one for Run 1 and one for Run 2. The values from both runs were then combined to give an average value of the mol% of *α*-pyranose in that particular sample according to Equation E.2:

$$\%\alpha\mathrm{P} = \frac{\text{Run 1}\,[\%\alpha\mathrm{P}(1) + \%\alpha\mathrm{P}(2) + \ldots\%\alpha\mathrm{P}(i)\,] + \text{Run 2}\,[\%\alpha\mathrm{P}(1) + \%\alpha\mathrm{P}(2) + \ldots\%\alpha\mathrm{P}(i)\,]}{2i} \qquad \text{[Eq. E.2]}$$

The uncertainty in the value of %*α*P (σ%*α*P) could then be obtained from Equation E.3:

$$\sigma\%\alpha\mathrm{P} = \frac{\%\alpha\mathrm{P}(\text{max value}) - \%\alpha\mathrm{P}(\text{min value})}{2\sqrt{2i}} \qquad \text{[Eq. E.3]}$$

An identical treatment can then be carried out using peaks assigned to the *β*-pyranose anomer, giving rise to a value for %*β*P and associated uncertainty σ%*β*P. The *α*- and *β*-furanose peaks account for a very small percentage of the species in solution (< 10 mol%) and so such an extensive treatment as was carried out for the pyranose configurations was not required. Instead, only two peaks (one for the *α*- and one for the *β*-furanose anomers) were integrated and summed together in order to give a single value for %F (and σ%F) in each sample.

When %*α*P and %*β*P had been calculated, a value for the %*α*P:%*β*P ratio (referred to as *α*/*β* in the text) can be calculated according to Equation E.4

$$\alpha/\beta = \frac{\%\alpha P}{\%\beta P} \qquad \text{[Eq. E.4]}$$

α/*β* has an associated uncertainty, σ(α/β), calculated according to Equation E.5:

$$\sigma(\alpha/\beta) = \frac{\%\alpha P}{\%\beta P}\sqrt{\left(\frac{\sigma\alpha P\%}{\%\alpha P}\right)^2 + \left(\frac{\sigma\%\beta P}{\%\beta P}\right)^2} \qquad \text{[Eq. E.5]}$$

E.2.2 Tabulated values of %αP, %βP, %F, and α/β for mono-uronates in the presence of various metal salts

Table E.9 Configurational equilibria of D-glucuronate under various conditions

D-glucuronate (Glc)									
Solution	**pH***	**%α P**	**±σ**	**%β P**	**±σ**	**%F**	**±σ**	**α/β**	**±σ**
No metal	7.5	42.4	*0.7*	56.2	*0.2*	1.4	*0.1*	0.75	*0.01*
1.0 M NaCl	7.5	42.2	*0.7*	56.6	*0.6*	1.2	*0.1*	0.75	*0.01*
1.0 M KCl	7.5	40.0	*0.8*	58.3	*0.5*	1.7	*0.3*	0.69	*0.01*
1.0 M $MgCl_2$	7.5	43.4	*0.9*	52.8	*0.3*	3.7	*0.3*	0.82	*0.02*
1.0 M $SrCl_2$	7.5	46.9	*0.6*	48.3	*0.1*	4.8	*0.2*	0.97	*0.01*
1.0 M $BaCl_2$	7.5	41.5	*0.4*	55.2	*0.7*	3.3	*0.3*	0.75	*0.01*
1.0 M $CaCl_2$	7.5	47.0	*0.6*	45.8	*0.3*	7.1	*0.0*	1.03	*0.01*
1.0 M CaI_2	7.5	46.9	*0.8*	44.7	*0.5*	8.4	*0.1*	1.05	*0.02*
1.0 M $Ca(NO_3)_2$	7.5	47.2	*0.5*	46.5	*0.2*	6.2	*0.4*	1.02	*0.01*
No metal	1.0	47.2	*0.6*	49.9	*0.2*	2.9	*0.2*	0.95	*0.01*
1.0 M NaCl	1.0	47.0	*0.6*	49.9	*0.2*	3.1	*0.2*	0.94	*0.01*
1.0 M KCl	1.0	45.6	*0.6*	51.5	*0.2*	2.8	*0.4*	0.89	*0.01*
1.0 M $MgCl_2$	1.0	48.0	*0.6*	48.6	*0.3*	3.4	*0.3*	0.99	*0.01*
1.0 M $SrCl_2$	1.0	47.9	*1.0*	47.6	*0.6*	4.4	*0.1*	1.01	*0.02*
1.0 M $BaCl_2$	1.0	47.8	*1.0*	47.2	*0.7*	4.8	*0.4*	1.01	*0.03*
1.0 M $CaCl_2$	1.0	46.5	*0.6*	48.6	*0.2*	4.8	*0.5*	0.96	*0.01*
1.0 M $ZnCl_2$	1.0	47.2	*1.0*	48.7	*0.9*	4.1	*0.5*	0.97	*0.03*

Table E.10 Configurational equilibria of D-galacturonate under various conditions

D-galacturonate (Gal)									
Solution	**pH***	**%α P**	**±σ**	**%β P**	**±σ**	**%F**	**±σ**	**α/β**	**±σ**
No metal	7.5	37.5	*0.2*	53.5	*0.4*	9.1	*0.2*	0.70	*0.01*
1.0 M NaCl	7.5	36.2	*0.3*	56.6	*0.4*	7.2	*0.1*	0.64	*0.01*
1.0 M KCl	7.5	33.3	*0.3*	59.7	*0.6*	7.1	*0.2*	0.56	*0.01*
1.0 M $MgCl_2$	7.5	38.1	*0.4*	49.5	*0.7*	12.4	*0.0*	0.77	*0.01*
1.0 M $SrCl_2$	7.5	46.6	*0.4*	45.6	*0.4*	7.8	*0.4*	1.02	*0.01*
1.0 M $BaCl_2$	7.5	36.0	*0.2*	59.0	*0.5*	5.0	*0.3*	0.61	*0.01*
1.0 M $CaCl_2$	7.5	48.9	*0.2*	39.4	*0.4*	11.7	*0.3*	1.24	*0.01*
1.0 M CaI_2	7.5	47.7	*1.0*	40.4	*1.0*	12.0	*0.9*	1.18	*0.04*
1.0 M $Ca(NO_3)_2$	7.5	48.1	*0.2*	40.3	*0.5*	11.6	*0.3*	1.19	*0.01*
No metal	1.0	42.4	*0.2*	47.7	*0.3*	9.8	*0.4*	0.89	*0.01*
1.0 M NaCl	1.0	40.8	*0.3*	50.7	*0.7*	8.5	*0.2*	0.80	*0.01*
1.0 M KCl	1.0	38.1	*0.2*	54.1	*0.7*	7.8	*0.1*	0.70	*0.01*
1.0 M $MgCl_2$	1.0	40.1	*0.8*	50.6	*0.9*	9.5	*0.6*	0.79	*0.02*
1.0 M $SrCl_2$	1.0	43.2	*0.3*	48.0	*0.3*	8.8	*0.2*	0.90	*0.01*
1.0 M $BaCl_2$	1.0	40.9	*0.4*	51.4	*0.5*	7.7	*0.5*	0.80	*0.01*
1.0 M $CaCl_2$	1.0	43.2	*0.3*	47.5	*0.7*	9.4	*0.2*	0.91	*0.01*
1.0 M $ZnCl_2$	1.0	42.0	*0.3*	48.5	*1.3*	9.6	*0.5*	0.87	*0.02*

Table E.11 Configurational equilibria of L-guluronate under various conditions

L-guluronate (Gul)									
Solution	pH*	%α P	±σ	%β P	±σ	%F	±σ	α /β	±σ
No metal	7.5	16.6	0.3	78.6	0.4	4.8	0.9	0.21	0.00
1.0 M NaCl	7.5	18.9	0.5	77.6	0.2	3.6	0.4	0.24	0.01
1.0 M KCl	7.5	15.6	0.4	80.7	0.2	3.7	0.5	0.19	0.01
1.0 M $MgCl_2$	7.5	19.6	0.4	74.4	0.5	6.0	0.5	0.26	0.01
1.0 M $SrCl_2$	7.5	51.3	0.4	42.6	0.7	6.2	0.3	1.20	0.02
1.0 M $BaCl_2$	7.5	35.1	0.1	60.8	0.5	4.1	0.1	0.58	0.00
1.0 M $CaCl_2$	7.5	54.7	0.8	36.6	0.7	9.0	0.3	1.50	0.03
1.0 M CaI_2	7.5	56.2	0.3	32.7	0.4	11.1	0.4	1.72	0.02
1.0 M $Ca(NO_3)_2$	7.5	48.5	1.3	40.7	1.2	10.8	0.1	1.19	0.05
No metal	1.0	16.7	0.2	79.0	0.2	4.2	0.4	0.21	0.00
1.0 M NaCl	1.0	19.0	0.3	77.5	0.5	3.5	0.2	0.25	0.00
1.0 M KCl	1.0	16.1	0.3	81.0	0.4	3.0	0.3	0.20	0.00
1.0 M $MgCl_2$	1.0	16.7	0.3	77.6	0.4	5.7	0.1	0.21	0.00
1.0 M $SrCl_2$	1.0	49.0	0.4	46.4	0.3	4.6	0.7	1.05	0.01
1.0 M $BaCl_2$	1.0	39.2	0.2	57.4	0.7	3.4	1.1	0.68	0.01
1.0 M $CaCl_2$	1.0	50.4	0.4	45.4	0.7	4.3	0.6	1.11	0.02
1.0 M $ZnCl_2$	1.0	17.8	0.8	76.8	0.4	5.4	0.5	0.23	0.01

Table E.12 Configurational equilibria of D-mannuronate under various conditions

D-mannuronate (Man)									
Solution	pH*	%α P	±σ	%β P	±σ	%F	±σ	α /β	±σ
No metal	7.5	67.1	0.8	28.4	0.3	4.7	0.5	2.36	0.04
1.0 M NaCl	7.5	63.7	0.6	31.1	0.4	5.3	1.2	2.05	0.03
1.0 M KCl	7.5	61.6	0.3	34.7	0.3	3.7	0.2	1.77	0.02
1.0 M $MgCl_2$	7.5	64.8	0.7	28.2	0.1	6.7	0.4	2.29	0.03
1.0 M $SrCl_2$	7.5	61.8	0.5	29.5	0.1	8.6	1.1	2.10	0.02
1.0 M $BaCl_2$	7.5	54.7	0.6	40.2	0.4	5.2	0.2	1.36	0.02
1.0 M $CaCl_2$	7.5	63.1	0.6	25.4	0.3	11.4	0.3	2.48	0.04
1.0 M CaI_2	7.5	58.9	0.7	28.9	0.6	12.2	0.4	2.04	0.05
1.0 M $Ca(NO_3)_2$	7.5	61.4	0.5	24.6	0.1	14.0	0.5	2.49	0.02
No metal	1.0	72.3	0.9	23.6	0.4	4.1	0.9	3.06	0.07
1.0 M NaCl	1.0	67.6	0.5	26.8	0.4	5.7	0.4	2.52	0.05
1.0 M KCl	1.0	65.1	1.5	29.5	0.1	5.4	0.1	2.21	0.05
1.0 M $MgCl_2$	1.0	67.7	0.5	27.4	0.5	4.6	0.4	2.47	0.05
1.0 M $SrCl_2$	1.0	62.9	0.9	27.2	0.4	9.8	0.2	2.31	0.05
1.0 M $BaCl_2$	1.0	60.2	1.0	31.8	0.3	8.1	0.4	1.90	0.04
1.0 M $CaCl_2$	1.0	64.3	1.0	25.7	0.3	10.0	0.5	2.50	0.05
1.0 M $ZnCl_2$	1.0	68.3	0.8	25.9	0.4	5.8	0.5	2.64	0.05

E.3 References

1 J. Burgess, in *Metal ions in solution*, Ellis Horwood Limited, Chichester, 1978, pp. 38–74.

2 J. Davies, S. Ormondroyd and M. C. R. Symons, *Trans. Faraday Soc.*, 1971, **67**, 3465–3473.

3 A. D. Buckingham, *Can. J. Chem.*, 1960, **38**, 300–307.

4 J. B. Hasted, D. M. Ritson and C. H. Collie, *J. Chem. Phys.*, 1948, **16**, 1–21.

Appendix F: Characteristic peaks used to confirm the identification of crystalline materials *via* Powder X-ray diffraction (PXRD) analysis.

Identified crystallite		Powder Diffraction File (PDF) number*	Characteristic peaks (2θ)	Normalised peak intensity	Miller indices		
Name	Formula				h	k	l
Sodium carbonate (Natrite)	Na_2CO_3	#00-019-130					
			30.1	90	0	0	2
			34.1†	60	0	2	0
			34.5†	45	-1	1	2
			35.2	100	3	1	0
			38.0	95	1	1	2
Metallic copper	Cu	#00-004-0836					
			43.3	100	1	1	1
			50.4	46	2	0	0
			74	20	2	2	0
Potassium chloride (Sylvite)	KCl	#00-001-0786					
			28.5	100	2	0	0
			40.7	60	2	2	0
			50.4	14	2	2	2
			66.8	12	4	2	0
Sodium chloride (Halite)	NaCl	#00-005-0628					
			31.7	100	2	0	0
			45.4	55	2	2	0
			56.5	15	2	2	2
Zinc(II) oxide (Zincite)	ZnO	#00-005-0664					
			31.7	71	1	0	0
			34.4	56	0	0	2
			36.3	100	1	0	1
Metallic nickel	Ni	#00-004-0850					
			44.5	100	1	1	1
			51.8	42	2	0	0
			76.4	21	2	2	0
Calcium carbonate (Calcite)	$CaCO_3$	#00-005-0586					
			29.4	100	1	0	4
			35.9	14	1	1	0
			39.4	18	1	1	3
			43.1	18	2	0	2
			47.4	17	0	1	8
			48.5	17	1	1	6
Calcium oxide	CaO	#00-004-0777					
			32.2	34	1	1	1
			37.4	100	2	0	0
			53.9	45	2	2	0
Calcium hydroxide	$Ca(OH)_2$	#00-004-0733					
			28.6	23	1	0	0
			34.1	100	1	0	1
			47.1	42	1	0	2
			50.8	36	1	1	0
			54.3	21	1	1	1
Magnesium oxide	MgO	#00-004-0829					
			36.9	10	1	1	1
			42.9	100	2	0	0
			62.3	52	2	2	0
Metallic cobalt	Co	#00-015-0806					
			44.2	100	1	1	1
			51.5	40	2	0	0
			75.8	25	2	2	0

* From the International Centre for Diffraction Data (ICDD) Powder Diffraction Database 4.1302 (2013)

† Detected as a single peak

Appendix G – Raw data from the FTIR analysis of alginates and related uronides

Table G.1 FTIR spectra of samples of sodium alginate

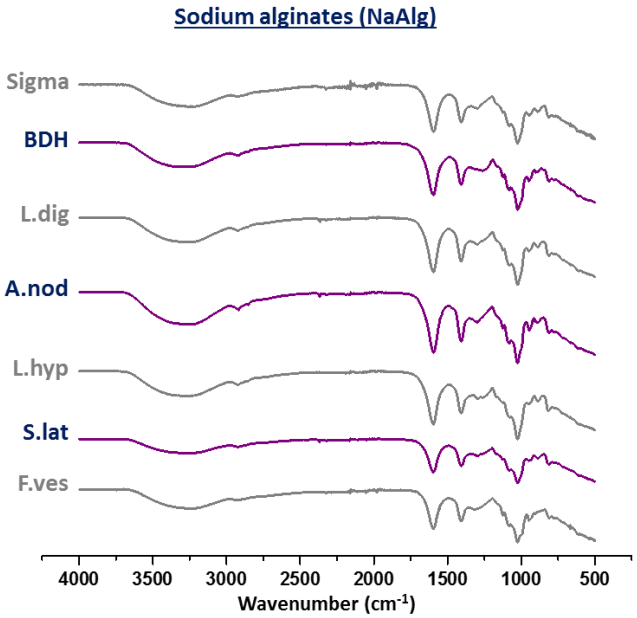

Table G.2 FTIR spectra of samples of copper(II) alginate

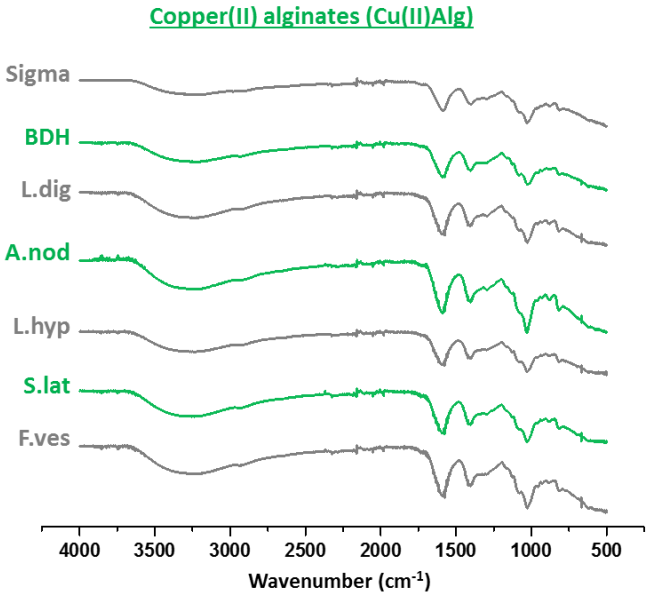

Table G.3 FTIR spectra of samples of calcium alginate

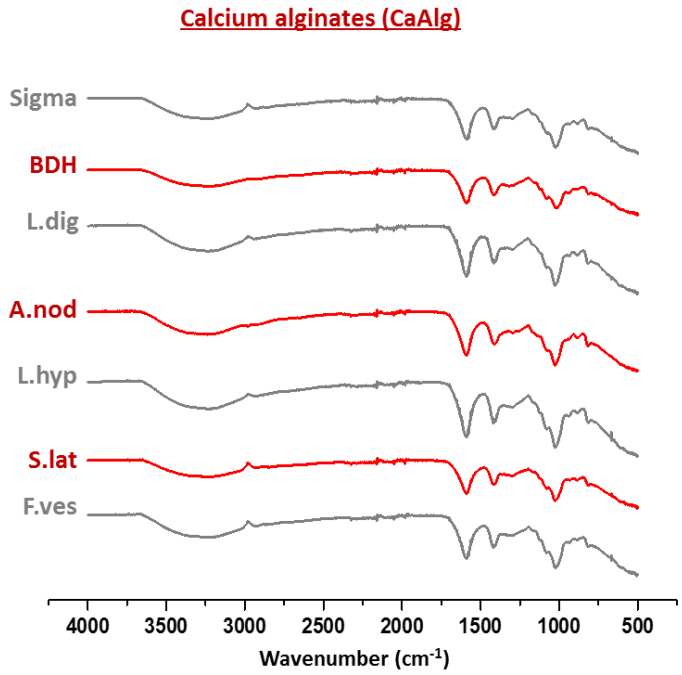

Table G.4 FTIR spectra of samples of alginic acid and various metal alginates

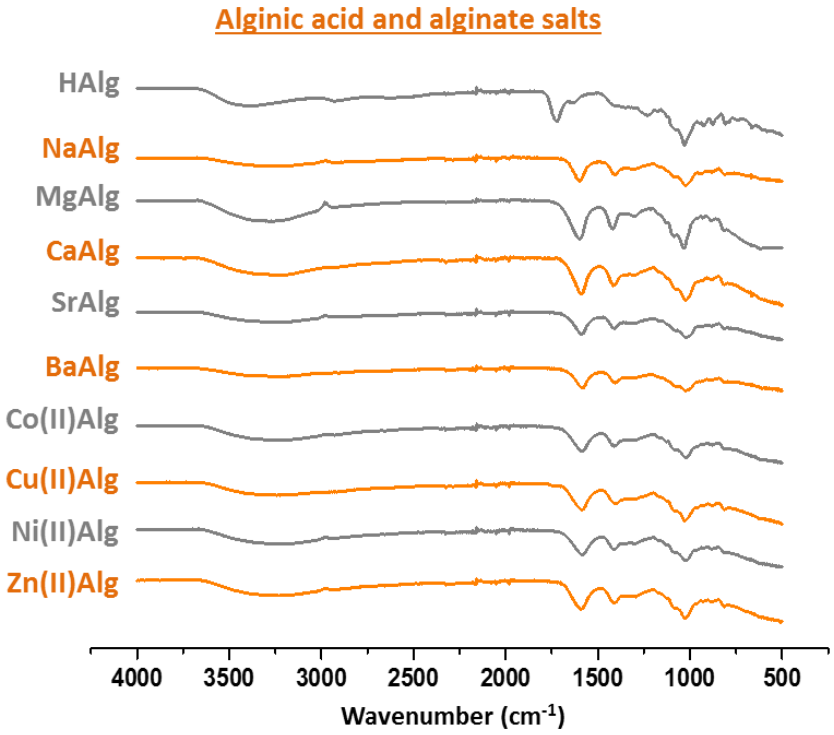

Table G.5 FTIR spectra of samples of pectin and various pectinate salts

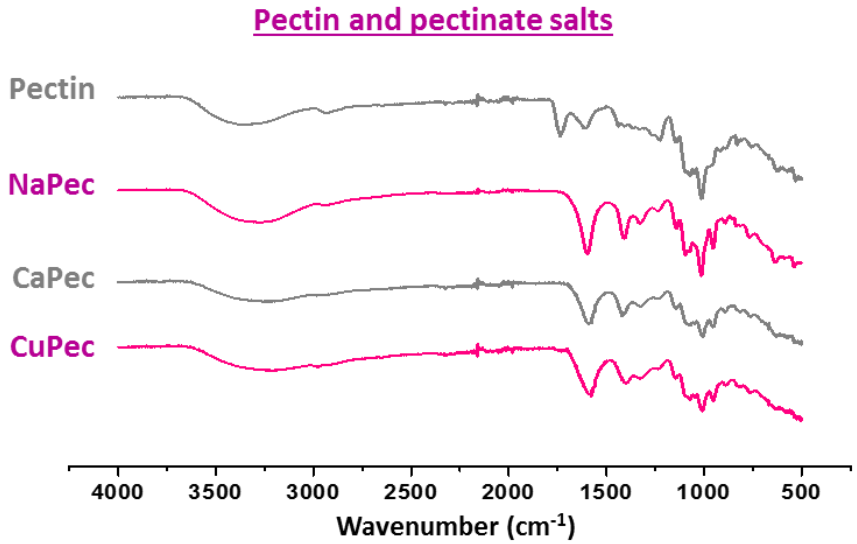

Table G.6 FTIR spectra of D-galacturonic acid and various D-galacturonate salts

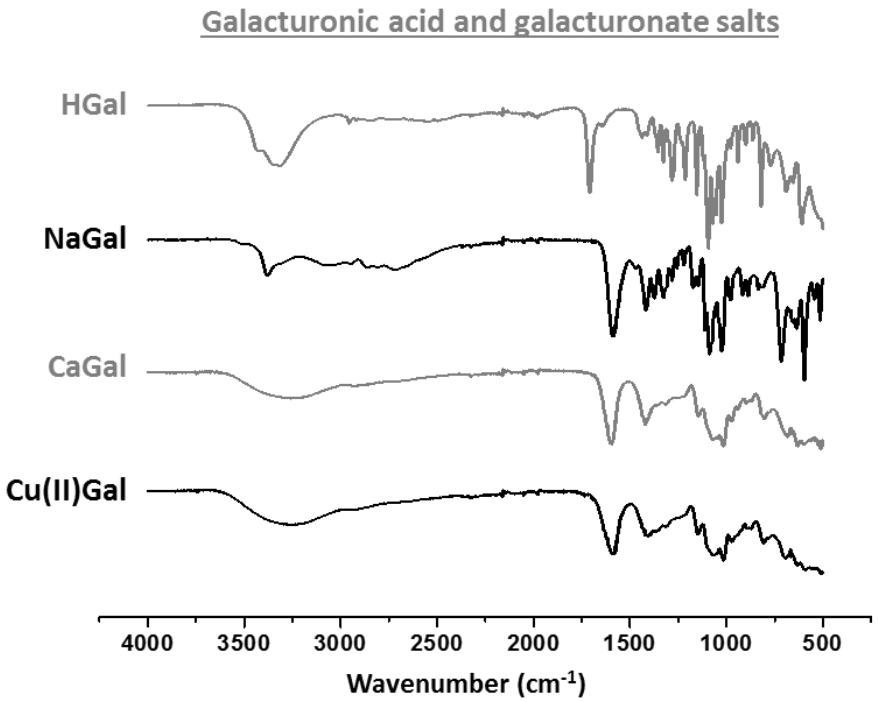

Table G.7 FTIR spectra of D-glucuronic acid and various D-glucuronate salts

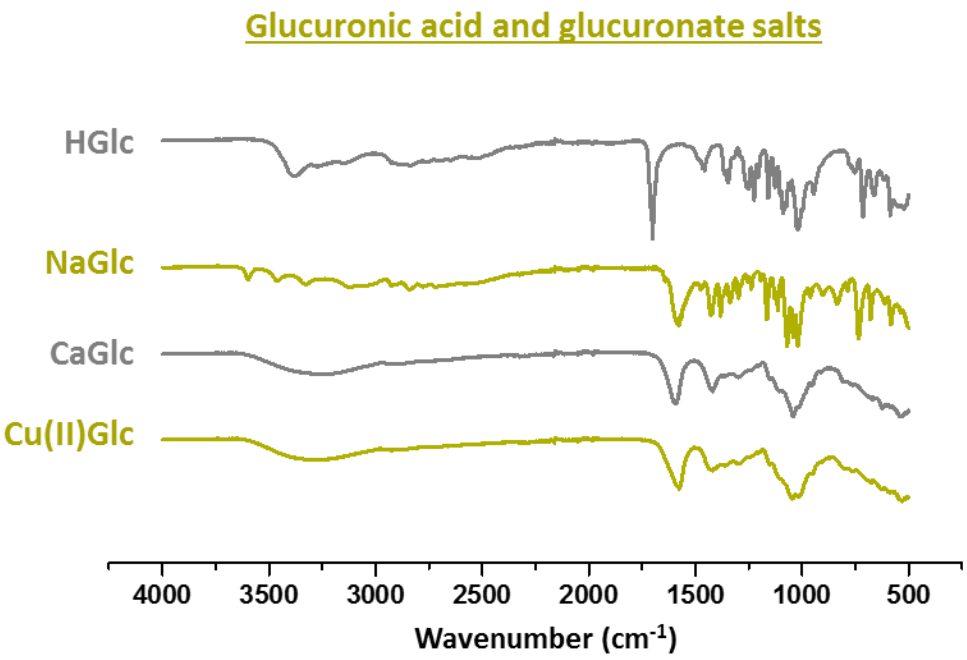

Appendix H – Results from the elemental analysis of alginates and related uronides

H.1 Results from elemental analyses

Table H.1 Elemental analyses of samples of sodium alginate

name **abbreviation**	**Source**	**H_2O content wt.%**	**Formula**	**Calculated (Calc) and experimentally determined (Exp) elemental analyses**	**C wt.%**	**H wt.%**	**M wt.%**
sodium alginate **NaAlg-SIG**	Sigma – used as received	11.8	$C_6H_7O_6Na$.(1.5 H_2O)	Calc	34.04	4.06	10.06
				Exp	29.37	3.91	10.21
sodium alginate-BDH **NaAlg-BDH**	BDH – used as received	14.5	$C_6H_7O_6Na$.(1.9 H_2O)	Calc	31.10	4.68	9.92
				Exp	30.18	4.04	8.68
sodium alginate-AN **NaAlg-AN**	Extracted from A. Nodosum	7.9	$C_6H_7O_6Na$.(0.9 H_2O)	Calc	33.50	4.17	10.69
				Exp	30.25	4.09	9.21
sodium alginate-LD **NaAlg-LD**	Extracted from L. Digitata	9.6	$C_6H_7O_6Na$.(1.2 H_2O)	Calc	32.88	4.30	10.49
				Exp	30.17	4.18	9.67
sodium alginate-FV **NaAlg-FV**	Extracted from F. Vesiculosis	13.7	$C_6H_7O_6Na$.(1.7 H_2O)	Calc	31.39	4.62	10.01
				Exp	30.06	3.83	8.97
sodium alginate-SL **NaAlg-SL**	Extracted from L. Saccharina	10.9	$C_6H_7O_6Na$.(1.3 H_2O)	Calc	32.41	4.40	10.34
				Exp	30.11	3.86	9.21
Sodium alginate-LH **NaAlg-LH**	Extracted from L. Hyperborea	9.1	$C_6H_7O_6Na$.(1.1 H_2O)	Calc	33.06	4.27	10.55
				Exp	29.16	3.60	8.94

For those extracted from seaweeds, %N was between 0.0 – 0.2 wt.%

Table H.2 Elemental analyses of samples of copper(II) alginate

name **abbreviation**	**Source**	**H_2O content wt.%**	**Formula**	**Calculated (Calc.) and experimentally determined (Exp.) elemental analyses**	**C wt.%**	**H wt.%**	**M wt.%**
Copper(II) alginate **Cu(II)Alg-SIG**	Prepared from NaAlg	11.2	$C_6H_7O_6Cu_{0.5}$.(1.4 H_2O)	Calc	30.93	4.29	13.64
				Exp	30.76	4.18	11.05
Copper(II) alginate-BDH **Cu(II)Alg-BDH**	Prepared from NaAlg-BDH	13.7	$C_6H_7O_6Cu_{0.5}$.(1.8 H_2O)	Calc	30.06	4.49	13.25
				Exp	27.79	4.01	10.20
Copper(II) alginate-AN **Cu(II)Alg-AN**	Prepared from NaAlg-AN	17.1	$C_6H_7O_6Cu_{0.5}$.(2.4 H_2O)	Calc	28.87	4.75	12.73
				Exp	27.83	4.04	11.15
Copper(II) alginate-LD **Cu(II)Alg–LD**	Prepared from NaAlg-LD	15.5	$C_6H_7O_6Cu_{0.5}$.(1.7 H_2O)	Calc	29.43	4.63	12.98
				Exp	27.32	4.02	11.89
Copper(II) alginate-FV **Cu(II)Alg–FV**	Prepared from NaAlg-FV	13.7	$C_6H_7O_6Cu_{0.5}$.(1.8 H_2O)	Calc	30.06	4.49	13.25
				Exp	27.91	3.92	13.76
Copper(II) alginate-SL **Cu(II)Alg–SL**	Prepared from NaAlg-SL	13.0	$C_6H_7O_6Cu_{0.5}$.(1.7 H_2O)	Calc	30.30	4.43	13.36
				Exp	27.96	4.02	11.71
Copper(II) alginate-LH **Cu(II)Alg-LH**	Prepared from NaAlg-LH	15.7	$C_6H_7O_6Cu_{0.5}$.(2.1 H_2O)	Calc	29.36	4.64	12.95
				Exp	27.55	4.09	11.76

For those from alginates extracted from seaweeds, %N was between 0.0 – 0.2 wt.%

Table H.3 Elemental analyses of samples of calcium alginate

name abbreviation	Source	H_2O content wt.%	Formula /unit	Calculated (Calc.) and experimentally determined (Exp.) elemental analyses	C wt.%	H wt.%	M wt.%
Calcium alginate **CaAlg-SIG**	Prepared from NaAlg	15.7	$C_6H_7O_6Ca_{0.5}$.(1.7 H_2O)	Calc	31.12	4.82	8.66
				Exp	31.35	4.55	8.25
Calcium alginate-BDH **CaAlg–BDH**	Prepared from NaAlg-BDH	14.3	$C_6H_7O_6Ca_{0.5}$.(1.8 H_2O)	Calc	31.64	4.71	8.80
				Exp	29.19	4.28	7.68
Calcium alginate-AN **CaAlg–AN**	Prepared from NaAlg-AN	15.6	$C_6H_7O_6Ca_{0.5}$.(2.0 H_2O)	Calc	31.16	4.81	8.67
				Exp	29.57	4.26	7.08
Calcium alginate-LD **CaAlg–LD**	Prepared from NaAlg-LD	16.6	$C_6H_7O_6Ca_{0.5}$.(2.2 H_2O)	Calc	30.79	4.88	8.56
				Exp	28.57	4.21	7.54
Calcium alginate-FV **CaAlg–FV**	Prepared from NaAlg-FV	14.1	$C_6H_7O_6Ca_{0.5}$.(1.8 H_2O)	Calc	31.72	4.69	8.82
				Exp	29.20	4.15	6.48
Calcium alginate-SL **CaAlg–SL**	Prepared from NaAlg-SL	18.0	$C_6H_7O_6Ca_{0.5}$.(2.4 H_2O)	Calc	30.28	4.99	8.42
				Exp	28.71	4.19	7.11
Calcium alginate-LH **CaAlg–LH**	Prepared from NaAlg-LH	14.6	$C_6H_7O_6Ca_{0.5}$.(1.9 H_2O)	Calc	31.53	4.73	8.77
				Exp	28.93	4.24	7.39

For those from alginates extracted from seaweeds, %N was between 0.0 – 0.2 wt.%

Table H.4 Elemental analyses of alginic acid and various metal alginates

name abbreviation	Source	H_2O content wt.%	Formula	Calculated (Calc.) and experimentally determined (Exp.) elemental analyses	C wt.%	H wt.%	M wt.%
Alginic acid **HAlg**	Prepared from NaAlg	7.0	$C_6H_8O_6$.(0.7 H_2O)	Calc	38.17	5.03	0.00
				Exp	37.28	4.83	0.18
Alginic acid **HAlg-B**	Sigma – used as received	7.9	$C_6H_8O_6$.(0.8 H_2O)	Calc	37.68	5.11	0.00
				Exp	37.79	4.83	0.32
Cobalt(II)alginate **Co(II)Alg**	Prepared from NaAlg	12.8	$C_6H_7O_6Co_{0.5}$.(1.7 H_2O)	Calc	30.71	4.45	12.55
				Exp	30.41	4.49	12.64
Nickel(II) alginate **Ni(II)Alg**	Prepared from NaAlg	13.7	$C_6H_7O_6Ni_{0.5}$.(1.8 H_2O)	Calc	30.41	4.52	12.39
				Exp	29.02	4.62	12.88
Zinc(II) alginate **Zn(II)Alg**	Prepared from NaAlg	13.3	$C_6H_7O_6Zn_{0.5}$.(1.8 H_2O)	Calc	30.06	4.44	13.64
				Exp	29.5	4.18	14.45
Magnesium alginate **MgAlg**	Prepared from HAlg-B	20.0	$C_6H_7O_6Mg_{0.5}$.(2.6 H_2O)	Calc	30.78	5.26	5.19
				Exp	30.43	5.33	4.73
Barium alginate **BaAlg**	Prepared from NaAlg	10.6	$C_6H_7O_6Ba_{0.5}$.(1.1 H_2O)	Calc	26.42	3.78	25.18
				Exp	24.64	3.53	27.17
Strontium alginate **SrAlg**	Prepared from NaAlg	10.6	$C_6H_7O_6Sr_{0.5}$.(2.6 H_2O)	Calc	29.42	4.08	17.89
				Exp	28.35	4.05	17.40

Table H.5 Elemental analyses of mono-uronic acids and their salts

name **abbreviation**	**Source**	**H_2O content wt.%**	**Formula**	**Calculated (Calc.) and experimentally determined (Exp.) elemental analyses**	C wt.%	H wt.%	M wt.%
D-glucuronic acid **HGlu**	Sigma – used as received	2.0	$C_6H_{10}O_7$.(0.2 H_2O)	Calc	36.37	5.32	0.00
				Exp	37.13	5.20	0.00
Sodium D-glucuronate **NaGlu**	Prepared from HGlu	3.0	$C_6H_9O_7Na$.(0.4 H_2O)	Calc	32.34	4.42	10.32
				Exp	29.37	4.71	9.82
Calcium D-glucuronate **CaGlu**	Prepared from HGlu	5.1	$C_6H_9O_7Ca_{0.5}$.(0.6 H_2O)	Calc	32.08	4.62	8.92
				Exp	30.74	4.73	7.90
Copper(II) D-glucuronate **Cu(II)Glu**	Prepared from HGlu	11.1	$C_6H_9O_7Cu_{0.5}$.(1.6 H_2O)	Calc	28.48	4.84	12.56
				Exp	27.60	4.09	14.93
D-galacturonic acid **HGal**	Sigma – used as received	9.7	$C_6H_{10}O_7$.(1.2 H_2O)	Calc	33.51	5.79	0.00
				Exp	34.00	5.68	0.03
Sodium D-galacturonate **NaGal**	Prepared from HGal	5.4	$C_6H_9O_7Na$.(0.7 H_2O)	Calc	31.54	4.58	10.06
				Exp	32.50	4.22	10.30
Calcium D-galacturonate **CaGal**	Prepared from HGal	7.7	$C_6H_9O_7Ca_{0.5}$.(1.0 H_2O)	Calc	31.20	4.80	8.68
				Exp	30.19	4.82	8.18
Copper(II) D-galacturonate **Cu(II)Gal**	Prepared from HGal	13.1	$C_6H_9O_7Cu_{0.5}$.(1.9 H_2O)	Calc	27.84	4.98	12.28
				Exp	28.21	4.34	13.49

Table H.6 Elemental analyses of pectin and various pectinate salts

name **abbreviation**	**Source**	**H_2O content wt.%**	**Experimentally determined elemental analyses** C wt.%	H wt.%	M wt.%
Pectin **HPec**	Sigma – used as received	11.4	37.66	5.13	1.40
Sodium pectinate **NaPec**	Prepared from HPec	17.4	29.63	4.31	7.95
Calcium pectinate **CaPec**	Prepared from NaPec	13.6	31.90	4.66	2.76
Copper(II) pectinate **Cu(II)Pec**	Prepared from NaPec	17.4	28.77	4.78	9.38

H.2 A note on the causes of discrepancies in the elemental analyses of uronates containing sodium

Table H.1 shows values for the wt.%C of **NaAlg** samples that are consistently lower than the theoretical values. It is believed that such a phenomena arises because of the formation of (highly stable) Na_2CO_3 within cold spots of the elemental analyser.[1] To test this theory, samples of pure $CaCO_3$ and $Cu_2(OH)_2CO_3$ were analysed, and were found to give values for their wt.%C within ± 0.01 of the theoretical value. Meanwhile, performing the same analysis on Na_2CO_3 under identical conditions, gave a result corresponding to less than half of the wt.% carbon content that was expected from the formula alone. Hence, it was concluded that the available equipment provides an underestimate of wt.%C for samples containing Na^+ ions.

1 K. Chandran, M. Kamruddin, S. Anthonysamy and V. Ganesan, in *Reactions and Mechanisms in Thermal Analysis of Advanced Materials*, eds. A. Tiwari and B. Raj, John Wiley & Sons, Inc., Hoboken, NJ, USA, 2015, pp. 333–392.

Appendix I – Results from the elemental analysis of kelps, and related biomass

Table I.1 Results from the elemental analysis of various kelp samples before and after treatment in solutions of either Ca^{2+} or Cu^{2+}

Species	Treatment	H_2O wt.%	Ash wt.%	Elemental analysis (wt.%)										C/H ratio
				C	H	N	S	Na	K	Mg	Ca	Sr	Cu	
Ascophyllum nodosum **(A.nod)**	Untreated	7.4	33.2	32.63	4.31	1.55	2.88	3.63	3.62	0.80	1.06	0.06	0.00	7.57
	Ca-treated	5.8	20.5	37.12	4.91	1.12	ND	0.00	0.00	0.00	1.59*	0.00	0.00	7.56
	Cu-treated	11.2	12.1	34.64	4.47	1.13	ND	0.00	0.00	0.00	0.00	0.00	2.72*	7.75
Laminaria digitata **(L.dig)**	Untreated	6.3	31.9	28.30	4.16	1.76	2.55	3.90	7.03	0.76	1.13	0.09	0.00	6.80
	Ca-treated	9.5	17.2	35.18	5.22	1.39	ND	0.00	0.00	0.00	2.73*	0.00	0.00	6.74
	Cu-treated	1.8	13.6	34.13	4.95	1.37	ND	0.00	0.00	0.00	0.00	0.00	1.14*	6.89
Laminaria hyperborea **(L.hyp)**	Untreated	5.3	31.4	32.77	4.88	2.21	2.43	2.54	6.91	0.54	0.93	0.11	0.00	6.72
	Ca-treated	10.8	17.7	35.85	4.96	1.57	ND	0.00	0.00	0.00	1.66*	0.00	0.00	7.23
	Cu-treated	6.8	12.6	34.67	4.80	1.51	ND	0.00	0.00	0.00	0.00	0.00	0.65*	7.22
Saccharina latissima **(S.lat)**	Untreated	6.1	26.6	30.85	4.32	2.11	2.08	3.01	4.30	0.64	0.79	0.06	0.00	7.14
	Ca-treated	3.8	15.7	36.31	5.28	1.79	ND	0.00	0.00	0.00	1.61*	0.00	0.00	6.88
	Cu-treated	6.0	13.9	34.45	4.89	1.81	ND	0.00	0.00	0.00	0.06	0.00	0.99*	7.04
Fucus vesiculosus **(F.ves)**	Untreated	6.0	40.9	35.98	4.37	1.53	2.40	2.41	3.73	0.60	0.89	0.09	0.00	8.23
	Ca-treated	4.6	18.4	37.56	4.88	1.61	ND	0.00	0.00	0.00	1.79*	0.00	0.00	7.70
	Cu-treated	4.4	12.8	36.37	4.56	1.48	ND	0.00	0.00	0.00	0.00	0.00	0.75*	7.98

*These results cannot be considered to be fully quantitative owing to an incomplete digestion of the biomass

Table I.2 Results from the elemental analysis of various samples of alginate-extracted algal-residue (**AE-AR**) before and after treatment in solutions of either Ca^{2+} or Cu^{2+}

Species	Treatment	Elemental analysis (wt.%)									C/H ratio
		C	H	N	Na	K	Mg	Ca	Sr	Cu	
Ascophyllum nodosum **(A.nod)**	Untreated	39.82	4.78	3.25	2.75	0.00	0.00	0.91	0.00	0.00	8.33
	Ca-treated	36.58	4.55	3.32	0.08	0.00	0.00	4.24	0.00	0.00	8.04
	Cu-treated	35.35	4.16	3.22	0.04	0.03	0.01	0.05	0.00	3.52	8.50
Laminaria digitata **(L.dig)**	Untreated	43.59	6.28	5.25	1.08	0.00	0.00	0.90	0.00	0.00	6.94
	Ca-treated	41.46	5.83	5.11	0.40	0.00	0.00	1.51	0.00	0.00	7.11
	Cu-treated	40.12	5.54	5.10	0.19	0.00	0.00	0.07	0.00	4.32	7.24
Laminaria hyperborea **(L.hyp)**	Untreated	42.23	5.37	3.86	2.00	0.00	0.00	0.13	0.00	0.00	7.86
	Ca-treated	39.44	4.94	3.74	0.16	0.00	0.00	2.75	0.00	0.00	7.98
	Cu-treated	38.85	4.86	3.77	0.07	0.02	0.01	0.06	0.00	2.85	7.99
Saccharina latissima **(S.lat)**	Untreated	42.41	5.47	5.16	2.39	0.00	0.00	0.44	0.00	0.00	7.75
	Ca-treated	40.01	5.53	4.96	0.12	0.00	0.00	2.37	0.00	0.00	7.24
	Cu-treated	39.12	5.3	4.94	0.01	0.01	0.01	0.02	0.00	2.98	7.38
Fucus vesiculosus **(F.ves)**	Untreated	39.05	4.82	3.05	3.60	0.00	0.00	0.69	0.00	0.00	8.10
	Ca-treated	35.73	4.35	3.01	0.06	0.07	0.02	4.17	0.00	0.00	8.21
	Cu-treated	34.93	4.05	3.15	0.07	0.03	0.02	0.03	0.00	3.40	8.62

Appendix J - Analysis of the M:G ratio of extracted alginates by ^{1}H NMR spectroscopy

J.1 Introduction

J.1.1 Background to methodology

As a linear copolymer of (1→4) linked α-L-guluronate (**G**) and β-D-mannuronate (**M**) residues, a number of methods have been developed to determine the monomeric composition (**M**:**G** ratio) and block structure (including the diad ratios **MM**:**GG**:**GM**, and triad ratios **GGG**:**GMM**:**GMG** etc.) of alginic acids.[1,2] In this regard, one of the most convenient and widely-utilised techniques revolves around the ^{1}H NMR spectroscopic analysis of samples of extracted alginate in an approach conceived initially by Penman and Sanderson,[3] and later developed by Grasdalen *et al.*[4–6] The method involves comparison of the integrals of a number of well-defined peaks in the deconvoluted anomeric region of a spectrum of a partially hydrolysed alginate sample. Since the devising of this method, the analysis of alginates by solution state ^{1}H NMR spectroscopy has become adopted as the American Society for Testing and Materials' (ASTM) standard procedure for obtaining compositional information of alginate block structures.[7] The ASTM methodology (as in the original procedures) includes a gentle acid hydrolysis to lower the M_w of the alginate and hence lower the viscosity of the solution, in addition to obtaining the ^{1}H NMR spectra at elevated temperatures (both to further reduce the viscosity and shift the HDO peak upfield of the anomeric region under investigation). The inclusion of a chelating agent (typically EDTA) to prevent line broadening by complexation of adventitious divalent cations to the alginate is now largely considered extraneous,[8] but is included in the following experiments for the sake of consistency.

J.1.2 Overview of data interpretation

The anomeric region in the ^{1}H NMR spectrum (approximately δ = 4.4 – 5.1 ppm) of partially hydrolysed alginates lies sufficiently to high frequency to enable confident assignment of particular signals to the corresponding protons in the polymer structure.[4,6] All signals originating from **G**(H_1), **G**(H_5), and **M**(H_1) (as depicted in Figure J.1) can be accounted for regardless of the neighbouring moieties to which the unit in question is adjoined.[†]

[†]The alginates are only partially hydrolysed in the analysis such that additional signals arising from newly formed terminal and reducing-end units are small enough to discount.

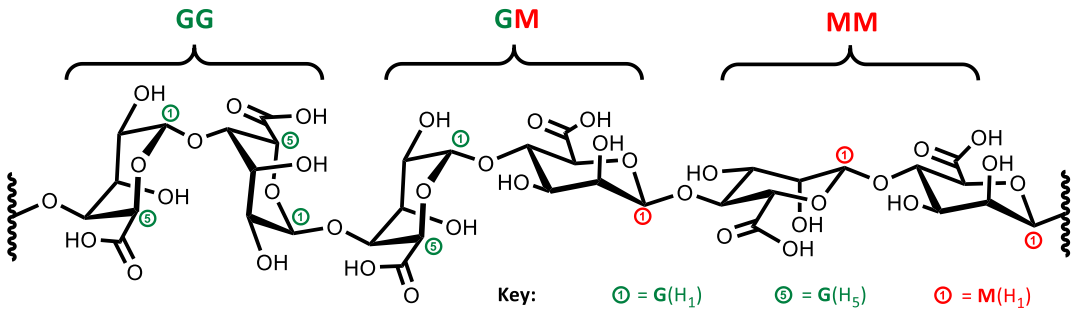

Figure J.1 Labelling of protons required for the analysis of alginates by ^{1}H NMR

Whilst the elevated temperatures (around 90 °C) at which the spectra are acquired shift the HDO signal to low freqeuncy and away from the peaks of interest there is, however, still some overlap between the **G**(H_5) and **M**(H_1) (see the example depicted in Figure J.2). Following a deconvolution analysis and peak identification according to the work of Grasdalen *et al.*[6] (see Table J.1), the intensities of appropriate signals can be summed in order to obtain compositional and structural information about the alginate. Here, the mathematical relationships given in Table J.2 can be used to determine the proportion of guluronate (F_G) and mannuronate (F_M) residues in the alginate chain, as well as the relative fraction of homo- (**MM** and **GG**) and hetero- (**GM** and **MG**) polymeric linkages (F_{MM}, F_{GG}, and $F_{GM,MG}$, respectively). From these relationships, the **M**:**G** ratio is defined as F_M: F_G. The data is also sufficient to establish information about the triad ratios (for example F_{MGM}:F_{MGG}), though this level of analysis was not deemed necessary for the work conducted in this thesis.

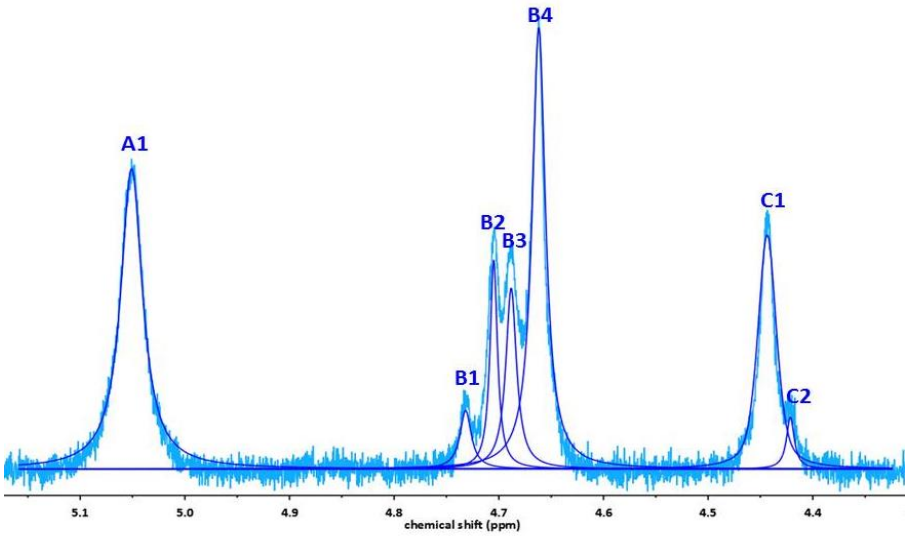

Figure J.2 Deconvolution of the anomeric region of ^{1}H NMR spectrum (500 MHz, 90 °C, D_2O, pD 7.0) of a sample of partially hydrolysed sodium alginate.

Table J.1 Assignments of peaks in Figure J.**2** according to Grasdalen *et al.*[6]

Peak name	Chemical shift δ (ppm)[a]	Assignment
A1	5.05	G (H_1)[b]
B1	4.73	GGM (H_5)
B2	4.70	MGM (H_5)
B3	4.69	MG (H_1)[c]
B4	4.66	MM (H_1)[d]
C1	4.44	GGG (H_5)
C2	4.42	MGG (H_5)

[a]Measured relative to the $(CH_3)_3Si$- signal of sodium 3-(trimethylsilyl)-1-propanesulphonate (δ = 0.00 ppm)
[b]Incorporating H_1 signal of GGG + MGG + GGM + MGM
[c]Incorporating H_1 signal of GMG + MMG
[d]Incorporating H_1 signal of GMM + MMM

Table J.2 Mathematical relationships between measured ^{1}H NMR signal intensities and chemical constitution of analysed alginates[7]

Summation of intensities of NMR signals according to the assignments in Table J.1*	**Converting signal intensities into chemical compositions:**
$\Sigma G = 0.5(A1 + C1 + C2 + 0.5(B1 + B2 + B3))$ $\Sigma M = B4 + 0.5(B1 + B2 + B3)$	$F_G = \Sigma G/(\Sigma M+\Sigma G)$ $F_M = \Sigma M/(\Sigma M+\Sigma G)$ $F_G + F_M = 1$
$\Sigma GG = 0.5(A1 + C1 + C2 - 0.5(B1 + B2 + B3))$ $\Sigma MM = B4$ $\Sigma MG = \Sigma GM = 0.5(B1 + B2 + B3)$	$F_{GG} = \Sigma GG/(\Sigma M+\Sigma G)$ $F_{MM} = \Sigma MM/(\Sigma M+\Sigma G)$ $F_{GM} = F_{MG} = \Sigma MG/(\Sigma M+\Sigma G)$ $F_{GG} + F_{GM} + F_{MG} + F_{MM} = 1$

*Where *A1*, *B1*, *B2*, etc. represent the measured intensity of the respective signals in the deconvoluted ^{1}H NMR spectrum of the alginate

J.2 Results and discussion

J.2.1 Compositional and structural analysis of alginates

The results of the compositional and structural analysis of alginates extracted from five wild brown macroalgae, two commercial samples, and a series of literature values are reported in Table J.3. For the alginates studied in this work, F_G values varied from 0.35 (*Ascophyllum nodosum*) to 0.66 (commercial *Laminaria hyperborea*), corresponding to a range of **M**:**G** ratios of 0.53 to 1.86. Unsurprisingly, the samples with higher guluronate contents also contained the highest proportion of **GG** linkages (represented by F_{GG}) and

vice versa for the mannuronate-rich samples. The proportion of hetero-polymeric linkages (represented by 2 X $F_{GM,MG}$) remained in the narrow range of 0.28 – 0.36, with the anticipated exception of the **G**-rich commercial *L. hyperborea*, which held an $F_{GM,MG}$ value of only 0.10.

Table J.3 Results of the ^{1}H NMR spectroscopic compositional and structural analysis of alginates from a number of wild seaweeds in comparison to commercial samples and literature values.

Alginate source	Alginate monomeric composition*			Alginate block structure*			Ref
	F_G	F_M	**M**:**G**	F_{GG}	F_{MM}	$F_{GM,MG}$	
This study:							
Laminaria digitata	0.43	0.57	**1.34**	0.25	0.39	0.18	This work
L. saccharina	0.47	0.53	**1.13**	0.29	0.35	0.18	This work
L. hyperborea	0.51	0.49	**0.95**	0.38	0.35	0.14	This work
L. hyperborea (BDH)**	0.66	0.34	**0.53**	0.56	0.25	0.10	This work
Macrocystis pyrifera (Sigma)**	0.44	0.56	**1.25**	0.26	0.38	0.18	This work
Fucus vesiculosus	0.56	0.44	**0.78**	0.40	0.28	0.16	This work
Ascophyllum nodosum	0.35	0.65	**1.86**	0.20	0.50	0.15	This work
Literature examples:							
L. digitata	0.41	0.59	**1.44**	0.25	0.43	0.16	9
L. digitata	0.38	0.62	**1.63**	0.25	0.49	0.13	4
L. saccharina (new blade)	0.35	0.65	**1.86**	0.25	0.55	0.10	9
L. saccharina (old blade)	0.46	0.54	**1.17**	0.32	0.40	0.14	9
L. hyperborea (blade)	0.55	0.45	**0.82**	0.38	0.28	0.17	9
L. hyperborea (stipe)	0.68	0.32	**0.47**	0.56	0.20	0.12	9
L. hyperborea (outer cortex)	0.75	0.25	**0.33**	0.66	0.16	0.09	9
L. hyperborea	0.70	0.30	**0.43**	0.66	0.26	0.04	4
M. pyrifera	0.39	0.61	**1.56**	0.16	0.38	0.23	9
M. pyrifera	0.37	0.63	**1.70**	0.23	0.49	0.14	10
F. vesiculosis	0.41	0.59	**1.44**	0.22	0.39	0.19	11
A. nodosum (fruiting body)	0.10	0.90	**9.00**	0.04	0.84	0.06	9
A. nodosum (old tissue)	0.36	0.64	**1.78**	0.16	0.44	0.20	9
A. nodosum	0.54	0.46	**0.85**	0.36	0.28	0.18	11
A. nodosum	0.40	0.60	**1.50**	0.20	0.40	0.20	4

*All reported to ± 0.01 except **M**:**G** ratio, which is reported to ± 0.02
**Commercial alginate (supplier in parentheses)

When comparing the **M**:**G** ratios and diad analyses obtained for samples in this work with literature values derived using the same technique, a good agreement is generally found. For example, the **M**:**G** ratios of 1.44 and 1.63 that have been reported for alginates from *L. digitata*,[4,9] correspond closely to the value of 1.34 for the alginate collected from the same species in this work. Similarly the F_{GG}, F_{MM}, and $F_{GM,MM}$ values for these three alginate samples are also in close agreement with each other. Indeed, given the variation in biochemical content of macroalgal samples generally, the similarities in alginate

composition and structure for similar species across different studies is perhaps quite surprising. The largest source of variation in this regard appears to be related to the age of the sample as well as the part of the algae from which the alginate is extracted. Thus, whilst the alginate of *A. nodosum* collected for this work has a similar composition to that from another study[9] (**M**:**G** ratios of 1.86 and 1.78 respectively), both are clearly quite different to alginate extracted from fruiting *A. nodosum* tissue (**M**:**G** ratios of 9.00). Similarly, the higher **M**:**G** ratio of the *L. hyperborea* alginate extracted as part of this work (0.95) in relation to others[9] (0.33 - 0.47) is indicative of the alginates having been taken from the different parts of the frond (in this case from the blade rather than the stipe and outer cortex). However, a more general understanding of the patterns and causes of variation in **M**:**G** ratio and alginate structure within samples of the same species appears to be lacking in current literature.

J.2.2 Repeatability of the analysis

With regards to the accuracy of the reported values, the ASTM suggest that, using this ^{1}H NMR methodology, a standard deviation in the value of F_G of ± 0.01 is achievable for values between 0.3 – 0.7 (a range that encompasses all of the measurements recorded here). Though extensive repeat experiments were not carried out for this study, repeating the analysis of alginate from *A. nodosum* on two independent occasions gave F_G values of 0.34 and 0.36, yielding a standard deviation of 0.01 and corroborating the error reported by the ASTM. Values of F_M, F_{GG}, F_{MM}, and $F_{GM,MG}$ are all also reported to ± 0.01, and the **M**:**G** ratio with an error of ± 0.02.

J.2.3 Implications of the M:G ratio for the thermochemical study of alginates

For the purposes of the thermochemical experiments carried out in Chapters 4 and 5 of this thesis, the macroalgae offer a useful range of **M**:**G** ratios and F_{GG}:F_{MM} structures. However, as further work was recommended to better elucidate the role that different stereochemical linkages have to play in the thermolysis of alginates (see Chapter 5), a more diverse selection of polymeric structures may be sought. In this case, it is suggested that systematic isolation of **M**-, **G**-, and **MG**- blocks be pursued *via* known methods,[12,13] as the necessary structural variation may be difficult to achieve through the use of naturally occurring samples alone.

J.3 Materials and methods

J.3.1 Preparing alginate samples for ^{1}H NMR spectroscopic analysis

Sodium alginate (20.0 ± 1.0 mg) obtained either commercially or through the extraction procedure detailed in Chapter 5 was first dissolved in deionised H_2O (40 mL). The pH of the algiante solution was lowered to 5.35 ± 0.05 through small additions of HCl (0.1 M) prior to heating of the stirred solution at 90 ˚C for 60 mins. Additional HCl was subsequently added to reduce the pH to 3.35 ± 0.05 and the solution was returned to the heat for a further 45 mins. Upon neutralisation (pH 7.0 ± 0.1) with NaOH (0.1 and 0.01 M), the partially-hydrolysed alginate was recovered by removal of the water *in vacuo*

(70 ˚C, 20 mbar). Prior to ^{1}H NMR spectroscopic analysis, the alginate was dissolved in D_2O (2.0 mL) (Apollo Scientific), dried *in vacuo* (70 ˚C, 20 mbar) and redissolved in D_2O (1.0 mL) containing sodium 3-(trimethylsilyl)-1-propanesulphonate (3.0 mg/mL D_2O) (Sigma) as a reference and disodium ethylenediaminetetraacetate dihydrate (1.0 mg/mL D_2O) (Sigma) as a chelating agent. The pH of the solution was, where necessary, returned to pH 7.0 ± 0.1 by small additions of NaOD (0.01 M) and then centrifuged (8000 rpm, 10 min) before transferring 500 μL to a Norell® XR-55-7 NMR tube (5.0 mm). The ^{1}H NMR spectrum of the sample was subsequently recorded at 90 ˚C on a Varian Inova 500 MHz spectrometer according to the parameters in Appendix D.

J.3.2 Analysis of the ^{1}H NMR spectra of digested alginate samples

Signals in the region 4.30 – 5.20 ppm (referenced against the $(C\underline{H}_3)_3Si$- signal of sodium 3-(trimethylsilyl)-1-propanesulphonate at δ = 0.00 ppm) were assigned according to the arguments in Section J.1.2. Following a baseline correction, deconvolution of the spectra was achieved using wholly Lorentzian line shapes with the A1:B1-4:C1-2 distribution depicted in Figure J.2, with small adjustments being made until the residual peak area between the real and simulated spectra was minimised. The intensities of the A, B, and C signals were then summed according to the relationships in Table J.2, and subsequently used to calculate F_G, F_M, F_{GG}, F_{MM}, and $F_{GM,MG}$.

J.4 References

1 P. Gacesa, *Carbohydr. Polym.*, 1988, **8**, 161–182.

2 A. I. Usov, *Russ. Chem. Rev.*, 1999, **68**, 957–966.

3 A. Penman and G. R. Sanderson, *Carbohydr. Res.*, 1972, **25**, 273–282.

4 H. Grasdalen, B. Larsen and O. Smidsrød, *Carbohydr. Res.*, 1979, **68**, 23–31.

5 H. Grasdalen, B. Larsen and O. Smisrod, *Carbohydr. Res.*, 1981, **89**, 179–191.

6 H. Grasdalen, *Carbohydr. Res.*, 1983, **118**, 255–260.

7 *ASTM F2259-03 (2008) - Determining the Chemical Composition and Sequence in Alginate by ^{1}H NMR*, 2008, vol. 3.

8 T. A. Davis, F. Llanes, B. Volesky, G. Diaz-Pulido, L. Mccook and A. Mucci, *Appl. Biochem. Biotechnol.*, 2003, **110**, 75–90.

9 M. Wilkinson, *Aquat. Conserv. Mar. Freshw. Ecosyst.*, 1992, **2**, 209–210.

10 T. A. Davis, F. Llanes, B. Volesky and A. Mucci, *Environ. Sci. Technol.*, 2003, **37**, 261–267.

11 L.-E. Rioux, S. L. Turgeon and M. Beaulieu, *Carbohydr. Polym.*, 2007, **69**, 530–537.

12 A. Haug, B. Larsen, O. Smidsrød, J. Møller, J. Brunvoll, E. Bunnenberg, C. Djerassi and R. Records, *Acta Chem. Scand.*, 1966, **20**, 183–190.

13 A. Haug, B. Larsen, O. Smidsrød, G. Eriksson, R. Blinc, S. Paušak, L. Ehrenberg and J. Dumanović, *Acta Chem. Scand.*, 1967, **21**, 691–704.

Appendix K – A note on the preparation and pyrolysis of Fe(III)Alg

Whilst this thesis has largely focussed on the coordination and pyrolysis behaviour of alginates bound to mono- and di-valent cations, there is also scope for considering the equivalent effects of trivalent metals. Here, Fe^{3+} is a suitable example. However, efforts to prepare the required **Fe(III)Alg** (see Figure K.1) using the same ion-exchange processes as for the **M^{2+}Alg** salts in Chapters 4 and 5, were not met with success. Recently, however, the team of Lun Yiu published work purporting to describe the pyrolysis behaviour of a sample of **Fe(III)Alg**, concluding that the results were very similar to samples of **HAlg**.[1]

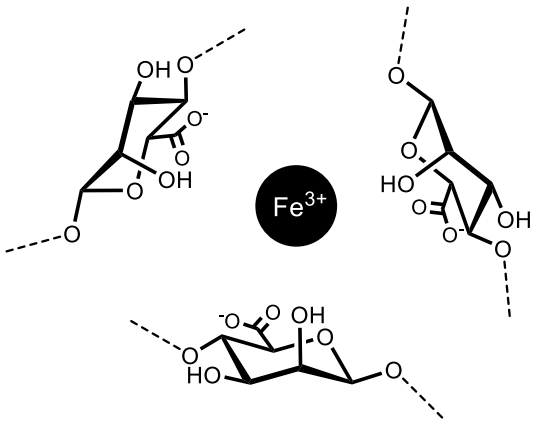

Figure K.1 Iron(III) alginate, **Fe(III)Alg**

Hence, for this thesis, an attempt was made to replicate the conditions of the study by Yiu and co-workers, in order to attempt to corroborate their results. In order to prepare samples of **Fe(III)Alg**, Yiu *et al.* started by soaking a sample of **NaAlg** in a 5.0 M solution of $FeCl_3$, before washing it and leaving it to dry in air. The authors carried out no further tests of the elemental composition of the product before proceeding to the thermochemical studies. Upon repeating the experiment of Yiu *et al.* for this thesis, the pH of the $FeCl_3$ solution was tested prior to addition of the **NaAlg**, and the was found to be very low (<< 1). At such low pH values, the carboxylate moieties of the alginate are protonated, and binding with an Fe^{3+} cation is expected to be weak, or non-existant.[2] Further examination of the material produced by replicating the methodology of Yiu *et al.*, revealed an absorption peak at 1720 cm^{-1} by FTIR analysis.[†] This peak is more consistent with the spectrum of **HAlg** than a metal-bound alginate (see Appendix G).[3] Additional elemental analysis of the prepared material revealed that it had a carbon content of 36.59 wt.%, close to the 37 – 38 wt.% that would be expected for a sample of **HAlg**. Finally, ICP analysis of the ash following combustion of the sample at 550 °C in excess oxygen, revealed an iron content of < 0.1 wt.%, far below the value that would be observed for **Fe(III)Alg**.

[†] The FTIR and elemental analyses of the material from the attempted preparation of **Fe(III)Alg** was conducted using the same methods as those employed for other metal alginates in Chapter 4.

Hence, it can be concluded that the methodology of Yiu *et al.* is not suitable for the preparation of **Fe(III)Alg** as the use of excessively harsh ion-exchange conditions serves simply to protonate the **NaAlg** starting material. Hence, instead of pyrolysing a sample of **Fe(III)Alg** as the authors believed, they actually studied **HAlg** (which is borne out by their Py-GCMS results).

There is still scope, therefore, to build on the work of Yiu *et al.*, and employ a more carefully controlled synthesis of **Fe(III)Alg** (with more complete characterisation) in order to explore further the pyrolysis behaviour of such a salt. Further work is therefore recommended in the study of the thermochemical characteristic of trivalent metal alginates.

1 Y. Liu, J.-S. Wang, P. Zhu, J.-C. Zhao, C.-J. Zhang, Y. Guo and L. Cui, *J. Anal. Appl. Pyrolysis*, 2016, **119**, 87–96.

2 K. Sreeram, *Biochim. Biophys. Acta - Gen. Subj.*, 2004, **1670**, 121–125.

3 S. K. Papageorgiou, E. P. Kouvelos, E. P. Favvas, A. a Sapalidis, G. E. Romanos and F. K. Katsaros, *Carbohydr. Res.*, 2010, **345**, 469–473.

Appendix L - Thermoanalytical methods utilised in the study of uronides and uronide-rich biomass

L.1 Introduction to thermal analysis

Thermal analysis covers a broad range of topics but broadly entails the probing of particular properties of a materials through the action of heat.[1] Thermochemical experiments were used extensively in the latter half of this thesis to explore the stability and degradation behaviour of uronide-based carbohydrates and uronide-rich biomass. Though sufficient methodological details are provided in the relevant chapters for the sake of reporting the research, this appendix provides a more extensive explanation of the choice and rationale of experimental techniques and methods of data analysis. Particularly, as the micropyrolyser (see Section L.3) was newly acquired, the work in this thesis constitutes the first use of the equipment for a methodological study; it is hoped that details in this appendix will help to inform future experiments with the apparatus – whatever their purpose may be.

As an organic material (carbohydrates or carbohydrate-rich biomass in this case) is heated it will eventually undergo thermal degradation *via* a number of observable stages. Certain parameters can be monitored at each stage to give insight into the thermolysis process (See Figure L.1). In this regard, the loss of mass of the sample is perhaps the easiest change to observe, giving rise to the field of thermogravimetric analysis (TGA).

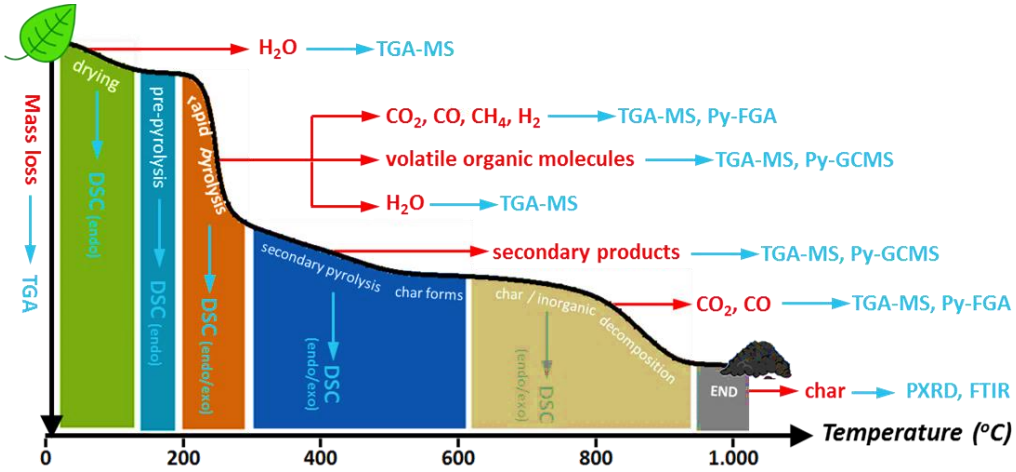

Figure L.1 The thermal degradation of a typical organic material with suggestions for suitable methods of analysis, including thermogravimetric analysis (**TGA**), thermogravimetric analysis coupled to mass spectrometry (**TGA-MS**), pyrolysis-fixed gas analysis (**Py-FGA**), pyrolysis-gas chromatography mass spectrometry (**Py-GCMS**), differential scanning calorimetry (**DSC**), Fourier transform infra-red spectroscopy (**FTIR**), and powder X-ray diffraction (**PXRD**).

The first mass loss event to occur as soon as the sample begins to be heated above ambient temperature is desorption of surface bound water (the drying stage).[*] As with the release of a number of species in pyrolysis, the desorbing water can also be followed by an evolved gas analysis (EGA) technique, such as TGA-mass spectrometry (TGA-MS). Next a period of pre-pyrolysis occurs in which the sample may be undergoing changes, but without the loss of mass (for example bond rearrangement or melting may be occurring). The main mass loss event – so called "rapid pyrolysis" follows, in which the sample thermally degrades with the release of a variety of volatilised compounds. The volatilised pyrolysate molecules can be followed through a combination of TGA-MS, pyrolysis-fixed gas analysis (Py-FGA) or pyrolysis-gas chromatography mass spectrometry (Py-GCMS). The latter technique is particularly useful for discerning the constitution of highly complicated pyrolysate mixtures. Secondary, often slower, reactions follow at higher temperatures as more functional groups are thermolytically removed to leave behind inorganic material supported on a carbon-rich char. The char may be subsequently studied by solid state analytical techniques, such as Fourier transform infra-red spectroscopy (FTIR), or powder X-ray diffraction (PXRD). As TGA and Py-GCMS were found to be particularly insightful for the work conducted in this thesis, those two techniques form the basis of the discussion in the following sections.

Of course, aside from monitoring the loss in mass and formation of thermolytically volatilised products, the heat flow to and from a sample can be measured (relative to a reference material placed under the same thermal conditions). So-called differential scanning calorimetry (DSC) can be used to define whether chemical changes in the sample are endothermic or exothermic.[2] Whilst a useful technique in itself, DSC was not used extensively in this thesis owing to difficulties in data interpretation when studying complex pyrolysis events (and consequently is not considered in detail in this appendix). However, there is certainly scope to make better use of the insights provided by DSC in future work, especially with regards to exploring changes occurring in the analyte during the "pre-pyrolysis" stage (see Figure L.1).

Finally, whilst many of the discussions in this appendix arise from consideration of thermoanalytical literature as a whole, specific citations are only made when a concept has been taken directly from a specific published work. It should be stressed, however, that the general development of this appendix and the author's understanding of thermal analysis was greatly informed by two key texts: one by Heal (on thermogravimetry)[3] and one by Moldoveanu (on micropyrolysis).[4]

---

[*] It is important to distinguish the volatilised water from the drying stage (sometimes referred to as moisture) from the water generated by the pyrolysis of the sample at higher temperatures. The moisture is dependant only on the hygroscopicity of the sample and the environment in which it is stored, whilst the water released during pyrolysis is a product of the thermolytic rearrangement of covalent bonds.

L.2 Thermogravimetric analysis (TGA)

L.2.1 TGA: background to the technique

Thermogravimetric analysis (or *thermogravimetry*) is a thermoanalytical technique that provides information on the change in mass of a sample upon the application of heat.[3] A typical setup for TGA apparatus is depicted in Figure L.2. In essence, a sample is suspended in a sample pan (usually ceramic) hung from a quartz wire (the *hang down*) and a furnace can be raised to surround the material, forming an air tight seal in the heating chamber. The heating output of the furnace can be carefully controlled and the temperature of the sample can be monitored by a nearby thermocouple. As the sample begins to thermally degrade, the balance very accurately detects changes to the mass and exports the data to yield a trace of the type depicted in Figure L.3. The first derivative of the mass *versus* temperature plot, the so-called DTG, makes significant mass loss events easy to identify and also gives useful insight into the kinetics of thermolysis.

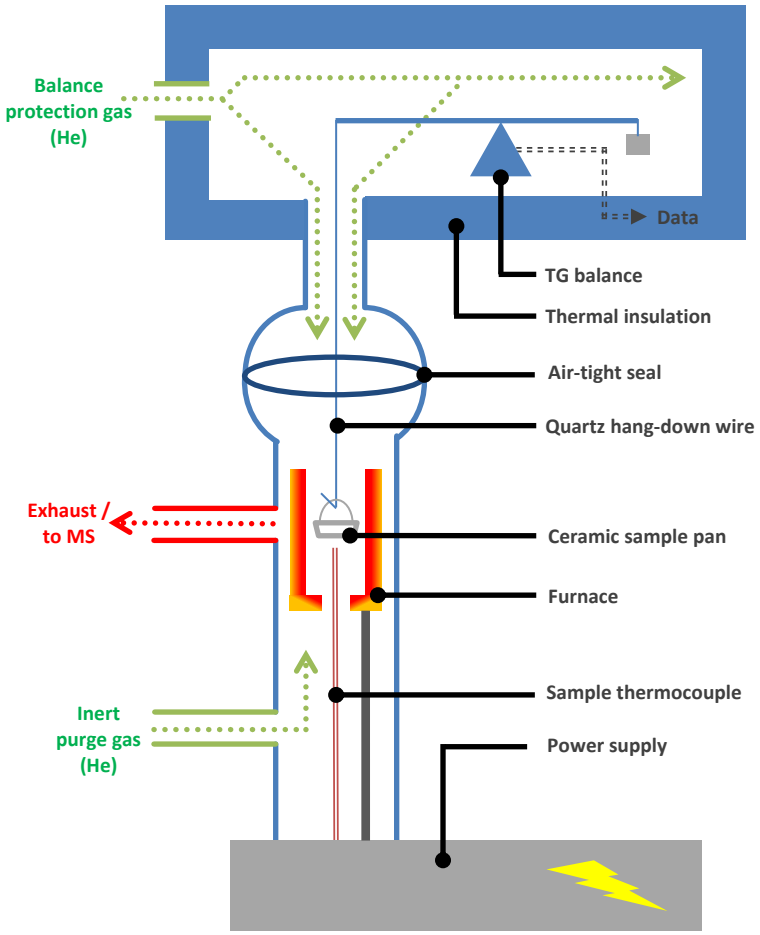

Figure L.2 Schematic of a hang down-type thermogravimetric analyser (TGA)

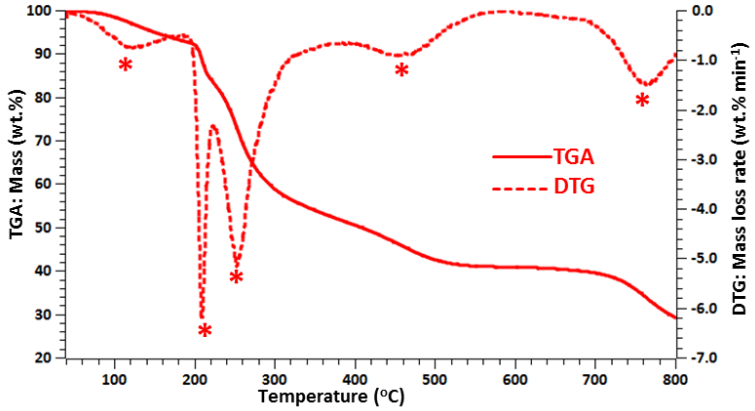

Figure L.3 Exemplar TGA plot and corresponding DTG curve. Significant mass loss events are marked with a ✱.

Of course, as is discussed elsewhere in this chapter, both the heating regime and heating atmosphere can have profound influences on the sample degradation behaviour. To avoid combustion of the organic material, the sample pan is purged with inert gas, which also serves the purpose of sweeping away any volatilised compounds as they are released (potentially transferring them to a secondary analyser such as an MS or FTIR, see Section L.2.2.4). A second, slightly faster, flow of inert gas is passed across the balance in order to protect it from any reactive compounds that may be given off. The balance is further protected by a layer of thermal insulation, which maintains as near to constant temperature as the furnace heats up.

The TGA equipment can be calibrated for mass (by using a set of standard micro-weights) and for temperature (by measuring the Curie point of a suitably well-defined alloy).[3] Standard samples can also be run routinely such as calcium oxalate (to ensure consistency of the results between calibrations)[3] or copper oxalate (to ensure that there is no oxygen in the inert gas supply).[5]

L.2.2 TGA: experimental methodology

L.2.2.1 TGA typical experimental configuration

All thermogravimetric experiments described in this thesis were carried out on a PerkinElmer® Pyris 1 TGA (unless otherwise stated). The balance was calibrated by using a set of standard micro-weights, and the temperature control by measuring the Curie point (T_C) of a set of standard alloy materials (alumel (T_C = 154 °C), Perkalloy (T_C = 596 °C), iron (T_C = 780 °C), Hisat-50 (T_C = 1000 °C), and nickel (T_C = 355 °C). The sample gas flow was typically Helium (CP grade, BOC) at 30 mL min^{-1}, though both N_2 and air were used in some cases (see Section L.2.4.1). Each sample was loaded into a clean ceramic boat and spread evenly prior to starting the experiment. Powdered samples of between 5 – 50 mg were used, with samples for direct comparison being measured using the same mass ± 20 wt.%. Data was extracted in X-Y format and processed using SciDAVis 1.D005, as outlined in Section L.2.3

For TGA-MS studies, the evolved sample gases were transferred directly to a Hiden HPR20 QIC mass spectrometer (which operates through an electron ionisation source at 70 eV and a quadrupole mass filter) *via* a ceramic-lined heated transfer line (see Figure L.4). A carrier gas of helium (CP grade BOC) flowing at 30 ml min^{-1} was used for all TGA-MS experiments; the manufacturer states that evolved gases reach the MS detector in under 0.3 seconds. The MSD was configured for Selective Ion Monitoring (SIM) of certain diagnostic m/z ratios as required.

Figure L.4 Pyris 1 TGA (left) coupled to a Hiden HPR20 mass spectrometer (right) *via* a ceramic-walled heated transfer line (manufacturer supplied image).

L.2.2.2 TGA Non-isothermal heating experiments

Non-isothermal heating experiments, where the temperature of the sample is increased continuously at a constant rate, were utilised extensively in the preparation of this thesis. A typical experiment, following calibration of the equipment (see Section L.2.1), would proceed as follows:

I. **Load**: A clean, empty ceramic pan was tared on the calibrated TGA balance. Powdered sample (typically 5 - 50 mg) was loaded into the pan and spread evenly, before carefully balancing the assemblage on the hang-down wire and sealing the furnace around the sample.
II. **Purge**: An inert purge gas (typically Helium, 50 ml min^{-1}) was passed over the sample for five minutes.
III. **Dry**: The sample was heated from ambient temperature to 100 °C at 10 °C min^{-1}, and held for 10 minutes. This isothermal drying period facilities the calculation of the moisture content of the sample (see Section L.2.3.2)
IV. **Experiment**: The sample was heated from 100 °C to the target temperature (typically 800 °C) at 10 °C min^{-1} still under the flow of purge gas. Compounds volatilised during this period were swept into an online MS for analysis (see Section L.2.2.4).
V. **End**: After reaching the target temperature, the furnace was allowed to cool fully prior to removal of the residual char either for disposal or further analysis. In some experiments, an additional isothermal period of 60 minutes was introduced upon reaching the target temperature to enable the formation of crystallites suitable for diffraction analysis (see Section L.2.2.3).

L.2.2.3 TGA Isothermal heating experiments

Isothermal TGA experiments proceed through the same steps as detailed in Section L.2.2.1, with the exception that the target temperature is held for a period of time. The technique is used in kinetic analysis to ramp quickly to a target temperature and then monitor mass loss events under constant-temperature conditions. The method can also help to separate thermal events that may be convoluted in non-isothermal experiments. In this thesis however, isothermal techniques were not utilised extensively, principally because the available equipment was not capable of ramping quickly and accurately enough to the target temperature. Instead, isothermal experiments were only used in the preparation of chars suitable for powder X-ray diffraction (PXRD) analysis. By adding a 60 minute isothermal period to the end of a typical run TGA experiments, any crystalline materials that had formed were able to grow in size and hence produce sharper peaks in the subsequent PXRD.

L.2.2.4 TGA On-line MS experiments

As a sample loses mass in a TGA experiment, the volatilised material can be swept by the flowing inert purge gas along a heated transfer line, through a quartz lined capillary tube and into a suitable detector. In the case of TGA-MS a mass selective detector (MSD) is utilised, which, when set to selected ion monitoring (SIM) mode, can be used to plot the intensity of indicative m/z ratios with time. As the delay between a compound being thermolytically evolved and it reaching the MSD is very low (< 0.3 s), the time at which an m/z peak is detected can be directly translated to the temperature of the sample at that point. In the experiments conducted in this thesis the m/z ratios for H_2O (m/z = 18), CO_2 (m/z = 44), CO (m/z = 28), and 2-furfural (m/z = 96 and 95) were monitored and hence the evolution of these compounds could be associated to specific mass loss events of the starting material as observed by TGA. As the MSD was not calibrated for those compounds, the m/z traces could only be interpreted qualitatively, with the exception of H_2O where quantitation was possible by reference to the mass lost during the isothermal drying period of the TGA program (see Section L.2.3.5).

L.2.3 TGA: data analysis

L.2.3.1 TGA data analysis: data truncation

The TGA apparatus used for experiments detailed in this thesis records data points every 1.0 s, which, at a typical heating rate of 10 °C min^{-1}, equates to one data point per 0.17 °C of temperature increase. For a typical TGA run (including an isothermal drying period) this amounts to over 5000 data points per thermogram. In order to process the data (including for example: correcting for moisture content, establishing kinetic parameters, overlaying spectra obtained from different machines etc.) data points were extracted every 3.0 s (two points per °C when heating at 10 °C min^{-1}) and subsequently plotted in SciDAVis 1.D005. To the naked eye, there is no difference in the shape of the resulting TGA curve following this truncation, but the data becomes much easier to manage and there is a significant reduction of noise in the DTG (see Figure L.5).

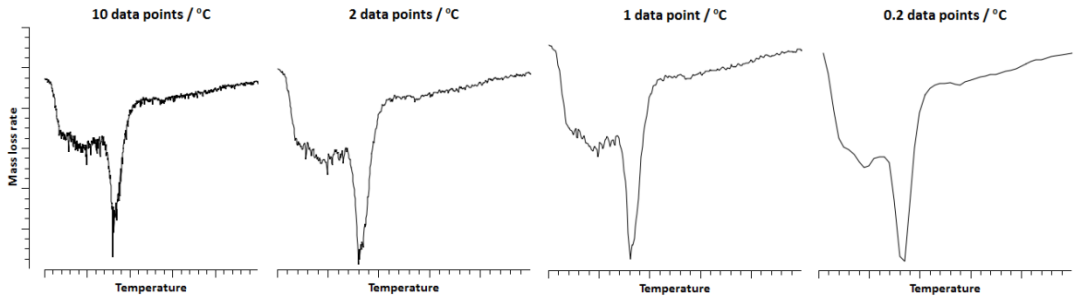

Figure L.5 Effect on an exemplar differential thermogram (DTG) of varying levels of data truncation.

L.2.3.2 TGA data analysis: moisture correction

Alginate and alginate-rich macroalgal samples readily absorb atmospheric moisture following their preparation, which must be accounted for when analysing their thermograms. In order to correct for the differing moisture contents of samples, an isothermal period (10 minutes at 100°C) was included in the majority of the TGA runs, over which time weakly bound water was removed. A temperature point (T,°C) was then chosen following the isothermal drying stage (typically T = 110°C) at which the mass was redefined as 100 wt.% according to Equation [L.1], and the experimental regime (usually heating at 10°C min^{-1}) was continued as normal. Figure L.6 demonstrates the importance of the moisture correction procedure in improving the agreement between samples that are identical in all but moisture content.

$$\text{Corrected mass (wt.\%) at Temperature, T(°C)} = \frac{100 \text{ X uncorrected mass (wt.\%) at Temperature, T(°C)}}{\text{uncorrected mass (wt.\%) at T = 110°C}} \quad \textbf{[L.1]}$$

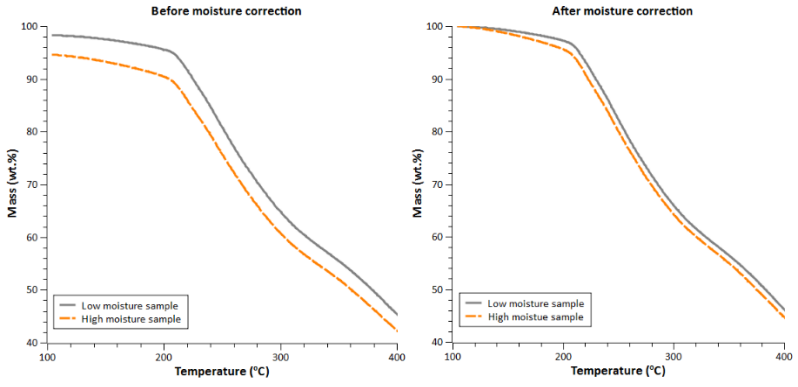

Figure L.6 TGA curves of low and high moisture variants of the same Ni(II)alginate sample before (left) and after (right) applying a moisture correction to the data.

L.2.3.3 TGA data analysis: smoothing

Differentiation of the (moisture corrected) TGA curve *via* the SciDAVis 1.D005 "Derivative" algorithm yields the (moisture corrected) DTG. The appearance of the DTG can be considerably improved by firstly truncating the data set (see Section L.2.3.1) and subsequently by applying a smoothing algorithm: in this case, a moving average applied across each 10 data points (or every 5°C). The smoothing is not just cosmetic, but facilitates consistent data analysis between samples when, for example, defining onset temperatures, by minimising gravimetric artefacts and random fluctuations (see Figure L.7).

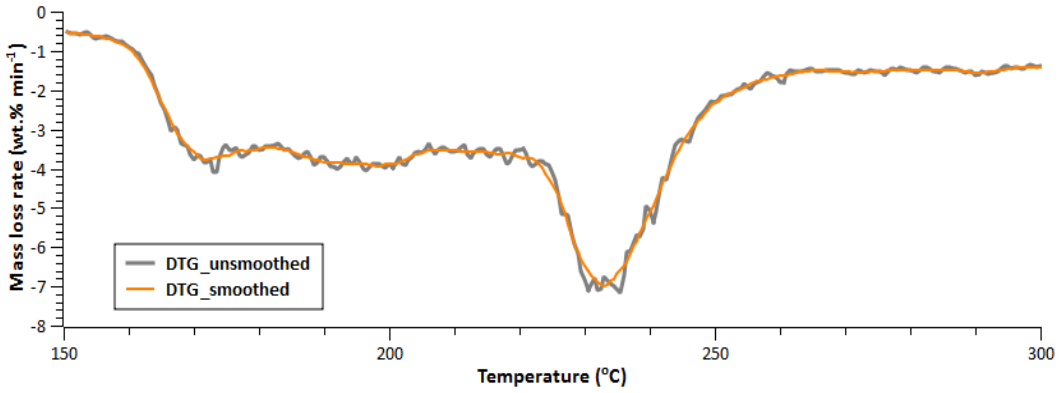

Figure L.7 Effect on an exemplar differential thermogram (DTG) of moving average smoothing.

L.2.3.4 TGA data analysis: defining indicative thermal events

Pyrolysis of alginates, and indeed most organic materials, typically proceed through three temperature-dependant, T (°C), stages:[†]

1. **Dehydration:** 25 °C ≤ T ≤ 150 °C
2. **Rapid pyrolysis:** 150 °C ≤ T ≤ 500 °C
3. **Secondary degradations and char formation:** 500 °C ≤ T

The second stage, rapid pyrolysis, is the most significant to the discussion in this thesis. The rapid pyrolysis behaviour between different samples can easily be compared by reference to indicative thermal events within the stage. These could include, for example, the temperature of the onset of rapid pyrolysis, the temperature(s) of maximum rate loss events, the temperature range over which rapid pyrolysis occurs, *etc.* Identifying indicative temperatures from thermograms can be a highly subjective exercise, and so a set of definitions were adhered to in order to ensure self-consistency (see Table L.1).

[†] Approximate temperature ranges, see full chapters for further details.

Table L.1 Definitions of pyrolysis events used in this thesis.

Pyrolysis event	Abbreviation	Definition
Rate of mass loss	$\frac{dm}{dT}$ (wt.% min^{-1})	Rate at which mass is lost with increasing temperature in the moisture-corrected thermogram
Initiation (onset) of rapid pyrolysis	T_i (°C)	The temperature in the moisture-corrected thermogram at which it is first true that: $\frac{dm}{dT} \geq 1.0$ wt.% min^{-1}
End of rapid pyrolysis	T_f (°C)	The temperature above T_i in the moisture-corrected thermogram at which it is first true that: $\frac{dm}{dT} \leq 1.0$ wt.% min^{-1}
Period of rapid pyrolysis	- (°C)	All temperatures (T) for which $T_i \leq T \leq T_f$
Temperature(s) of maximal mass loss rate	T_{max1}, T_{max2}, T_{max3} … (°C)	Temperatures within the period of rapid pyrolysis in which: $\frac{d^2m}{dT^2} = 0$ *Expressed as: temperature* (°C) [*rate* (wt.% min^{-1})]
% mass lost over period of rapid pyrolysis	$\Delta M(T_i - T_f)$ (wt.%)	$\frac{(\text{Mass at } T = T_i) - (\text{Mass } T = T_f)}{\text{Moisture-corrected starting mass}}$ X 100
% mass lost by 500 °C	ΔM(500) (wt.%)	$\frac{\text{Mass at } T = 500}{\text{Moisture-corrected starting mass}}$ X 100

L.2.3.5 TGA data analysis: TGA-MS and calculating the thermolysis yield of H_2O

The MSD yields a plot of intensity of a selected m/z ratio at each point in time, which can be related back to a corresponding temperature on the thermogram. Hence, all peaks in the MSD data can be related to specific mass loss events in the thermogravimetric analysis. As stated in Section L.2.2.4, m/z ratios were selected to observe the formation of H_2O, CO_2, CO, and 2-furfural with increasing temperature. Whilst a lack of calibration method meant that these plots could not be used quantitatively in the case of CO_2, CO, and 2-furfural, a technique was developed to obtain a yield of H_2O from the m/z intensity *versus* time trace. As a drying period was included at the start of each TGA experiment during which time the mass loss of the sample was attributable wholly to the desorption of surface bound H_2O, the intensity *versus* time plot for that period could be integrated to

obtain a relationship between mass of H_2O and area (see Figure L.8). Hence, though prone to errors from drifting baselines and ill-defined limits, the method allows for an estimate of the mass of H_2O generated during pyrolysis to be generated. Given the difficulty of estimating the H_2O yield from Py-GCMS analysis (See Section L.3.3.7), the technique discussed here proved to be valuable as water can be the largest product fraction in the pyrolysis of carbohydrates.

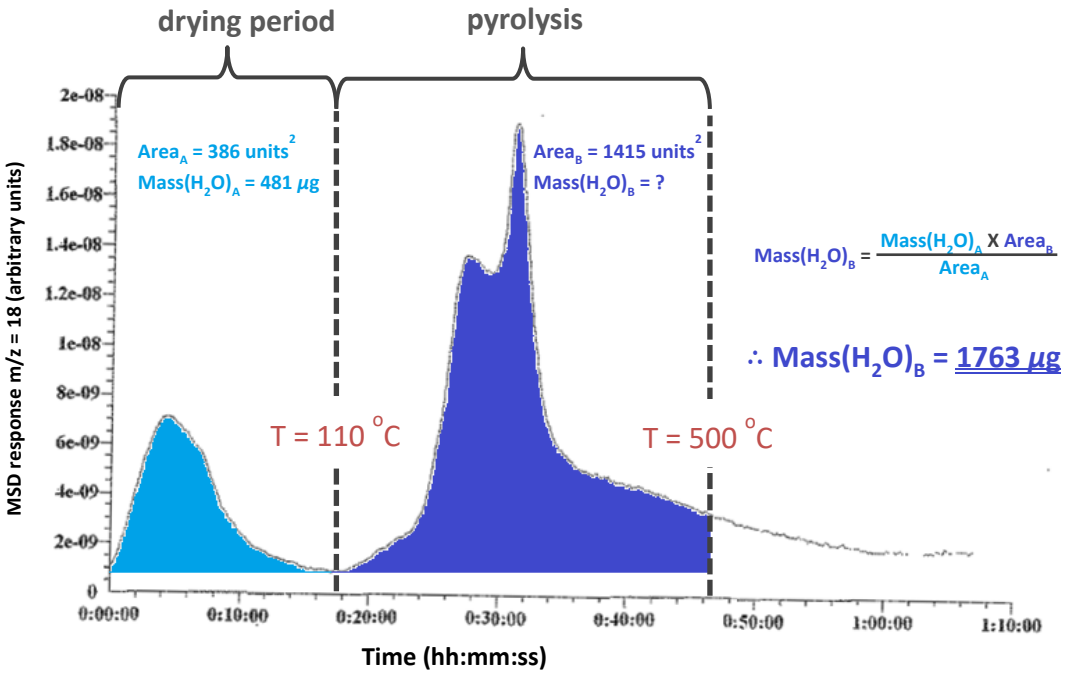

Figure L.8 MSD response (m/z = 18) with time for a TGA-MS experiment to demonstrate how the water generated in pyrolysis may be calculated be reference to the mass of moisture lost during the drying period.

L.2.3.6 TGA data analysis: errors and repeatability

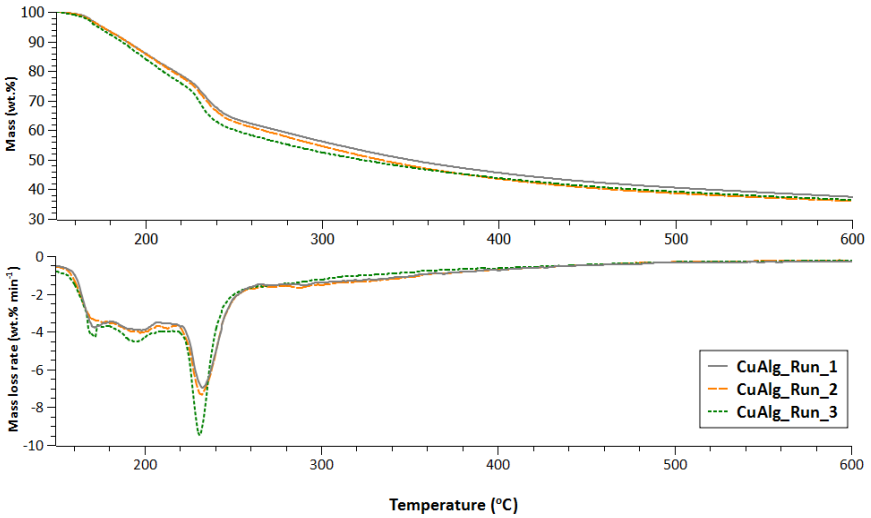

Figure L.9 Three thermograms of the same sample performed under the same nominal conditions, but at different intervals.

Variability in the TGA analysis of biomass can arise through a number of pathways – changing calibrations of the machine, fluctuations in gas flow, inhomogeneity of the starting material. To combat such errors, samples were always analysed in batches, with at least two repeats being carried for each identical run (and more if necessary). Typical standard deviations for various measured pyrolysis parameters are shown in Table L.2. Here it can be seen that the repeatability of the technique for measuring the water released during pyrolysis by TGA-MS (see Section L.2.3.5) is quite poor.

Table L.2 List of standard deviations for commonly measured pyrolysis parameters

Parameters	Unit	Example	Typical standard deviation
Temperature	^{o}C	T_i, T_f, T_{max}	± 3 °C
Mass loss rate	wt.% min^{-1}	Rate[T_{max1}]	± 0.5 wt.% min^{-1}
Mass loss	wt.%	$\Delta M(T_i - T_f)$	± 1 wt.%
Mass H_2O	wt.%	Yield of H_2O from pyrolysis	± 6 wt.%

L.2.4 TGA: additional parameter considerations

L.2.4.1 The role of heating atmosphere in TGA

Many studies have noted the differences observed in the thermal behaviour of alginic acid and alginates in air as opposed to under an inert atmosphere.[6–9] For pyrolysis studies, where aerobic oxidation is to be avoided, flowing He or N_2 is frequently used as the reaction medium. In preliminary studies carried out for this thesis, swapping between He and N_2 did not appear to have a significant impact on the initial stages of alginate pyrolysis (see Figure L.10 for the example of alginic acid). Indeed, Coburn demonstrated that alginic acid pyrolysis proceeds identically until 300 °C in both pure N_2 and N_2 containing 10 mol.% O_2, though at higher temperatures the latter sample undergoes a large mass loss event that was absent in the inert atmosphere experiment.[10] Coburn's data demonstrates the importance of using a pure inert gas flow to avoid inconsistent results. In this regard, it was noticed in the preliminary stages of this thesis that performing thermogravimetric analysis on alginic acid on two different machines (both with a supply of N_2 as the inert atmosphere) gave significantly different results (See Figure L.10). The secondary mass loss event observed on Machine 2 at temperatures > 300 °C was attributed to the effects of trace oxygen in the N_2 supply. The presence of O_2 in Machine 2 was subsequently confirmed by holding a sample of carbon (Sigma Aldrich) at 1000 °C for 60 minutes in the N_2 atmosphere, under which conditions a 30 wt.% mass loss was observed due to combustion of the sample.

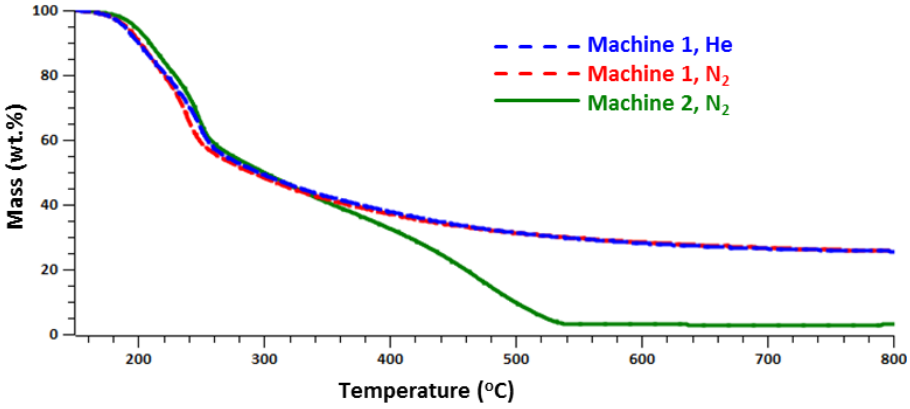

Figure L.10 Repeated TGA analysis (10 °C min^{-1}, gas flow 30 mL min^{-1}) of alginic acid under different conditions. The N_2 supply of Machine 2 was believed to have a slightly higher O_2 content than in Machine 1, inducing an oxidative mass loss event at T > 300 °C that is absent under truly inert conditions.

The problem of trace O_2 in N_2 gas supplies proved to be particularly problematic in the case of high temperature isothermal experiments conducted to produce chars for powder X-ray diffraction (PXRD) analysis. For example, whilst Cu(II)-alginate showed a degradation to Cu^0 irrespective of the choice of inert atmosphere, at higher temperatures the N_2 supply facilitated re-oxidation to Cu_2O and then to CuO, which was not observed when the experiments were repeated under He (see Figure L.11). Indeed, the formation of copper oxides in place of copper metal in the thermolysis of copper oxysalts is a well-established test for the detection of trace oxygen in thermal analysis apparatus.[5]

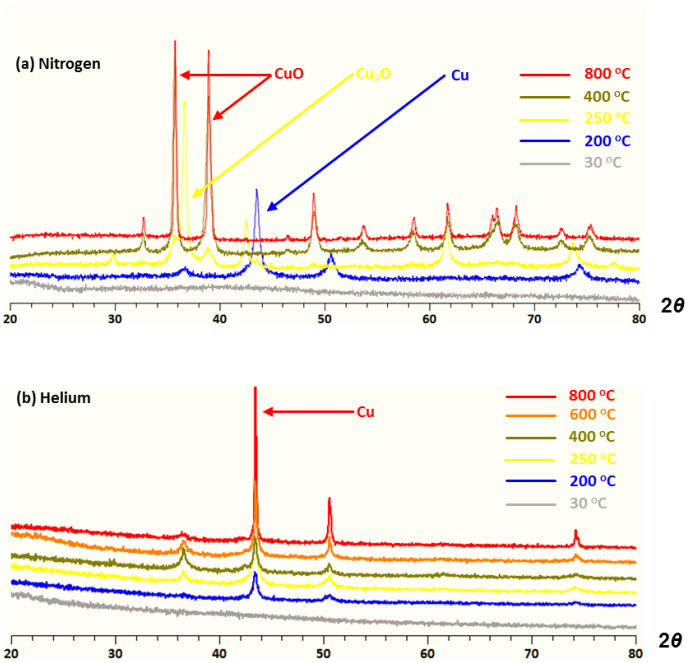

Figure L.11 Powder X-ray diffraction (PXRD) patterns of chars derived from Cu(II)-alginate pyrolysed at different temperatures for 60 minutes under (a) nitrogen and (b) helium.

As a consequence of the difficulties encountered with nitrogen as the thermolysis atmosphere, all of the final TGA experiments presented in this thesis (unless otherwise stated) were conducted in helium, which has a far lower trace oxygen content. The effect of small amounts of O_2 in the purge gas is, however, worthy of further investigation as under industrial pyrolysis conditions the atmosphere would likely not be as pure as the Helium used throughout this thesis.

L.2.4.2 The role of sample mass

When conducting a TGA experiment, the choice of initial sample mass can be quite important, owing to differing rates of heat and mass transfer to/from the particles under investigation.[3] There may, however, be particular reasons for using a high sample mass (for example to maximise the product yields for onward analysis) or low sample mass (for example due to limited sample amount or for extremely intumescent samples*). Two sets of experiments were carried out for all of the alginates studied in this thesis: one utilising ~5 mg of sample, and one with ~30 mg. Between the two sets, there was found to be no difference (within error) of the two thermograms obtained (see example of alginic acid in Figure L.12). A similar experiment conducted by Coburn also observed no change in the thermogram of alginic acid when 2 mg and 20 mg of sample was used.[10] Hence, whilst best efforts were always made to keep sample size constant between TGA experiments that were to be directly compared, these preliminary experiments indicated that small fluctuations in the starting mass would be of no significance to the results.

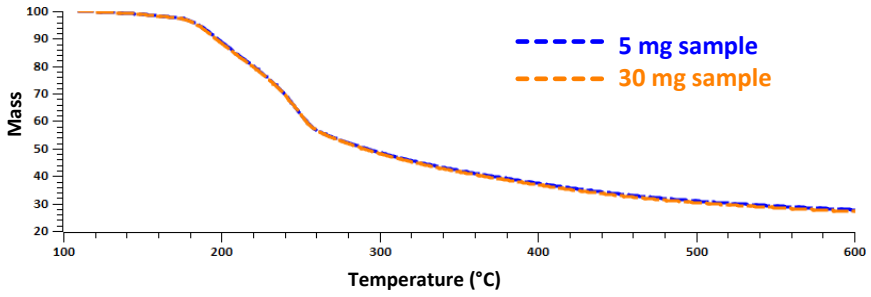

Figure L.12 Moisture corrected thermogram analysis (10 °C min^{-1}, Helium 30 mL min^{-1}) of alginic acid of different original starting masses.

L.3 Pyrolysis-Gas Chromatography Mass Spectrometry (Py-GCMS)

L.3.1 Py-GCMS: background to the technique[4, 11, 12]

Whilst TGA is a useful tool for obtaining time-resolved information about the thermolysis of an organic material, it offers limited information about the products being volatilised.

* Intumescent samples must be considered carefully. For example some sodium uronate salts were found to swell to such an extent that, at elevated temperatures, they forced the TGA furnace open and ignited upon contact with air!

In order to obtain information (especially quantitative information) about thermally evolved compounds, a micropyrolyser (referred to as a *pyroprobe*) coupled to a suitable means of analysis such as mass spectrometry (Py-MS) or gas chromatography-mass spectrometry (Py-GCMS) can be used. Py-GCMS holds the advantage of being able to separate out complex product mixtures prior to their analysis by a mass selective detector (MSD), and hence this technique was used prominently in the preparation of this thesis. The micropyrolyser system can be further coupled to a fixed gas analyser (FGA), which comprises a gas chromatograph (GC) and thermal conductivity detector (TCD). The purpose of the FGA is to provide a quantitative measure of the yield of non-condensable gases (such as CO_2, CO, H_2, CH_4, and, potentially, H_2O), which are incompatible with the GCMS setup designed to detect volatile organic pyrolysis products.

One of the main advantages of a micropyrolyser system lies in the method of heating. A finely powdered sample is packed into a quartz tube and held in place by two plugs of quartz wool, which also serve as heat transfer agents (see Figure L.13a). The quartz tube is placed inside a tightly wound platinum heating element capable of very rapid (20 °C ms^{-1}) and very accurate heating (see Figure L.13b). The ability to perform pyrolysis on the second timescale minimises the degree of secondary reactions that take place following initial pyrolysis, helping to preserve primary reaction produce for analysis and minimise the yield of char. Secondary reactions are further suppressed by the ability to use very small sample sizes (on the order of 100 μg) facilitating rapid diffusion of the evolved volatile components from the pyrolysis reaction interface.

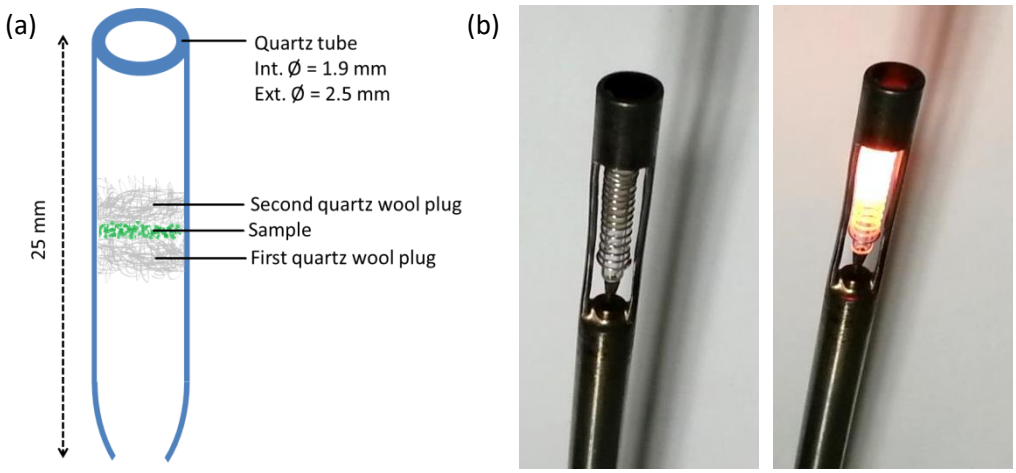

Figure L.13 (a) Schematic of a quartz sample tube used for Py-GCMS (b) Photo of a quartz sample tube loaded into the pyroprobe element before (left) and during (right) heating.

Of course, the pyroprobe itself forms only a very small part of a complex array of experimental equipment. The full Py-GCMS-FGA system is depicted schematically in Figure L.14) and the relevant steps in the procedure of a pyrolysis experiment are outlined below:

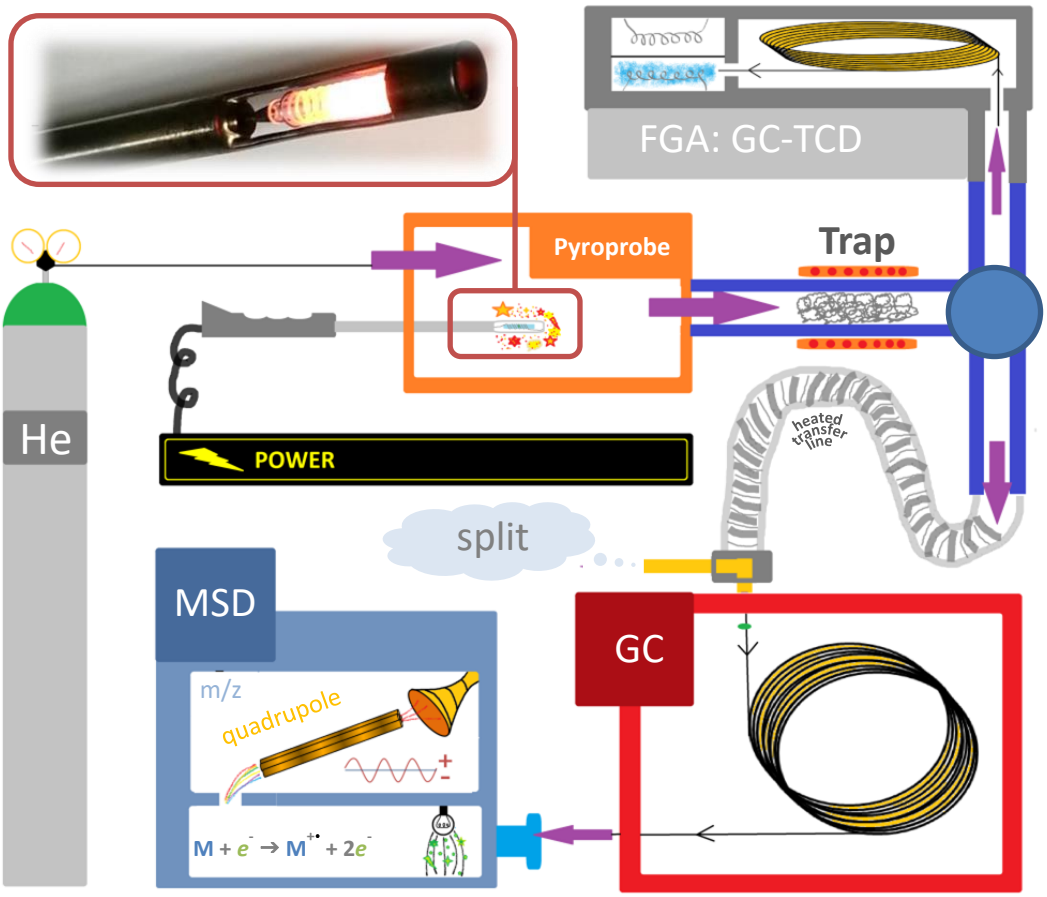

Figure L.14 Schematic cartoon of a typical pyrolysis gas-chromatography mass-spectrometry (Py-GCMS) setup, with additional fixed gas analysis (FGA).

I. **Load** The sieved sample is loaded into a quartz tube packed with quartz wool (depicted in Figure L.13a). The tube is inserted into the coiled platinum heating element of a pyroprobe unit.

II. **Purge** The pyroprobe unit is inserted horizontally into the air-tight housing, and sealed by a Swagelok fixing. A helium purge gas sweeps out any residual oxygen whilst the heated housing brings the probe and surroundings to thermal equilibrium.

III. **Pyrolysis** Power is supplied to the platinum heating coil of the pyroprobe, which heats at a very high rate (typically 120 000 more quickly than the TGA apparatus) to a pre-defined temperature. The temperature is held for a short period whilst pyrolysis takes place and the products are liberated.

IV. **Trapping** Volatile molecules are swept quickly from the heated pyrolysis chamber by the inert gas flow and onto a trapping material. The trapping material holds an affinity for a number of functional groups, and is maintained at a cold temperature to induce condensation of the product.

V. **Fixed gas analysis (FGA)** Fixed gases (CO_2, CO, H_2 etc.) are not absorbed by the trap and flow directly into fixed gas analyser (FGA) comprising a gas chromatograph (GC) coupled to a thermal conductivity detector (TCD).

VI. **Transfer of volatiles to gas chromatograph (GC)** Once the pyrolysis reaction is complete, the volatile products captured by the trap can be desorb by heating. The products are first desorbed by heating the trap and then (following the flipping of a valve to re-direct the gas flow) the pyrolysate compounds are swept into the injection port of the GC. A flow of helium splits the product stream to dilute the amount of material transferred to the GC column.

VII. **GC** The complex pyrolysate mixture is swept along the GC column where it is separated out according to the differing volatilities of the compounds and their affinity for the column lining material. The separation can be controlled by different means such as the gas flow rate and the temperature program of the GC-oven.

VIII. **Mass selective detection (MSD)**[12] Once at the end of the column, the compounds are swept into the mass spectrometer unit. Firstly, in the ionisation chamber, high energy electrons (70 eV) bombard the eluting molecules to yield positively charged ions. Next, the ions are accelerated and passed down a quadrupole of varying electric field to filter ions based on their mass to charge ratio (m/z) prior to detection. By cycling quickly through the selected m/z ratios, a snapshot of the ion fragments at each point in time is built up.

IX. **Data analysis** The GCMS yields a plot of the ion fragments detected over time. The characteristic fragmentation patterns, as well as the time at which they are found to elute from the column, can be used to assign the identity of the detected species. Quantitative work is also possible.

X. **Char yield** By measuring the mass of the pyrolysed sample immediately before and after pyrolysis, an assessment of the quantity of residual char can be made.

Careful optimisation of each of these step was required, as even small variations can have drastic results. In this regard, the investigations of Brown *et al.* prove to be particularly useful, as the authors explore the many parameters that should be considered when operating a micropyrolyser similar to that used in this work.[13]

L.3.2 Py-GCMS: experimental methodology

L.3.2.1 Py-GCMS Sample preparation

The small mass of material required for Py-GCMS analysis (typically 0.1 - 0.3 mg) necessitates special consideration in terms of sample preparation, especially if quantitation is required (see Sections L.3.3.6 - L.3.3.9). The protocol used in this thesis is outlined in Figure L.15. Firstly, the powdered analyte material is sieved to a suitable size to generate a homogeneous sample, and then left to attain equilibrium with the atmospheric moisture in a screw-cap vial with a sufficiently large headspace. A clean quartz tube packed with a plug of fine quartz wool (depicted previously in Figure L.13a) was weighed empty on a Sartorius SE2 microbalance prior to being loaded with material and re-weighed, giving the sample mass by difference (see below for further details). A second plug of quartz wool was inserted into the tube and packed down on top of the sample to ensure efficient heat transfer during the experiment. The loaded tube was

subsequently used for Py-GCMS analysis, with weighing before and immediately afterwards to determine the mass loss on pyrolysis. After this process, the sample and quartz wool were disposed of and the quartz tube cleaned ready for re-use.

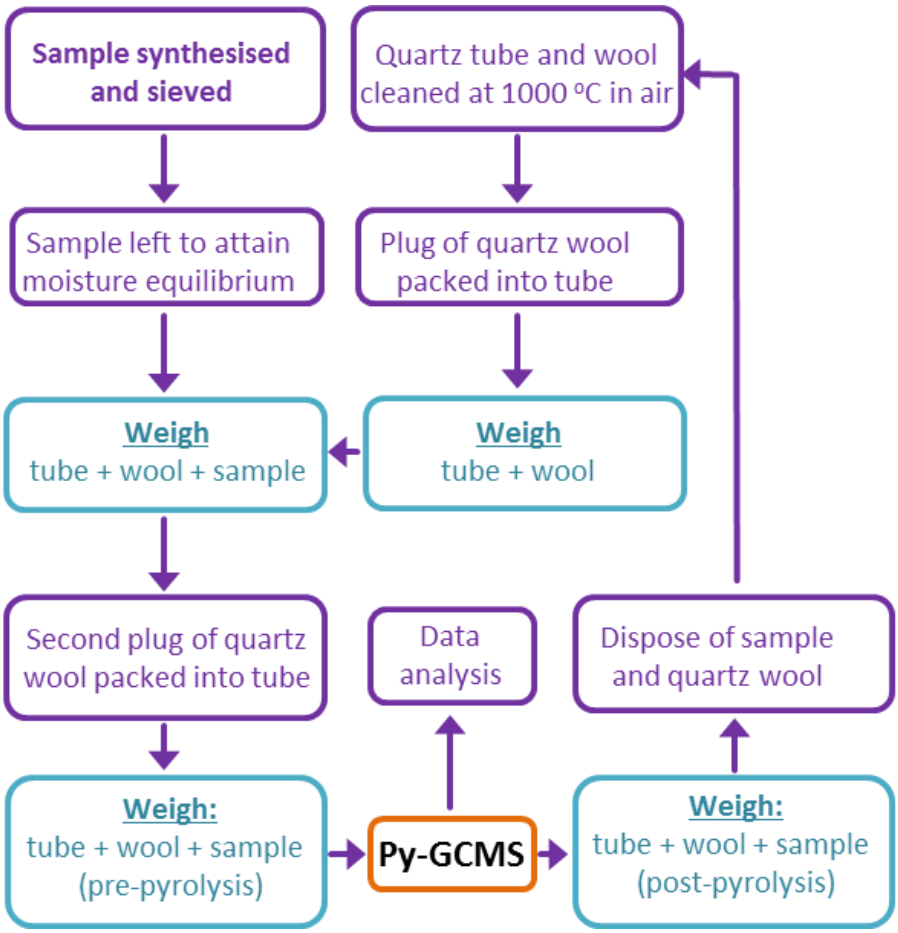

Figure L.15 Steps in the preparation of samples for quantitative Py-GCMS.

The high sensitivity of the Py-GCMS instruments require stringent precautions to be taken in order to minimise the influence of contaminant peaks on the resulting chromatograms. Quartz tubes and wool were cleaned prior to use by heating them to 1000 °C in air to remove any residual organic contaminants. Whilst nitrile gloves could be worn to handle clean quartz tubes (thereby avoiding the transfer of sebaceous oils), quartz wool could only be manipulated using stainless steel tweezers as otherwise peaks were detected due to contamination from the rubber. Samples were transferred into the quartz Py-GCMS tubes using the end of a glass Pasteur pipette.

In order to facilitate quantitative pyrolysis (see Sections L.3.3.6 - L.3.3.9), an accurate measurement of the sample loading was required. Quantification of the mass of sample used could be established using a Sartorius SE2 precision microbalance, though the manipulation of such small amounts present complications beyond those encountered at

typical lab scales. Potential errors met whilst weighing out micro-masses for Py-GCMS are outlined in Table L.3,[14] along with suitable measures to prevent or minimise them.

Table L.3 Potential errors associated with accurately weighing out samples for quantitative Py-GCMS analysis on a high performance microbalance[14]

Error	Description	Preventative measure
Eccentric error	Differences in measured weight according to the position and orientation of the sample tube on the pan	Tin foil cylinder used to keep the tube central and vertical
Static error	A build-up of static charge causes the balance to drift. Additionally, particles may "leap" on to or off of the tube.	Balance earthed. Wear an anti-static wristband. Leave statically charged samples in the balance to attain equilibrium. Wipe tube with lint-free lens cloth to remove statically adhered particles prior to weighing.
Tube gaining/losing quartz wool or fibres	Quartz wool is lost from the tube or the tube picks up stray fibres in between measurements. This was found to be the most frequent cause of large discrepancies.	Wool packed tightly into tube. Loose wool fibres meticulously removed by blowing air over weighing area prior to measurement. Weighed tubes covered in aluminium foil to prevent dust settling.
Temperature induced instability of balance	A large thermal gradient between the sample and the weighing pan can cause the balance to drift.	Samples weighed in the morning / evening when temperature was stable. Tubes handled with tweezers to avoid heat transfer from fingers.
Change in calibration of high sensitivity balance between measurements	The "zero" of the balance will drift over time with, for example changes in temperature, air pressure, relative humidity etc.	Before and after measurements taken with as small a time gap as possible. Weighing was not carried out on days with extremes of temperature.

L.3.2.2 Py-GCMS typical experimental configuration

The coupling of a pyrolyser, analytical equipment, and intermediary traps and transfer lines requires careful consideration of a number of parameters, outlined in Table L.4. The parameters used in this thesis were based partly on those of Brown *et al.*, who optimised an identical piece of equipment to investigate the pyrolysis of cellulose.[13]

Table L.4 Experimental parameters used in Py-GCMS experiments.

Parameter	Setting used	Comment
Pyroprobe (CDS 5200)		
Pyroprobe housing (accessory) temperature	100 °C for 5 min prior to pyrolysis. 105 °C for 2 min after pyrolysis.	-
Pyroprobe heating	Heating at 20 °C ms^{-1} to temperature (*e.g.* 500 °C) and held for time (*e.g.* 20 s)	-
Trap	Tenax® TA (poly(2,6-diphenylphenylene oxide))	150 mg, 20 – 35 mesh
Trap absorb/desorb	50 °C (2 minutes) / 280 °C (2 minutes)	-
Purge gas flow	Helium (CP grade, BOC), 15.0 ± 0.5 ml min^{-1}	By Ellutia 7000 Flowmeter
Transfer line temperature	300 °C	-
Quartz sample tube	CDS (L = 25, ID = 1.9, OD = 2.5 mm)	Cleaned at 1000 °C in air
Quartz wool	H. Baumbach, 4 μm diameter	Cleaned at 1000 °C in air
Sample size	100 – 250 μg 250 - 60 mesh / 63 - 250 μm	Weighed on a Sartorius SE2 microbalance
Gas Chromatograph (Agilent 7820A GC)		
Column	Thermo Scientific TraceGold: capillary TG-1701MS (60 m X 250 μm X 0.25 μm)	14% cyanopropylphenyl 86% dimethyl polysiloxane
Inlet temperature	300 °C	-
Septum	Agilent CrossLab 9.5 mm inlet septum	-
Oven program	40 °C (hold 2 mins), heat at 10 °C min^{-1} to 250 °C (hold 10 mins). Total = 33 mins	Longer run times (60+ mins) did not show extra peaks
Column head pressure	Initial = 10.7 psi (40 °C) Final = 24.36 psi (250 °C)	Pressure changed to maintain constant column flow rate
Column flow rate	Constant flow = 0.68 mL min^{-1}	Kept constant even as temperature ramps
Split ratio	235:1 (and 400:1 in some cases)	-
Mass Spectrometer Detector (Agilent 5977E MSD)		
Tune	Perfluorotributylamine m/z 69, 219, and 502	Weekly or as required
MS source temperature	230 °C	-
MS quad temperature	150 °C	-
Electron Ionisation (EI)	EI energy = 70 eV	Positive ion electron ionisation
Mass detection range	1.6 – 300 amu (in 0.1 amu increments)	Full Scan Mode
Detection scan rate	781 amu s^{-1}	-
Gain factor	25:1	-
Solvent delay	5 minutes	No products elute in this period
Analysis	Agilent *MassHunter* B.06.00	NIST 11.L (MS library)
Fixed Gas Analyser (TCD CDS 5500)		
Oven parameters	35 °C (hold 5 mins), heat at 20 °C min^{-1} to 250 °C (hold until end of GCMS run)	-
Column	Carboxen 1000 (60-80 mesh): packed	I.D. = 1/8”, L = 9’
TCD bridge current	150 mA	-
Carrier gas flow	Helium (CP grade, BOC), 15.0 ± 0.5 ml min^{-1}	By Ellutia 7000 Flowmeter
Analysis	ChromPerfect 6.0.10	-

The chronology of the Py-GCMS experiment is also important to ensure the optimal transfer of pyrolysate material to the various analytical detectors (see Figure L.16). Once the quartz sample tube has been loaded into the pyroprobe element, and the probe then secured into the housing, an equilibration period of five minutes is initiated. During this initial five minute period helium is flowed (15.0 mL min^{-1}) and the pyroprobe housing is maintained at 100 °C to bring the equipment to thermal equilibrium and to replicate the isothermal drying period employed in the equivalent TGA experiments (see Section L.2.2.2). Following the equilibration period, the pyroprobe is triggered, heating to a typical reaction temperature of 500 ± 5 °C at a typical rate of 20 °C ms^{-1}. Once the probe is at temperature (which occurs in well under one tenth of a second), an isothermal reaction period of 20 seconds was sufficient to ensure full pyrolysis of the material under investigation. From the start of the isothermal reaction period liberated volatiles are swept by the helium flow onto the trap, whilst non-condensable gases (fixed gases) proceed to the fixed gas analyser (FGA), which is triggered automatically to start running.*

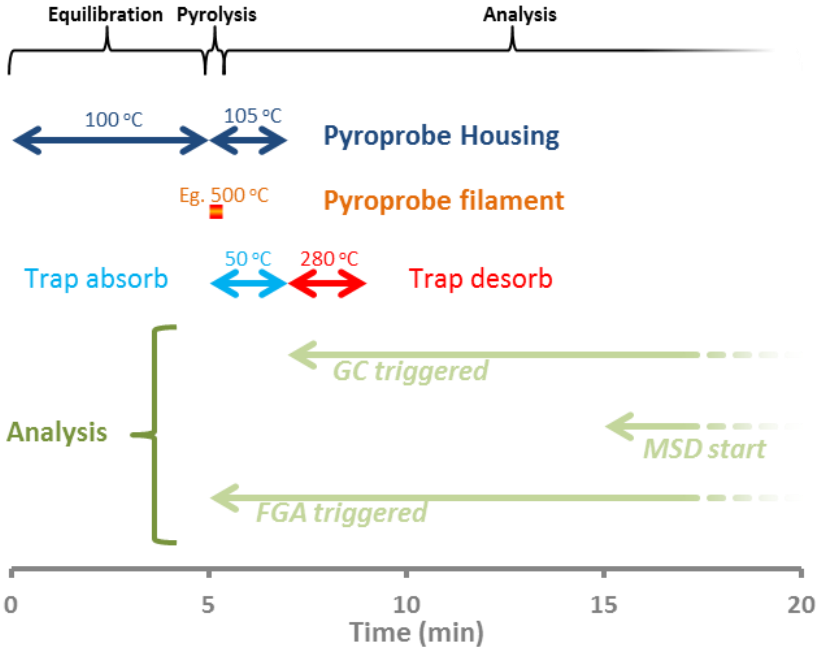

Figure L.16 Chronology of a Py-GCMS experiment.

The trap is maintained at 50 °C for a full two minutes from the start of the isothermal reaction period to enable absorption of all volatile pyrolysate, after which time it is heated to 280 °C for a further two minutes to release the trapped compounds into the injection port of the GCMS *via* a heated transfer line. The GC is primed to start automatically as soon as pyrolysate begins to desorb from the trap, with the MSD beginning to detect after a five minute delay (included to protect the ion-source filament whilst no analyte compounds were eluting). The procedure then extends for as long as is

* Note that the increase in temperature of the pyroprobe housing from 100 °C to 105 °C at the start of the isothermal reaction period has no practical significance.

necessary for the GCMS and FGA to finish their respective runs, prior to cleaning and resetting the apparatus and analysis of the data (see Section L.3.3). Generally it was found that all compounds were cleanly transferred from the trap and from the column during the analysis period, meaning that additional cleaning of this equipment was not required between each run (unless large quantities of poorly volatile material was generated, see Section L.3.4.4).

Finally, in order to discern the retention time and MS fingerprint of standard reference compounds, samples of the pure material (Sigma Aldrich) were transferred to a quartz tube (approximately 10 μg for solids or 100 nL for liquids) and heated at 500 °C under the conditions listed above. For highly volatile species the five minute equilibration period was skipped, and for thermally unstable compounds, a lower temperature (100 – 300 °C) was used as required. Some compounds were also identified as being well-documented products originating from the pyrolysis of a parent molecule (for example the formation of acetic acid from the thermolysis of ethyl acetate).[15]

L.3.3 Py-GCMS: data analysis

L.3.3.1 Py-GCMS data analysis: overview

The rapid pyrolysis of even very simple organic molecules can yield hundreds of volatile products. Whilst this level of complexity can provide valuable insight into the degradation pathways of a material, there is an associated cost in terms of time of computation and analysis of the data. The most common method of interpreting a pyrolysis experiment is through Py-GCMS, whereby, following pyrolysis, compounds are first separated *via* online gas chromatography (GC) and then analysed *via* a coupled mass spectrometer (MS) (see Section L.3.1 for details). Thus, a typical data-set from a Py-GCMS experiment is no different from that of any other direct injection GCMS analysis, with the possible exception of the complexity of the former compared to the latter. Despite their apparent similarities, direct injection GCMS and Py-GCMS data sets are often treated quite differently in the literature. Whilst quantitative interpretation of direct injection GCMS is routine, a similar treatment of Py-GCMS data is rare owing to difficulties associated with the inclusion of an internal reference or the making up of calibration standards for the multitude of formed products. Consequently, the vast majority of Py-GCMS studies found in the literature are either purely qualitative or semi-quantitative, with absolute quantitation being much less common, and attempts to attain a mass balance extremely scarce.

In lieu of a standard methodology for analysing Py-GCMS data, the following sections outline in detail the approaches used in this thesis along with their rationale. Sections L.3.3.3-L.3.3.5 detail qualitative and semi-quantitative methods for Py-GCMS analysis, in which volatile pyrolysis products are identified and their selectivities determined based on relative peak area. Whilst much insight can be gained from these internally referenced studies, a more holistic view of pyrolysis is desirable – especially when considering the pyrolysis of materials for industrial-scale applications. With this in mind Sections L.3.3.6-

L.3.3.9 detail attempts to quantify absolutely the volatile, char, moisture, and fixed gas yields, with a view to obtaining a pyrolysis mass-balance (discussed in L.3.3.9).

L.3.3.2 Py-GCMS data analysis: preliminary measures and data clean-up

In the first instance, acquired Py-GCMS data must be processed to a state where it is suitable for interpretation and analysis. For this thesis, the following preliminary measures were undertaken:

I. **Background spectra** At the start of each day, a blank pyrogram was run whereby the trap was desorbed into the GCMS to provide a background spectrum. Thus, persistent contaminants (for example siloxane from the GC column) could be disregarded in subsequent analysis.

II. **Discounting m/z values** The choice of range of m/z values detected can have a large impact on the interpretation of the subsequent dataset. Whilst m/z = 300 is a sensible upper limit (with m/z = 500 not revealing any new peaks), the lower limit is less straightforward. Detecting over too wide a range can generate a "noisy" spectrum, whilst detecting over too narrow a range can lead to truncation of peaks (see Figure L.17). Hence, in this work, all m/z values from 1.6 – 300 were detected but then m/z = 4.0, 18.0, 28.0, 32.0, and 44.0 (± 0.2 in each case) corresponding respectively to signals from He, H_2O, N_2/CO, O_2 and CO_2 were filtered from the data following acquisition.[†]

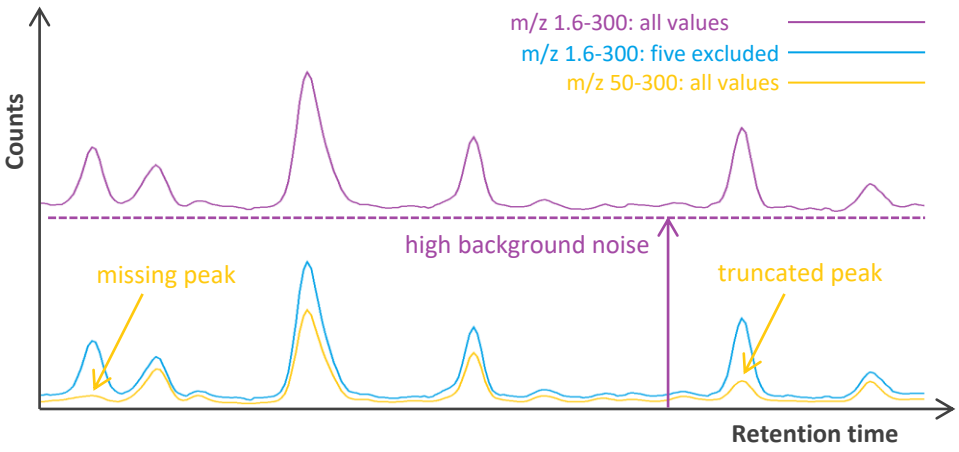

Figure L.17 The effect of choice of m/z range on data analysis in Py-GCMS.

[†]Technical note: owing to a glitch in the version of the *MassHunter* software, extracting the total ion chromatogram (TIC) and excluding the selected masses does not perform the desired function. Instead, the exclusion is achieved by generating an extracted ion chromatogram (EIC) with all of the m/z values in the range 1.6-300 included, except 4.0, 18.0, 28.0, 32.0, 44.0 (±0.2).

III. **Signal to noise ratio (SNR) check** A one minute section of the chromatogram with no pyrolysate signals was selected to represent the "noise" signal. The height of each detected peak was then measured against the noise signal to give the signal to noise ratio (SNR). Peaks with SNR < 1.0 were disregarded for the purposes of the analysis.

IV. **MSD sensitivity check (quantitative pyrolysis only)** In the absence of an internal standard, as might be used in direct injection GCMS, another solution must be sought to ensure detector consistency between samples. Here, the carrier gas signal (Helium, m/z = 4.0) measured at the same point in each run (a time selected to be when no other compounds were eluting) could be used to ensure that the MSD sensitivity was not drifting significantly between samples. Over a period of one week with heavy usage (70 runs), the He signal at retention time = 12.00 minutes was recorded with a mean value 3.01 X 10^6 and a standard deviation of ± 0.15 X 10^6, indicating the drift in the sensitivity of the MSD was not significant over this period. Re-tuning was carried out once per week or if significant drift in the He signal was detected. Experiments intended for direct comparison were run within the same tune. Hence, whilst the He signal was not used explicitly for quantitative purposes, it was a useful data quality control measure.

L.3.3.3 Py-GCMS qualitative data analysis: compound identification and classification

The pyrolysis of even the most simple molecules can give rise to many hundreds of products. Whilst on-line GC helps to separate pyrolysate compounds, and MSD can provide a unique fragmentation pattern for each one, identification is still a non-trivial exercise. Advances in MS libraries and database-searching algorithms have helped to simplify the task by providing likely candidates for a peak identity *via* probability based matching (PBM), though an unambiguous assignment can only be truly made by matching the retention time and MS fingerprint with a standard sample of that compound.[4] Whilst standard compounds were utilised where possible, they could not be supplied for every identified species, hence other methods of assignment are shown in Table L.5. A full list of all the compounds detected throughout the work undertaken in this thesis is given in Appendix N. A code is provided with each compound to signify how it was assigned to provide an indication of the certainty of the ascribed chemical identity (see Table L.5).

Interpretation of the extensive lists of pyrolysate compounds produced by each starting material can be greatly simplified by identifying suitable chemical groupings. Whilst some studies classify molecules based on carbon number or molecular weight for instance, for uronide pyrolysis, grouping based on common chemical moieties was found to be most convenient. The groupings utilised in this thesis are outlined in Table L.6, along with the code used to identify an assigned molecule as a member of a particular class.

Table L.5 Methods for assigning chemical identities of compounds detected in Py-GCMS.

Code	Method of chemical identification
A	Matching of MS fragmentation pattern and retention time to a well-defined standard
B	Matching of MS fragmentation pattern from similar studies in the literature
C	Matching of MS fragmentation pattern and retention time of the known degradation product of a well-defined standard
D	NIST MS library match, probability ≥ 95%
E	NIST MS library match, probability ≥ 90%
F	NIST MS library match, probability ≥ 85%
G	NIST MS library match, probability ≥ 80%
H	NIST MS library match, probability ≥ 70%
T	Tentative assignment based on informed inference
*****	Assignment includes the possibility of closely related isomers/tautomers

Table L.6 Classification of chemicals generated in Py-GCMS experiments.

Class	Chemical classification	Common chemical feature
O	**Aliphatic or small oxygenated molecules**	*Acyclic alkanes and alkenes including those with ester, ketone, aldehyde, ether, alcohol, ketene, and carboxylic acid moieties*
Ar	**Aromatic or cyclohexene derivative**	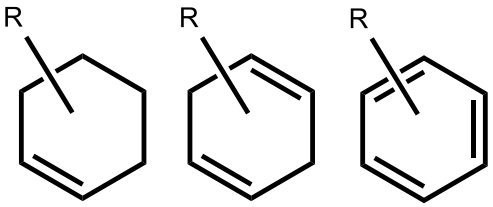
CP	**Cyclopentene derivative**	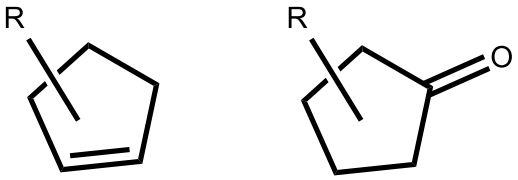
FN	**Furanone derivative**	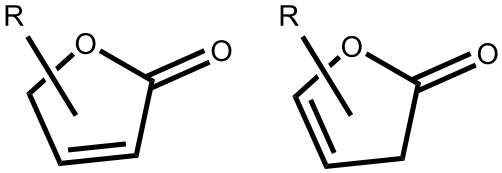
FR	**Furan derivative**	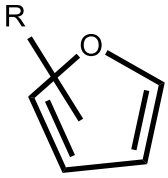

Continued…

FF	**Furfural derivative**	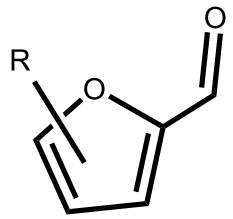
N	**Containing a heteroatom (X)**	*X is typically nitrogen, though some iodine compounds were also detected*
U	**Unknown**	*Could not be identified*
AH	**Anhydrosugar**	*Containing an intramolecular ether derived by elimination of water from the parent saccharide. These compounds were problematic for Py-GCMS.*

L.3.3.4 Py-GCMS semi-quantitative data analysis: total peak area (TPA) and normalised total peak area (nTPA)

Once the pyrogram has been pre-processed (see Section L.3.3.2) and pyrolysate compounds have been identified and classified, the peaks can be integrated to establish the total ion count that makes up their area. The integration for each peaks was carried out by hand, above the level of the noise. When two peaks overlapped, the measured area was split manually according to the approximate proportion of the two compounds as judged from the intensity of their respective MS signals. Once integrated, the individual peak areas can be summed together to give a total peak area (TPA).

The TPA can be affected by:

- The mass of material originally pyrolysed
- The transfer efficiency of pyrolysate to the MSD
- The split ratio of the GC
- The ionisation efficiency of the pyrolysate material
- The sensitivity of the MSD
- The gain factor of the MSD

Assuming, in the first instance, that the split ratio of the GC remains constant, the sensitivity of the MSD remains constant (which can be verified by reference to the helium signal at a specified time, see Section L.3.3.2), the gain factor of the MSD remains constant, the ionisation efficiency of each compound is the same, and that each compound is transferred to the MSD with equal efficiency, then the TPA is purely a function of the amount of material that is originally pyrolysed. As the mass of the original material is known (see Section L.3.2.1), then the TPA can be normalised according to either Equation [L.2] or [L.3]. Thus, the normalised TPA (nTPA) can be used as a measure of the yield of volatile compounds to be generated per unit of starting material.

For well-defined chemicals:

$$\text{normalised total peak area (units mol}^{-1}) = \frac{\sum \text{integrated Py-GCMS peaks (units)}}{\text{moles of pyrolysable starting material (mol)}} \quad \textbf{[L.2]}$$

For biomass:

$$\text{normalised total peak area (units } \mu\text{g}^{-1}) = \frac{\sum \text{integrated Py-GCMS peaks (units)}}{\text{moisture-corrected starting mass } (\mu\text{g})} \quad \textbf{[L.3]}$$

The nTPA is a fairly arbitrary measure when considered in isolation, though it can be useful to compare the nTPA values of two different materials under given conditions. In this case, the largest nTPA in the set being compared is usually set as 100 for convenience, and the other values are subsequently quoted relative to that.

Of course, the problem with using the nTPA as a measure of the yield of volatile organic substances, is that it relies on the assumption that all detected compounds have the same ionisation efficiency in the MSD. The second requisite assumption, that all compounds are transferred with equal efficiency from the pyrolysis chamber to the MSD is also dubious. Whilst similar compounds are expected to ionise to roughly similar degrees,[12,16] and the transfer of chemical species with similar volatilities is expected to be approximately constant, without deriving a relative response factor for each individual compound, the level of required correction is not known. Hence, whilst the nTPA is a useful first indicator of the yield of volatile material released in pyrolysis, it is only an expedient substitute for equivalent values derived from properly calibrated standards.

With the above discussion in mind, the treatment of anhydrosugars in Py-GCMS analysis of carbohydrates must be given special attention. The poor volatility of anhydrosugars (compared to furanic and small oxygenate pyrolysis products) meant that these compounds were excluded from calculations involving peak area.[‡] This issue is discussed further in Section L.3.4.4.

L.3.3.5 Py-GCMS semi-quantitative data analysis: product %selectivity by peak area

Once the total peak area (TPA) has been determined (see Section L.3.3.4), the % selectivity (by peak area) towards each individual compound can be calculated according to Equation [L.4].

$$\text{selectivity by peak area (\%)} = \frac{\text{integrated area of compound peak (units)}}{\text{total peak area (units)}} \text{ X } 100 \quad \textbf{[L.4]}$$

[‡] With the exception of levoglucosenone, which is considered an anhydrosugar but with a much higher volatility than is typical of this class of compounds.

Owing to the problematic assumptions underpinning the calculation of TPA as well as the negation of other products fractions (char, anhydrosugars, fixed gases etc.), the %selectivity by peak area has a somewhat restricted definition. However, %selectivity by peak area still serves as a useful initial metric for estimating the likely composition of the volatile fraction of pyrolysis and is one of the most ubiquitous methods of analysis of micropyrolysis data (see many examples in the *Journal of Analytical and Applied Pyrolysis*).[17–23] Furthermore, as the %selectivity by peak area is self-contained (that is to say, it is not dependant on consideration of external factors such as the starting mass of the material, the split ratio of the GC, the sensitivity of the MSD etc.), this metric is much less prone to error than some of the fully quantitative methods described in the following sections.

L.3.3.6 Py-GCMS quantitative data analysis: 2-furaldehyde yield

As stated in L.3.3.1, to properly quantify the yield of a pyrolysate compound by Py-GCMS analysis, a "relative response factor" must be calculated. Whilst in direct injection GCMS, mixtures of calibration standards are simple to prepare and run through the equipment, Py-GCMS presents difficulties in terms of preparing a well-defined quantity of volatile material from the probe to the GC injection port. As 2-furfural proved to be a particular compound of interest, a procedure was developed to calibrate specifically for this species. Here, standard solutions of 2-furfural (Sigma Aldrich) were made up in toluene (AR grade) at concentrations of 0.0 - 0.1 M, and 0.50 μL transferred by means of a Hamilton 1.00 μL microsyringe to a quartz pyrolysis tube packed with quartz wool. The quartz tube was quickly loaded into the pyroprobe and the pyrolysis program (heating at 20 °C ms^{-1} to 300 °C, hold for 60 seconds) initiated immediately without the usual 5 minute equilibration period. The rest of the Py-GCMS run then proceeded as before.[§] Through this procedure, the Py-GCMS was shown to behave linearly to increasing 2-furfural quantities (see Figure L.18) and hence a calibration equation was obtained for two different GC split ratios, from which the peak area of 2-furfural could be translated to a molar quantity. Assuming the MSD sensitivity remains constant between Py-GCMS runs (which could be verified by reference to the internal helium signal, see Section L.3.3.2), then a molar quantity of furfural could be calculated for all compounds pyrolysed.

[§] The large excess of toluene in comparison to furfural necessitated the inclusion of a 10 minute solvent delay at the start of the GCMS run to protect the MSD.

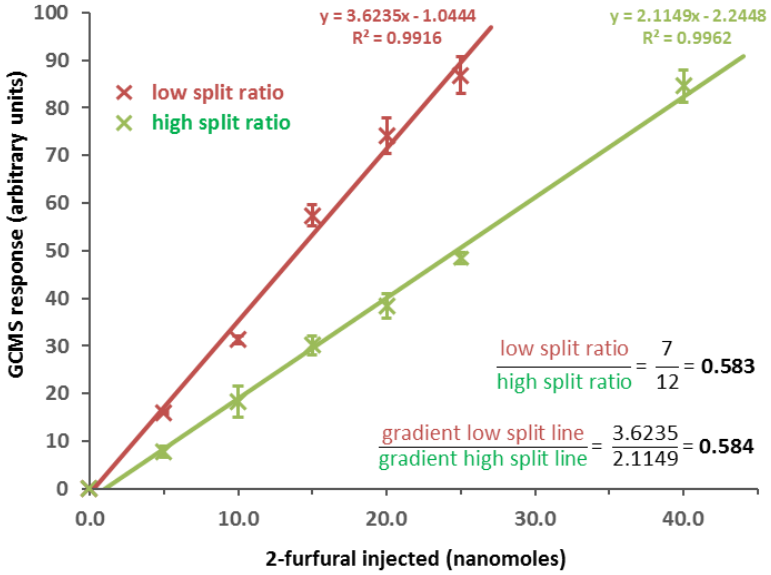

Figure L.18 Exemplar plot of the Py-GCMS response to varying amounts of 2-furfural obtained at two different GC split ratios. Each marker represents the mean value of three independent runs and error bars depict the standard deviation.

Having established the number of moles of 2-furfural formed during the pyrolysis of the material, a yield of 2-furfural for each pyrolysed compound could be discerned in absolute terms according to Equation [L.5] (for uronides – yield as a mol.% of the starting quantity of uronate monomer) or Equation [L.6] (for biomass – yield as a mol.%C of the starting molar quantity of carbon).

$$\text{yield of 2-furfural (mol.\%)} = \frac{\text{moles of 2-furfural formed}}{\text{moles of uronide monomer pyrolysed}} \text{ X } 100 \qquad \textbf{[L.5]}$$

$$\text{yield of 2-furfural (mol.\%C)} = \frac{\text{moles of 2-furfural formed X 5}}{\text{moles of carbon in mass of pyrolysed biomass}} \text{ X } 100 \qquad \textbf{[L.6]}$$

L.3.3.7 Py-GCMS quantitative data analysis: fixed gas yield

The pyrolyser can also be coupled to a fixed gas analyser (FGA), which comprises a gas chromatograph (GC) and thermal conductivity detector (TCD). The purpose of the FGA is to provide a quantitative measure of the yield of non-condensable gases (such as CO_2, CO, H_2, and CH_4) that bypass the trap, as well as potentially H_2O. As the addition of the FGA equipment came much later in the preparation of this thesis, the degree of method development is accordingly much less. As in the case of the Py-GCMS analysis of 2-furaldhehyde (see Section L.3.3.6), identifying a suitable calibration method was the first challenge to quantifying permanent gas yields. Whilst direct injection of a standard gas mix may well prove to be the best method of calibrating the equipment (which has a separate injection port suitable for this process), such mixes are expensive and not always readily available. As TGA-MS and similar studies had indicated that CO_2 and H_2O were the

predominant fixed gases generated in the experiments conducted here, a method was developed to quantify these species from the thermolysis of $NaHCO_3$. Here, the clean and well defined thermolysis of $NaHCO_3$ was utilised to yield stoichiometric quantities of CO_2 and H_2O (see Equation [L.7]).[3]

$$2\ NaHCO_3 \xrightarrow[20\ °C\ ms^{-1}]{300\ °C,\ 20\ s} Na_2CO_3 + H_2O + CO_2 \qquad \textbf{[L.7]}$$

By pyrolysing different quantities of $NaHCO_3$ and integrating the area of appropriate peak in the resulting GC-TCD, a calibration line could be established for CO_2 (see Figure L.19). Unfortunately, such a well-behaved response could not be replicated for the corresponding H_2O calibration (potentially due to losses on the trap), and so other methods were sought to quantify the yield of generated water (see Section L.3.3.9).

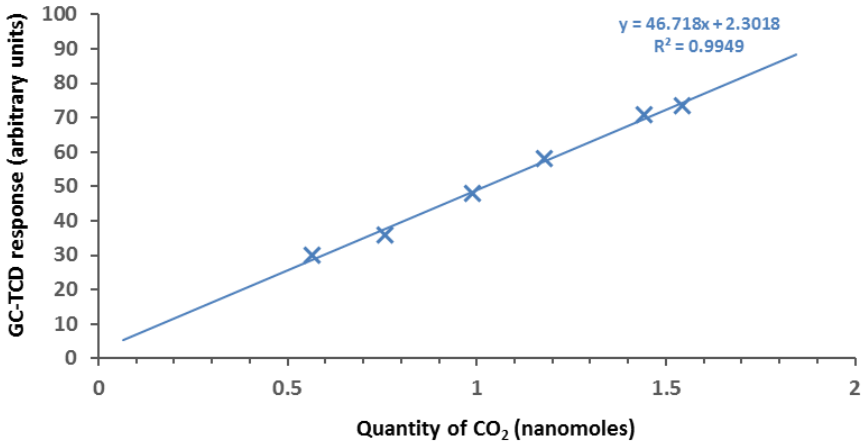

Figure L.19 Response of the CG-TCD of the fixed gas analyser to quantities of CO_2 evolved from the pyrolysis of $NaHCO_3$ at 300 °C.

L.3.3.8 Py-GCMS quantitative data analysis: char yields

The char yield, defined as the mass of solid material remaining at the end of the Py-GCMS experiment relative to the amount of starting material, is easily calculated by weighing the sample tube before and immediately after pyrolysis to establish the mass loss (see Equation [L.8]). In order for the char yield derived from Py-GCMS analysis to be comparable with that derived from TGA experiments, a moisture correction was applied (similar to the procedure in Section L.2.3.2). The moisture correction simply involved deducting the mass of moisture in the sample (which was known from TGA analysis) from the starting sample mass (see Equation [L.9]). Similarly a yield for the "organic char" (the char calculated as if there was no moisture or metal ions in the sample) can be calculated using Equation [L.10].

$$\text{char yield (wt.\%)} = \frac{\text{sample mass after pyrolysis}}{\text{sample mass before pyrolysis}} \text{ X } 100 \qquad \textbf{[L.8]}$$

$$\text{moisture-corrected char yield (wt.\%)} = \frac{\text{sample mass after pyrolysis}}{\text{sample mass before pyrolysis - mass of moisture in sample}} \text{ X } 100 \quad \textbf{[L.9]}$$

$$\text{organic char yield (wt.\%)} = \frac{\text{sample mass after pyrolysis - mass of metal in sample}}{\text{sample mass before pyrolysis - mass of (moisture + metal in sample)}} \text{ X } 100 \quad \textbf{[L.10]}$$

These technique for the calculation of yields of char suffer from problems of repeatability, as the extremely small sample sizes (coupled with the necessity of leaving gaps in time between measurements on the micro-balance) means that errors are common (see Section L.3.2.1 and L.3.3.10). Consequently, the quoted values for char yield from Py-GCMS are likely to be underestimates as, for example, mass lost due to evaporated moisture from the surface of the quartz tube, or losses of small amounts of quartz wool give a false impression of mass lost by the sample during pyrolysis. Suggestions for further improvement to this measurement technique are made in Section L.3.4.4.

L.3.3.9 Py-GCMS quantitative data analysis: mass balance

In Chapter 4, an attempt to calculate the mass balance of the pyrolysis of **Na-, H-, Ca,** and **Cu(II)-Alg** at 500 °C was made. Here, the following contributions were considered:

- Yield of **2-FF** (calculated according to the method in Section L.3.3.6)
- Yield of **CO** and **CO_2** (calculated according to the method in Section L.3.3.7)
- Yield of **H_2O** (calculated according to the method in Section L.2.3.5)
- Yield of **organic char** (calculated according to the method in Section L.3.3.8)
- Yield of **other volatile organic compounds** (calculated by using the 2-FF calibration in Section L.3.3.6)

The final contribution to the mass balance on this list (the yield of **other volatile organic compounds**) was calculated by assuming that compound identified in the Py-GCMS trace had the same relative response factor as 2-FF. Hence, the calibration plot derived for 2-FF in Section L.3.3.6, was applied directly to estimate the number of moles of each of the other compounds detected in the pyrolysate. Clearly, such an assumption is invalid, but as a first approximation it is a useful metric.

Strictly speaking, the yield of H_2O calculated by TGA-MS (see Section L.2.3.5) is also not a good indicator of the amount of water released during a Py-GCMS experiment, and this is another significant shortcoming of the mass balance.

Finally, as was discussed in Section L.3.3.8, the char yields calculated from Py-GCMS also have a very large error associated with them.

Hence, whilst the pyrolysis mass balance calculated according to the above method was a good first approximation, there are a number of significant improvements that can be made in the future.

L.3.3.10 Py-GCMS data analysis: errors and repeatability

Repeatability between samples analysed by Py-GCMS was found to be extremely good. Running identical samples run under similar conditions frequently yields pyrograms that are virtually superimposable on one another (after accounting for differences in scale due to the original sample quantity). Owing to a greater heterogeneity biomass samples, they generally show slightly poorer reproducibility (in terms of the resultant pyrogram) than do model compounds (such as alginates), though consistency between runs was still good enough so as not to necessitate a large number of repeat measurements. With this in mind, all Py-GCMS experiments were run at least twice, with three or more repeats being carried out as required. Hence, values of the various measurements made by Py-GCMS represent an average of all of those repeats (with obviously erroneous results being disgarded) and errors are quoted as being plus or minus the standard deviation. A summary of the typical errors and their underlying cause is provided in Table L.7.

Table L.7 A summary of errors encountered in quantitative Py-GCMS analysis

Quantity	Typical units[a]	Principle cause(s) of errors	Typical standard deviation
Normalised total peak area	units/mol units/μg	Consistency of integration technique. Mass of sample used.	< 10 % of value
%Selectivity (by peak area)	%	Consistency of integration	< 10 % of value
Char yield	wt.%	Mass of sample post-pyrolysis. Char yield overestimated due to other mass lost by sample.	± 6 wt.%
2-furfural yield	mol.% mol.%C	Mass of sample used	± 5% of value
CO_2 yield	mol.% mol.%C	Mass of sample used	< 1 % of value
H_2O yield	mol.% wt.%	Derived from TGA-MS. Uncertainties in integration of peaks	± 6 wt.%

[a]Units depend on whether the starting material is defined in terms of moles of uronate, moles of carbon or by mass.

L.3.4 Py-GCMS: additional parameter considerations

L.3.4.1 The role of sample dimension Py-GCMS: particle size

Mettler *et al.*[24,25] and Brown *et al.*[13] have demonstrated the important role that sample dimension can play in the micropyrolytic analysis of polysaccharides. Large differences in the pyrolysis product spectrum of cellulose can be observed for samples of various thicknesses, as evolved compounds must travel through differing amounts of reactive matter before escaping the pyrolysis interface.[25] Hence, controlling the size of the particles used in Py-GCMS experiments (typically achieved by sieving) is important. In most experiments reported in this thesis, a mixture of particles were used from within the range 63 – 250 μm (with an approximately even distribution across that bracket). In order

to establish whether differences in mass transport within the particles across within the selected range was important, a set of preliminary experiments were carried out following additional fractionation (small particles of between 63 – 125 μm, and larger ones of between 200 – 250 μm) with pyrolysis for 20 s at 500 °C. Here it was shown that, within the size ranges chosen, both model compounds and macroalgae did not show statistically significant differences in their product selectivity when using small particles, large particles, or a mixture of particles (see Figure L.21).

L.3.4.2 The role of sample dimension in Py-GCMS: sample mass

As explained in Section L.3.4.1 and elsewhere,[13,24,25] the sample dimension can be a critical factor in determining the product slate of a pyrolysis experiment. Whilst the range of particle sizes employed in this thesis was sufficiently narrow to negate differences in mass transport between sample batches (as demonstrated in Section L.3.4.1), it was also important to investigate the effect of the actual mass of sample loaded into the pyrolysis tube each time. Here, different masses of Cu(II)-alginate were pyrolysed (500 °C, 20 °C ms^{-1}, 20 seconds, He 15.0 ml min^{-1}) at a range of masses spanning the order of magnitude (10 – 100 μg) relevant to work in this thesis. The yield (reported as a normalised peak area) and %selectivity (by peak area) of 2-furfural was used as a marker to identify effects due to the changing sample mass. As is depicted in Figure L.20, there is clearly a linear relationship between the sample mass pyrolysed and the amount of 2-furfural produced whilst the %selectivity remains constant (within the bounds of error) across the range of masses. These experiments clearly demonstrate that small changes in sample dimension due to different masses of sample used are unimportant on the scale of the experiments conducted in this thesis. In addition, changing the split ratio of the GC did not appear to significantly alter either the yield of selectivity of 2-furfural production either (following correction of the GC response by a normalising arithmetical factor).

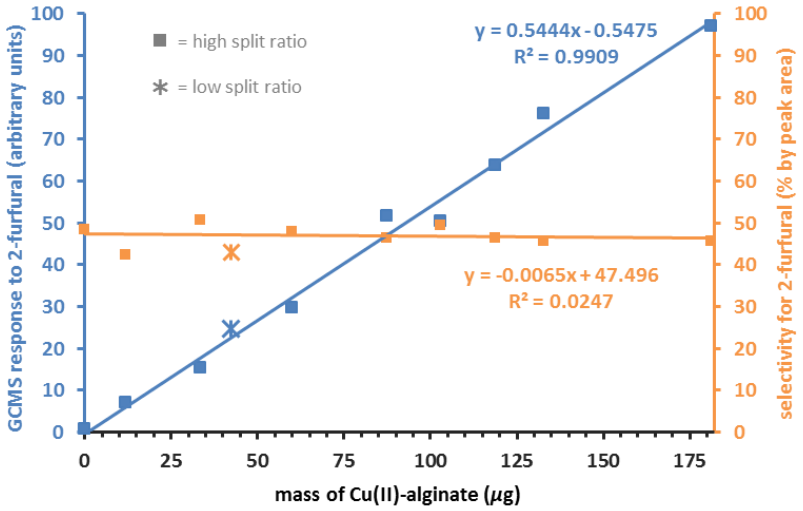

Figure L.20 GCMS response and %selectivity (by peak area) for 2-furfural from the pyrolysis (500 °C, 20 °C ms^{-1}, He 15 mL min^{-1}) of varying masses of Cu(II)-alginate.

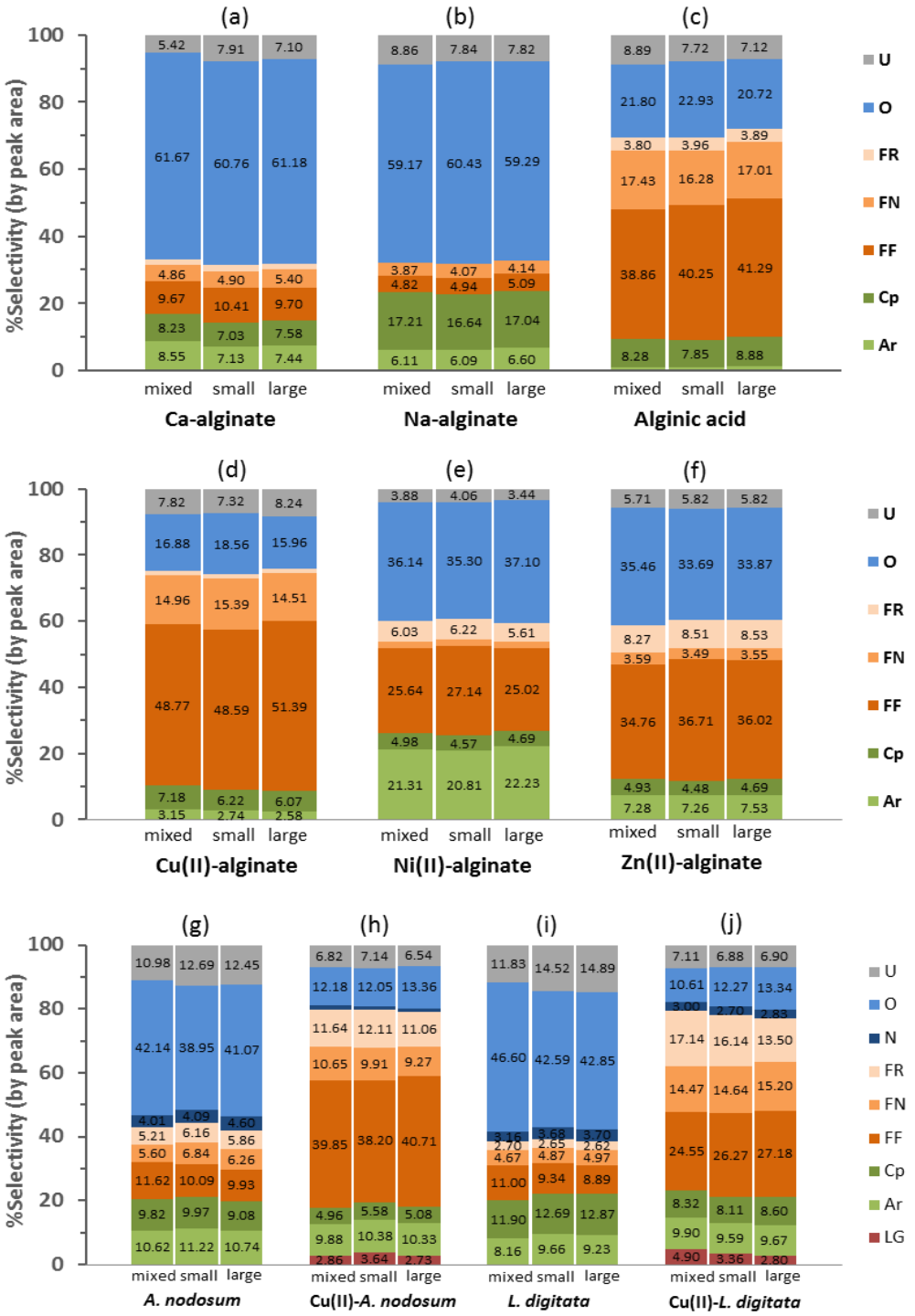

Figure L.21 %Selectivity (by peak area) of product fractions in the Py-GCMS (500 °C, 20 °C ms^{-1}, 20 s, He 15 ml min^{-1}) analysis of (a)-(f) alginates, and (g)-(j) macroalgae with different particle sizes (mixed = 63 – 250 μm, small = 63 – 125 μm, large = 200 – 250 μm). Product fraction codes are: U = unknown, O = aliphatics and small oxygenates, N = heteroatom-containing, FR = furan-derivatives, FN = furanone-derivatives, FF = furfural-derivatives, Cp = cyclopentene-derivatives, Ar = aromatic and cyclohexene-derivatives, LG = levoglucosenone). The size of each fraction is also expressed numerically as a % by peak area.

L.3.4.3 Py-GCMS: comparison with TGA

Whilst Py-GCMS and TGA both operate by thermally decomposing a sample, the results from these two methods are typically not directly comparable. The principle difference between the two techniques is the rate of heating of the sample, whilst TGA experiments usually involve heating between 1 – 100 °C min^{-1} (in the regime of slow – medium pyrolysis), Py-CMS is carried out at rates on the order of 100 000 °C min^{-1} (flash pyrolysis).[26] Such a discrepancy in heating rate has been known to have a profound effect on the product distribution of the pyrolysis.[27] In order to probe quite the extent of the difference between the techniques, several model compounds (alginic acid, Na-, Ca-, and Cu(II)-alginates) were pyrolysed *via* Py-GCMS but under TGA-like conditions (heating at 10 °C min^{-1} to 600 °C). Qualitative analysis of the results indicated that, under the slower heating regime in the Py-GCMS, the yield of volatile material was decreased in all cases relative to the equivalent flash experiments. This drop in yield was anticipated based on the likely increase in secondary reactions at lower heating rates. Interestingly, the high % selectivity by peak area of **HAlg** and **Cu(II)Alg** for 2-furfural was maintained at the lower heating rate, whilst **NaAlg**, and **CaAlg** showed a shift towards the formation of aromatic compounds such as toluene (though these results were not analysed quantitatively).

Hence, whilst TGA data obtained at a slower rate is unsurprisingly not directly relatable to the results obtained by flash Py-GCMS, the former remains a useful technique for probing the kinetics of thermolysis and indicating changes in the stability of a material due to, for example, a bound metal ion. The role of heating rate in uronide thermolysis generally remains to be an area for further investigation.

L.3.4.4 Future improvements to the Py-GCMS technique

As Py-GCMS is a rapidly developing field, and one currently lacking the rigorously defined standard methodologies that exist in other methods of thermal analysis, such as TGA and DSC, there are a number of improvements that could be made to better improve upon the techniques described in the previous sections. These suggestions apply both specifically to the analysis of uronides by Py-GCMS and also more generally:

I. Quantifying anhydrosugars

It is well known that anhydrosugars (including species such as levoglucosan, dianhydromannitol, and uronolactones) can be the dominant products in carbohydrate pyrolysis, but their quantification is less straight forward than for other classes of product.[13,28,29] Difficulties arise due to the much lower volatility of anhydrosugars compared to other pyrolysis products.[13] Hence, whilst 2-furfural boils at 162 °C at atmospheric pressure,[30] levoglucosan boils at 385 °C,[31] meaning that in Py-GCMS the latter compound is not transferred cleanly to and from the trap, and does not give well defined chromatographic peaks.[13] This effect was particularly noticed in the work conducted here with uronides as liberated uronolactones were found to be extremely difficult to desorb completely from the trap. As a consequence, in the analysis of Py-GCMS data in this thesis

anhydrosugars were excluded from all calculations of peak area,* and no attempts were made to quantify them. Of course, the difficulties associated with anhydrosugars also extend to quantifying liberated mono- and oligo-saccharides, which are also extremely poorly volatile when compared to other pyrolysis products.

One potential solution to improving the analysis of anhydrosugars and equivalent compounds is *in situ* silylation.[4] Here, a small amount of (trimethylsilyl chloride) TMSCl is included in the pyrolysis vessel (the quartz tube in this case) such that under the reaction conditions hydroxyl groups are converted to trimethylsilyl ethers. The change of functional group bought about by the added silane reduces H-bond and dipole-dipole interactions, and increases the volatility of the liberated pyrolysis products – assisting in the transfer of the analyte from the pyroprobe to the GC and improving chromatographic resolution (i.e. narrow elution time). The process is becoming more routine in Py-GCMS and has, for example, been employed successfully in a recent study of the carbohydrates present in degraded wood samples.[32] There is scope for adopting this technique for the quantification of uronolactones and other anhydrosugars relevant to the thermolysis of macroalgal biomass.

II. Quantifying low molecular weight compounds

Just as poorly volatile compounds are difficult to quantify by Py-GCMS, other low molecular weight species prove to be problematic. Hence, H_2O shows a partial affinity to the trap that, at small sample sizes, made quantification impossible, whilst formic acid could not be detected even when desorbed directly from the pyroprobe. Potential future solutions could include the use of tandem traps (composed of a series of trapping materials with different functional group affinities) or bypassing the trap completely and performing pyrolysis in "direct" pyrolysis mode.

III. Increasing the mass of pyrolysed sample

In the experiments carried out through this thesis, a deliberately small sample size (0.1 – 0.2 mg). Whilst there are a number of advantages of minimising sample quantity (such as minimising the influence of mass transport control in reaction pathways), the restricted sample size helped to prevent overloading of the trap, GC-column, and MSD, which can be particularly problematic when highly selective pyrolysis reactions occur. However, as described in Sections L.3.2.1 and L.3.3.8, the use of small sample sizes also maximises the error associated with obtaining accurate masses of material, particularly in the case of char yield (which

* With the exception of levoglucosenone, which, whilst considered an anhydrosugar, has a boiling point of with a boiling point of 254 °C at atmospheric pressure,[34] rendering it sufficiently volatile to analyse.

requires for a measurement to be taken before and after pyrolysis). There would, therefore, be benefits to increasing the sample size in terms of more accurately determining the amount of solid remaining at the end of the experiment. Furthermore, a key objective of future work will be to probe the degree to which mass transport effects uronide/macroalgal biomass at a larger scale, hence again increasing the sample size may be warranted. In the case of a study utilising >1 mg of sample, the gain on the MSD could be reduced and the split ratio of the GC increased in order to provide signals of a similar intensity to those from samples on the order of 0.1 mg.

IV. Improving the accuracy of calculations of %yield from Py-GCMS analysis

As the experiments conducted in the preparation of this thesis were largely exploratory, the quantification of 2-furfural was a secondary consideration. As such, there are further optimisations that could be carried out to improve the accuracy of the subsequent calculations. For example, the MSD was operated in "scan mode" for the purpose of this work, however selective ion monitoring (SIM) could be employed to measure the intensity of particular diagnostic m/z ratios (m/z = 96 and m/z = 95 in the case of 2-furfural) with a higher level of accuracy.[33] Of course, as stated above, increasing the mass of sample pyrolysed would also serve to minimise errors in the %yield calculations. Finally, these methods, in addition to the calibration procedure explained in Section L.3.3.6, could be employed to quantify other compounds detected in the pyrolysate to build up a more realistic impression of the absolute yields of volatile organic compounds generated by pyrolysis.

L.4 Acknowledgements

The author wishes to thank members of the RSC Thermal Methods Group for useful discussions regarding techniques in thermal analysis. Dr. Li Li, Dr. Ben Smith, and Michael Lamb are thanked for their support in setting up the Py-GCMS equipment and for suggestions on experimental design. The author is also grateful to Dr. Emily Unsworth for providing training on the microbalance and Doug Carswell for experimental support in performing thermogravimetric analysis.

L.5 References

1 P. J. Haines, *Principles of Thermal Analysis and Calorimetry*, Royal Society of Chemistry, Cambridge, 2002.

2 P. G. Laye, in *Handbook of Thermal Analysis and Calorimetry : Vol 1 Principles and practice*, 1998, vol. 1, pp. 55–93.

3 G. R. Heal, in *Principles of Thermal Analysis and Calorimetry*, Royal Society of Chemistry, Cambridge, 2002, pp 10 - 54

4 S. C. Moldoveanu, in *Techniques and Instrumentation in Analytical Chemistry*, Elsevier, Amsterdam, 1998, Vol. 20, pp. 217–315.

5 J. Mullens, A. Vos, R. Carleer, J. Yperman and L. C. Van Poucke, *Thermochim. Acta*, 1992, **207**, 337–339.

6 J. P. Soares, J. E. Santos, G. O. Chierice and E. T. G. Cavalheiro, *Eclética Química*, 2004, **29**, 57–64.

7 M. P. Segato and É. T. G. Cavalheiro, *J. Therm. Anal.*, 2007, **87**, 737–741.

8 K. Anastasakis, A. Ross and J. Jones, *Fuel*, 2011, **90**, 598–607.

9 A. Ross, C. Hall, K. Anastasakis, A. Westwood, J. Jones and R. J. Crewe, *J. Anal. Appl. Pyrolysis*, 2011, **91**, 344–351.

10 S. Coburn, PhD thesis, University of Greenwich, UK 2006.

11 H. M. McNair and J. M. Miller, *Basic Gas Chromatography*, John Wiley & Sons, Inc., Hoboken, NJ, USA, 2009.

12 J. H. Gross, in *Mass Spectrometry: A textbook. 2nd edition.*, Springer Berlin Heidelberg, Berlin, Heidelberg, 2011, pp. 21–66.

13 F. Ronsse, D. Dalluge, W. Prins and R. C. Brown, *J. Anal. Appl. Pyrolysis*, 2012, **95**, 247–256.

14 A. Reichmuth, S. Wunderli, M. Weber and V. R. Meyer, *Microchim. Acta*, 2004, **148**, 133–141.

15 K. Saito, T. Sasaki, I. Yoshinobu and A. Imamura, *Chem. Phys. Lett.*, 1990, **170**, 385–388.

16 J. A. Beran and L. Kevan, *J. Phys. Chem.*, 1969, **73**, 3866–3876.

17 Y. Wan, P. Chen, B. Zhang, C. Yang, Y. Liu, X. Lin and R. Ruan, *J. Anal. Appl. Pyrolysis*, 2009, **86**, 161–167.

18 J.-W. Choi, J. H. Choi, D. J. Suh and H. Kim, *J. Anal. Appl. Pyrolysis*, 2015, **112**, 141–149.

19 K. Kebelmann, A. Hornung, U. Karsten and G. Griffiths, *J. Anal. Appl. Pyrolysis*, 2013, **104**, 131–138.

20 Q. Lu, C. Q. Dong, X. M. Zhang, H. Y. Tian, Y. P. Yang and X. F. Zhu, *J. Anal. Appl. Pyrolysis*, 2011, **90**, 204–212.

21 A. Pattiya, J. O. Titiloye and A. V. Bridgwater, *J. Anal. Appl. Pyrolysis*, 2008, **81**, 72–79.

22 H. Yuan, S. Xing, Huhetaoli, T. Lu and Y. Chen, *J. Anal. Appl. Pyrolysis*, 2015, **112**, 325–332.

23 M. M. Smits, R. Carleer and J. V. Colpaert, *J. Anal. Appl. Pyrolysis*, 2016, **118**, 335–342.

24 M. S. Mettler, S. H. Mushrif, A. D. Paulsen, A. D. Javadekar, D. G. Vlachos and P. J. Dauenhauer, *Energy Environ. Sci.*, 2012, **5**, 5414–5424.

25 A. D. Paulsen, M. S. Mettler and P. J. Dauenhauer, *Energy & Fuels*, 2013, **27**, 2126–2134.

26 A. V. Bridgwater, *Biomass and Bioenergy*, 2012, **38**, 68–94.

27 T. R. Carlson, T. P. Vispute and G. W. Huber, *ChemSusChem*, 2008, **1**, 397–400.

28 X. Gong, Y. Yu, X. Gao, Y. Qiao, M. Xu and H. Wu, *Energy & Fuels*, 2014, **28**, 5204–5211.

29 S. C. Moldoveanu, in *Techniques and Instrumentation in Analytical Chemistry*, Elsevier, Amsterdam, 2010, vol. 28, pp. 471–526.

30 K. J. Zeitsch, in *Sugar Series: the chemistry and technology of furfural and its many by-products*, 2000, vol. 13, pp. 234–239.

31 T. Shoji, H. Kawamoto and S. Saka, *J. Anal. Appl. Pyrolysis*, 2014, **109**, 185–195.

32 D. Tamburini, J. J. Łucejko, M. Zborowska, F. Modugno, W. Prądzyński and M. P. Colombini, *J. Anal. Appl. Pyrolysis*, 2015, **115**, 7–15.

33 J. H. Gross, in *Mass Spectrometry: A textbook. 2nd edition.*, Springer Berlin Heidelberg, Berlin, Heidelberg, 2011, pp. 651–684.

34 S. Kudo, Z. Zhou, K. Yamasaki, K. Norinaga and J. Hayashi, *Catalysts*, 2013, **3**, 757–773.

Appendix M – Glossary of compounds detected in the Py-GCMS analysis of uronides and uronide-rich biomass

M.1 Aliphatics and small oxygenates (O)

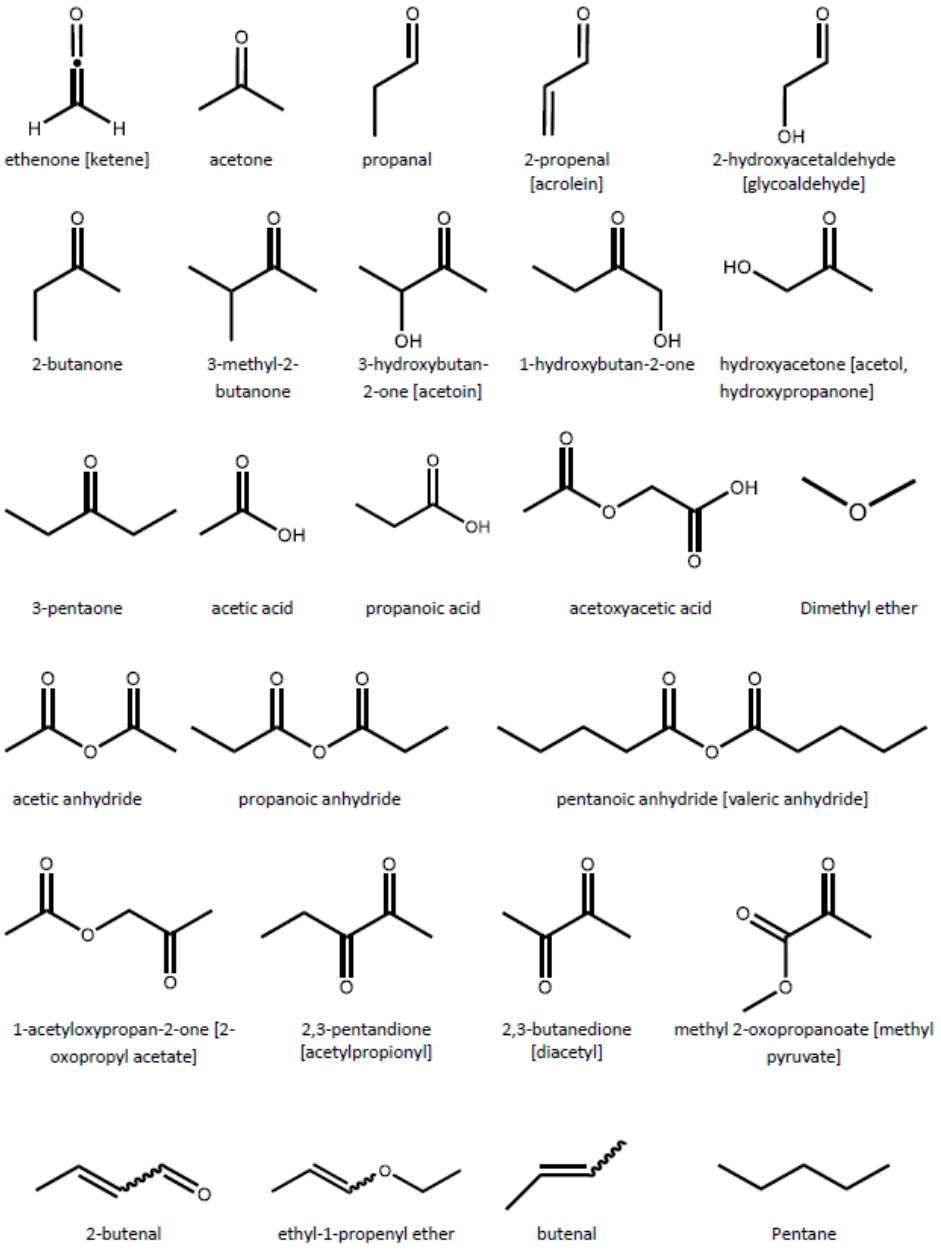

M.2 Furanone derivatives (FN)†

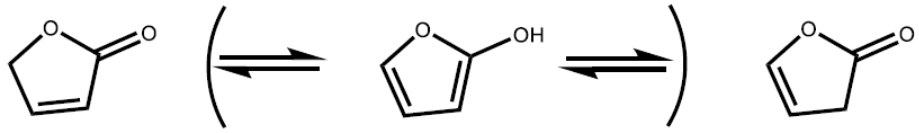

2-(5H)-furanone (2-hydroxyfuran) 2-(3H)-furanone

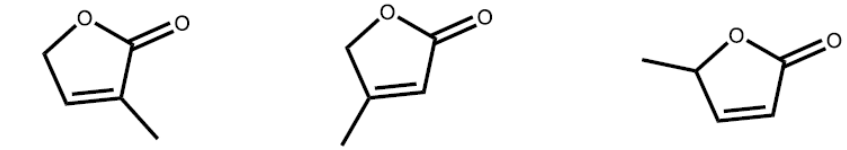

3-methyl-2-(5H)-furanone 4-methyl-2-(5H)-furanone 5-methyl-2-(5H)-furanone

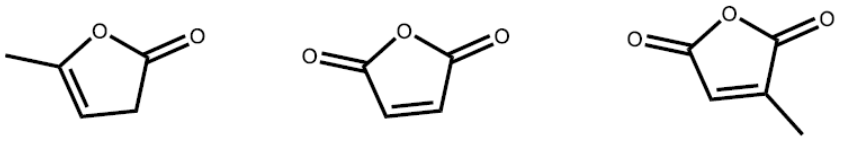

5-methyl-2-(3H)-furanone 2,5-furandione [maleic anhydride] 3-methyl-2,5-furandione

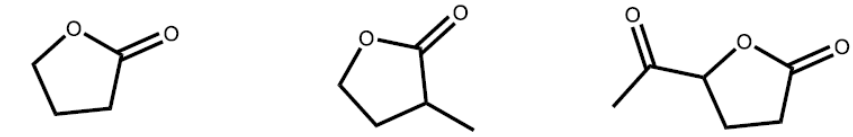

dihydro-2(3H)-furanone [butyrolactone] 3-methyldihydro-2(3H)-furanone 5-acetyldihydro-2(3H)-furanone

M.3 Cyclopentene derivatives (CP)†

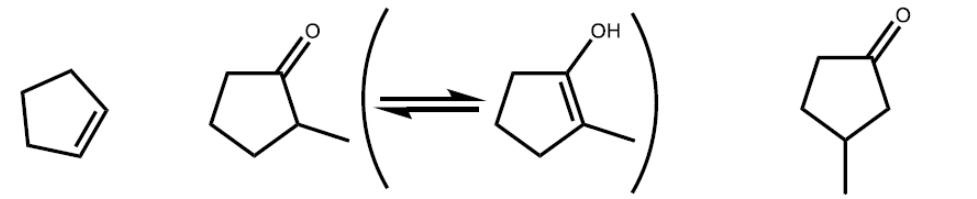

cyclopentene 2-methylcyclopentanone (2-methylcyclopenten-1-ol) 3-methylcyclopentanone (3-methylcyclopenten-1-ol)

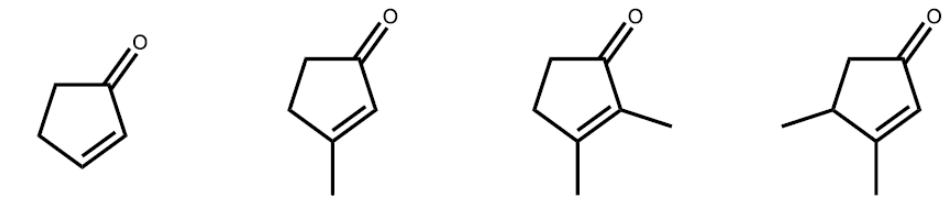

2-cyclopenten-1-one 3-methl-2-cyclopenten-1-one 2,3-dimethyl-2-cyclopenten-1-one 3,4-dimethyl-2-cyclopenten-1-one

† Names of common tautomeric forms shown in parentheses and depicted in some illustrative cases

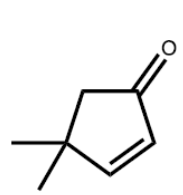

4,4-dimethyl-
2-cyclopenten-1-one

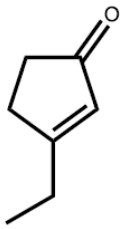

3-ethyl-
2-cyclopenten-1-one

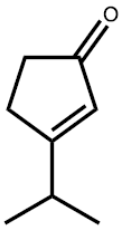

3-isopropyl-
2-cyclopenten-1-one

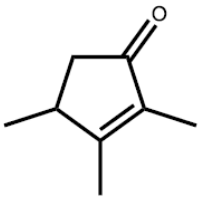

2,3,4-trimethyl-
2-cyclopenten-1-one

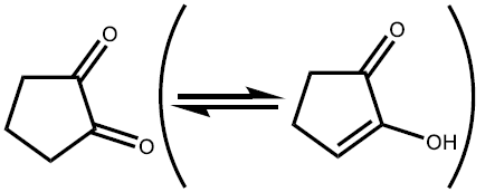

1,2-cyclopentanedione

(2-hydroxy-2-cyclopenten-
1-one)

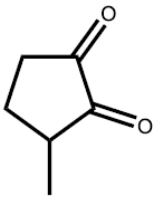

3-methyl-cyclopentane-1,3-
dione
(2-hydroxy-3-methyl-2-
cyclopenten-1-one)

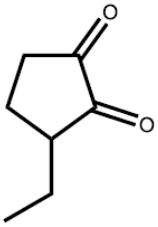

3-ethyl-cyclopentane-1,3-
dione
(2-hydroxy-3-ethyl-2-
cyclopenten-1-one)

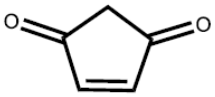

4-cyclopenten-1,3-dione

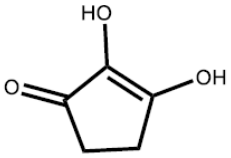

2,3-dihydroxy-2-cyclopenten-1-one
[reductic acid]

M.4 Furan derivatives (FR)

furan

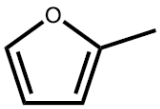

2-methylfuran

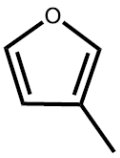

3-methylfuran

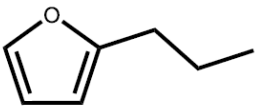

2-propylfuran

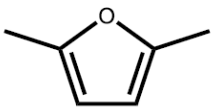

2,5-dimethylfuran

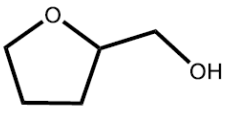

tetrahydro-2-furanmethanol
[tetrathydrofurfuryl alcohol]

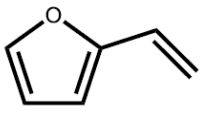

2-vinylfuran

2,3-dihydrofuran

M.5 Furancarboxaldehyde derivatives (FF)

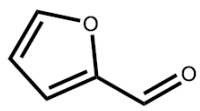

2-furancarboxyaldehyde
[2-furfural]

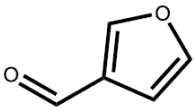

3-furancarboxaldehyde
[3-furfural]

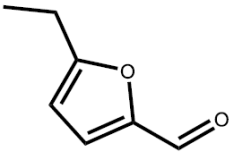

5-ethyl-
2-furancarboxaldehyde
[5-ethylfurfural]

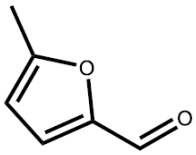

5-methyl-
2-furancarboxaldehyde
[5-methylfurfural]

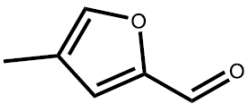

4-methyl-
2-furancarboxaldehyde
[4-methylfurfural]

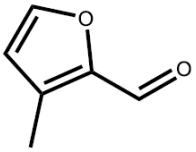

3-methyl-
2-furancarboxaldehyde
[3-methylfurfural]

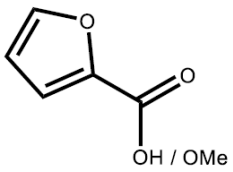

furan-2-carboxylic acid /
methyl ester
[2-furoic acid /
methyl-2-furoate]

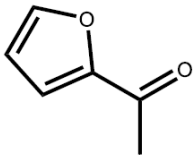

1-(2-furanyl)-ethanone
[2-acetylfuran]

M.6 Aromatics and cyclohexene derivatives (Ar)

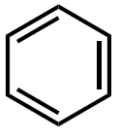

benzene

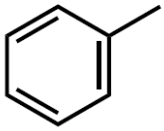

methylbenzene
[toluene]

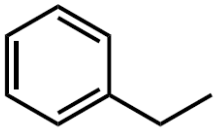

ethylbenzene

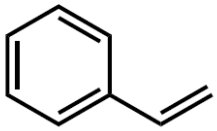

vinylbenzene
[styrene]

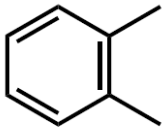

1,2-dimethylbenzene (*o*-
xylene)

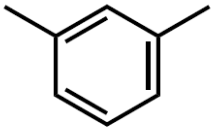

1,3-dimethylbenzene
[*m*-xylene]

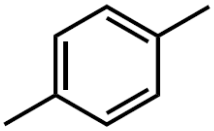

1,4-dimethylbenzene
[*p*-xylene]

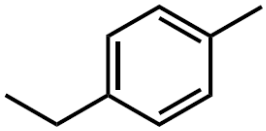

1-ethl-4-methylbenzene
[*p*-ethyltoluene]

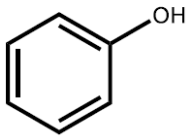

phenol

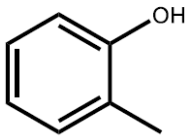

2-methylphenol
[*o*-cresol]

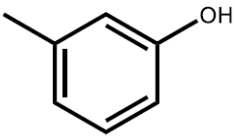

3-methylphenol
[*m*-cresol]

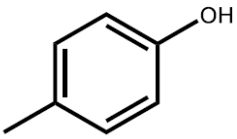

4-methylphenol
[*p*-cresol]

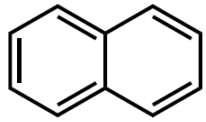
bicyclo[4.4.0]deca-1,3,5,7,9-pentene [napthalene]

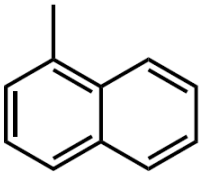
1-methylbicyclo[4.4.0]deca-1,3,5,7,9-pentene [1-methylnapthalene]

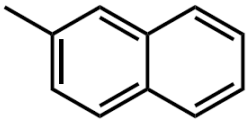
2-methylbicyclo[4.4.0]deca-1,3,5,7,9-pentene [2-methylnapthalene]

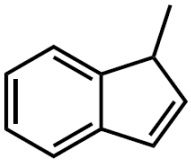
1-methylindene

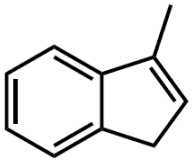
3-methylindene

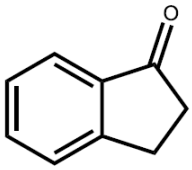

1-indanone

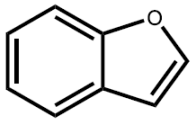

benzofuran

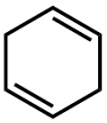
1,4-cyclohexadiene

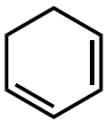
1,3-cyclohexadiene

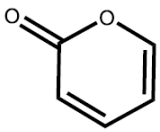

2-pyrone

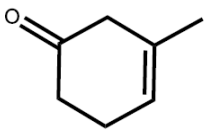

3-methyl-3-cyclohexen-1-one

M.7 Heteroatom containing (N)

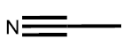

acetonitrile

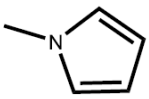

N-methylpyrrole [1-methylpyrole]

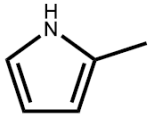

2-pyrrole

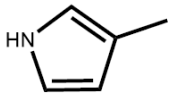

3-pyrrole

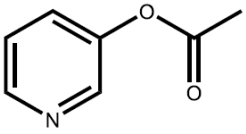

3-hydroxypyridine monoactetate [3-acetoxypyridine]

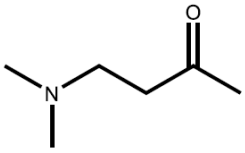

4-(dimethylamino)-2-butanone

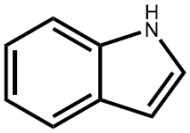

indole

Iodomethane

M.8 Levoglucosenone (LGO)

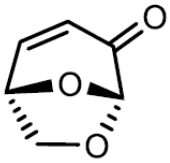

6,8-dioxabicyclo[3.2.1]oct-2-en-4-one [levoglucosenone]

Appendix N: Detection and identification of compounds in Py-GCMS analysis

Classification Key

O	Aliphatic & small oxygenates
Ar	Aromatic & cyclohexene
CP	Cyclopentene derivative
FN	Furanone derivative
FR	Furan derivative
FF	Furfural derivative
N	Heteroatom-containing
U	Unknown
AH	Anhydrosugar

Method of Identification

A	Comparison to standard
B	Comparison to literature (Moldoveanu)
C	Known degradation product of standard
D	NIST data match ≥ 95%
E	NIST data match ≥ 90%
F	NIST data match ≥ 85%
G	NIST data match ≥ 80%
H	NIST data match ≥ 70%
T	Tentative assignment
*	Isomers/tautomers possible

RT (min)	Name (alternative name)	Mw	Class	Identification	Characterisitic fragments m/z (normalised relative intensities)				
5.13	ethenone (ketene)	42.0	O	B, C	**42** (100)				
5.26	2-butene	56.1	O	D, *	**64** (7)	**56** (20)	**41** (37)	**39** (37)	
5.52	unknown	60.0	U		**60**				
5.60	pentane	72.2	O	E	**70** (33)	**55** (67)			
5.83	furan	68.1	FR	A	**68** (52)	**39** (48)			
6.04	2-propenal (acrolein)	56.1	O	D	**56** (27)	**55** (17)	**29** (16)	**27** (24)	**26** (16)
6.05	1,3-cyclopentadiene	66.1	Cp	E	**66** (62)	**65** (38)			
6.05	Iodomethane	141.9	N	G	**142** (70)	**127** (30)			
6.13	acetone	58.1	O	A	**58** (27)	**43** (73)			
6.23	unknown	-	U		**72** (4)	**43** (78)	**29** (17)		
6.57	2,3-dihydrofuran	70.1	FR	E	**70** (10)	**41** (60)	**40** (30)		
6.57	acetonitrile	41.1	N	D	**41** (53)	**40** (29)	**39** (12)	**38** (6)	
6.77	2-methylfuran	82.1	FR	A	**82** (38)	**81** (24)	**53** (24)	**39** (14)	
6.96	3-methylfuran	82.1	FR	D	**82** (45)	**81** (27)	**53** (27)		
7.06	cyclohexadiene	80.1	Ar	F	**80** (29)	**79** (48)	**77** (24)		

7.27	2,3-butanedione (diacetyl)	86.1	O	A	**86** (17)	**43** (83)				
7.33	2-butanone	72.1	O	A	**72** (21)	**57** (7)	**43** (72)			
7.52	3-pentanone	86.1	O	G	**86** (3)	**79** (4)	**57** (38)	**29** (55)		
7.71	benzene	78.1	Ar	D	**78** (58)	**77** (13)	**52** (10)	**51** (10)	**50** (10)	
8.04	2-hydroxyacetaldehyde (glycoaldehyde)	60.1	O	E	**60** (4)	**32** (27)	**31** (42)	**29** (27)		
8.13	unknown mixture	-	U		**96** -	**81** -	-	-	-	-
8.18	dimethyl ether	46.1	O	E	**46** (25)	**45** (20)	**44** (20)	**29** (35)		
8.21	2,5-dimethylfuran	96.1	FR	E	**96** (37)	**95** (30)	**81** (15)	**53** (19)		
8.48	2-butenal	70.1	O	E, *	**70** (32)	**69** (14)	**41** (30)	**39** (25)		
8.54	acetic acid	60.1	O	C	**60** (26)	**45** (35)	**43** (39)			
8.75	3-methyl-2-butanone	86.1	O	G, B	**86** (9)	**55** (18)	**43** (73)			
8.75	4-(dimethylamino)-2-butanone	115.2	N	G	**58** (46)	**43** (22)	**42** (22)	**30** (10)		
8.76	2-pentanone	86.1	O	E	**86** (10)	**71** (5)	**60** (10)	**45** (15)	**43** (60)	
8.85	2-vinylfuran	94.1	FR	E	**94** (52)	**66** (18)	**65** (30)			
8.94	2,3-pentanedione (acetylpropionyl)	100.1	O	F	**100** (13)	**57** (25)	**43** (63)			
9.29	ethyl-1-propenyl ether	86.1	O	F	**86** (41)	**58** (14)	**57** (18)	**29** (27)		
9.38	hydroxyacetone (acetol, hydroxypropanone)	74.1	O	A	**74** (13)	**43** (75)	**31** (13)			
9.49	methylbenzene (toluene)	92.1	Ar	A	**92** (36)	**91** (64)				
9.76	*N* -methylpyrrole (1-methylpyrrole)	81.1	N	E	**81** (32)	**80** (28)	**78** (4)	**53** (8)	**40** (14)	**31** (14)
10.12	3-hydroxybutanone (acetoin)	88.1	O	D	**88** (8)	**45** (51)	**43** (41)			
10.24	propanoic acid	74.1	O	C	**74** (26)	**73** (17)	**57** (9)	**45** (17)	**29** (17)	**27** (14)
10.27	acetic anhydride	102.1	O	A	**43** (100)					
10.56	propanoic anhydride	130.1	O	A	**57** (64)	**29** (24)	**27** (12)			
10.19	methyl 2-oxopropanoate (methyl pyruvate) or isomer	102.1	O	E, B*	**102** (12)	**59** (6)	**43** (82)			
11.18	acetoxyacetic acid	76.1	O	H	**75** (12)	**74** (10)	**43** (79)			
11.24	1-hydroxy-2-butanone (2-oxobutanol)	88.1	O	F	**88** (11)	**57** (89)				
11.26	ethylbenzene/dimethylbenzene (xylene)	106.2	Ar	G, *	**106** (19)	**91** (67)	**67** (15)			
11.40	dimethylbenzene (xylene)	106.2	Ar	D, *	**106** (36)	**91** (64)				
11.55	furanone tautomer	84.1	FN	C, *	**84** (36)	**55** (45)	**39** (8)	**27** (12)		
11.63	2-cyclopenten-1-one derivative?		CP	T	**98** (46)	**70** (14)	**55** (21)	**45** (18)		
11.80	furanone tautomer	84.1	FN	T, *	**84** (52)	**54** (37)	**55** (11)			
11.81	3-furancarboxaldehyde (3-furfural)	96.1	FF	A	**96** (36)	**95** (40)	**67** (5)	**39** (20)		
11.90	2-methylcyclopentanone	98.1	CP	E	**98** (19)	**83** (6)	**70** (6)	**69** (13)	**55** (23)	**42** (32)

11.98	methyl 2-oxopropanoate (methyl pyruvate) or isomer	102.1	O	G, B*	**102** (9)	**43** (91)				
11.98	unknown		U		**91** (42)	**106** (21)	**43** (38)			
12.07	propanal	58.1	O	F	**58** (46)	**29** (54)				
12.07	2,5-furandione (maleic anhydride)	98.1	FN	G	**98** (50)	**54** (50)				
12.08	vinylbenzene (styrene)	104.2	Ar	E	**104** (50)	**103** (25)	**78** (25)			
12.17	3-methylcyclopentanone	98.1	CP	G	**98** (21)	**69** (25)	**56** (14)	**55** (23)	**42** (17)	
12.36	2-furancarboxaldehyde (2-furfural)	96.1	FF	A	**96** (39)	**95** (38)	**67** (3)	**39** (21)		
12.38	2-cyclopenten-1-one	82.1	CP	E, B	**82** (56)	**54** (22)	**53** (22)			
12.57	2-propylfuran	110.2	FR	G	**110** (19)	**81** (49)	**53** (32)			
12.70	3-methylpyrrole	81.1	N	E	**81** (33)	**80** (54)	**53** (13)			
12.78	unknown	98.2		U	**112** (9)	**96** (27)	**81** (42)	**67** (22)		
12.78	2-methylpyrrole	81.1	N	E	**81** (36)	**80** (48)	**53** (16)			
12.90	unknown		U		**120** (3)	**91** (10)	**59** (31)	**44** (34)	**43** (21)	
13.04	4-methylethylbenzene (4-ethyltoluene)	120.2	Ar	H	**120** (20)	**105** (80)				
13.06	tetrahydro-2-furanmethanol (tetrathydrofurfuryl alcohol)	102.1	FR	A	**71** (55)	**43** (28)	**41** (18)			
13.12	5-methyl-2(3H)-furanone	98.1	FN	E	**98** (31)	**55** (41)	**43** (28)			
13.14	1-acetyloxypropan-2-one (2-oxopropyl acetate)	116.1	O	E, B	**116** (6)	**86** (12)	**43** (82)			
13.14	unknown		U		**72** (4)	**43** (78)	**29** (17)			
13.37	cyclopentene / cyclopentanone derivative		CP	D	**96** (34)	**67** (37)	**53** (18)	**39** (11)		
13.47	unknown		U		**103** (7)	**87** (36)	**72** (11)	**44** (46)		
13.48	alkylated furan derivative		FR	T	**110** (8)	**98** (14)	**95** (20)	**83** (14)	**55** (14)	**43** (30)
13.61	2-acetylfuran (1-(2-furanyl)-ethanone)	110.1	FF	A	**110** (26)	**95** (63)	**39** (11)			
13.68	unknown mixture		U		**95** -	**67** -	-	-	-	-
13.74	3- or 4-methyl-2-furancarboxaldyde (3- or 4- methylfurfural)	110.1	FF	T	**110** (40)	**109** (28)	**81** (13)	**53** (19)		
13.77	4-cyclopentene-1,3-dione	96.1	CP	D, C	**96** (37)	**68** (20)	**54** (20)	**42** (24)		
13.93	3-methyl-3-cyclohexen-1-one	110.2	Ar	G	**110** (17)	**96** (13)	**95** (17)	**82** (8)	**68** (13)	**67** (33)
13.94	4-cyclopentene-1,3-dione	96.1	CP	D	**96** (38)	**68** (20)	**54** (18)	**42** (25)		
14.17	3-methyldihydro-2(3H)-furanone	100.1	FN	F	**98** (35)	**68** (19)	**40** (27)	**39** (19)		
14.22	1,2-cyclopentanedione (≡ 2-hydroxy-2-cyclopenten-1-one)	98.1	CP	B, C, E, *	**98** (38)	**70** (6)	**69** (13)	**55** (23)	**42** (19)	
14.29	cyclopentanone derivative		CP	T	**112** (23)	**68** (26)	**43** (26)	**40** (25)		
14.30	unknown		U		**124** -	**105** -	**81** -	-	-	-
14.31	pentanoic anhydride (valeric anhydride)	186.3	O	E	**85** (83)	**57** (17)				
14.39	benzofuran	118.1	Ar	E	**118** (48)	**90** (22)	**89** (22)	**63** (9)		

14.50	methyl-2-furoate	126.1	FF	E	**126** (20)	**95** (67)	**39** (13)				
14.61	unknown mixture		U		**-** -	-	-	-	-	-	
14.73	5-methyl-2-furancarboxaldyde (5-methylfurfural)	110.1	FF	A	**110** (36)	**109** (31)	**81** (4)	**53** (19)	**39** (4)	**37** (4)	
14.79	unknown		U		**124** (24)	**81** (39)	**68** (36)				
14.87	2,3-dimethyl-2-cyclopenten-1-one	110.2	CP	E	**110** (33)	**95** (17)	**67** (50)				
15.02	unknown		U		**128** (16)	**127** (13)	**113** (13)	**86** (29)	**69** (29)		
15.06	3-methyl-2-cyclopenten-1-one	96.1	CP	B, F	**96** (38)	**81** (17)	**67** (26)	**53** (20)			
15.07	N-containing heterocycle?	110.0	N	T	**110** (33)	**69** (17)	**52** (50)				
15.17	dihydro-2(3H)-furanone (butyrolactone)	86.1	FN	F	**86** (18)	**85** (8)	**69** (3)	**56** (15)	**42** (55)		
15.25	3,4-dimethyl-2-cyclopenten-1-one	110.2	CP	H	**110** (22)	**95** (35)	**67** (22)	**43** (22)			
15.32	unknown		U		**85** (38)	**57** (18)	**55** (13)	**31** (10)	**29** (21)		
15.38	2-(5H)-furanone	84.1	FN	A, *	**84** (28)	**55** (49)	**39** (10)	**27** (13)			
15.52	5-methyl-2(5H)-furanone	98.1	FN	F	**98** (22)	**83** (17)	**69** (8)	**55** (31)	**43** (22)		
15.52	unknown mixture		U		**118** -	**114** -	-	-	-	-	
15.66	3-methyl-2,5-furandione	112.1	FR	E	**68** (43)	**40** (21)	**39** (36)				
15.83	2-pyrone	96.1	Ar	C, E	**96** (28)	**68** (40)	**39** (33)				
15.83	3-methyl-1,2-cyclopentanedione (≡ 2-hydroxy-3-methyl-cyclopenten	112.1	CP	B, D, *	**112** (28)	**84** (9)	**83** (9)	**69** (21)	**57** (14)	**55** (19)	
15.93	4,4-dimethyl-2-cyclopenten-1-one	110.2	CP	F	**110** (28)	**95** (17)	**67** (40)	**39** (15)			
16.03	3-methyl-2(5H)-furanone	98.1	FN	G	**98** (36)	**69** (36)	**44** (27)				
16.08	unknown		U		**128** (26)	**113** (26)	**87** (14)	**72** (10)	**58** (24)		
16.18	phenol	94.1	Ar	E	**94** (75)	**66** (25)					
16.18	unknown		U		**132** (38)	**131** (62)					
16.36	unknown		U		**110** (32)	**94** (27)	**82** (41)				
16.46	unknown		U		**138** (2)	**95** (13)	**39** (3)	**54** (82)			
16.52	3-ethyl-2-hydroxy-2-cyclopenten-1-one	126.2	CP	E	**126** (33)	**111** (8)	**97** (8)	**83** (21)	**70** (8)	**55** (21)	
16.65	unknown		U		**128** (73)	**72** (27)					
16.67	2,3,4-trimethyl-2-cyclopenten-1-one	124.2	CP	F	**124** (23)	**109** (30)	**81** (30)	**79** (17)			
16.69	1-methylindene	130.2	Ar	G	**130** (31)	**129** (25)	**128** (15)	**115** (29)			
16.80	3-isopropyl-2-cyclopenten-1-one	124.2	CP	G	**124** (28)	**123** (16)	**109** (16)	**109** (16)	**81** (24)		
16.86	3-ethyl-2-cyclopenten-1-one	110.2	CP	G	**110** (30)	**81** (30)	**67** (20)	**53** (20)			
16.92	3-methylindene	130.2	Ar	G	**130** (29)	**129** (28)	**128** (14)	**115** (29)			
16.92	methylphenol (cresol)	108.1	Ar	E	**108** (39)	**107** (35)	**90** (10)	**77** (16)			
17.20	cyclopentenone derivative		CP	T	**126** (40)	**83** (20)	**64** (13)	**55** (27)			

17.35	3-hydroxypyridine monoacetate (3-acetoxypyridine)	137.1	N	E	**137** (10)	**95** (48)	**43** (29)	**39** (14)		
17.38	unknown		U		**124** (23)	**123** (14)	**110** (12)	**109** (16)	**95** (14)	**81** (21)
17.46	methylphenol (cresol)	108.1	Ar	E	**108** (39)	**107** (36)	**79** (13)	**77** (13)		
17.58	5-ethyl-2-furancarboxaldyde (5-ethylfurfural)	124.1	FF	H	**124** (14)	**109** (14)	**108** (14)	**107** (14)	**96** (22)	**95** (20)
17.68	bicyclo[4.4.0]deca-1,3,5,7,9-pentene (napthalene)	128.2	Ar	E	**128** (100)					
17.81	4-methyl-2(5H)-furanone	98.1	FN	E	**98** (26)	**69** (74)				
17.96	furan-2-carboxylic acid (2-furoic acid)	112.1	FF	A	**112** (43)	**95** (37)	**39** (20)			
18.18	6,8-dioxabicyclo[3.2.1]oct-2-en-4-one (levoglucosenone)	126.1	AH	E (94%)	**126** (2)	**98** (23)	**97** (13)	**96** (18)	**68** (25)	**53** (19)
18.36	unknown		U		**136** (10)	**130** (21)	**124** (12)	**121** (16)	**102** (24)	**65** (16)
18.68	unknown		U		**138** (15)	**122** (33)	**107** (52)			
19.16	5-acetyldihydro-2(3H)-furanone	128.1	FN	D	**128** (5)	**85** (48)	**57** (10)	**43** (19)	**29** (19)	
19.23	methylbicyclo[4.4.0]deca-1,3,5,7,9-pentene (methylnapthalene)	142.2	Ar	E, B, *	**143** (7)	**142** (42)	**141** (38)	**115** (13)		
19.24	unknown mixture		U		**142** -	**95** -	-	-	-	-
19.45	2,3-dihydroxy-2-cyclopenten-1-one (reductic acid)	114.1	CP	A, T	**114** (37)	**86** (7)	**84** (22)	**56** (35)		
19.51	methylbicyclo[4.4.0]deca-1,3,5,7,9-pentene (methylnapthalene)	142.2	Ar	E, B, *	**143** (7)	**142** (42)	**141** (38)	**115** (13)		
19.63	unknown		U		**128** (19)	**56** (81)				
19.76	unknown		U		**138** (20)	**113** (53)	**70** (27)			
19.81	unknown		U		**131** (21)	**91** (79)				
19.93	1-indanone	146.1	Ar	E	**132** (29)	**104** (29)	**103** (15)	**98** (13)	**78** (14)	
20.52	5-hydroxymethyl-2-furancarboxaldeyde (HMF)	126.1	FF	A	**126** (19)	**109** (3)	**97** (32)	**69** (11)	**41** (21)	**39** (13)
20.95	indole	117.2	N	E	**117** (53)	**90** (24)	**89** (16)	**63** (6)		
22.78	unknown anhydrosugar		AH		**162** (43)	**108** (22)	**80** (17)	**52** (17)		
23.50	lactone	176.1	AH	A	**86** (19)	**73** (15)	**71** (23)	**57** (34)	**55** (9)	
24.36	unknown anhydrosugar		AH		**176** (32)	**108** (30)	**80** (15)	**52** (15)	**39** (8)	
?	formic acid (NIST library)		O	A - not found	**46** (44)	**45** (29)	**29** (27)			

Appendix O – Additional Py-GCMS data for uronides and uronide-rich biomass

O.1 Full lists of compounds liberated at 500 °C by CaAlg, NaAlg, HAlg, and Cu(II)Alg, as detected by Py-GCMS

O.1.1 Compounds liberated by CaAlg at 500 °C

Compound	Class	RT	peak area	STDEV
cyclohexadiene	Ar	7.06	0.93	0.00
benzene	Ar	7.71	0.56	0.04
methylbenzene (toluene)	Ar	9.51	1.47	0.01
ethylbenzene/dimethylbenzene (xylene)	Ar	11.25	0.47	0.03
dimethylbenzene (xylene)	Ar	11.39	1.07	0.09
4-methylethylbenzene (4-ethyltoluene)	Ar	13.04	0.38	0.09
2-pyrone + 3-methyl-1,2-cyclopentanedione	Ar	15.85	0.81	0.09
Phenol + unknown	Ar	16.19	0.96	0.01
1-methylindene	Ar	16.69	0.31	0.05
3-methylindene	Ar	16.92	0.48	0.09
methylphenol (cresol)	Ar	17.45	0.83	0.14
1-indanone	Ar	19.93	0.31	0.04
1,3-cyclopentadiene	Cp	6.06	1.10	0.02
2-cyclopenten-1-one derivative?	Cp	11.63	0.43	0.01
cyclopentene / cyclopentanone derivative	Cp	13.38	1.30	0.02
4-cyclopentene-1,3-dione	Cp	13.94	1.05	0.01
1,2-cyclopentanedione	Cp	14.22	1.44	0.09
3-methyl-2-cyclopenten-1-one	Cp	15.07	1.22	0.02
3,4-dimethyl-2-cyclopenten-1-one	Cp	15.25	0.22	0.00
4,4-dimethyl-2-cyclopenten-1-one	Cp	15.93	0.94	0.09
2,3-dihydroxy-2-cyclopenten-1-one (reductic acid)	Cp	19.46	0.56	0.04
3-furancarboxaldehyde (3-furfural)	FF	11.81	0.47	0.02
2-furancarboxaldehyde (2-furfural)	FF	12.36	7.97	0.11
2-acetylfuran (1-(2-furanyl)-ethanone)	FF	13.61	0.38	0.00
5-methyl-2-furancarboxaldyde (5-methylfurfural) + unknown	FF	14.64	0.86	0.02
furanone tautomer	FN	11.54	0.53	0.00
furanone tautomer	FN	11.81	0.47	0.02
furan-2,5-dione (maleic anhydride)	FN	12.07	0.56	0.04
dihydro-2(3H)-furanone	FN	15.17	0.48	0.01

(butyrolactone)				
2-(5H)-furanone	FN	15.33	0.91	0.05
3-methyl-2(5H)-furanone	FN	16.03	0.54	0.01
4-methyl-2(5H)-furanone	FN	17.81	0.53	0.05
5-acetyldihydro-2(3H)-furanone	FN	19.17	0.86	0.04
2,3-dihydrofuran	FR	6.57	0.42	0.06
2-methylfuran	FR	6.78	1.19	0.04
2-butene	O	5.26	0.96	0.07
pentane	O	5.56	1.09	0.07
2-propenal (acrolein)	O	6.06	1.10	0.02
acetone	O	6.16	8.06	0.07
2,3-butanedione (diacetyl)	O	7.27	5.19	0.03
2-butanone	O	7.27	3.90	0.02
3-pentanone	O	7.52	1.10	0.05
2-hydroxyacetaldehyde (glycoaldehyde)	O	8.05	3.63	0.33
acetic acid	O	8.53	5.46	0.41
2-pentanone	O	8.76	1.25	0.01
2,3-pentanedione (acetylpropionyl)	O	8.93	1.96	0.51
ethyl-1-propenyl ether	O	9.29	1.11	0.11
hydroxyacetone (acetol, hydroxypropanone)	O	9.51	10.32	0.05
3-hydroxybutanone (acetoin) + propanoic acid + acetic anhydride	O	10.14	6.57	0.59
acetoxyacetic acid	O	11.18	1.82	0.06
methyl 2-oxopropanoate (methyl pyruvate)	O	11.98	4.08	0.23
propanal	O	12.07	0.56	0.04
1-acetyloxypropan-2-one (2-oxopropyl acetate)	O	13.14	3.53	0.04
unknown	U	6.23	3.58	0.01
unknown mixture	U	13.68	0.48	0.01
unknown mixture	U	15.52	0.49	0.01
unknown mixture	U	16.47	0.39	0.18
unknown	U	18.40	0.49	0.03

O.1.2 Compounds liberated by NaAlg at 500 °C

Compound	Class	RT	peak area	STDEV
cyclohexadiene	Ar	7.07	0.59	0.03
ethylbenzene/dimethylbenzene (xylene)	Ar	11.25	0.44	0.03
dimethylbenzene (xylene)	Ar	11.39	0.60	0.06
3-methyl-3-cyclohexen-1-one	Ar	13.93	0.44	0.02
phenol	Ar	16.18	1.12	0.18
methylphenol (cresol)	Ar	16.92	1.18	0.01
methylphenol (cresol)	Ar	17.47	0.99	0.06
1-indanone	Ar	19.91	0.77	0.05
1,3-cyclopentadiene	Cp	6.04	1.18	0.01
2-methylcyclopentanone	Cp	11.90	0.67	0.04
3-methylcyclopentanone	Cp	12.17	0.55	0.01
cyclopentene / cyclopentanone derivative	Cp	13.37	1.92	0.01
1,2-cyclopentanedione (2-hydroxy-2-cyclopenten-1-one)	Cp	14.20	1.44	0.15
2,3-dimethyl-2-cyclopenten-1-one	Cp	14.87	0.51	0.01
3-methyl-2-cyclopenten-1-one	Cp	15.06	2.27	0.01
3,4-dimethyl-2-cyclopenten-1-one	Cp	15.25	0.71	0.01
3-methyl-1,2-cyclopentanedione (2-hydroxy-3-methyl-cyclopenten-1-one)	Cp	15.84	1.84	0.09
4,4-dimethyl-2-cyclopenten-1-one	Cp	15.93	2.73	0.11
3-ethyl-2-hydroxy-2-cyclopenten-1-one	Cp	16.52	0.73	0.03
2,3,4-trimethyl-2-cyclopenten-1-one	Cp	16.67	1.14	0.03
3-isopropyl-2-cyclopenten-1-one	Cp	16.80	0.39	0.01
3-ethyl-2-cyclopenten-1-one	Cp	16.86	0.67	0.02
cyclopentenone derivative	Cp	17.20	0.49	0.13
2-furancarboxaldehyde (2-furfural)	FF	12.38	3.44	0.01
2-acetylfuran (1-(2-furanyl)-ethanone) + unknown	FF	13.67	1.01	0.04
5-ethyl-2-furancarboxaldyde (5-ethylfurfural)	FF	17.58	0.37	0.06
2-(5H)-furanone	FN	15.33	0.51	0.01
3-methyl-2(5H)-furanone + unknown m/z 126	FN	16.04	1.82	0.13
4-methyl-2(5H)-furanone	FN	17.81	0.64	0.17
5-acetyldihydro-2(3H)-furanone	FN	19.16	0.91	0.09
pentane	O	5.56	0.76	0.11
acetone	O	6.16	3.97	0.16
2,3-butanedione (diacetyl)	O	7.27	7.37	0.08
3-pentanone	O	7.52	0.99	0.17
2-hydroxyacetaldehyde	O	8.02	4.38	0.44

(glycoaldehyde)				
acetic acid	O	8.54	2.69	0.28
2-pentanone	O	8.76	1.19	0.04
2,3-pentanedione (acetylpropionyl)	O	8.93	1.05	0.01
ethyl-1-propenyl ether	O	9.29	0.52	0.04
hydroxyacetone (acetol, hydroxypropanone)	O	9.39	21.69	0.16
3-hydroxybutanone (acetoin)	O	10.10	0.92	0.02
propanoic anhydride	O	10.10	0.92	0.02
acetic anhydride	O	10.10	0.92	0.02
acetoxyacetic acid	O	11.18	2.90	0.00
methyl 2-oxopropanoate (methyl pyruvate)	O	11.97	6.58	0.26
propanal	O	12.07	0.78	0.02
1-acetyloxypropan-2-one (2-oxopropyl acetate)	O	13.14	1.58	0.03
unknown	U	6.23	5.95	0.71
unknown	U	17.38	1.44	0.08
unknown	U	18.68	0.81	0.08
Unknown m/z 146	U	20.52	0.33	0.04
unknown m/z 110	U	12.78	0.35	0.01

O.1.3 Compounds liberated by HAlg at 500 °C

Compound	Class	RT	peak area	STDEV
2-pyrone	Ar	15.818	0.95	0.43
2-cyclopenten-1-one derivative?	Cp	11.616	0.47	0.14
cyclopentene / cyclopentanone derivative	Cp	13.395	0.53	0.06
4-cyclopentene-1,3-dione	Cp	13.768	0.90	0.29
4-cyclopentene-1,3-dione	Cp	13.931	1.23	0.16
1,2-cyclopentanedione (2-hydroxy-2-cyclopenten-1-one)	Cp	14.168	2.74	0.06
3-methyl-2-cyclopenten-1-one	Cp	15.058	0.68	0.04
3,4-dimethyl-2-cyclopenten-1-one	Cp	15.234	0.62	0.03
2,3-dihydroxy-2-cyclopenten-1-one (reductic acid)	Cp	16.225	0.49	0.01
2,3-dihydroxy-2-cyclopenten-1-one (reductic acid)	Cp	19.456	0.63	0.09
2-furancarboxaldehyde (2-furfural)	FF	12.349	37.53	1.56
2-acetylfuran (1-(2-furanyl)-ethanone)	FF	13.598	0.48	0.11
5-methyl-2-furancarboxaldyde (5-methylfurfural)	FF	14.718	0.85	0.04
furanone tautomer	FN	11.535	1.35	0.15
furanone tautomer + [furan-3-carboxaldehyde (3-furfural)]	FN	11.745	12.46	1.51
5-methyl-2(3H)-furanone	FN	13.116	0.73	0.12
2-(5H)-furanone	FN	15.322	2.89	0.63
furan	FR	5.813	1.51	0.16
2-methylfuran	FR	6.756	1.26	0.05
2-vinylfuran	FR	8.833	1.03	0.03
2-propenal (acrolein)	O	6.044	1.19	0.19
acetone	O	6.146	2.52	0.11
2,3-butanedione (diacetyl)	O	7.245	9.10	0.64
2-hydroxyacetaldehyde (glycoaldehyde)	O	8.012	2.01	0.28
2-butenal	O	8.467	0.74	0.04
acetic acid	O	8.542	1.69	0.25
propanal	O	12.071	2.10	0.36
pentanoic anhydride (valeric anhydride)	O	14.311	2.45	0.18
unknown	U	6.213	3.26	0.77
unknown (m/z 110)	U	13.469	0.41	0.06
unknown mixture	U	14.589	0.99	0.05
unknown (m/z 124)	U	14.793	0.57	0.03
unknown m/z 112	U	15.519	0.82	0.12
unknown m/z 112	U	15.926	1.20	0.61
unknown mixture	U	16.178	0.80	0.03
unknown mixture	U	18.356	0.85	0.03

O.1.4 Compounds liberated by Cu(II)Alg at 500 °C

Compound	Class	RT	peak area	STDEV
benzofuran	Ar	14.39	1.24	0.10
2-pyrone	Ar	15.82	1.91	0.08
cyclopentene / cyclopentanone derivative	Cp	13.40	0.77	0.10
4-cyclopentene-1,3-dione	Cp	13.77	1.00	0.14
4-cyclopentene-1,3-dione	Cp	13.94	1.18	0.02
1,2-cyclopentanedione (2-hydroxy-2-cyclopenten-1-one)	Cp	14.17	3.52	0.76
3-methyl-2-cyclopenten-1-one	Cp	15.07	0.71	0.12
2-furancarboxaldehyde (2-furfural)	FF	12.35	47.14	0.91
2-acetylfuran (1-(2-furanyl)-ethanone)	FF	13.60	0.71	0.08
5-methyl-2-furancarboxaldyde (5-methylfurfural)	FF	14.72	0.92	0.03
furanone tautomer	FN	11.54	1.37	0.12
furanone tautomer + [furan-3-carboxaldehyde (3-furfural)]	FN	11.75	7.41	0.55
5-methyl-2(3H)-furanone	FN	13.12	1.10	0.16
2-(5H)-furanone	FN	15.33	4.24	0.12
5-methyl-2(5H)-furanone	FN	15.52	0.83	0.19
2-methylfuran	FR	6.75	1.24	0.11
ethenone (ketene)	O	5.83	2.46	0.49
2-propenal (acrolein)	O	6.03	1.34	0.28
acetone	O	6.14	2.57	0.06
2,3-butanedione (diacetyl)	O	7.25	3.22	0.17
2-hydroxyacetaldehyde (glycoaldehyde) + unknown mix	O	8.02	1.56	0.20
2-butenal	O	8.47	0.90	0.07
acetic acid	O	8.55	2.91	0.43
propanal	O	12.07	1.94	0.22
unknown	U	6.21	2.92	0.23
unknown	U	11.62	0.77	0.16
unknown (m/z 110)	U	13.48	0.73	0.07
unknown	U	15.95	1.56	0.50
unknown	U	16.18	1.03	0.12
unknown	U	18.36	0.81	0.03

O.2 Normalised total peak areas and conversion data from the Py-GCMS analysis of metal alginates at 500 °C

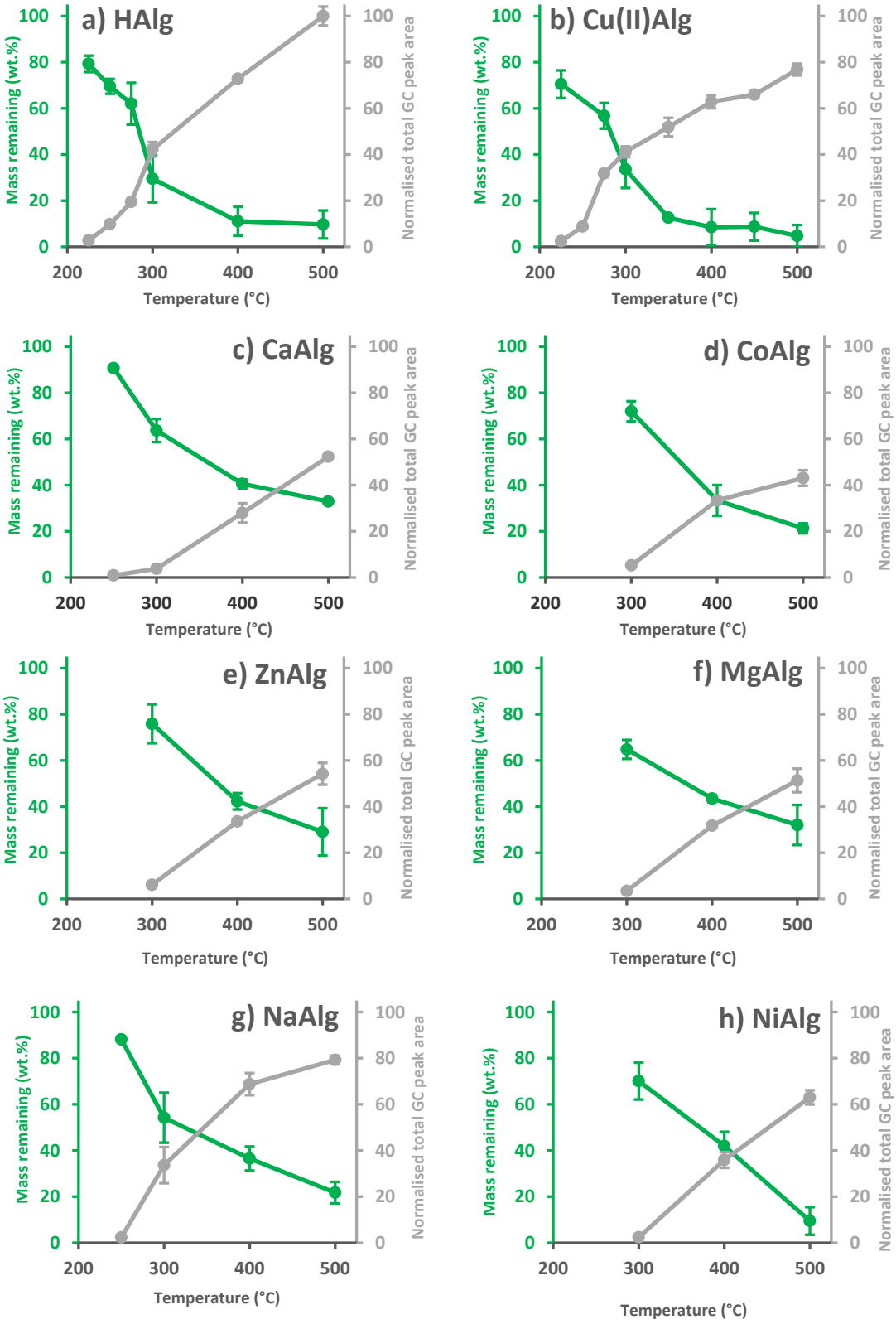

Figure O.1 Plots of remaining organic mass and total GC peak areas (normalised against **HAlg** at 500 °C) for (a) **HAlg**, (b) **Cu(II)Alg**, (c) **CaAlg**, (d) **CoAlg**, (e) **ZnAlg**, (f) **MgAlg**, (g) **NaAlg**, **and** (h) **NiAlg** pyrolysed at various temperatures under He.

Appendices P – T

Additional literature reviews and publications

Appendix P - Additional literature relating to the role of native and non-native metal ions in the pyrolysis of terrestrial biomass

Appendix Q - Additional literature relating to the thermal stability of carboxylic acids and their corresponding metal salts

Appendix R - Papers published during the preparation of this thesis

Appendix S - "Thermochemical processing of macroalgae: a late bloomer in the development of third−generation biofuels?" J. S. Rowbotham, PW Dyer, HC Greenwell, and MK Theodorou, Biofuels, *2012*, **3**(4), 441–461

Appendix T - "Copper(II)-mediated thermolysis of alginates: a model kinetic study on the influence of metal ions in the thermochemical processing of macroalgae" J. S. Rowbotham, P. W. Dyer, H. C. Greenwell, D. Selby, and M. K. Theodorou, Interface Focus, *2013*, **3**(1), 20120046

Appendix P – Additional literature relating to the role of native and non-native metal ions in the pyrolysis of terrestrial biomass

P.1 Introduction

Co-feeding catalyst material with the biomass in pyrolysis is now a widely accepted strategy for improving yields and selectivities towards desired compounds, however, some authors have questioned the degree to which metal ions already contained within the biomass matrix might also play a modifying role.[1] The following section explores how such "intrinsic" metal-ions might be controlled in advance of further discussion of their role in pyrolysis. Ultimately, these discussions of the pyrolysis of metal-doped terrestrial biomass are a useful source of comparison for the work performed in this thesis on metal-doped aquatic biomass.

P.1.1.1 Indigenous and artificially-incorporated metals in terrestrial biomass

Depending on the biomass in question, metal-ions bound indigenously within the samples are typically very low (<< 2 wt.%), especially in the terrestrial sphere.[2] Frequently, the natural metal-profile of biomass is dominated by alkali and alkali-earth species, but may vary considerably depending on the local environment to which the feedstock has been exposed.[2] These metal ions may exist in the form of salts, loosely bound within the biomass, or individual metal ions ionically coordinated to anionic moieties in the sample.[3,4] Either way, it is desirable to control the metal profile of the biomass by removing, replacing or enriching a particular metal species, dependent on the desired thermochemical outcome). In this regard, researchers have devised a number of methods to alter the metal profile of biomass, and these are summarised in Figure P.1 and below:

- **Dry mixing (see Figure P.1a):** a metal salt is ground (dry) with the biomass feedstock. The technique gives poor contact between the biomass and the metal ions, and the identity of the counter-anion can also be extremely influential to subsequent thermochemistry.[3,5]

- **Wet-impregnation (see Figure P.1b):** the biomass is soaked in a solution of metal salt.[4,6] The metal penetrates much more thoroughly into the biomass matrix, however the counter-anion still remains, and may play an important role in subsequent thermochemistry.[3,7–9]

- **Ion-exchange (see Figure P.1c):** in biomass with suitable anionic functional groups (such as the carboxylate moiety of a uronic acid)[10] the indigenously bound counter-cations may be replaced by soaking in a solution of the salt of a metal for which the feedstock has a higher affinity.[6,8,13] In theory, the anion of the salt does not remain in the biomass.

- **Acid-washing (see Figure P.1d):** acid washing has the effect of removing any loosely bound metal salts or ionically bound metal ions from the biomass.[6,12–15] A water wash or washing with a non-metallic salt may also be employed towards achieving the same effect.[16]

- **Acid-washing / wet-impregnation (see Figure P.1e):** a combined approach of acid washing (to remove metal salts) followed by wet-impregnation (to re-introduce a salt of choice) can be used to control the metal profile of the biomass.[17,18]

- **Acidification / neutralisation (see Figure P.1f):** a combined approach of acid washing (to remove metal salts by acidifying anionic functional groups) followed by neutralisation (to re-introduce a metal ion of choice) could also be utilised.

Of course, it is quite possible that more than one metal-introduction mechanism might be operative at any one time, including a combination of wet-impregnation and ion-exchange.[6,8] As such, it is important to analyse the biomass before and after the introduction of a new metal ion, to ensure the desired effect has been implemented. Indeed, authors have pointed out that different loadings of the same metal ion can give rise to significant differences in subsequent thermochemical reactions.[19–23] The following section will provide a brief overview of the literature relating to the role of intrinsic metal ions in the pyrolysis of terrestrial biomass to provide a point of comparison for equivalent discussions of kelp biomass later in this chapter.

P.1.1.2 Implications of the presence of metal ions in the pyrolysis of terrestrial biomass

As was noted in above, naturally occurring metal ions are often found encompassed within the organic matrix of a biomass sample. Given the activity of metal-based catalysts in pyrolysis generally, it is highly likely that such indigenous metal ions should play a mediating role in subsequent pyrolysis treatment of the biomass. Given this fact, the impact of the presence of such indigenous metal ions on biomass thermochemistry is a surprisingly unexplored subject matter. Indeed Mettler *et al.*, cited the influence of these "*natural catalysts*"[*] as one of the top ten fundamental challenges facing pyrolysis research.[1] Meanwhile, early investigators such as Geoffrey Richards and co-workers recognised that there was potential to exploit the presence of inherently bound metal species by doping-in those with preferential properties (according to the method outlined above).[4,6,24–26]

[*] The term "*natural catalysts*" was coined by Mettler and co-workers, but is not adopted here for two reasons. Firstly, it is important to make a distinction between those metal ions that have been deliberately incorporated within the biomass, *versus* those that occur naturally. Whilst both types of metal ion may be considered to be "intrinsic" to the biomass, their origins are clearly different. Secondly, a judgement as to whether the metal ion in question is acting as a catalyst depends on an insight into what reactions are taking place during pyrolysis, which is not often readily available.

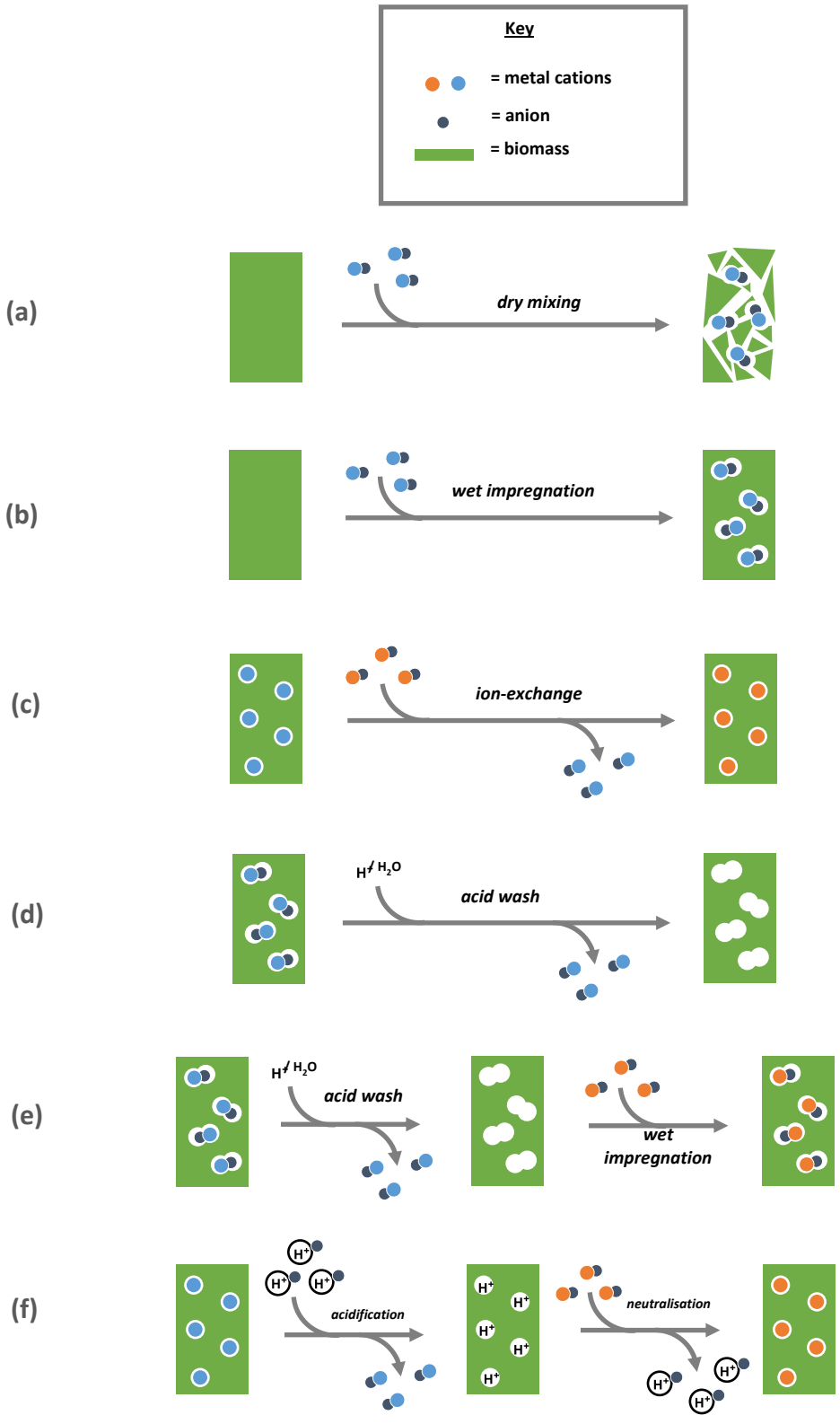

Figure P.1 Methods for controlling the metal profile of biomass: (a) dry-mixing, (b) wet impregnation, (c) ion-exchange, (d) acid-washing, (e) sequential acid washing and wet impregnation, and (f) sequential acidification and neutralisation of the biomass.

Richards and his team made many pioneering discoveries in this field, especially regarding the role of Cu^{2+} (which is of particular interest to the discussions later in Chapter 5).[4,25,26] Whilst the work of Richards and his successors has not led to a unified theory of the role of metal-ions in the pyrolysis of biomass (partly owing to wide variations in the composition of types of biomass studied)[2] a number of general trends can be highlighted:

- **s-block metals**

In general, s-block ions tend to decrease the amount of volatile hydrocarbons released from cellulosic biomass, diminishing the yield of bio-oil. [4,6] Typically, the degree of inhibition follows the trend: [13]

$$K^+ > Na^+ > Ca^{2+} > Mg^{2+}$$

Similarly, the same ions give rise to lower levels of anhydrosugars such as levoglucosan (LG – see Figure P.2),[27–30] higher levels of small oxygenated molecules (acetol, acetic acid, formic acid, glyoxal, and hydroxyacetaldehyde – see Figure P.2),[20,31] and are frequently found to promote char formation.[4,6,13,27,28,30,32] Acid-washing the metals from the biomass has been demonstrated to reverse the aforementioned effects and give a higher yield of aromatic compounds.[13–15,33] Finally, it is worth mentioning that s-block ions have been associated with slagging and fouling in the reactor, as the metals (or their oxysalts) are volatilised at higher temperatures.[34,35]

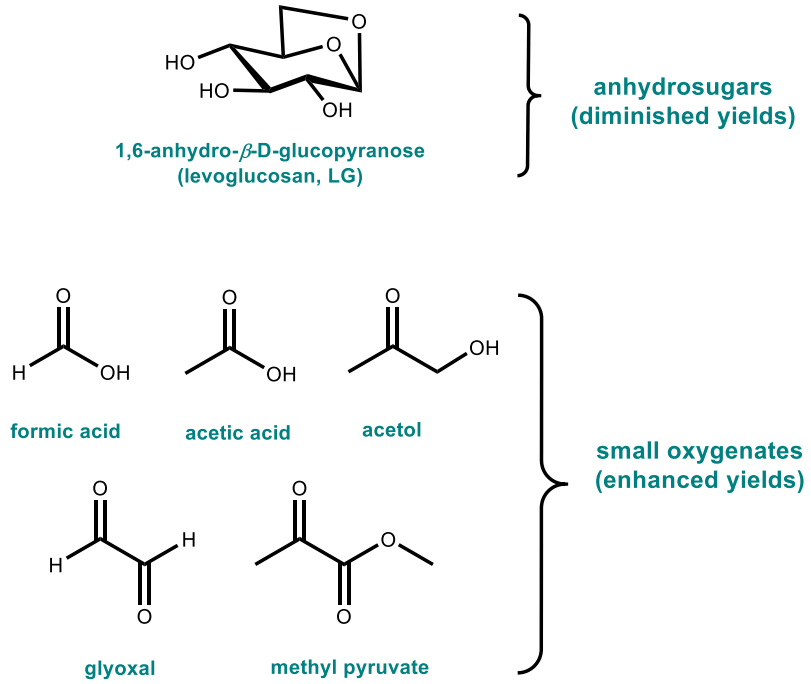

Figure P.2 Effect of s-block ions on various classes of products arising from the pyrolysis of cellulosic biomass

- **d-block metals**

The are many examples of d-block metals lowering the onset temperature required for pyrolysis in samples of wood[18,36,37] and cellulosic filter paper,[20] albeit to varying degrees. The same metal ions have also been found to alter the gas : char : oil ratio in for example, eucalyptus,[9] newspaper, [4] and wood,[38] though, again, the effects can vary widely. Cu^{2+} and Fe^{2+} have been shown to give both higher and lower yields of bio-oil,[20,39] though, regardless of the yield, they tend to increase the calorific value of the fraction.[39] Biomass impregnated with Zn^{2+} was found to deliver higher yields of 2-FF at lower temperatures (depending on the metal loading),[22,23,40] and Ni^{2+} has been found to decrease the amount of liberated aromatic compounds,[21,32,41] whilst increasing H_2 production.[21,38] In most cases, the yield of levoglucosenone (LGO) was found to be increased by doping biomass with d-block metals, possibly by enhanced degradation of LG (see Figure P.3).[4,22,23,42]

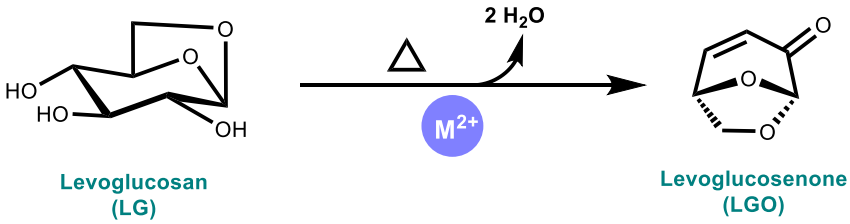

Figure P.3 LG degradation as a possible route to the formation of LGO in the pyrolysis of cellulosic biomass impregnated with d-block metal ions (M^{2+}).[42]

Some authors have noted discrepancies between the thermochemical influence of d-block metal ions on different components of lignocellulosic biomass. For example, lignin is largely unaffected, cellulose is affected more severely at high temperatures, and hemi-cellulose is affected at low temperatures.[18] Presumably, such observations indicate that the metal ions play differing roles in both the primary and secondary stages of degradation,[18,32,*] dependent upon the component and type of metal binding present.[4]

Finally, a number of studies have been made to probe the fate of the d-block cations during the pyrolysis of terrestrial biomass. Crystalline Cu^0 has been found to form at temperatures between 350 - 400°C in cellulosic feedstocks doped with $CuCl_2$.[4,25,26,39] Similarly, Ni^0 nanoparticles have been detected between 400 – 500°C in $NiCl_2$ rich samples,[19,41,43] and ZnO by 500°C following impregnation with $ZnCl_2$.[9] Authors have variously suggested that Ni^{2+}, Cu^{2+}, and Zn^{2+} proceed through an amorphous $M_xO_yH_z$ phase, to form MO.[4,9,19] The former two metals are then reduced further by high temperature reaction with either CO or the carbon-rich char to yield M^0.[19,39,41,43] At low temperatures, the metals could be recovered in about 90 – 95 % yield from the char fraction of the pyrolysate.[19,39]

[*] A more detailed discussion of the distinction between metal involvement in primary *versus* secondary pyrolysis reactions is contained in Chapter 4, Section 4.3.2.4.

P.2 References

1 M. S. Mettler, D. G. Vlachos and P. J. Dauenhauer, *Energy Environ. Sci.*, 2012, **5**, 7797–7809.

2 S. V. Vassilev, D. Baxter, L. K. Andersen, C. G. Vassileva and T. J. Morgan, *Fuel*, 2012, **94**, 1–33.

3 Z. A. Mayer, A. Apfelbacher and A. Hornung, *J. Anal. Appl. Pyrolysis*, 2012, **94**, 170–176.

4 G. N. Richards and G. Zheng, *J. Anal. Appl. Pyrolysis*, 1991, **21**, 133–146.

5 L. Zhang, B. Zhang, Z. Yang and Y. Yan, *RSC Adv.*, 2014, **4**, 39145–39155.

6 W.-P. Pan and G. N. Richards, *J. Anal. Appl. Pyrolysis*, 1990, **17**, 261–273.

7 D. Zhao, Y. Dai, K. Chen, Y. Sun, F. Yang and K. Chen, *J. Anal. Appl. Pyrolysis*, 2013, **102**, 114–123.

8 J. Wang, M. Zhang, M. Chen, F. Min, S. Zhang, Z. Ren and Y. Yan, *Thermochim. Acta*, 2006, **444**, 110–114.

9 S. Eibner, F. Broust, J. Blin and A. Julbe, *J. Anal. Appl. Pyrolysis*, 2015, **113**, 143–152.

10 W. F. DeGroot, *Carbohydr. Res.*, 1985, **142**, 172–178.

11 W. F. DeGroot and F. Shafizadeh, *J. Anal. Appl. Pyrolysis*, 1984, **6**, 217–232.

12 L. Jiang, S. Hu, L. Sun, S. Su, K. Xu, L. He and J. Xiang, *Bioresour. Technol.*, 2013, **146**, 254–260.

13 K. Wang, J. Zhang, B. H. Shanks and R. C. Brown, *Appl. Energy*, 2015, **148**, 115–120.

14 A. Aho, N. DeMartini, A. Pranovich, J. Krogell, N. Kumar, K. Eränen, B. Holmbom, T. Salmi, M. Hupa and D. Y. Murzin, *Bioresour. Technol.*, 2013, **128**, 22–29.

15 I. Y. Eom, K. H. Kim, J. Y. Kim, S. M. Lee, H. M. Yeo, I. G. Choi and J. W. Choi, *Bioresour. Technol.*, 2011, **102**, 3437–3444.

16 A. Saddawi, J. Jones, A. Williams and C. Le Coeur, *Energy & Fuels*, 2012, 120119162934000.

17 A. Saddawi, J. Jones and A. Williams, *Fuel Process. Technol.*, 2012, **104**, 189–197.

18 H. Yuan, S. Xing, Huhetaoli, T. Lu and Y. Chen, *J. Anal. Appl. Pyrolysis*, 2015, **112**, 325–332.

19 Y. Richardson, J. Blin, G. Volle, J. Motuzas and A. Julbe, *Appl. Catal. A Gen.*, 2010, **382**, 220–230.

20 P. T. Williams and P. A. Horne, *Renew. Energy*, 1994, **4**, 1–13.

21 F. X. Collard, J. Blin, A. Bensakhria and J. Valette, *J. Anal. Appl. Pyrolysis*, 2012, **95**, 213–226.

22 Q. Lu, Z. Wang, C. Q. Dong, Z. F. Zhang, Y. Zhang, Y. P. Yang and X. F. Zhu, *J. Anal. Appl. Pyrolysis*, 2011, **91**, 273–279.

23 Q. Lu, C. Q. Dong, X. M. Zhang, H. Y. Tian, Y. P. Yang and X. F. Zhu, *J. Anal. Appl. Pyrolysis*, 2011, **90**, 204–212.

24 W. P. Pan and G. N. Richards, *J. Anal. Appl. Pyrolysis*, 1989, **16**, 117–126.

25 G. N. Richards and G. Zheng, *Energy & Fuels*, 1995, **9**, 136–140.

26 T. G. Devi, M. P. Kannan and G. N. Richards, *Fuel*, 1990, **69**, 1440–1447.

27 I. Y. Eom, J. Y. Kim, T. S. Kim, S. M. Lee, D. Choi, I. G. Choi and J. W. Choi, *Bioresour. Technol.*, 2012, **104**, 687–694.

28 H. Hwang, S. Oh, T. S. Cho, I. G. Choi and J. W. Choi, *Bioresour. Technol.*, 2013, **150**, 359–366.

29 S. Hu, L. Jiang, Y. Wang, S. Su, L. Sun, B. Xu, L. He and J. Xiang, *Bioresour. Technol.*, 2015, **192**, 23–30.

30 H. Hwang, S. Oh, I. G. Choi and J. W. Choi, *J. Anal. Appl. Pyrolysis*, 2015, **113**, 27–34.

31 D. J. Nowakowski and J. Jones, *J. Anal. Appl. Pyrolysis*, 2008, **83**, 12–25.

32 A. Khelfa, A. Bensakhria and J. V. Weber, *J. Anal. Appl. Pyrolysis*, 2013, **101**, 111–121.

33 D. Mourant, Z. Wang, M. He, X. S. Wang, M. Garcia-Perez, K. Ling and C. Z. Li, *Fuel*, 2011, **90**, 2915–2922.

34 D. Keown, G. Favas, J. Hayashi and C. LI, *Bioresour. Technol.*, 2005, **96**, 1570–1577.

35 D. J. Lane, P. J. van Eyk, P. J. Ashman, C. W. Kwong, R. de Nys, D. A. Roberts, A. J. Cole and D. M. Lewis, *Energy & Fuels*, 2015, **29**, 2542–2554.

36 V. a. Beliy and E. V. Udoratina, *Cent. Eur. J. Chem.*, 2014, **12**, 1294–1303.

37 S. E. Kinata, K. Loubar, M. Paraschiv, A. Bouslamti, C. Belloncle and M. Tazerout, *J. Anal. Appl. Pyrolysis*, 2013, **104**, 210–217.

38 K. Bru, J. Blin, A. Julbe and G. Volle, *J. Anal. Appl. Pyrolysis*, 2007, **78**, 291–300.

39 W. J. Liu, K. Tian, H. Jiang, X. S. Zhang, H. S. Ding and H. Q. Yu, *Environ. Sci. Technol.*, 2012, **46**, 7849–7856.

40 S. J. Oh, S. H. Jung and J. S. Kim, *Bioresour. Technol.*, 2013, **144**, 172–178.

41 Y. Richardson, J. Motuzas, A. Julbe, G. Volle and J. Blin, *J. Phys. Chem. C*, 2013, **117**, 23812–23831.

42 P. Rutkowski, *J. Anal. Appl. Pyrolysis*, 2012, **98**, 86–97.

43 Y. Shen, C. Areeprasert, B. Prabowo, F. Takahashi and K. Yoshikawa, *RSC Adv.*, 2014, **4**, 40651–40664.

Appendix Q – Additional literature relating to the thermal stability of carboxylic acids and their corresponding metal salts

Q.1 Introduction

In this thesis (and elsewhere) the carboxylate moiety has been recognised as a pivotal functional group in dictating the possible pathways of uronide thermolysis. This appendix explores the thermal stability of carboxylic acids (Section Q.2) and carboxylates more generally (Section Q.3). Naturally, these subjects have been reviewed elsewhere,[1–4] and this appendix serves only to highlight the points salient to the degradation mechanisms discussed in earlier chapters. An additional discussion of the thermal stability of related metal carbonates is provided in Section Q.4 as the formation of such salts is a frequent occurrence during the metal-mediated thermolysis of carboxylates moieties.

Q.2 Thermal degradation of carboxylic acids by thermal decarboxylation

Q.2.1 Mechanistic overview of thermal decarboxylation

The thermolysis of carboxylic acids proceeds majoratively *via* thermal decarboxylation and, consequently, the importance of this mechanism for the deoxygenation of biomass is now being realised.[5–7] However, systematic analyses of the factors that promote and inhibit the thermal elimination of carbon dioxide from carboxylic acid bearing molecules are surprisingly lacking. Intramolecular thermal decarboxylation is commonly assumed to proceed *via* deprotonation of the hydroxyl group combined with heterolytic C-C bond cleavage to yield a carbanion, proton, and CO_2 (see Figure Q.1).[1,8]

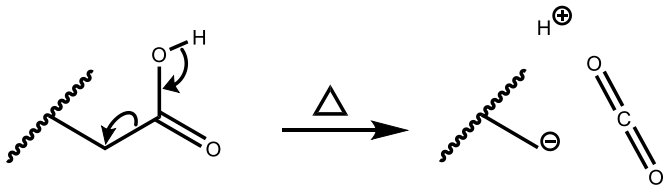

Figure Q.1 Thermal decomposition of a carboxylic acid moiety *via* deprotonation followed by heterolytic bond scission to release CO_2

The heterolytic bond cleavage pathway to CO_2 elimination from a carboxylic acid is achieved by simultaneous donation of electron density into C=O (π) and C-C (σ*) orbitals. Promoting these electron transfers should, in turn, promote decarboxylation. Naturally, abstraction of the proton from the hydroxyl group of the acid facilitates C=O formation and, as such, thermal decarboxylation occurs much more rapidly in water than in non-ionising solvents or under solvent-free conditions (such as those found in a typical pyrolysis experiment).[1,4] Hence, whilst malonic acid will only slowly eliminate carbon dioxide at 140 °C under dry, inert conditions, it rapidly decarboxylates at 70 °C in aqueous conditions (where the lability of the proton is dramatically increased) (see Figure Q.2).[4]

In addition to proton abstraction, the favourability of thermal decarboxylation can be increased by stabilisation of the resulting carbanion, typically in the form of an electron accepting substituent acting as a sink for the charge accumulated in the high energy C-C (σ*) orbital (see Figure Q.2).[8] Indeed, in the absence of such carbanion stabilisation, many carboxylic acids can be remarkably resistant to anhydrous thermal decarboxylation with, for example, oleic acid being largely undegraded even at 750 °C.[4] When the high thermal stability of long alkyl chain carboxylic acids is contrasted with, for example, the readily degradable derivatives of malonic acids, the importance of the substituent on the *α*-carbon towards promoting pyrolytic decarboxylation can be readily recognised.[4]

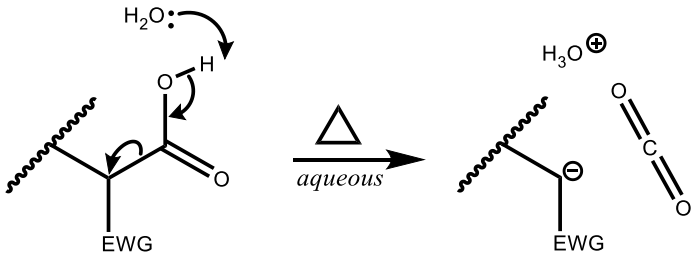

Figure Q.2 Promotion of thermal decarboxylation by water-mediated proton abstraction and by the presence electron withdrawing groups (EWGs) on the *α*-carbon

In some cases, a substituent may serve a dual purpose in decarboxylation; assisting in both proton abstraction and simultaneously stabilising the resultant carbanion. Here, *β*-keto acids form a class of widely cited examples, readily undergoing decarboxylative enol formation (see Figure Q.3).[9] Of course, the various thermolytic routes available to a *α*-hydroxy and *β*-hydroxy substituted carboxylic acids are of significant interest to uronic acid thermochemistry and are discussed in more detail in the main body of the text.

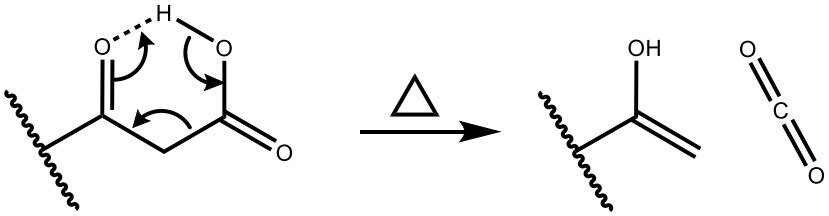

Figure Q.3 Thermal decarboxylation of *β*-keto acids

Q.2.2 Alternative mechanisms for thermal decarboxylation

Whilst the thermal decarboxylation mechanism described in Section Q.2.1 is the most frequently referenced in textbooks, in a review of the subject in 1951, Brown highlighted a number of other potential routes.[1] A second heterolytic pathway giving rise to a hydride and carbocation (see Figure Q.4a), or a radical mechanism following a homolytic C-C bond cleavage (see Figure Q.4b) can both be conceived of.[1] In reality, the mechanisms as written in Figures Q.4a and Q.4b would be extremely unlikely to occur, as they both rely on the formation of highly unstable electron-rich hydrogen species. If, however, the hydrogen bound to the carboxylic acid moiety was replaced with a suitable electron accepting group such as a metal ion (which is considered later in this appendix) or, in the case of the homolytic pathway, a radical initiator (such as a peroxy-group),[10,11] the pathways become much more likely.

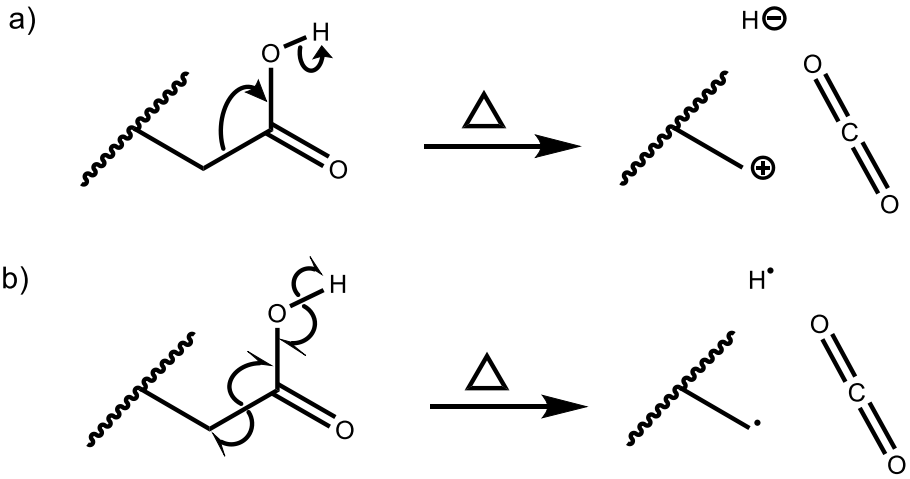

Figure Q.4 Alternative methods for thermal decarboxylation by (a) heterolytic and (b) homolytic C-C bond cleavage, both producing electron-rich hydrogen and electron-deficient carbon species.[1]

The mechanisms outlined in Figure Q.4 are also rendered unfavourable by the formation of electron-deficient carbon species (either a carbocation or radical). However, again, the stability of such species can be greatly improved by suitable neighbouring substituents, especially by the presence of electron donating groups such as an ether oxygen. The donation of electron density from the oxygen lone pair into the empty or partly filled carbon 2p orbital lowers the energy of the species by giving rise to a net-bonding interaction (see Figure Q.5).[12] Ultimately, therefore, electron donating interactions serve to increase the likelihood of decarboxylation occurring through one of the mechanisms outlined in Figure Q.4, and, in the earlier chapters of this thesis, it was argued that the saccharide ring oxygen plays just such a stabilising role during thermolysis of uronic acids.

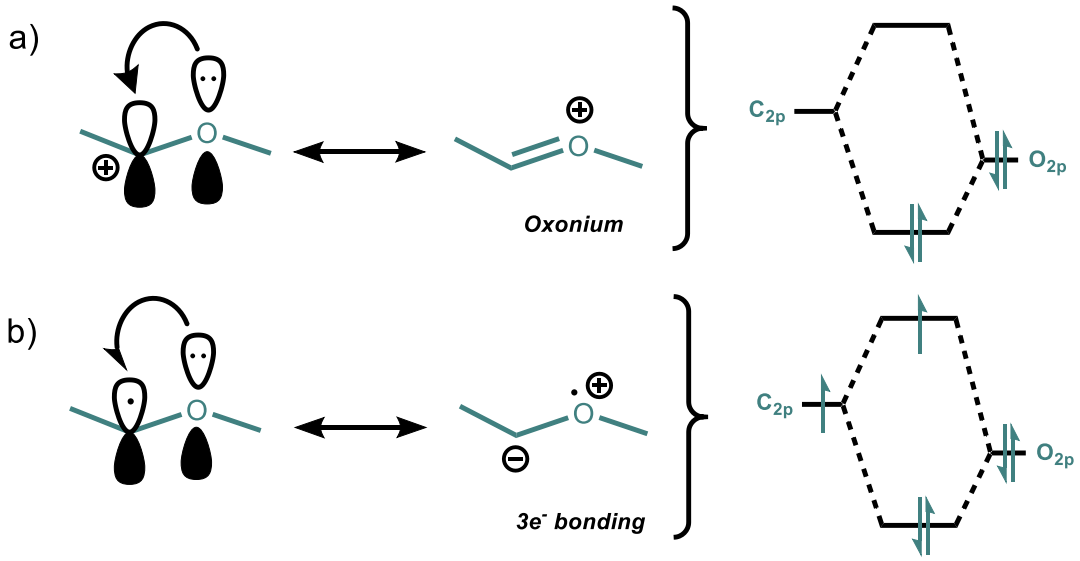

Figure Q.5 Routes to stabilising an electron-deficient carbon atom following thermal decarboxylation by (a) heterolytic and (b) homolytic mechanisms

Q.2.3 The potential role of metal ions in thermal decarboxylation

With the above discussions in mind, it is fruitful to consider the likely effect of a metal ion on the thermally activated decarboxylation of organic acids. In the case of the mechanism described in Section Q.2.1 (defined in Figure Q.1), a metal ion would inhibit elimination of CO_2 by withdrawing electron density from the C-O^- moiety and consequently preventing population of the C=O (π) orbital. Indeed, such a theory is borne out experimentally when sodium and potassium salts of carboxylic acids in THF have been found to thermally eliminate CO_2 with increased rapidity in the presence of crown ethers, which serve to neutralise the electron withdrawing ability of the K^+ or Na^+ ion.[13] However, it is also possible to imagine the metal ion playing alternative roles, perhaps by thermally destabilising the carboxylate anion through polarisation (as is found in the thermochemistry of carbonates, see Section Q.4)[14] or, in the case of redox active metals, by providing a sink for the electrons in the rupturing C-C bond, promoting the two mechanisms described in Section Q.2.2 (and defined in Figure Q.4).

Unfortunately, systematic experimental studies that purpose to investigate the thermal stability of s- and d-block metal carboxylates in relation to their parent acids are scarce. Furthermore, comparison between different pyrolysis studies is limited by the often differing experimental conditions that are used. As such, the mechanisms of the metal-mediated thermolysis of even very simple carboxylate salts are still debated. The following sections will examine the literature pertaining to three carboxylic acids (namely oxalic, malonic, and succinic acids) for which there is sufficient data on the thermolysis of their corresponding carboxylates to draw some general conclusions on the role of the complexed cation.

Q.3 Thermal stability of metal carboxylates†

Q.3.1 Thermal stability of metal oxalates

The oxalates are by far the class of carboxylate for which the most thermal analysis data exists, with extensive experimental and review articles having been prepared by Dollimore[2,15,16] and, more recently, Galwey and Brown.[3] Their conclusions are summarised in this section.

Free oxalic acid is known to pyrolyse under anhydrous conditions at around 140 °C to yield formic acid and CO_2, though the precise mechanism is still contested (see Figure Q.6).[4,17]

† All discussions refer to thermolysis of the salt under a dry, inert atmosphere – typically flowing N_2

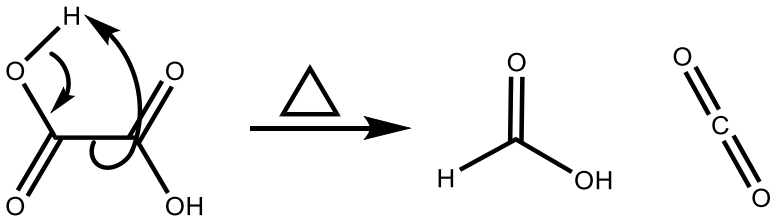

Figure Q.6 Potential mechanism of the thermal decomposition of oxalic acid[4]

The complexation of a metal ion to oxalic acid to yield the corresponding oxalate salts is found, in all cases, to increase the thermal stability of the anion, though by differing amounts depending on the metal in question.

Plot Q.1 indicates the temperatures at which various s- and d-block metal oxalates undergo thermal decomposition (only the primary stage is depicted). The determined thermal stability series for metal oxalates is as follows:

(least stable) ⟶ *(most stable)*

$$H^+ < Cu^{2+} < Pb^{2+} < Ni^{2+} < Zn^{2+} \approx Co^{2+} < Sr^{2+} \approx Ca^{2+} \approx Mg^{2+} < Na^+ \approx Ba^{2+} < K^+ < Li^+$$

Plot Q.1 Temperatures for the primary stage of thermolysis of oxalate salts under N_2

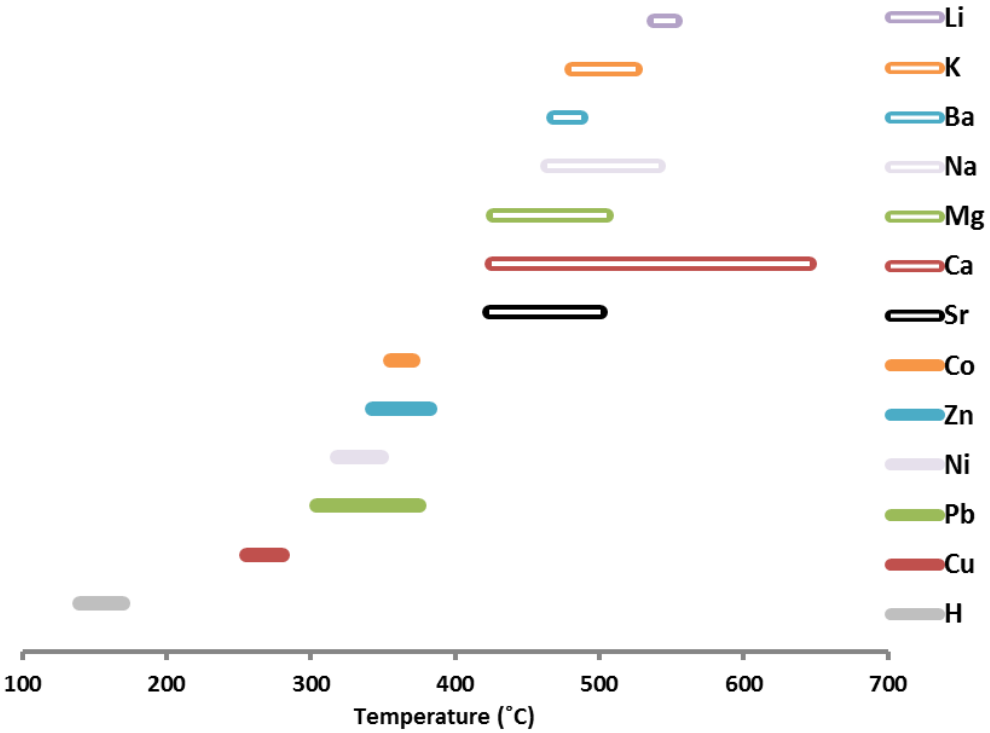

Aside from altering the temperature of pyrolysis, the metal species bound to the oxalate may also influence the mechanism of decomposition. The possible reaction pathways have been sorted into three classes (see Figure Q.7) depending on whether the metal compound formed following initial thermolysis is a carbonate (type (A)), oxide (type (B)), or zero valent metal (type (C)).[2] Oxalates of types (A) and (B) proceed through thermolytic rupture of a C-O bond, where type (C) behaviour results from M-O bond cleavage.[3] The thermal behaviour of the oxalates in this regard has been linked to their electronegativity characteristics, with more electropositive metals preferentially following route (A), and the more electronegative through route (C).[2]

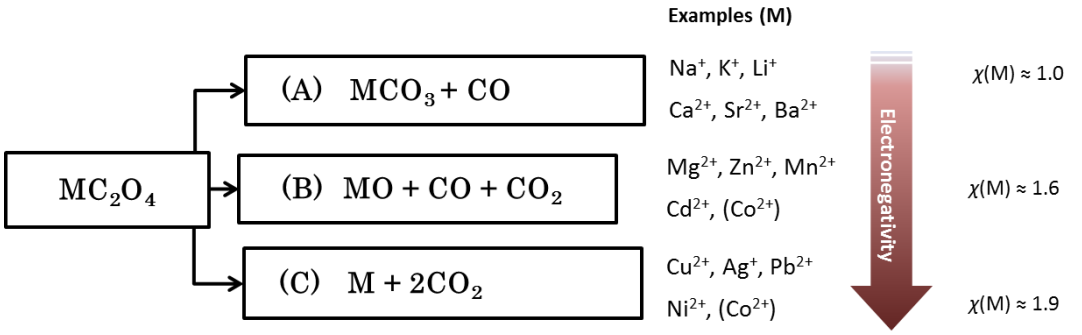

Figure Q.7 Products of the thermal decomposition of metal oxalates under N_2 depending on the electronegativity of the coordinated cation.[2] (Note: both Co and CoO have been detected in the case of anoxic cobalt(II) oxalate thermolysis).

Q.3.2 Thermal stability of metal malonates

The thermal behaviour of malonic acid and some representative metal malonate salts have been investigated under a number of different atmospheres,[18–20] however, as above, the discussion here is limited to pyrolysis undertaken in inert conditions (typically dry N_2). The acid itself undergoes facile decarboxylation from 140 °C to yield, predominantly, CO_2 and acetic acid (see Figure Q.8).[20]

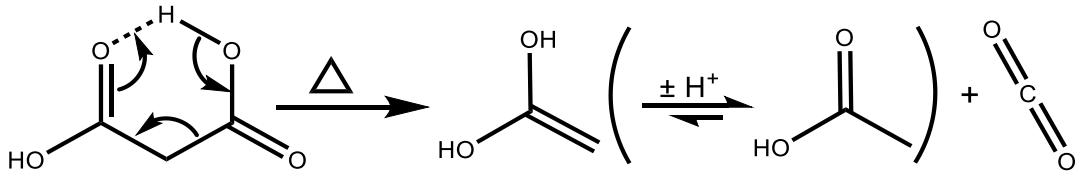

Figure Q.8 Potential mechanism of the thermal decarboxylation of malonic acid

The addition of a bound metal ion increases the thermolysis temperature (see Plot Q.2), according to the following trend:[3,20]

(least stable) ⟶ *(most stable)*

$H^+ < Cu^{2+} < Zn^{2+} \approx Co^{2+} < Ni^{2+} < Na^+ < Ca^{2+}$

In all cases, a mixture of CO and CO_2 were produced from the thermolysis reaction, and the metal went on to form the same inorganic residues as discussed in the case of oxalate degradation (see Figure Q.7). There are, however, notable differences in the detected organic products, with Na^+, Co^{2+}, and Zn^{2+} salts all yielding acetone whilst the corresponding Ni^{2+} and Cu^{2+} counterparts instead form acetic acid.[20] The similarities of the thermolysis products of Ni(II) and Cu(II) malonates with those of free malonic acid has led to the theory that the compounds undergo a similar decarboxylative mechanism, with a marked exothermic event at 256 °C (copper(II) malonate) being ascribed to that step.[20,‡]

Plot Q.2 Temperatures for the primary stage of thermolysis of malonate salts under N_2.[3,20]

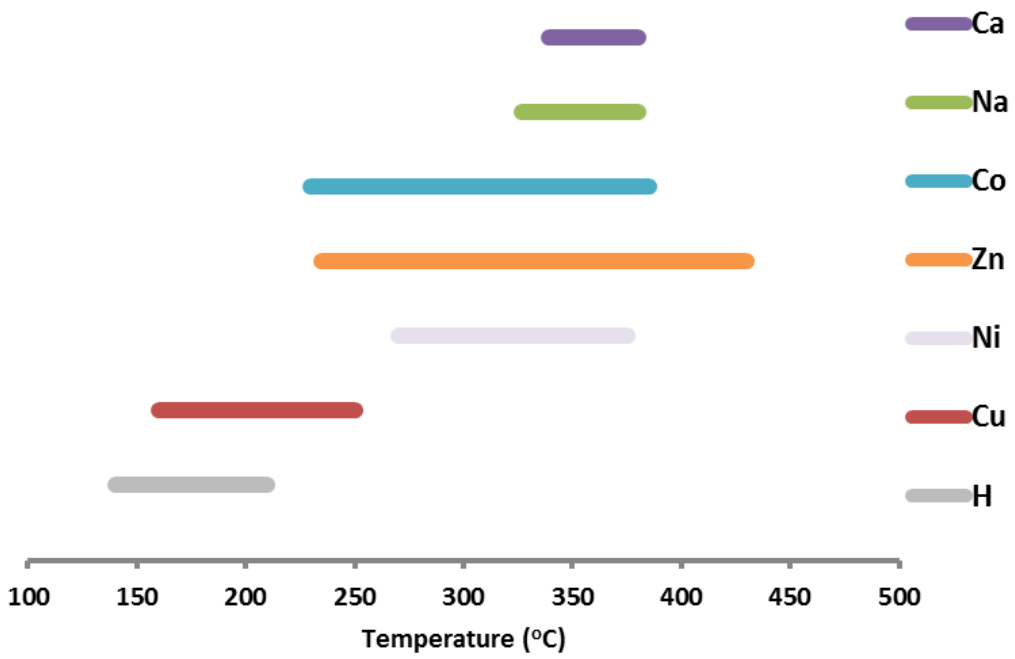

Q.3.3 Thermal stability of metal succinates

The thermal behaviour of succinic acid and some representative metal succinate salts have been investigated under a number of different atmospheres,[18,21,22] however, as above, the discussion here is limited to pyrolysis undertaken in dry N_2. Succinic acid differs from both malonic and oxalic acids in that it is stable towards thermal decarboxylation, instead undergoing vaporisation (from 165 °C)[22] and anhydride formation (from 200 °C),[4] as shown in Figure Q.9.

‡ The authors highlight an exothermic event for nickel(II) malonate at 404 °C with the same decarboxylative attribution, but it is much less pronounced than in the case of the copper(II) malonate.

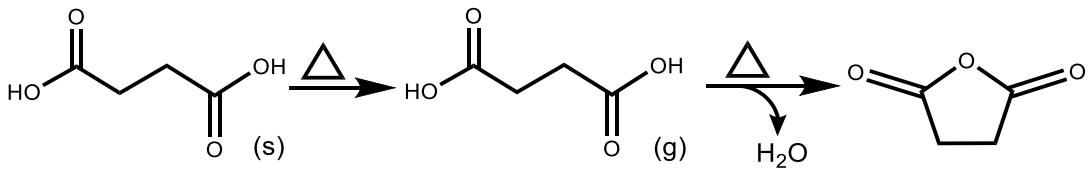

Figure Q.9 Thermal decomposition of succinic acid

The corresponding metal succinate salts are found to undergo thermal decomposition at higher temperatures than the parent acid (see Plot Q.3), and according to the following stability series:[22]

(least stable) ⟶ *(most stable)*

$$\mathbf{Cu^{2+} < Ni^{2+} \approx Co^{2+} < Ni^{2+} < Zn \approx Na^{+}}$$

Plot Q.3 Temperatures for the primary stage of thermolysis of succinate salts under N_2[22]

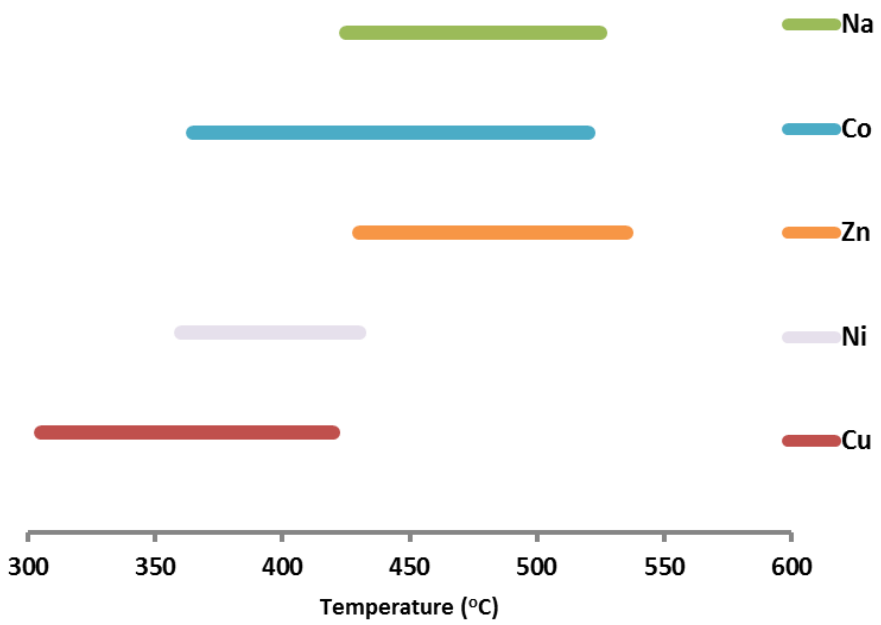

There does not, however, appear to be a link between the products of succinic acid pyrolysis (principally succinic anhydride) and the corresponding metal succinates, which form a mixture of CO and CO_2, as well as CH_4 (Na^+, Zn^{2+}, Co^{2+}, Ni^{2+}), acetone (Na^+), propanoic acid (Co^{2+}, Ni^{2+}), and propenoic acid (Cu^{2+}). As with the equivalent malonates and oxalates, a combination of carbonates (for Na^+), oxides (for Co^{2+}, Zn^{2+}, Cu^{2+}, and Ni^{2+}) and zero-valent metals (for Co^{2+}, Cu^{2+} and Ni^{2+}) were thought to be generated by the reactions.[22] Hence, though the parent succinic acid is not known to undergo thermal decarboxylation, there is evidence to suggest that certain metal ions (Cu^{2+} in this case) can promote this reaction pathway, conceivably by the $1e^-$ or $2e^-$ reductions outlined in Figure Q.10 Finally it is worth noting that, in all cases, the succinate salts were much more

thermally stable than their malonate counterparts as a consequence of the additional methylene unit in the alkyl bridge between the two carboxylates.[18,20,22]

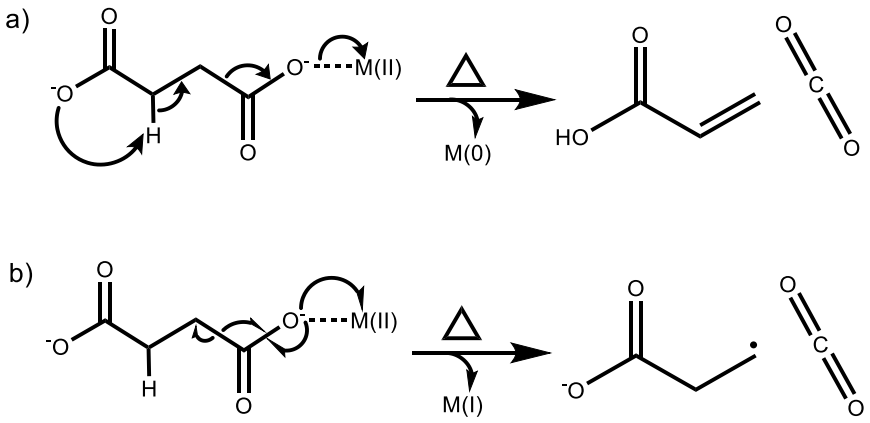

Figure Q.10 Potential mechanistic route for the metal-mediated decarboxylation of succinic acid *via* a) $2e^-$ reduction and b) $1e^-$ reduction of the coordinated metal, M, where M = Cu in this case.

Q.3.4 Thermal stability of metal carboxylates: general trends

In their review of the field, Galwey and Brown remarked that there is "no general agreement concerning the chemical parameters that control the thermal reactivities of metal carboxylates or the initial step in their reaction", but instead highlighted some patterns shared by the species discussed above (amongst others).

1) ***Metal ions typically increase the thermolysis temperature of their parent acids, but by different amounts***

The thermal stability trend for metal carboxylates is typically:

(least stable) ⟶ *(most stable)*

$H^+ \approx Cu^{2+} < Co^{2+} \approx Ni^{2+} \approx Zn^{2+} <$ alkali metals ≈ alkali earth metals

As stated above, the underlying causes of this pattern are unknown. Whilst some metals serve to promote certain thermolysis pathways unavailable to the free acid (such as Cu(II)-mediated decarboxylation of succinates) others may considerably inhibit these reactions (such as in the case of Na-mediated malonate thermolysis). Whilst the electropositivity and polarising nature of the metal ion undoubtedly play a role, other factors (such as the readiness of the bound metal ion to undergo reduction) play a part. Without detailed knowledge of the preferred thermolysis mechanism in the case of each carboxylic acid, it is very difficult to make conclusions as to what the role of a bound metal ion will be.

2) *Thermal stability of metal carboxylates is linked in part to the reduction potential of the metal species*

The patterns of thermal stability associated with carboxylates salts led Galwey and Brown to propose that the reduction potentials of the respective metals (see Table Q.1) may act as a controlling factor. Indeed, there is a notable correlation between the order of thermal stabilities for the carboxylates discussed in this appendix with the oxidising ability of the metal ion as it is found in the salt. This relationship between the two factors gives weight to the notion of carboxylate thermal decomposition proceeding *via* metal-mediated decarboxylation, where a redox active metal species (for example Ag^{+}, Cu^{2+}, Ni^{2+}) accepts one or two electrons liberated from the rupturing M-O or C-C bond. Similarly, alkali and alkali earth metals are too stable towards reduction to be able to activate decarboxylation. Naturally, there is still scope for additional work in this area, and, in actuality, the picture is likely to be far more complicated (for example, the possibility of sequential reductions or other routes to charge transfer), but the metal redox potentials still serve as a useful empirical predictive tools for the time being.

Table Q.1 Electrode reduction potentials, $E^{ø}$ (V), of processes relevant to metal-mediated decarboxylation reactions

Reduction half reaction			$E^{ø}$ / V
$2CO_2 + 2H^+ + 2e^-$	→	$H_2C_2O_4$	-0.43
$Ag^+ + e^-$	→	Ag	+0.80
$Cu^{2+} + 2e^-$	→	Cu	+0.34
$Cu^{2+} + e^-$	→	Cu^+	+0.16
$Ni^{2+} + 2e^-$	→	Ni	-0.23
$Co^{2+} + 2e^-$	→	Co	-0.28
$Zn^{2+} + 2e^-$	→	Zn	-0.76
$Al^{3+} + 3e^-$	→	Al	-1.66
$Mg^{2+} + 2e^-$	→	Mg	-2.36
$Na^+ + e^-$	→	Na	-2.71
$Ca^{2+} + 2e^-$	→	Ca	-2.87
$Sr^{2+} + 2e^-$	→	Sr	-2.89
$Ba^{2+} + 2e^-$	→	Ba	-2.91
$K^+ + e^-$	→	K	-2.93
$Li^+ + e^-$	→	Li	-3.05

3) *Copper(II) carboxylate salts behave atypically to most other metal carboxylates*

The unusual thermal properties of copper(II) carboxylates when compared to other such metal salts has been frequently noted, with the thermal behaviour of many copper(II) carboxylates (including oxalate,[23] malonate,[24] squarate,[25] and formate[26] amongst others[3,27]) giving rise to entire experimental investigations in their own right. Whilst the formation of Cu^0 is a common feature of the decomposition of many of these Cu(II) oxysalts, there is still significant disagreement as to how the reduction process occurs.[3,23,27] Possibilities include Cu^{2+} undergoing a single $2e^-$ reduction (to yield Cu^0

directly), two sequential 1e$^-$ reductions (proceeding through a $Cu^{2+} \rightarrow Cu^{+} \rightarrow Cu^{0}$ pathway), or reactant gases released in the pyrolysis (such as CO/CO_2) complicating the observed redox behaviour with additional steps. Significant evidence exists for substantial levels of Cu^+ being formed within thermally degrading Cu(II) carboxylates,[3] but more work has been advocated to more fully understand these complex reactions.

In addition, copper(II) carboxylates have frequently been demonstrated to decompose exothermically under inert atmospheres (as demonstrated by differential scanning calorimetry, DSC),[16,20] which, in the case of copper(II) oxalate for example, relates to a heat release of 33 KJ mol^{-1} over the course of thermolysis.[23] Copper(II) salts are unusual in displaying this exothermic behaviour as for the vast majority of metal carboxylates under inert conditions thermolysis is endothermic, and driven instead by the large entropic favourability of the reaction at high temperatures.[2,16] Unsurprisingly, the principal stage of the thermal decomposition of all the metal carboxylates discussed in this appendix are exothermic when conducted in an oxidative atmosphere.[12,15,16,18] The exothermic stage in Cu(II)-carboxylate degradation has been linked to the decarboxylation of the anion.[20]

Q.4 Thermal stability of metal carbonates[14]

As discussed in previous sections, carbonates can be an important product in pyrolysis and their formation (or lack thereof) offers clues as to the pyrolysis pathway of the parent compound. Additionally, knowledge of the temperature required to thermally decompose any carbonates formed in the initial stages of pyrolysis can be important for interpreting thermogravimetric data, as their degradation is often accompanied by the release of CO_2. Whilst some carbonates are not thermodynamically stable even at room temperature ($CuCO_3$ for example), others may remain intact to well above 1000 °C, melting and vaporising before their decomposition temperature is reached (Li_2CO_3 for example). This behaviour has been linked to the polarising nature of the metal ion in question, with highly charge dense cations distorting the CO_3^{2-} anion, causing destabilisation, and increasing the likelihood of thermal decarboxylation occurring.

The calculated standard Gibbs free energies of decomposition of various metal carbonates is shown in Plot Q.4 over a range of temperatures relevant to carboxylate pyrolysis. Of course, there are several factors to consider when discussing carbonate thermolysis (kinetic stability for example), but simple thermodynamic arguments serve as an excellent predictive tool. From Plot Q.4 it can be seen that Cu(II), Ni(II), Zn(II) and Co(II) cannot form carbonates under typical carboxylate pyrolysis temperatures (> 200 °C). Conversely, Li^+, Na^+, K^+, Ca^{2+}, Sr^{2+}, and Ba^{2+} will all, evidently, form stable carbonates under the temperatures encountered in a typical organic pyrolysis (< 600 °C). Mg^{2+} (and, though it is not frequently encountered, Pb^{2+}) is an interesting borderline case, with carbonate formation and subsequent decomposition conceivably occurring during (or soon after) the primary pyrolysis event of the parent carboxylate under investigation.

Plot Q.4 Calculated standard Gibbs free energies of thermal decomposition (ΔG˚) of various metal (M) carbonates from 0 – 1200 K.[14]

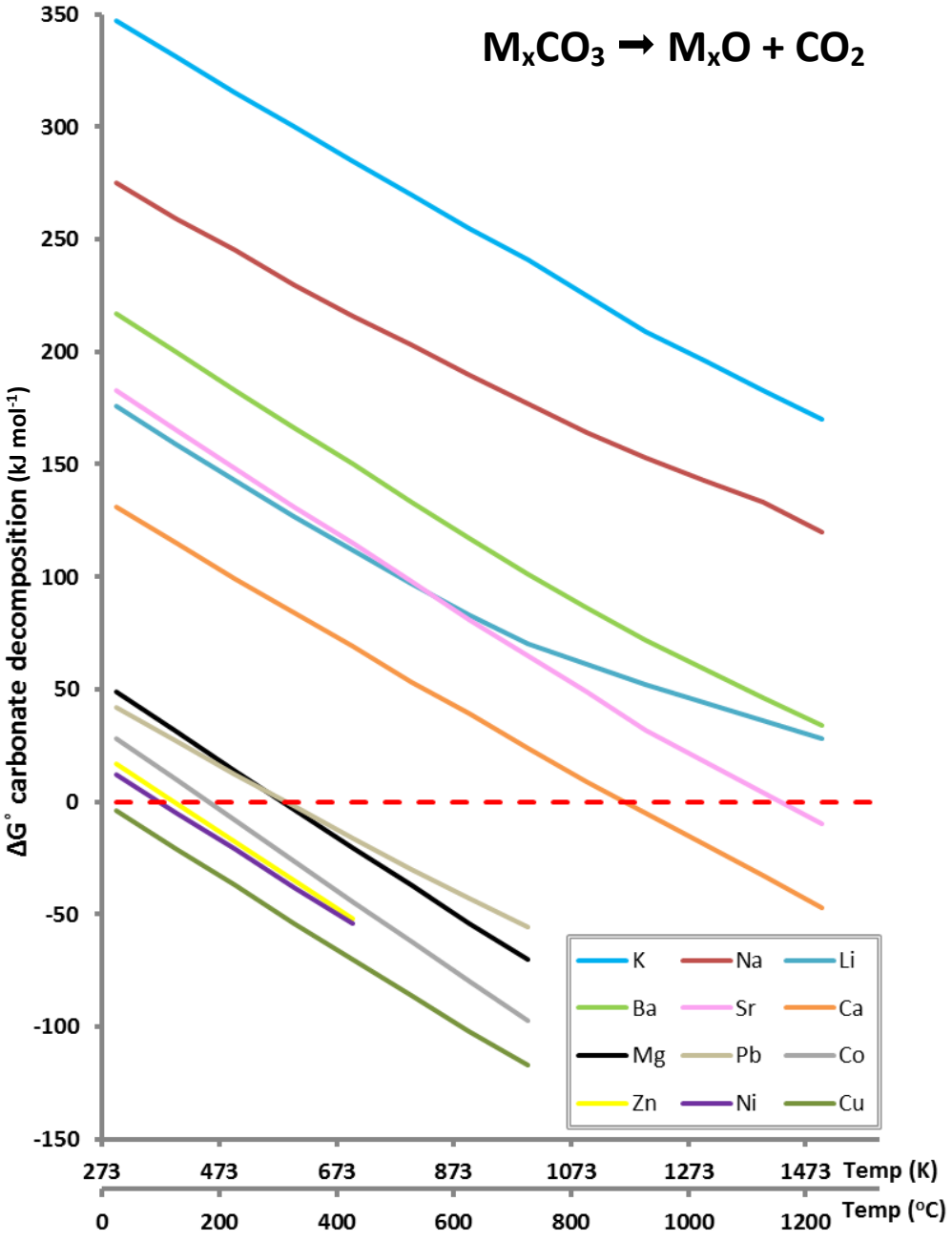

Q.5 References

1 B. R. Brown, *Q. Rev. Chem. Soc.*, 1951, **5**, 131–146.

2 D. Dollimore, *Thermochim. Acta*, 1987, **117**, 331–363.

3 A. K. Galwey and M. E. Brown, *Chapter 16 The thermal decompositions of metal salts of organic acids*, Elsevier, Amsterdam, 1999.

4 S. C. Moldoveanu, in *Techniques and Instrumentation in Analytical Chemistry*, Elsevier, Amsterdam, 2010, vol. 28, pp. 471–526.

5 J. M. Clark, M. R. Nimlos and D. J. Robichaud, *J. Phys. Chem. A*, 2014, **118**, 260–274.

6 J. M. Clark, M. R. Nimlos and D. J. Robichaud, *J. Phys. Chem. A*, 2015, **119**, 501–516.

7 G. J. S. Dawes, E. L. Scott, J. Le Nôtre, J. P. M. Sanders and J. H. Bitter, *Green Chem.*, 2015, **17**, 3231–3250.

8 R. W. Hanson, *J. Chem. Educ.*, 1987, **64**, 591–595.

9 M. B. Smith and J. March, in *March's Advanced Organic Chemistry*, John Wiley & Sons, Inc., Hoboken, NJ, USA, 2006, pp. 752–852.

10 B. Abel, J. Assmann, M. Buback, C. Grimm, M. Kling, S. Schmatz, J. Schroeder and T. Witte, *J. Phys. Chem. A*, 2003, **107**, 9499–9510.

11 E. T. Denisov and A. F. Shestakov, *Kinet. Catal.*, 2013, **54**, 22–33.

12 L. Somsák and R. J. Ferrier, *Adv. Carbohydr. Chem. Biochem.*, 1991, **49**, 37–92.

13 D. H. Hunter, V. Patel and R. a. Perry, *Can. J. Chem.*, 1980, **58**, 2271–2277.

14 K. H. Stern, in *High Temperature Properties and Thermal Decomposition of Inorganic Salts with Oxyanions*, CRC Press, Boca Raton, 2000, pp. 15–51.

15 D. Dollimore, D. L. Griffiths and D. Nicholson, *J. Chem. Soc.*, 1963, 2617–2623.

16 D. Dollimore and D. L. Griffiths, *J. Therm. Anal.*, 1970, **2**, 229–250.

17 A. Górski and A. D. Kraśnicka, *J. Therm. Anal.*, 1987, **32**, 1229–1241.

18 B. S. Randhawa and K. Gandotra, *J. Therm. Anal. Calorim.*, 2006, **85**, 417–424.

19 F. J. Caires, L. S. Lima, C. T. Carvalho, R. J. Giagio and M. Ionashiro, *Thermochim. Acta*, 2010, **497**, 35–40.

20 F. J. Caires, D. J. C. Gomes, A. C. Gigante, L. S. Lima, C. T. Carvalho and M. Ionashiro, *Brazilian J. Therm. Anal.*, 2014, **2**, 12–16.

21 F. J. Caires, L. S. Lima, C. T. Carvalho and M. Ionashiro, *Thermochim. Acta*, 2010, **500**, 6–12.

22 C. J. Caires, L. S. Lima, C. T. Carvalho and M. Ionashiro, *Eclética Química*, 2010, **35**, 73–80.

23 E. Lamprecht, G. M. Watkins and M. E. Brown, *Thermochim. Acta*, 2006, **446**, 91–100.

24 N. J. Carr and A. K. Galwey, *Proc. R. Soc. A Math. Phys. Eng. Sci.*, 1986, **404**, 101–126.

25 A. K. Galwey, M. A. A. Mohamed, S. Rajam and M. E. Brown, *J. Chem. Soc. Faraday Trans. 1 Phys. Chem. Condens. Phases*, 1988, **84**, 1349–1356.

26 A. K. Galwey, D. Jamieson and M. E. Brown, *J. Phys. Chem.*, 1974, **78**, 2664–2670.

27 A. K. Galwey and M. A. Mohamed, *Thermochim. Acta*, 1994, **239**, 211–224.

Appendix R - Papers published during the preparation of this thesis

- **"Thermochemical processing of macroalgae: a late bloomer in the development of third–generation biofuels?"** J. S. Rowbotham, PW Dyer, HC Greenwell, and MK Theodorou, Biofuels, *2012*, **3**(4), 441–461 **[see Appendix S]**

- **"An introduction to pyrolysis and catalytic pyrolysis: versatile techniques for biomass conversion"** L. Li, J. S. Rowbotham, H. C. Greenwell, and P. W. Dyer in "New and Future Developments in Catalysis: Catalytic Biomass Conversion", S. L. Suib, Ed., Elsevier, Netherlands, *2013*, 173-208

- **"Copper(II)-mediated thermolysis of alginates: a model kinetic study on the influence of metal ions in the thermochemical processing of macroalgae"** J. S. Rowbotham, P. W. Dyer, H. C. Greenwell, D. Selby, and M. K. Theodorou, Interface Focus, *2013*, **3**(1), 20120046 **[see Appendix T]**

- **"The future of alcohol-based biofuels: will we see the death of ethanol and birth of butanol?"** J. S. Rowbotham, H. C. Greenwell, and M. Adcock, Biofuels, *2014*, **5**(4), 365–368

Chapters 2 – 5 are also currently being re-written as individual manuscripts for submission to appropriate journals.

Appendix S

“Thermochemical processing of macroalgae: a late bloomer in the development of third−generation biofuels?”

J. S. Rowbotham, PW Dyer, HC Greenwell, and MK Theodorou, Biofuels, *2012*, **3**(4), 441–461

Thermochemical processing of macroalgae: a late bloomer in the development of third-generation biofuels?

Biofuels (2012) 3(4), 441–461

JS Rowbotham[1], PW Dyer[1‡], HC Greenwell[*2‡] & MK Theodorou[3,4]

This article offers a critical overview of the recent developments in thermochemical processing of macroalgae, a field that has been comparatively neglected when viewed against the vast wealth of research into alternative biofuel production methods and feedstocks. However, advances in thermochemical techniques have led to a flurry of activity into the applicability and use of macroalgae. Recent research has demonstrated that macroalgae may be used to produce bioresources in a similar way to many conventional terrestrial feedstocks and, indeed, may also possess a number of advantages (notably by not competing for land that could be used for food and forestry, nor requiring extensive use of nitrogenous fertilizers). With this in mind, it is suggested that many of the criticisms that have led to previous disinterest in thermal processing of macroalgae are not valid. Nevertheless, only through the continuation of these recent endeavors can macroalgal biomass, via broader and successively larger scale experimentation, demonstrate itself to be a competitive source of renewable energy.

Preface: biofuels from biomass

It is widely acknowledged that the dawn of the technological age coupled with an ever increasing global population has driven mankind's hunger for energy to unprecedented levels. The relationship between energy demand and supply is growing increasingly strained and, consequently, the efforts to obtain cheap, dependable and sustainable sources of energy are rapidly intensifying. However, the degree to which the global energy infrastructure will be able to meet these challenges, both now and in the future, is not yet certain. Furthermore, the impact of the colossal increase in energy consumption and, specifically, the increase in anthropogenic GHG emissions that accompany it, look set to be environmentally catastrophic [1]. Endeavors to find energy sources that are not only renewable, but that facilitate mitigation of the effects of climate change, appeal both to the environmentalist and the economist alike. Nowhere are these endeavors more pertinent than in the search for alternatives to fossil **fuels**. With peak oil production thought to be reached sometime this decade [2], the increasing volatility in global geopolitics and the continuing escalation in atmospheric CO_2 concentrations, the desire to alleviate mankind's dependence on fossil fuels is not only prudent, but essential. Biofuels, therefore, represent the closest surrogate to conventional fossil fuels, but with the added benefits of sustainability, carbon neutrality, a supply route that is secure and the potential to offer growth to countries previously economically barren through a lack of fuel reserves.

Today, a number of methods have been developed for deriving fuels from a plethora of biomass feedstocks [3]; these fall broadly into three categories: biological processing, chemical processing and **thermochemical** processing (**Table 1**). Although chemical and biochemical

[1]Centre for Sustainable Process Chemistry, Department of Chemistry, Durham University, South Road, Durham, DH1 3LE, UK
[2]Department of Earth Sciences, Durham University, South Road, Durham, DH1 3LE, UK
[3]Centre for Process Innovation, Wilton Centre, Wilton, Redcar, TS10 4RF, UK
[4]School of Biological & Biomedical Sciences, Durham University, South Road, Durham, DH1 3LE, UK
*Author for correspondence: E-mail: chris.greenwell@durham.ac.uk
‡Authors contributed equally

FUTURE SCIENCE

10.4155/BFS.12.29 ISSN 1759-7269

Table 1. Examples of processing options for biomass.

Process examples	Products	Ref.
Biological		
Fermentation	Ethanol	[7]
Anaerobic digestion	Biogas	[7]
Chemical		
Extraction followed by transesterification	Biodiesel	[82]
Extraction followed by multifarious chemical transformations	High-value chemicals	[137]
Direct chemical treatment	High-value chemicals	[138,139]
Thermochemical		
Gasification	Gas	[55]
Pyrolysis	Gas, bio-oil and biochar	[6]
Combustion	Heat and CO_2	[3]

transformations are viable options for fuel production and investigations into their implementation are, quite rightly, being given significant attention, thermochemical processing methods offer a number of advantages. First, they represent the most direct route for biomass processing as, in most cases, the biomass can be processed whole with very little pretreatment or prior extraction steps. Second, the choice and versatility of the range of products that can be obtained from thermochemical processing, including gases (syngas, methane and hydrogen), liquids (hydrocarbon fuels and valuable chemicals) and chars, is impressive and could be tailored according to market needs [4]. In contrast, processes such as fermentation (producing ethanol or butanol) and anaerobic digestion (primarily producing methane) essentially offer no flexibility in terms of their primary products. Third, thermochemical processes can be operated under continuous conditions – an advantage that can lower the cost of, for example, fast **pyrolysis** by as much as three-times compared with batch methods, such as fermentation [5]. For these reasons, thermochemical methods are worthy of deeper consideration.

Key terms

Fuels: This term is used extensively throughout the article to refer to substances that have the potential to provide energy on an industrial scale. The phrase 'biofuel' is therefore used to represent fuels that are sourced sustainably through the processing of biological feedstocks.

Thermochemical: Also known as thermolysis – a process that involves the degradation of a compound through the application of heat.

Pyrolysis: Thermochemical process in which a compound is heated to high temperatures in the absence of oxygen in order to decompose it into three phases: solid (char), liquid (oil) and gas.

Combustion: Thermochemical process whereby a compound is heated in excess oxygen until it is fully burned releasing heat.

Biochar: Solid fraction of products from the thermochemical processing of biomass.

Gasification: Decomposition of a compound into various gaseous products, facilitated by heating to very high temperatures in controlled amounts of oxygen and/or steam.

An introduction to thermochemical methods

Aside from conventional biological and chemical transformations, biomass can be broken down and subsequently converted into useable fuels through the application of heat. The main types of thermochemical methods that have been used in such applications are outlined in **Figure 1** and discussed in detail below.

▪ Pyrolysis

Overview of biomass pyrolysis

Pyrolysis is the process of heating a substance to the point of thermal degradation in the presence of sufficiently low concentrations of oxygen so as to avoid significant levels of **combustion**. It has been the subject of a number of comprehensive reviews, notably by Balat *et al.* [6] and, more recently, Bridgwater [7,8] amongst others [9,10]. Although pyrolysis methods can vary considerably, it is believed that the energy consumed is only approximately 15% of that contained in the original feed and so the process offers a tantalizing energy profit margin [8]. This attractive energy balance is, however, decreased for feedstocks with high moisture content, since energy is wasted as dehydration occurs, something that makes dry starting materials desirable.

Needless to say, the choice of potential pyrolysis feedstocks is so extensive that a thorough literature analysis could easily sustain an entire thesis. Some notable reviews do, however, provide a commendable overview of this aspect [10,11]. Indeed, recent studies have utilized materials with varying chemical compositions from both the terrestrial and aquatic spheres, including woods, rice husks, bagasse, jatropha cake, microalgae, duck weed, cotton seed, sewage sludge and many more [11–26].

Irrespective of the starting feed, the resulting pyrolysis products are generally categorized as solid (char), liquid (tar/oil) and gas. The art of pyrolysis lies in controlling the distribution of these three product fractions through the manipulation of a number of variables (i.e., temperature, heating rate and residence time); hence, the design of the experimental set up is vital **(Table 2)**.

Products of pyrolysis

Biochar

Char is the solid residue remaining at the end of the pyrolysis process, which usually contains high levels of hydrogen and approximately 60 wt% carbon (with any remaining mass being made up of inorganic constituents, principally metal oxides known as ash). Most of the carbon in the char is present as fixed carbon (coke), although significant levels of volatile organic species may still be present (through either surviving the thermal degradation process or reforming after it) [27]. Coke can remain stable for many hundreds of years and so **biochar** offers unrealized possibilities as a carbon sequestration agent [28]. Furthermore, the elemental carbon present can potentially be used in a wide manner

of industrial applications, from simply burning as a solid fuel in boilers to use as an agrochemical, or even in the manufacture of carbon nanotubes [9]. Further **gasification** of char can also produce a hydrogen-rich fuel source, suitable for use in fuel cells or hydrogenation processes [9]. Biochar is, therefore, a relatively underestimated output of the pyrolysis process and there are currently extensive research efforts seeking to fully explore its composition (as derived from a variety of feedstocks) and potential uses [27]. Indeed, this biochar accounts for some 25% of the energy of the products and may, therefore, be utilized to make the pyrolysis process energetically self-sufficient [8].

Bio-oil

Bio-oil (or biocrude) is the liquid fraction obtained from pyrolysis, and represents a potentially lucrative source of both energy and high-value commodity chemicals **(Figure 1)** [29]. It is composed of a water-rich aqueous phase containing multifarious oxygenated hydrocarbons and an organic tar phase laden with heavier, long-chain hydrocarbons. The combination of polar species and lengthy carbon-chain molecules means that bio-oil has a viscosity that can be up to 1000-times that of water, a feature that poses difficulties for storage and transport. A review by Bridgwater highlights some common properties of bio-oils [30]. First, the oxygen content can be as high as 50 wt%, leading to **higher heating values** (HHVs) as low as 15–18 MJ/kg, disappointing when viewed against conventional diesel with a HHV of approximately 45 MJ/kg. The high concentration of organic acids in the oil often leads to very low pH values making the liquid corrosive towards metallic components and, thus, difficult to store. This storage problem is exacerbated by the instability of the oxygenated compounds, which tend to polymerize over time, further increasing the viscosity and contributing to the difficulties associated with utilizing bio-oil as a fuel. However, the technical problems surrounding bio-oils usage should not cloud perceptions of their potential value as both an energy supply and source of chemicals. It is widely recognised that bio-oil would probably need to undergo some form of upgrading before being utilized. This might involve hydrotreating the oils (deoxygenation through combination with hydrogen at high pressures) [31] or catalytic upgrading of the vapors over zeolites and other catalysts [32]. Some of the multiple routes for upgrading and applying bio-oils have been reviewed extensively by Butler *et al.* [10], Bridgwater [8], Huber *et al.* [33] and Zhang *et al.* [34]; many of the catalytic processes have also been described by Bulushev and Ross [35].

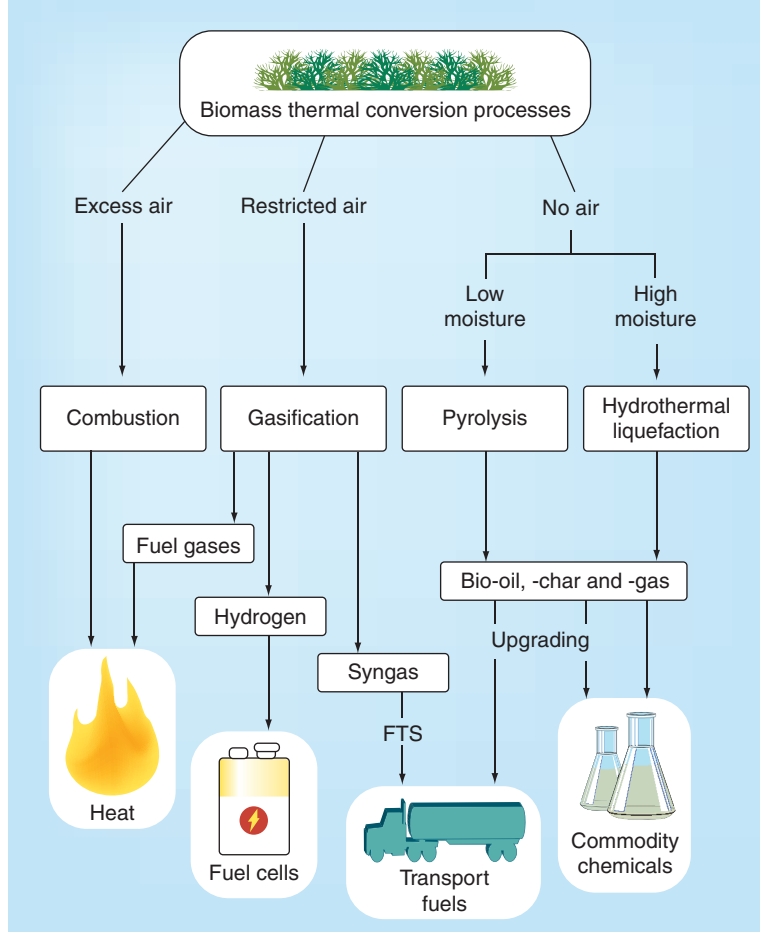

Figure 1. Products resulting from thermochemical treatment of biomass.
FTS: Fischer–Tropsch synthesis.
Modified with permission from [6].

Table 2. A comparison of process parameters and outputs from different classes of pyrolysis.

Pyrolysis class	Heating rate (°C/min^{-1})	Pyrolysis temperature range (°C)	Residence time	Approximate product distributions (%)		
				Oil	Char	Gas
Flash	1000–10,000	900–1300	<0.5 s	75 (25% H_2O)	12	13
Fast	100–1000	500–900	<2 s	60 (30% H_2O)	20	20
Intermediate	50–100	400–500	10–20 s	50 (50% H_2O)	25	25
Slow	10	~400	Min to h	30 (70% H_2O)	35	35

Adapted with permission from [7].

Key terms

Bio-oil: Known also as biocrude; the liquid fraction of the products from thermochemical processing of biomass. It is a mixture of an aqueous phase and an organic phase (tar). Both of these phases are complex and contain a vast number of different chemical species.

Higher heating value: Measure of the calorific value of a substance whereby the condensation of water, which is produced as a product of combustion, is factored in to the total energy change.

Biogas: Gaseous fraction resulting from the thermochemical processing of biomass.

Fischer–Tropsch synthesis: Process in which syngas or biosyngas (a mixture of predominantly CO and H_2) are passed over a transition metal catalyst in order to produce a range of alkanes/alkenes (and, to a lesser extent, oxygenates), which can be further upgraded or used as a fuel source.

Hydrothermal liquefaction: Thermochemical process whereby a feedstock is decomposed by the action of moderate heating in a high pressure aqueous environment.

Biogas

The pyrolysis-derived **biogas** fraction may account for as little as 10 wt% of the total products, but can be considerably higher depending on the heating rate and vapor residence time, as well as particle size, catalyst loading and rate of char removal. The gas is primarily composed of CO, CO_2, CH_4 and H_2, which all clearly have potential to be utilized directly as feedstocks or fuels; for example, in **Fischer–Tropsch synthesis** (FTS) or gas-to-liquid processes **(Figure 1)**. Short-chain alkanes and alkenes, which are useful feedstocks for the chemical industry, are also present in smaller concentrations in the biogas [9].

Stages of pyrolysis

Many terrestrial plants, which have been the most common focus of pyrolysis investigations, are comprised of lignocellulosic materials. It has been reported that the thermolysis of cellulose is endothermic, but that of lignin is exothermic. Overall, however, the ratio of these two components is such that pyrolysis of most feedstocks tends to be an exothermic process [36]. Pyrolysis, is thought to proceed via a three-stage process consisting of dehydration followed by principle degradation, and then a slow stage in which further decomposition, volatilization and char formation occur. Mechanisms explaining how each of these different stages occurs are usually only generic in nature owing to the complexity of the myriad of processes occurring simultaneously. The decomposition pathways usually include depolymerization (cellulose to glucose is common) followed by hydrolysis, oxidation, dehydration and decarboxylation [36]. Of particular interest are the mechanisms behind the formation of aromatic compounds, as they usually make up a significant proportion of the organic fraction of the resulting bio-oil [37]. Huber and Corma proposed a route whereby aromatics are obtained from Diels–Alder reactions and aldol condensations between fully and partially dehydrated products [38]. However, there is still much work to be done in this area in order to identify the pathways of the formation of key compounds.

Catalytic pyrolysis

In order to better improve upon the results obtained from conventional pyrolysis of the type discussed above, the process can be modified to include a catalyst. The presence of a catalyst directly in the pyrolysis vessel during the thermolysis process can achieve one or more of the following objectives:

- A reduction in the activation energy of the biomass decomposition, thereby facilitating pyrolysis at a lower temperature;
- An improvement in the quality of the resulting bio-oils by deoxygenating at the point of pyrolysis;
- The alteration of the product distribution in terms of oil:gas:char ratios;
- Facilitating rapid, *in situ* upgrading of the organic products.

The design of catalysts for inclusion in the pyrolysis of biomass is a field of ever-increasing importance as it has become clear that the successful implementation of such thermochemical processes on an industrial scale will inevitably rely on some sort of catalytic assistance. Indeed, various reviews have focused specifically on the catalytic aspect of the processes [35,39,40].

Consequently, a number of catalysts, including metal oxides, zeolites [40], transition metal-based systems [41] and ionic liquids [42], have been integrated directly into the biomass pyrolysis process with varying results. Generally, although an increase in bio-oil yield is not always seen, the liquid fraction will usually demonstrate substantial deoxygenation (and, consequently, an increase in calorific value and decrease in viscosity) upon inclusion of a catalyst. A study by Wang *et al.* revealed that activated alumina (aluminium oxide) was the most effective catalyst (in terms of both yield and deoxygenation) compared with Al-SBA-15 and ZSM-5 (both alumino-silicate heterogeneous solid acid catalysts) in the pyrolysis of herb residue industrial wastes [43]. The alumina produced oil with an HHV of 25.94 MJ/kg and a yield of 34.26 wt% at 450°C compared with an oil with a slightly lower yield and HHV of only 18.66 MJ/kg when no catalyst was included. Furthermore, the inclusion of catalysts has been found to facilitate pyrolysis at lower temperatures by decreasing the activation energy, thereby increasing the thermal efficiency of the process for a variety of different biomass feeds [39].

Hydrothermal liquefaction

Overview of hydrothermal liquefaction of biomass

In contrast to pyrolysis, **hydrothermal liquefaction** (HTL) employs much lower temperatures (<400°C) and higher pressures (up to 25 MPa). Crucially, however, unlike the low moisture levels needed for pyrolysis, HTL requires significant water content in the reactor (<85 wt%) and is, therefore, perfectly suited to the conversion of wet biomass such as biowaste [44] or algae [45]. These

HTL processing parameters, which are either slightly above (supercritical) or slightly below (subcritical) the critical point (at ~374°C and 22 MPa) of the water, enable it to act as both a solvent for organic species and as a provider of hydrogen radicals, which facilitate deoxygenation [46,47].

Consequently, HTL processing has given liquid yields as high as 82.1 wt% for biomass (grassland perennials, dry basis) at 374 K, 22.5 MPa, without the use of a catalyst [48]; this is far higher than might be expected from the equivalent pyrolysis (typically 30–40 wt%). A direct, side-by-side evaluation of pyrolysis and HTL has been carried out using microalgae as the feedstock [49]. In this study, pyrolysis was found to produce significantly lower oil yields (23–29 wt%) compared with 41 wt% for HTL upon the removal of the water soluble fraction and bio-oil of a slightly lower calorific value (29.30–33.62 MJ/kg for pyrolysis compared with 34.21 MJ/kg for HTL). Although the high pressures required make HTL initially sound unfeasible, the process is actually energetically favorable. This is partly due to the omission of an energy-intensive drying step, such as that required for processing via pyrolysis and so, for wet biomasses, HTL appears to be the most viable option for thermochemical processing [50].

Catalytic HTL

As with pyrolysis, a number of opportunities exist for both integrated catalysis and catalytic product upgrading post-reaction. Notably in this context, metal ions inherently present in the biomass have been thought to exert a catalytic effect on the thermolysis, but this notion has not been fully exploited or understood [46]. Indeed, the addition of a variety of salts and bases has been employed to probe such phenomena, predominantly on wood-based feedstocks, in order to catalyze the liquefaction process. For example, Ogi *et al.* tested $CaCO_3$, $Ca(OH)_2$, Na_2CO_3, NaOH, HCOONa, NaCl, K_2CO_3, KOH and HCOOK [51], whilst Karagöz *et al.* used RbOH, CsOH [52] and K_2CO_3 [53], with a selection of others having also been investigated [54]. In each case, the typical effect of the basic catalysts (under subcritical HTL conditions) was to supress char yields and increase oil yields. However, more work needs to be undertaken to explore the precise role of the catalyst in both subcritical and supercritical HTL, as for wet biomass, it may prove to be the optimal method for extracting fuels.

▪ Gasification

Overview of gasification of biomass

Gasification of biomass proceeds initially by the same route as pyrolysis: first dehydration occurs, followed by primary cracking and, finally, a slower sustained degradation. To achieve gasification, the feed is heated to much higher temperatures than in pyrolysis and subjected to longer residence times to facilitate the decomposition into simple, combustible gaseous molecules (the 'producer gas') consisting of CH_4, H_2 and CO (and, to a lesser extent, carbon dioxide and nitrogen) [3,7,9,33,55,56]. Unlike pyrolysis, a gasifying agent such as air, steam or oxygen-enriched air is often fed simultaneously into the reactor.

The quality and composition of the product gas is intimately linked to the feedstock, conditions and gasifying agent. Generally, air is found to give the poorest product gas quality (LHV = 5 MJ/m^3), followed by oxygen (LHV = 10–12 MJ/m^3), with steam giving the best (LHV = 15–20 MJ/m^3) [7]. The quality of the gas product can be improved by a subsequent cleanup step that removes tars (which would be liquid under ambient conditions), halogens, sulphur compounds, dust and other contaminents. The gases can then be used for electricity production, synthesis of chemicals and the production of fuels via FTS [56,57]. The hydrogen fraction obtained is also of growing interest due to its potential use in fuel cells. Furthermore, inclusion of water in the basic gasification process, so-called hydrothermal gasification, can be used to minimize char yield as the high-temperature water is better able to solvate the solid matter [58]. Thus, again, wet biomass feedstocks are of growing interest, particularly as a means of recovering useful energy from organic/water waste streams [59].

Catalytic gasification

Aside from the utilization of catalysts in postgasification FTS/gas-to-liquid upgrading of the gaseous products, which generate hydrocarbons suitable for fuel applications, there are numerous benefits to incorporating a catalyst directly into the gasification process. This type of methodology has been reviewed by Sutton *et al.* who state that a suitable primary catalyst must be effective in the removal of tars, improve gas quality, resist deactivation, and be easily regenerated, robust and reasonably inexpensive [60]. To this end, dolomites, olivines (both naturally occurring minerals), alkali metal salts and supported metal catalysts (including nickel supported on dolomite) have all been incorporated into biomass gasification [35]. Notably, de Lasa *et al.* reported that using CaO as a catalyst could lower the gasification temperature of cellulose, aspen and cedar by up to 150°C, while simultaneously increasing yields of CO, CO_2, CH_4 and H_2 [61].

▪ Biomass combustion

Overview of biomass combustion

Combustion through the ignition of biomass in ample oxygen can generate temperatures of between 800 and

Key terms

Biosorption: Process in which contaminants can become concentrated within biomass through passive absorption and are subsequently retained by binding to the cellular structure.

Biodiesel: Fuel consisting of long-chain alkyl esters derived from processing of lipid-containing biomass. Can be used as a fuel additive or on its own after engine modification.

1000°C. This is generally quite an inefficient method of extracting energy from biomass, especially if oxygen and moisture contents in the feeds are high, with an average energy conversion between 20 and 40 wt% being achieved in commercial combustion facilities [3]. Moreover, the energy density of unprocessed biomass is quite low and so transport of large volumes is not sustainable without prior refinement. Methods for predicting the HHV from the proximate analysis have been developed, providing a simple route to estimating the energy of combustion from a feedstock [62]. Although HHVs can be quite high for woody biomasses, they are generally disappointing for other forms of bioderived materials. This low calorific value combined with the need to pretreat the biomass (e.g., by chopping and grinding) means that combustion is quite an inefficient option for thermal processing [63].

Thermochemical processing of macroalgae

▪ Macroalgae as a feedstock

Terrestrial versus aquatic biomass: wetter is better

In recent years, biofuels derived from terrestrial sources have gained an increasingly negative image. In 'The Biofuel Delusion', Giampietro and Mayumi give a damning appraisal of the impacts of the explosion in biofuels activity over the last few decades [64]. Specifically, they cite fuels derived from terrestrial biomass as having caused a boom in global food prices, as well as having generated a net carbon gain in the atmosphere. This is far from the environmentally and economically beneficial solution that biofuels propose to offer. Indeed, some researchers no longer see biofuels as a viable energy source, a stance typified by David Mackay who claimed that "*in a European country like Britain, [biofuels] can deliver so little power, I think they are scarcely worth talking about*" [65]. Thus, biofuels are in danger of becoming ostracized by the sustainable energy community as a frivolous experiment that went awry.

The tensions that arise when plants are grown preferentially for biofuel production at the expense of food crops and carbon-sequestering forests is the primary criticism of biofuels; consequently one potential solution is to utilize aquatically sourced biomass. The likes of micro- and macro-algae, invasive aquatic plants and weeds, make up approximately 50 wt% of the planet's biomass resources [66]. They hold a number of advantages over terrestrial feedstocks, the most obvious being that they do not compete for land and freshwater with agriculture and forestry and, consequently, energy derived from algal processing is not to the detriment of food production or carbon sinks. Indeed, by growing in the ocean, macroalgae can utilize the 70% of the planet for which there is currently comparatively little competition. These 'third-generation' biofuels could well be part of the answer to restoring confidence in bioenergy.

Macroalgae background

Macroalgae is a term referring to approximately 9000 species of multicellular eukaryotic aquatic plants colloquially known as seaweed. They fall into three divisions: brown algae (Phaeophyceae: 2000 species including the genera *Laminaria*, *Fucus* and *Sargassum*); red algae (Rhodophyceae: 6000 species including the genera *Gelidium*, *Palmaria* and *Porphyra*); and green algae (Chlorophyceae: 1200 species including the genera *Ulva* and *Codium*). As with most weeds, macroalgae are considered by many to be nothing more than a nuisance, as they exhibit exceedingly high growth rates [67] and some brown algae can reach sizes of up to 60 m in length [68]. Indeed, the green tide algal blooms that result from species such as *Ulva prolifera* can have something of a malevolent presence. For example, 1 million tons of this macroalgae had to be cleared from the Qingdao region of China in 2008 [69]. Prompted by eutrophication of waters through anthropogenic pollution, the blooms may generate noxious fumes of H_2S as they rot and can severely damage the affected ecosystem through deoxygenation as they degrade. Aside from such dangers, these blooms also represent an enormous waste of natural resources to the extent that it is estimated that less than 1% of the world's macroalgae biomass is currently utilized [66].

Despite this overriding image as nuisance species, macroalgae are in fact industrially valuable and versatile commodities. Across the globe, seaweeds are harvested from the wild or farmed in aquacultures in order to produce foods, cosmetics and fertilizers from the phycocolloids and alginates, which are extracted from them [70]. Clearly, however, if macroalgae were to be utilized in higher volumes than are currently consumed, they would have to be farmed artificially on a much larger scale. A myriad of cultivation technologies have been imagined and considered for this task [67,71,72], which, critically, do not compete for the land and fresh water that must be reserved for food production. With the availability of 15–20 dry tonnes of macroalgae per hectare per year, countries with extensive coastlines are considering the possibility of large-scale cultivation of the crop. China, Indonesia, Ireland, the UK and Denmark, amongst others, have all begun to assess the scale of possible seaweed bioenergy industries, with the west

coast of Scotland (at one point the world capital of kelp cultivation) estimated to generate up to 4735 km^2 of harvestable macroalgae by 2050 [73].

There is reason to believe that certain physiological traits of macroalgae would make their large-scale cultivation environmentally beneficial. First, the photosynthetic efficiency of some macroalgae (6–8%) is three- or four-times greater than terrestrial biomass (1.8–2.2%) and, **hence, they absorb carbon more effectively**. This carbon is removed to an aquatic environment, which better enables sequestration to the ultimate sink (the deep ocean [74]) and so macroalgae are excellent agents for CO_2 remediation [67]. Furthermore, it has been speculated that the production of iodine from macroalgae could also act as an atmospheric cooling agent [66] and so there are considerable benefits to cultivating this class of biomass as far as climate change mitigation is concerned. In addition, the **biosorption** properties of macroalgae enable it to scavenge heavy metals and excess nutrients from aquatic environments [67]. Thus, seaweeds have been utilized to remove toxic metals such as cadmium [75] and arsenic [76] from waters, as well as acting as a biofilter to remove 90–99% of the nitrogen and 70–98% of the phosphorus produced by marine animals, which would otherwise contribute to the levels of eutrophication behind harmful blooms of microalgae [77]. Similarly, the ability of marine macroalgae to grow profusely in accessible coastal zones (in both temperate as well as tropical regions) means that they can also assist in the bioremediation of the run-off from land-based agriculture.

Macroalgae composition

With the need for flexible fronds to withstand stormy marine conditions, macroalgae do not contain high levels of lignocellulose. Thus, macroalgae differ quite substantially in their composition compared with rigid terrestrial feedstocks, which are rich in cellulose (straws and grasses) or lignin (woody biomass) [78]. Since lignocellulosic materials decompose at comparatively high temperatures (of the order of 330°C), macroalgae present a potentially significant energy-beneficial alternative for onward conversion, as their thermolysis takes place over lower temperature regimes (see the section 'Thermodynamic studies of macroalgae thermolysis'). It should also be stressed that macroalgae differ quite considerably from microalgae, specifically in terms of their lipid content, which can be as high as 80 wt% for the latter [79,80]. Much of the 'algal biofuels' debate is centered around lipid extraction from microalgae and its subsequent transesterification to produce **biodiesel** [81,82]. However, lipid extraction followed by transesterification has been shown to be ineffective for macroalgae [83], with yields of fatty acids peaking at only approximately 10 wt%, even when the extraction procedure has been fully optimized [84,85]. Consequently, most analyses claiming to consider the viability of 'algal biofuels' neglect macroalgae altogether [65,86]. However Ross, of the University of Leeds, has been particularly influential in leading the reappraisal of macroalgae, specifically brown seaweeds, as feedstocks for the thermochemical production of biofuels, stressing that the high carbohydrate content in most species of macroalgae means that they are well suited to this kind of processing [68]. These carbohydrates come primarily in the form of free sugars such as mannitol and also laminarin, fucoidan, alginic acid and other polysaccharides (a typical kelp composition profile is given in **Table 3**). Furthermore, **macroalgae differ considerably from terrestrial biomass feedstocks** in their comparatively high levels of nitrogen (from the protein content) and sulfur (from the fucoidan) along with a total halogen content of between 0.5 and 11 wt% (compared with 1–1.5 wt% for most land-based feedstocks) [68].

It should be noted however, that the observations outlined above are only generalizations; the exact chemical compositions of macroalgae vary between species. Alginates (the salts of alginic acid) are, for example, very

Table 3. The typical chemical constituents of brown algae.

Compound	Typical content (wt%)	Structure
Alginic acid	≈ 25	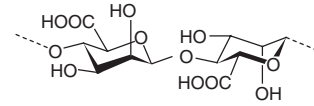
Fucoidan	≈ 5	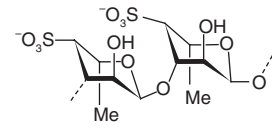
Mannitol	≈ 5	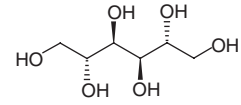
Lipids	≈ 5	Monoglycerides, diglycerides, triglycerides and phospholipids
Laminarin	≈ 10	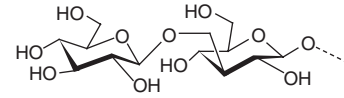
Cellulose	≈ 5	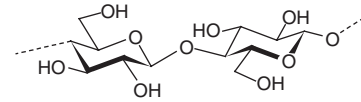
Proteins	≈ 15	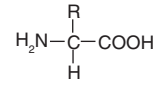
Ash	≈ 30	$K^+/Na^+/Ca^{2+}$/metals

Adapted with permission from [9].

prevalent in brown algae, but completely absent from red and green genera. Additional compositional variations are also found within single species, both seasonally and geographically, as illustrated by the pioneering work of Black in the 1950s [87,88]. The impact of this seasonal variation in the context of thermochemical treatments was considered recently by Ross *et al.* for the case of *Laminaria digitata* [89]. It was found that harvesting the feedstock in July, when photosynthetic activity is at a peak, was optimal as carbohydrate content (and consequently HHVs) is highest. In contrast, protein, ash and alginic acid concentrations were found to peak during the winter months as the stores of sugars were depleted. Although this variation appears to limit the utility of macroalgae as a feedstock, it is clearly less drastic than the seasonality exhibited by terrestrial crops, which are, in general, completely unavailable for large periods of the year.

Another notable difference between macroalgae and terrestrial feedstocks comes from their unique biosorption properties. Their ability to sequester metallic ions from the surrounding seawater lead macroalgae to naturally exhibit higher metal contents than found in other biomass types. Brown algae in particular are prone to accumulate alkali and alkali earth metal ions, notably K^+, Na^+ and Ca^{2+}, which are usually found in concentrations in the order of 10^4 ppm [89]. These metals are found to act as binding agents for parallel chains of polymeric alginic acid, providing the seaweed with support in the absence of lignin and giving the extracted alginates their famous gelatinous properties [90]. Trace elements, including heavy metals and transition metals, are detected in much smaller quantities in macroalgae, but still at concentrations thousands of times higher than those found in the surrounding seawater [88]. Both the abundance and concentration of trace metals are found to vary seasonally and the impact of their presence on the thermochemical treatment of macroalgae is considered below [88,89].

Clearly, the carbohydrate content of macroalgae could be utilized in the production of fuels. The routes available for this process are numerous and some have already been discussed. As neither lipid extraction (followed by transesterification) nor anaerobic digestion are currently considered to be economically viable options, other processing methods must be considered for the role of converting algal biomass to fuels [83,91]. Novel chemical transformations [92], fermentation [93,94] and thermochemical upgrading all show potentially promising results as candidates for this task, despite being largely ignored in most biofuel appraisals. The following section will examine the case for the thermochemical upgrading of macroalgae to deliver useful chemicals and fuel materials.

Historical perspective on the thermochemical processing of macroalgae

The derivation of useful chemicals from seaweed via thermochemical processing is, by no means, a novel idea. Indeed, the incineration of kelps (large brown algae) to obtain soda ash dates back to the 1720s, where the process was integral to the growth of the soap and glass manufacturing industries [95]. The method was later exploited in the same manner to extract potash and iodine, and by 1820 some 20,000 tons of kelp were being harvested in the Outer Hebrides, Scotland, alone [95]. As the industry began to decline, those seeking to keep their businesses afloat sought to derive other valuable products from the seaweed and, in 1862, these endeavors led to the discovery of oily distillates from the thermal treatment of macroalgae [96,97]. However, further analysis of these oily products did not take place until the early 1920s when they were found to be side products in the manufacturing of potash from kelp in the USA [98,99]. Later in that decade, the British Fuel Research Board commissioned Tupholme to undertake a study to explore the potential of deriving combustible resources from the pyrolysis of seaweeds [100]. This study found that treatment of a mixed feed of different air-dried *Laminaria* species at 600°C gave rise to a 20 wt% yield of a gaseous product with a calorific value of 3.7 MJ/m^3 [101]. By modern standards, the gas would be considered to be of quite low quality; however, the British Fuel Research Board did recognize potential in the process. Unfortunately, the decision to proceed with larger scale investigations was not met with financial backing and the notion of using seaweed as a feedstock for deriving fuels was abandoned in the wake of the rapid development of the petrochemical industry [95].

For the next few decades, research into the thermochemical treatment of macroalgae for fuel almost completely died out. Nevertheless, the pyrolysis of seaweed was still being researched for use as a novel taxonomic tool for distinguishing different macroalgal species, with subsequent gas chromatographic analyses acting as a fingerprint [102–106]. It was not until 1978, with the work of Morgan and Smith, that a comprehensive evaluation of how pyrolysis could be used to decompose macroalgae for biofuels was undertaken [107]. Their study involved pyrolysing *Fucus serratus*, a brown alga, at 300, 450 and 800°C. However, in each case the relatively low yield of liquid hydrocarbon (4 wt%) prompted them to conclude that it was "*unlikely that simple pyrolysis [of macroalgae] would be an economic prospect in the foreseeable future*" [107]; a prophecy that was subsequently met by a further three decades of inactivity in the field.

With pressing concerns about conventional energy sources and with the vast wealth of research that has been undertaken into the thermochemical processing

Table 4. Species and composition of macroalgae that have been subjected to thermochemical investigations for biofuels production.

Species	Moisture (wt%)	Ash (wt%)	VM	FC	C (wt%)	H (wt%)	O† (wt%)	N (wt%)	S (wt%)	HHV‡ (MJ/kg)	Thermochemical method	Ref.
Laminaria japonica	7.65	28.28	53.10	10.97	30.60	4.89	26.51	1.51	0.56	13.14	Pyrolysis/ microwave/ combustion/ gasification	[24,78,108,130,133]
Undaria pinnatifid	9.50	25.84	53.62	11.04	34.01	4.99	21.61	3.34	0.71	14.99	Pyrolysis	[108]
Fucus serratus	11.40	18.60	45.50	24.20	33.50	4.78	28.02	2.39	1.31	14.13	Pyrolysis/ gasification	[68,106,130]
Sargassum pallidum	10.30	36.44	44.60	8.30	22.64	4.90	21.34	2.96	1.42	10.80	Pyrolysis	[78]
Dictyopteris divaricata	5.00	24.67	57.62	12.71							Pyrolysis	[118]
Laminaria hyperborea	12.40	11.20	53.50	21.50	34.97	5.31	32.94	1.12	2.06	15.01	Pyrolysis	[76,68]
Fucus vesiculoses	12.30	11.80	51.40	23.80	32.88	4.77	33.28	2.53	2.44	13.62	Pyrolysis	[76,68]
Macrocystis pyrifera	8.00	18.50	42.40	33.40	27.30	4.08	38.20	2.03	1.89	10.16	Pyrolysis	[76,68]
Laminaria digitata	13.70	10.00	53.40	25.30	31.59	4.85	36.52	0.90	2.44	12.99	Pyrolysis	[66,68,89]
Ascophyllum nodosum	6.20	14.50									Microwave pyrolysis	[66]
Chorda filum	13.10	9.90	52.20	24.90	39.14	4.69	30.13	1.42	1.62	16.01	Pyrolysis	[68]
Sargassum natans	10.46	29.09	48.85	11.60	25.90	5.57	24.18	3.58	1.22	12.56	Combustion/ pyrolysis	[122]
Bifurcaria bifurcata	~10§	23.80			32.50	4.44	26.99	1.15	1.12	13.38	Gasification	[130]
Alaria esculenta	~10§	27.30			28.40	3.75	28.47	1.59	0.49	10.84	Gasification	[130]
Laminaria saccharina	9.20	24.20			31.30	3.70	28.50	2.40	0.70	11.86	HTL	[124]
Sargassum patens	14.38	17.77	55.49	12.36	40.18	5.22	19.47	2.00	0.98	17.86	HTL	[126]
Ulva prolifera	9.83	12.46	68.79	8.92	32.89	4.67	35.21	2.51	2.43	13.29	Pyrolysis/HTL	[69,119,128]
Ulva lactuca	4.93	24.72	58.38	11.97						12.89	Pyrolysis	[118]
Ulva pertusa	8.00	19.60	59.30	13.10						11.50	Pyrolysis	[115]
Cladophora coelothrix	~10§	10.50			32.10	4.10	39.30	4.00		11.69	Pyrolysis	[113]
Cladophora patentiramea	~10§	25.20			22.50	2.80	37.00	2.50		6.76	Pyrolysis	[113]
Chaetomorpha indica	~10§	10.80			20.60	2.90	52.70	3.00		4.89	Pyrolysis	[113]
Chaetomorpha linum	~10§	12.50			26.00	3.50	44.80	3.20		8.26	Pyrolysis/HTL	[113,127]
Cladophoropsis sp.	~10§	33.30			20.50	2.50	31.80	1.90		6.08	Pyrolysis	[113]

†Calculated by difference.
‡Calculated using equations from Channiwala and Parikh [62].
§Estimated moisture content based on drying conditions reported in reference.
FC: Fixed carbon; HHV: Higher heating values; HTL: Hydrothermal liquefaction; VM: Volatile matter.

Table 4. Species and composition of macroalgae that have been subjected to thermochemical investigations for biofuels production (cont.).

Species	Moisture (wt%)	Ash (wt%)	VM	FC	C (wt%)	H (wt%)	O (wt%)	N (wt%)	S (wt%)	HHV (MJ/kg)	Thermochemical method	Ref.
Ulva flexuosa	~10[§]	19.40			26.20	3.80	36.50	4.10		9.08	Pyrolysis	[114]
Cladophora vagabunda	~10[§]	33.80			28.60	2.90	21.30	3.40		10.34	Pyrolysis	[114]
Caulerpa taxifolia	~10[§]	13.10			26.80	3.40	44.60	2.10		8.44	Pyrolysis	[114]
Ulva clathrata	13.30	37.09	41.82	7.79	22.74	6.27	16.19	3.14	1.27	12.95	Pyrolysis/ combustion	[117,123,134]
Ulva rigida	4.93	26.00	61.41	12.59							Microwave pyrolysis	[122]
Cladophora fracta			65.60	28.10							Pyrolysis/ gasification	[108,140]
Codium fragile					39.70	6.10		4.10	3.90		HTL	[141]
Porphyra tenera	6.41	10.44	69.66	13.49	40.60	4.65	30.51	6.13	1.26	16.31	Pyrolysis	[109]
Pophyra yezoensis	9.20	31.30	36.80	22.10						10.60	Pyrolysis	[118]
Plocamium telfairiae	11.70	33.20	30.60	24.30						12.30	Pyrolysis	[118]
Corallina pilulifera	10.50	38.60	32.20	18.40						9.70	Pyrolysis	[118]
Grateloupia filicina	4.69	22.37	55.93	17.01						13.17	Pyrolysis	[119]
Gracilaria cacalia	11.65	14.84	54.50	19.01	31.11	5.60	33.93	0.83	2.04	13.83	Microwave pyrolysis/ combustion	[66,134]

[†]Calculated by difference.
[‡]Calculated using equations from Channiwala and Parikh [62].
[§]Estimated moisture content based on drying conditions reported in reference.
FC: Fixed carbon; HHV: Higher heating values; HTL: Hydrothermal liquefaction; VM: Volatile matter.

of other types of biomass, many have recognized that the case for macroalgae pyrolysis must be re-evaluated. Consequently, the last 3 years have witnessed something of a bloom in terms of the number of papers published on the subject. These reports detailed studies of approximately 40 species of macroalgae (red, green and brown), along with a number of model algal compounds, that have been subjected to pyrolysis and other thermochemical processes in order to try and obtain bioresources (Table 4).

▪ Pyrolysis of macroalgae

Product analysis

Bio-oil

As discussed earlier, bio-oil is a major product of pyrolysis of land-based plant materials and this is no exception for macroalgae. As with terrestrial feedstocks, bio-oil yields often increase with pyrolysis temperature, reaching a peak at approximately 500°C [107–109]. Analyses have been made of the oils resulting from the conventional pyrolysis (temperatures of 200–875°C) of the main carbohydrates found in macroalgae [110], as well as oils obtained from the pyrolysis of six types of brown algae (*Undaria pinnatifid*, *Laminaria japonica* [109], *F. serratus* [107], *Laminaria hyperborea*, *Fucus vesiculosus* and *Macrocystis pyrifera* [76]), one red alga (*Porphyra tenera* [109]) and one green (*Cladophora fracta* [108]). Although the total liquid yield can be quite high from pyrolysis (*F. serratus* 42 wt% at 800°C; *C. fracta* 44.6 wt% at 875°C; *U. pinnatifid* 39.5 wt%; *L. japonica* 37.5 wt% and *P. tenera* 47.4 wt%, all at 500°C), the water content is usually significant and, consequently, the HHV of the pyrolysis oils is low, between 6.75 and 12.24 MJ/kg. If the aqueous and organic fractions are separated and considered in isolation, however, the picture improves considerably. The organic phase has an oxygen content (~17 wt%) that is approximately four-times lower than in the original liquid (~70 wt%) and lower than in the equivalent woody biomass derived bio-oil (~30 wt%) [109]. Consequently, the HHV values for the organic fraction of the macroalgae bio-oil are much higher, between 23.33–33.57 MJ/kg. This low oxygen, high hydrocarbon phase is rich in aromatic and phenolic compounds, and has an unusually high

nitrogen content in the form of pyrrole and indole derivatives, reflecting the higher nitrogen level of macroalgae compared with those of terrestrial feedstocks. However, the organic phase of the bio-oil is obtained from macroalgae in fairly low yields on its own (only 4 wt% for *F. serratus*, and 22, 16 and 28 wt% for the *Undaria, Laminaria* and *Porphyra,* respectively), so it is useful to consider the impact of dehydrating the aqueous fraction and combining the two. Inevitably, with the increased oxygen content, the HHV values of the combined material decrease by approximately 20–25%; these values are still higher than those achieved from some land-based biomass [11], but lower than the values found through processing microalgae [26].

The aqueous phase resulting from macroalgae pyrolysis is composed of hundreds of relatively small oxygenated compounds such as furfurals, ketones, aldehydes, acids, furans and alcohols. The exact origins of the compounds in this complex medley is something of a mystery, but a better understanding has been provided through the work of Ross *et al.* [110]. Their recent analysis of the degradation behavior of the principal carbohydrates that make up brown seaweeds will be invaluable to future macroalgal bio-oil analyses. Through coupling the pyrolysis reactor to a gas chromatography-mass spectrometer, Ross studied the fragmentation of alginic acid, mannitol, laminarin and fucoidan over the temperature range 200–800°C and determined that the former two compounds decompose over one temperature region, whereas the latter two decompose over two temperature regions. Other investigations have concentrated on the thermal decomposition of metal alginates and alginic acid in order to model the degradation of macroalgae by heat [78,111–113]. Critically, it was found that the decomposition of these model algal compounds take place at lower temperatures than the constituents of many terrestrial biomasses. Although some authors criticize the use of 'model compounds' in thermochemical studies [8], it is doubtless that the characteristic mass-loss profiles and product spectra obtained by Ross will be decisive in deconvoluting results from pyrolysis of real macroalgal specimens. Indeed, they equip the experimenter with the ability to 'fingerprint' a macroalga sample in a way analogous to that used by the early the early taxonomic researchers, but now with the possibility for deciphering the complex thermal degradation processes involved in pyrolytic transformations. A schematic representation of the various carbohydrate fragmentation pathways is given in **Figure 2**. It is important to mention that, despite having a clearer understanding of what the various carbohydrate components degrade into and at what temperatures, there is still relatively little understanding of the mechanism by which these processes occur.

Biochar

Levels of residual solid (char) are noticeably higher following macroalgae pyrolysis than those resulting from terrestrial biomass sources owing to the high levels of ash and fixed carbon present in many of the seaweed samples analyzed to date [68]. The yields of this char can be as high as 60 wt% [109] although, as with the pyrolysis discussed earlier, these are found to decrease with increasing temperature and are usually approximately 20–40 wt% at the point of highest oil yield [68,109]. The char offers potential as a high-value side product and so significant analyses of its composition, production and possible applications have been undertaken by Bird *et al.* [114]. Having collected eight species of green tide algae and paralyzed them at temperatures between 305 and 507°C, Bird *et al.* determined the physiochemical parameters of each of the chars, noting the low carbon content (20.5–30.2 wt%) and relatively high nitrogen content (1.9–4.0 wt%), both of which are representative of the levels in the corresponding seaweeds. Furthermore, the char samples were found to have high levels of extractable inorganic nutrients (P, K, Ca and Mg) and high pH (8–10). Bird concluded that the char would be of significant use to the agricultural community as a soil ameliorant and fertilizer, which he later confirmed through a series of trials [115]. These studies also substantiated the claim that algal biochar would serve as an effective carbon sequestration agent as it contains approximately 30 wt% of trapped carbon, which could subsequently be buried.

Biogas

The gaseous products of macroalgae pyrolysis do not differ significantly from those obtained through the pyrolysis of other biomasses. In both cases, the gaseous yields are found to increase with temperature and are approximately 20–30 wt% at the point of highest oil yield for the macroalgae [107,109]. CO_2 constitutes approximately 90 vol% of the gas produced at lower pyrolysis temperatures (300°C), although this can drop to as low as 50 vol% at higher temperatures (600°C) as secondary tar cracking reactions lead to the evolution of new gases, particularly C_1-C_4 vapors. H_2 and CO constitute the bulk of the remaining gases in fractions obtained at temperatures above 500°C, with yields of approximately 10 and 5 vol%, respectively [109].

Thermodynamic studies of macroalgae thermolysis

In order to establish the thermodynamic parameters of the pyrolysis process, a number of detailed thermal studies have been carried out on a variety of macroalgae species [69,78,116–121], as well as on a set of model carbohydrate compounds [110]. In both cases, the decomposition was found to take place in three distinct

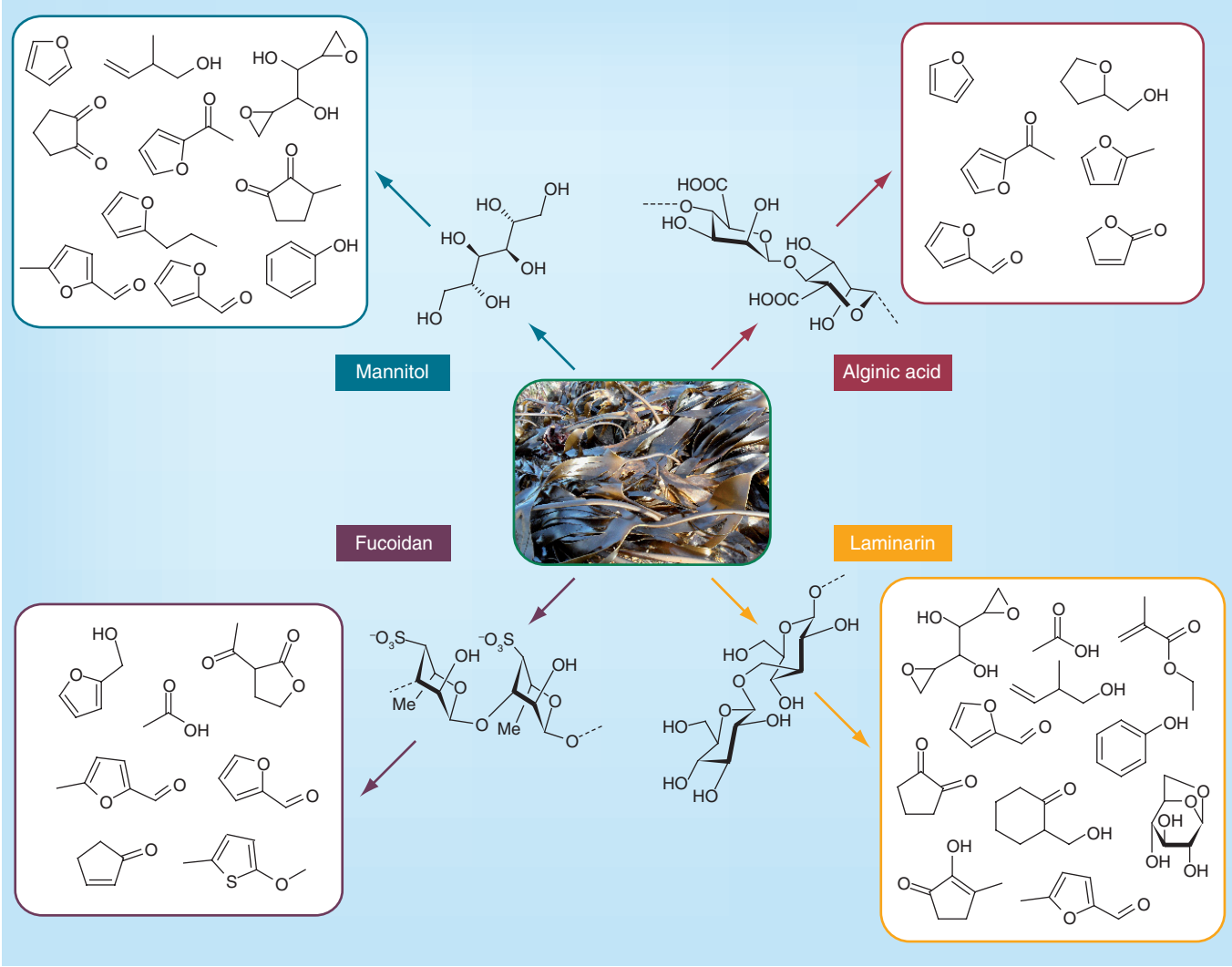

Figure 2. Origins of the main fragments from the pyrolysis of the principle carbohydrates in brown algae.
Data from [110].

stages: dehydration, followed by the main pyrolysis/devolatilization and, finally, a slow decomposition step [69,78,116,118,120]. The onset of seaweed thermolyis, specifically the devolatilization stage, generally takes place at a lower temperature than that for terrestrially grown materials by approximately 50°C **(Table 5)**, although clearly this depends on the individual constituents of the biomass. It was also noted that the heating rate was instrumental in determining the activation energy, thus, a rate of 20°C min^{-1} was found to give the lowest activation energy for *U. prolifera*, but use of different species may require further optimization. Ultimately, however, no detailed mechanism has been put forward for the pyrolysis reactions themselves and there is scope for work in this area. A better understanding of the degradation pathways will allow more efficient processing techniques to be designed.

Further considerations

Effect of catalysts on macroalgae pyrolysis

There is considerable evidence to suggest that the ash content of macroalgae makes the pyrolysis process autocatalytic (see the section 'Effect of pretreatment on macroalgae pyrolysis') with Na ions (present at 10^4 ppm levels) having been shown to promote decomposition of alginates at a lower temperature than do calcium ions [112]. Lee *et al.* are the only group to have specifically studied the effects of an added catalyst upon pyrolysis **(Figure 3)** [24]. Their investigation into the effects of meso-MFI-zeolite and nanoporous Al-MCM-48 on the pyrolysis of *Laminaria japonica* demonstrated that, in both cases, an overall increase in gas yield (from 13 to 24 wt%) and a 15 wt% decrease in oxygen content was achieved in the presence of these catalysts. The study showed that the zeolite gave the greatest yield

of phenolics, aromatics and nitrogen compounds and that the Al-MCM-48 gave the highest yield of hydrocarbons (~8 wt% at 500°C). Further investigations into catalytic pyrolysis are, therefore, ongoing.

Effect of microwave irradiation on macroalgae pyrolysis

A recent novel innovation has been the application of microwave technology to the pyrolysis process. Two studies, one by Budarin *et al.* [66] and the other by Jun *et al.* [122], have analyzed the products of the microwave pyrolysis of *Gracilaria*, *L. digitata*, *Ascophyllum nodosum* [66] and *Ulva rigida* [122] with mixed results. Microwave technology has been found to be ideally suited to treating algal biomass as their elevated water content facilitates the high heating rates needed to deliver high bio-oil yields. Thus, bio-oil yields were found to be highest with approximately 7.5 wt% initial water; this is approximately the moisture content of most macroalgae samples (Table 4). A maximum oil yield of 21 wt% was obtained by Budarin *et al.*, which had a low water content (2.2 wt%) and middling HHV (22.1 MJ/Kg), although a disappointingly low pH (2.8), reflecting the relatively high concentrations of organic acids. However, these figures are impressive given the extremely low temperatures (~130°C using a 200/300 W microwave) required for decomposition via microwave-mediated pyrolysis. Curiously, the mass of the sample used in the pyrolysis also had a dramatic influence on both bio-oil yield and composition, an effect attributed to the slower diffusion of volatile vapors in the larger samples. The study by Jun *et al.* on *U. rigida* was conducted at much higher temperatures than that by Budarin *et al.* and, consequently, the bio-oil yield was lower (~8 wt%) as a result of the onset of secondary decomposition processes [122]. Jun *et al.* also reported the usual high nitrogen and oxygen levels in the resulting bio-oil but, more encouragingly, also noted an increased ester yield, a reduced yield of carboxylic acids (and consequently higher pH) and a high number of long linear chain hydrocarbons, which increase the HHV of the oil.

Effect of pretreatment on macroalgae pyrolysis

As previously stated, macroalgae typically have a high metal content (especially Na, K, Ca and Mg) and it is widely believed that these ions may exert a catalytic effect on decomposition [68,78,109,110,118,123]. For example, a study by Ross *et al.* concluded that Na ions are particularly effective at catalysing alginate thermolysis [112]. However, formation of inorganic oxides (ash) through the presence of metal ions dramatically increases the chances of fouling and slagging in the reactor and is often heralded as one of the principle disadvantages of macroalgae as a feedstock [68]. Most algae have an alkali index (a measure of amount of alkali oxide in the biomass per unit of energy) of approximately 16–82 kg alkali/GJ, where values of above 0.34 kg alkali/GJ are seen to

Table 5. Thermodynamic parameters for biomass thermolysis.

Species	Activation energy (KJ mol^{-1})	Pyrolysis temperatures (°C)		Ref.
		Temperature range of devolatization stage	Temperature of maximum mass loss rate	
Macroalgae				
Ulva pertusa	149	199–305	251	[116]
Ulva prolifera	228	175–551	248–271	[69]
Ulva prolifera	25–50	186	255	[120]
Laminaria japonica	208	192–372	252–285	[78]
Sargassum pallidum	203	172–414	258–304	[78]
Ulva clathrata	230	192–540	261	[142]
Pophyra yezoensis	154	187–378	280–312	[118]
Plocamium telfairiae	241	196–370	233–277	[118]
Corallina pilulifera	245	178–365	226–293	[118]
Laminaria digitata	104	200–550	260–310	[110]
Microalgae				
Spirulian platensis	83	210–560	360	[143]
Chlorella protothecoides	45	180–540	340	[143]
Dunaliella tertilecta	146	185–382	285	[144]
Terrestrial				
Wheat straw	130–175	230–400	300–350	[145]
Rice husk	80	225–350	300	[146]
Cotton stalks	41	480–630		[147]
Sunflower shells	74	300–600		[148]
Cornstalk	60–90	214–400	350	[120]
Sawdust	120–155	239–430	380	[120]
Constituents of macroalgae				
Sodium alginate	188	204–285	232	[78]
Alginic acid	112	150–555	225	[110]
Fucoidan	247	175–750	202	[110]
Laminarin	102	175–685	342	[110]
Mannitol	139	220–400	336	[110]
Constituents of terrestrial biomass				
Cellulose	200	305–496	332	[149]
Hemicellulose	100	240–696	281	[149]
Lignin	80	219–508	363	[149]

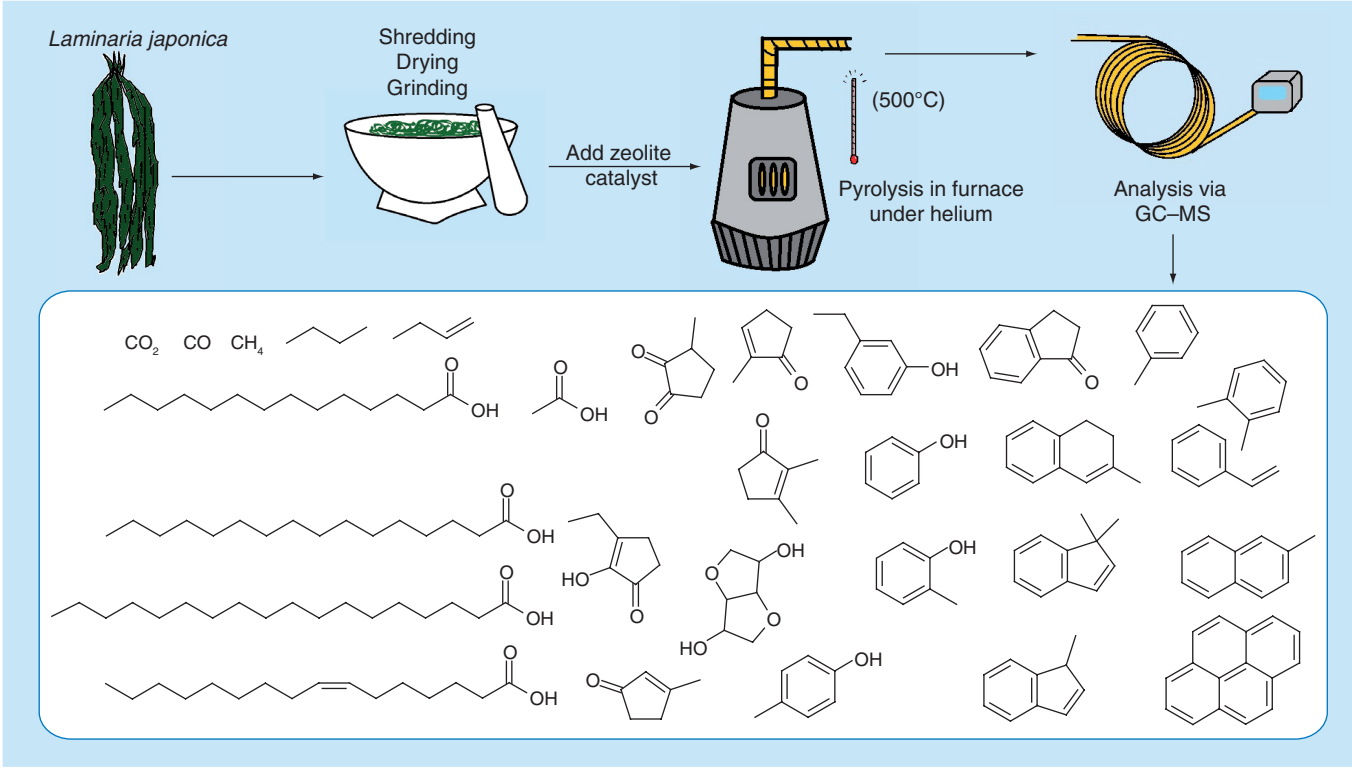

Figure 3. The pyrolysis of *Laminaria japonica* over a zeolite catalyst.
Data from [24].

guarantee fouling [68]; therefore, a dramatic reduction in metal content would be required for pyrolysis to be considered as a processing option. However, studies into the pretreatment of macroalgae, principally by Ross *et al.* [76], but also by Bae *et al.* [109], showed that by first washing the feedstock in acid the Mg, K, Na and Ca ion concentration could be reduced by up to 90% and the levels of trace mineral content, nitrogen and halogens are also significantly diminished. The effect of the removal of impurities on the pyrolysis product is, however, difficult to ascertain. It is known that some of the biopolymers (laminarin and fucoidan) and mannitol are also partially removed by acid and, thus, an increase in the furfural content of the bio-oil is seen, owing to the predominance of the alginic acid in the feed [76]. Park *et al.* did report a slight decrease in bio-oil yield due to acid washing and also pointed out increased yields of 2,4-nonadiyne, 2,2,6,6-tetra-methyl-4-piperidinone and 2-pyridinone, which was attributed to a smaller degree of secondary cracking as a result of the decrease in ash content [109]. Clearly, more research is desirable in this area.

▪ HTL of macroalgae

Overview

The exceptionally high moisture content of macroalgae (~80 wt% initial water content; 10 wt% residual moisture when dried below 100°C) means that HTL seems like a natural option for the thermochemical processing of this under-utilized bioresource. Given that HTL has been found to be a viable option for microalgae conversion [49] and for various invasive aquatic plants [124], it is not surprising that related studies for macroalgae have produced similarly encouraging results. For example, a study by Anastasakis and Ross examined the hydrothermal processing of *Laminaria saccharina* to determine the effects of water:biomass ratio, temperature, residence time and catalyst loading [125]. After removal of the water-soluble fraction, a maximum bio-oil yield of 19.3 wt% was obtained, which represents one of the highest achieved to date; an achievement that is doubly impressive given the relatively high HHV of 36.5 MJ/kg (a value higher than that exhibited by heavy crude oil [126]). Anastasakis and Ross' study found that a short residence time (15 min) was the most productive in terms of bio-oil yield; beyond this, the small molecules formed from biomass degradation have a tendency to re-polymerise. A temperature of 350°C and water:biomass loading of 1:10 were reported as being the most effective conditions. These operating parameters were also shown to be optimal for the liquefaction of *Sargassum patens C. Agardh* [127], giving a 32.01 wt% bio-oil yield with a HHV of

27.1 MJ/kg (after extraction of the aqueous phase), and also for *Chaetomorpha linum*, where the overall energy yield was found to be more efficient than extraction by supercritical CO_2 and subsequent transformation [128]. A separate study performed on the green algae, *U. prolifera*, afforded a yield of 23.0 wt% bio-oil (with a HHV of 29.89 MJ/kg) using a temperature of 300°C, a residence time of 30 min and a Na_2CO_3 catalyst loading of 5 wt% [129].

All of the resulting bio-oils in the above studies were found to contain a considerable diversity of products (as is also found for pyrolysis) including a host of ketones, aldehydes, phenols, alkenes and aromatics. Zhou *et al.* have recently reported that, upon changing the reaction medium from water to methanol and ethanol, the bio-oils resulting from the HTL of *U. prolifera* bear a resemblance to biodiesel, rich in fatty acid methyl and ethyl esters [130]. Again, heterocyclic nitrogen compounds were found to be more abundant in all of the above cases than in terrestrially derived bio-oils, owing to the high N content in the feedstock. The oils could, therefore, be upgraded by deoxygenation and denitrification through established catalytic upgrading methods to produce fuels that could be more easily integrated into existing fossil fuel dependent infrastructures [34].

Catalytic HTL

To date, no studies have been reported that explore the effect of a catalyst on the HTL of macroalgae as rigorously as for feedstocks such as microalgae [45]. Although some of the above studies did consider the impact of adding either KOH [125] or Na_2CO_3 [127,129] to HTL processes, the effects proved minimal. The catalysts decreased the bio-oil yield slightly in the cases of *L. saccharina* [125] and *S. patens C. Agardh* [127], and the aqueous fraction was seen to increase marginally. However, in both cases, the HHV of the bio-oil was almost unaffected by the catalyst addition, although the pH of the resulting oils were found to be slightly higher (as would be expected from the addition of basic salts). Interestingly, when the products were separated, the majority of the alkali earth metal content of the original seaweed was found to have been transferred to the aqueous fraction and was largely absent from the organic oil and biochar phases (leaving the latter products more suitable for use in combustion processes). The metal-rich aqueous phase therefore has the potential to be recycled into the seaweed cultivation process, where the minerals are required as nutrients, or into other agricultural applications [125]. Thus, the addition of a catalyst has not been seen to endow any particular advantages; however, now knowledge of the optimal reaction conditions has been established, it is likely that more insightful investigations into suitable catalyst can take place.

▪ Gasification of macroalgae

Although the production of biogas from macroalgae via biological methods has been considered elsewhere [90], gasification via thermochemical treatment is less explored, despite the fact that wet feedstocks are of particular interest as their inherent water content is thought to help suppress char formation [58]. Ross *et al.* have suggested that macroalgae could potentially be gasified and that their high ash content may aid in tar cracking, making the process autocatalytic [68]. Only two studies to date have set out to examine these claims empirically. Sinağ *et al.* examined four species of seaweed, both individually and as a combined batch, under supercritical water gasification conditions [131], while Dermirbas studied the steam gasification of *C. fracta* [108]. Both investigations reported CO_2, H_2 and CH_4 as the gaseous products with very low char yields (an effect believed to be due to the increasing dissolution of organics into the aqueous layer leading to reduced opportunities for polymerization [58]) and an increased hydrogen yield at higher temperatures (up to 54.7 vol.% of the total gaseous products at 1225 K [108]). Notably, the algae used by Sinağ *et al.* were seen to produce only trace amounts of CO, as it was consumed in the water–gas shift (Equation 1), which may itself be catalyzed by the inorganic metal salts present in the seaweed:

$$CO_{(g)} + H_2O_{(g)} \rightleftharpoons CO_{2(g)} + H_{2(g)}$$

Equation 1

Thus, work by both Sinağ and Dermirbas showed that macroalgae produce yields of hydrogen that are lower than those obtained through the gasification of microalgae, but higher than from terrestrial mosses and twice as large as from some lignocellulosic materials [132], meaning that macroalgae could well become of use to the hydrogen economy.

▪ Combustion of macroalgae

In the incisive critique of macroalgae as a thermochemical feedstock for biofuel manufacture by Ross *et al.*, it was suggested that high moisture, halogen and metal content combined with a low HHV makes macroalgae a decidedly unattractive option for conventional combustion [68]. Indeed, a number of more in-depth analyses have returned similar conclusions [123,133–136]. For example, a study by Lamare and Wing reported the calorific values of 28 macroalgae species found around the coasts of New Zealand on a dry, ash-free basis [136]. HHVs of between 4.35 and 14.02 MJ/kg were found, much in line with the values reported in Table 4, which range from 4.89 to 17.86 MJ/kg, but average at 11.87 MJ/kg. When these figures are compared with those obtained for an equivalent study of 16 samples of

various terrestrial biomasses [63], which ranged between 15 and 20.1 MJ/kg and averaged at 18.34 MJ/kg, it can be seen that seaweeds have quite a low raw energy content. Interestingly, when the thermodynamics of seaweed combustion have been studied [123,134], it has been observed that macroalgae have lower ignition temperatures than woody biomasses do. In the case of macroalgae, this ignition proceeds via a homogenous mechanism (pyrolysis followed by ignition of evolved volatile components and subsequent ignition of the char). The ensuing combustion is, however, clearly not as exothermic as that for terrestrially derived samples, such as woods, and the alkali metal content of the macroalgae again raises concerns about fouling in the reactor [123,133,134]. The evolution of higher levels of NO_x and SO_2 due to the enhanced nitrogen and sulfur content of macroalgae is also undesirable, as is the release of halogen compounds [123]. Thus, seaweed is generally not considered as a viable feedstock for combustion.

A perspective

Many of the ethical, political, economic and environmental arguments for integrating biofuels into our energy infrastructure are appealing on a theoretical basis, but the reality is somewhat different. The clamor to produce crops that are suitable for fuel production has been blamed for having a deleterious impact on global food prices and a potentially detrimental effect on the environment. Consequently, biofuels derived from aquatic media represent a tantalizing opportunity as far as renewable energy sources are concerned. Therefore, it seems strange that this opportunity has been so underexploited in the case of macroalgae, a natural resource that is abundant, rapidly replenished and, in some cases, a nuisance when left unused.

Until now, research in this field has been erratic and inconsistent. The decision to ignore macroalgae as an energy resource has been the *status quo* for three decades and is based on sporadic reports that employed now outdated methods. It would be remiss not to give macroalgae, and its processing via modern thermochemical techniques, the reappraisal it deserves, especially when biofuels, as a whole, are facing such a crisis of confidence. Recently, however, a re-evaluation does appear to have started to take place, as is evidenced by the wealth of research that has been carried out in the UK, Ireland, China, The Netherlands and other countries that benefit from extensive coastlines and healthy seaweed stocks. Therefore, the macroalgae renaissance has benefited significantly from the work of the likes of Ross and colleagues at the University of Leeds, who have assessed a variety of macroalgal feedstocks for their suitability in thermochemical processing and provided foundations on which the field can grow. Their work will set the precedent for how future investigations should be carried out.

Critics have cited the high moisture and ash contents, as well as the poor bio-oil quality, as rendering the thermochemical processing of seaweed an impossibility. Recent work has demonstrated, however, that it is not beyond the wit of the researcher to overcome these problems. Indeed, improved techniques, such as HTL and microwave-assisted pyrolysis, have shown macroalgae to be a well suited and viable feedstock. Furthermore, an added benefit of using macroalgae as fuel/energy feeds is that some of the metals that they accumulate have been shown to exhibit catalytic properties in the pyrolysis process itself. Although the bio-oil produced from thermochemically treating macroalgae would not be suitable for direct replacement of petroleum, diesel or kerosene, through the use of established post-process catalytic upgrading technologies this could be achieved. Moreover, a detailed analysis of macroalgae-derived bio-oil has shown it to have significant value of its own accord, both as a fuel additive and as a source of high-value chemicals, and biochar has been shown to exhibit significantly beneficial properties as a fertilizer and carbon sequestering agent.

The early results of research re-evaluating the case for macroalgae have drawn some fairly clear conclusions. The products of thermochemical processing are versatile and easy to obtain, although, in the case of most seaweeds, their final energy yield is lower than some terrestrial feedstocks. However, the fact that, from a thermochemical point of view, macroalgae have been shown to be net energy producing [74] and that, with cultivation, stocks are available in such high abundances without competing for land and fresh water, should be sufficient evidence to justify the utilization of macroalgae as a fuel source in the broadest sense. Since macroalgae are already of global commercial interest (as a potash source, cattle feed, food sources, extracts in food and pharmaceuticals) established cultivation methods amenable to scale-up already exist. Indeed, sited and managed correctly macroalgae farms would bioremediate, sequester CO_2, prevent eutrophication and even enhance marine biodiversity. When these environmental benefits are considered it is seen that macroalgae offer unique and exciting possibilities as sustainable feedstocks.

However, in a world searching for a 'miracle cure' for the energy crisis, the recent flurry of research has demonstrated that macroalgae simply (and understandably) cannot offer one. Unfortunately, it is invariably the anticipation that a feedstock should be able to offer a direct replacement for petrochemicals that leads to disinterest when it is found not to be able to do so; nowhere is this more evident than in the case of macroalgae. Yet,

in times of uncertainty, we must adopt the mantra of making the best use of the resources we have available and the benefits of utilizing macroalgae are potentially too numerous to continue to ignore.

Future perspective

Progress should adopt a slow and cautious approach, with rigorous investigation taking precedence over excessively hasty, large-scale endeavors and overly ambitious claims. Particular attention over the next few years should be devoted to exploring the fundamental mechanisms associated with the thermolysis of both macroalgae and biomass generally. Clearly, a better understanding of these processes will facilitate the design of more efficient upgrading methods and effective catalysts in order to optimize both the economics and resource utilization efficiency. With the elucidation of the basic facts, increasingly large pilot-scale projects can be undertaken, which will allow for better prediction of the true potential of macroalgae; it is conceivable that these projects may start to take place over the next 10–15 years. As it stands, the data for modeling the macro-implementation of algal processing is not available and so reports that purpose to offer economic analyses are fundamentally flawed, containing only tenuous speculation and misleading conclusions. We will therefore be in a much better position to judge the viability of an algae biofuel economy by 2020–2030.

The recent advances in thermochemical processing of macroalgae have just scratched the surface of this under-utilized feedstock and, ultimately, long-term investment of both time and resources is desirable to facilitate significant further development. It should be recognized that, whatever the future holds for following generations, they will not be fortunate enough to benefit from millions of years of fossil fuel reserves as we have done. They will, however, always have seaweed. With careful, meticulous investigation and the continuing implementation of innovative methodology, there is no reason why macroalgae cannot play an increasingly important role in the provision of both the energy and the chemicals on which our civilization is built.

Financial & competing interests disclosure

The authors are grateful to The Centre for Process Innovation, Durham University, and the Engineering and Physical Sciences Research Council for financial support. The authors have no other relevant affiliations or financial involvement with any organization or entity with a financial interest in or financial conflict with the subject matter or materials discussed in the manuscript apart from those disclosed.

No writing assistance was utilized in the production of this manuscript.

Executive summary

An introduction to thermochemical methods

- A general discussion of the pyrolysis, hydrothermal liquefaction, gasification and combustion of biomass is given. Particular emphasis is placed on the reaction conditions and the nature of the resulting solid, liquid and gaseous product fractions including their potential utility to the energy and chemical industries. Relevant catalysts that can be incorporated into the processes are also considered.

Thermochemical processing of macroalgae

- The various thermochemical processing techniques presented in the introduction are discussed in the context of macroalgae. The last three years have shown a rapid increase in interest in using macroalgae as a sustainable feedstock and the recent results in this area are summarized.

A perspective

- An analysis is given on why the development of macroalgae as a feedstock for thermochemical processing has been relatively slow over the last few decades compared with the interest in terrestrial plants. Recent results are contextualized and used to demonstrate how, by careful continuation of this work, macroalgae could become a lucrative and sustainable source of both energy and chemicals in the future.

References

Papers of special note have been highlighted as:

- ■ of interest
- ■■ of considerable interest

1 Solomon S, Qin D, Manning M *et al. Contribution of Working Group I to the Fourth Assessment Report of the Intergovernmental Panel on Climate Change*. IPCC, Cambridge, UK (2007).

2 Owen NA, Inderwildi OR, King DA. The status of conventional world oil reserves –hype or cause for concern? *Energy Policy* 38(8), 4743–4749 (2010).

3 McKendry P. Energy production from biomass (part 2): conversion technologies. *Bioresour. Technol.* 83(1), 47–54 (2002).

4 Haveren JV, Scott EL, Sanders J. Bulk chemicals from biomass. *Biofuels Bioprod. Bioref.* 2, 41–57 (2008).

5 Vispute TP, Zhang H, Sanna A, Xiao R, Huber GW. Renewable chemical commodity feedstocks from integrated catalytic processing of pyrolysis oils. *Science* 330, 1222–1227 (2010).

6 Balat M, Balat M, Kırtay E, Balat H. Main routes for the thermo-conversion of biomass into fuels and chemicals. Part 1: pyrolysis systems. *Energy Convers. Manage.* 50(12), 3147–3157 (2009).

■ **Useful overview of pyrolysis processes for biomass.**

7 Bridgwater AV. Biomass for energy. *J. Sci. Food Agric.* 86, 1755–1768 (2006).

8 Bridgwater AV. Review of fast pyrolysis of biomass and product upgrading. *Biomass Bioenergy* 38, 1–27 (2011).

9 Goyal HB, Seal D, Saxena RC. Bio-fuels from thermochemical conversion of renewable resources: a review. *Renew. Sust. Energy Rev.* 12(2), 504–517 (2008).

10 Butler E, Devlin G, Meier D, McDonnell K. A review of recent laboratory research and commercial developments in fast pyrolysis and upgrading. *Renew. Sust. Energy Rev.* 15(8), 4171–4186 (2011).

■ **Comprehensive review of the utility of the pyrolysis process for a number of biomass classes.**

11 Mohan D, Pittman CU, Steele PH. Pyrolysis of wood/biomass for bio-oil: a critical review. *Energy Fuels* 20(3), 848–889 (2006).

12 Inguanzo M, Domínguez A, Menéndez JA, Blanco CG, Pis JJ. On the pyrolysis of sewage sludge: the influence of pyrolysis conditions on solid, liquid and gas fractions. *J. Anal. Appl. Pyrol.* 63(1), 209–222 (2002).

13 Pattiya A, Titiloye J, Bridgwater AV. Fast pyrolysis of cassava rhizome in the presence of catalysts. *J. Anal. Appl. Pyrol.* 81(1), 72–79 (2008).

14 Zhang H, Xiao R, Huang H, Xiao G. Comparison of non-catalytic and catalytic fast pyrolysis of corncob in a fluidized bed reactor. *Bioresour. Technol.* 100(3), 1428–1434 (2009).

15 Kirszensztejn P, Przekop R, Tolińska A, Maćkowska E. Pyrolytic and catalytic conversion of rape oil into aromatic and aliphatic fractions in a fixed bed reactor on Al_2O_3 and Al_2O_3/B_2O_3 catalysts. *Chem. Pap.* 63(2), 226–232 (2009).

16 Wang J, Zhang M, Chen M *et al.* Catalytic effects of six inorganic compounds on pyrolysis of three kinds of biomass. *Thermochim. Acta* 444(1), 110–114 (2006).

17 Nowakowski DJ, Jones JM, Brydson RMD, Ross AB. Potassium catalysis in the pyrolysis behaviour of short rotation willow coppice. *Fuel* 86(15), 2389–2402 (2007).

18 Murata K, Somwongsa P, Larpkiattaworn S, Liu Y, Inaba M. Analyses of liquid products from catalytic pyrolysis of *Jatropha* seed cakes. *Energy Fuels* 25, 5429–5437 (2011).

19 Pütün E. Catalytic pyrolysis of biomass: effects of pyrolysis temperature, sweeping gas flow rate and MgO catalyst. *Energy* 35(7), 2761–2766 (2010).

20 Demiral I, Sensöz S. The effects of different catalysts on the pyrolysis of industrial wastes (olive and hazelnut bagasse). *Bioresour. Technol.* 99(17), 8002–8007 (2008).

21 Williams PT, Nugranad N. Comparison of products from the pyrolysis and catalytic pyrolysis of rice husks. *Energy* 25, 493–513 (2000).

22 Pan P, Hu C, Yang W *et al.* The direct pyrolysis and catalytic pyrolysis of *Nannochloropsis* sp. residue for renewable bio-oils. *Bioresour. Technol.* 101(12), 4593–4599 (2010).

23 Babich IV, van der Hulst M, Lefferts L *et al.* Catalytic pyrolysis of microalgae to high-quality liquid bio-fuels. *Biomass Bioenergy* 35(7), 3199–3207 (2011).

24 Lee HW, Jeon J-K, Park SH *et al.* Catalytic pyrolysis of *Laminaria japonica* over nanoporous catalysts using Py-GC/MS. *Nanoscale Res. Lett.* 6(1), 500 (2011).

25 Park HJ, Dong J-I, Jeon J-K *et al.* Effects of the operating parameters on the production of bio-oil in the fast pyrolysis of Japanese larch. *Chem. Eng. J.* 143, 124–132 (2008).

26 Miao X, Wu Q, Changyan Y. Fast pyrolysis of microalgae to produce renewable fuels. *J. Anal. Appl. Pyrol.* 71(2), 855–863 (2004).

27 Grierson S, Strezov V, Shah P. Properties of oil and char derived from slow pyrolysis of *Tetraselmis chui*. *Bioresour. Technol.* 102(17), 8232–8240 (2011).

28 Lehmann J, Gaunt J, Rondon M. Bio-char sequestration in terrestrial ecosystems – a review. *Mitigat. Adapt. Strat. Global Change* 11(2), 403–427 (2006).

29 Bozell JJ, Petersen GR. Technology development for the production of biobased products from biorefinery carbohydrates – the US Department of Energy's "Top 10" revisited. *Green Chem.* 12(4), 539–554 (2010).

30 Bridgwater AV. Biomass fast pyrolysis. *Therm. Sci.* 8(2), 21–49 (2004).

31 Furimsky E. Catalytic hydrodeoxygenation. *Appl. Catal. A Gen.* 199(2), 147–190 (2000).

32 Nokkosmäki MI, Kuoppala ET, Leppämäki EA, Krause AOI. Catalytic conversion of biomass pyrolysis vapours with zinc oxide. *J. Anal. Appl. Pyrol.* 55(1), 119–131 (2000).

33 Huber GW, Iborra S, Corma A. Synthesis of transportation fuels from biomass: chemistry, catalysts, and engineering. *Chem. Rev.* 106(9), 4044–4098 (2006).

34 Zhang Q, Chang J, Wang T, Xu Y. Review of biomass pyrolysis oil properties and upgrading research. *Energy Convers. Manage.* 48(1), 87–92 (2007).

35 Bulushev DA, Ross JRH. Catalysis for conversion of biomass to fuels via pyrolysis and gasification: a review. *Catal. Today* 171(1), 1–13 (2011).

36 Demirbas A. Mechanisms of liquefaction and pyrolysis reactions of biomass. *Energy Convers. Manage.* 41(6), 633–646 (2000).

37 Wang Y, Li X, Mourant D *et al.* Formation of aromatic structures during the pyrolysis of bio-oil. *Energy Fuels* 26(1), 241–247 (2011).

38 Huber GW, Corma A. Synergies between bio- and oil refineries for the production of fuels from biomass. *Angew. Chem. Int. Ed.* 46(38), 7184–7201 (2007).

39 Hu C, Yang Y, Luo J *et al.* Recent advances in the catalytic pyrolysis of biomass. *Front. Chem. Sci. Eng.* 5(2), 188–193 (2011).

40 Shi K, Shao S, Huang Q *et al.* Review of catalytic pyrolysis of biomass for bio-oil. Presented at: *2011 International Conference on Materials for Renewable Energy and Environment.* Shanghai, China, 20–22 May 2011.

41 Samolada MC, Papafotica A, Vasalos IA. Catalyst evaluation for catalytic biomass pyrolysis. *Energy Fuels* 14(10), 1161–1167 (2000).

42 Du J, Liu P, Liu Z-H, Sun D-G, Tao C-Y. Fast pyrolysis of biomass for bio-oil with ionic liquid and microwave irradiation. *J. Fuel Chem. Technol.* 38(5), 554–559 (2010).

43 Wang P, Zhan S, Yu H, Xue X, Hong N. The effects of temperature and catalysts on the pyrolysis of industrial wastes (herb residue). *Bioresour. Technol.* 101(9), 3236–3241 (2010).

44 Yin S, Dolan R, Harris M, Tan Z. Subcritical hydrothermal liquefaction of cattle manure to bio-oil: effects of conversion parameters on bio-oil yield and characterization of bio-oil. *Bioresour. Technol.* 101(10), 3657–3664 (2010).

45 Duan P, Savage PE. Hydrothermal liquefaction of a microalga with heterogeneous catalysts. *Ind. Eng. Chem. Res.* 50, 52–61 (2011).

46 Kruse A, Gawlik A. Biomass conversion in water at 330–410°C and 30–50 MPa. Identification of key compounds for indicating different chemical reaction pathways. *Ind. Eng. Chem. Res.* 42(2), 267–279 (2003).

47 Blaschek HP, Ezeji T, Scheffran J. *Biofuels from Agricultural Wastes and Byproducts*. Wiley-Blackwell, IO, USA, 208–211 (2010).

48 Zhang B, von Keitz M, Valentas K. Thermochemical liquefaction of high-diversity grassland perennials. *J. Anal. Appl. Pyrol.* 84(1), 18–24 (2009).

49 Jena U, Das KC. Comparative evaluation of thermochemical liquefaction and pyrolysis for bio-oil production from microalgae. *Energy Fuels* 25, 5472–5482 (2011).

50 Yang Y, Feng C, Inamori Y, Maekawa T. Analysis of energy conversion characteristics in liquefaction of algae. *Resour. Conserv. Recy.* 43(1), 21–33 (2004).

51 Ogi T, Yokoyama S, Koguchi K. Direct liquefaction of wood by alkaline earth salt in an aqueous phase. *Chem. Lett.* 14(8), 1199–1202 (1985).

52 Karagöz S, Bhaskar T, Muto A, Sakata Y. Catalytic hydrothermal treatment of pine wood biomass: effect of RbOH and CsOH on product distribution. *J. Chem. Technol. Biotech.* 80(10), 1097–1102 (2005).

53 Karagöz S, Bhaskar T, Muto A, Sakata Y. Hydrothermal upgrading of biomass: effect of K_2CO_3 concentration and biomass/water ratio on products distribution. *Bioresour. Technol.* 97(1), 90–98 (2006).

54 Toor SS, Rosendahl L, Rudolf A. Hydrothermal liquefaction of biomass: a review of subcritical water technologies. *Energy* 36(5), 2328–2342 (2011).

55 Balat M, Balat M, Kırtay E, Balat H. Main routes for the thermo-conversion of biomass into fuels and chemicals. Part 2: gasification systems. *Energy Convers. Manage.* 50(12), 3158–3168 (2009).

56 Demirbas A. Biorefineries: current activities and future developments. *Energy Convers. Manage.* 50(11), 2782–2801 (2009).

57 Kreutz TG, Larson ED, Liu G, Williams R. Fischer-Tropsch fuels from coal and biomass. Presented at: *25th Annual International Pittsburgh Coal Conference*. Pittsburgh, PA, USA, 29 September–2 October 2008.

58 Karayıldırım T, Sınağ A, Kruse A. Char and coke formation as unwanted side reaction of the hydrothermal biomass gasification. *Chem. Eng. Technol.* 31(11), 1561–1568 (2008).

59 Elliott DC, Neuenschwander GG, Hart TR *et al.* Chemical processing in high-pressure aqueous environments. 7. Process development for catalytic gasification of wet biomass feedstocks. *Ind. Eng. Chem. Res.* 43(9), 1999–2004 (2004).

60 Sutton D, Kelleher B, Ross JRH. Review of literature on catalysts for biomass gasification. *Fuel Process. Technol.* 73(3), 155–173 (2001).

61 de Lasa H, Salaices E, Mazumder J, Lucky R. Catalytic steam gasification of biomass: catalysts, thermodynamics and kinetics. *Chem. Rev.* 111(9), 5404–5433 (2011).

62 Channiwala SA, Parikh PP. A unified correlation for estimating HHV of solid, liquid and gaseous fuels. *Fuel* 81(8), 1051–1063 (2002).

63 Demirbaş A. Calculation of higher heating values of biomass fuels. *Fuel* 76(5), 431–434 (1997).

64 Giampietro M, Mayumi K. *The Biofuel Delusion: The Fallacy of Large-Scale Agro-Biofuel Production*. Earthscan, London, UK (2009).

65 Mackay DJC. *Sustainable Energy – Without the Hot Air*. UIT, Cambridge, UK (2009).

66 Budarin VL, Zhao Y, Gronnow MJ *et al.* Microwave-mediated pyrolysis of macro-algae. *Green Chem.* 13, 2330–2333 (2011).

■■ **Excellent example of advanced thermochemical methods demonstrating that macroalgae have more to offer as a feedstock than was previously thought.**

67 Gao K, McKinley KR. Use of macroalgae for marine biomass production and CO_2 remediation: a review. *J. Appl. Phycol.* 6, 45–60 (1994).

68 Ross AB, Jones JM, Kubacki M, Bridgeman T. Classification of macroalgae as fuel and its thermochemical behaviour. *Bioresour. Technol.* 99(14), 6494–6504 (2008).

■■ **Classic evaluation of the potential of macroalgae as a feedstock for pyrolysis, covers many of the points raised in this perspective and is an excellent starting point for future investigations.**

69 Li D, Chen L, Zhao J *et al.* Evaluation of the pyrolytic and kinetic characteristics of *Enteromorpha prolifera* as a source of renewable bio-fuel from the Yellow Sea of China. *Chem. Eng. Res. Des.* 88(5–6), 647–652 (2010).

70 Chapman VJ. Seaweeds and their uses. *Aqua. Botany* 12, 389–390 (1982).

71 Wilcox HA. The ocean as a supplier of food and energy. *Experientia* 38(1), 31–35 (1982).

72 Buck BH, Buchholz CM. The offshore-ring: a new system design for the open ocean aquaculture of macroalgae. *J. Appl. Phycol.* 16, 355–368 (2004).

73 The Department of Energy and Climate Change. *2050 Pathways Analysis.* HM Government, London, UK (2010).

■ **Outlines the UK government's renewable energy option up to the year 2050. One such consideration is the large-scale cultivation of macroalgae.**

74 Aresta M, Dibenedetto A, Barberio G. Utilization of macro-algae for enhanced CO_2 fixation and biofuels production: Development of a computing software for an LCA study. *Fuel Process. Technol.* 86, 1679–1693 (2005).

75 Lodeiro P, Cordero B, Barriada JL, Herrero R, Sastre de Vicente ME. Biosorption of cadmium by biomass of brown marine macroalgae. *Bioresour. Technol.* 96(16), 1796–1803 (2005).

76 Ross AB, Anastasakis K, Kubacki M, Jones JM. Investigation of the pyrolysis behaviour of brown algae before and after pre-treatment using PY-GC/MS and TGA. *J. Anal. Appl. Pyrol.* 85, 3–10 (2009).

77 Xu D, Gao Z, Zhang X *et al.* Evaluation of the potential role of the macroalga *Laminaria japonica* for alleviating coastal eutrophication. *Bioresour. Technol.* 102(21), 9912–9918 (2011).

78 Li D, Chen L, Yi X, Zhang X, Ye N. Pyrolytic characteristics and kinetics of two brown algae and sodium alginate. *Bioresour. Technol.* 101(18), 7142–7136 (2010).

79 Singh A, Nigam PS, Murphy JD. Renewable fuels from algae: an answer to debatable land based fuels. *Bioresour. Technol.* 102(1), 10–16 (2011).

80 Chen Y-C. The biomass and total lipid content and composition of twelve species of marine diatoms cultured under various environments. *Food Chem.* 131(1), 211–219 (2012).

81 Greenwell HC, Laurens LML, Shields RJ, Lovitt RW, Flynn KJ. Placing microalgae on the biofuels priority list: a review of the technological challenges. *J. R. Soc. Interface* 7(46), 703–726 (2010).

82 Smith B, Greenwell HC, Whiting A. Catalytic upgrading of tri-glycerides and fatty acids to transport biofuels. *Energy Environ. Sci.* 2(3), 262–271 (2009).

83 Bastianoni S, Coppola F, Tiezzi E *et al.* Biofuel potential production from the Orbetello lagoon macroalgae: a comparison with sunflower feedstock. *Biomass Bioenergy* 32(7), 619–628 (2008).

84 Suganya T, Renganathan S. Optimization and kinetic studies on algal oil extraction from marine macroalgae *Ulva lactuca*. *Bioresour. Technol.* 107, 319–326(2011).

85 Maceiras R, Rodríguez M, Cancela A, Urréjola S, Sánchez A. Macroalgae: raw material for biodiesel production. *Appl. Energy* 88(10), 3318–3323 (2011).

86 Kovacevic V, Wesseler J. Cost–effectiveness analysis of algae energy production in the EU. *Energy Policy* 38(10), 5749–5757 (2010).

87 Black WAP. The seasonal variation in weight and chemical composition of the common British Laminariaceae. *J. Mar. Biol. Ass. UK* 29, 45–72 (1950).

88 Black WAP, Mitchell RL. Trace elements in the common brown alae and in the sea water. *J. Mar. Biol. Ass. UK* 30(3), 575–584 (1952).

89 Adams JMM, Ross AB, Anastasakis K *et al.* Seasonal variation in the chemical composition of the bioenergy feedstock *Laminaria digitata* for thermochemical conversion. *Bioresour. Technol.* 102(1), 226–234 (2011).

90 Horn SJ. *Bioenergy from Brown Seaweeds*. Department of Biotechnology, Norweigian University of Science and Technology, Trondheim, Norway (2000).

91 Demirbas A. Use of algae as biofuel sources. *Energy Convers. Manage.* 51(12), 2738–2749 (2010).

92 Bora K, Jeong J, Shin S *et al.* Facile single-step conversion of macroalgal polymeric carbohydrates into biofuels. *Chem. Sust. Chem.* 3(11), 1273–1275 (2010).

93 Adams JM, Gallagher JA, Donnison IS. Fermentation study on *Saccharina latissima* for bioethanol production considering variable pre-treatments. *J. Appl. Phycol.* 21(5), 569–574 (2009).

94 Østgaard K, Indergaard M, Markussen S, Knutsen SH, Jensen A. Carbohydrate degradation and methane production during fermentation of *Laminaria saccharina* (*Laminariales, Phaeophyceae*). *J. Appl. Phycol.* 5(3), 333–342 (1993).

95 Woodward FN. The Scottish Seaweed Research Association. *J. Mar. Biol. Ass. UK* 29(3), 719–725 (1951).

96 Stanford ECC. *Chem. News Lond.* 5(121), 167 (1862).

97 Stanford ECC. On the economic applications of seaweed. *J. Soc. Arts* 10, 185–195 (1862).

98 Spencer GC. Potash from kelp: III – the preliminary examination of kelp distillates. *J. Ind. Eng. Chem.* 12(8), 786–792 (1920).

99 Turrentine JW, Schoaff PS. Potash from kelp: the experimental plant of the United States Department of Agriculture. Preliminary paper. *J. Ind. Eng. Chem.* 11(9), 864–874 (1919).

100 Tupholme CHS. Carbonization of seaweed. *Chem. Met. Eng.* 32, 81–82 (1926).

101 Guiry MD, Blunden G. *Seaweed Resources in Europe: Uses and Potential*. John Wiley & Sons Ltd, Chichester, UK (1991).

102 Bird CJ, Helleur RJ, Hayes ER, McLachlan J. Analytical pyrolysis as a taxonomic tool in *Gracilaria* (Rhodophyta: Gigartinales). *Hydrobiologia* 151/152(1), 207–211 (1987).

103 Nichols HW, Anderson DJ, Shaw JI, Sommerfield MR. Pyrolysis-gas-liquid chromatographic analysis of Chlorophycean and Rhodophycean algae. *J. Phycol.* 4(4), 362–368 (1968).

104 Helleur RJ, Hayes ER, Jamieson WD, Craigie JS. Analysis of polysaccharide pyrolysate of red algae by capillary gas chromatography-mass spectrometry. *J. Anal. Appl. Pyrol.* 8, 333–347 (1985).

105 Helleur RJ, Hayes ER, Craigie JS, McLachlan JL. Characterization of polysaccharides of red algae by pyrolysis-capillary gas chromatography. *J. Anal. Appl. Pyrol.* 8, 349–357 (1985).

106 Hardy FG, Scott GW, Sisson PR, Lightfoot NF. Pyrolysis mass spectrometry as a technique for studying inter- and intraspecific relationships in the genus fucus. *J. Mar. Biolog. Assoc. U.K.* 78(1), 35–42 (1998).

107 Morgan PJ, Smith K. Potentiality of seaweed as a resource: analysis of the pyrolysis products of *Fucus serratus*. *Analyst* 103, 1053–1060 (1978).

108 Demirbas MF. Biofuels from algae for sustainable development. *Appl. Energy* 88(10), 3473–3480 (2011).

109 Bae YJ, Ryu C, Jeon J-K *et al.* The characteristics of bio-oil produced from the pyrolysis of three marine macroalgae. *Bioresour. Technol.* 102(3), 3512–3520 (2011).

110 Anastasakis K, Ross AB, Jones JM. Pyrolysis behaviour of the main carbohydrates of brown macro-algae. *Fuel* 90(2), 598–607 (2011).

■■ **Offers an explanation for the origins of some of the main products seen in the pyrolysis of macroalgae. It will be an invaluable resource to researchers beginning to explore the fundamental mechanism of thermolysis in more detail.**

111 Soares JP, Santos JE, Chierice GO, Cavalheiro ETG. Thermal behavior of alginic acid and its sodium salt. *Ecl. Quím. São Paulo* 29(2), 53–56 (2004).

112 Ross AB, Hall C, Anastasakis K *et al.* Influence of cation on the pyrolysis and oxidation of alginates. *J. Anal. Appl. Pyrol.* 91(2), 344–351 (2011).

113 Said AA, Hassan RM. Thermal decomposition of some divalent metal alginate gel compounds. *Polym. Deg. Stab.* 39(3), 393–397 (1993).

114 Bird MI, Wurster CM, de Paula Silva PH, Bass AM, de Nys R. Algal biochar –production and properties. *Bioresour. Technol.* 102(2), 1886–1891 (2011).

■ **The biochar is a potentially valuable side product of thermochemical processing. This is one of the most comprehensive analyses of biochar derived from macroalgae.**

115 Bird MI, Wurster CM, De Paula Silva PH, Paul NA, De Nys R. Algal biochar: effects and applications. *GCB Bioenergy* 4(1), 61–69 (2011).

116 Ye N, Li D, Chen L, Zhang X, Xu D. Comparative studies of the pyrolytic and kinetic characteristics of maize straw and the seaweed *Ulva pertusa*. *PLoS ONE* 5(9), 1–6 (2010).

117 Wang S, Jiang XM, Wang N *et al.* Research on pyrolysis characteristics of seaweed. *Energy Fuels* 21(6), 3723–3729 (2007).

118 Li D, Chen L, Zhang X, Ye N, Xing F. Pyrolytic characteristics and kinetic studies of three kinds of red algae. *Biomass Bioenergy* 35(5), 1765–1772 (2011).

119 Wang J, Wang G, Zhang M *et al.* A comparative study of thermolysis characteristics and kinetics of seaweeds and fir wood. *Process. Biochem.* 41(8), 1883–1886 (2006).

120 Zhao H, Yan H, Liu M, Zhang C, Qin S. Pyrolytic characteristics and kinetics of the marine green tide macroalgae, *Enteromorpha prolifera*. *Chin. J. Oceanol. Limnol.* 29(5), 996–1001 (2011).

121 Zhao H, Yan H, Dong S *et al.* Thermogravimetry study of the pyrolytic characteristics and kinetics of macro-algae *Macrocystis pyrifera* residue. *J. Therm. Anal. Calorim.* doi:10.1007/s10973-011-2102-8 (2011) (Epub ahead of print).

122 Jun W, Mingqiang C, Shaomin L *et al.* Pyrolysis of *Ulva rigida* by microwave heating. Presented at: *2011 International Conference on Materials for Renewable Energy and Environment.* Shanghai, China, 20–22 May 2011.

123 Wang S, Jiang XM, Han XX, Liu JG. Combustion characteristics of seaweed biomass. 1. Combustion characteristics of *Enteromorpha clathrata* and *Sargassum natans*. *Energy Fuels* 23(10), 5173–5178 (2009).

124 Catallo WJ, Shupe T, Eberhardt TL. Hydrothermal processing of biomass from invasive aquatic plants. *Biomass Bioenergy* 32(2), 140–145 (2008).

125 Anastasakis K, Ross AB. Hydrothermal liquefaction of the brown macro-alga *Laminaria saccharina*: effect of reaction conditions on product distribution and composition. *Bioresour. Technol.* 102(7), 4876–4883 (2011).

126 Vaezi M, Passandideh-Fard M, Moghiman M, Charmchi M. Gasification of heavy fuel oils: a thermochemical equilibrium approach. *Fuel* 90(2), 878–885 (2011).

127 Li D, Chen L, Xu D *et al.* Preparation and characteristics of bio-oil from the marine

brown alga *Sargassum patens C. Agardh*. *Bioresour. Technol.* 104, 737–742 (2011).

128 Aresta M, Dibenedetto A, Carone M, Colonna T, Fragale C. Production of biodiesel from macroalgae by supercritical CO_2 extraction and thermochemical liquefaction. *Environ. Chem. Lett.* 3(3), 136–139 (2005).

■ **Demonstrates the suitability of macroalgae for hydrothermal conversion processes.**

129 Zhou D, Zhang L, Zhang S, Fu H, Chen J. Hydrothermal liquefaction of macroalgae *Enteromorpha prolifera* to bio-oil. *Energy Fuels* 24(7), 4054–4061 (2010).

130 Zhou D, Zhang S, Fu H, Chen J. Liquefaction of macroalgae *Enteromorpha prolifer*a in sub-/supercritical alcohols: direct production of ester compounds. *Energy Fuels* 26(4), 2342–2351 (2012).

131 Schumacher M, Yanık J, Sınağ A, Kruse A. Hydrothermal conversion of seaweeds in a batch autoclave. *J. Supercrit. Fluid* 58(1), 131–135 (2011).

132 Yanik J, Ebale S, Kruse A, Saglam M, Yuksel M. Biomass gasification in supercritical water. Part 1. Effect of the nature of biomass. *Fuel* 86(15), 2410–2415 (2007).

133 Bruhn A, Dahl J, Nielsen HB *et al.* Bioenergy potential of *Ulva lactuca*: biomass yield, methane production and combustion. *Bioresour. Technol.* 102(3), 2595–2604 (2011).

134 Yu LJ, Wang S, Jiang XM, Wang N, Zhang CQ. Thermal analysis studies on combustion characteristics of seaweed. *J. Therm. Anal. Calorim.* 93(2), 611–617 (2008).

135 Conesa JA, Domene A. Biomasses pyrolysis and combustion kinetics through n-th order parallel reactions. *Thermochim. Acta* 523, 176–181 (2011).

136 Lamare MD, Wing SR. Calorific content of New Zealand marine macrophytes. *N. Z. J. Mar. Freshwater Res.* 35(2), 335–341 (2001).

137 Corma A, Iborra S, Velty A. Chemical routes for the transformation of biomass into chemicals. *Chem. Rev.* 107(6), 2411–2502 (2007).

138 Binder JB, Raines RT. Simple chemical transformation of lignocellulosic biomass into furans for fuels and chemicals. *J. Am. Chem. Soc.* 131(5), 1979–1985 (2009).

139 Robinson JM, Banuelos E, Barber WC *et al.* Chemical conversion of biomass polysaccharides to liquid hydrocarbon fuels and chemicals. *Prepr. Pap. Am. Chem. Soc. Div. Fuel Chem.* 44(2), 224–227 (1999).

140 Demirbaş A. Production of biodiesel from algae oils. *Energy Source A.* 31(2), 163–168 (2008).

141 Daneshvar S, Salak F, Ishii T, Otsuka K. Application of subcritical water for conversion of macroalgae to value-added materials. *Ind. Eng. Chem. Res.* 51(1), 7–84 (2011).

142 Hui Z, Huaxiao Y, Mengmeng Z, Song Q. Pyrolysis characteristics and kinetics of macroalgae biomass using thermogravimetric analyzer. *Proc. World. Acad. Sci. Eng. Technol.* 65, 1161–1166 (2010).

143 Peng W, Wu Q, Tu P, Zhao N. Pyrolytic characteristics of microalgae as renewable energy source determined by thermogravimetric analysis. *Bioresour. Technol.* 80(1), 1–7 (2001).

144 Shuping Z, Yulong W, Mingde Y, Chun L, Junmao T. Pyrolysis characteristics and kinetics of the marine microalgae *Dunaliella tertiolecta* using thermogravimetric analyzer. *Bioresour. Technol.* 101(1), 359–365 (2010).

145 Cai JM, Bi LS. Kinetic analysis of wheat straw pyrolysis using isoconversional methods. *J. Therm. Anal. Calorim.* 98(1), 325–330 (2009).

146 Sharma A, Rao TR. Kinetics of pyrolysis of rice husk. *Bioresour. Technol.* 67, 53–59 (1999).

147 Shuangning X, Zhihe L, Baoming L, Weiming Y, Xueyuan B. Devolatilization characteristics of biomass at flash heating rate. *Fuel* 85, 664–670 (2006).

148 Zabaniotou AA, Kantarelis EK, Theodoropoulos DC. Sunflower shells utilization for energetic purposes in an integrated approach of energy crops: laboratory study pyrolysis and kinetics. *Bioresour. Technol.* 99(8), 3174–3181 (2008).

149 Orfao JJM, Antunes FJA, Figueiredo JL. Pyrolysis kinetics of lignocellulosic materials – three independent reactions model. *Ind. Eng. Chem Res.* 78, 349–358 (1999).

Appendix T

“Copper(II)-mediated thermolysis of alginates: a model kinetic study on the influence of metal ions in the thermochemical processing of macroalgae”

J. S. Rowbotham, P. W. Dyer, H. C. Greenwell, D. Selby, and M. K. Theodorou, Interface Focus, *2013*, **3**(1), 20120046

Interface Focus

rsfs.royalsocietypublishing.org

Research

Cite this article: Rowbotham JS, Dyer PW, Greenwell HC, Selby D, Theodorou MK. 2013 Copper(II)-mediated thermolysis of alginates: a model kinetic study on the influence of metal ions in the thermochemical processing of macroalgae. Interface Focus 3: 20120046. http://dx.doi.org/10.1098/rsfs.2012.0046

One contribution of 9 to a Theme Issue 'Biofuels, science and society'.

Subject Areas:
chemical biology, environmental science, chemical engineering

Keywords:
alginate, biofuel, copper, pyrolysis, thermochemistry, seaweed

Authors for correspondence:
P. W. Dyer
e-mail: p.w.dyer@durham.ac.uk
H. C. Greenwell
e-mail: chris.greenwell@durham.ac.uk

Copper(II)-mediated thermolysis of alginates: a model kinetic study on the influence of metal ions in the thermochemical processing of macroalgae

J. S. Rowbotham[1], P. W. Dyer[1], H. C. Greenwell[2], D. Selby[2] and M. K. Theodorou[3,4]

[1]Centre for Sustainable Process Chemistry, Department of Chemistry, [2]Department of Earth Sciences, and [3]School of Biological and Biomedical Sciences, Durham University, South Road, Durham DH1 3LE, UK
[4]Centre for Process Innovation, Wilton Centre, Wilton, Redcar TS10 4RF, UK

Thermochemical processing methods such as pyrolysis are of growing interest as a means of converting biomass into fuels and commodity chemicals in a sustainable manner. Macroalgae, or seaweed, represent a novel class of feedstock for pyrolysis that, owing to the nature of the environments in which they grow coupled with their biochemistry, naturally possess high metal contents. Although the impact of metals upon the pyrolysis of terrestrial biomass is well documented, their influence on the thermochemical conversion of marine-derived feeds is largely unknown. Furthermore, these effects are inherently difficult to study, owing to the heterogeneous character of natural seaweed samples. The work described in this paper uses copper(II) alginate, together with alginic acid and sodium alginate as model compounds for exploring the effects of metals upon macroalgae thermolysis. A thermogravimetric analysis–Fourier transform infrared spectroscopic study revealed that, unusually, Cu^{2+} ions promote the onset of pyrolysis in the alginate polymer, with copper(II) alginate initiating rapid devolatilization at 143°C, 14°C lower than alginic acid and 61°C below the equivalent point for sodium alginate. Moreover, this effect was mirrored in a sample of wild *Laminaria digitata* that had been doped with Cu^{2+} ions prior to pyrolysis, thus validating the use of alginates as model compounds with which to study the thermolysis of macroalgae. These observations indicate the varying impact of different metal species on thermochemical behaviour of seaweeds and offer an insight into the pyrolysis of brown macroalgae used in phytoremediation of metal-containing waste streams.

1. Introduction

Biofuels represent one of a number of renewable technologies that aim to alleviate an overdependence on fossil-derived hydrocarbons. However, in recent years, the social, financial, climatological, ecological and political impacts of certain biofuels, such as corn-derived ethanol and palm oil-based biodiesel, have been highly contested [1]. With this in mind, so-called 'advanced' biofuels, derived primarily from feedstocks such as waste and non-edible plant matter, have awoken interest from the scientific community and beyond [2].

Although advanced biofuels are naturally more sustainable than their earlier counterparts, there are inevitable technological difficulties associated with the requirement to treat complex, heterogeneous, multi-component feedstocks, which may be difficult to upgrade using conventional biomass processing techniques such as fermentation and anaerobic digestion [3]. Consequently, thermochemical processing methods such as pyrolysis, hydrothermal liquefaction and gasification (all of which use heat to convert the feed) have come to the fore as versatile treatment options [4]. In this context, a diverse range of raw materials have now been considered for the production of fuels and chemicals,

Royal Society Publishing
Informing the science of the future

including woods [5], bagasse [6], rice husks [7], tyres [8], duck weed [9] and sewage sludge [10].

One type of feedstock that has demonstrated considerable potential in thermochemical processing are macroalgae [11–14]. Macroalgae, or *seaweed*, are a group of fast-growing aquatic organisms that include some 9000 species worldwide [15]. Owing to the need for structural flexibility in turbulent coastal environments, macroalgae consist predominantly of elastic polysaccharides such as laminarin, carrageenan, agarose and alginic acid [16,17]; a stark contrast to the rigid lignocellulosic support required by terrestrial flora. These differences in biochemical composition mean that macroalgae offer unique opportunities in terms of thermochemical processing and its resulting products compared with their land-based counterparts. Moreover, seaweeds have the added advantages of high photosynthetic efficiencies (up to four times greater than terrestrial plants) and not competing with forestry and agriculture for land and fresh water [18,19].

Phaeophyceae (brown macroalgae, of which the orders Laminariales and Fucales are colloquially known as *kelp*) are common around the coasts of northern Europe [16] with considerable interest in their utilization as a feedstock for manufacturing commodity chemicals, dating back to the early seventeenth century [20]. More recently, work has demonstrated that kelps (including *Laminaria digitata*) show promise in thermochemical processes such as pyrolysis, because of their abundance, the diverse range of products they can afford and their relatively low thermal decomposition temperatures [11,12]. However, comparative investigations of macroalgae in thermochemical applications are hampered by the inherent heterogeneous nature of the samples collected for study [11]. This is particularly problematic because both the carbohydrate and metal contents vary considerably as a function of season, geographical location, local environment, induced stress conditions and by species [21–23], meaning studies that examine only a single sample of seaweed can be severely restricted in the generality and applicability of their conclusions. Consequently, investigations that use appropriate model compounds rather than whole biomass are of interest. Such an approach circumvents the problems associated with natural variance in biochemical composition and reveals fundamental trends, including the origins of various products and the key decomposition temperatures of certain constituents, thereby allowing pyrolysis processes to be better understood and, ultimately, optimized [24].

A particular area where model compounds can assist is in the prediction of the thermochemical behaviour of a biomass feedstock as a function of metal content. This parameter is particularly important since the presence of naturally occurring metals has been found to influence greatly the pyrolysis behaviour of various biomass types [25,26]. For example, potassium ions have been demonstrated to alter the kinetics of thermolysis (lowering both the first-order activation energy and onset temperature of rapid pyrolysis) of short rotation willow coppice, as well as promoting the conversion of complex molecules such as levoglucosan to more simple compounds, including acetic and formic acid [26,27].

Despite the established impact of metal ions in biomass thermochemical processing, their role is generally not well understood and has only been investigated for a few types of feedstock. Developing such insights for macroalgae feedstocks where the metal concentrations can be remarkably high (of the order of 10–20% of the dry weight [12]) is imperative. Indeed, significantly, few of the investigations to date feature a full analysis of the metal profile in the feedstock [28–30]. However, it should be noted that these types of studies are complicated because samples of metal-free macroalgae are not readily accessible as metal ion extraction (by acid washing for example) typically results in significant alteration of the biomolecular matrix that is under investigation [31,32]. Furthermore, a number of recent studies have started to probe the effects of directly incorporating metal-based catalysts into various biomass pyrolysis processes (including macroalgal studies [33]) with a view to influencing the resulting product distributions and selectivity [34,35]. Again, however, in order to optimize catalyst integration in an effective manner, a clear understanding of the nature and impact of naturally occurring metals is of great importance.

In order to circumvent the issues associated with macroalgal sample heterogeneity and metal ion removal for thermolysis studies, alginic acid (consisting of alternating blocks of unbranched binary copolymers of 1,4-linked α-D-mannuronic (M) and β-L-guluronic (G) acid residues) and the corresponding metal alginate salts constitute a promising set of compounds with which to model the effects of metals. Alginate materials not only constitute between 10 and 40 wt% of the dry weight of many common kelps [22], but they are also largely responsible for the metal sequestering properties of brown macroalgae (figure 1) [36]. Thus, studies of discrete metal alginate salts can be used to model macroalgal thermal degradation, exemplifying the effects of a particular metal ion on pyrolysis without the results being convoluted by processes related to the decomposition of other compounds in the rest of the biomass.

A number of studies have explored the effects of various metals on alginate thermal stability using thermogravimetric analysis (TGA), a technique that measures the volatilization of a sample by recording mass loss as a function of temperature [37–44]. However, many of these TGA-based investigations have been carried out under oxidative conditions, where combustion is the predominant reaction. Consequently, these studies are poor models for understanding pyrolysis behaviour, which requires an inert environment. However, one study by Ross and co-workers examined both pyrolysis (in a nitrogen atmosphere) and oxidation (in air) of alginic acid and the corresponding sodium and calcium salts [44]. This study showed that calcium alginate degrades at a higher temperature than the sodium counterpart, which decomposes at a temperature closer to that of the parent acid. Both salts generated pyrolysis products similar to those from alginic acid, although the sodium salt equivalent gives rise to a significantly higher proportion of cyclopentenone derivatives. These observations indicate the influence that other metal ions may have on pyrolysis kinetics (i.e. temperatures, rate of pyrolysis, Arrhenius parameters) and resultant products from alginates and, crucially, raise the question of the degree to which these effects are mirrored during the pyrolysis of whole macroalgal biomass.

The work presented here aims to further the understanding of the impact of metals, widening the present studies on alginate thermolysis with alkali and alkaline earth metals to include d-block elements, which are found in some seaweed samples at concentrations many thousands of times higher than the surrounding seawater [45]. Studies to probe such effects are complex because, despite the passive nature of the biosorption process, macroalgae show preferences for certain metals above

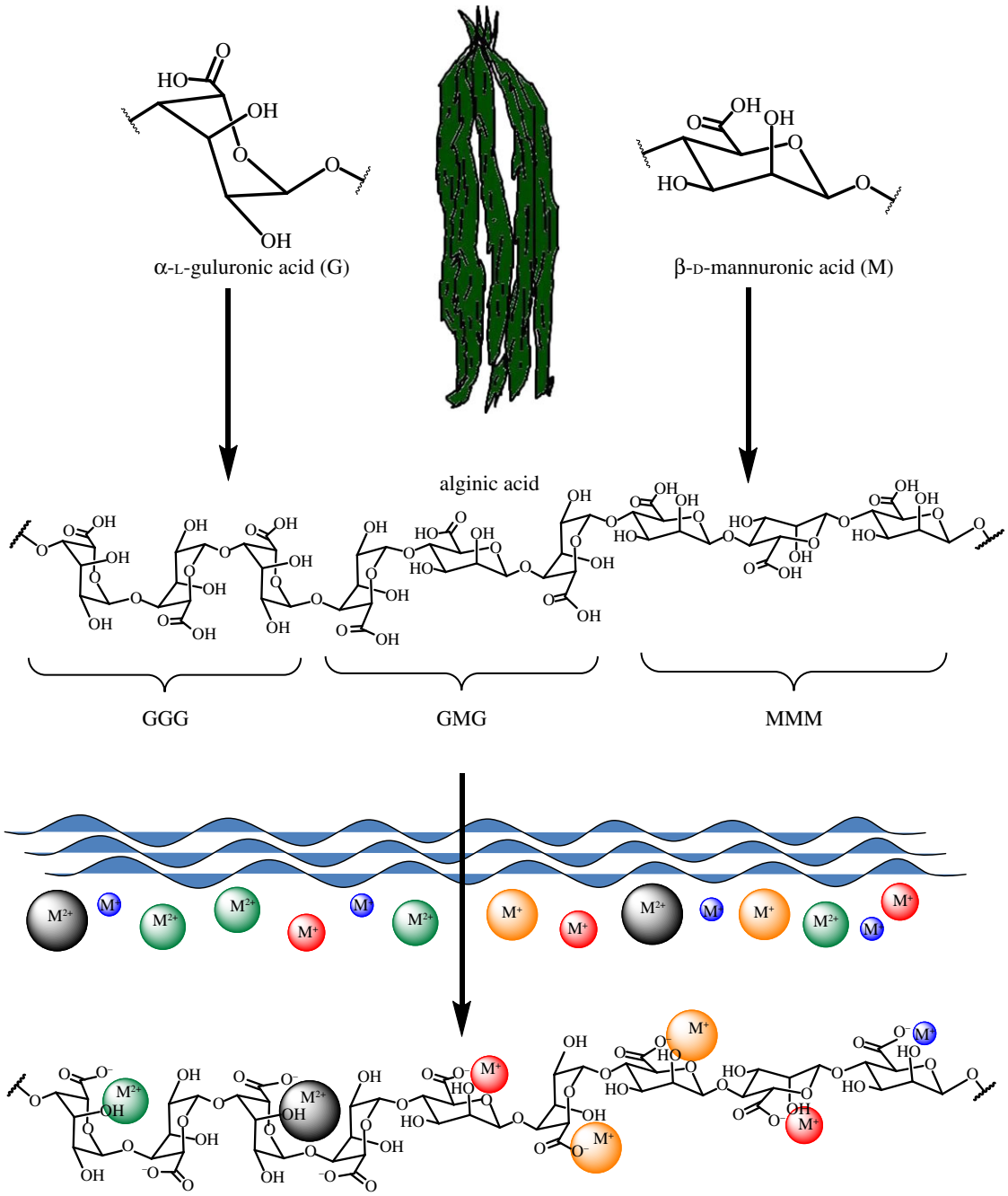

Figure 1. Schematic of the mode of uptake of various mono- and di-valent metallic ions found in seawater by α-L-guluronic acid and β-D-mannuronic acid, which polymerize to form alginic acid (and the corresponding alginate salts) in large quantities in brown macroalgae [36]. (Online version in colour.)

others, with the relative affinities (shown in figure 2) having been determined for divalent metal species. The observed trend is not easily explained, but it is thought to originate from the so-called 'egg box' model of divalent cation binding to alginates [46], in which some M^{2+} ions fit the anionic cavities provided by two parallel strands of β-L-guluronic acid better than others (figure 3) [47]. Indeed, brown macroalgae harvested from copper-polluted water exhibit particularly high concentrations of Cu^{2+} ions, which is a direct consequence of the high affinity of alginates for copper [48,49].

Accordingly, the following study will examine the effects of Cu^{2+} ions on the slow pyrolysis (i.e. at a heating rate less than 50°C min^{-1} [50]) of alginates via TGA. However, in addition to this, it is also desirable to analyse the degree to which these findings are applicable to the outcomes of the thermal treatment of samples of real seaweed biomass. In

$$Pb^{2+} > Cu^{2+} > Cd^{2+} > Ba^{2+} > Sr^{2+} > Ca^{2+} > Co^{2+} > Ni^{2+} > Mn^{2+} > Mg^{2+}$$

Figure 2. The affinity of alginic acid in *L. digitata* for various divalent cations [47].

order to facilitate such a comparison, the metals inherently present in a sample of macroalgae can be almost completely ion exchanged with Cu^{2+} ions by soaking the seaweed in a copper-containing solution and, subsequently, the resulting copper(II)-doped macroalgae can be subjected to the same TGA treatment as the model copper(II) alginate compound. This approach will allow for a wider discussion on the methodological validity of using model compounds for studying biomass pyrolysis and the importance of characterizing the full metal content of a feedstock prior to its thermal analysis, a practice that is not currently commonplace.

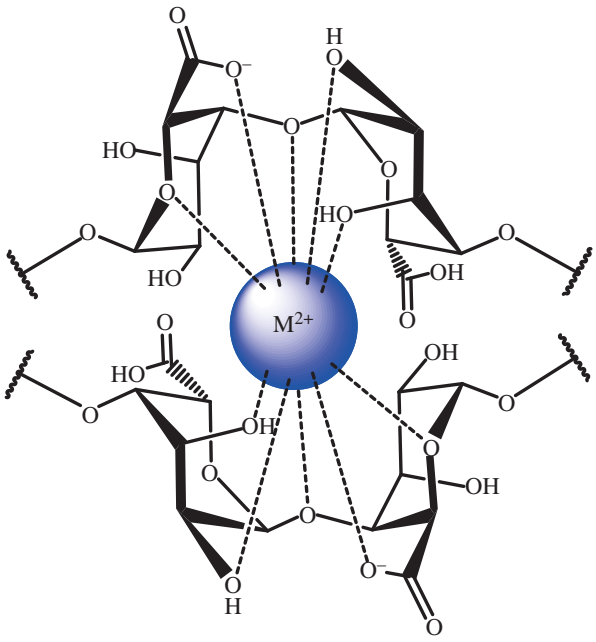

Figure 3. The 'egg box' model of divalent cation bonding in alginic acid [46]. (Online version in colour.)

2. Materials and methods

Alginic acid (H-Alg) and sodium alginate (Na-Alg) were obtained in powdered form from Sigma Aldrich and used as received.

2.1. Preparation of copper(II) alginate (Cu-Alg)

Copper(II) alginate (Cu-Alg) was prepared via an ion exchange protocol by suspending sodium alginate (2.0 g) in a solution of $Cu(NO_3)_2$ (100 ml, 1.0 M) and stirring vigorously for 6 h at room temperature, according to the following reaction:

$$2\text{Na-Alg} + Cu^{2+} \leftrightharpoons \text{Cu-Alg}_2 + 2Na^{+}. \tag{2.1}$$

The resulting light blue gelatinous precipitate was subsequently isolated by filtration, washed thoroughly with deionized water and dried to a constant weight at 80°C, which led to the isolation of a dark green solid.

2.2. Thermal analysis of H-Alg, Na-Alg and Cu-Alg

The alginic acid and two metal alginate powders were ground and sieved to 250 µm. The three samples were then subsequently dried at 105°C overnight, immediately prior to the TGA experiments, in order to attain similar moisture contents since both the alginate materials and alginic acid are hygroscopic. TGA experiments were carried out on the dried, ground samples of the H-, Na- and Cu-Alg using a Perkin Elmer Pyris 1 analyser by loading 20.0 ± 0.5 mg of the sample evenly into a platinum pan and subsequently heating from 25 to 900°C at 5, 10, 20, 30 and 40°C min^{-1} under a flow of dry N_2 at 25 ml min^{-1}. The first derivative of the TGA data yielded the differential thermogravimetric profile (DTG). Coupled thermogravimetric analysis–Fourier transform infrared spectroscopic (TGA-FTIR) analyses of the three alginate samples were also carried out by heating the powders to 1000°C at 10°C min^{-1} on a TA Q500 V6.7 Build 203 coupled to a Nicolet IS 10 infrared spectrometer. Differential scanning calorimetry (DSC) analyses were conducted on a TA Instruments DSC analyser (Q1000, v. 9.9, build 303) by placing 5.0 ± 0.5 mg of sample into an aluminium sample pan, crimping it shut and then heating from 30 to 500 at 10°C min^{-1} under a flow of dry N_2 at 50 ml min^{-1}. For comparison, TGA of powdered samples of Na_2CO_3, $CaCO_3$ and $CuCO_3$ (each obtained from Sigma Aldrich and used as received) was also undertaken.

2.3. Kinetic analysis

TGA of H-, Na- and Cu-Alg was carried out at five different heating rates (β), in order to determine the energy of activation (E_a) and pre-exponential factor (A) for the thermal degradation of the samples at certain points in the pyrolysis process. This was achieved by adopting a previously used method, based on the approach described below [51].

During thermolysis, a sample will lose mass through volatilization. Hence, a degree of conversion α_n of the sample at a temperature T_n can be defined:

$$\alpha_n = \frac{m_0 - m_n}{m_0 - m_\infty}, \tag{2.2}$$

where m_0 is the initial mass of the sample, m_n is the mass at temperature T_n and m_∞ is the final mass. Thus, the rate of thermolysis, or the rate of change of α with time, t, can be described by a temperature-dependant Arrhenius expression, $k(T)$, scaled by a function $f(\alpha)$, the *conversion function*:

$$\frac{d\alpha}{dt} = f(\alpha)\, k(T). \tag{2.3}$$

The conversion function reflects the mechanistic nature of the thermolysis process that is taking place. Assuming, crudely, that there is a single first-order reaction taking place at any particular temperature during the pyrolysis being studied, and which occurs uniformly throughout the biomass sample, this may be defined as

$$f(\alpha) = (1 - \alpha). \tag{2.4}$$

The constant rate at which the sample is heated, β, can simply be defined as the change of temperature, T, with time, t:

$$\beta = \frac{dT}{dt}. \tag{2.5}$$

Combining equations (2.3) and (2.4) gives

$$\frac{d\alpha}{dT} = \frac{1}{\beta}(1 - \alpha)\, k(T). \tag{2.6}$$

Since the Arrhenius function $k(T)$ has the form

$$k(T) = A \exp\left(\frac{-E_a}{RT}\right), \tag{2.7}$$

it is possible to define

$$\frac{d\alpha}{dT} = \frac{1}{\beta}(1 - \alpha)\, A \exp\left(\frac{-E_a}{RT}\right), \tag{2.8}$$

and thus the experimentally determined turning points of the DTG profile represent the maximum volatilization rates, i.e.

$$T = T_{max} \text{ when } \frac{d^2\alpha}{dT^2} = 0. \tag{2.9}$$

Hence, by rearrangement the following expression is obtained:

$$\ln\left(\frac{\beta}{T_{max}^2}\right) = \ln\left(\frac{RA}{E_a}\right) - \frac{E_a}{RT_{max}}. \tag{2.10}$$

And so, from a graph of $\ln(\beta/T_{max}^2)$ versus $1/T_{max}$, the values of E_a and A can be calculated [51].

2.4. Preparation of macroalgae (*Laminaria digitata*)

Samples of *L. digitata* were harvested from Marsden Bay, South Shields, UK (54°58′42.58″ N, 1°23′0.97″ W) on 28 October 2011 (figure 4). The samples were washed in distilled water to remove the majority of the sand and grit, and frozen at −18°C within 4 h of harvest. After being allowed to thaw naturally at room temperature for 8 h, the macroalgae were shredded, dried to a constant weight at 80°C, and ground and sieved to 250 µm. The dry, powdered macroalgae samples were either used immediately or returned to storage at −18°C.

Figure 4. *L. digitata* collection site: Marsden Bay, South Shields, UK.

Table 1. Partial elemental analysis of H-Alg, Na-Alg and Cu-Alg.

	C (wt%)	H (wt%)	N (wt%)	Na (wt%)	Cu (wt%)
alginic acid (H-Alg)	39.94	4.54	0	0.39	0.05
sodium alginate (Na-Alg)	33.95	3.72	0	10.60	0.05
copper(II) alginate (Cu-Alg)	32.29	3.62	0	0.03	14.81

2.5. Cu^{2+} ion exchange in *L. digitata*

The alkali and alkaline earth metals inherently present in a sample of wild *L. digitata* were replaced with Cu^{2+} ions via an ion-exchange process: the *L. digitata* (as prepared in §2.4) were suspended in a solution of $Cu(NO_3)_2$ (100 ml, 1.0 M) and stirred vigorously for 6 h at room temperature. The ion-exchanged macroalgae were subsequently isolated by filtration, washed thoroughly with deionized water (100 ml) and dried to a constant weight at 80°C.

2.6. Thermal analysis of *L. digitata*

Both the untreated *L. digitata*, and the Cu^{2+} ion-exchanged *L. digitata* were dried overnight at 105°C immediately prior to analysis. TGA experiments were carried out on the dried, ground seaweed samples using a Perkin Elmer Pyris 1 analyser. Samples of 20.0 ± 0.5 mg were loaded into a platinum pan and spread evenly. The sample was subsequently heated from 25°C to 900°C at a heating rate (β) of 10°C min^{-1} under a flow of dry N_2 at 25 ml min^{-1}. The first derivative of the TGA plot yielded the DTG profile.

DSC analyses were performed on a TA Instruments DSC analyser (Q1000, v. 9.9, build 303) by placing 5.0 ± 0.5 mg of sample into an aluminium pan, crimping it shut and then heating from 30 to 500°C at 10°C min^{-1} under a flow of dry N_2 at 50 ml min^{-1}.

2.7. Elemental analyses

C, H and N compositions of all samples were determined by combustion on an Exeter Analytical CE440 elemental analyser by the Analytical Department of the Chemistry Department, Durham University.

The concentrations of 26 common metals in the *L. digitata* (known to be present in significant concentrations from previous investigations [22,23]) were determined via inductively coupled plasma mass spectrometry analysis (ICP-MS) using a Thermo Fisher X–Series II analyser; the analysed samples were prepared by Carius tube digestion in a concentrated, ultrapure HNO_3:HCl mix (3 : 1 by volume). The Cu and Na concentrations in H-, Na- and Cu-Alg were also determined using this method. Fluka analytical *Trace*SELECT ultrapure acids and standards were used in the analyses and high-purity deionized water was used throughout.

3. Results and discussion

3.1. Pyrolysis of alginic acid and alginates

Samples of alginic acid (H-Alg), sodium alginate (Na-Alg) and copper(II) alginate (Cu-Alg) were prepared as in §2.1. Examination of their elemental analysis profiles (table 1) reveals that the exchange of sodium for copper ions occurred almost completely, with the equilibrium depicted in equation (2.1) lying predominantly to the right-hand side, an effect predicted in earlier studies on the affinity of alginates for Cu^{2+} ions (see §1) [47,48].

A comparison was made of the pyrolysis behaviour of Cu-Alg against that of H-Alg and Na-Alg in order to probe the effect of the Cu^{2+} ions in the alginate structure [36]. Broadly, it was found that for all three compounds, thermal degradation occurred in three discrete temperature windows (phases 1–3) defined by T_i (the onset of rapid pyrolysis) and T_f (the end of rapid pyrolysis). However, despite this apparent similarity, it was found that the behaviour of the different materials within these three temperature regimes varied dramatically, as demonstrated by the DTG (figure 5*a*) and TGA (figure 5*b*) curves. In particular, a detailed analysis of the three distinct pyrolysis regions highlights the dramatic influence exerted by the presence of the metal ions on the pyrolysis of the alginic acid polymer.

3.1.1. Phase 1: $25^{o}C \leq T < T_i$

The small mass loss (around 5 wt%) observed in this region for H-, Na- and Cu-Alg is attributed to simple loss of moisture,

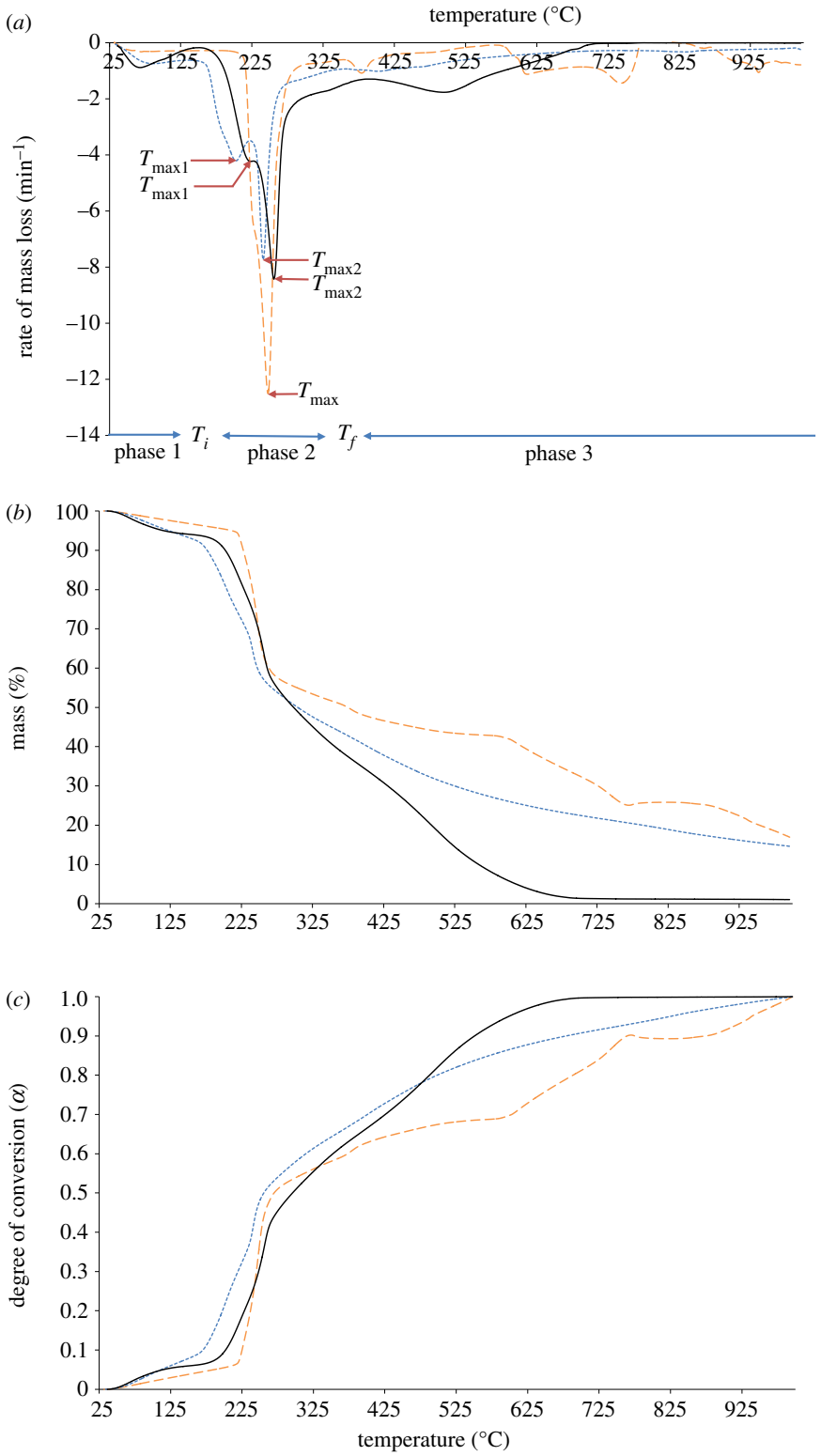

Figure 5. The (*a*) DTG, (*b*) TGA and (*c*) degree of conversion profiles for the thermolysis of H-Alg, Na-Alg and Cu-Alg over the temperature range 25–1000°C obtained with a heating rate (β) of 10°C min^{-1} under N_2. Dashed line, Na; dotted line, Cu; solid line, H.

which had re-absorbed following drying to a constant weight at 105°C prior to the TGA, consistent with the hygroscopic nature of these materials [24,28,52–54]. This is in agreement with the large endothermic peak during this temperature region on the DSC curve featured in figure 6, which results from water evaporating from the sample.

3.1.2. Phase 2: $T_i < T < T_f$

The region of the TGA profile that lies between T_i and T_f is arguably the most important when considering biomass pyrolysis in general (and that of related model materials) because it is within this window that the maximum degree of volatilization takes place, with between 40 and 50 wt% of the initial mass of the sample being lost. T_i corresponds to the temperature where rapid pyrolysis begins to take effect. With a heating rate, β, of 10°C min^{-1} the value of T_i varies with Cu-Alg (150°C) < H-Alg (161°C) < Na-Alg (207°C). During this period of rapid pyrolysis, several notable features appear at T_{max} (the temperature at which the maximum mass loss rate occurs) signified by an intense peak in the DTG curve. A summary of the values of T_i, T_f and T_{max} for H-Alg, Na-Alg and Cu-Alg recorded at five different

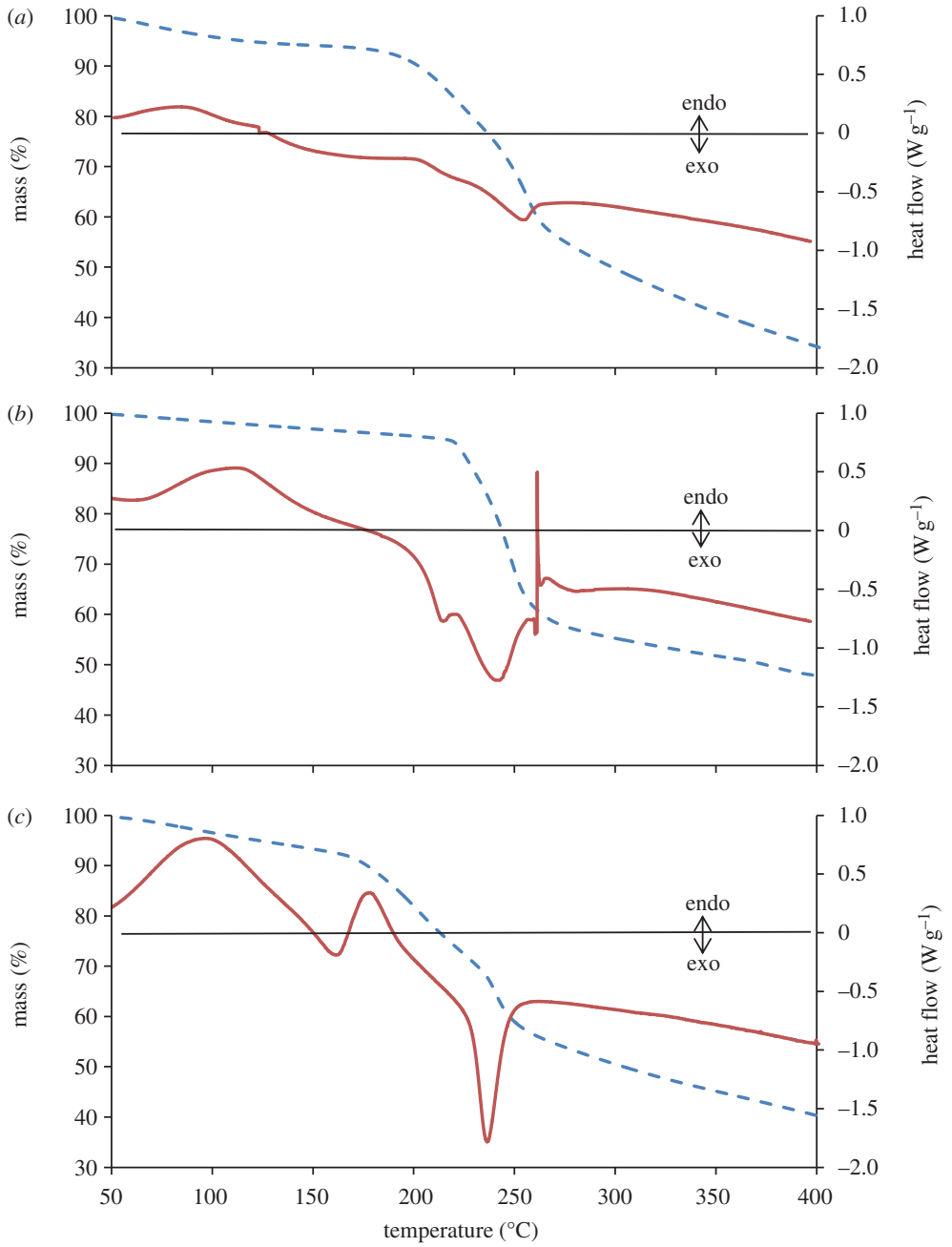

Figure 6. Comparison of TGA (dashed line) and DSC (solid line) curves for (*a*) H-Alg, (*b*) Na-Alg, and (*c*) Cu-Alg over the temperature range 50–400°C obtained with a heating rate (β) of 10°C min^{-1} under N_2.

heating rates (β) is given in table 2. It can be seen that the H-Alg and Cu-Alg samples show two peaks (T_{max1} and T_{max2}), whereas the Na-Alg only shows one (simply T_{max}); the latter represents a much greater rate of mass loss and occurs at a similar temperature to H-Alg T_{max2}. This indicates that the first step in the pyrolysis pathway is somehow inhibited (relative to H-Alg) by the Na^+ ions until some critical temperature (207°C), after which the subsequent reactions occur very rapidly. Many of the reactions that cause the rapid volatilization of the solid feedstock are not well understood and there is still much work to be done to gain a better understanding of this pyrolysis phase, both in the case of alginates and for biomass in general [55]. Interestingly, however, the DSC profiles for H-Alg, Na-Alg and Cu-Alg during this phase of pyrolysis (figure 6) all show sharp exothermic peaks, revealing that the net effect of the reactions that lead to the rapid volatilization stage is to release heat, presumably as more thermodynamically stable compounds are formed from the decomposition.

T_f marks the end of the period of rapid volatilization and varies as Cu-Alg (270°C) < H-Alg (275°C) < Na-Alg (283°C); this is a much smaller temperature range than that for T_i, where approximately 60°C separates Cu-Alg from Na-Alg. This appears to be because the Na-Alg demonstrates a much higher mass loss rate during the period T_i to T_f. Consequently, although the onset of rapid pyrolysis for Na-Alg begins at a higher temperature than for both Cu-Alg and H-Alg, volatilization of the sodium salt proceeds very quickly with mass loss ending at a temperature only slightly higher than those recorded for copper(II) alginate and alginic acid.

3.1.3. Phase 3: $T_f < T \leq 1000$°C

The region from T_f onwards is generally regarded as being a period of slower, sustained degradation in biomass pyrolysis. Reaction processes occurring within this region are thought to consist mainly of secondary pyrolysis reactions, tar

Table 2. Key kinetic and thermal parameters in the pyrolysis of H-Alg, Cu-Alg and Na-Alg.

		pyrolysis temperatures (°C)				
	β (°C min^{-1})	T_i	T_{max1}	T_{max2}	T_{max}	T_f
H-Alg	5	157	210	246	—	267
	10	161	216	254	—	275
	20	168	220	256	—	278
	30	176	228	261	—	286
	40	180	233	264	—	289
	E_a (kJ mol^{-1})	—	174	269	—	—
	ln A	—	36	55	—	—
	R^2	—	0.95	0.98	—	—
Cu-Alg	5	143	184	231	—	261
	10	150	196	239	—	270
	20	156	202	242	—	277
	30	162	208	247	—	287
	40	164	215	249	—	292
	E_a (kJ mol^{-1})	—	123	248	—	—
	ln A	—	24	52	—	—
	R^2	—	0.98	0.98	—	—
Na-Alg	5	204	—	—	239	271
	10	207	—	—	246	283
	20	215	—	—	249	286
	30	221	—	—	252	296
	40	225	—	—	250	298
	E_a (kJ mol^{-1})	—	—	—	340	—
	ln A	—	—	—	73	—
	R^2	—	—	—	0.88	—

cracking, char formation and the degradation of thermally robust inorganic constituents [24,28,52–54]. Consequently, the rate of mass loss is considerably lower than that in phase 2, with the final mass achieved corresponding to the amount of char produced.

For biomass such as macroalgae, the residual char is primarily composed of carbon and inorganic materials, such as metal oxides and metal carbonates, which form as the metal ions bound to the alginates react with the organic matrix upon degradation [44]. Some of the inorganic salts may be products of secondary reactions, such as the formation of metal carbonates from the reaction between CO_2 (released throughout the pyrolysis process) and other metal oxides. To survive to the char stage, however, the inorganic constituents need to be thermally robust, and some may degrade prior to 1000°C. Figure 7 shows the TGA/DTG profiles of some of the inorganic constituents (namely copper, sodium and calcium carbonate) that may be expected to form during the pyrolysis of the Na-Alg and Cu-Alg. $CuCO_3$ degrades to CuO and CO_2 at around 300°C (with a later, much smaller mass loss at around 900°C, as the CuO begins to form Cu_2O [56]; figure 7). Consequently, no peak is seen that corresponds to the degradation of $CuCO_3$ in the pyrolysis of Cu-Alg between T_f and 1000°C. Conversely, pure Na_2CO_3, which melts at around 850°C, does not start to significantly volatilize until temperatures above 1000°C [57] and hence no features arising from this material were observed. However, a high temperature thermal decomposition feature is apparent during the pyrolysis of Na-Alg, something that has been attributed to small quantities of calcium ion impurities present in the alginate that initially react to form $CaCO_3$ [44], and which subsequently decomposes at temperatures around 700°C (figure 7) [58]. The H-Alg material contains only trace inorganic content and is virtually completely degraded by 650°C. Thus, in the higher temperature regions (more than 650°C), there are no regions of significant mass loss in the TGA profile that correspond to the degradation of inorganic salts.

As expected, the inorganic materials present in the Cu-Alg and Na-Alg materials are not fully volatilized by 1000°C. Metal oxides that form during pyrolysis such as Cu_2O, CuO and Na_2O remain intact, something that results in higher char yield for the Cu-Alg and Na-Alg samples (14.6 and 17.0 wt%, respectively), compared with that from H-Alg (1.1 wt%) [12]. Consequently, by using TGA data directly, it is difficult to compare the effects of metals in the thermal degradation of metal-rich biomass samples, as the relative mass loss is smaller as a result of the significant amounts of inorganic char formed. Thus, to gain a deeper insight into the rate of volatilization of the important organic

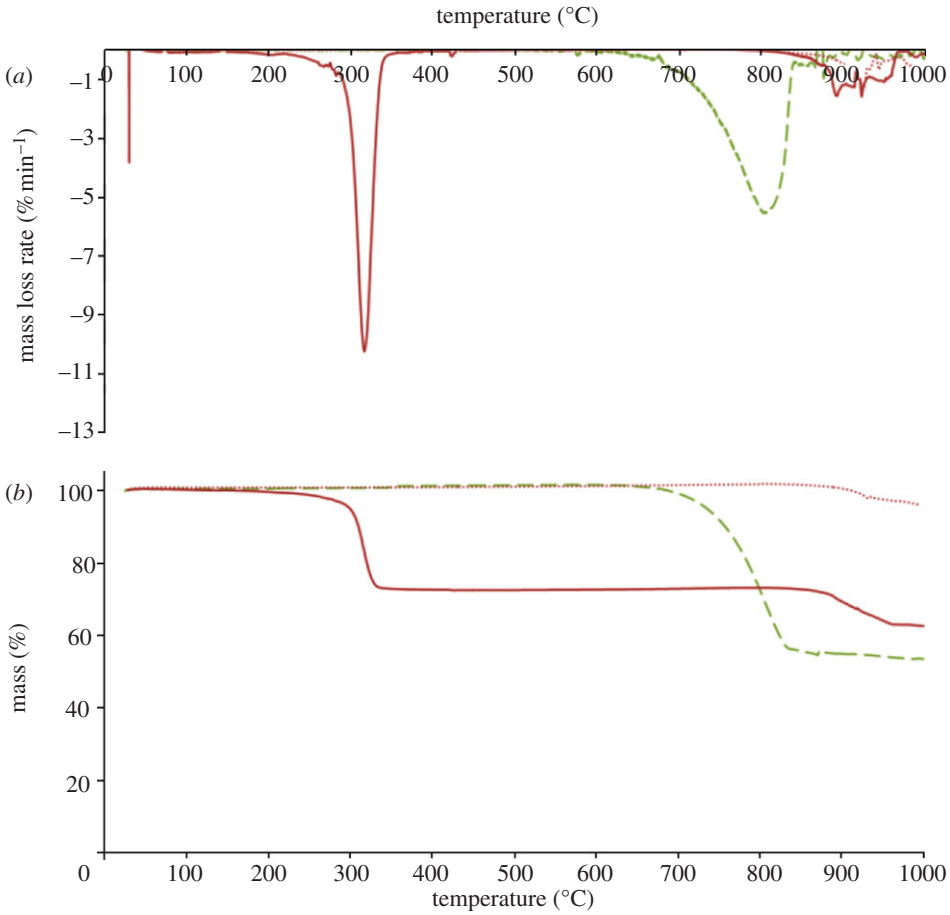

Figure 7. The (*a*) DTG and (*b*) TGA profiles for the thermolysis of Na_2CO_3, $CuCO_3$ and $CaCO_3$ over the temperature range 25–1000°C obtained with a heating rate (β) of 10°C min^{-1} under N_2. Dashed line, Ca; solid line, Cu; dotted line, Na.

constituents of the biomass occurring during pyrolysis, a plot of the degree of conversion α (defined in equation (2.2)) against temperature, as depicted in figure 5*c*, can be informative. This degree of conversion (α) does not include the amount of residual char and only considers matter that is volatilizable below the maximum temperature used in the experiment, 1000°C. Consequently, samples such as Cu-Alg and Na-Alg, which have comparably high inorganic content (with 10–15 wt% consisting of metal ions), can be compared directly with H-Alg, which is almost entirely organic. Thus, whereas the TGA profiles suggest that the extent of mass loss of Na-Alg with temperature is consistently lower than for H-Alg, when the mass lost is considered as a fraction of the total amount volatilized (i.e. the degree of conversion), it can be seen that there is a period between 240°C and 330°C where the Na-Alg has lost a greater proportion of its volatilizable mass than has H-Alg, indicating that the Na^+ ions promote pyrolysis between these temperatures.

Furthermore, the TGA data suggest that the H-Alg and Cu-Alg materials are comparable in terms of the extent of mass lost upon pyrolysis to 285°C. However, if the degree of conversion data α are examined, it becomes apparent that the samples of H-Alg and Cu-Alg do not achieve the same value until a pyrolysis temperature of 480°C. This latter observation indicates that the Cu^{2+} ions promote pyrolysis of the organic matter over a much wider temperature range than would be apparent from the TGA profile alone. Indeed, the data presented in figure 5*c* also clearly demonstrate that the presence of Cu^{2+} ions inhibits the later stages (phase 3) of alginic acid pyrolysis quite considerably

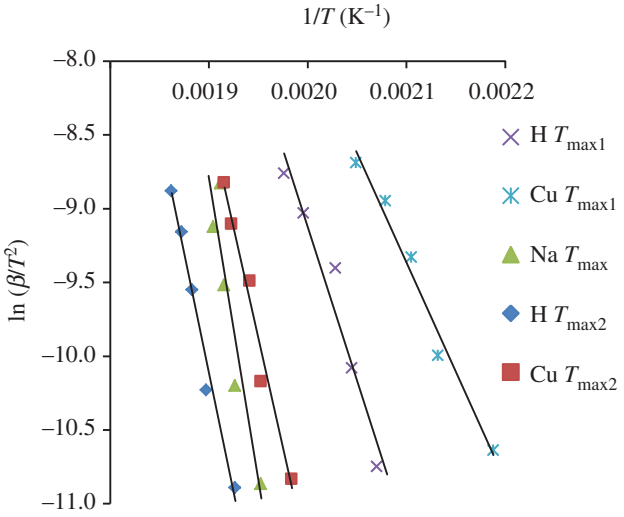

Figure 8. Plot of $\ln(\beta/T^2)$ versus $1/T$ (with T in kelvin) at the points of maximum volatilization of H-Alg, Cu-Alg and Na-Alg, pyrolysed at $\beta = 5$, 10, 20, 30 and 40°C min^{-1}.

(cf. H-Alg and Na-Alg) and severely slows down the rate of volatilization above approximately 500°C.

This observation contradicts previous studies, where the presence of mono- (Na^+) and divalent (Ca^{2+}, Co^{2+}) metal ions have all been shown to inhibit the onset of pyrolysis of alginates relative to that of the parent acid [43,44]. By contrast, the results presented here indicate that Cu^{2+} ions clearly shift the onset of pyrolysis to a lower temperature

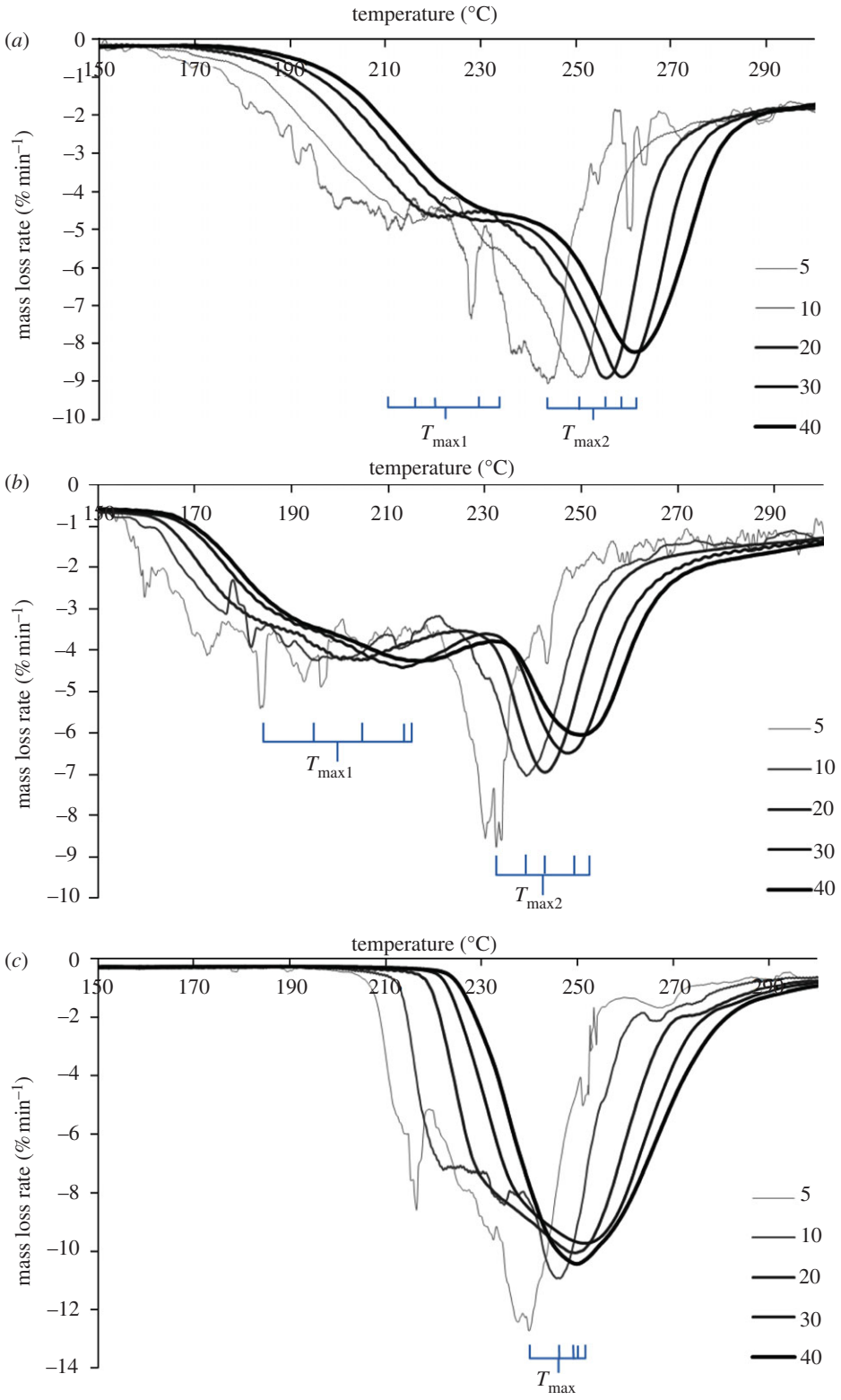

Figure 9. The DTG profiles for the main pyrolysis region of (*a*) H-Alg, (*b*) Cu-Alg and (*c*) Na-Alg at heating rates (β) of 5, 10, 20, 30 and 40°C min^{-1} under N_2.

with respect to the (practically) metal-free alginic acid. To explain this phenomenon, however, requires a better understanding of the interaction of the metal ions with both the mannuronic and guluronic acid residues that comprise the alginates as it appears that, though the alginic acid shows a high affinity for Cu^{2+} ions, the presence of such ions also serves to destabilize the polymer at higher temperatures. In order to better quantify the observed trend in thermal stability (i.e. Cu-Alg < H-Alg < Ca-Alg), a kinetic study was carried out for the second stage of pyrolysis for all three compounds. The mathematical details of the model used are elaborated in §2.3, but the principle behind the analysis was to plot $\ln(\beta/T_{max}^2)$ versus $1/T_{max}$, where T_{max} represents a point of maximum mass loss rate (identified as a turning point in the DTG profile) for five different heating rates ($\beta = 5$, 10, 20, 30 and 40°C min^{-1}).

From this plot (figure 8), the gradient can be used to extract the energy of activation, E_a, for the reaction(s) occurring at that point in the pyrolysis, with the intercept giving the pre-exponential factor, A. The plots in figure 9 show the

DTG profiles at the five different heating rates (β). As β increases, the DTG curve maintains a similar shape, but is shifted to a higher temperature; this is a well-documented effect that arises owing to the delay in heat transfer to the samples being analysed [59]. The results of the kinetic analyses are summarized in table 2. The energy of activation, E_a, was calculated for two points in the pyrolysis (T_{max1} and T_{max2}) for H-Alg and Cu-Alg, and at one point (T_{max}) for Na-Alg obtained from the peaks in the DTG profiles (figure 5*a*). The values of E_a give an indication of the energy required to initiate the reaction(s) occurring at that temperature in the pyrolysis, and so they provide a useful comparison of the ease of volatilization of the compounds relative to each other. It is unsurprising then that the trends in the values of E_a reflect the trends in the values of T_i ($T_{i(\text{Cu-Alg})} < T_{i(\text{H-Alg})}$), thus $E_a(T_{max1})_{\text{Cu-Alg}} < E_a(T_{max1})_{\text{H-Alg}}$ and $E_a(T_{max2})_{\text{Cu-Alg}} < E_a(T_{max2})_{\text{H-Alg}}$ and thus the kinetic data further corroborate the observation that Cu^{2+} ions promote volatilization in the rapid pyrolysis phase with respect to H-Alg. Further comparison with Na-Alg is not straightforward however, as the DTG profiles (figure 9*c*) are not well resolved. Consequently, only one value of T_{max} (and thus E_a) can be determined for Na-Alg (table 2) from the single, broad peak, which is clearly associated with a larger number of reactions than the separate, narrower peaks in the Cu-Alg and H-Alg spectra. This gives rise to the correspondingly large value of E_a for sodium alginate, which cannot meaningfully be correlated with the values of E_a determined for the other compounds.

Finally, coupled TGA-FTIR analysis gives insight into aspects of the thermal degradation pathways of H-Alg, Na-Alg and Cu-Alg, and the differences between them. Figure 10 shows that the primary volatile component product for this 'slow' pyrolysis, in all three cases, is CO_2, as evidenced by the intense absorbance at 2360 cm^{-1}; this observation has been reported previously from studies using coupled TGA–gas-chromatography/mass spectrometry (Py-GC-MS) [42,44]. Interestingly, if the intensity of the IR absorbance at 2360 cm^{-1} is plotted against temperature during the pyrolysis of H-Alg, Na-Alg and Cu-Alg over the temperature range 150–300°C (figure 11*a*), the trace can be seen to completely replicate the trend in mass loss shown in the equivalent section of the TGA curve (figure 11*b*). Thus, it is possible that the rapid period of pyrolysis that begins at T_i (discussed above) is most likely attributable to decarboxylation of the carboxylate group of the alginates, which explains the rapid release of CO_2.

Beyond the temperature region 150–300°C, the amount of CO_2 evolved is seen to increase to a maximum in the case of Cu-Alg and H-Alg, but decrease in the case of Na-Alg. This decrease is a consequence of the reaction between CO_2 and sodium salts such as Na_2O, from which Na_2CO_3 can form, thus retaining the CO_2 until decomposition at much higher temperatures (figure 11*c*) [44]. Of course, the formation of carbonates is not possible in the case of the Cu-Alg (because $CuCO_3$ is not stable at these temperatures; figure 7), and for H-Alg, which does not contain significant metallic species for carbonates to form. The amount of CO_2 released is highest in H-Alg (as evidenced by the larger area under the curve in figure 11*c*), which is expected owing to the higher carbon content of the starting material compared with the metal salts.

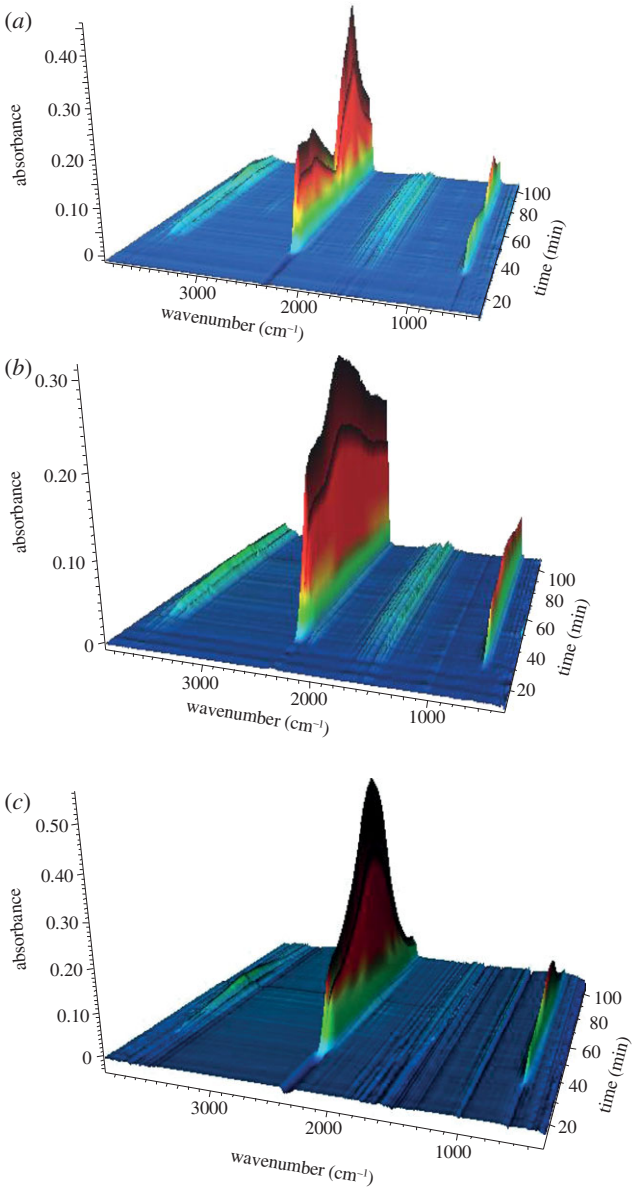

Figure 10. TGA-FTIR profile for the thermolysis of (*a*) Na-Alg, (*b*) Cu-Alg and (*c*) H-Alg over the temperature range 25–1000°C obtained with a heating rate (β) of 10°C min^{-1} under N_2.

Other minor peaks in the TGA-FTIR profile indicate that a number of other compounds may be evolved in the pyrolysis processes. Earlier studies have suggested that the minor peaks observed between 1500 and 1800 cm^{-1} in the IR spectrum that begin to appear after around 300°C (absorbance around 0.02) could be due to a mixture of small, volatile, organic molecules bearing carbonyl groups such as formaldehyde, acetone and furfural, among others [42,44].

3.2. Influence of metals on the pyrolysis of macroalgae

In order to test the applicability of the results from the study of model biomass compounds (H-Alg, Na-Alg, Cu-Alg) described in §3.1, whereby Cu^{2+} ions were shown to promote the onset of pyrolysis of alginic acid, an actual sample of macroalgal biomass should be subject to thermal degradation to test for similar effects. Indeed, previous studies have examined the role of metals in macroalgae pyrolysis by removing them completely and analysing the metal-stripped materials. However, this approach requires the macroalgae to be treated via washing with acid, something that has the additional

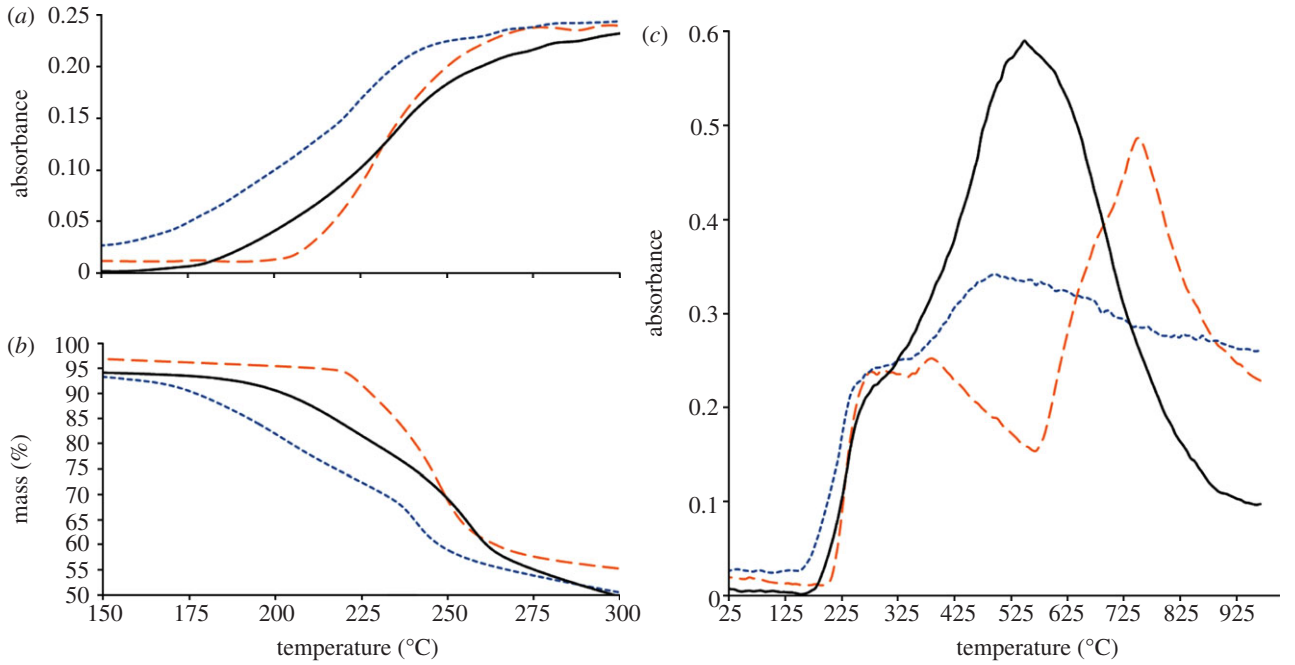

Figure 11. (*a*) Plot of absorbance at 2360 cm^{-1} versus temperature for the thermolysis of Na-Alg, Cu-Alg and H-Alg over the temperature range 150–300°C obtained with a heating rate (β) of 10°C min^{-1} under N_2. (*b*) TGA profile for the thermolysis of Na-Alg, Cu-Alg and H-Alg over the temperature range 150–300°C obtained with a heating rate (β) of 10°C min^{-1} under N_2. (*c*) Plot of absorbance at 2360 cm^{-1} versus temperature for the thermolysis of Na-Alg, Cu-Alg and H-Alg over the temperature range 25–1000°C obtained with a heating rate (β) of 10°C min^{-1} under N_2. Dashed line, Na; dotted line, Cu; solid line, H.

detrimental effect of removing a significant fraction of the soluble organic constituents such as mannitol and fucose and potentially hydrolysing some of the carbohydrates [31,32]. Consequently, it is very difficult to determine which effects upon the pyrolysis are due to the presence or absence of the metals, and which result from the removal of the soluble biomolecules. Here, we present a different and novel approach whereby instead of removing the metals, samples of seaweed are saturated with one particular metal species (in this case copper) to determine the effects on pyrolysis with minimal alteration to the volatilizable organic matter. This methodology is especially suited to the study of brown macroalgae, which have an extremely high affinity for Cu^{2+} ions, making it possible to achieve very high levels of ion exchange with relative ease [48].

To this end, a sample of wild *L. digitata* was subject to a metal ion exchange process, which resulted in replacement of around 93 per cent of the alkali, alkaline earth and other trace metals by Cu^{2+} ions. Table 3 depicts the elemental compositions of the *L. digitata* samples pre- and post-impregnation via ion exchange. It was found that the original seaweed, as collected, contained around 122 000 ($\pm$1000) $mg_{metal}/kg_{dry\text{-}seaweed}$, which was increased to 161 000 ($\pm$1000) $mg_{metal}/kg_{dry\text{-}seaweed}$ after copper-ion exchange, accompanied by a slight decrease in carbon content (2.0 wt%). The data reported in table 3 also suggest that, within experimental uncertainty, electroneutrality of the seaweed was maintained according to equation (2.1). Furthermore, the low nitrate content of the ion-exchanged material indicates that the copper detected was bound to the biomass and not residual $Cu(NO_3)_2$ used for impregnation, which was removed during the washing stages.

The two samples of *L. digitata* (the unadulterated sample and its Cu-exchanged counterpart) were pyrolysed under the same experimental conditions as described earlier for H-, Na- and Cu-Alg ; the results are shown in the TGA/DTG plots in figure 12. Generally speaking, these analyses reveal that the Cu-doped macroalgae sample shows the same mass loss regions as the H-, Na- and Cu-Alg samples; dehydration, rapid pyrolysis and slow degradation phases are readily identifiable. Notably, although the onset of rapid pyrolysis occurs at a higher temperature for the real macroalgae biomass samples relative to those of the model compounds, the Cu^{2+} ions are seen to exert a similar influence and Cu-doped macroalgae ($T_i = 164$°C) are observed to begin rapid pyrolysis at a lower temperature compared with the unadulterated macroalgae ($T_i = 180$°C). The same trend is also true for the values of T_{max} (T_{max}(Cu(II)-L.dig) = 236°C compared with T_{max}(L.dig) = 254°C). However, at T_f, the two seaweed samples begin to show remarkably similar mass loss profiles, something that continues until around 650°C, where the unadulterated macroalgae show a very slight additional mass loss relative to the Cu-exchanged. This latter mass loss is most likely to be a result of thermolysis of $CaCO_3$ (as shown by the data presented in figure 7), which forms owing to the sizeable concentration of Ca^{2+} present in the biomass (2.5 wt%). Thus, the conclusions drawn from the kinetic studies on the model alginate compounds are also true in the case of actual macroalgal biomass: the presence of Cu^{2+} ions promotes pyrolysis at lower temperatures, but does not assist in the later stages of high temperature volatilization.

The similarities between the thermal behaviour of the model compound (copper(II) alginate) and the real biomass (copper(II)-doped *L. digitata*) can be further demonstrated by reference to the DSC profiles (figure 13*a*). These analyses show that, broadly, the major exotherms for the Cu-Alg overlap with those of the copper(II)-doped *L. digitata*, with the peaks in the heat flow to the latter material being less pronounced owing to the presence of other (thermally stable)

Table 3. Partial elemental profile of unadulterated *L. digitata* and *L. digitata* treated in a solution of Cu^{2+} ions.[a]

element[b]:	Cr	Ba	Li	Mn	Fe	Ni	Zn	Rb	Mo	Ag	Pb	Na	Mg	Al	K	Ca	Sr	Cu	Total	C (wt%)	H (wt%)	N (wt%)
unadulterated *L. digitata*																						
(mg/kg$_{seaweed}$)	2	14	1	4	116	1	52	9	0	1	1	42 268	13 344	345	39 787	25 002	1727	3	**122 677**	37.6	5.2	1.6
(mmol/kg$_{seaweed}$)	0.04	0.10	0.14	0.07	2.07	0.02	0.80	0.11		0.01		1837	556	12.8	1020	625	19.6	0.05	**4075**			
charge	2 +	2 +	1 +	2 +	2 +	2 +	2 +	1 +	2 +	1 +	2 +	1 +	2 +	3 +	1 +	2 +	1 +	2 +	**5285**[c]			
Cu(II)-doped *L. digitata*																						
(mg/kg$_{seaweed}$)	13	4	0	1	173	10	11	0	1	21	9	3638	35	430	286	159	26	156 295	**161 112**	35.6	4.8	1.9
(mmol/kg$_{seaweed}$)	0.25	0.03		0.02	3.09	0.17	0.17		0.01	0.19	0.04	158	1.46	15.9	7.33	3.98	0.30	2442	**2633**			
charge	2 +	2 +	1 +	2 +	2 +	2 +	2 +	1 +	2 +	1 +	2 +	1 +	2 +	3 +	1 +	2 +	1 +	2 +	**5116**[c]			

[a]On a dry basis.
[b]Be, Co, Ga, Cd, Cs, Bi, Tl and V were also detected but below milligram per kilogram levels.
[c]The sum of moles of each element multiplied by its charge.

compounds in the rest of the biomass. The main difference between the two thermograms is a small endothermic event beginning at around 170°C in the DSC curve of Cu-Alg, which, when compared with the TGA data for Cu-Alg (figure 6*c*), is apparently associated with the onset of rapid devolatilization. The event is not, however, a feature in the DSC curve of the copper(II)-doped seaweed due to the smaller proportion of alginate in the sample coupled with potential insulating effects and, conceivably, exothermic events originating from other components present in the biomass. Thus, when these complicating factors are accounted for, it can be seen that the Cu-Alg effectively mimics the thermal behaviour of the copper(II)-doped *L. digitata*, and the sharp exothermic event at around 235°C in the pyrolysis of the real biomass can easily be assigned to the degradation of the alginate. An interesting comparison can then be made between the results of the DSC analysis of the copper-doped seaweed sample with those of the unadulterated *L. digitata* (figure 13*b*), for which the latter material displays a much less well-defined profile. It can be seen that the peaks in the thermogram of the unadulterated *L. digitata* are generally broader and more numerous, reflecting the varying influences of the many different metal ions on the thermolysis of the biomass, with some inhibiting that stage of decomposition (such as Ca^{2+}) and some promoting it (such as Cu^{2+}).

These results demonstrate the validity of using alginates as model compounds with which to predict the thermochemical behaviour of brown seaweed biomass. Thus, the kinetic parameters established in §3.1 can be used in the development of larger scale macroalgae processing operations, particularly in the modelling of low temperature slow pyrolysis or torrefaction as a pre-treatment in biomass gasification [60]. Clearly, however, much more work is required, predominantly in determination of the product stream and the effects of reaction conditions, before a more complete model can be used to analyse large scale thermochemical processes and the economic and energetic implications.

Together, the data presented here show that macroalgae that have been exposed to copper-enriched aqueous environments (such as in some industrial wastewater streams [61,62]) should be easier to pyrolyse than samples rich in alkali and alkaline earth metals. Indeed, it is conceivable that macroalgae could be used in the remediation of wastewater streams contaminated with other metals (such as cadmium) and then ion exchanged in a copper solution prior to pyrolysis. Of course, the exception to this proposition would be for macroalgae enriched in Pb^{2+} ions (for which alginates show an even higher affinity than for Cu^{2+} ions; figure 2) [63]. The effects of Pb^{2+} ions on macroalgae thermolysis will consequently make for an interesting comparison with Cu^{2+}, but there is an inherent difficulty in such experiments owing to the toxicity of lead. Such studies, if achievable, may even help to shed light on the interactions between alginates and divalent cations.

4. Conclusions and outlook

The complex nature of the thermal behaviour of seaweeds demonstrated throughout this study indicates that their thermolysis pathways are not straightforward and that the TGA and DSC profiles encompass a myriad of diverse reactions. Thus the requirement to make comparative studies with model compounds is very relevant, as they can help to

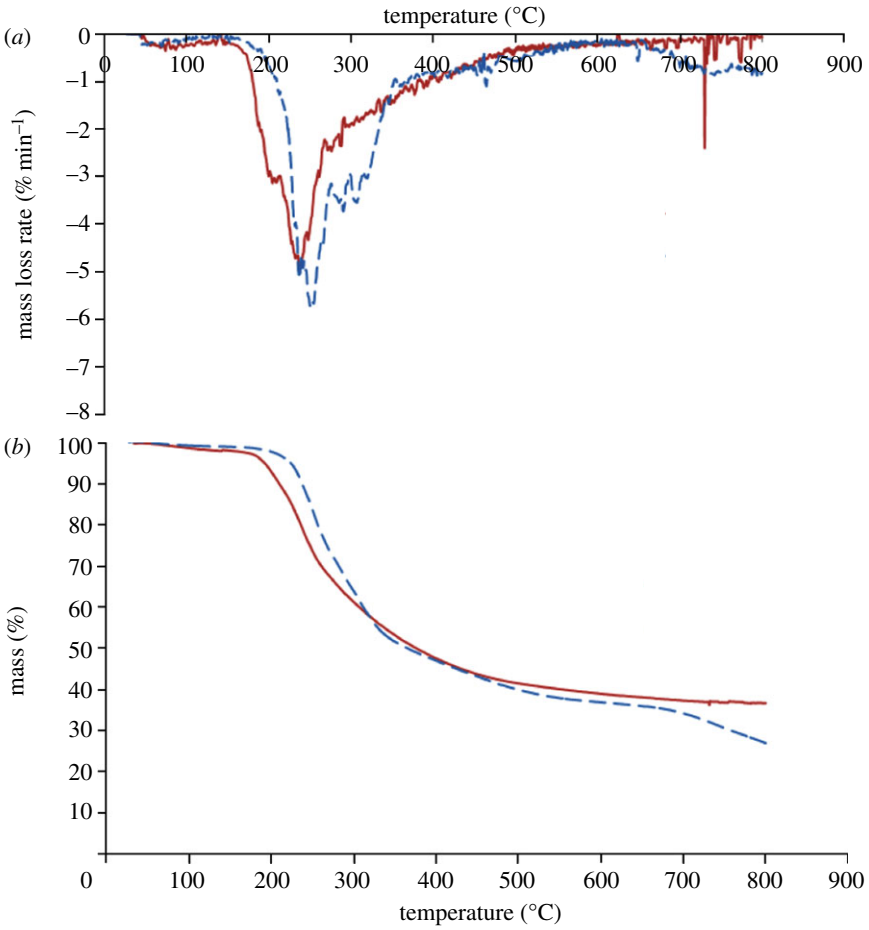

Figure 12. The (*a*) DTG and (*b*) TGA profiles for the thermolysis of raw *L. digitata* and *L. digitata* treated in a solution of Cu^{2+} ions in the range 25–800°C with a heating rate (β) of 10°C min^{-1} under N_2. Solid line, copper(II)-doped *L. digitata*; dashed line, *L. digitata*.

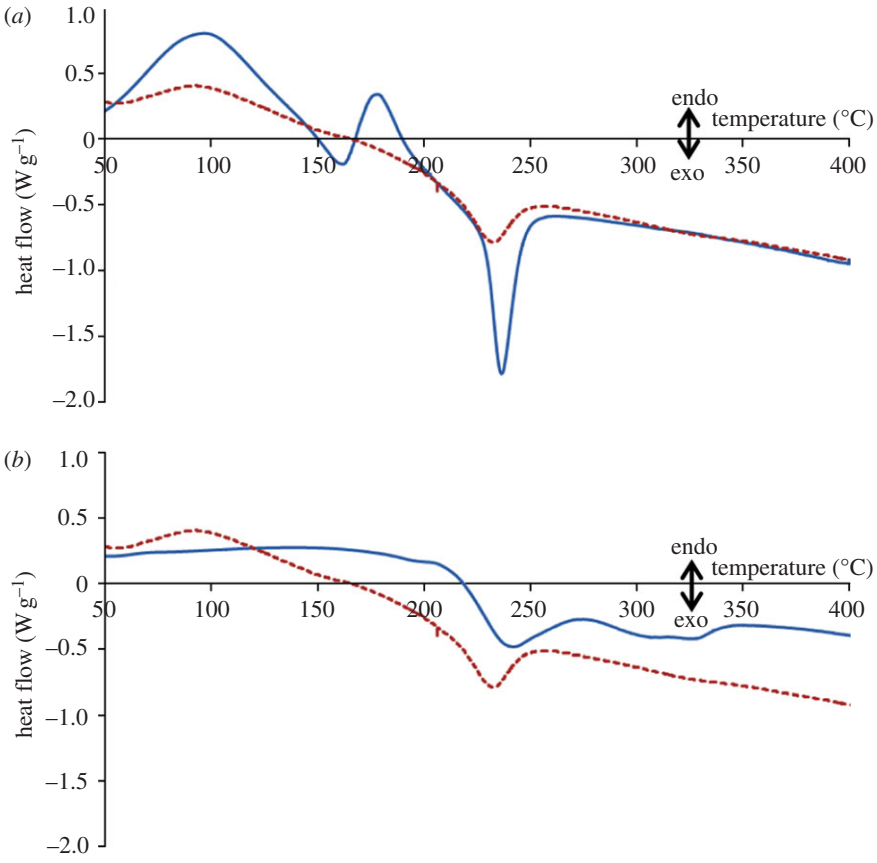

Figure 13. (*a*) Comparison of DSC curves for copper(II) alginate (solid line) and copper(II)-doped *L. digitata* (dotted line) over the temperature range 50–400°C obtained with a heating rate (β) of 10°C min^{-1} under N_2. (*b*) Comparison of DSC curves for unadulterated *L. digitata* (solid line) and copper(II)-doped *L. digitata* (dotted line) over the temperature range 50–400°C obtained with a heating rate (β) of 10°C min^{-1} under N_2.

pinpoint the important factors necessary for the study of biomass pyrolysis without the complication of sample heterogeneity. In this respect, copper(II) alginate was found to be a convincing compound with which to model the effects of Cu^{2+} ions on a sample of brown macroalgae. Consequently, though only samples of *L. digitata* were examined, the agreement between the model study and the study using whole biomass suggests that the findings in this paper should be applicable to most brown (alginate-containing) macroalgae.

Here, Cu^{2+} ions have been found to have a dramatic impact on the thermal stability of polymeric alginic acid, promoting the onset of pyrolysis where other mono- and divalent cations have been found to inhibit it. This effect is evidenced by a reduction in temperature of the onset of rapid pyrolysis of copper(II) alginate compared with the parent alginic acid that, as might be expected, is also accompanied by a lowering of the activation energies at various points in the conversion pathway. It is not accurate, however, to describe the copper as acting catalytically towards the pyrolysis of the alginic acid as, at elevated temperatures (more than 500°C), the Cu^{2+} ions clearly begin to inhibit conversion of the solid into volatile compounds. Indeed, with such a multitude of reactions taking place over the course of the pyrolysis process, the exact role of the copper is difficult to discern, but it clearly appears to destabilize the alginate polymer and, consequently, is beneficial during the early stages of pyrolysis, the region that is of most importance in the production of biofuels and chemicals.

Given the high affinity of alginates and, consequently, macroalgae for Cu^{2+} ions, it is anticipated that other samples of brown seaweed grown in or around copper-contaminated wastewater streams will demonstrate effects similar to those described above. This highlights the importance of establishing the metal profile of a sample of macroalgae prior to analysis, especially in the case of comparative studies, such as those that compare different species or the effects of different catalysts. It is likely that a greater understanding of the destabilizing effects of Cu^{2+} ions reported in this paper will be accompanied by a better understanding of the interaction of seaweed biomass with metal ions as a whole, which in turn opens the way to better utilization of macroalgae as a resource.

The authors are grateful to the Centre for Process Innovation, Durham University, and the Engineering and Physical Sciences Research Council for their financial support of this work. Thanks are owed to C. Patterson and Prof. N. Robinson of Durham University, for assistance with ICP-MS, R. Wout for advice on macroalgae collection and identification and D. Carswell for performing DSC analyses. The authors also thank E. J. Pickering and R. Cornell of the University of Cambridge for their help in obtaining TGA-FTIR data.

References

1. Giampietro M, Mayumi K. 2009 *The biofuel delusion: the fallacy of large-scale agro-biofuel production*. London, UK: Earthscan.
2. Inderwildi O, King D. 2009 Quo vadis biofuels? *Energy Environ. Sci.* **2**, 343–346. (doi:10.1039/b822951c)
3. Bridgwater AV. 2006 Biomass for energy. *J. Sci. Food. Agric.* **86**, 1755–1768. (doi:10.1002/jsfa.2605)
4. Goyal HB, Seal D, Saxena RC. 2008 Bio-fuels from thermochemical conversion of renewable resources: a review. *Renew. Sust. Energy Rev.* **12**, 504–517. (doi:10.1016/j.rser.2006.07.014)
5. Mohan D, Pittman CU, Steele PH. 2006 Pyrolysis of wood/biomass for bio-oil: a critical review. *Energy Fuels* **20**, 848–889. (doi:10.1021/ef0502397)
6. Demiral I, Sensöz S. 2008 The effects of different catalysts on the pyrolysis of industrial wastes (olive and hazelnut bagasse). *Bioresour. Technol.* **99**, 8002–8007. (doi:10.1016/j.biortech.2008.03.053)
7. Williams PT, Nugranad N. 2000 Comparison of products from the pyrolysis and catalytic pyrolysis of rice husks. *Energy* **25**, 493–513. (doi:10.1016/S0360-5442(00)00009-8)
8. Williams PT, Brindle AJ. 2002 Catalytic pyrolysis of tyres: influence of catalyst temperature. *Fuel* **81**, 2425–2434. (doi:10.1016/S0016-2361(02)00196-5)
9. Muradov N, Fidalgo B, Gujar AC, T-Raissi A. 2010 Pyrolysis of fast-growing aquatic biomass—*Lemna minor* (duckweed): characterization of pyrolysis products. *Bioresour. Technol.* **101**, 8424–8428. (doi:10.1016/j.biortech.2010.05.089)
10. Inguanzo M, Domínguez A, Menéndez JA, Blanco CG, Pis JJ. 2002 On the pyrolysis of sewage sludge: the influence of pyrolysis conditions on solid, liquid and gas fractions. *J. Anal. Appl. Pyrol.* **63**, 209–222. (doi:10.1016/S0165-2370(01)00155-3)
11. Rowbotham JS, Dyer PW, Greenwell HC, Theodorou MK. 2012 Thermochemical processing of macroalgae: a late bloomer in the development of third-generation biofuels? *Biofuels* **3**, 441–461. (doi:10.4155/bfs.12.29)
12. Ross AB, Jones JM, Kubacki M, Bridgeman T. 2008 Classification of macroalgae as fuel and its thermochemical behaviour. *Bioresour. Technol.* **99**, 6494–6504. (doi:10.1016/j.biortech.2007.11.036)
13. Budarin VL, Zhao Y, Gronnow MJ, Shuttleworth PS, Breeden SW, Macquarrie DJ, Clark JH. 2011 Microwave-mediated pyrolysis of macroalgae. *Green Chem.* **13**, 2330–2333. (doi:10.1039/c1gc15560a)
14. Lewis J, Salam F, Slack N, Winton F, Hobson L. 2011 Product options for the processing of marine macroalgae. Summary report on behalf of the Crown Estate, CPI, Wilton, UK.
15. Hardy G, Guiry MD. 2003 *A check-list and atlas of the seaweeds of Britain and Ireland*. London, UK: The British Phycological Society.
16. Guiry MD, Blunden G. 1991 *Seaweed resources in Europe: uses and potential*. Chichester, UK: John Wiley & Sons Ltd.
17. Holdt SL, Kraan S. 2009 Bioactive compounds in seaweed: functional food applications and legislation. *J. Appl. Phycol.* **23**, 543–597. (doi:10.1007/s10811-010-9632-5)
18. Gao K, McKinley KR. 1994 Use of macroalgae for marine biomass production and CO_2 remediation: a review. *J. Appl. Phycol.* **6**, 45–60. (doi:10.1007/BF02185904)
19. Aresta M, Dibenedetto A, Barberio G. 2005 Utilization of macroalgae for enhanced CO_2 fixation and biofuels production: development of a computing software for an LCA study. *Fuel Process. Technol.* **85**, 1679–1693. (doi:10.1016/j.fuproc.2005.01.016)
20. Woodward FN. 1951 The Scottish Seaweed Research Association. *J. Mar. Biol. Assoc. UK* **29**, 719–725. (doi:10.1017/S0025315400052899)
21. Marinho-Soriano E, Fonseca PC, Carneiro MAA, Moreira WSC. 2006 Seasonal variation in the chemical composition of two tropical seaweeds. *Bioresour. Technol.* **97**, 2402–2406. (doi:10.1016/j.biortech.2005.10.014)
22. Black WAP. 1950 The seasonal variation in weight and chemical composition of the common British Laminariaceae. *J. Mar. Biol. Assoc. UK* **29**, 45–72. (doi:10.1017/S0025315400056186)
23. Adams JMM, Ross AB, Anastasakis K, Hodgson EM, Gallagher JA, Jones JM, Donnison IS. 2011 Seasonal variation in the chemical composition of the bioenergy feedstock *Laminaria digitata* for thermochemical conversion. *Bioresour. Technol.* **102**, 226–234. (doi:10.1016/j.biortech.2010.06.152)
24. Anastasakis K, Ross AB, Jones JM. 2011 Pyrolysis behaviour of the main carbohydrates of brown macro-algae. *Fuel* **90**, 598–607. (doi:10.1016/j.fuel.2010.09.023)

25. Williams PT, Horne PA. 1994 The role of metal salts in the pyrolysis of biomass. *Renew. Energy* **4**, 1–13. (doi:10.1016/0960-1481(94)90058-2)
26. Nowakowski DJ, Jones JM, Brydson RMD, Ross AB. 2007 Potassium catalysis in the pyrolysis behaviour of short rotation willow coppice. *Fuel* **86**, 2389–2402. (doi:10.1016/j.fuel.2007.01.026)
27. Fuentes M, Nowakowski D, Kubacki M, Cove J, Bridgeman T, Jones JM. 2008 Survey of influence of biomass mineral matter in thermochemical conversion of short rotation willow coppice. *J. Energy Inst.* **81**, 234–241. (doi:10.1016/j.biortech.2011.01.031)
28. Li D, Chen L, Yi X, Zhang X, Ye N. 2010 Pyrolytic characteristics and kinetics of two brown algae and sodium alginate. *Bioresour. Technol.* **101**, 7131–7136. (doi:10.1016/j.biortech.2010.03.145)
29. Daneshvar S, Salak F, Otsuka K. 2012 Macroalgae pyrolysis and its devolatilisation kinetics. In *3rd Int. Conf. on Chemistry and Chemical Engineering*, vol. 38, pp. 77–81. Singapore: IACSIT Press.
30. Zhao H, Yan H, Liu M, Zhang C, Qin S. 2011 Pyrolytic characteristics and kinetics of the marine green tide macroalgae, *Enteromorpha prolifera*. *Chin. J. Oceanol. Limnol.* **29**, 996–1001. (doi:10.1007/s00343-011-0095-6)
31. Ross AB, Anastasakis K, Kubacki M, Jones JM. 2009 Investigation of the pyrolysis behaviour of brown algae before and after pre-treatment using PY-GC/MS and TGA. *J. Anal. Appl. Pyrol.* **85**, 3–10. (doi:10.1016/j.jaap.2008.11.004)
32. Larsen B, Salem DMSA, Sallam MAE, Mishrikey MM, Beltagy AI. 2003 Characterization of the alginates from algae harvested at the Egyptian Red Sea coast. *Carbohydr. Res.* **338**, 2325–2336. (doi:10.1016/S0008-6215(03)00378-1)
33. Lee HW, Jeon JK, Park SH, Jeong KE, Chae HJ, Park YK. 2011 Catalytic pyrolysis of *Laminaria japonica* over nanoporous catalysts using Py-GC/MS. *Nanoscale Res. Lett.* **6**, 500. (doi:10.1186/1556-276X-6-500)
34. Wang J, Zhang M, Chen M, Min F, Zhang S, Ren Z, Yan Y. 2006 Catalytic effects of six inorganic compounds on pyrolysis of three kinds of biomass. *Thermochim. Acta* **444**, 110–114. (doi:10.1016/j.tca.2006.02.007)
35. Shi K, Shao S, Huang Q, Liang X, Jiang L, Li Y. 2011 Review of catalytic pyrolysis of biomass for bio-oil. *Int. Conf. Mater. Renew. Energy Environ.* **1**, 317–321. (doi:10.1109/ICMREE.2011.5930821)
36. Davis TA, Volesky B, Mucci A. 2003 A review of the biochemistry of heavy metal biosorption by brown algae. *Water Res.* **37**, 4311–4330. (doi:10.1016/S0043-1354(03)00293-8)
37. Khairou KS. 2002 Kinetics and mechanism of the non-isothermal decomposition. I. Some divalent cross-linked metal-alginate ionotropic gels. *J. Therm. Anal.* **69**, 583–588. (doi:10.1023/A:1019920108863)
38. Said AA, Hassan RM. 1993 Thermal decomposition of some divalent metal alginate gel compounds. *Polym. Deg. Stab.* **39**, 393–397. (doi:10.1016/0141-3910(93)90015-B)
39. Zaafarany IA. 2010 Non-isothermal decomposition of Al, Cr and Fe cross-linked trivalent metal-alginate complexes. *J. King Abdul. Uni.* **22**, 193–202. (doi:10.4197/Sci.22-1.13)
40. Said AA, Abd El-Wahab MMM, Hassan RM. 1994 Thermal and electrical studies on some metal alginate compounds. *Thermochim. Acta* **233**, 13–24. (doi:10.1016/S0040-6031(99)80002-1)
41. Zhang J, Ji Q, Shen X, Xia Y, Tan L, Kong Q. 2011 Pyrolysis products and thermal degradation mechanism of intrinsically flame-retardant calcium alginate fibre. *Polym. Deg. Stab.* **96**, 936–942. (doi:10.1016/j.polymdegradstab.2011.01.029)
42. Zhang J, Ji Q, Wang F, Tan L, Xia Y. 2012 Effects of divalent metal ions on the flame retardancy and pyrolysis products of alginate fibres. *Polym. Deg. Stab.* **97**, 1034–1040. (doi:10.1016/j.polymdegradstab.2012.03.004)
43. Pathak TS, Kim JS, Lee SJ, Baek DJ, Paeng KJ. 2008 Preparation of alginic acid and metal alginate from algae and their comparative study. *J. Polym. Environ.* **16**, 198–204. (doi:10.1007/s10924-008-0097-4)
44. Ross AB, Hall C, Anastasakis K, Westwood A, Jones JM, Crewe RJ. 2011 Influence of cation on the pyrolysis and oxidation of alginates. *J. Anal. Appl. Pyrol.* **91**, 344–351. (doi:10.1016/j.jaap.2011.03.012)
45. Black WAP, Mitchell RL. 1952 Trace elements in the common brown algae and in sea water. *J. Mar. Biol. Assoc. UK* **30**, 575–584. (doi:10.1017/S0025315400012984)
46. Rees DA. 1981 Polysaccharide shapes and their interactions: some recent advances. *J. Pure Appl. Chem.* **53**, 1–14. (doi:10.1351/pac198153010001)
47. Haug A, Smidsrød O. 1970 Selectivity of some anionic polmers for divalent metal ions. *Acta Chem. Scand.* **24**, 843–854. (doi:10.3891/acta.chem.scand.24-0843)
48. Antunes WM, Luna AS, Henriques CA, da Costa ACA. 2003 An evaluation of copper biosorption by a brown seaweed under optimized conditions. *Electron. J. Biotechnol.* **6**, 174–185.
49. Patrón-Prado M, Acosta-Vargas B, Serviere-Zaragoza E, Méndez-Rodríguez LC. 2010 Copper and cadmium biosorption by dried seaweed *Sargassum sinicola* in saline wastewater. *Water Air Soil Pollut.* **210**, 197–202. (doi:10.1007/s11270-009-0241-3)
50. Balat M, Balat M, Kirtay E, Balat H. 2009 Main routes for the thermo-conversion of biomass into fuels and chemicals. I. Pyrolysis systems. *Energy Convers. Manag.* **50**, 3147–3157. (doi:10.1016/j.enconman.2009.08.014)
51. Ledakowicz S, Stolarek P. 2002 Kinetics of biomass thermal decomposition. *Chem. Pap.* **56**, 378–381.
52. Li D, Chen L, Zhang X, Ye N, Xing F. 2011 Pyrolytic characteristics and kinetic studies of three kinds of red algae. *Biomass Bioenergy* **35**, 1765–1772. (doi:10.1016/j.biombioe.2011.01.01)
53. Li D, Chen L, Zhao J, Zhang X, Wang Q, Wang H, Naihao Y. 2010 Evaluation of the pyrolytic and kinetic characteristics of *Enteromorpha prolifera* as a source of renewable bio-fuel from the Yellow Sea of China. *Chem. Eng. Res. Des.* **88**, 647–652. (doi:10.1016/j.cherd.2009.10.011)
54. Orfao JJM, Antunes FJA, Figueiredo JL. 1999 Pyrolysis kinetics of lignocellulosic materials—three independent reactions model. *Fuel* **78**, 49–58. (doi:10.1016/S0016-2361(98)00156-2)
55. Demirbaş A. 2000 Mechanisms of liquefaction and pyrolysis reactions of biomass. *Energy Convers. Manag.* **41**, 633–646. (doi:10.1016/S0196-8904(99)00130-2)
56. Frost R, Ding Z, Kloprogge J, Martens W. 2002 Thermal stability of azurite and malachite in relation to the formation of mediaeval glass and glazes. *Thermochim. Acta* **390**, 133–144. (doi:10.1016/S0040-6031(02)00127-2)
57. Kim JW, Lee HG. 2001 Thermal and carbothermic decomposition of Na_2CO_3 and Li_2CO_3. *Metall. Mater. Trans. B* **32**, 17–24. (doi:10.1007/s11663-001-0003-0)
58. Halikia I, Zoumpoulakis L, Christodoulou E, Prattis D. 2001 Kinetic study of the thermal decomposition of calcium carbonate by isothermal methods of analysis. *Eur. J. Min. Process. Environ. Prot.* **1**, 89–102.
59. Heal GR. 2002 Thermogravimetry and derivative thermogravimetry. In *Principles of thermal analysis and calorimetry* (ed. PJ Haines), ch. 2, pp. 10–54. Cambridge, UK: RSC.
60. Chen Q, Zhou JS, Liu BJ, Mei QF, Luo ZY. 2011 Influence of torrefaction pretreatment on biomass gasification technology. *Chinese Sci. Bull.* **56**, 1449–1456. (doi:10.1007/s11434-010-4292-z)
61. Yu Q, Mathemickal JT, Yin P, Kaewsarn P. 1999 Heavy metal uptake capacities of common marine macro algal biomass. *Water Res.* **33**, 1534–1537. (doi:10.1016/S0043-1354(98)00363-7)
62. Dean JG, Bosqui FL, Lanouette KH. 1972 Removing heavy metals from waste water. *Environ. Sci. Technol.* **6**, 518–522. (doi:10.1021/es60065a006)
63. Vieira DM, da Costa ACA, Henriques CA, Cardoso VL, de Franca FP. 2007 Biosorption of lead by the brown seaweed *Sargassum filipendula*—batch and continuous pilot studies. *Electron. J. Biotechnol.* **10**. (doi:10.2225/vol10-issue3-fulltext-3)